Exploring the Epigenome of Neurons and Glia *in Vitro* to determine their Utility as a Model for Alzheimer's Disease.

Submitted by Jennifer Louise Imm

To the University of Exeter

as a thesis for the degree of

Doctor of Philosophy in Medical Studies

In March 2020

I certify that all material in this thesis which is not my own work has been identified and that no material has previously been submitted and approved for the award of a degree by this or any other University.

Signature: ……………………………………………………………..

ABSTRACT

Alzheimer's disease is a progressive neurodegenerative condition that is characterised by distinct neuropathological changes. Within the last decade post mortem human brain samples have been used to show that there are robust epigenetic changes occurring in the brain during disease. However, as these samples are collected shortly after death they are a reflection of only the very end stages of disease.

Through the exposure of differentiated adult cells to exogenous reprogramming factors it is now possible to generate induced pluripotent stem cells which have the potential to differentiate into any cell type in the body. Over recent years reseach has moved towards using these stem cells to generate neurons or microglia in order to study diseases of ageing such as Alzheimer's disease. However, there are relatively few epigenetic studies that have been undertaken using induced pluripotent stem cells. As there are global cellular epigenetic changes occurring during the induction of pluripotency and re-differentiation it is critical to ensure we understand the DNA methylation changes occurring during normal neuronal differentiation before using these as a model of Alzheimer's disease or other diseases of ageing.

The aim of this thesis is to first characterise the DNA methylation changes that are occurring in neuronal and microglial models that are exposed to AD-relevant exposures such as differentiation and maturation, drug treatment and immune challenge. This will largely be achieved through measuring DNA methylation using the Illumina Infinium HumanMethylationEPIC BeadChip array which provides information on the DNA methylation levels at over 850,000 loci across the genome.

<u>ACKNOWLEDGEMENTS</u>

At the start of this PhD journey I could never have anticipated just how challenging it would be or how much determination it would require. Now at the end of that journey I can say honestly that I am a stronger and more resilient person despite the challenges throughout. However, this is not a journey I have undertaken alone, and there are so many people who have helped me in different ways and without them I most certainly wouldn't have made it this far.

First and foremost I have to thank my truly wonderful supervisors, Professor Katie Lunnon, Dr Talitha Kerrigan and Dr Aaron Jeffries. You have provided me with endless amounts of advice, wisdom and support each and every day over the last four and a half years. There were most certainly moments throughout my PhD where I didn't feel I could continue, but with your incredible support and continuous guidance I am still sat here today writing these words. Without doubt I know that none of this would have been possible without you and there are few words that can truly capture how grateful I am to have had you as my supervisors.

I would also like to thank everyone within the Complex Disease Epigenetics Group, in particular those of you that have made each day enjoyable and have prevented me from going (even more) insane. Firstly, to Janou, the best business partner and desk neighbour I could ask for. No one has made me cry with laughter more, and shared my appreciation for weird murder cases, awful motivational quotes or googly eyes (sorry Sam!) quite as much as you have. My PhD experience wouldn't have been anywhere near as amazing without you, so thank you for everything, there are so many wonderful times and memories I will remember forever. Next to Sam, one of the loveliest yet rantiest people I have

had the pleasure of knowing. Thank you for allowing me to complain at will, for the mutual tormemting, stupid jokes, and all the fun both inside and outside of work. There is genuinely no-one who could ever come close to replacing you, and the office just won't be the same without you once you go to Oxford. To "the boys" Rob, Michael, Lachlan, Josh and Leo, whilst some of you haven't been in the office all that long, you have all had such a positive impact on my life. Before I started I had no idea how much I would enjoy chunksertions, improving the english language or having completely innapropriate conversations all of the time, now however I can't imagine work without them! To Adam, for the laughs, allowing me to supply you vast amounts of sugar, and generally putting up with all my antics over the years. I have always enjoyed the "what have you done now" look in your eyes that's teamed with a smirk, and hope I get to cause so many more of these looks over the next few years. To Bex, thank you for always being there to give me advice, for letting me borrow your cats, for obsessing over TV shows with me, for being an amazing canoeing partner and for all the fun times we have shared. To Ehsan, my statistics and analysis guru, you have helped me so much these last few years and without your help a lot of what of it would not have been possible. Thank you to everyone else within the Epigenetics group, there are too many of you to thank individually but know I am grateful to every single one of you for the support you have given me, all the amazing memories and I look forward to continuing to work with you all in the future.

Last, but definitely not least, I would like to thank my wonderful, if slightly barmy family. You have been there through every piece of homework, exam, trial and tribulation for my entire life. I truly appreciate the all of the support,

encouragement and unending amounts of love you have given me. I couldn't dream of having a better family.

Finally, I would like to dedicate this thesis to my Mum, Tracy Imm, without whom none of it would have been possible. Not only have you always encouraged me to be the absolute best I could be academically, you also taught me to be kind, loving, strong, and so much more, all of which I am eternally grateful for. Who would have thought the little girl who thought she would only get C's at GCSE could have gone on to complete a PhD?! Well I can say with certainty that without you in her life she most likely wouldn't, you are truly the best Mum in the world.

TABLE OF CONTENTS

TABLE OF FIGURES

TABLE OF TABLES

PUBLICATIONS ARISING FROM THIS THESIS

Imm, J., Kerrigan, T.L., Jeffries, A., and Lunnon, K., *Using induced pluripotent stem cells to explore genetic and epigenetic variation associated with Alzheimer's disease.* Epigenomics, 2017. **9**(11): p. 1455-1468.

Thei, L., **Imm, J,.** Kaisis, E., Dallas, M.L., and Kerrigan, T.L., *Microglia in Alzheimer's disease: a role for ion channels.* Frontiers in Neuroscience, 2018. 12:676.

Crawford, B., Craig, Z., Mansell, G. White, I., Smith, A., Spaull, S., **Imm J**., Hannon, E., Wood, A., Yaghootkar, H., Ji, Y., Mullins, N., Lewis, C.M.,4, Mill, J., Murphy, T.M., DNA methylation and inflammation marker profiles associated with a history of depression. Human Molecular Genetics, 2018. 27(16): p. 2840-2850.

Imm, J., Pishva, E., Ali, M., Kerrigan, T.L., Jeffries, A., Burrage, J., Glaab, E., Cope, E.L., Jones, K.M., Allen, N.D., and Lunnon, K., *Characterization of DNA methylomic signatures in induced pluripotent stem cells during neuronal differentiation*. 2020. Under Review.

DECLARATIONS

The samples used in this study were obtained from several different sources. In **chapter 3** all of the samples used were from Professor Nicholas Allen at the University of Cardiff. In **chapter 4** the iPSC-derived microglia were from Dr Sally Cowley at the University of Oxford and the iPSC-derived neurons were from Dr Elena Ribe of the University of Oxford. In **chapter 5** the SV40 microglia were purchased from Accegen Biotech.

All laboratory work in this thesis was carried out by myself with a couple of exceptions; in **chapter 3 and 5** the Illumina Infinium HumanMethylationEPIC arrays were done by Dr Joe Burrage, in **chapter 4** the Illumina Infinium HumanMethylationEPIC arrays were performed with the assistance of Dr Adam Smith.

All bioinformatics and statistical analyses performed in **chapter 4** were performed by me, under the guidance of Professor Katie Lunnon and Dr Ehsan Pishva. The trajectory modelling and gene-gene interactions in **chapter 3** and the epigenome wide association studies in **chapter 5** were performed with the assistance of Dr Ehsan Pishva.

ABBREVIATIONS

Abbreviation	Term
Δ	% change in methylation
AD	Alzheimer's disease
27K array	Illumina Infinium HumanMethylation27K Array
450K array	Illumina Infinium HumanMethylation450K Array
5-caC	5-carboxylcytosine
5-fC	5-formylcytosine
5-hmC	5-hydroxymethylcytosine
5-mC	5-methylcyosine
AA	Ascorbic acid
APOE	Apolipoprotein E
APP	Amyloid precursor protein
ARUK ODDI	Alzheimer's Research UK Oxford Drug Discovery Institute
Aβ	Amyloid Beta
BAZ2	Bromodomain adjacent to zinc-finger domain
BBB	Blood brain barrier
BDNF	Brain derived neurotrophic factor
BET protein	Bromodomain and extra terminal motif proteins
BMI	Body mass index
BMP	Bone morphogenic protein
BP	Biological pathway
BRD	Bromodomain
BS	Bisulphite
CC	Cellular component
CCR7	Chemokine receptor 7
CGI	CpG islands
CH3	Methyl group
CNS	Central nervous system
CR3	Complement receptor 3
CSF1	Colony stimulating factor
DLB	Dementia with lewy bodies
DMP	Differentially methylated position
DMR	Differentially methylated region
DNMT	DNA methyltransferase
DOT1L	Disruptor of telomeric silencing 1-like
E8F	Essential 8 flex media
EDTA	Ethylenediaminetetraacetic acid
EMPs	Erythromyeloid progenitors
EOAD	Early onset Alzheimer's disease
EPIC array	Illumina Infinium HumanMethylationEPIC Array
ESC	Embryonic stem cell
ETC	Electron transport chain
EWAS	Epigenome wide association study
EZH2	Enhancer of zeste polycomb repressive complex 2
FAD	Familial Alzheimer's disease
FDR	False discovery rate

FTD	Frontotemporal dementia
GABA	Gamma-aminobutyric acid
GAM	General additive model
GDNF	Glial derived neurotropic factor
GO	Gene ontology
GREAT	Genomic regions enrichment of annotations tool
GWAS	Genome wide association study
HAT	Histone acetyltransferase
HD	Huntington's disease
HKDM	Histone lysine demethylase
HMT	Histone methyltransferase
HSCs	Hematopoietic stem cells
IKKβ	IκB kinase β
iNOS	Inducible nitric oxide synthetase
iNs	Induced neurons
iPSC	Induced pluripotent stem cell
IQR	Interquartile range
JMJD3	Jumanji domain containing-3
KMR	Methyl lysine readers
L3MBTL	L3MBTL Histone Methyl-Lysine Binding Protein 3
L3MBTL3	Lethal(3)malignant brain tumour-like protein 3
LDN	LDN193189
LOAD	Late onset Alzheimer's disease
LPS	Lipopolysaccharide
MAD	Median absolute derivation
MAF	Minor allele frequency
MAPK	Mitogen activated protein kinase
MAPT	Microtubule associated protein tau
MF	Molecular function
MHC	Major histocompatibility complex
MLL	Mixed lineage leukaemia
MMM	Microglial maintenance medium
NFTs	Neurofibrillary tangles
NHTR	Nuclear hormone transcription regulator
NO	Nitric oxide
NPC	Neuronal precursor cell
NSAID	Non-steroidal anti-inflammatory drug
OR	Odds ratio
Ox-E8	Oxford essential 8 media
PBS	Phosphate buffered saline
PC	Principal component
PCA	Principal component analysis
PCI	Phenol:chloroform:isopropyl alcohol
PCR	Polymerase chain reaction
PD	Parkinson's disease
PET	Positron emission tomography
PKMT	Protein lysine methyltransferases
PKN	Prior knowledge network

PRMT	Protein lysine arginine transferases
PRS	Polygenic risk score
PSEN1	Presenilin1
PSEN2	Presenilin2
p-Tau	Hyperphosphorylated tau
QC	Quality control
qPCR	Quantitative polymerse chain reaction
RefSeq	Reference sequence
ROS	Reactive oxygen species
RT	Room temperature
SB	SB431542
SCC	Strongly connected component
SCM1	Synaptojuice media 1
SCM2	Synaptojuice media 2
SETD7	SET containing domain 7
SNP	Single nucleotide polymorphism
Te	Tris-EDTA
TET	Ten eleven translocation
TF	Transcription factor
TGF-β	Transforming growth factor-beta
TI	Trajectory inference
TLR4	Toll like receptor 4
TSS	Transcription start site
UCSC	University of California Santa Cruz
UTR	Untranslated regions
VaD	Vascular dementia
WD	Aspartic acid
WD40	WD repeat protein family
WDR5	WD repeat-containing protein 5
WGCNA	Weighted gene correlation network analysis
WGS	Whole genome sequencing
WIN	WRD5-interacting

CHAPTER 1 : <u>INTRODUCTION</u>

This chapter reviews research that has been undertaken in the field of Alzheimer's disease (AD), with a particular emphasis on epigenetic studies and work in induced pluripotent stem cells (iPSCs) to date. The work presented in this chapter reviewing iPSCs to study epigenetic variation in AD is based on a published review, on which I am first author [1], which can be found in Appendix A.

1.1 Alzheimer's Disease (AD)

Dementia is an umbrella term that covers several diseases that all have similar symptoms, which are associated with neurodegeneration. AD is the most prevalent neurodegenerative disorder and accounts for approximately 60-80% of all dementia cases worldwide [2]. The disease is characterised by the accumulation of amyloid beta (Aβ) plaques, intracellular neurofibrillary tangles (NFTs) of hyperphosphorylated tau [3] and loss of synaptic connections [4]; taken together these lead to neuronal cell death. This is accompanied by cognitive and behavioural changes, such as memory impairments, language disturbance and hallucinations. The early cognitive decline in AD can be attributed to the degeneration of cholinergic neuronal cells found in the cortical and limbic brain regions such as the hippocampus [5] and the basal forebrain [6].

1.1.1 Types of AD

AD can be broken down into two subtypes, early onset AD (EOAD) and late onset AD (LOAD). EOAD accounts for relatively few cases, between to 1-5% and the disease has a symptomatic onset of before 65 years of age [7]. EOAD is usually attributed to autosomal dominant mutations in three genes, which are amyloid precursor protein (*APP*), presenilin1 (*PSEN1*) and presenilin2 (*PSEN2*).

Therefore these cases of EOAD can be inherited and so are often termed familial AD (FAD).

Most AD cases are late-onset, starting after the age of 65, and sporadic, with no defined aetiology. However, in recent years, large cohort collections and the relatively inexpensive cost of assessing genetic variation through genome-wide association studies (GWAS) has allowed the identification of common variants associated with risk of developing LOAD. These studies have demonstrated that LOAD is multifactorial with many different genes and single nucleotide polymorphisms (SNPs) being implicated in, and contributing to, disease onset and progression [8].

1.1.2 Prevalence and Financial Burden

It is estimated that 46.8 million people worldwide are affected by dementia, with this set to double every 20 years, reaching 131.5 million people in 2050 [9]. Despite 5.2% of people over the age of 60 living with dementia only around 1 in 4 people with AD have been diagnosed [10]. Furthermore, due to the rising number of AD cases the economic burden of the disease is also increasing; it has been calculated that the global cost of dementia was $818 billion in 2015, with this set to become $2 trillion by 2030. Some regions have seen large increases in cost with the greatest being an increase by ~300% in sub-Saharan Africa, whilst overall the worldwide increase is ~35% [10]. This is because the life expectancy of developing countries is increasing and the number of people aged above 60 in these regions is growing faster than in other countries [11].

1.1.3 Disease Progression and Pathological Hallmarks

Despite LOAD and EOAD having different causes and ages of onset, the progression and pathology of these subtypes are broadly the same. As previously stated AD can be characterised by the accumulation of Aβ plaques and NFTs of hyperphosphorylated tau. The deposition of these tangles does not occur at random, but follows a distinct and characteristic pattern [12-15], starting in the neocortex and then the hippocampus [16], whilst other regions, such as the cerebellum, remain relatively unaffected [17]. This specific topographical distribution correlates with, and explains, the characteristic symptoms of AD; the hippocampus and neocortex are well known for being involved in controlling emotions, memory and higher brain function [18, 19]. The cerebellum on the other hand is responsible for the coordination, motor and voluntary movements, and there are far fewer aberrations in these in AD patients when compared with the prevalence of other symptoms [20]. There is already considerable pathology before the disease is diagnosed [21], with the onset of symptoms sometimes occurring at least 10 years after Aβ is first deposited [22]. This apparent delay in the appearance of symptoms is caused by there being a threshold of cholinergic loss before the brain can no longer compensate and ameliorate the deficit [16].

1.1.4 Causes of LOAD

Despite decades of molecular research into LOAD aetiology, relatively little is known about the exact mechanisms that initiate AD pathology or drive AD progression. Whilst it is known that certain genetic mutations can increase one's risk of disease (see section 1.1.4.4), it is unclear through which mechanism these are acting. In general, there are three hypotheses that try and explain AD

aetiology. These are the amyloid hypothesis, the tau tangle hypothesis, and the inflammatory hypothesis.

1.1.4.1 The Amyloid Hypothesis

As previously stated, it is known that certain mutations within the *APP*, *PSEN1* and *PSEN2* genes are disease causing. The proteins that these genes code for are all involved in the proteolytic cleavage of APP into several different proteins. APP can be processed through two pathways: the amyloidogenic and non-amyloidogenic pathway, and it is the amyloidogenic pathway that produces several isoforms of Aβ (figure 1.1) [23]. In the non-amyloidogenic pathway APP is first cleaved by α-secretase (encoded for by *ADAM10*) followed by γ-secretase, forming AICD, sAPPα and p3. However, in the amyloidogenic pathway APP is cleaved by β-secretase (encoded for by *BACE1*) and then γ-secretase to form sAPPβ, AICD and Aβ. Interestingly, *PSEN1* and *PSEN2* both encode for proteins that are subunits of the γ-secretase complex [24-26].

Whilst Aβ has normal cellular functions such as playing a role in synaptic plasticity [27], kinase activation [28] and oxidative stress protection [29], too much causes aggregation and the formation of plaques. Interestingly, the aggregation rate varies between the different isoforms of Aβ, for example the fastest aggregation rate can be attributed to $Aβ_{1-42}$ and so this isoform is more likely to form neurotoxic amyloid plaques [30]. These mutations (in *APP*, *PSEN1* and *PSEN2*) shift the balance of APP processing more towards the amyloidogenic pathway, therefore changing the $Aβ_{42}/Aβ_{40}$ ratio. This has been shown to cause an increase in the aggregation rate of Aβ and therefore can contribute to the onset of AD [31].
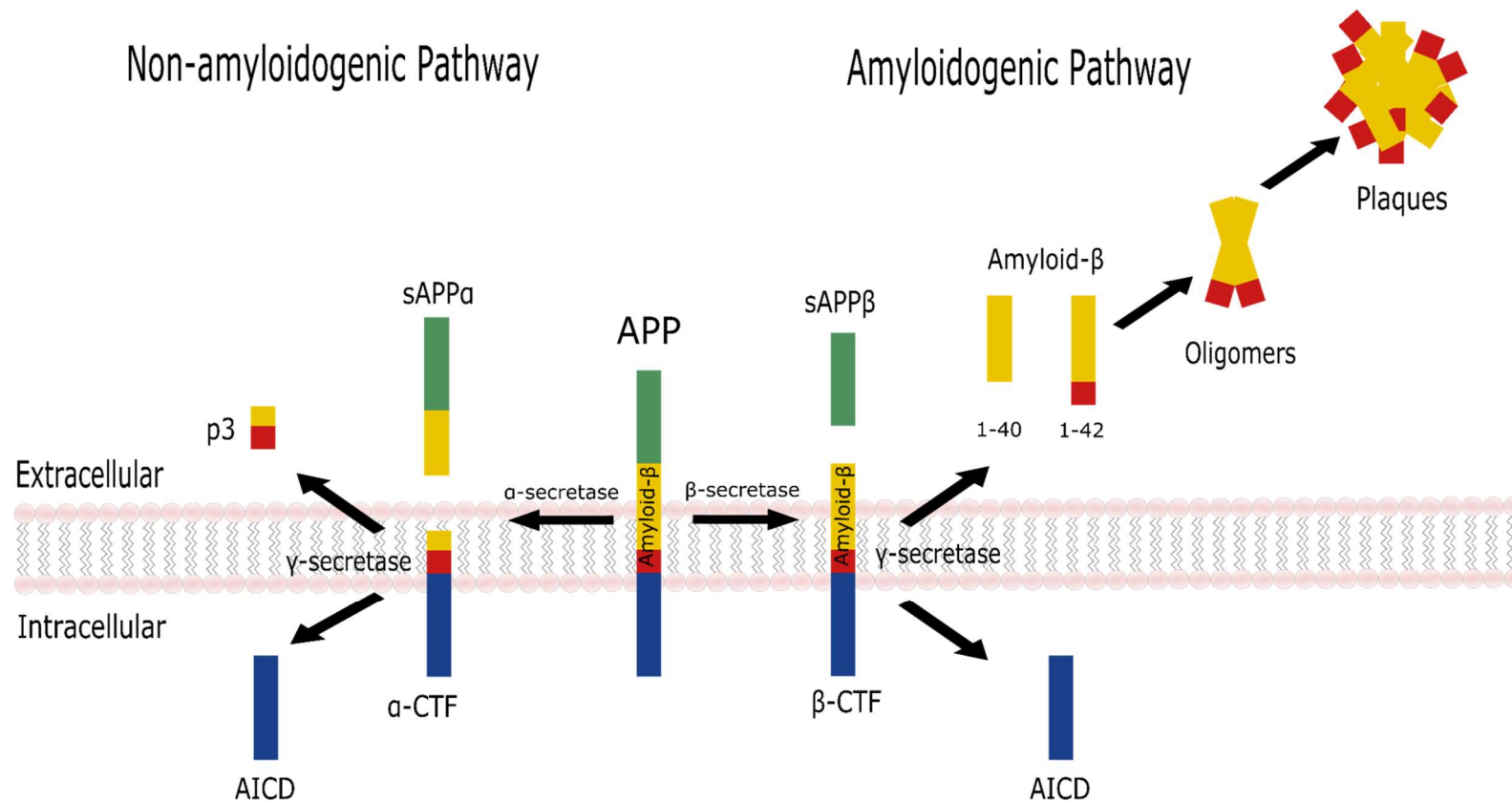
Figure 1.1. Proteolytic cleavage of APP through the amyloidogenic and non-amyloidogenic pathways.

In the non-amyloidogenic pathway APP is first cleaved by α-secretase followed by γ-secretase, forming AICD, sAPPα and p3. However, in the amyloidogenic pathway APP is cleaved by β-secretase and then γ-secretase to form sAPPβ, AICD and amyloid-β (Aβ). Mutations in APP, PSEN1 or PSEN2 that shift the balance towards the amyloidogenic pathway result in the formation of more oligomers and plaques made of Aβ.

1.1.4.2 The Tau Tangle Hypothesis

Tau, which is encoded for by the microtubule associated protein tau (*MAPT*) gene, plays important physiological roles in microtubule assembly and stabilisation [32]. Altogether there are six isoforms in the brain, which vary in length, the number of microtubule binding domains (3R or 4R) and inserts of 29 amino acids in the N-terminus (0N, 1N or 2N) they contain [33]. In three of the isoforms of Tau there are three microtubule binding domains (0N3R, 1N3R, 2N3R) and in the other three there are four microtubule binding domains (0N4R, 1N4R, 2N4R) [33].

Alongside Aβ plaques, the accumulation of intracellular Tau into NFTs is another hallmark of AD. The exact mechanisms through which these NFTs develop are still un-clear, but the phosphorylation and de-phosphorylation of Tau is thought to play a critical role (figure 1.2). NFTs in the brains of AD patients compared to non-AD patients are enriched for abnormally hyperphosphorylated Tau (p-Tau) [34]. This p-Tau is unable to bind to tubulin, therefore preventing microtubule assembly, alongside this it can also disrupt the microtubules directly [35, 36]. Dysfunctional networks of microtubules within neurons cause disturbances to critical cellular functions such as axonal transport [37] and synaptic integrity [38]. P-Tau is also able to sequester normal physiological Tau causing further cellular disruption [39]. The progression of p-Tau accumulation within the brain, measured as Braak staging (figure 1.3), correlates with disease severity [40] and is therefore thought to play a key role in the initiation and progression of disease. Tau deposition first begins in prodromal AD in the transentorhinal cortex (stages I/II) before spreading further during mid-stage AD into the limbic regions (stage

III/IV) and finally during late stage disease is widespread throughout the neocortex (stage V/VI).

Whilst there have been no mutations in *MAPT* implicated in AD, *MAPT mutations* are sufficient to cause diseases such as frontotemporal dementia (FTD). The *MAPT* mutations linked to FTD have been shown to be missense or deletion mutations that reside either in the coding region or intronic region located close to the splice donor site of the intron following exon ten [41-43]. These mutations are believed to affect how tau interacts with microtubules, reducing their stability and ability to form [44-47]. Intronic mutations are generally located at positions +3, +13, +14 and +16 within the intron following the alternatively spliced exon 10 [48, 49]. Using exon trapping it has been shown that intronic mutations lead to increased splicing of exon ten which can also be seen in brain tissue from patients known to have intronic *MAPT* mutations [50, 51]. This is reflected by a change in the 3R to 4R isoform ratio creating an overproduction of the 4R isoform [42, 52]. Exploring these mutations and the effects they have is of importance for AD as it can help the understanding of how tau pathology may lead to neurodegeneration. Until relatively recently it was believed that it was not possible to develop AD without the presence of Aβ plaques. However, imaging studies have shown that tau tangles do occur in the absence of amyloid. Using positron emission tomography (PET) to look at the presence of both Aβ plaques and tau and their association with cognitive performance it was shown that in the absence of tau memory, language and executive function were unaffected even in the presence of Aβ plaques [53]. This suggests that it is in fact tau that causes cognitive decline, independently of Aβ.
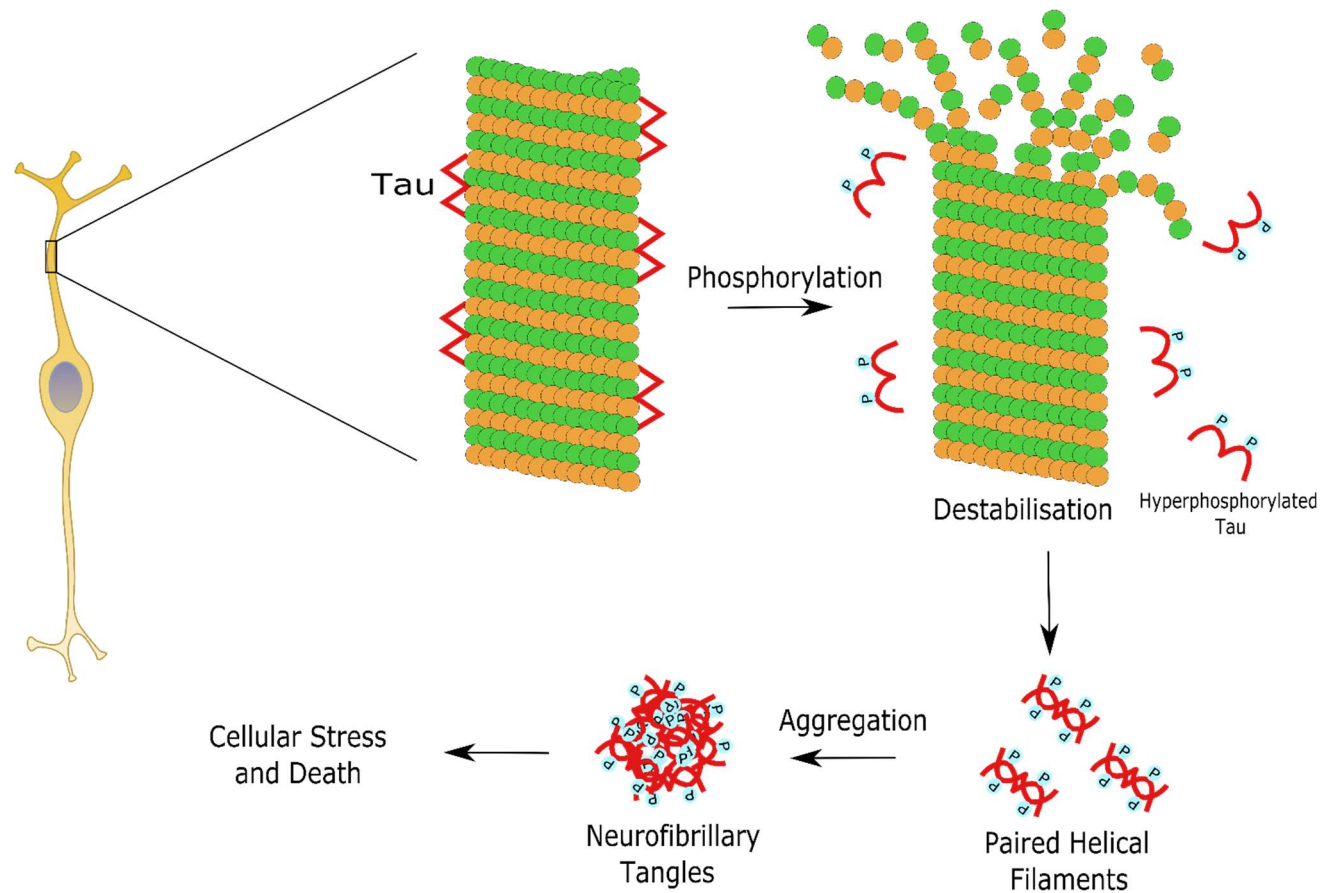
Figure 1.2. Schematic diagram to illustrate the hyperphosphorylation of Tau.

Within neuronal cells Tau mediates the stabilisation of microtubules by binding to tubulin dimers. If hyperphosphorylated Tau dissociates from the microtubules, this causes them to destabilise. Hyperphosphorylated Tau is prone to aggregation first into paired helical filaments and then neurofibrillary tangles. These tangles of Tau are neurotoxic and can cause cellular stress and death.
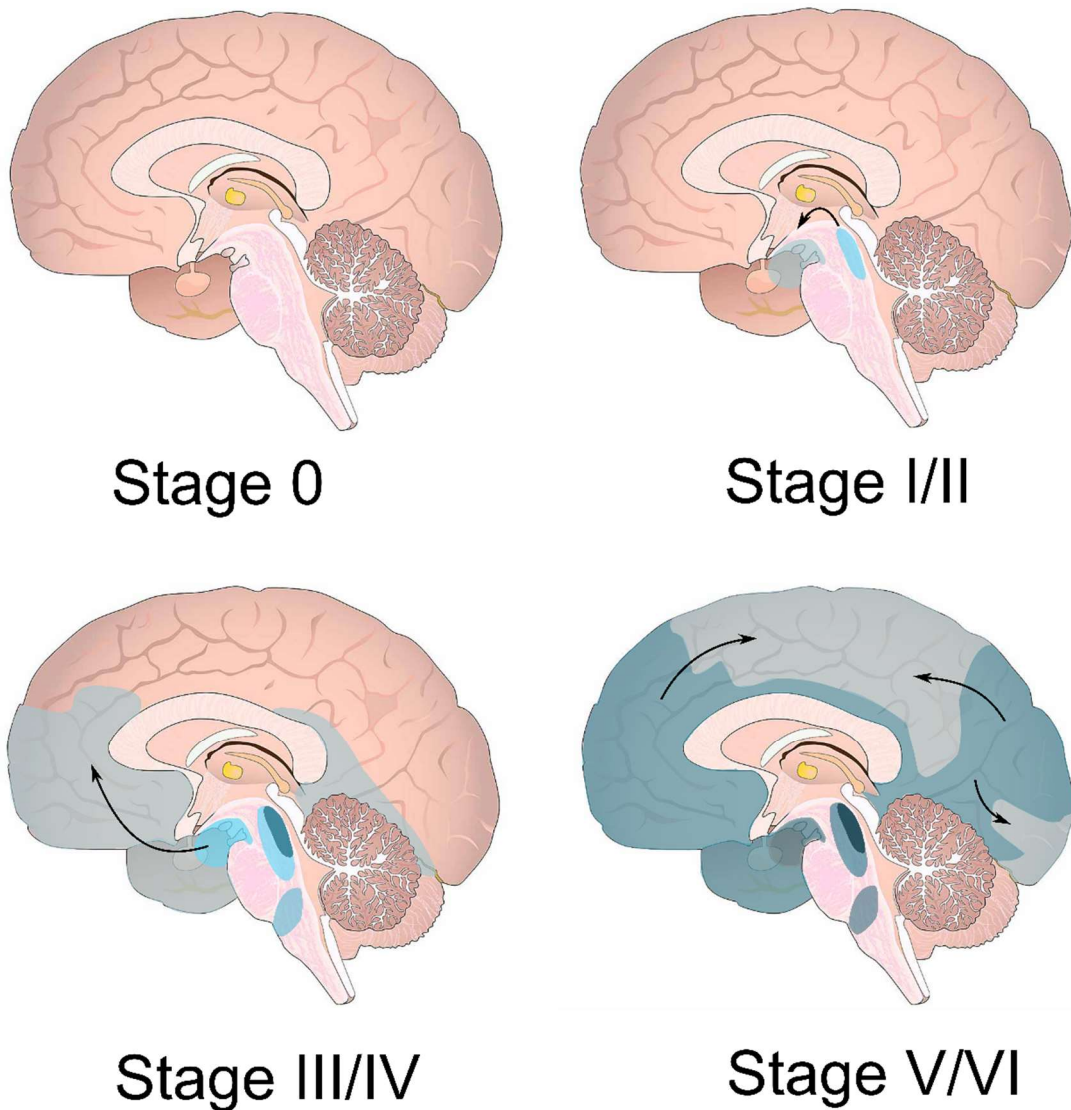
Figure 1.3. Schematic diagram to illustrate the spread of Tau throughout the brain, which is known as Braak staging.

In the prodromal phases of disease (stage I/II) Tau deposition can be seen in the transentorhinal regions of the brain, before spreading to the limbic areas during the mid-stage (stage III/IV) , and finally into the neocortex in late stage AD (stage V/VI). Where the shade of blue indicates the level of tau deposition from light blue = least deposition to dark blue = considerable deposition. Image adapted from BioRender.

1.1.4.3 Innate Immunity and AD

Of increasing interest is the involvement of the innate immune system in AD, particularly the role of microglia. Microglia are the resident immune cells in the brain and spinal cord, and play important roles in neurodevelopment, immune surveillance, disease and homeostasis [54]. Unlike neurons and other glial cell types, microglia are of haematopoietic lineage, arise early during development [55], and are derived from erythromyeloid progenitors (EMPs) in the yolk sac [56]. There is increasing evidence to suggest that microglia play a key role in AD risk and pathogenesis [57]. Under normal physiological conditions they are highly ramified and their function is highly regulated by molecular factors in the central nervous system (CNS) [58]. Upon activation microglia become less ramified, develop a more rounded cell body with shorter processes and express a wide range of different mediators [59]. Through chronic/recurrent activation of microglia during ageing, or the presence of Aβ plaques in AD, this can trigger morphological changes and alterations in intracellular and cell surface antigens reminiscent of an activated cell [60]. These microglia are said to be "primed" and are in a pre-activated state [61, 62]. These primed microglia have increased expression of inflammatory markers such as major histocompatibility complex (MHC) class II molecules, complement receptor 3 (CR3) and are also less ramified [63-66] (figure 1.4). Once primed, microglia give a heighted response to inflammatory stimuli [60]. This exaggerated immune reaction activation is accompanied by the secretion of inflammatory molecules, which can be detrimental to surrounding neurons [67] (figure 1.4). However, microglial priming by Aβ does not necessarily only occur after Aβ deposition, but can also occur before plaques are even formed; Maezawa and colleagues have shown that

nanomolar concentrations of Aβ oligomers can activate microglia and induce microglial-mediated neuronal cell death [68].

To date, anti-inflammatory drugs have proved unsuccessful in ameliorating the microglia-induced neuronal death [69]. This is because the relationship between the innate immune system and AD is incredibly complex, and the immune response to plaques can be beneficial or damaging depending on the context [70-72]. It is also likely that these studies were also undertaken too late, once the priming and damage had already occurred, but it has been suggested that long term non-steroidal anti-inflammatory drugs (NSAIDs) can give a decreased risk of developing AD [73].
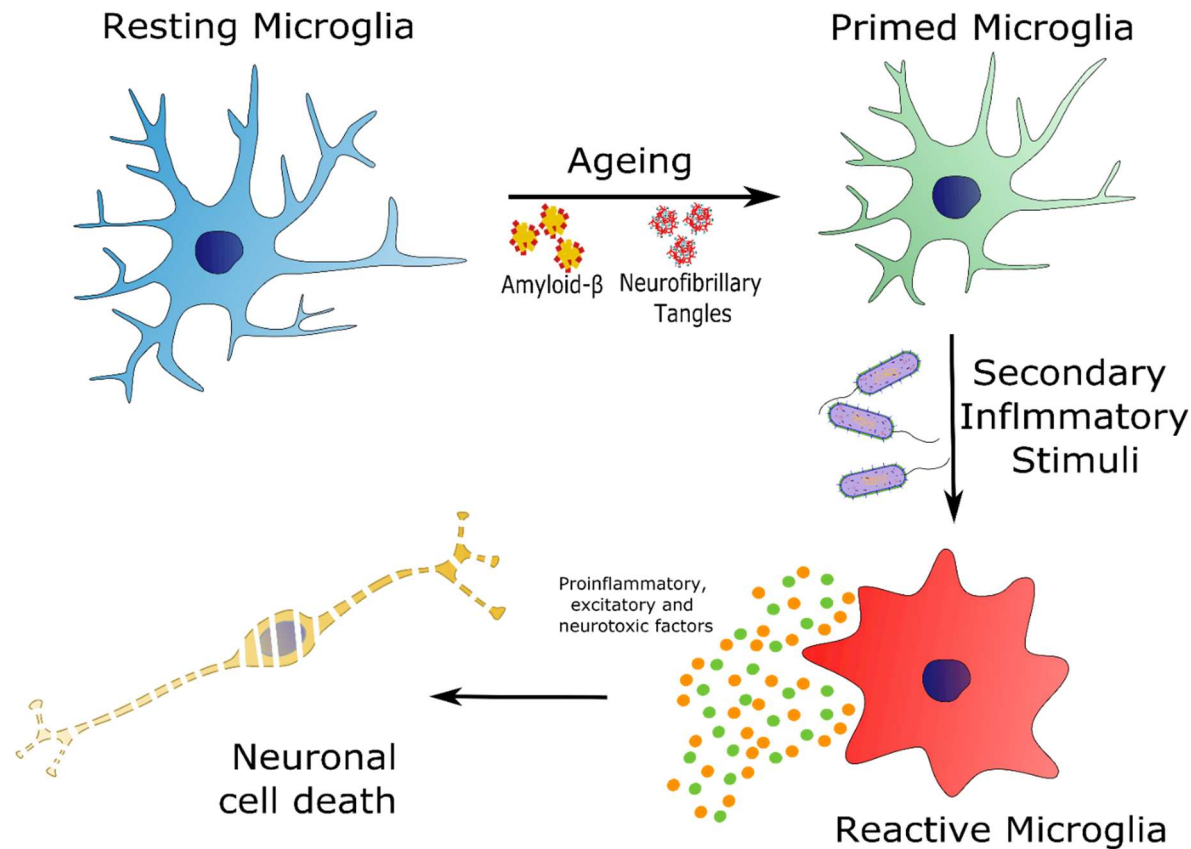
Figure 1.4. Schematic illustrating the role of microglial activation in AD.

Under physiological conditions microglia have a highly ramified morphology. Throughout ageing microglia are repetitively stimulated, and also as a response to chronic Aβ in AD they become primed. Following this priming, when they encounter secondary stimuli such as inflammatory mediators as a response to a systemic infection they undergo a heightened response. This response results in the release of proinflammatory, excitatory and neurotoxic factors which can result in the death of surrounding neuronal cells.

<u>1.1.4.4 Genetics of LOAD</u>

The mutations known to cause FAD are within genes that are all involved in the APP processing pathway. On the other hand, the causes of LOAD are far less defined; despite there being a genetic component to LOAD there are no mutations/SNPs that are sufficient to cause disease alone. From GWAS it has been shown that the gene most robustly associated with LOAD is Apolipoprotein E (*APOE*), which encodes a polymorphic glycoprotein that is involved in the transport of cholesterol and other lipids [74] alongside neuronal growth [75] and tissue repair [76]. There are three isoforms of *APOE* that all correspond to allelic variation at a single locus, *ε2*, *ε3* and *ε4*, which can be distinguished by cysteine to arginine substitutions at the amino acid positions 112 and 158 [77]. The *ε4* variant confers increased risk of developing LOAD, with each additional copy of the risk allele lowering the mean age of onset [78]. Whilst *APOE ε4* accounts for approximately 20% of genetic risk for developing LOAD it cannot explain all of disease incidence, as not everyone who is homozygous for *ε4* develops AD [79]. Aside from *APOE* there are numerous other SNPs that have been implicated in LOAD from numerous GWAS. In 2013, there was a meta-analysis of nearly 75,000 individuals which nominated 19 common genetic variants, of which 11 were novel disease loci [80] (see table 1.1). Interestingly, many of the GWAS loci nominated for AD can be linked to amyloid processing or inflammation. More recently, two larger meta-analyses of AD GWAS were published; Kunkle and colleagues identified 25 risk loci in ~95,000 individuals [81], whilst Jansen et al nominated 29 risk variants, implicating over 200 genes, by analysing >450,000 individuals, by using an AD-by-proxy phenotype [82]. The genes identified were in pathways relating to immune regulation, lipid related processes and degradation of amyloid precursor proteins [82]. Whilst the risk variants that have

been identified from GWAS only confer a relatively modest effect size, with odds ratios (ORs) between 0.73 and 1.22 per loci investigated [83], it is thought that these could act cumulatively to cause the onset of degeneration. Scientists have generated polygenic risk scores (PRS) for AD, which combine the effects of many disease-associated SNPs to predict disease risk [84] and recently it has been reported that the PRS prediction captures nearly all common genetic risk for AD [85]. However, another study has demonstrated that collectively common SNPs for AD only account for a third of phenotypic variance in AD [86]. Recent efforts to explain the missing heritability of AD have used sequencing approaches to identify rare variants, with a larger effect size, with SNPs in *PLD3*, *TREM2*, *TM2D3* and *PICALM* being nominated in recent years [87-91].

SNP	Chr:Position	Closest Gene	Odds Ratio
rs6656401	1:207692049	*CR1*	1.18
rs6733839	2:127892810	*BIN1*	1.22
rs10948363	6:47487762	*CD2AP*	1.10
rs11771145	7:143110762	*EPHA1*	0.90
rs9331896	8:27467686	*CLU*	0.86
rs983392	11:59923508	*MS4A6A*	0.90
rs10792832	11:85867875	*PICALM*	0.87
rs4147929	19:1063443	*ABCA7*	1.15
rs3865444	19:51727962	*CD33*	0.94
rs9271192	6:32578530	*HLA-DRB5– HLA-DRB1*	1.11
rs28834970	8:27195121	*PTK2B*	1.10
rs11218343	11:121435587	*SORL1*	0.77
rs10498633	14:92926952	*SLC24A4 RIN3*	0.91
rs8093731	18:29088958	*DSG2*	0.73
rs35349669	2:234068476	*INPP5D*	1.08
rs190982	5:88223420	*MEF2C*	0.93
rs2718058	7:37841534	*NME8*	0.93
rs1476679	7:100004446	*ZCWPW1*	0.91
rs10838725	11:47557871	*CELF1*	1.08
rs17125944	14:53400629	*FERMT2*	1.14
rs7274581	20:55018260	*CASS4*	0.88

Table 1.1. Summary table of SNPs associated with AD, which reach genome wide significance in Lambert et al, 2013 [80]

Abbreviations: Chr. = Chromosome

1.2 Genomic Regulation

Epigenetic processes mediate the reversible regulation of gene expression, occurring independently of DNA sequence, acting principally through chemical modifications to DNA and nucleosomal histone proteins [92]. Epigenetic modifications serve to inform the transcriptional machinery whether a gene is to be transcribed or not. It is epigenetic processes that allows every cell type in the body to express different proteins and have distinct morphologies and functions, despite containing the same genetic material [93]. There are several epigenetic mechanisms, including DNA modifications, histone modifications and microRNA-based mechanisms (figure 1.5).
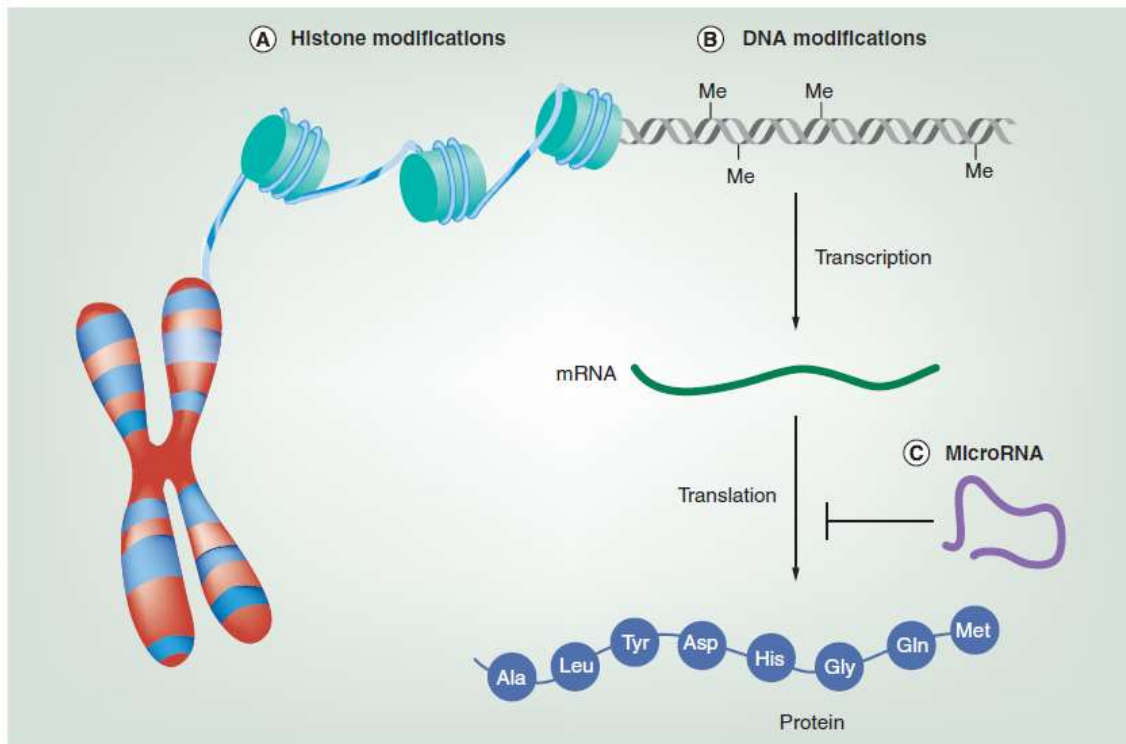
Figure 1.5. Diagram to illustrate the different epigenetic mechanisms that have been identified.

 (A) Regulation of chromatic structure through post-translational modifications to histone proteins. This can include: acetylation, methylation, SUMOylation, ubiquitylation, citrullination and ADP-ribosylation. **(B)** Addition of chemical tags to DNA to the 5' end of a cytosine nucleotide. This creates 5-methylcytosine (5-mC) – the most commonly studied epigenetic mark, 5-hydroxymethylcytosine (5-hmC), 5-carboxylcytosine (5-caC) and 5-formycytosine (5-fC). **(C)** Small RNA molecules, such as microRNA (miRNA) can also affect gene expression either through degrading mRNA or altering protein translation.

1.2.1 DNA Modifications

The most widely studied epigenetic modification in human studies is that of DNA methylation, given it is the most stable and longest lasting change [94, 95]. This is because it can be robustly assessed using extracted genomic DNA, thus meaning it has been the focus of many human epidemiological epigenetic studies to date [96]. 5-methylcytosine (5-mC) is formed when a methyl group (CH_3) is added to the 5' position of the pyrimidine ring of a cytosine within a CpG dinucleotide by DNA methyltransferases (DNMT). 5-mC has been shown to block transcription by preventing the binding of transcription factors (TFs) and promoting methyl-binding proteins to initiate chromatin compaction [97]. However, it is not always the case that DNA methylation leads to gene silencing. More recently it has been demonstrated that methylation that lies within the gene body itself may be associated with transcriptional activation [98-100].

DNA methylation is not the only cytosine modification, 5-hydroxymethylcytosine (5-hmC) [101, 102], 5-formylcytosine (5-fC), and 5-carboxylcytosine (5-caC) [103, 104] have all been described in recent years and are formed from the sequential oxidation of 5-mC by ten eleven translocation (TET) enzymes (figure 1.6). These modifications, 5-hmC in particular, has been shown to be enriched in certain areas of the brain [105-107] and also in stem cells [108], with between 0.4-0.7% [106] and 4-6% [109] total nucleotides being hydroxymethylated respectively. Lowering TET levels within stem cells, and therefore also 5-hmC levels, has been shown to impair self renewal and promote the loss of the stem cell phenotype [110, 111]. Interestingly, in contrast to 5-mC it has been demonstrated that 5-hmC has the opposing effect and generally promotes transcription [112].
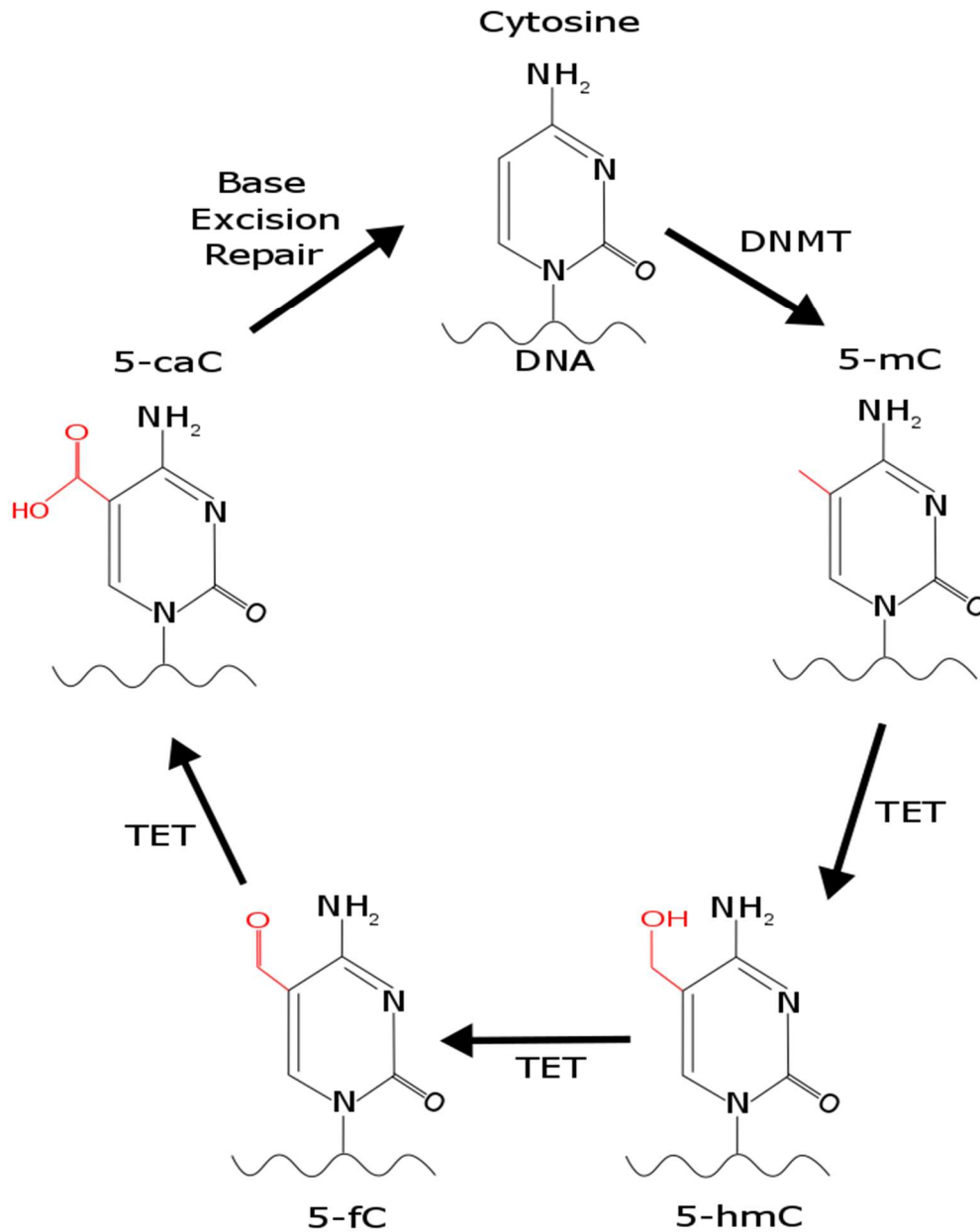
Figure 1.6. DNA modifications shown throughout the de-methylation process.

Cytosine is first methylated, to 5-mC, by a DNA methyl transferase enzyme (DNMT). This can then be sequentially oxidised into 5-hmC, 5-fC and 5-caC by ten eleven translocation (TET) enzymes. To return to cytosine the base is excised by base excision

1.2.2 Other Epigenetic Mechanisms

Alongside cytosine modifications, histone modifications and small RNA based mechanisms also alter the expression of genes. As with DNA modifications there are several different chemical marks which can be added to histones to alter their function.

As the focus of this PhD thesis is on DNA methylation I have chosen to focus on this epigenetic mechanism only. However, I do acknowledge that there are other epigenetic mechanisms that may play a role in the onset and progression of AD.

1.2.3 DNA Methylation Studies in AD

Initial studies investigating DNA modifications in AD focussed on global methylation analyses using immunofluorescence. These were inconsistent in findings; Mastroeni and colleagues demonstrated a significant decrease in 5-mC and 5-hmC in entorhinal cortex neurons and glia in AD patients when compared to controls [113, 114]. They have also shown that the affected twin in a monozygotic twin pair had decreased DNA methylation in cortical neurons [115] and decreased 5-mC and 5-hmC in hippocampal neurons and glia [113] compared to the unaffected twin. However, other studies have shown increased global 5-mC and 5-hmC in AD patients [116] and in AD neurons [117]. Due to the inconsistencies between studies attention has changed to investigating 5-mC and 5-hmC change at single nucleotide resolution.

One way in which this was achieved was through the use of array based methodologies. The earliest array based technologies assessed AD-associated 5-mC changes at <27,000 loci genome wide using the Illumina Infinium 27K

methylation BeadChip array (27K array). One study, which identified 948 CpG sites (mapped to 918 unique genes) showed nominally significant AD-associated DNA methylation changes [118]. Sanchez-Mut *et al* also used this array and investigated hippocampal DNA methylation in five Braak stage I-II cases, five Braak stage III-IV cases, five Braak stage V-VI and five controls (Braak stage 0). They identified Braak-associated DNA methylation at four loci, two of which resided within the *DUSP22* gene and one each in the *CLDN15* and *QSCN6* genes [119].

The 27K array has since been superseded by the Illumina Infinium 450K methylation BeadChip array (450K array), which can determine the DNA methylation status of >485,000 loci across the genome. It is this technology that has been most widely used to assess epigenetic variation in AD. In 2014, two independent papers were published back to back that both identified four overlapping signals (*ANK1, RPL13, RHBDF2* and *CDH23*), which had not previously been associated with AD [120, 121]. Interestingly, in the Lunnon *et al* paper, two of the top four most significant differentially methylated positions (DMPs) resided in the *ANK1* gene, located only 91bp apart. These changes were found only in brain regions known to be affected by AD, such as the prefrontal cortex, entorhinal cortex and superior temporal gyrus, but not other unaffected brain regions such as the cerebellum [120]. However, a recent study has used pyrosequencing to assess DNA methylation across an 119bp region of the *ANK1* gene, which includes those two CpG sites, in a range of different brain regions in different dementias and showed *ANK1* hypermethylation in AD cerebellum, although not at the two sites covered by the 450K array [122]. Interestingly, this study also showed that *ANK1* hypermethylation in the entorhinal cortex is seen

in AD, Huntington's disease (HD) and Parkinson's disease (PD). In individuals with Dementia with lewy bodies (DLB), or Vascular dementia (VaD), DNA hypermethylation was only seen in individuals with co-exisiting AD pathology. The same group have also recently shown robust neuropathology-associated DNA methylation in the *HOXA* gene cluster. In this study they used the 450K array to identify a 48kb region, spanning 208 CpGs, which demonstrated increased DNA methylation in the prefrontal cortex and superior temporal gyrus tissue. The top ranked probe within the *HOXA3* gene was also validated in two independent cohorts [123]. Taken together, these studies have provided the first robust and replicable evidence of an association between differential DNA methylation and AD.

Whilst these studies have undoubtedly provided valuable insight into the role of epigenetic dysfunction in AD, they were performed on bulk brain tissue. Having multiple cell types present within each tissue sample can add noise to the data and whilst this can be controlled to some extent in the analysis, this is not ideal. Furthermore, AD is characterised by alterations in the abundance of neurons and glia, which further confounds the problem. In order to try and combat this issue, Gasparoni *et al*, performed the first epigenome-wide association study (EWAS) on FACS sorted neuronal and non-neuronal (glia) nuclei from post mortem brain [124]. They were able to show Braak-associated changes in neurons and glia that replicate the previous findings, and confirms the cell type of origin of the *ANK1* (glia) and *HOXA3* (neuron) signals.

The latest iteration of the methylation array is the Illumina Infinium EPIC array (EPIC array), which is able to interrogate methylation at over 850,000 loci

genome wide at single nucleotide resolution. One study by Marioni *et al* used this newest array to investigate the relationship between accelerated DNA methylation, or epigenetic age, and AD risk factors relating to lifestyle, genetics and cognitive reserve. DNA methylation at certain loci has shown to change robustly with age and based on this there have been numerous algorithms developed which are able to predict biological age from an individuals methylome [125, 126]. Using epigenome-wide DNA methylation data from 5,100 people they reported significant associations between epigenetic age acceleration and body mass index (BMI), socioeconomic status, high blood pressure and smoking [127]. This study highlights the potential importance of specific lifestyle factors in the onset of AD and suggests that modifying these may lower AD risk, although more longitudinal studies are needed to disentangle these relationships further.

Overall through many studies, some of which are discussed here, it has been shown that specific DNA methylation changes are consistently and robustly associated with AD pathology. However, these relationships are complex and further studies need to be undertaken in order to elucidate the precise mechanisms and establish whether these epigenetic changes are causative or merely a consequence of the disease process.

1.3 Modelling AD

There are a number of different model organisms that have been used to investigate AD-associated changes including rodent models, *Drosophila melanogaster* and neuronal cell culture models. In this section I will initially focus on rodent models, as these have been the most widely utilised. Subsequently, I will discuss newer methodologies involving stem cell models and how these are being used to model AD.

1.3.1 Rodent Models of AD

To fully understand and characterise a disease, extensive modelling must take place to elucidate the mechanisms underlying disease aetiology. Traditionally, this has been achieved by several methods, including both animal (murine) models and primary patient cell lines. Whilst both approaches have their own merits, they can prove inconvenient and do not completely and accurately reflect human disease. At present, the AD research field has had a heavy focus on disease modelling through the use of transgenic mouse models [128], as there is a well-developed understanding of genetic manipulation techniques in this organism. Furthermore, mice are more phylo-genetically related to humans than other simpler model organisms such as *Drosophila melanogaster* and *Caenorhabditis elegans*, although these do allow for more experimental control than mice. Due to the close relation of mice to humans they also have great utility in studying familial AD using transgenic mice containing mutations in the *APP* and *PSEN* genes. This has led to advances in our understanding of multiple aspects of AD, in particular amyloid pathology and the differential effects of the various Aβ peptides. However, despite the extensive use of these transgenic models to study AD, they do not accurately recapitulate AD, as the

mice do not display overt neurodegeneration [129-131], have amyloid plaques [132], nor do they model sporadic LOAD.

Whilst they have proven useful for modelling autosomal disease, such as familial AD, the mouse models do not have extensive utility for studying sporadic AD, which has both polygenic and environmental components. Even if it were possible to model the genetics of sporadic AD in transgenic mice the effect sizes of each associated variant would be small and therefore difficult to determine phenotypic outcome. However, there have been murine studies that have targeted replacement of the endogenous murine *Apoe* gene with human *APOE-ε4*. These mice demonstrated reduced spatial learning and a reduction in dendritic spine density in the medial entorhinal cortex [133]. In another study where *APOE* (both *ε3/ε3* and *ε4/ε4*) mice were crossed with mice containing a mutant human form of *APP*, the *APOE-ε4*x*APP* mice displayed significantly worse spatial memory performance than their *APOE-ε3*x*APP* counterparts, but this was also associated with insulin dysfunction [134].

1.3.2 iPSCs and iPSC-derived Neurons as Models

A more promising avenue for modelling SNPs in complex diseases, such as sporadic AD, is using stem cell technology. Embryonic stem cells (ESCs), which are derived from the inner cell mass of an embryo (blastocyst), have the ability to differentiate into any cell in the body [135]. Due to their inherent plasticity, and as genomic variation can be assessed relatively inexpensively through polymerase chain reaction (PCR), microarray, or sequencing technology, there is the potential that they could be used to study the effect of disease-associated SNPs on the functionality of specific cell types. However, whilst useful, the ethical issues

implicated with using embryo derived ESCs are numerous. Recent advances in stem cell technology have allowed the production of stem cells derived from adult tissue, such as blood, urine and fibroblasts (figure 1.7) [136]. These iPSCs have almost identical characteristics to ESCs: they share the same morphology, can differentiate into any cell type in the body, have unlimited growth and have the same expression pattern of genes [137]; potentially making them a very powerful tool in research. One concern of using iPSCs is that of X-inactivation in female cells, whereby one of the X chromosomes is randomly inactivated. It was previously a concern that iPSCs may not consistently and efficiently undergo X-inactivation. However, a recent study investigated X-inactivation in ESCs and iPSCs using over 700 high-throughput sequencing samples. They demonstrated that whilst there is heterogeneity in X-inactivation and *XIST* expression in the ESCs this was not the case for iPSCs which maintained an inactivated X chromosome [138].

The most common method of using stem cells to study neurological diseases is by differentiating iPSCs into neurons (figure 1.8). Through this process different growth factors are added into the culture media to promote cellular differentiation to neuronal cell types. Two growth factors in particular are used to differentiate iPSCs into a neuronal cell type, SB431542 (SB) and LDN193189 (LDN), through a process named dual SMAD inhibition. Dual SMAD inhibition rapidly differentiates iPSCs into early neuroectoderm [139] by blocking two signalling pathways. These pathways use two SMADs, bone morphogenic (BMP) and transforming growth factor-beta (TGF-β), for signal transduction. By blocking these pathways *OCT4* expression decreases and *PAX6* expression increases, leading to the formation of neuronal rosettes [140].

Whilst these two growth factors are common to most neuronal differentiation protocols, there are numerous other growth factors and small molecules used in order to terminally differentiation and mature iPSC derived-neurons [141]. For example, glial cell line-derived neurotrophic factor (GDNF), brain derived neurotrophic factor (BDNF) and ascorbic acid (AA) can be used. These three factors have been shown to support the survival and promote the growth and differentiation of new synapses and neurons [142-144].

Many of the methodologies used to generate iPSC-derived neurons were developed in order to generate specific neuronal cell types and few have been created in order to enhance and accelerate functional maturation. One which has been created with this in mind is the synaptojuice medias developed by Kemp *et al* [145]. Their differentiation protocol requires the serial addition of two supplemented medias in order to enhance the two phases of neuronal development, neurogenesis and synaptogenesis. A list of all the growth factors used in these two medias (SCM1 and SCM2) can be found below in figure 1.8. Cells matured through this protocol exhibit comparatively larger cellular capacitance and relatively hyperpolarised resting membrane potentials. Not only this, but functionally mature neurons can be generated within 21 days, roughly half the time it would take with other methods [145]. However, whilst this methodology does decrease differentiation time, it does not promote the growth of specific neuronal cell types, nor was it generated to support long term maintenance.

Whilst it is now possible to create iPSC-derived neurons of different subtypes the earliest studies using iPSC-derived neurons simply served to try and recapitulate AD findings from other models such as post-mortem human brain and rodent models. From these studies it was demonstrated that neuronal survival and function were comprised when the iPSC-derived neurons were treated with exogenous Aβ [146-150]. Alongside this, iPSC-derived neurons which were derived from both LOAD and EOAD patients had increased $A\beta_{1-42}$ production and elevated $A\beta_{1-40}/A\beta_{1-42}$ ratio [151-156]. For example, iPSC-derived cortical neurons containing the *PSEN2* N141I mutation demonstrated both an increase in $A\beta_{1-40}/A\beta_{1-42}$ ratio and a decrease in the maximum number of spikes following depolarising injection, both of which were ameliorated in isogenic controls [153]. Besides aberrant Aβ production there are also aggregates of hyperphosphorylated tau in AD. During the normal timeframe of neuronal differentiation in culture, iPSC-derived neurons do not express the mature 4R isoform of tau. It is not until they were cultured for extended periods, ~360 days in vitro, that the mature 4R isoform was co-expressed alongside 3R tau [157]. Despite this, even without the mature 4R isoform, EOAD neurons harbouring an *APP* duplication had increased GSK-3β activity and a concomitant increase in phosphorylated tau levels [158].
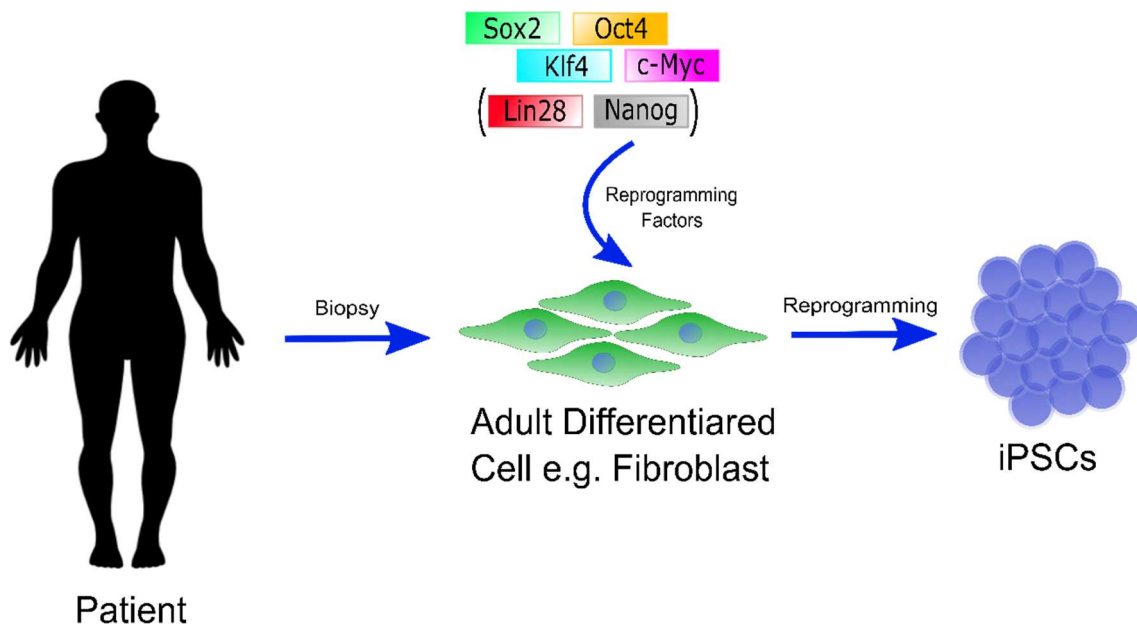
Figure 1.7. A simplified schematic representing the reprogramming of differentiated adult cells into iPSCs.

This technique, as first described by Takahashi and Yamanaka in 2006, uses four reprogramming factors to de-differentiate adult somatic cells into iPSCs. Lin28 and Nanog, shown in brackets, are sometimes also used during de-differentiation.
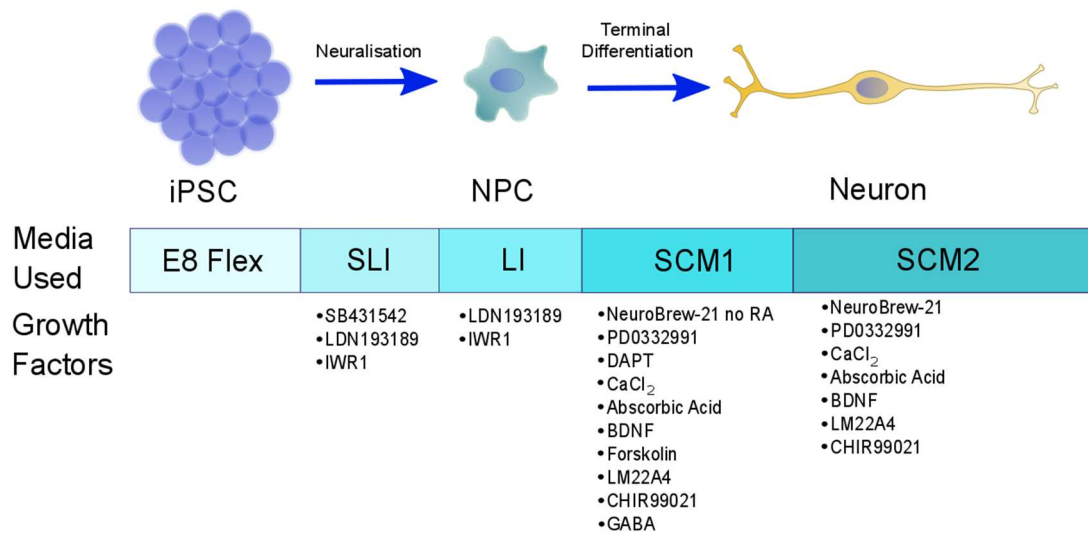
Figure 1.8. A simplified schematic representing the differentiation of iPSCs into neurons.

The medias and growth factors used to promote neuronal differentiation are shown. These include; two SMAD inhibitors: SB and LDN and IWR1 which inhibits the WNT signalling pathway. The components for SCM1/2 were formulated to promote neurogenesis and synaptogenesis [145].

1.3.3 iPSC-derived Microglia

Until recently, it had been difficult to generate iPSC-derived microglia, with much scepticism for the reported studies as the microglia were made from induced hematopoietic stem cells (HSCs). HSCs have the potential to give rise to other cell types such as blood derived macrophages and as already stated microglia arise from EMPs (see section 1.1.4.3). In order to generate EMPs from the iPSCs, Muffat *et al* developed a serum free media that contains high levels of IL-34 and colony stimulating factor 1 (CSF1) [159]. These conditions were chosen as the media mimics the brain cerebrospinal fluid and the factors have been shown to be necessary for microglia differentiation and maintenance. These cells were shown to express many of the cell surface markers of microglia including TMEM118, P2RTY12/13, HEXB and GPR34. Alongside this, the resulting cells were also highly phagocytic and a transcriptomic analysis showed they resemble human primary foetal and adult microglia [159]. This is not the only protocol that has been developed to generate iPSC-derived microglia, and there are now several different methods available [160-163].

Since the development of these protocols there has been significant interest in using the resulting cells to study the impact of various immune-related AD-associated SNPs; one such mutation is the R47H mutation of *TREM2*. Interestingly, in knock-in mice harbouring the human R47H mutation in *TREM2* was aberrantly spliced, however, this was not found to be the case in human primary and iPSC-derived microglial models [164]. Other functional studies have also demonstrated that missense mutations cause TREM2 to accumulate in its immature form, meaning it is not processed normally and therefore is not trafficked to the cell surface. Despite this the microglia still undergo normal

differentiation and are able to perform phagocytosis and still respond to immune stimuli [165]. This suggests that certain *TREM2* mutations can have subtle effects, perhaps reflecting the later onset of disease [165]. Alongside *TREM2,* iPSC-derived microglia have also been used to further investigate the relationship between *APOE* genotype and AD. A study by Lin *et al* demonstrated that *APOE* status was linked to the gene expression in biological pathways such as lipid metabolism or immune responses [166]. In addition to this cells carrying the *APOE4* variant were shown to have impaired Aβ42 clearance when compared to isogenic controls [166].

1.3.4 Other Cellular Models used to Investigate AD

To overcome some of the caveats of iPSC-derived neurons, in particular those related to cellular immaturity, other ways of modelling neurological disorders such as AD have emerged. One of these are induced neurons (iNs), which are similar to iPSC-derived neurons in that they are generated from differentiated adult tissue, but differ in the fact that they do not pass through a stem cell intermediate phase [167]. As iNs do not pass through this intermediate stage they have been shown to retain the epigenetic, metabolomic and transcriptomic age of the fibroblasts they were derived from [168, 169]. Alongside this, iNs are easier to make, quicker to produce, taking only a couple of few weeks, and are much cheaper than iPSC-derived cells. Whilst this maintenance of age and cost-effectiveness have obvious advantages for studying diseases of ageing there are a few limitations which means they have not been widely adopted. Firstly, their major limitation is that the number of iNs you can generate is finite as there are no stages within reprogramming that are expandable. This means that iNs are not suitable for studies requiring large amounts of cells such as some large drug

screens [170]. Secondly, it has been shown that the original culture conditions of the fibroblasts can impact on the resulting neurons and therefore cause interindividual heterogeneity or mosaicism when compared to the clonal nature of iPSC-derived cells [171]. Finally, whilst it is possible to generate iPSC-derived neurons from a variety of differentiated tissues including but not limited to fibroblasts [136], keratinocytes [172] and blood cells [173] the same cannot be said for iNs. Currently only pericytes and skin fibroblasts have been used to successfully derive iNs from adult tissue, but as pericytes are quite hard to obtain from donors, fibroblasts remain the only feasible option for generating iNs.

The other cellular model being used increasingly more frequent to study neurological diseases such as AD are those of cerebral organoids. Cerebral organoids are conceptually very similar to iPSC-derived cells as they are too are derived from iPSCs, the main difference is that the organoids are grown in 3D rather than the traditional 2D culture used for iPSC-derived neurons [174]. The creation of organoids relies upon the ability of iPSCs to self-organise, and through the use of exogenous factors form organised structures resembling distinct regions of the brain [174]. One recent study demonstrated that organoids derived from both down syndrome and EOAD patients displayed progressive accumulation of Aβ and tau into structures resembling plaques and NFTs, but that these aggregations were absent from control organoids [175]. Alongside monoculture organoid models triculture models have also been developed to increase physiological relevance. Using this system organoids containing neurons, astrocytes and microglia to model AD pathophysiology and the model displayed Aβ aggregation, tau hyperphosphorylation, neuroinflammatory activity and the release of NO [176]. However, despite being physiologically more

relevant organoid models do have their limitations. One limitation to modelling AD with organoids relates to the maturity of the resulting cells, much like iPSC-derived neurons grown in 2D, cerebral organoids have been shown to have a transcriptional profile representative of a prenatal brain [175, 177]. Alongside this another limitation is that of the lack of vascularisation, which can result in insufficient neuronal maturation and overall limits the amount of time the organoids can be maintained in culture [174, 178].

1.4 Using iPSCs to Model Epigenetic Changes

1.4.1 Epigenetic Changes Associated with Inducing Pluripotency

Associated with inducing pluripotency are the global cellular epigenetic changes that allow the cells to alter gene expression and become iPSCs. These changes to epigenetic mechanisms, such as DNA methylation, are known to regulate which parts of the DNA are transcribed and change throughout development and differentiation in order to restrict what types of cells the precursors can become (figure 1.9) [179].

Despite being functionally identical, several groups report that iPSCs have different DNA methylation profiles and gene expression patterns to ESCs [180-183]. Similarly, whilst grown in 3D, cerebral organoids too have been demonstrated to have the epigenetic signature of fetal human brain, but their development does seem to parallel that of human cortical development [184]. Some groups attribute this variation due to an 'epigenetic memory' where iPSCs show residual DNA methylation patterns that are typical of the tissue they originate from [185]. These differentially methylated regions (DMRs) were shown to affect the differentiation potential of the newly formed iPSCs. For example, iPSCs derived from neural and fibroblast progenitors maintained DNA methylation marks at sites associated with haematopoietic lineages, which decreased the potential for these iPSCs to form blood cells. Subsequently, it is possible to reverse these restricting methyl marks by increasing the cells passage number or treatment with chromatin modifying compounds [185]. This treatment is associated with a decrease in DNA methylation at haematopoietic loci and therefore an increase in blood cell fate potential. Therefore, although it would

appear that this epigenetic memory can affect the differentiation potential of cells initially, this effect is actually only transient. It has also been observed that certain subsets of cells can become stuck in a partially reprogrammed state. This is due to inefficient DNA demethylation at certain sites or the incomplete repression of TFs [186]. Despite this, these aberrations can be rectified using RNA inhibition of TFs or treatment with DNA methylase inhibitors. Another potential source of epigenetic variation between ESCs and iPSCs is the microenvironment in which the iPSCs have been generated. Cooper and Newman have demonstrated that there is some correlation between cells' gene expression patterns and the laboratory the cell lines are derived from [187, 188]. This demonstrates that the environment can affect the epigenome and therefore downstream gene expression of cell lines. To fully assess the differences in the epigenomes between iPSCs and ESCs, Lister *et al,* utilized a shotgun bisulphite sequencing technique (MethylIC-seq) to look at the whole-genome DNA methylome at single base-pair resolution [189]. This demonstrated that, overall, ESCs and iPSCs are similar, but that there are some inherent differences between their DNA methylomes. The reprogramming of somatic cells generated hundreds of DMRs that could be attributed to both memory from the somatic cell and iPSC-specific DNA methylation patterns that are susceptible during the reprogramming process as many DMRs were consistent across independent iPSC lines [181]. All of these studies demonstrate that there are fundamental differences in both the epigenome and gene expression patterns of ESCs and iPSCs. However, there are ways to rectify some of these differences meaning that iPSCs still have utility as disease models.
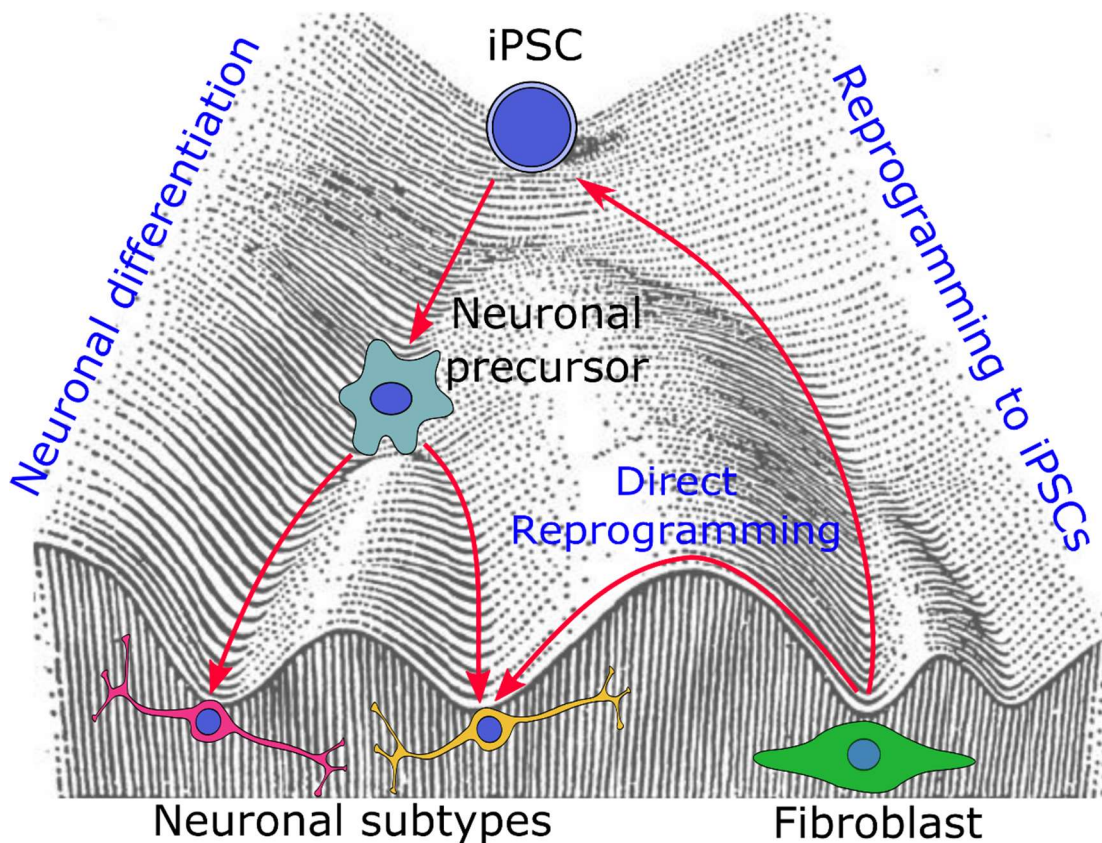
Figure 1.9. Epigenetic mechanisms regulate cell fate and differentiation.

In order to create iPSCs from differentiated adult tissue such as fibroblasts global cellular changes to epigenetic mechanisms, such as DNA methylation, are necessary as these epigenetic mechanisms regulate cell fate and differentiation. Undifferentiated pluripotent cells, such as iPSCs, start at the top of the landscape, and throughout differentiation they move further down the landscape becoming more specialised and undergoing epigenetic changes which reflect this. To reprogramme differentiated cells such as fibroblasts back into the pluripotent state you have to reset these epigenetic marks, effectively pushing the cells back to the top of the landscape. Adapted from [179].

1.5 Conclusions

Through the use of GWAS in human samples and studies in rodent models clear links between genetic variation and disease progression have been established [80, 82, 128-134]. However, in the case of LOAD, genetic variation is not sufficient in all cases to cause disease, as exemplified by the fact that approximately 40% of monozygotic twins are discordant for AD [190]. In recent years EWAS studies have been undertaken to understand the contribution of non-genetic factors to AD onset and progression [120, 121, 123]. Whilst these studies have provided clear and robust evidence for epigenetic dysfunction in AD the majority have been performed using postmortem brain tissue, which only offer a snapshot of DNA methylation profiles at the very end stages of life. Furthermore, these studies simply highlight an association with disease, and do not show whether nominated loci are actually causal in the disease process. Although rodent models can be utilised to study AD longitudinally, these are all models of FAD, which have limited utility for studying sporadic disease that has both genetic and environmental contributions. In order to establish how DNA methylation changes throughout the life course and in diseases it is now important to use human based models which can be followed over time to track these changes, such as iPSC-derived neuronal models and human derived cell lines. This thesis aims to characterise a number of different human and iPSC models with relevance to AD.

1.6 Hypothesis and Aims

As it has previously been demonstrated that there is epigenetic dysfunction occurring in AD, this thesis hypothesises that there are methylomic changes occurring within neuronal and microglial cells when they are exposed to AD-relevant exposures and that these changes can be linked to relevant biological pathways.

In order to address this hypothesis this thesis aims to:

1. Investigate the epigenomic changes that occur during iPSC differentiation and maturation into neurons.

2. Investigate the epigenomic changes induced by epigenetic modulators in iPSC-derived neurons and microglia.

3. Investigate the epigenomic changes induced by Lipopolysaccharide (LPS) immune challenges in a microglial cell line.

CHAPTER 2 : <u>MATERIALS AND METHODS</u>

2.1 Cell Culture

This section outlines the general methods that were used to culture cells on a regular basis. For cell line specific culture and differentiation methodology please see the relevant chapter. Please see table 2.1 for more information on the cell lines used in each chapter.

All work done in this section was undertaken in a class II laminar flow hood that had been turned on and allowed to equilibrate for at least half an hour before use. During this time any appropriate reagents were warmed either through use of a water bath or drying oven set to 37°C. Once equilibrated the laminar flow hood was thoroughly decontaminated by spraying and wiping down all surfaces and side panels with 70% ethanol. At least once a week the laminar was also deep cleaned (by using 1% Rely+On Virkon (12358667, Fisher Scientific) solution followed by 70% ethanol). Before being placed into the laminar flow hood all items and equipment were thoroughly sterilised first by being sprayed with 70% ethanol. After completion of cell culture work the laminar flow hood was again sterilised using 70% ethanol before being switched off.

Chapter	Cell Line Name	Tissue	Sex	Transformation method	Passage No.	No. of Biological/Technical Replicates	Seeding Density (cells/well)	Reference
3	33Q	Fibroblasts	Female	Lentivirus	-	3x Technical	-	[191]
4	CTR M3 36S	Keratinocytes	Male	Sendai virus	-	3x Technical	300,000	[192]
	SFC840-03-03	Fibroblasts	Female	Sendai virus	-	3x Biological	750,000	[193]
5	SV40	Primary microglia	Male	Lenti-SV40 lentivirus	6	3x Technical	100,000	-

Table 2.1. Information on cell lines used in each chapter.

Detailed information for the cell line(s) used in each chapter. The chapter the cell line was used in, the name of the line, the tissue it was derived from, the sex of the person the line was derived from, the transformation method, passage number at which they were used, number of replicates, seeding density and reference for each cell line is detailed where available.

2.1.1 Thawing and Recovery

Cells in long term storage were kept in liquid nitrogen using Cryostor (Sigma Aldrich). Cells were defrosted by partially immersing the cryovial into a 37°C water bath until only a small ice crystal remained. Once defrosted the cryovial was transferred into the laminar flow hood where all cell culture work was undertaken. The cell suspension was then transferred into a 15mL falcon tube containing the relevant pre-warmed media. Cells were pelleted by centrifugation for three minutes at 1,000rpm (Megafuge 16R, Thermo Fisher), and the resulting pellet resuspended in media containing 1xRevitacell™ cell supplement (1:100, Gibco). Resuspended cells were placed into the correct size flask or culture plate and kept in a humidified incubator at 37°C, with 5% CO_2. Revitacell™ supplement was removed after 24 hours by changing the media on the cells.

2.1.2 Changing Media

The relevant media was first warmed to 37°C in a water bath or drying oven. Once up to temperature media and relevant equipment were sterilised with 70% ethanol and placed into the laminar flow hood. Following this, cells were then carefully moved from the incubator into the laminar flow hood, being sprayed with ethanol before being placed into the laminar flow hood. Using good aseptic technique, the lid of the flask was removed and spent media removed using a stripette and pipet aid. Waste media was then placed into a flask containing 1% Virkon in order to kill any free-floating cells. Fresh media was then placed into the relevant wells/flasks, being careful not to wash it over the culture and dislodge the cells. Waste media was left in Virkon solution for at least 20 minutes before being disposed of.

2.1.3 Cryopreserving Cells

To freeze down cells they were first washed in phosphate buffered saline (PBS; Gibco), treated with Ethylenediaminetetraacetic acid (EDTA; Gibco) or Accutase (Gibco) (depending on cell type/stage) and washed with media as described in section 2.1.2. After washing, cells were detached from the base of the well using 1mL Cryostor/well and the suspension placed into a cryovial. Vials of cells were placed into isopropanol tubs for the first 48 hours before being moved to liquid nitrogen storage long term.

2.2 DNA Extraction

This section outlines in detail the method used to extract DNA from cell pellets in Chapters 4, 5 and 6. All plastic-ware used during this protocol were sterile and DNase free. Before starting the laboratory benches were cleaned using Alconox (Sigma Aldrich) and 70% ethanol to remove contaminants and any DNases present. The DNA extraction workflow is depicted in figure 2.1 below.

2.2.1 Overview of DNA Isolation using a Phenol Chloroform Based Protocol

Extracting genomic DNA using a phenol-chloroform method has been widely used and has been shown to yield high quality DNA for downstream purposes [194]. The method below is an adaptation of the phenol-chloroform method developed by Sambrook *et al.* [194]. Reagents used for the extraction can be found in tables 2.2, 2.3 and 2.4.

2.2.2 Lysis and Digestion of Cells

Cell pellets were resuspended in 1mL lysis buffer (table 2.2). Subsequently, to degrade any RNA present, 2µL of RNase-A (working concentration 20µg/mL; Fisher Scientific) was added to each sample and these were then incubated at 37°C for two hours. To facilitate protein degradation, 20µL of Proteinase K (20mg/mL; Sigma Aldrich) was added and the sample was incubated for a further two to three hours at 50°C. The sample was then cooled to room temperature before proceeding to nucleic acid purification.

2.2.3 Purification of Nucleic Acids

Phase lock tubes were prepared by adding vacuum grease to the lid of a 2mL Eppendorf tube and centrifuging the tube at room temperature (RT) for 10 minutes at 3,000 rpm. The cooled lysed cell suspension prepared in section 2.2.2 was then added to the phase lock tube, before being topped up with Phenol:Chloroform:Isopropyl alcohol (PCI). The tube was then inverted 20x to mix and was centrifuged at 13,000 rpm for 15 minutes at RT. The top layer was then transferred to a new 2mL Eppendorf and 1mL of chloroform was added. The tube was inverted 20x to mix and was then centrifuged at 13,000 rpm for 15 minutes at RT. The top aqueous layer was carefully transferred to a new tube and the chloroform extraction step was repeated.

2.2.4 Precipitation of DNA

Sufficient 100% ice-cold ethanol was added to the purified nucleic acid solution to fill the Eppendorf tube. Subsequently, the samples were placed at -20°C overnight. After 12-16 hours the samples were centrifuged at 13,000 rpm for 15 minutes at RT, the DNA was precipitated, forming a white pellet at the base of the tube. The supernatant was removed and the pellet was carefully washed with 1mL 70% ethanol so as not to dislodge the pellet. The sample was then centrifuged at 13,000 rpm for 10 minutes, before repeating the 70% ethanol wash step. The supernatant was removed by pipetting and the sample was left to air dry for 30 minutes. Finally, the pellet was resuspended in 200µL Tris-EDTA (Te) buffer (table 2.3) and left to dissolve overnight. Once dissolved DNA was stored at 4°C until needed for downstream experiments.
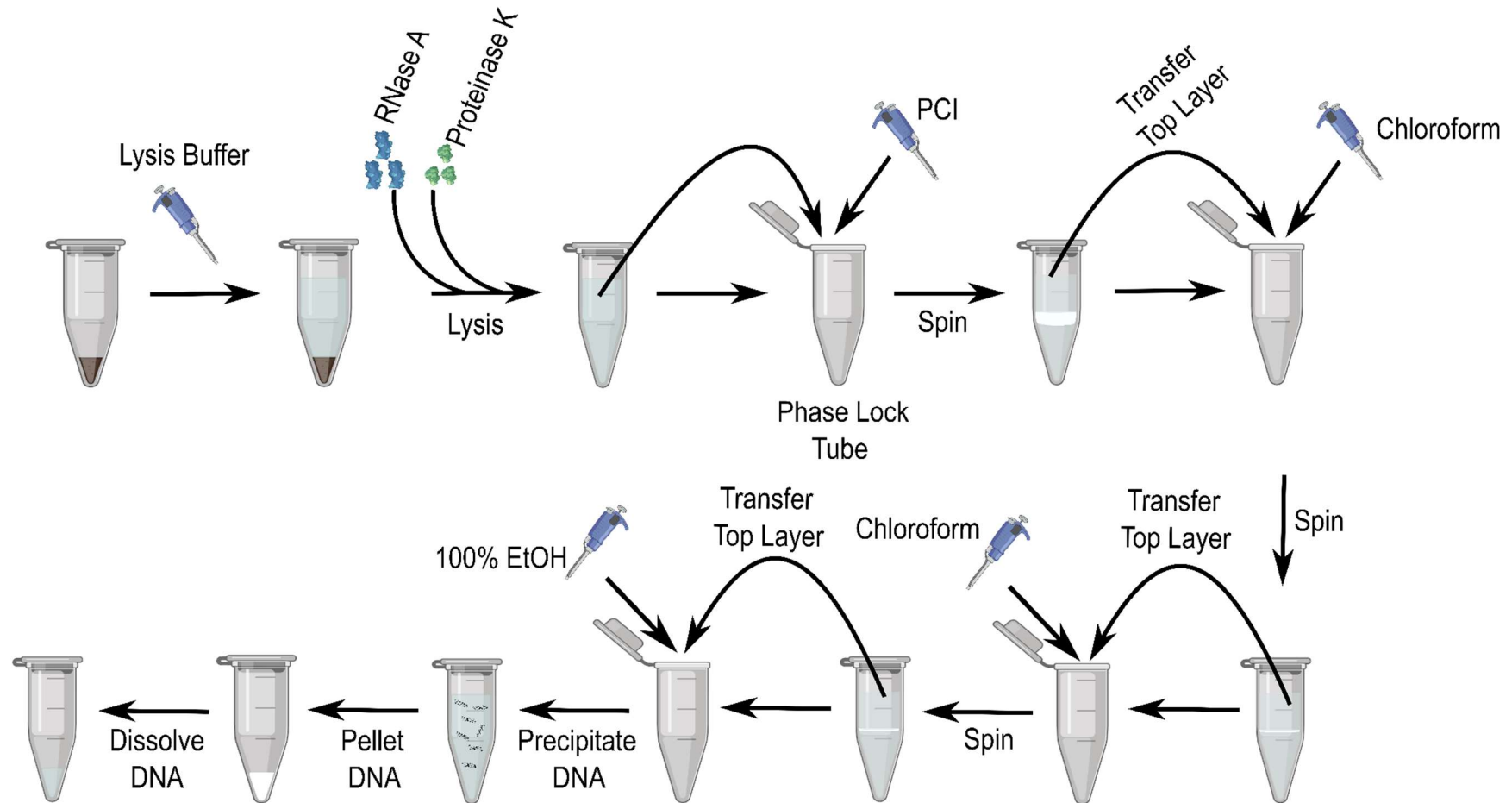
Figure 2.1. Diagram to illustrate DNA extraction workflow.

Once collected and pelleted the cells were lysed using RNase A and proteinase K. The nucleic acids were then purified from this lysed cell solution through the concurrent addition of PCI and chloroform spinning whilst centrifuging between each addition. Once purified the DNA was precipitated using ice-cold 100% ethanol. Following precipitation, the DNA was pelleted and dissolved in Te.

2.2.5 Determining the Quantity of Extracted DNA

2μL of DNA was used to quantify DNA using spectrophotometry (NanoDrop 8000) and check quality. The quality was assessed by checking the 260/280 and 230/280 ratios, which for pure DNA should be above 1.8 and ~2, respectively.

Name	Storage	pH	Final Concentration	Supplier	Catalogue No.
NaCl	RT	-	75mM	Sigma Aldrich	S3014
Tris-HCl	RT	8	10mM	VWR	733-1654
EDTA	RT	8	25mM	Fisher Scientific	11568896
10% SDS	RT	-	$\frac{1}{20}$th final volume	Sigma Aldrich	L3771
H_2O	RT	-	-	-	-

Table 2.2. Reagents required to make lysis buffer.

Where RT signifies room temperature.

Name	Storage	pH	Volume (mL)	Supplier	Catalogue No.
1M Tris-HCl	RT	8	10	VWR	733-1654
0.5M EDTA	RT	8	0.2	Fisher Scientific	11568896
H_2O	RT	-	990	-	-

Table 2.3. Reagents required to make 1x Te buffer.

The solution was filtered with a 0.5micron filter and autoclaved before use. Where RT signifies room temperature.

Name	Storage	Concentration	Supplier	Catalogue No.
Proteinase K Solution	-20°C	20mg/mL	Fisher Scientific	10172903
Ribonuclease A (from bovine pancreas)	-20°C	20µg/mL	Sigma Aldrich	R6513
Phenol/chloroform/ Isoamyl Alcohol (PCI)	4-8°C	100%	Fisher Scientific	13148563
Chloroform (CHCl$_3$)	RT	100%	Sigma Aldrich	C2432
Ethanol	-20°C	100%	Sigma Aldrich	E7023
NaCl	RT	75mM	Sigma Aldrich	S3014
Ethanol	RT	70%	Sigma Aldrich	E7023
Elution Buffer (Te)	RT	200-300 µL/sample	See table 2.3	-

Table 2.4. Other reagents required for phenol-chloroform extraction.

Where RT signifies room temperature.

2.3 DNA Sodium Bisulphite (BS) Treatment

BS treatment, which was originally described in 1992 by Frommer *et al.* [195] is a methodology that allows you to accurately measure DNA modifications at the base-pair level. Through this method un-modified cytosines are converted into uracils, and so after PCR amplification the uracils become a thymine. However, if a cytosine is modified, *i.e.* contains a methyl or hydroxymethyl group, it is protected from conversion and so will not become a thymine. It is this difference that allows you to distinguish whether a cytosine was originally modified or not. BS treatment using the EZ-96 DNA Methylation-Gold^{TM} Kit (Zymo D5007) requires 500ng of high quality DNA (in a volume of 20μL) to provide enough starting material to profile cytosine modifications using the Illumina Infinium Methylation bead arrays, which is the profiling methodology used in all data chapters of this thesis. The method outlined below is an adaptation of the BS treatment methodology developed by the manufacturer. For the original protocol please visit https://www.zymoresearch.eu/media/amasty/amfile/attach/_D5007_EZ-96_DNA_Methylation-Gold_Kit_ver.2.1.5.pdf

2.3.1 Starting Material

500ng (25ng/μL in 20μL) of DNA was added to each well of a 96 well PCR plate.

2.3.2 Sodium BS Conversion

To each DNA sample in the 96 well plate, 130μL CT conversion reagent (table 2.5) was added and mixed by pipetting. The PCR plate was sealed and transferred to a thermal cycler (Thermo Fisher, Veriti) and run under the following conditions: 98°C for

10 minutes, 64°C for 2.5 hours and then 4°C for up to 24 hours. Once the cycle was completed, 600µL of M-binding buffer was added to the wells of a Zymo-Spin™ I-96 binding plate mounted on a collection plate. The samples were transferred from the conversion plate into the Zymo-Spin™ I-96 binding plate and mixed by pipetting. The plate was centrifuged at 3,000 *x* g for 5 minutes and the flow through was discarded. Subsequently, 400µL of M-wash buffer (table 2.6) was added to each well and the plate was centrifuged again at 3,000 *x* g for 5 minutes. Following this, 200µL of M-desulphonation buffer was added to each well and the plate was incubated at room temperature for 15 minutes. The plate was then centrifuged at 3,000 *x* g for 5 minutes and the flow through was discarded. Samples were washed using 400µL of M-wash buffer, centrifuged at 3,000 *x* g for 5 minutes and the flow through discarded. A further 400µL of M-wash buffer was added to the samples, which were then centrifuged at 3,000 *x* g for 10 minutes. The Zymo-Spin™ I-96 binding plate was placed onto an elution plate and 15µL of M-elution buffer was added directly onto each well of the binding plate. The plate was incubated at room temperature for 5 minutes and then centrifuged at 4,000 *x* g for 3 minutes. Subsequently, a further 15µL of M-elution buffer was added to the plate and the incubation and centrifugation step was repeated. The eluted DNA could then be used immediately for downstream analysis, or store at -20°C for later use. For longer term storage BS treated DNA was kept at -80°C.

Reagent	Volume (mL)	Supplier
M-dissolving buffer	0.5	Zymo
M-dilution buffer	3	Zymo
CT conversion reagent	Bottle provided	Zymo
Ultra-pure H_2O	9	User

Table 2.5. CT conversion reagent required for BS conversion using the Zymo EZ-96 DNA Methylation-Gold^{TM} Kit.

The CT conversion reagent is provided as a powder and must be dissolved prior to use and mixed at room temperature with regular vortexing and shaking for 15 minutes.

Reagent	Volume (mL)	Supplier
M-wash buffer	36	Zymo
100% ethanol	144	User

Table 2.6. Reagents required to make the M-wash buffer for BS conversion using the Zymo EZ-96 DNA Methylation-Gold^{TM} Kit.

2.4 Infinium Human Methylation EPIC BeadChip Array

By combining whole genome amplification of BS treated DNA with array based scoring of CpG loci, the EPIC array makes it possible to assess 5mC levels of 863,904 loci across the genome [196]. The EPIC array builds on the previous iteration of this technology, the Illumina Infinium Human Methylation 450K array, and contains >90% of the original CpGs plus an additional 413,743 CpGs [197]. Importantly, the EPIC array covers 99% of the Reference Sequence (RefSeq) database genes, and includes coverage of important regulatory regions such as CpG islands (CGIs) (>95% covered), shores (>90% covered), shelves (>80% covered), 3' and 5' untranslated regions (UTRs), promoters, enhancers and CpGs within gene bodies [196].

In order to quantify 5-mC levels, the signal intensity of each probe is measured using an Illumina iScan by generating beta values, a measure of DNA methylation. Within the BeadChip there are two different types of probe used to assess methylation, these are termed type I and type II probes (figure 2.3). Type I probes have two separate probe sequences per CpG one each to cover the methylated and unmethylated CpG. The hybridisation of an unmethylated BS converted DNA strand to an unmethylated bead allows for the single base pair extension and incorporation of a labelled ddNTP nucleotide which matches the nucleotide which is immediately upstream of the CpG. However, if an unmethylated DNA strand hybridises to a methylated bead then there is a 3' mismatch pairing at the probe and single base pair extension is not possible. The same method/steps is used for the detection of methylated BS treated DNA, but in reverse. Whereas, the same bead is used to measure both methylated and unmethylated CpG for the type II probes. These bead sequences were designed to

match both the BS treated methylated and unmethylated DNA sequences. This is achieved by allowing the cytosine of interest, the target of the single base pair extension and replacing the rest of the cytosines within the probe sequence with degenerate R bases that can hybridise to both C and T bases (where C represents methylated and T represents unmethylated loci).

2.4.1 EPIC Array Protocol

In this section I will describe the methodology required to perform the Illumina Infinium HumanMethylationEPIC BeadChip Array. All reagents described are provided as part of the array kit, unless otherwise stated. Please see figure 2.2 for the experimental workflow.

2.4.1.1 Preparation for amplification

In the first stage of this protocol the BS DNA is denatured and neutralised in order to prepare it for overnight amplification. First, 20µL of MA1 reagent was pipetted into each well of an MSA4 plate, before 7µL of BS DNA from the BS elution plate was added in to the corresponding wells of the MSA4 plate. Following this, 4µL of 0.1M NaOH was added to each well and the MSA4 plate was sealed using a 96-well cap mat, having ensured that the orientation of the cap matches that of the plate. Each plate was then vortexed for one minute and centrifuged at 280 x g for one minute. The plate was then incubated for ten minutes at room temperature. After this incubation, 68µL of RPM solution and 75µL of MSM solution was added into each well and the plate was re-sealed with the 96-well cap mat. The plate was then mixed by inverting it ten times, before centrifuging at 280 x g for one minute. The plate was then incubated in an Illumina hybridisation oven for 20-24 hours at 37°C.

2.4.1.2 Fragmentation of DNA

The MSA4 plate was removed from the hybridisation oven and centrifuged at 50 x g for one minute. Following this, 50μL of FMS solution was added to each well and the plate was sealed with a 96-well cap mat. The plate was then vortexed for one minute at 1,600 rpm before being centrifuged at 50 x g for one minute. The sealed plates were then placed on a heat block set to 37°C for one hour.

2.4.1.3 Precipitation of DNA

After the DNA had been fragmented, the plate was removed from the heat block and 100μL of PM1 was added to each well and the plate sealed with a 96-well cap mat. The samples were then vortexed at 1,600rpm for one minute followed by a 37°C incubation for five minutes. After this incubation step, the samples were centrifuged at 50 x g at 22°C for one minute. Subsequently, 300μL of 100% 2-propanol (Sigma Aldrich) was added to each well, the plate was carefully sealed with a new 96-well cap mat, inverted at least ten times to mix the contents thoroughly and then incubated at 4°C for 30 minutes. Following this incubation stage the plate was centrifuged at 3,000 x g for 20 minutes at 4°C. The cap mat was then discarded, the supernatant removed and the plate was left uncovered and inverted for one hour at room temperature to air dry the pellet.

2.4.1.4 Resuspension of DNA

26μL of RA1 reagent was added to each pellet and then the plate was heat sealed with a foil seal for five minutes before being placed the in a hybridisation oven at 48°C

for one hour. After this incubation stage, the plate was vortexed at 1,800 rpm for one minute and then centrifuged at 280 x g for one minute.

2.4.1.5 Hybridisation to BeadChip

Before hybridisation can begin the hybridisation chambers were first prepared as follows. First, the hybridisation chambers were placed into the corresponding gaskets and then 800µL of PB2 solution was placed into the reservoir of each chamber. Once the reservoirs were filled the chamber lid was replaced and kept at room temperature until needed.

The resuspended samples in the MSA4 plate were placed on the heat block at 95°C for 20 minutes to denature the samples. After this incubation step, the plate was removed from the heat block and allowed to cool to room temperature for 30 minutes. Once cooled, the plate was pulse centrifuged at 280 x g for one minute and the BeadChips were removed from 2-8°C storage 15µL of each DNA sample was pipetted onto the appropriate BeadChip section, the hybridisation inserts containing the BeadChips were loaded into the hybridisation chamber, the chamber was closed and placed in a hybridisation oven at 48°C with continuous movement for 16-24 hours.

2.4.1.6 Washing the BeadChip

The hybridisation chambers were removed from the oven and allowed to cool for 25 minutes. During this time two wash dishes were prepared, containing 200mL of PB1, the multi-sample BeadChip alignment fixture filled with 150mL of PB1 solution and the-flow through chamber. Once cooled the BeadChips were removed from the chambers one by one and the coverseal removed, before immediately inserting the BeadChips

into the wash rack and submerging them fully into the PB1 solution. Once all the BeadChips were in the wash rack, the rack was then moved up and down for one minute with slow gentle agitation. Subsequently, the wash rack was moved to another wash dish containing fresh PB1, again ensuring the BeadChips were fully submerged.

2.4.1.7 Assembly of Flow-Through Chambers

Each BeadChip was placed into a black frame that had been set up in the multi-sample BeadChip alignment fixture pre-filled with PB1 solution aligning the barcode with the ridges in the fixture, placing a clear spacer onto the top of each BeadChip and a clean glass back plate on top of the clear spacer. The metal clamps were attached to the flow through chamber and the clear plastic spacers were trimmed from the flow through chamber assembly.

2.4.1.8 Single Base Pair Extension and Staining

The water circulator was filled to the appropriate level and set so the chamber rack reached a temperature of 44°C. Once the chamber rack had reached this temperature each flow through chamber was placed in the chamber rack and then the following steps were undertaken using the Tecan dilution robot:

1. 150μL of RA1 was dispensed and incubated for 30 seconds.
    a. This step was repeated five times
2. 450μL of XC1 was dispensed and incubated for ten minutes
3. 450μL of XC2 was dispensed and incubated for ten minutes
4. 200μL of TEM was dispensed and incubated for 15 minutes
5. 450μL of 95% formamide/1mM EDTA was dispensed and incubated for one minute.

     a. This step was then repeated

6. The temperature of the chamber rack was changed to the temperature stated on the side of the STM tube, which is normally 32°C.

7. 450μL of XC3 was dispensed and incubated for one minute.

     a. This step was then repeated

8. 250μL of STM was dispensed and incubated for ten minutes

9. 450μL of XC3 was dispensed and incubated for one minute

     a. This step was repeated after which five minutes were waited before moving on.

10. 250μL of ATM was dispensed and incubated for ten minutes

11. 450μL of XC3 was dispensed and incubated for one minute

     a. This step was repeated after which five minutes were waited before moving on.

12. 250μL of STM was dispensed and incubated for ten minutes

13. 450μL of XC3 was dispensed and incubated for one minute

     a. This step was repeated after which five minutes were waited before moving on.

14. 250μL of ATM was dispensed and incubated for ten minutes

15. 450μL of XC3 was dispensed and incubated for one minute

     a. This step was repeated after which five minutes were waited before moving on.

16. 250μL of STM was dispensed and incubated for ten minutes

17. 450μL of XC3 was dispensed and incubated for one minute

     a. This step was repeated after which five minutes were waited before moving on.

18. 450µL of XC3 was dispensed and incubated for five minutes

19. Incubate for a further five minutes

Once this staining was completed, the flow through chambers were immediately removed and placed horizontally on the lab bench.

2.4.1.9 Washing and Coating the BeadChips

A wash dish containing a wash rack was filled with PB1 reagent. Each flow through chamber was sequentially dismantled and each BeadChip was immediately placed into the wash rack, before slowly moving the wash rack up and down in the solution ten times and then soaking the BeadChips for five minutes. The BeadChips in the wash rack were then transferred to a second wash dish containing XC4 solution, and the rack was moved slowly up and down ten times, before soaking the BeadChips for five minutes. The BeadChips were removed from the XC4 and placed horizontally to dry in a vacuum desiccator for one hour at 508mmHg (0.68 bar), or until the XC4 was completely dry on the arrays. Once dry, the underside of each BeadChip was cleaned with 70% ethanol.

2.4.1.10 Imaging the BeadChips

Four BeadChips at a time were loaded into the Illumina iScan and the Methylation NXT settings were used to image the array.

.
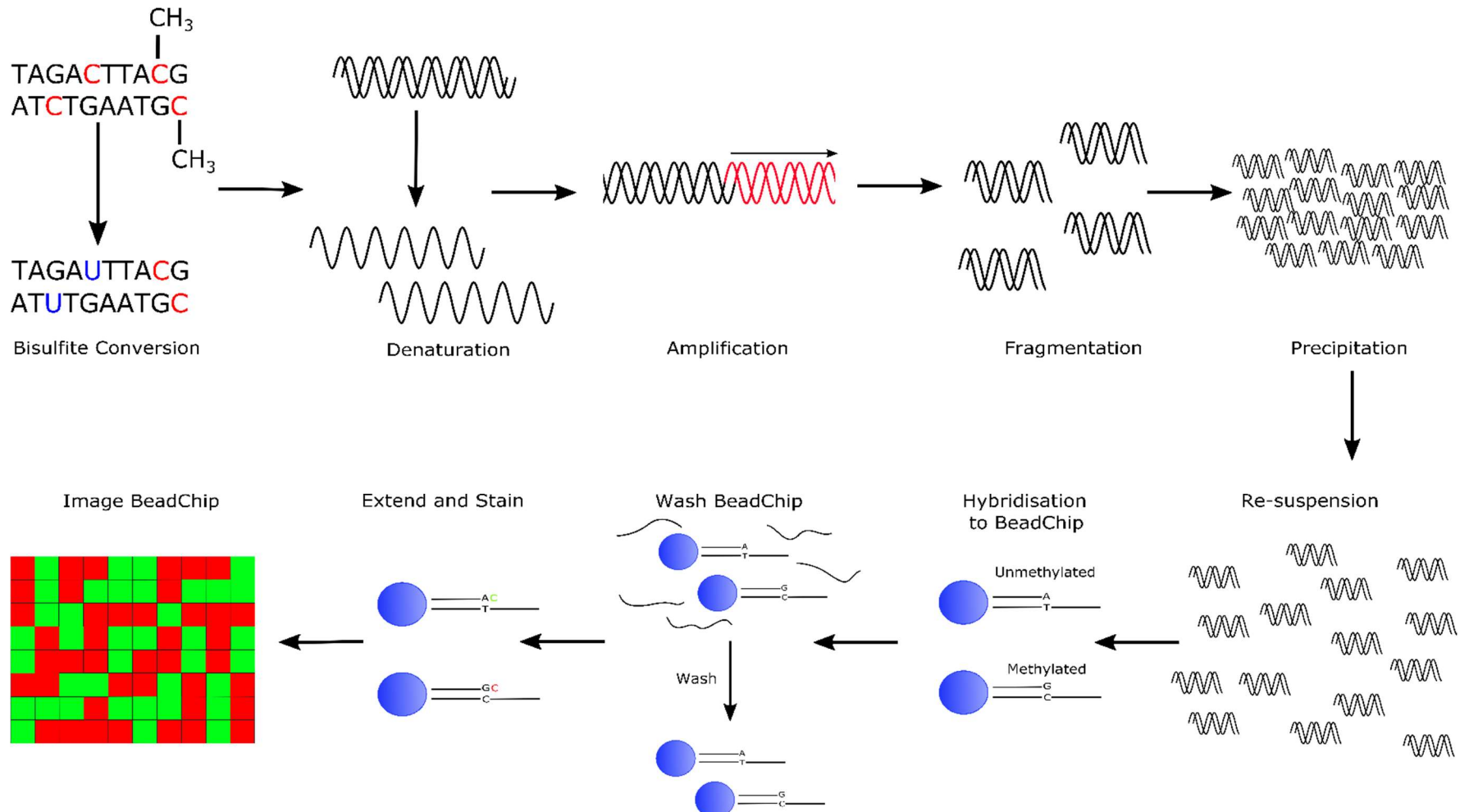
Figure 2.2. Diagram to illustrate the Illumina EPIC array workflow.

Diagram to illustrate the various experimental steps throughout the EPIC array protocol. After the DNA is bisulfite converted it is denatured and amplified by PCR before being fragmented and precipitated. Following this the precipitates DNA is re-suspended and hybridised to the BeadChip, which after washing can be stained and then imaged using an Illumina iScan.
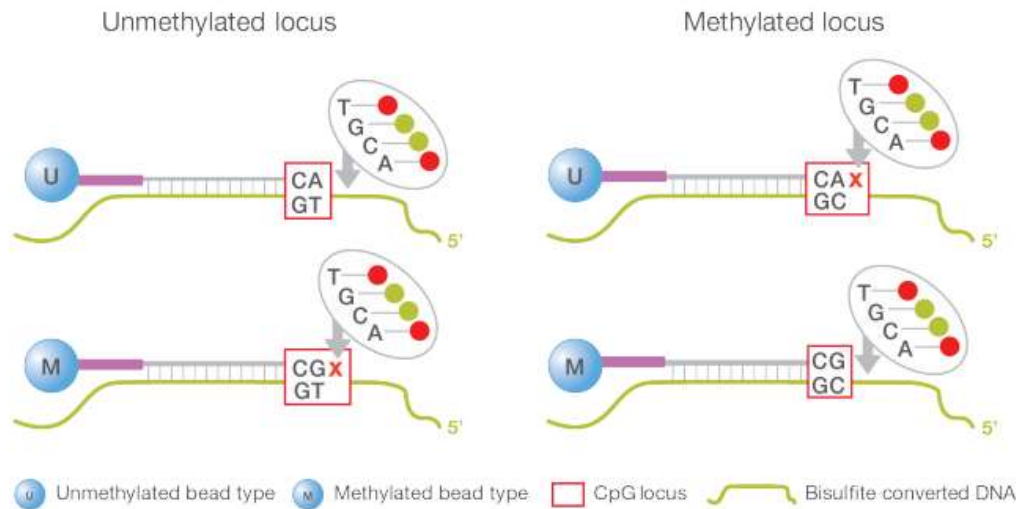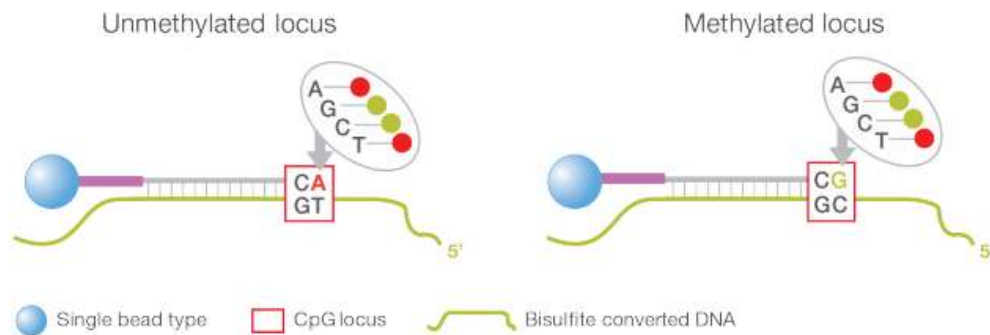
Figure 2.3. Illustration of type I and II (Infinium I and II respectively) probe designs.

On the EPIC BeadChip there are two probe types: type I, which uses two probe sequences per CpG and type II which uses just one probe per CpG. For type I probes the U bead measures the unmethylated signal and the M bead measures the methylated signal. The type II probes measure both methylated and unmethylated CpGs on the same bead. Taken from [196].

2.4.2 Data Quality Control (QC) and Normalisation

The DNA methylation level at each CpG locus was determined by generating β-values, which represent the ratio of the intensity of the fluorescent signal for the methylated and unmethylated beads. The β-values for each probe lies between zero (all cytosines at that loci are unmethylated) and one (all cytosines at that loci are methylated). The β-values can be calculated using the following equation:

$$\beta = \frac{Intensity\ of\ M}{Intensity\ of\ M + Intensity\ of\ U + 100}$$

2.4.2.1 Assessing Median Methylated and Unmethylated Signal Intensity

The median methylated and unmethylated sample intensity for each sample were calculated and plotted against one another in order to ensure that the hybridisation to the BeadChip was successful and that the signal intensities for each sample were above background levels. Median sample intensities were coloured both by chip and position on each BeadChip to check whether these were having any effect on intensity.

2.4.2.2 Determining Bisulfite Conversion Efficiency

Another way to assess data quality is to determine the bisulfite conversion efficiency. The "bscon" function in the wateRmelon package [198] uses the sample intensities of the fully methylated control probes on the array to calculate the percentage bisulfite conversion of each sample. This percentage can be used to determine how well the bisulfite conversion went during the DNA preparation. Typically samples with a bisulfite conversion of less than 80% will be excluded.

2.4.2.3 Determining Epigenetic and Mitotic Age

In order to calculate the epigenetic or biological age of samples the Horvath coefficients were extracted. There are 391 probes on the EPIC array whose DNA methylation profile has been shown to robustly change throughout ageing, these probes were used to generate an algorithm which can be used to predict the biological age of samples from methylation data [126]. This data was then uploaded and submitted to the latest version of the Horvath epigenetic age calculator at https://dnamage.genetics.ucla.edu/home [126].

To determine the mitotic age of samples the MiAge calculator was used. This is an algorithm that uses the methylation profile of 268 probes to predict the number of cellular divisions a cell has undergone [199]. The 268 probes relevant to the MiAge calculator were extracted and used in conjunction with MiAge algorithm to generate estimates of the number of cellular divisions.

2.4.2.4 Pfilter

To filter samples and probes by detection p-value the "pfilter" function in the wateRmelon package was used [198]. This removes samples that contain more than one percent (by default) of probes above the 0.05 detection p-value threshold and probes with any samples with a beadcount less than three or more than one percent above the p-value threshold.

2.4.2.5 Normalisation using Dasen

Normalisation was performed using the "dasen" function within the wateRmelon package [198]. Dasen uses quantile normalisation, which normalises by type I and type II probe background levels first.

One limitation of the EPIC BeadChip array technology is the difference in performance between the two bead types [200]. More specifically, the β-values which are generated from the type I probes are in general more reliable and accurate than the values generated from the type II probes. In order to address this there have been a number of data normalisation methods developed. The wateRmelon package within R offers a range of different normalisation methods [198], of which Dasen was used within this thesis as it has consistently been shown to be the best performing method in our group.

Another caveat of the BeadChip array is the presence of SNPs in close proximity to the CpG of interest, which have been shown to confound the data generated [201, 202], meaning therefore that the 5-mC levels detected may be a reflection of the underlying genetic variation. Furthermore, a proportion of the probes on the array have been shown to cross hybridise with other genomic locations and as a result do not accurately reflect the DNA methylation at the specific loci of interest [201, 202]. In order to overcome this any probes which have been identified as cross-hybridising or contain SNP variation were removed prior to any analysis, using the probe annotations provided by McCartney *et al* [203].

Further details on data QC and on specific analytical methods or pipelines can be found in the relevant data chapter(s) and are also available to view online at: https://github.com/ji241/JenniferImmThesis.

CHAPTER 3 : CHARACTERISATION OF DNA METHYLOMIC SIGNATURES IN IPSCS DURING NEURONAL DIFFERENTIATION

The work presented in this chapter is based on work submitted for publication and is currently under review at Epigenomics (Imm et al, 2020). A copy of the submitted manuscript can be found in Appendix C.

3.1 Introduction

The process of ageing very heterogeneous with some people developing age-related conditions far earlier than others. Not only do age-related changes affect tissues and organs but also affect cells and their organelles [204]. These changes can include changes to mitochondrial function [205], the extracellular matrix [206] and also transcriptional and epigenetic changes [207-209]. In the introduction to this chapter I will briefly introduce the cellular changes that occur during ageing and focus on DNA methylation changes over time especially within the brain.

3.1.1 Cellular Changes Associated with Ageing

As we age one of the organelles that is particularly affected is the mitochondria. With time the electron transport chain (ETC) becomes less efficient, causing more reactive oxygen species (ROS) to leak into the cell and also reduced production of ATP [210]. This increase in ROS causes further mitochondrial damage and globally more cellular damage [211]. Whilst it is believed that ROS can have homeostatic functions and are released as a stress mechanism in order to promote cellular survival at some point during ageing, the levels of ROS can ultimately elicit more harm than good and begin to cause age-associated cellular damage [212].

Another hallmark of ageing is cellular senescence, which is the stable arrest of the cell cycle alongside characteristic phenotypic changes [213-215]. Alongside

the shortening of telomeres [216] there are other mechanisms that cause senescence, including DNA damage to the *INK4/ARF* genes [215]. The levels of INK4a and ARF have been shown to correlate robustly with chronological age in the vast majority of tissues analysed in both humans and mice [217, 218] and have been linked to many different pathologies, including AD, through GWAS [219].

Ageing can also be characterised by deregulation or changes in alternative splicing [220]. Alternative splicing is a key mechanism for cellular homeostasis and survival, and is dysregulated in diseases of ageing such as AD [221-223]. One example of how alternative splicing can result or affect ageing is at the *LMNA* gene which encodes for LamininA/C. A mutation within this protein (C608T) causes a new 5' splice site to be generated and therefore causes the formation of truncated form of the protein which is associated with the disease Hutchinson-Gilford progeria syndrome [224, 225]. Progeria is a disease of accelerated ageing where the people who have the disease display age related phenotypes much earlier in life such as atherosclerosis, hardening of the arteries and cardiovascular diseases [226]. Another way in which alternative splicing can affect ageing is through the dysregulated splicing of DNA repair genes. This leads to increased DNA damage and cellular stress and therefore to cellular ageing [227].

3.1.2 DNA Methylation Changes associated with Ageing

Recent evidence suggests that epigenetic mechanisms such as DNA methylation may play a role in ageing [228-232]. Changes in DNA methylation at particular loci across the genome have been shown to have robust and replicable

methylation changes over time [233-235] and these can used to accurately predict age in a variety of tissues [125, 236-238]. DNA methylation changes begin very early in life, with longitudinal studies in blood showing that during the first five years in early life there are large increases in DNA methylation, and that these changes in methylation occur even within the first year of life [239, 240]. Studies of DNA methylation throughout ageing within monozygotic twins have also demonstrated that changes to DNA methylation are independent of genotype, as the twins have diverging patterns of methylation over time, demonstrating that these epigenetic changes at least in part are influenced by our environment [241, 242]. "Epigenetic drift" is one mechanism that is theorised to play a role in cellular ageing and refers to stochastic alterations to the DNA methylome over time with age. This drift leads to inter-individual divergence in DNA methylation over time and is likely caused by accumulation of epigenetic changes brought on by environmental exposures [241, 242]. Characteristic robust and reproducible DNA methylation changes at specific loci over time as a result of age have now been used to derive an epigenetic clock which is able to predict biological age from epigenetic profiles [125].

3.1.3 DNA Methylation Changes associated within the Ageing CNS

DNA methylation is known to regulate early neuronal development as increased promoter methylation at pluripotency and germ-line specific genes ultimately determines pluripotency repression in progenitors [243]. For the first few years after birth there are large increases in DNA methylation at 16 of 50 genes which have been determined to be important in CNS development and growth with changes within the cerebral cortex being involved specifically in neuronal differentiation [244]. Whilst there are quite dramatic changes to DNA methylation

throughout early development and childhood, each age period are distinct from one another in terms of methylation changes within the prefrontal cortex [245]. The most dramatic changes occur during the prenatal period, slowing down considerably after birth and then continuing to slow further throughout life. Interestingly, the transition between postnatal to foetal is characterised by prenatal demethylation to postnatal methylation.

One of the hallmarks of advancing age is the slow decline of cognitive function, including aberrations in memory [246]. Generally it is believed that there is a global decrease in DNA methylation with increased age, but that this is dependent on the context and the loci in question [247, 248]. In the mature CNS it has been shown that long-term memory and synaptic plasticity are modulated by the activity of DNMTs in the hippocampus and that these processes can be affected by the deregulation of methylation [249]. The decreased capacity for neurogenesis throughout ageing has been attributed to the global hypomethylation that is seen in the brain [250]. DNMTs mediate the DNA methylation process and have also been shown to be linked to memory and cognitive function. Using young and aged mice it has been shown that Dnmt3a2 expression in the hippocampus decreases throughout ageing and that recovery of the Dnmt3a2 levels rescues cognitive functioning [251]. Taken together these studies suggest that DNA methylation is an important mechanism for regulating age-associated cognition.

3.1.4 Modelling Cellular Trajectory

Genome-wide "omics" datasets, such as for DNA methylation provide an opportunity to study dynamic cellular processes such as cell cycle, cellular activation and differentiation [252, 253]. Using epigenomics data it is possible to computationally study these processes using trajectory inference (TI) modelling or pseudotime analysis. TI methods order the cells/samples based on patterns in the data, for example, based on the changes in DNA methylation profile [254]. Through the creation of lineage trajectories using TI methods it is possible to untangle dynamic processes and work out which changes are contributing to the trajectory.

There are now over 70 TI methods available all with differing underlying characteristics and algorithms. Generally, there are two main differences between methods, which are (1) the type of trajectory they are able to detect and (2) whether they fix the topology of the trajectory. Early methodologies relied upon the user to input the topology parameters or the topologies to be fixed using algorithms [255-257]. However, more recent methods, such as SCORPIUS, are able to also infer the trajectory, which is computationally more complex [258].

3.1.5 Using iPSC-derived Neurons to Model Diseases of Ageing

In order to best model any disease, such as diseases of ageing, it is important that we select the most appropriate model possible. Over recent years one model system that has garnered considerably more use for modelling diseases of ageing, is that of iPSC-derived neurons. These iPSCs have been shown to be functional, expressing neuron specific proteins and having the ability to fire mature action potentials [145]. Whilst iPSCs have numerous advantages over

other model systems, it is important to also recognise their potential limitations. For example, although they have been shown to be electrophysiologically mature [145], with numerous protocols having now been developed to accelerate this electrophysiological maturity, they have also been shown to be transcriptomically immature [259].

To utilise iPSC-derived neurons to study epigenomic aberrations in disease fully it is important to first have an understanding of what is happening under disease-free conditions. This should include identifying an epigenetic trajectory signature associated with neuronal differentiation and maturation and to assess the epigenetic maturity of the resultant neurons. This data will then be able to inform future studies, allowing the better interpretation of disease specific epigenomic dysfunction, as well as allowing the identification of specific limitations that would need to be addressed moving forward.

3.2 Hypothesis and Aims

As epigenetic mechanisms are known to regulate cell fate and differentiation this chapter hypothesises that there are methylomic changes occurring as iPSCs differentiate and mature into neurons and that these changes are occurring in cellular pathways functionally relevant to the neuronal cell type.

In order to address this hypothesis the aims of this chapter are:

1. To determine the biological age of differentiated iPSC-derived neuronal cells.

2. To identify the biological pathways that are changing throughout neuronal differentiation.

3. To use DNA methylation patterns to create a cellular trajectory throughout differentiation and maturation.

4. To use the loci important within the trajectory to look at gene-gene interaction and biological function.

3.3 Methods

3.3.1 Cell culture

Information in this section covers the conditions needed to grow, maintain and differentiate iPSCs into mature neurons.

3.3.1.1 Sources of Cells

Cells referred to within this project as "33Q" were a gift from Professor Nicholas Allen at the University of Cardiff. These cells were generated and validated externally (HD33i.8) by Mattis et al [260].

3.3.1.2 Neuralisation and Expansion into Neuronal Precursors

Neurogenesis was conducted using a 2D-monolayer based system, through the addition of regulatory signalling molecules (table 3.1, figure 1.8) to iPSCs at a high confluency. Day 0-7, differentiation was first induced using SLI media which contained 2% NeuroBrew-21 without retinoic acid, 10µM SB, 1µM LDN and 1.5µM IWR1. Media was changed daily, and cells were passaged 1:2 on day 8. On day 8, after passaging, cells were changed to LI media containing 2% NeuroBrew-21 without retinoic acid, 200nM LDN and 1.5µM IWR1. Media was changed daily between days 8 and 16. Following these differentiation steps NPCs were formed which could be expanded in NPC expansion media, terminally differentiated or frozen down for later use.

3.3.1.3 Terminal Differentiation into Neurons

To plated day 16 NPCs, SCM1 medium was added for the first 7 days post plating, which contained Advanced DMEM:F-12 (with Glutamax), 2%

NeuroBrew21 (Miltenyi Biotec), 2μM PD0332991 (Selleckchem), 10μM DAPT (Sigma-Aldrich), 0.6mM $CaCl_2$ (to give 1.8 mM total $CaCl_2$ in final complete medium; Sigma-Aldrich), 200μM ascorbic acid (Sigma Aldrich), 10ng/mL brain-derived neurotrophic factor (BDNF, Miltenyi Biotec), 1μM LM22A4 (Tocris Bioscience), 10μM forskolin (Tocris Bioscience), 3μM CHIR 99021 (Tocris Bioscience), and 300μM gamma-aminobutyric acid (GABA, Tocris Bioscience). From 8 days post plating, the NPCs were cultured in SCM2 medium, which contained 1:1 Advanced DMEM/F-12 (with Glutamax):Neurobasal A (Life Technologies), 2% NeuroBrew21 with retinoic acid (Miltenyi Biotec), 2μM PD0332991 (Selleckchem), 3μM CHIR 99021 (Tocris Bioscience), 0.3mM $CaCl_2$ (to give 1.8 mM total $CaCl_2$ in final complete medium; Sigma-Aldrich), 200μM ascorbic acid (Sigma-Aldrich), 10ng/mL BDNF (Miltenyi Biotec), and 1μM LM22A4 (Tocris Bioscience). This media was generated as part of a rapid maturation protocol outlined in [261].

For an outline of the experimental workflow please refer to figure 3.1 below.

3.3.1.4 Media Used for Each Cellular Stage

Cell Stage	Media Name	Media Components	Working Concentration	Supplier	Catalogue Number
iPSC	Essential 8	Essential 8 basal medium	-	Life Technologies	A1517001
		Essential 8 supplement	1x	Life Technologies	A1517001
D1-7 NPC	SLI	Advanced DMEM/F-12 + Glutamax	-	Life Technologies	11524436
		NeuroBrew-21 without retinoic Acid	2%	Miltenyi Biotec	130-097-263
		SB431542	10µM	Abcam	ab120163
		LDN193189	1µM	Sigma Aldrich	SML0559-5MG
		IWR1	1.5µM	Tocris	3532
D8-15 NPC	LI	Advanced DMEM/F-12 + Glutamax	-	Life Technologies	11524436
		NeuroBrew-21 without retinoic Acid	2%	Miltenyi Biotec	130097263
		LDN193189	200nM	Sigma Aldrich	SML0559-5MG
		IWR1	1.5µM	Tocris	3532
D16-NPC	Expansion Media	Advanced DMEM/F-12 + Glutamax	-	Life Technologies	11524436
		NeuroBrew-21 with retinoic Acid	2%	Miltenyi Biotec	130-093-566
		FGF2	20ng/mL	Fisher Scientific	10222253
D1-7 TDN	SCM1	Advanced DMEM/F-12 + Glutamax	-	Life Technologies	11524436
		NeuroBrew-21 without retinoic Acid	2%	Miltenyi Biotec	130097263
		PD0332991	2µM	Tocris Biotechne	4786
		DAPT	10µM	Tocris Biotechne	2634
		CaCl2	1.8mM	Sigma Aldrich	449709
		Ascorbic Acid	200µM	Sigma Aldrich	BP461
		BDNF	10ng/mL	Tocris Biotechne	248-BD-025/CF
		Forskolin	10µM	Tocris Biotechne	1099
		LM22A4	1µM	Tocris Biotechne	4607
		CHIR 99021	3µM	Tocris Biotechne	4423
		GABA	300µM	Tocris Biotechne	344
D8- TDN	SCM2	Advanced DMEM/F-12 + Glutamax	-	Life Technologies	11524436
		NeuroBasal A	-	Life Technologies	11570556

		NeuroBrew-21 with retinoic Acid	2%	Miltenyi Biotec	130097263
		PD0332991	2µM	Tocris Biotechne	4786
		CHIR 99021	3µM	Tocris Biotechne	4423
		CaCl2	1.8mM	Sigma Aldrich	449709
		Ascorbic Acid	200µM	Sigma Aldrich	BP461
		BDNF	10ng/mL	Tocris Biotechne	248-BD-025/CF
		LM22A4	1µM	Tocris Biotechne	4607

Table 3.1. Media used and their components for each cellular stage.

Where D1-7 NPC is the media used for the first seven days of differentiation into neuronal precursors, D8-15 NPC is the media used for day 8-15 of differentiation into neuronal precursors, D16 NPC is the media to maintain and expand the cells at the neuronal precursor stage, D1-7 TDN is the media used for the first seven days of terminal differentiation into neurons, and D8- TDN is the media used to complete terminal differentiation and mature neuronal cells.
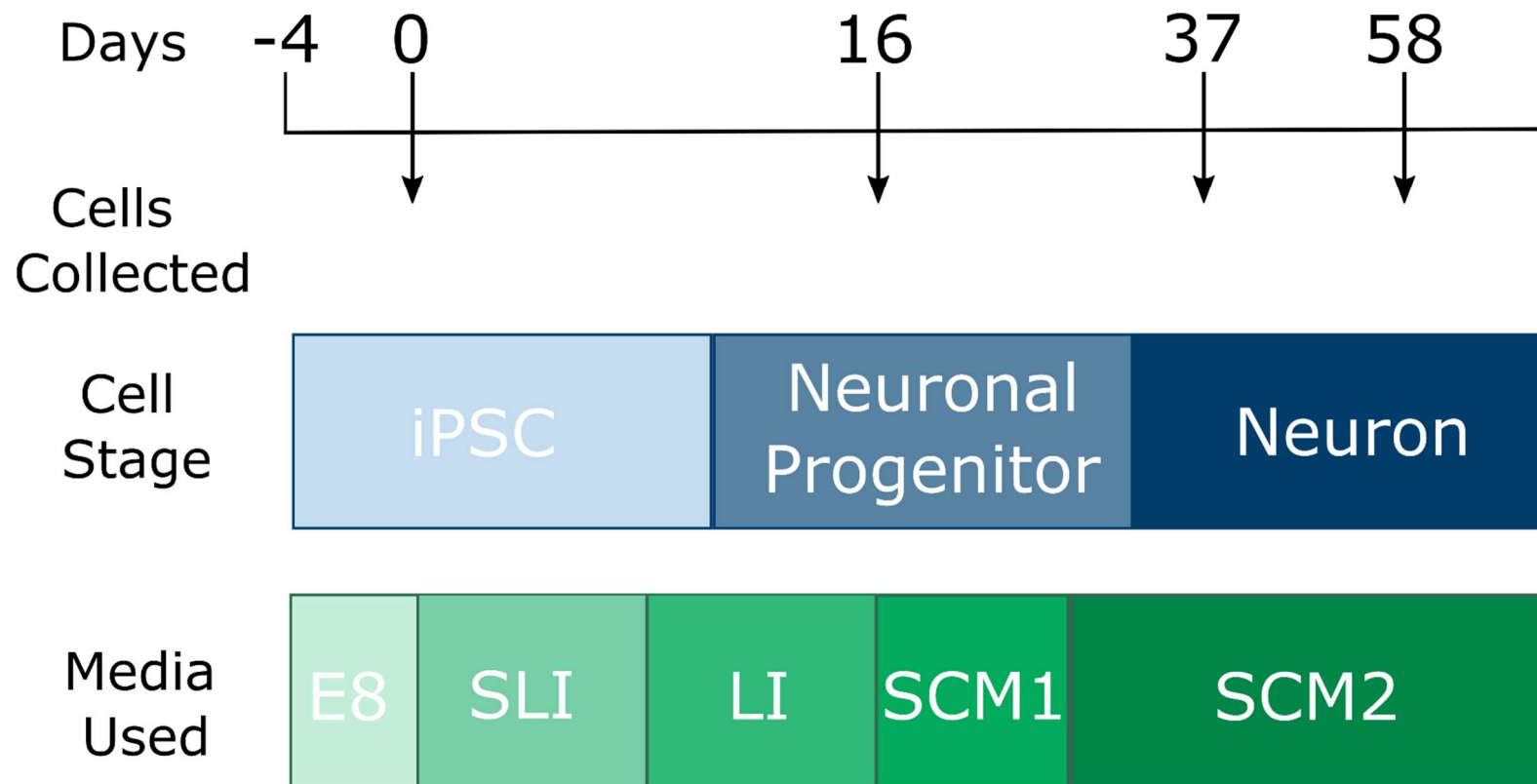
Figure 3.1. Diagram outlining the experimental workflow.

33Q iPSCs were plated out at day -4 and allowed to grow in culture for four days before being collected. The remaining cells then began neuralisation and were collected on day 16 once neuronal progenitors had been formed. Following this, the final cells were terminally differentiated and collected after either a further 37 or 58 days. The diagram above illustrates the days the cells were collected at which cellular stage this represents and the media that was used for each stage. The constituents of each media can be found above in table 3.1.

3.3.2 DNA Extraction and Methylation Profiling and Quantification

DNA was extracted from cell pellets and bisulfite treated prior to quantification of DNA methylation using the Illumina EPIC array. Please refer to sections 2.2 for information on DNA extraction, section 2.3 for details on bisulfite conversion and section 2.4 or figure 2.2 for a detailed outline of the EPIC array protocol.

3.3.3 Data QC

For an outline of the QC and normalisation methods used in this chapter please see sections 2.4.2. All data analyses in this chapter were performed using R version 3.4.3. Signal intensities were imported into R using the methylumi package [262]. Initial QC checks were conducted using functions within the methylumi and wateRmelon packages [198, 262].

Using the default setting of one percent, the "pfilter" function detected two samples and 12,962 probes and 7,170 sites to be above the detection threshold. The two samples which failed this metric, were the iPSC samples labelled "D4_2" and "D4_3". These samples were removed at this point.

3.3.4 Data Analysis

Outlined in this section are the analysis steps conducted in order to assess and quantify the DNA methylation changes occurring throughout iPSC differentiation to neuronal cells.

3.3.4.1 Correlation between Epigenetic and Mitotic Age

In order to assess the correlation between the epigenetic and mitotic age Pearson's product-moment correlation was used. This was using the "cor.test" function within the default statistics package of R.

3.3.4.2 Weighted Gene Correlation Network Analysis (WGCNA)

Network analysis was performed on normalized DNA methylation (β)-values using WGCNA [263]. Pair-wise correlations were used to identify modules of highly co-methylated probes. An unsigned network was created using the "blockwiseModules" function from the WGCNA package [264] based on a block size of 10,000 and using a soft threshold parameter of 20. Each module was then labelled with a unique colour identifier. Module-trait relationship was determined using linear regression, and four modules were shown to be significant after multiple test correction (blue, black, greenyellow and red).

Pathway analysis was used to give biological or functional meaning to the CpG sites that contributed the most to each significant module. This was achieved using the "gometh" function from the missMethyl package [265] alongside the Gene Onotology (GO) repository. The "gometh" function was chosen as it adjusts for the number of CpGs per gene. Probes were sorted by module membership in each module and the top 15% were used for pathway analysis. Briefly, pathways were downloaded from the GO website (http://geneontology.org/) and genes with at least one Illumina probe annotated to it and which mapped to at least one GO pathway were included. Pathways were filtered to those containing between 10 and 2,000 genes and a list of significant pathways ($P < 0.05$) was identified as described previously [266].

3.3.4.3 Probe Filtering and Dimensionality Reduction

In order to robustly determine variable CpG sites median absolute deviation (MAD) was calculated and the upper fifth percentile was used as a cut off to determine the most variable probes throughout differentiation and maturation. Principal component analysis (PCA) without scaling probes by their variance was then used to reduce the number of dimensions within the dataset whilst maintaining as much relevant information as possible.

3.3.4.4 Pseudotime Trajectory Analysis

To create a pseudotime trajectory throughout the different cellular stage the "infer_trajectory" and "draw_trajectory_plot" functions of the SCORPIOUS package [258] were used, respectively. The first two principal components of the methylation data were subjected as the coordinate of the samples to the "infer_trajectory" function, which performs k-means clustering. This calculates the distance matrix between cluster centres and finds the shortest path that connects all cluster centres using a custom distance function before finally fitting a curve to the given data using principal curves [258].

Next, to identify the loci with the largest contribution to the trajectory, I regressed each CpG sites methylation values on the pseudotime variable that had been in the trajectory modelling, using a general additive model (GAM). This allowed the detection of non-linear methylation patters occurring throughout neuronal differentiation. The CpG loci which remained significant after Bonferroni multiple testing correction were taken as robust markers for neuronal differentiation and were therefore used for further downstream analyses.

3.3.4.5 Calculating Euclidean Distance

Euclidean distance was calculated prior to the trajectory modelling in order to cluster the samples to identify their similarity to one another. This information was then represented as a dendrogram.

3.3.4.6 Gene Ontology (GO) Enrichment Analysis

Pathway analysis was used to give biological or functional meaning to the CpG sites that contributed the most to the trajectory analysis. This was achieved using the "gometh" function from the missMethyl package [265] alongside the GO repository. The "gometh" function was chosen as it adjusts for the number of CpGs per gene.

In order to add additional meaning to the pathway analysis outputs the online platform REVIGO was used (available at: http://revigo.irb.hr/) [267]. The significantly altered pathways (determined by GO ID) and p-value significance values were added to the online portal with the GO term database being set to *Homo sapien* and the semantic similarity measure as Resnik. Once analysed the treemaps for the altered biological processes (BP), molecular functions (MF) and cellular components (CC) were generated and created.

3.3.4.7 Gene-gene Interaction Network Analysis

I used Metacore (Clarivate Analytics) to obtain a set of functional regulatory interactions between the unique genes that were annotated to the CpG sites with the largest contribution to the trajectory inference model. The Metacore database is a repository of manually curated and experimentally validated directed gene-gene interactions that have been based on existing literature. This high level of curation and

validation enables us to create highly confident interaction network maps. The network reconstruction was restricted to interactions contained within the categories of "transcriptional regulation", "influence on expression", "co-regulation of transcription" and "regulation", which have all been reported in humans. When available the type of interaction, *i.e.* activation or inhibition, was provided. Next, the igraph package (version 1.1.2) [268] was used to calculate the strongly connected component (SCC) from the network obtained through the Metacore database. Following this the "network analyser" tool from Cytoscape (version 3.4.0) [269] was employed to conduct the network topographical analysis to identify the key genes within the network based on their connectivity.

3.4 Results

3.4.1 Outcome of the QC Pipeline

The results in this section outline the quality control process undertaken in order to ensure the data was of sufficient quality before undertaking any downstream analyses.

3.4.1.1 Median Sample Intensities Highlight Potential Problems

To check the signal intensities for each sample were above background level the methylumi package was used to extract and quantify the fluorescent intensities for each probe. Following this, the median methylated and unmethylated signal intensities for each sample were calculated (table 3.2). By plotting the median methylated signal intensity against the median unmethylated signal intensity (figure 3.2) If was able to determine whether the median signal intensities are above the background level of intensity, which is generally assigned a value of 1000. Two iPSC samples in our dataset, D4_2 and D4_3, have signal intensities which are close to or around the background signal intensity level and were therefore considered for exclusion from the study. However, as they were close to the cut off threshold, they were kept in so I could see if they also failed on any other QC metrics.

Next, I assessed whether there was any variation introduced into the data by the BeadChip the samples were on or the position within the BeadChip. To do this the samples were coloured by BeadChip and position on the BeadChip and methylated and unmethylated signal intensities were plotted (figure 3.3). In the data whilst the BeadChip itself doesn't affect the signal intensities (figure 3.3B) the position of the sample within the BeadChip does affect the intensity (figure 3.3A). Samples which

107

were located on row1 coloumn1 (R01C01) and row2 column1 (R02C01) have lower methylated and unmethylated median signal intensity than any other of the positions. However, the effect was not large enough to consider removing samples.

Cell Stage	Day of Differentiation	Replicate	Sample ID	Median Methylated Intensity	Median Unmethylated Intensity
iPSC	4	1	D4_1	2320	1429
		2	D4_2	1136	1032
		3	D4_3	992	811
		4	D4_4	1781	1146
NPC	16	1	D16_1	4369	2199
		2	D16_2	3769	2001
		3	D16_3	3645	1667
		4	D16_4	3105	1632
Neuron-D37	37	1	D37_1	3394	1767
		2	D37_2	3298	1572
		3	D37_3	3637	1496
		4	D37_4	3633	1403
Neuron-D58	58	1	D58_1	3315	1819
		2	D58_2	3476	1789
		3	D58_3	2748	1232
		4	D58_4	3407	1480

Table 3.2. Median methylated and unmethylated intensities for each sample.

Using the methylumi package [262] the signal intensities for sample were extracted and the medians calculated. For each sample shown above is the sample ID, day of differentiation, replicate number, the corresponding cell stage, median methylated intensity and median unmethylated intensities.

Median Sample Intensities
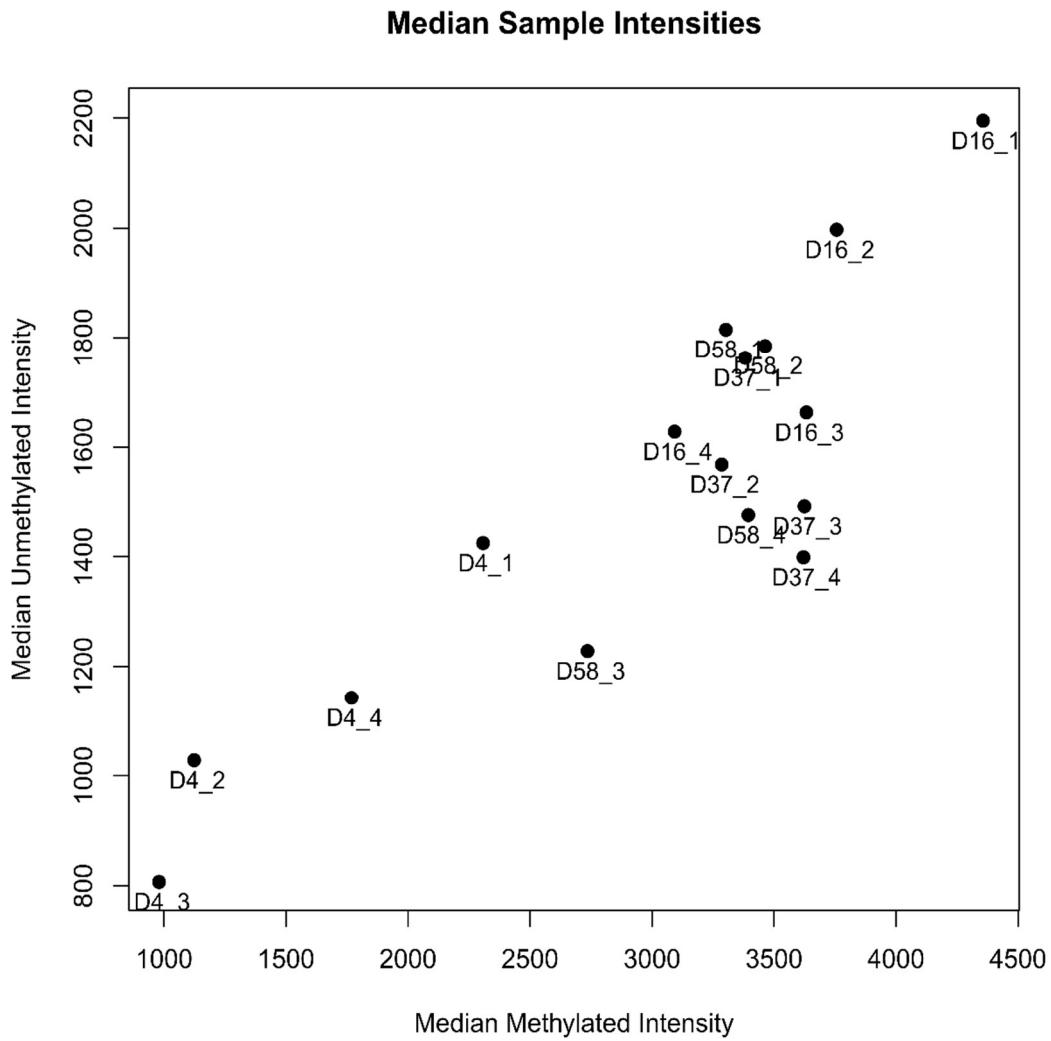
Figure 3.2. Median methylated and unmethylated signal intensities.

Using the methylumi package [262] the signal intensities for sample were extracted and the medians calculated. Scatterplot showing the median methylated and unmethylated signal intensities for each sample. Each point is labelled with the corresponding sample ID.
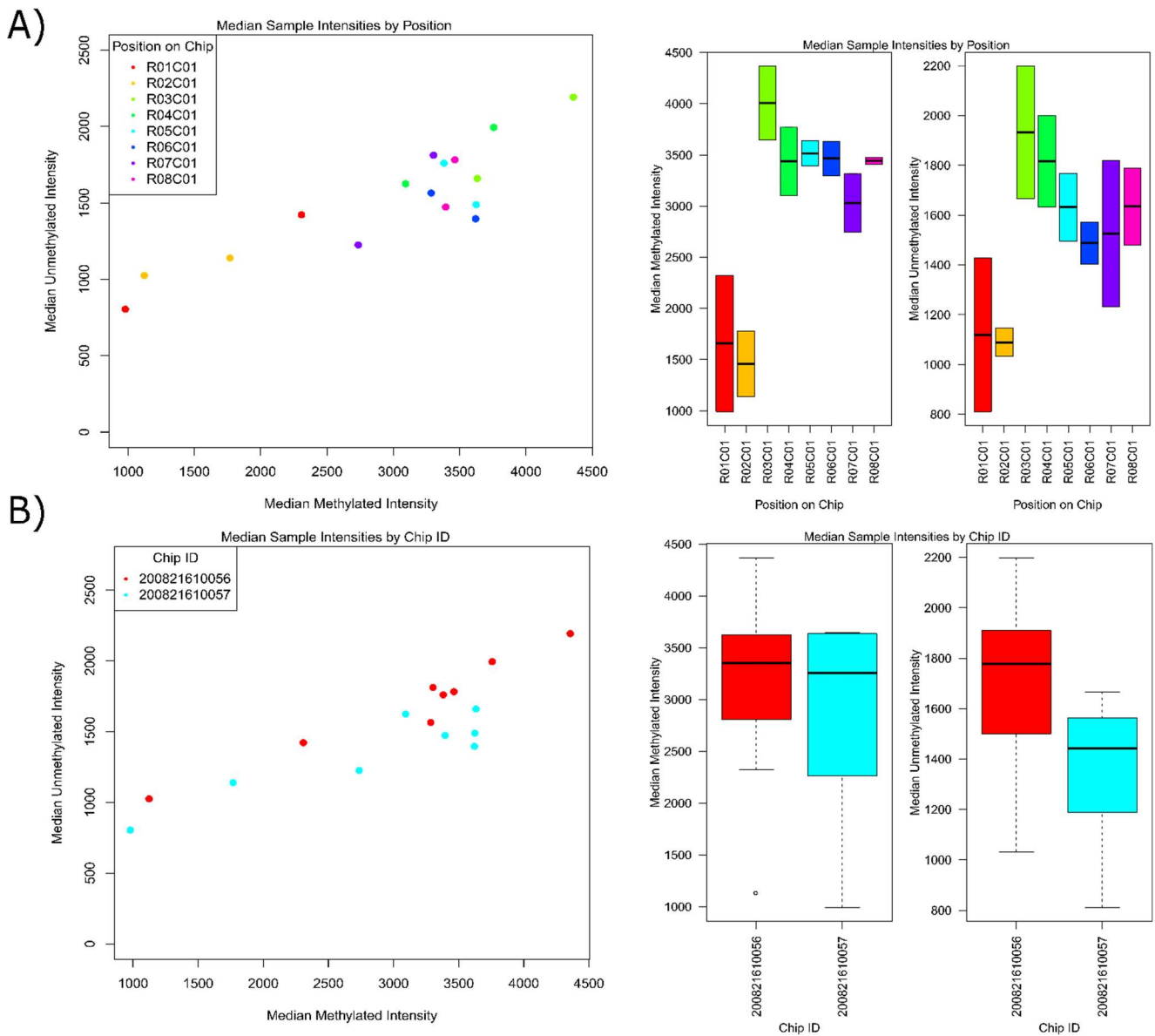
Figure 3.3. Median signal intensities plotted by Chip ID and position on BeadChip.

Median methylated and unmethylated sample intensities were calculated for each BeadChip and each of the eight positions on the BeadChip. **(A)** Median signal intensities coloured by position as a scatterplot and boxplot. **(B)** Median signal intensities coloured by Chip ID as a scatterplot and boxplot. Error bars indicate 1.5x interquartile range (IQR).

3.4.1.2 All Samples have a Good Bisulfite Conversion Efficiency

Bisulfite conversion is the process which converts unmethylated cytosines to uracils and consequently to thymines during PCR allowing unmethylated and methylated cytosines to be distinguished from one another once the EPIC array has been run. Therefore, it is of great importance that the bisulfite conversion efficiency is high and is detecting the true levels of methylated and unmethylated loci. Within the EPIC array there are several loci which are known to be fully methylated, using the "bscon" function of the wateRmelon package [198] within R it is possible to convert the fluorescence intensity of these probes for each sample into an easy to understand percentage conversion efficiency. The lowest generally accepted bisulfite conversion efficiency is 80% and any samples that have a percentage conversion less than this should be removed. All of the samples within this study have a bisulfite conversion efficiency of greater than 90% and therefore do not need to be removed based on this metric (figure 3.4A).
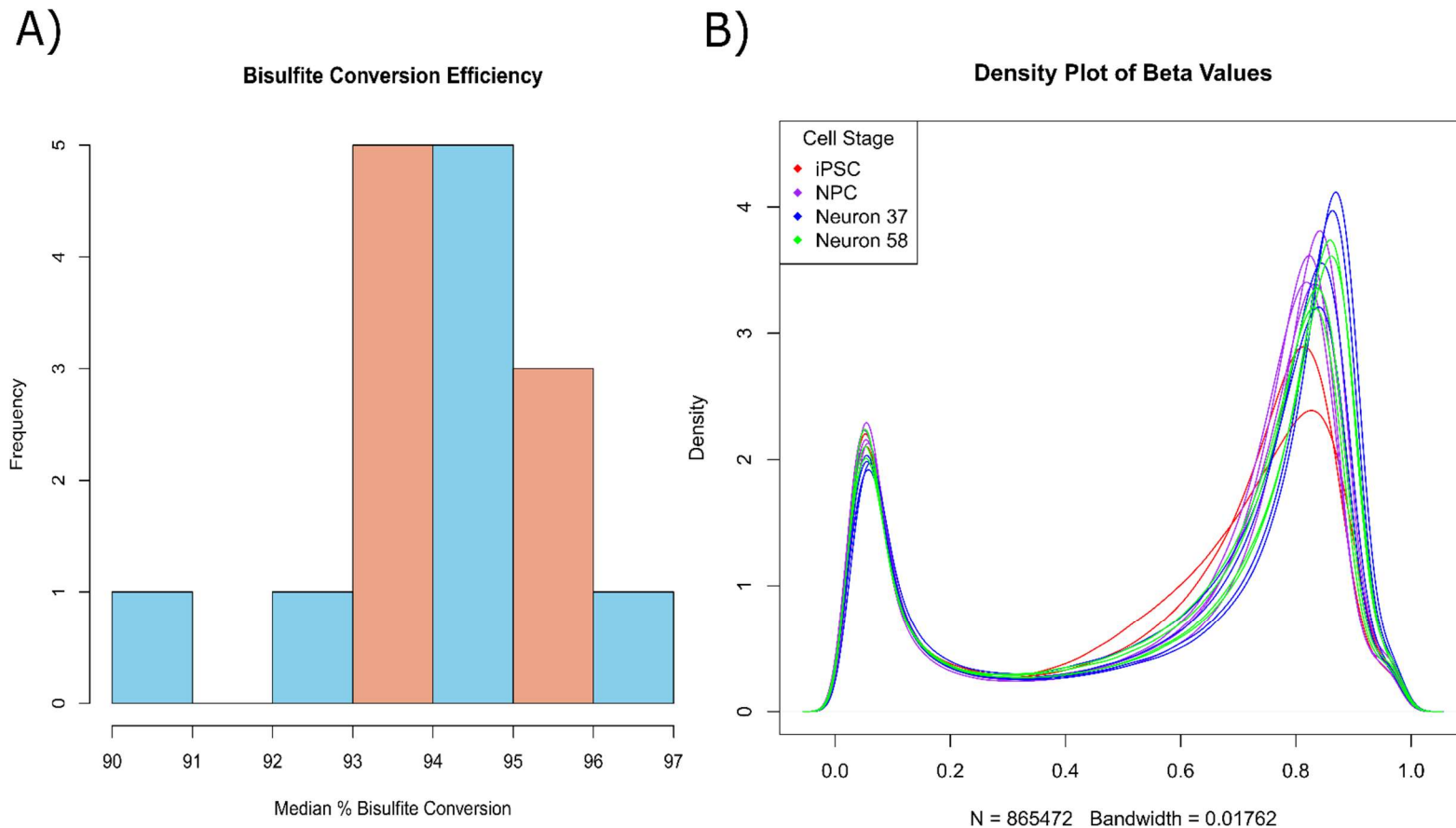
Figure 3.4. Bisulfite conversion efficiency and β-density plot.

(A) Using the fully methylated probes within the array the bisulfite conversion efficiency of each sample was calculated and represented in a histogram. **(B)** The DNA methylation level at each locus was determined using β -values, which are the ratio of fluorescence signal intensity for the methylated and unmethylated beads. The β-values of each probe of each sample were plotted on a β-density plot.

3.4.1.3 β-Density Demonstrates Bimodal Distribution of Methylation

To determine the methylation level at each locus on the EPIC array β-values for each locus are generated. β-values are calculated by taking the ratio of the intensity for the fluorescent signal for the methylated and unmethylated beads. As this value is a ratio the β-value for each probe lies between zero and one, where zero indicates all cytosines at this locus are unmethylated and a value of one means all cytosines at this locus are methylated. The majority of loci within the genome will either be almost completely fully methylated or completely unmethylated, depending on whether the gene they are annotated to is being expressed or not. To check that our data falls in line with this the β-values for each sample were plotted on a density plot (figure 3.4B). It is clear that for the vast majority of samples and loci that this holds true. However, it is of note that for some of the iPSC samples there is an increase in hemi-methylation (having a β-value between 0.2 and 0.8) and a decrease in fully methylated loci. This would suggest that there is more hemi-methylation present in the iPSC samples over the more differentiated cell types.

3.4.1.4 Two Samples are Removed by P-filtering

The final stage in the QC pipeline is to filter samples and probes by detection p-value. This was achieved using the "pfilter" function in the wateRmelon package [198], which removes samples that contain more than one percent (by default) of probes above the 0.05 detection p-value threshold and probes with any samples with a beadcount less than three or more than one percent above the p-value threshold. Using the default setting of one percent, the pfilter function identified two samples, 12,962 sites with a beadcount count less than three and 7,170 sites having 1% samples with a detection p-value above the detection threshold. The two samples which failed this metric were

the D4_2 and D4_3 samples which also had low median signal intensities. Due to these samples failing the pfilter test and also being on the borderline of having too low signal intensities it was decided that they should be removed from the study.

3.4.2 Dasen Normalisation of Methylation Data

In order to make meaningful comparisons between the samples within the dataset the data needs to be transformed using normalisation. Normalisation was performed using the "dasen" function within the wateRmelon package [198]. Dasen involves quantile normalisation that normalises by type I and type II probe background levels first. After dasen normalisation the median methylated and unmethylated signal intensities become much closer together and consistent across samples (table 3.3; figure 3.5).

By plotting the normalised β-values it is possible to see that when plotting all probes on the array the peaks which are towards the extremes (*i.e.* fully methylated and fully unmethylated loci) are much tighter, this is especially true for the fully methylated probes (figure 3.6A). By plotting β-values by probe type it is clear that the type I probes contribute more to the fully unmethylated peak (figure 3.6B) and the type II probes contribute more to the fully methylated peak (figure 3.6C) post normalisation.

Cell Stage	Day of Differentiation	Replicate	Sample ID	Median Methylated Intensity	Median Unmethylated Intensity
iPSC	4	1	D4_1	3340.000	1636.643
		4	D4_4	3340.000	1636.643
NPC	16	1	D16_1	3340.000	1636.643
		2	D16_2	3340.214	1636.643
		3	D16_3	3339.943	1636.643
		4	D16_4	3340.214	1697.286
Neuron-D37	37	1	D37_1	3340.357	1636.500
		2	D37_2	3340.357	1637.214
		3	D37_3	3340.429	1637.214
		4	D37_4	3339.786	1637.500
Neuron-D58	58	1	D58_1	3340.429	1637.168
		2	D58_2	3340.357	1637.500
		3	D58_3	3340.214	1637.500
		4	D58_4	3340.429	1636.643

Table 3.3. Median methylated and unmethylated intensities after dasen normalisation.

Using the wateRmelon package [198] dasen quantile normalisation was performed and the median intensities calculated. For each sample shown above is the corresponding cell stage, day of differentiation, replicate number, sample ID, day of differentiation, the corresponding cell stage, median methylated intensity and median unmethylated intensities after dasen normalisation.

Median Sample Intensities after Normalisation
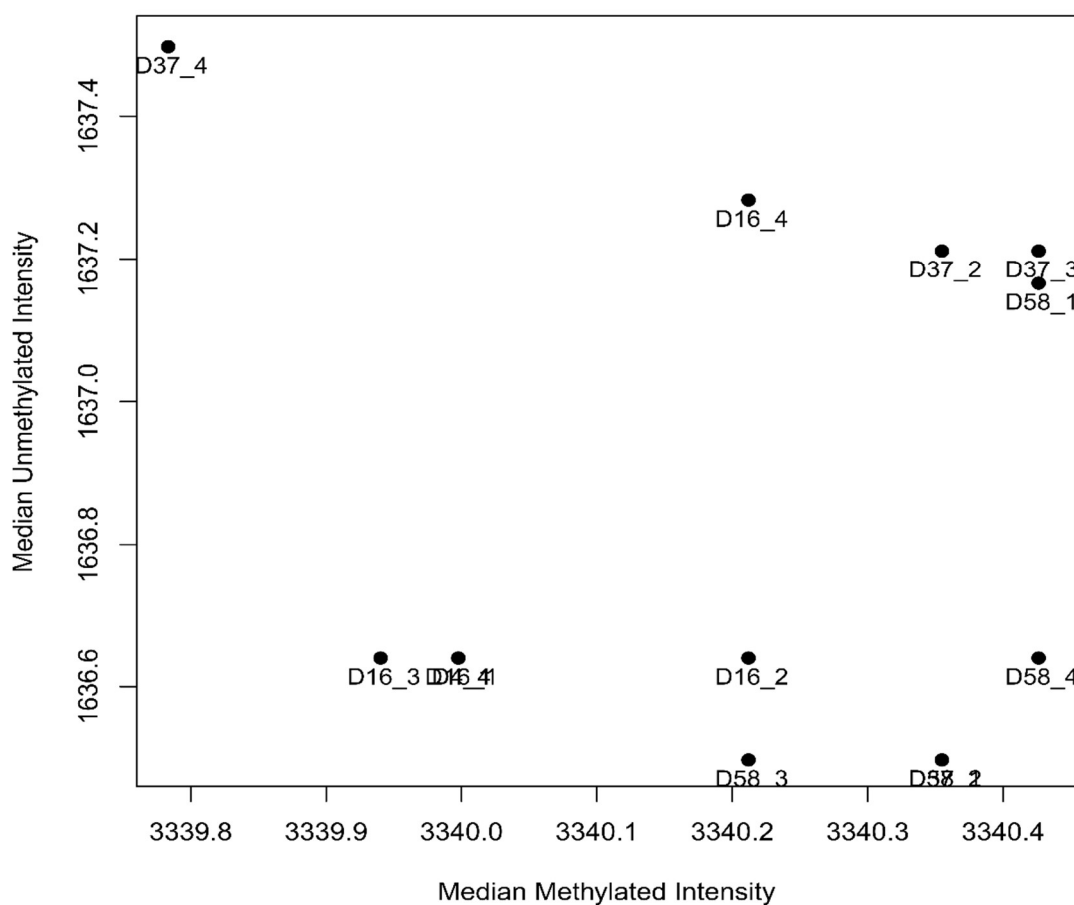
Figure 3.5. Median methylated and unmethylated sample intensities after Dasen normalisation.

Quantile normalisation was performed using dasen [198] to generate the normalised median methylated and unmethylated signal intensities. Graphical representation of median signal intensities relative to each other.
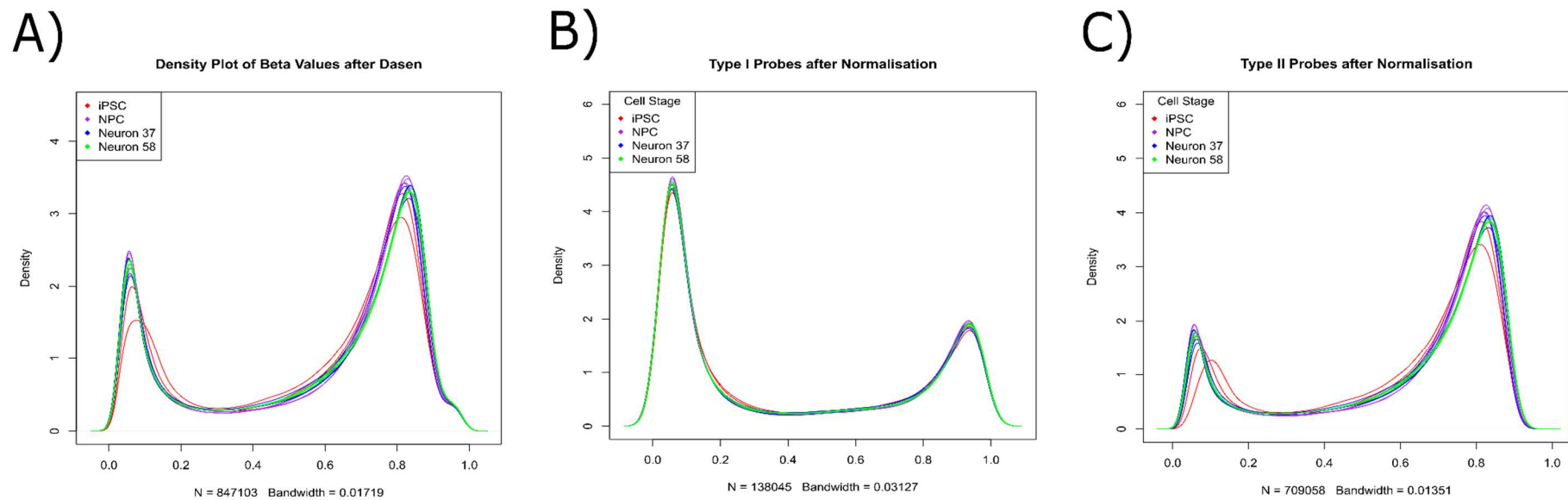
Figure 3.6. β-density plots by probe type.

Normalised β-values were generated and plotted using dasen quantile normalisation **(A)**. Probes were separated based on whether they were type I **(B)** or type II probes **(C)** and plotted individually.

3.4.3 Assessing Metrics of Maturity throughout Neuronal Differentiation

In this section I have used DNA methylation at numerous loci to examine/assess metrics of maturity within the different cellular stages throughout differentiation and maturation.

3.4.3.1 iPSC-derived Neuronal Cells have an Immature Epigenome

One concern when using iPSC-derived neurons to study diseases of advanced age is the biological age of the neurons. I have used the Horvath epigenetic age calculator to predict epigenetic age based on DNA methylation profiles assessed by the EPIC array [126]. This is an algorithm which takes the DNA methylation levels of 391 loci in order to give a prediction of biological age. The biological age of each sample can be seen in table 3.4 and these have been plotted in figure 3.7. From this analysis it is possible to see that whilst the epigenetic age of the cells increases with differentiation and maturation, even the most mature samples still have a negative biological age This demonstrates that the even the oldest iPSC-derived neurons in this study still have an epigenomic profile representative of foetal neurons.

3.4.3.2 Mitotic Age Stops Increasing after Terminal Differentiation

An important metric of ageing is the number of cell divisions a cell has been through. Assessing this in our samples is particularly of interest as differentiated neurons are post-mitotic and should therefore cease dividing and replicating. In order to determine the number of cellular divisions I used the MiAge calculator [199]; this algorithm is able to predict mitotic age using the DNA methylation profile of 268 probes from the methylation array. Similarly to the epigenetic ages, our data shows an increase in mitotic age over the first three time points (iPSC, NPC and day 37 neurons), but unlike

epigenetic age it plateaus or slightly decreases between the two terminally differentiated time points (table 3.4; figure 3.8).

Cell Stage	Day of Differentiation	Replicate	Sample ID	Epigenetic Age (years)	No. of Cell Divisions
iPSC	4	1	D4_1	-0.534	472.08
		4	D4_4	-0.755	429.273
NPC	16	1	D16_1	-0.665	679.434
		2	D16_2	-0.552	647.998
		3	D16_3	-0.584	652.024
		4	D16_4	-0.439	566.607
Neuron-D37	37	1	D37_1	-0.407	828.816
		2	D37_2	-0.487	1003.885
		3	D37_3	-0.445	776.052
		4	D37_4	-0.588	817.212
Neuron-D58	58	1	D58_1	-0.412	733.566
		2	D58_2	-0.427	698.652
		3	D58_3	-0.392	718.764
		4	D58_4	-0.566	779.269

Table 3.4. Epigenetic and mitotic ages of iPSCs as they differentiate into neurons.

Using the Horvath epigenetic age calculator [126] and MiAge calculator [199], the epigenetic age, *i.e.* years, and mitotic age, *i.e.* number of cell divisions were calculated for each sample. For each sample shown above is the corresponding cell stage, day of differentiation, replicate number, sample ID, epigenetic age and mitotic age.
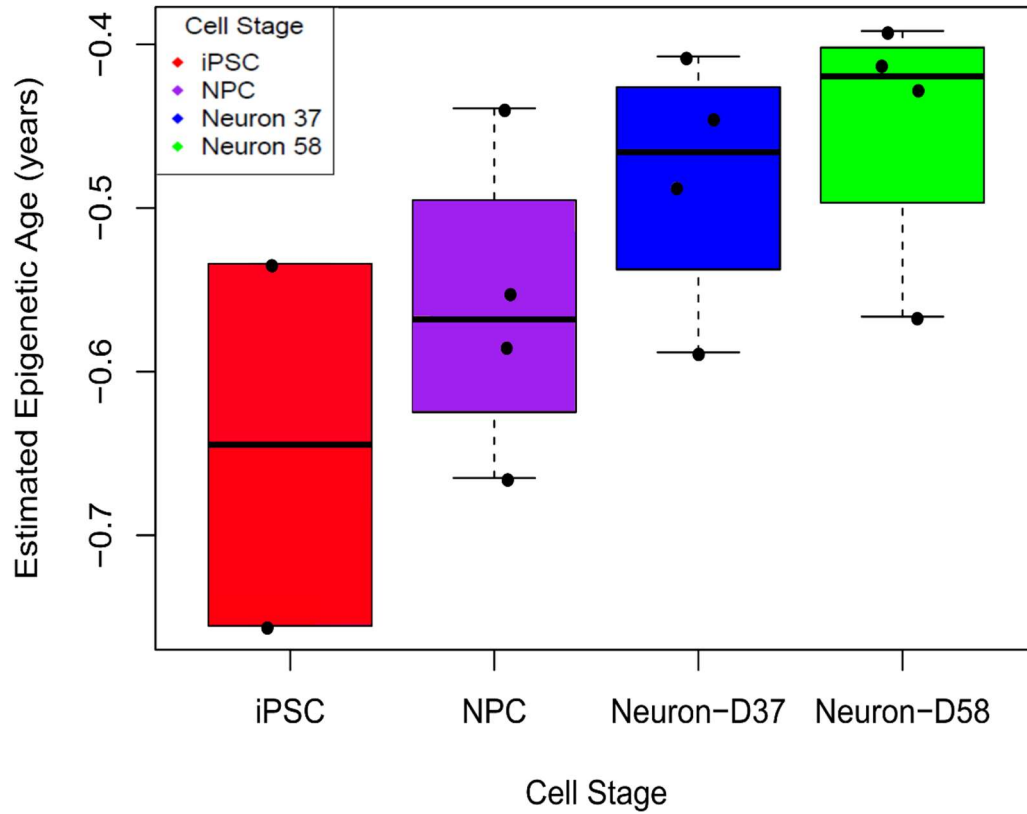
Figure 3.7. Epigenetic age increases throughout neuronal differentiation.

Using the latest iteration of the Horvath epigenetic age calculator online [126], the epigenetic ages of each sample were calculated. Where red represents the iPSC stage, purple the NPC stage, blue the neurons differentiated for 37 days post terminal differentiation and green the neurons differentiated for 58 days post terminal differentiation. Error bars are 1.5x IQR.

Mitotic Age Prediction
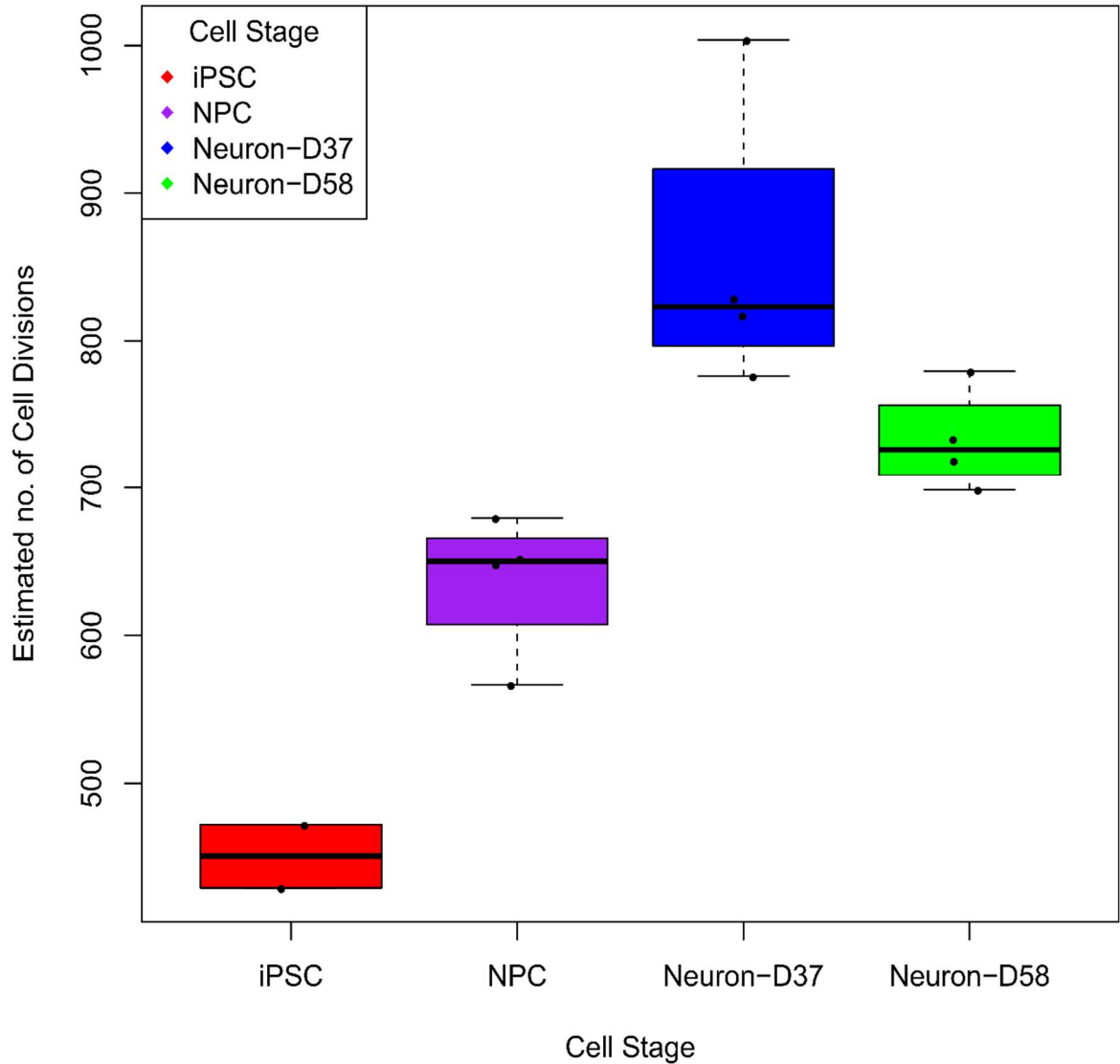
Figure 3.8. Mitotic age stops increasing after terminal differentiation.

Using the coefficients of the MiAge calculator [199] the mitotic ages of each sample were derived. Where red represents the iPSC stage, purple the NPC stage, blue the neurons differentiated for 37 days post terminal differentiation and green the neurons differentiated for 58 days post terminal differentiation. Error bars are 1.5x IQR.

3.4.3.3 There is No Correlation between Epigenetic and Mitotic Age

To test whether there is any correlation between epigenetic age and the number of divisions a cell has gone through Person's correlation was used. From this it is clear that whilst there is some correlation between epigenetic and mitotic age this correlation is not significant (figure 3.9; r value=0.426, p=0.129). Interestingly, representing the data in this way it is possible to see that on the whole the neuronal D37 samples have undergone more cell divisions than the neuronal D58 samples. As cell division is known to stop once terminal differentiation has occurred I also wanted to test whether the correlation improved if the D58 neuronal samples were not included. However, removing these samples did not improve the correlation (r value=0.486, p=0.155)

Correlation Between Epigenetic and Mitotic Age
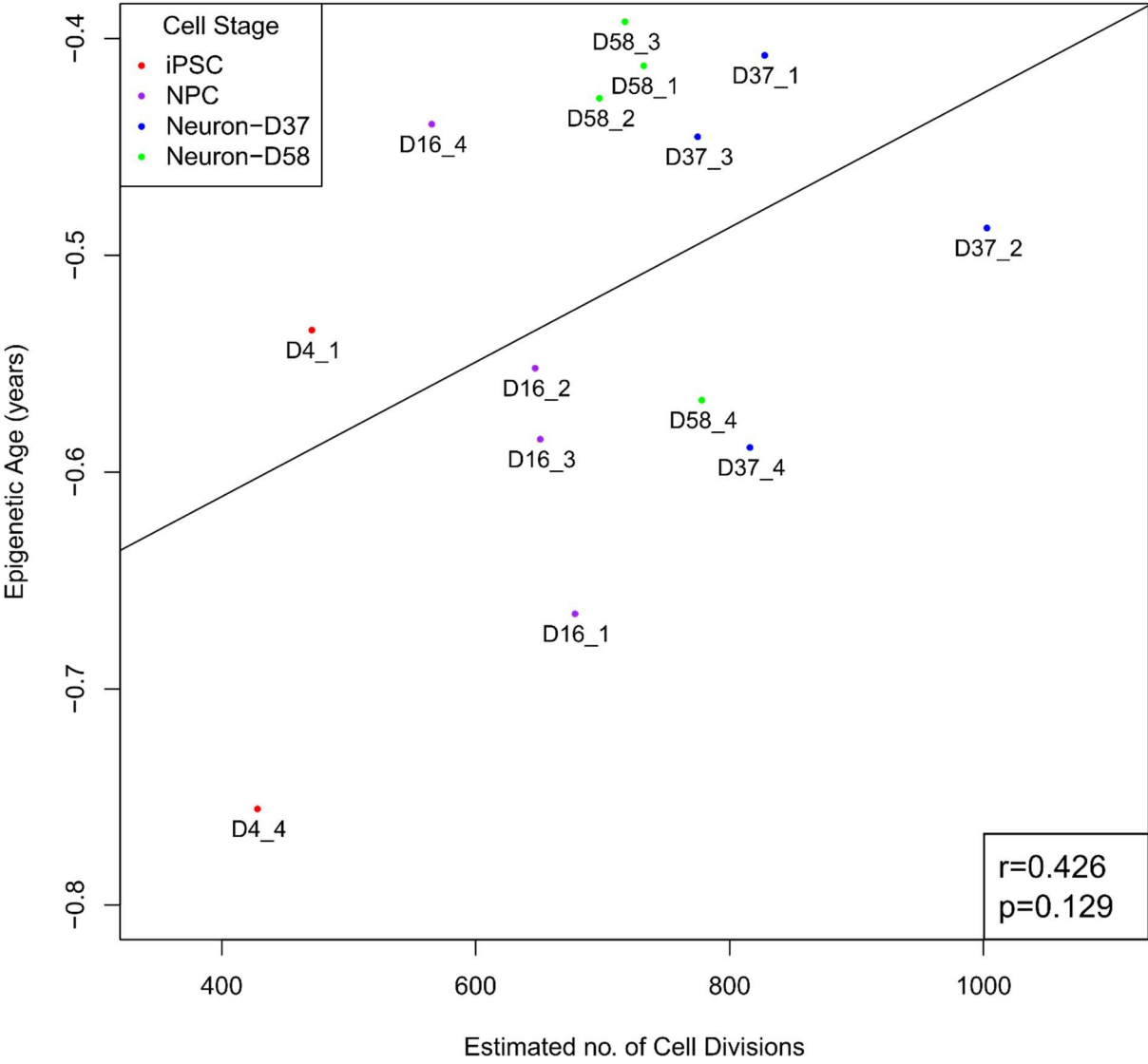
Figure 3.9. There is no correlation between epigenetic and mitotic age.

Using Pearson's product-moment correlation the relationship between epigenetic age and mitotic age was assessed and the results plotted. Where red indicates the iPSC samples, purple the NPCs, blue the neurons differentiated for 37 days post terminal differentiation and green the neurons differentiated for 58 days post terminal differentiation. The line of best for the correlation is also shown.

3.4.4 Non-CpG Loci are more Hemi-methylated in iPSCs

As depicted in figure 3.4B there is an increase in hemi-methylation in the iPSC samples. It has previously been demonstrated that stem cells contain more CpH hemi-methylation (where H stands for any base other than cytosine) [270] and so to determine whether this was the case in these iPSC samples probes were grouped on the basis of whether they were CpG or CpH. After this it was possible to plot only the hemi-methylated CpG and CpH probes (having a β-value between 0.2 and 0.8) to ascertain where the hemi-methylation was present (figure 3.10). From this analysis it is possible to see that for the most part the CpG probes on the array have higher β-values than the non-CpG probes on the array, but also that within the non-CpG group the iPSC samples have an increase in hemi-methylation.
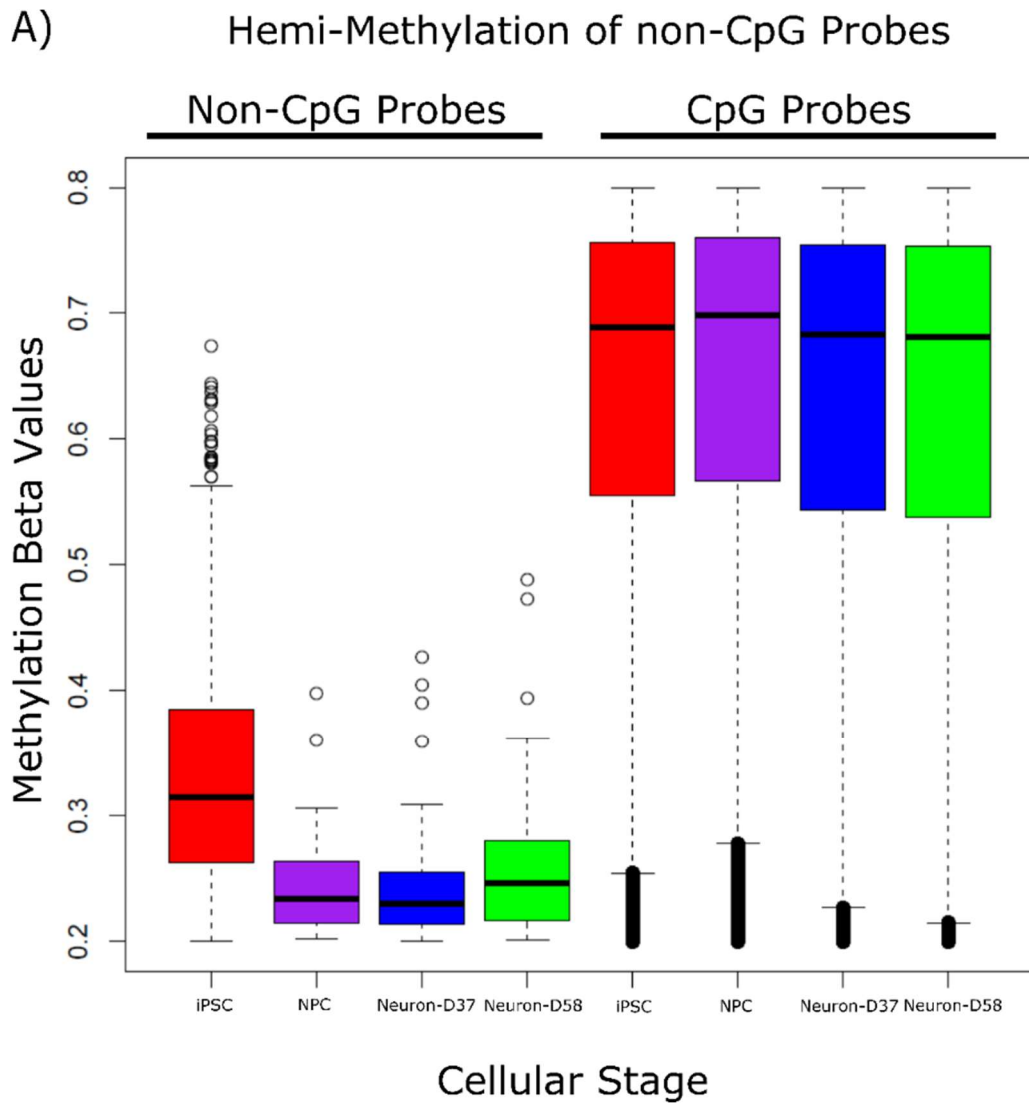
Figure 3.10. Non-CpG probes are hemi-methylated in iPSCs.

After dasen normalisation probes were grouped on the basis of whether they were a CpG or CpH probe. Probes containing β-values between 0.2 and 0.8 (hemi-methylated probes) were then plotted, where red represents the iPSC stage, purple the NPC stage, blue the neurons differentiated for 37 days post terminal differentiation and green the neurons differentiated for 58 days post terminal differentiation. Error bars are 1.5x IQR.

3.4.5 Biological Function of DNA Methylation Levels

In this section I will describe and analyse the methods used in order to provide biological meaning to the DNA methylation changes occurring during neuronal differentiation and maturation. This has been achieved using WGCNA and pathway analysis.

3.4.5.1 WGCNA Identifies Four Modules of Co-Methylated Loci

To identify groups of probes that have similar methylation changes over time WGCNA was used. Briefly, after the construction of blockwise modules of 10,000 probes pairwise correlations were used to identify groups of linearly co-methylated loci. This analysis identified 26 modules of co-methylated probes, eight of which are modules of progressive hypomethylation and fourteen of which are modules of progressive hypermethylation throughout differentiation. Of these 26 modules four remained significant after correction for multiple testing (figure 3.11). These were the black, blue greenyellow and red modules (p=0.001, p=2.00x10^{-4}, p=4.00x10^{-6} and p=3.00x10^{-6}, respectively). The blue, black and greenyellow modules were modules of hypomethylation over time (figure 3.11B-D) and the red module was made of probes becoming hypermethylated throughout differentiation (figure 3.11E). For the most part the iPSC, NPC and day 58 terminally differentiated groups have relatively little methylation variation according to the module eigengene, with the day 37 terminally differentiated neurons having a larger amount of variation within the group. This would suggest that there are still large amounts of DNA methylation level variation within the day 37 group as they have not yet become fully mature or completely differentiated.
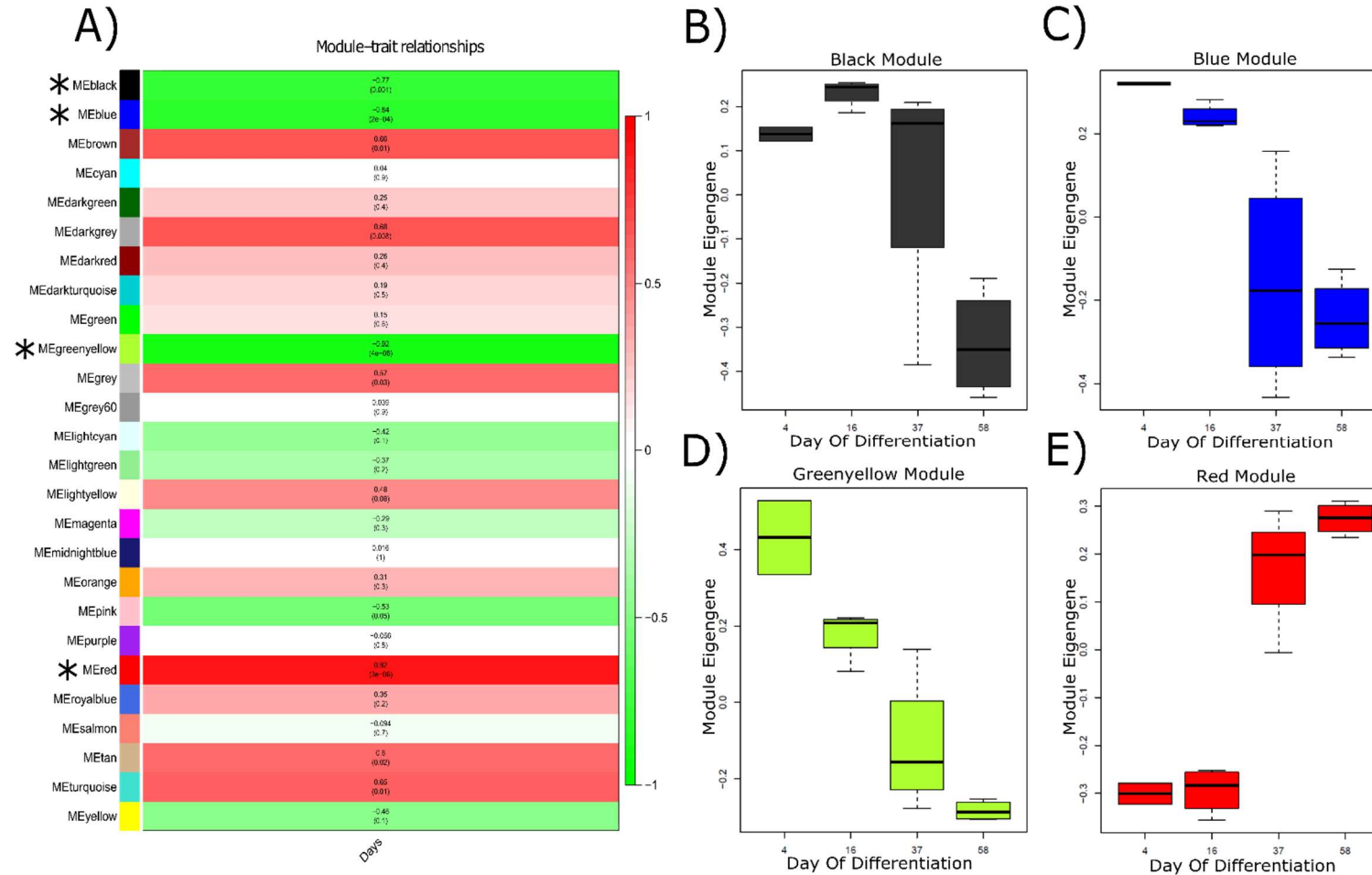
Figure 3.11. WGCNA identifies four significant modules across differentiation.

WGCNA was used to identify modules or groups of loci that had similar linear changes in DNA methylation throughout differentiation. **(A)** This analysis identified 26 modules, four of which still remained significant after multiple testing correction. These are the black, blue, greenyellow and red modules which are highlighted with an *, where red signifies an increase in methylation over time and green signifies decreasing methylation over time. **(B)-(E)** Boxplots depicting the change in methylation of the module eigengene throughout neuronal differentiation for the black, blue, greenyellow and red modules respectively. Error bars are 1.5x IQR.

129

3.4.5.2 Pathway Analysis Implicates Neuronal Differentiation, Neurogenesis and Transcriptional Regulation

In order to provide biological meaning to the modules identified during WGCNA GO pathway analysis was performed on the top 15% probes within the module (based on module membership). After the top 15% probes were extracted there were 2,005, 3,410, 1,266 and 2,037 probes in the black, blue, greenyellow and red modules, respectively. The GO repository allows us to input the genes annotated to each loci within each module and provides us with the various biological pathways that are enriched in these modules. The top ten pathways for each module are provided in tables 3.5 to 3.8. The black module is associated with biological pathways which are associated with becoming a neuron (table 3.5). This includes FDR significant pathways such as neuron differentiation, generation of neurons and neurogenesis. As I was differentiating the cells into neurons this is encouraging and is perhaps to be expected. The blue module is also associated with becoming a neuron and pulls out similar biological pathways, although the genes within these pathways are distinct from those in the black module (table 3.6). On the other hand, the greenyellow module is made up of pathways involved in response to ions, transcriptional repression, regulatory DNA binding and signal transduction (table 3.7). This suggest that this module is involved more in the underlying processes required to make neurons such as gene expression changes and intracellular signalling rather than the physical changes. It is however worth noting that unlike the other modules, none of the pathways identified in the greenyellow module passed FDR correction. Finally, similarly to the black and blue modules, the red module is also associated with pathways involved in neuronal differentiation and generation (table 3.8). However,

interestingly the red module is made of probes becoming hypermethylated rather than

hypomethylated over time.

GO Term	Description	No. of Genes in Pathway	No. of Genes in Module	P-Value	FDR
GO:0030182	neuron differentiation	1222	127	4.18×10^{-6}	0.034
GO:0048699	generation of neurons	1342	134	1.25×10^{-5}	0.043
GO:0022008	neurogenesis	1439	140	1.55×10^{-5}	0.043
GO:0048666	neuron development	972	106	3.67×10^{-5}	0.076
GO:0008092	cytoskeletal protein binding	836	88	9.99×10^{-5}	0.143
GO:0031175	neuron projection development	827	93	1.06×10^{-3}	0.143
GO:0048468	cell development	1884	164	1.21×10^{-3}	0.143
GO:0030030	cell projection organization	1328	124	2.34×10^{-3}	0.241
GO:0007409	axonogenesis	422	55	2.98×10^{-3}	0.273
GO:1902259	regulation of delayed rectifier potassium channel activity	15	6	3.95×10^{-3}	0.316

Table 3.5. Top ten GO terms associated with black module identified through WGCNA.

Shown for each pathway is the corresponding GO ID, pathway descriptor number of genes annotated to the pathway, the number of genes in our list in the pathway, uncorrected p-value and false discovery rate (FDR)-adjusted p-value. Pathways are ordered by significance.

GO Term	Description	No. of Genes in Pathway	No. of Genes in Module	P-Value	FDR
GO:0030182	neuron differentiation	1222	228	4.17×10^{-16}	3.44×10^{-12}
GO:0048699	generation of neurons	1342	242	1.17×10^{-15}	4.83×10^{-12}
GO:0022008	neurogenesis	1439	252	2.34×10^{-15}	5.55×10^{-12}
GO:0048666	neuron development	972	196	2.69×10^{-15}	5.55×10^{-12}
GO:0031175	neuron projection development	827	169	8.05×10^{-13}	1.33×10^{-9}
GO:0048468	cell development	1884	287	6.93×10^{-12}	9.52×10^{-9}
GO:0048858	cell projection morphogenesis	583	131	2.21×10^{-11}	2.48×10^{-8}
GO:0016358	dendrite development	195	63	2.40×10^{-11}	2.48×10^{-8}
GO:0030030	cell projection organization	1328	220	2.91×10^{-11}	2.58×10^{-8}
GO:0048812	neuron projection morphogenesis	568	128	3.13×10^{-11}	2.58×10^{-8}

Table 3.6. Top ten GO terms associated with blue module identified through WGCNA.

Shown for each pathway is the corresponding GO ID, pathway descriptor number of genes annotated to the pathway, the number of genes in our list in the pathway, uncorrected p-value and false discovery rate (FDR)-adjusted p-value. Pathways are ordered by significance.

GO Term	Description	No. of Genes in Pathway	No. of Genes in Module	P-Value	FDR
GO:0035864	response to potassium ion	14	5	2.03 x10^{-3}	1
GO:0001227	transcriptional repressor activity, RNA polymerase II transcription regulatory region sequence-specific binding	176	18	0.001	1
GO:0044212	transcription regulatory region DNA binding	769	53	0.001	1
GO:0000975	regulatory region DNA binding	771	53	0.001	1
GO:0001067	regulatory region nucleic acid binding	772	53	0.001	1
GO:1990837	sequence-specific double-stranded DNA binding	648	45	0.002	1
GO:0023019	signal transduction involved in regulation of gene expression	18	4	0.002	1
GO:0071889	14-3-3 protein binding	23	6	0.003	1
GO:0061180	mammary gland epithelium development	65	10	0.003	1
GO:0033865	nucleoside bisphosphate metabolic process	32	5	0.003	1

Table 3.7. Top ten GO terms associated with greenyellow module identified through WGCNA.

Shown for each pathway is the corresponding GO ID, pathway descriptor number of genes annotated to the pathway, the number of genes in our list in the pathway, uncorrected p-value and false discovery rate (FDR)-adjusted p-value. Pathways are ordered by significance.

GO Term	Description	No. of Genes in Pathway	No. of Genes in Module	P-Value	FDR
GO:0030182	neuron differentiation	1222	165	4.88×10^{-10}	2.01×10^{-6}
GO:0022008	neurogenesis	1439	185	5.60×10^{-10}	2.01×10^{-6}
GO:0048699	generation of neurons	1342	176	7.30×10^{-10}	2.01×10^{-6}
GO:0045595	regulation of cell differentiation	1483	170	5.41×10^{-8}	1.11×10^{-3}
GO:0048666	neuron development	972	134	7.46×10^{-8}	1.23×10^{-3}
GO:0007417	central nervous system development	891	116	1.92×10^{-7}	2.64×10^{-3}
GO:0045664	regulation of neuron differentiation	545	84	2.36×10^{-7}	2.68×10^{-3}
GO:0051960	regulation of nervous system development	753	106	2.68×10^{-7}	2.68×10^{-3}
GO:0050767	regulation of neurogenesis	665	96	2.94×10^{-7}	2.68×10^{-3}
GO:0048468	cell development	1884	209	3.77×10^{-7}	2.68×10^{-3}

Table 3.8. Top ten GO terms associated with red module identified through WGCNA.

Shown for each pathway is the corresponding GO ID, pathway descriptor number of genes annotated to the pathway, the number of genes in our list in the pathway, uncorrected p-value and false discovery rate (FDR)-adjusted p-value. Pathways are ordered by significance.

3.4.6 Trajectory Modelling

This section of the results covers the creation of the trajectory network, the identification of biological pathways that are contributing to this network and the gene interactions within the network.

3.4.6.1 Trajectory Inference

To further explore how DNA methylation changes throughout neuronal differentiation I undertook trajectory inference modelling to create a cellular lineage trajectory and create groups of probes which were becoming hyper- or hypomethylated throughout differentiation. To generate the lineage trajectory (figure 3.12A) principal component analysis was used to reduce the number of dimensions within the dataset whilst maintaining as much information as possible. The dataset was reduced to only contain the five percent most variable CpG probes (41,811 loci) and 14 principal components, of which the first two components explained 78% of the variation in the data. Once this was completed the pseudotime of the trajectory was estimated. The first two principal components were then used alongside pseudotime to plot the samples according to stage of differentiation/maturation (figure 3.12A). Samples within each cellular stage clustered together, with the exception of one Day 37 neuron sample, which clustered with the Day 58 neuron samples. This could indicate that this sample had aged quicker than the others in the same group; however, when I checked the "epigenetic age" of this sample, it was surprisingly the second youngest of the four Day 37 neuronal samples. To ensure this sample was not a general outlier I clustered all 14 samples based on Euclidean distance (prior to the trajectory inference analysis). This highlighted that this Day 37 sample was not an outlier in general and clustered together with the Day 58 samples (figure 3.13).

Using the pseudotime created in the lineage trajectory a GAM was fitted to cluster together and order probes by whether they are becoming progressively hypomethylated or hypermethylated throughout differentiation. Where blue represents progressive hypomethylation and red progressive hypermethylation it is not surprising to see that there are large numbers of probes that have progressive methylation changes over time (figure 3.12B). There are 4,206 probes becoming hypomethylated with time and 1,662 probes becoming hypermethylated across neuronal differentiation. The probe that undergoes the largest DNA methylation change over time is one that becomes progressively hypomethylated during differentiation and is not annotated to a gene using the University of California Santa Cruz (UCSC) repository (figure 3.12C) [271]. However, using the Genomic Regions Enrichment of Annotations Tool (GREAT) it was possible to determine the closest gene to this loci is that of C-C chemokine receptor type 7 (CCR7; table 3.9) [272].
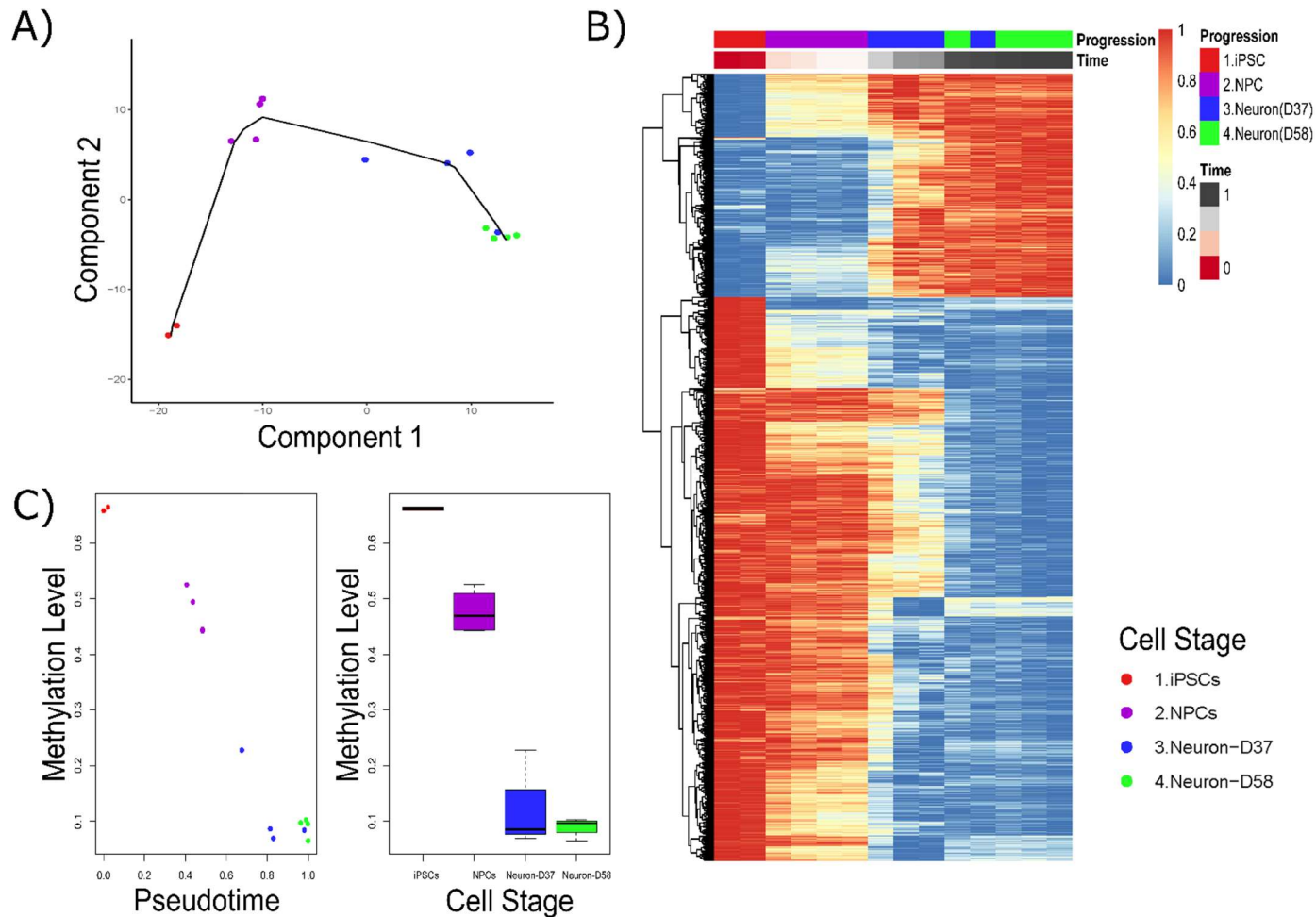
Figure 3.12. Trajectory modelling and module construction.

(A) To create the trajectory model dimensionality reduction was first performed, using PCA, followed by estimating pseudo-time to model the lineage trajectory using k-means clustering, a custom distance algorithm and principal curves. **(B)** Using the pseudo-time estimation a generalised additive model was used to determine which probes were becoming hypo-methylated (blue) or hyper-methylated (red) over time. **(C)** DNA methylation changes occurring at the top differentially methylated probe throughout differentiation. Left: plot of β-value (y-axis) against pseudotime (x-axis) and right: plot of β-value (y-axis) against cellular stage (x-axis). Error bars are 1.5x IQR.

Probe ID	Direction of change	Uncorrected p-value	Bonferroni p-value	Chromosome	Genomic position	Illumina gene annotation (UCSC)	GREAT gene annotation
cg00908292	↓	1.71×10^{-13}	7.16×10^{-9}	17	38699009	-	CCR7 (+22714)
cg15190241	↓	1.11×10^{-12}	4.67×10^{-8}	1	168368506	-	TBX19 (+118229)
cg14171824	↓	2.02×10^{-12}	8.47×10^{-8}	1	2006656	PRKCZ	PRKCZ (+24748)
cg25653165	↓	3.16×10^{-12}	1.32×10^{-7}	5	179569548	RASGEF1C	RASGEF1C (-4200)
cg21105928	↓	3.17×10^{-12}	1.32×10^{-7}	15	40143956	GPR176	GPR176 (+69136)
cg04901527	↓	3.49×10^{-12}	1.46×10^{-7}	10	117832870	GFRA1	GFRA1 (+200108)
cg01933515	↓	4.67×10^{-12}	1.95×10^{-7}	14	96532698	C14orf132	C14orf132 (+27038)
cg24737914	↓	4.82×10^{-12}	2.02×10^{-7}	7	5739289	RNF216	RNF216 (+82080)
cg00177101	↓	5.46×10^{-12}	2.29×10^{-7}	9	120545390	-	TLR4 (+78741)
cg02331902	↓	5.82×10^{-12}	2.44×10^{-7}	5	90610303	-	ARRDC3 (+68872)
cg11702768	↓	9.47×10^{-12}	3.96×10^{-7}	9	34567202	CNTFR-AS1	CNTFR (+22532)
cg20109624	↓	1.04×10^{-11}	4.36×10^{-7}	16	81254265	PKD1L2	BCMO1 (-17787)
cg02268851	↓	1.23×10^{-11}	5.13×10^{-7}	11	47545207	CELF1	CELF1 (+332)
cg02603875	↓	1.27×10^{-11}	5.33×10^{-7}	5	152871549	GRIA1	GRIA1 (-182)
cg26181096	↓	1.39×10^{-11}	5.80×10^{-7}	22	41876619	ACO2	ACO2 (+11491)
cg01170387	↓	1.58×10^{-11}	6.62×10^{-7}	16	31076818	ZNF668	ZNF668 (-443)
cg17957761	↓	1.69×10^{-11}	7.09×10^{-7}	19	46478879	-	NOVA2 (-2076)
cg04314308	↑	1.99×10^{-11}	8.32×10^{-7}	19	19336150	NCAN	NCAN (+13369)
cg03534428	↓	2.14×10^{-11}	8.96×10^{-7}	19	42972740	LIPE-AS1	CXCL17 (-25541)
cg03724874	↓	2.22×10^{-11}	9.28×10^{-7}	3	111719291	TAGLN3	TAGLN3 (+1706)
cg13313697	↓	2.26×10^{-11}	9.44×10^{-7}	5	152870740	GRIA1	GRIA1 (-991)
cg12379611	↓	2.85×10^{-11}	1.19×10^{-6}	10	17045387	CUBN	CUBN (+126442)
cg13617441	↓	2.87×10^{-11}	1.20×10^{-6}	3	34886005	-	ARPP21 (-795872)
cg21762380	↓	3.10×10^{-11}	1.30×10^{-6}	9	93063697	LINC01508	DIRAS2 (+341688)
cg02103771	↑	3.45×10^{-11}	1.44×10^{-6}	12	113531238	DTX1	DTX1 (+35744)

cg00622618	↓	3.50×10^{-11}	1.46×10^{-6}	6	38288376	BTBD9	BTBD9 (+319323)
cg10859605	↑	3.61×10^{-11}	1.51×10^{-6}	8	30255368	RBPMS	RBPMS (+13342)
cg15167636	↓	3.62×10^{-11}	1.51×10^{-6}	12	90485193	-	ATP2B1 (-382586)
cg20780998	↓	3.71×10^{-11}	1.55×10^{-6}	X	12996931	-	TMSB4X (+3703)
cg08332866	↓	4.02×10^{-11}	1.68×10^{-6}	17	35017916	-	MRM1 (+59916)
cg16627786	↑	4.45×10^{-11}	1.86×10^{-6}	22	19711051	GP1BB	GP1BB (+584)
cg24135615	↓	4.71×10^{-11}	1.97×10^{-6}	17	37042201	LASP1	LASP1 (+16090)
cg08960385	↓	4.74×10^{-11}	1.98×10^{-6}	20	43367613	-	KCNK15 (-6807)
cg01956293	↓	4.76×10^{-11}	1.99×10^{-6}	2	145212605	ZEB2	ZEB2 (+66015)
cg02494279	↓	5.47×10^{-11}	2.29×10^{-6}	18	23395233	-	SS18 (+275355)
cg01079726	↓	5.71×10^{-11}	2.39×10^{-6}	14	100485682	-	EVL (-45932)
cg08811227	↓	6.15×10^{-11}	2.57×10^{-6}	16	24697469	-	TNRC6A (-43564)
cg19902443	↓	6.58×10^{-11}	2.75×10^{-6}	20	11899807	BTBD3	BTBD3 (+28332)
cg04122918	↓	6.63×10^{-11}	2.77×10^{-6}	14	73146313	DPF3	DPF3 (+214495)
cg27587033	↓	6.76×10^{-11}	2.83×10^{-6}	1	2006032	PRKCZ	PRKCZ (+24124)
cg24692861	↓	7.49×10^{-11}	3.13×10^{-6}	3	155524344	C3orf33	C3orf33 (-290)
cg02879029	↓	7.62×10^{-11}	3.19×10^{-6}	8	10829962	XKR6	PINX1 (-132577)
cg17835180	↓	8.07×10^{-11}	3.38×10^{-6}	X	12995592	-	TMSB4X (+2364)
cg16306978	↑	8.55×10^{-11}	3.58×10^{-6}	2	21266953	APOB	APOB (-9)
cg07584840	↓	8.84×10^{-11}	3.70×10^{-6}	12	94579928	PLXNC1	PLXNC1 (+37430)
cg06538238	↓	9.78×10^{-11}	4.09×10^{-6}	6	29588575	GABBR1	GABBR1 (+12386)
cg22334705	↓	1.04×10^{-10}	4.34×10^{-6}	14	60174988	RTN1	RTN1 (+162695)
cg18630264	↓	1.04×10^{-10}	4.36×10^{-6}	4	140707850	MAML3	MGST2 (+120929)
cg09972881	↑	1.05×10^{-10}	4.39×10^{-6}	12	53298822	KRT8	KRT8 (+21430)
cg13053505	↑	1.09×10^{-10}	4.57×10^{-6}	4	4854459	-	MSX1 (-6933)

Table 3.9. The top 50 of 5,866 probes comprising the epigenetic trajectory signature identified through general additive modelling.

Shown for each loci are its probe ID, direction of change (*i.e.* increasing(↑) or decreasing(↓) methylation), uncorrected p-value, bonferroni corrected p-value, the chromosome it resides on, its genomic position, the gene it is annotated to according to the Illumina (UCSC) manifest and the closest annotated gene via GREAT annotation, with distance upstream (+) or downstream (-) in bp. Probes are ordered by significance.
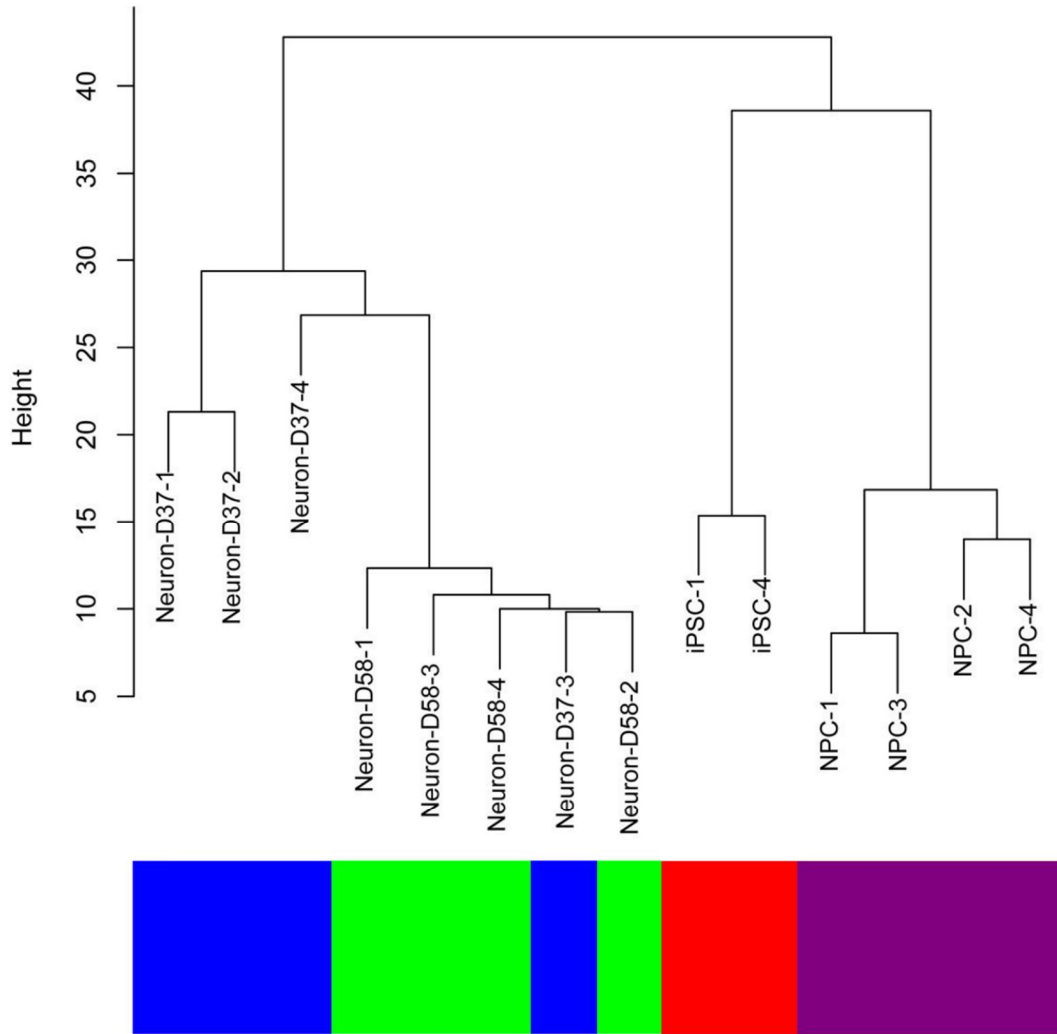
Figure 3.13. Clustering of samples based on Euclidean distance.

By calculating and clustering samples based on their Euclidean difference (prior to trajectory inference) it is clear that the D37 sample which clusters with the D58 samples is not a general outlier.

3.4.6.2 Pathway Analysis Implicates Development, Signalling and Transcription

In order to give meaning to the trajectory model and determine the functional implications of the probes on which it is based I used GO pathway analysis to identify the cellular pathways which are undergoing change during differentiation. To do this the loci that had the most significant methylation changes throughout differentiation were grouped together according to whether they were becoming progressively hypomethylated or hypermethylated over time (4,206 and 1,662 probes, respectively). The genes annotated to these probes were then searched in the GO repositories in order to find biological processes in which these genes are enriched. The progressively hypermethylated loci resided in genes that featured in pathways relating to head development, signalling, cell surface receptor signalling, transcriptional activity and cell-cell junctions (figures 3.14; table 3.10). The progressively hypomethylated loci were associated with neuron projection development, synaptic activity and gated channel activity (figures 3.15; table 3.11).

GO Term	GO Descriptor	Ontology	No. genes in pathway	No. genes in our list	P-value	FDR	Genes
GO:0000976	transcription regulatory region sequence-specific DNA binding	MF	777	71	6.45×10^{-9}	2.99×10^{-5}	NFAT5; SIX2; VAX1; JDP2; NACC2; GLIS1; DNMT3A; ELF3; FOXK1; FOXS1;
GO:0000977	RNA polymerase II regulatory region sequence-specific DNA binding	MF	725	67	1.12×10^{-8}	2.99×10^{-5}	NFAT5; SIX2; VAX1; JDP2; NACC2; GLIS1; DNMT3A; ELF3; FOXK1; FOXS1;
GO:0043565	sequence-specific DNA binding	MF	1088	86	1.31×10^{-8}	2.99×10^{-5}	NFAT5; SIX2; VAX1; FOXN3; FOXP4; JDP2; NACC2; GLIS1; DNMT3A; ELF3;
GO:1990837	sequence-specific double-stranded DNA binding	MF	819	72	1.53×10^{-8}	2.99×10^{-5}	NFAT5; SIX2; VAX1; JDP2; NACC2; GLIS1; DNMT3A; ELF3; FOXK1; FOXS1;
GO:0001012	RNA polymerase II regulatory region DNA binding	MF	731	67	1.69×10^{-8}	2.99×10^{-5}	NFAT5; SIX2; VAX1; JDP2; NACC2; GLIS1; DNMT3A; ELF3; FOXK1; FOXS1;
GO:0044212	transcription regulatory region DNA binding	MF	891	76	3.33×10^{-8}	4.80×10^{-5}	NFAT5; SIX2; RAI1; VAX1; JDP2; GABPB2; NACC2; GLIS1; DNMT3A; ELF3;
GO:0001067	regulatory region nucleic acid binding	MF	893	76	3.80×10^{-8}	4.80×10^{-5}	NFAT5; SIX2; RAI1; VAX1; JDP2; GABPB2; NACC2; GLIS1; DNMT3A; ELF3;
GO:0098609	cell-cell adhesion	BP	811	71	1.31×10^{-7}	1.27×10^{-3}	PTPRU; CDH16; MAD2L2; COL13A1; UNC5D; CLDN19; CTNND2; DSP; DTX1; GPC4
GO:0003690	double-stranded DNA binding	MF	909	74	1.32×10^{-7}	1.27×10^{-3}	NFAT5; SIX2; VAX1; JDP2; NACC2; GLIS1; DNMT3A; ELF3; FOXK1; FOXS1;
GO:0007155	cell adhesion	BP	1384	107	1.43×10^{-7}	1.27×10^{-3}	PTPRU; EDIL3; CDH16; PLXNC1; EFS; SPON2; SPON1; MAD2L2; EMID1; COL13A1;

Table 3.10. Results of GO pathway analysis of loci that become progressively hypermethylated through differentiation.

Shown is the top ten pathways identified through GO pathway analysis. For each pathway is the GO ID, pathway descriptor, number of genes annotated to the pathway, the number of genes in our list in the pathway, uncorrected p-value and false discovery rate (FDR)-adjusted p-value. Pathways are ordered by significance.

A)

REVIGO GO Biological Pathways Treemap

143

B)

REVIGO GO Molecular Function Treemap

C)

REVIGO GO Cellular Component Treemap
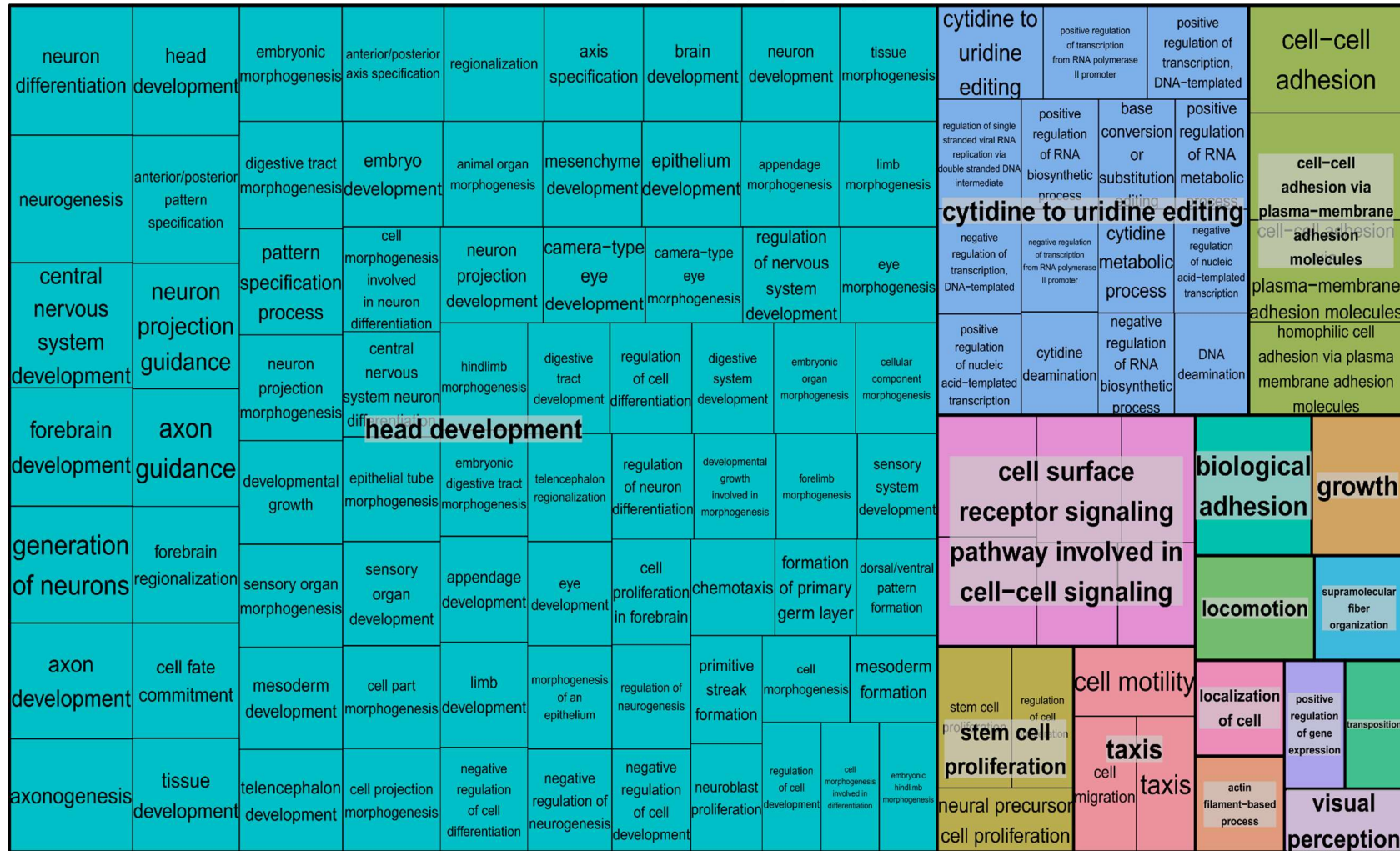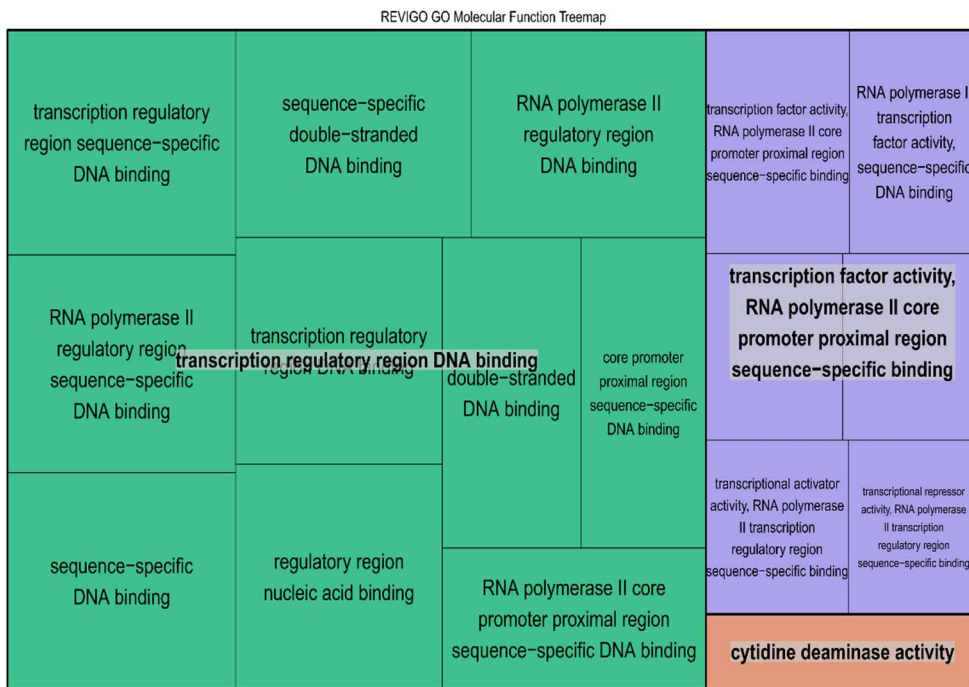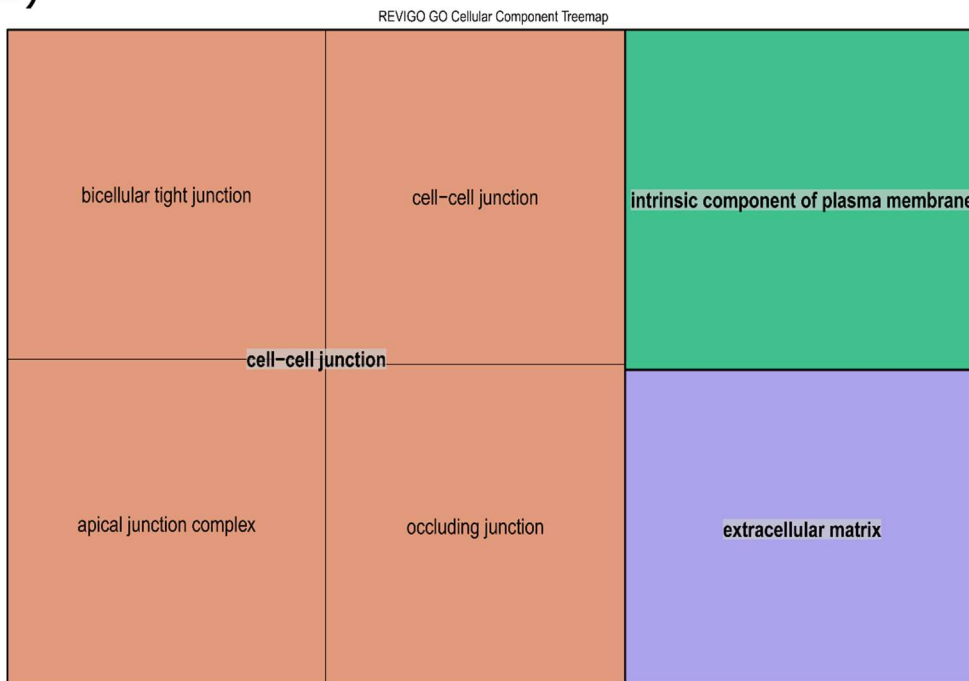
Figure 3.14. Pathway analysis of loci becoming progressively hypermethylated throughout differentiation.

Gene ontology (GO) enrichment analysis was performed on the 1,662 loci shown to become progressively hypermethylated throughout neuronal differentiation. Treemaps illustrating the pathways relating to **(A)** biological pathways (BP), **(B)** cellular components (CC) and **(C)** molecular functions (MF) that are changing throughout differentiation are shown. For each treemap, terms relating to the same pathway are grouped together and have been given the same colour, the term that summarises the grouped pathways is at the centre of each section and is written in bold text.

GO Term	GO Descriptor	Ontology	No. genes in pathway	No. genes in our list	P-value	FDR	Genes
GO:0097458	neuron part	CC	1686	293	3.46×10^{-11}	3.06×10^{-7}	CDH13; FARP1; KATNB1; CACNG3; BASP1; BAIAP2; ADCY2; PPARGC1A; STMN2; CIT;
GO:0045202	synapse	CC	1152	220	4.77×10^{-10}	2.11×10^{-6}	GPC6; CDH11; CDH13; FARP1; WASF2; APC2; RTN3; CACNG3; BAIAP2; NRG3;
GO:0048666	neuron development	BP	1069	209	1.09×10^{-9}	3.21×10^{-6}	FOXO6; CDH4; CDH11; FRY; PLXNC1; FARP1; UBE4B; CDKN1C; KATNB1; ADARB1;
GO:0043005	neuron projection	CC	1286	228	1.51×10^{-9}	3.35×10^{-6}	CDH13; FARP1; KATNB1; CACNG3; BASP1; BAIAP2; ADCY2; PPARGC1A; STMN2; FAM107A;
GO:0048858	cell projection morphogenesis	BP	635	142	2.58×10^{-8}	3.91×10^{-5}	CDH4; CDH11; PLXNC1; FARP1; WASF2; ADARB1; BAIAP2; SEMA4D; SEMA3C; B3GNT2;
GO:0048812	neuron projection morphogenesis	BP	620	139	2.70×10^{-8}	3.91×10^{-5}	CDH4; CDH11; PLXNC1; FARP1; ADARB1; BAIAP2; SEMA4D; SEMA3C; B3GNT2; ZFYVE27;
GO:0120039	plasma membrane bounded cell projection morphogenesis	BP	634	141	3.80×10^{-8}	3.91×10^{-5}	CDH4; CDH11; PLXNC1; FARP1; WASF2; ADARB1; BAIAP2; SEMA4D; SEMA3C; B3GNT2;
GO:0031175	neuron projection development	BP	939	183	3.89×10^{-8}	3.91×10^{-5}	FOXO6; CDH4; CDH11; FRY; PLXNC1; FARP1; UBE4B; KATNB1; ADARB1; SEC24B;
GO:0036477	somatodendritic compartment	CC	819	152	3.97×10^{-8}	3.91×10^{-5}	FARP1; KATNB1; CACNG3; BAIAP2; ADCY2; PPARGC1A; STMN2; CIT; CHRM5; TRIM9;
GO:0032990	cell part morphogenesis	BP	654	142	8.98×10^{-8}	7.46×10^{-5}	CDH4; CDH11; PLXNC1; FARP1; WASF2; ADARB1; BAIAP2; SEMA4D; SEMA3C; B3GNT2;

Table 3.11. Results of GO pathway analysis of loci that become progressively hypomethylated through differentiation.

Shown is the top ten pathways identified through GO pathway analysis. For each pathway is the GO ID, pathway descriptor, number of genes annotated to the pathway, the number of genes in our list in the pathway, uncorrected p-value and false discovery rate (FDR)-adjusted p-value. Pathways are ordered by significance.

A)

REVIGO GO Biological Pathways Treemap
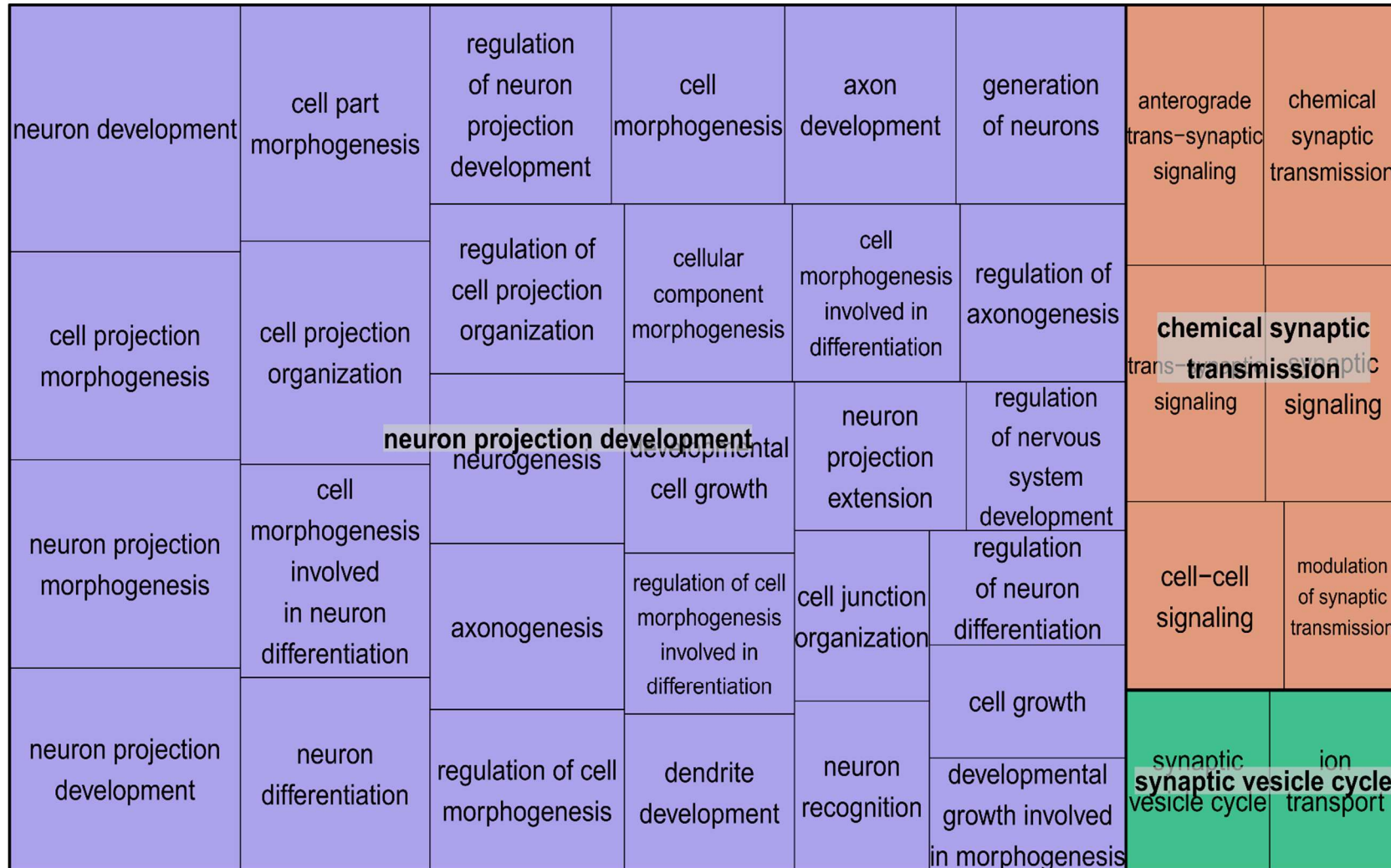
B)
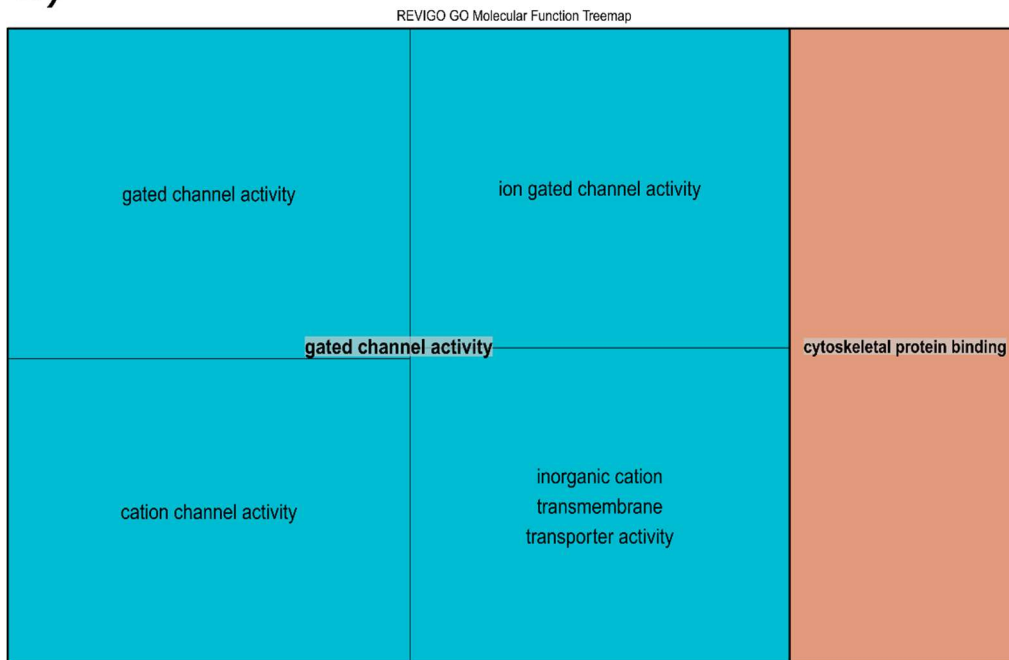
C)
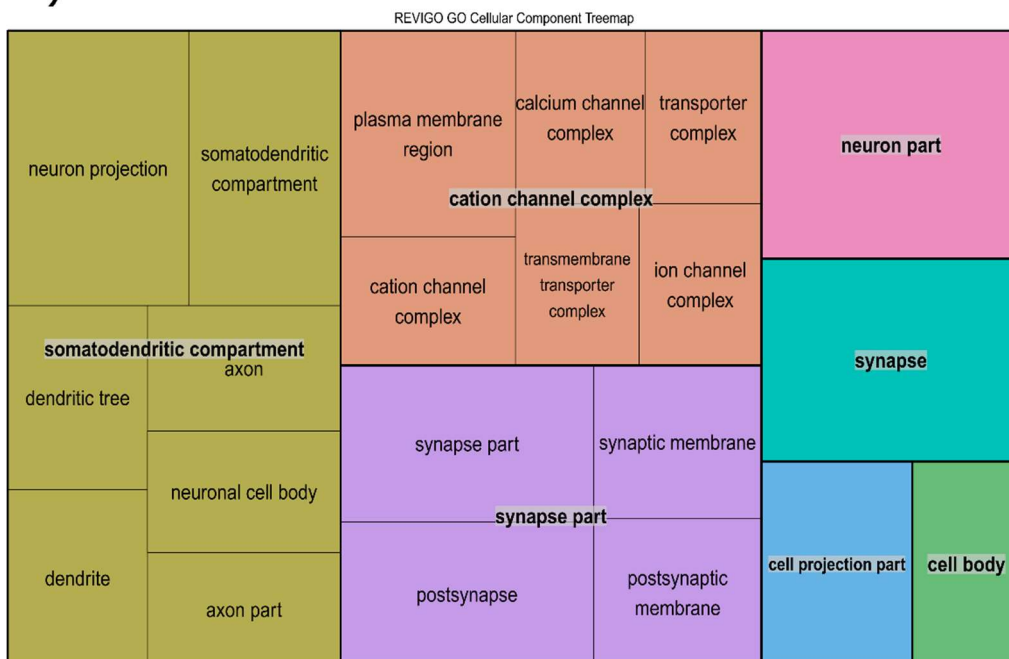
Figure 3.15. Pathway analysis of loci becoming progressively hypomethylated throughout differentiation.

Gene ontology (GO) enrichment analysis was performed on the 4,206 loci shown to become progressively hypomethylated throughout neuronal differentiation. Treemaps illustrating the pathways relating to **(A)** biological pathways (BP), **(B)** cellular components (CC) and **(C)** molecular functions (MF) that are changing throughout differentiation are shown. For each treemap, terms relating to the same pathway are grouped together and have been given the same colour, the term that summarises the grouped pathways is at the centre of each section and is written in bold text.

<u>3.4.6.3 Transcriptional Regulation is a Highly Interconnected Process</u>

<u>during Neuronal Differentiation</u>

To explore the connectivity between key genes that display progressive DNA methylomic changes through differentiation gene-gene interaction analyses were performed on the Bonferroni significant loci. Out of the 5,874 significant loci 2,352 loci were annotated to unique genes. From this a prior knowledge network (PKN) was obtained, which contained 602 genes and 1,158 interactions between these genes. Within this PKN there was only one SCC which was comprised of 50 genes and 138 interactions between them, so that every gene within the SCC can be reached through any other gene in the network (figure 3.16; table 3.12). This network analysis highlighted key genes within the network based on particular characteristics including their out-degree (the set of targets they regulate), in-degree (set of upstream regulating genes), betweenness centrality (most influential genes as determined by the shortest path lengths in the network) and their clustering coefficient (measure of tendency to cluster with other genes in the network). Interestingly, *STAT3, TCF7L2* and *LHX2* are the top genes based on their edge counts (number of upstream regulators) and their out-degree (number of downstream target genes). *STAT3* also has the highest betweenness centrality of 0.043 which suggests that it plays a large role within the network.

In order to ascertain more information about the functions of the top 50 most connected genes in the network a manual function search for each gene was undertaken. Of these top 50 genes 36 (72%) are involved in transcriptional regulation and include genes coding for proteins that are transcriptional activators, repressors and hormone receptor transcriptional regulators. Of these 36 genes 25 are specifically transcription factors which accounts for 50% of the

top 50 most connected genes. Interestingly, of the 22% of genes in the network that aren't involved in transcriptional regulation 14% are genes that are known to be involved in epigenetic regulation.

Gene name	Betweenness Centrality	Closeness Centrality	Clustering Coefficient	Edge Count	Indegree	Neighbourhood Connectivity	Outdegree	Function
STAT3	0.04345	0.37748	0.01997	71	9	9.43	62	Transcription factor
LHX2	0.01637	0.35092	0.00186	66	3	3.32	63	Transcription factor
CDKN1A	0.00058	1	0.0161	60	58	10.68	2	Cell cycle regulator
TCF7L2	0.0191	0.34628	0.01481	56	4	8.73	52	Transcription factor
ETS1	0.01263	0.29362	0.00716	52	4	6.37	48	Transcription factor
RUNX1	0.01469	0.30945	0.01568	43	7	8.5	36	Transcription factor
GATA4	0.01931	0.25409	0.03409	34	14	14.39	20	Transcription factor
SMAD3	0.00844	0.26041	0.0252	32	4	10.19	28	Transcriptional regulator
PAX6	0.01644	0.29865	0.02381	31	10	11.43	21	Transcription factor
SMARCA4	0.00607	0.30651	0.02094	30	1	10.86	29	Chromatin remodellor
KDM6B	0.00588	0.24575	0.01984	28	2	10.29	26	Histone demethylase
NR5A2	0.01974	0.2422	0.00833	26	4	7.84	22	Transcription factor
THRB	0	0.24009	0.00395	23	0	4	23	NHTR
BCL6	0.01245	0.28388	0.04978	23	11	16.64	12	Transcription factor
PPARGC1A	0.02024	0.25271	0.05952	22	11	17.52	11	Transcriptional coactivator
NFATC1	0.00469	0.24691	0.03095	22	6	13.24	16	Transcription factor
BMI1	0.00515	0.27404	0.02381	21	4	14.33	17	Chromatin remodellor
RARB	0.00132	1	0.00952	21	16	9.14	5	NHTR
ATF3	0.02981	0.31245	0.06053	21	11	17.3	10	Transcription factor
THRA	0	0.25391	0.00952	21	0	6.67	21	NHTR
BCL2	0	0	0.07368	20	20	22.15	0	Apoptosis inhibitor
RXRA	0.00212	0.26945	0.00263	20	1	6.65	19	Transcription factor

SALL4	0.00992	0.28897	0.0719	19	6	18.67	13	Transcription factor
NR4A1	0.00078	0.91667	0.04248	18	8	11.78	10	Transcription factor
ZBTB20	0.00028	0.23217	0.00327	18	1	7.17	17	Transcription factor
DNMT3B	0.00226	0.26586	0.03309	17	1	13.76	16	DNA methyltransferase
MEIS1	0.00807	0.26122	0.02917	17	9	13.19	8	Transcriptional activator
PBX1	0.01088	0.30764	0.07143	16	5	19.4	11	Transcription factor
HDAC4	0.00233	0.19141	0.01429	15	1	10.73	14	Histone deacetylase
NCOA2	0.0013	0.20809	0.01648	14	1	12.93	13	Transcriptional coactivator
CD44	0	0	0.09341	14	14	26.29	0	Cell surface receptor
COL2A1	0	0	0.00549	14	14	11.79	0	Component of collagen
BCL11B	0.01648	0.28445	0.02564	13	2	17.85	11	Transcriptional repressor
CHD7	0.00272	0.1532	0.01282	13	3	7.38	10	Chromatin remodellor
TEAD1	0.00104	0.17285	0.01923	13	1	9	12	Transcription factor
PAX3	0.00911	0.22896	0.02564	13	8	14.54	5	Transcription factor
KDM2B	0	0.26348	0	13	0	6.46	13	Histone demethylase
NCOR2	0.0005	0.20172	0.03846	13	2	14.69	11	Transcriptional corepressor
NR2F1	0.00139	0.23343	0.02273	12	1	11.92	11	NHTR
ERG	0.00477	0.26419	0.03788	12	3	14.75	9	Transcription factor
ESRRG	0.0016	0.2032	0.03636	12	4	13.09	8	NHTR
EGFR	0	0	0.05303	12	12	25.33	0	Cell surface receptor
EBF1	0.00132	0.17466	0.01515	12	4	12.58	8	Transcription factor
TCF4	0.00199	0.17328	0.04545	11	2	16.27	9	Transcription factor
ZBTB16	0.00846	0.26485	0.02727	11	7	12.18	4	Transcription factor
COL1A2	0	0	0.07273	11	11	23.82	0	Component of collagen
DNMT3A	0.00235	0.21081	0.00909	11	1	7.45	10	DNA methyltransferase

NR4A2	0.00108	0.68	0.02727	11	2	10.91	9	Transcription factor
SREBF2	0	1	0	11	0	2	11	Transcription factor
SOX5	0.00004	0.8125	0.00909	11	1	4.45	10	Transcription factor

Table 3.12. A subnetwork of 50 genes constituting the strongly connected component (SCC) in the gene-gene interaction network, highlighting the methylomic changes occuring throughout neuronal differentiation.

Using Cytoscape a SCC comprised of 50 genes was identified alongside information on the key features of these 50 genes. Shown for each gene is the betweenness centrality, closeness centrality, clustering coefficient, edge count, indegree, neighbourhood connectivity, outdegree and function (based on manually curated search. NHTR = nuclear hormone transcription regulator.
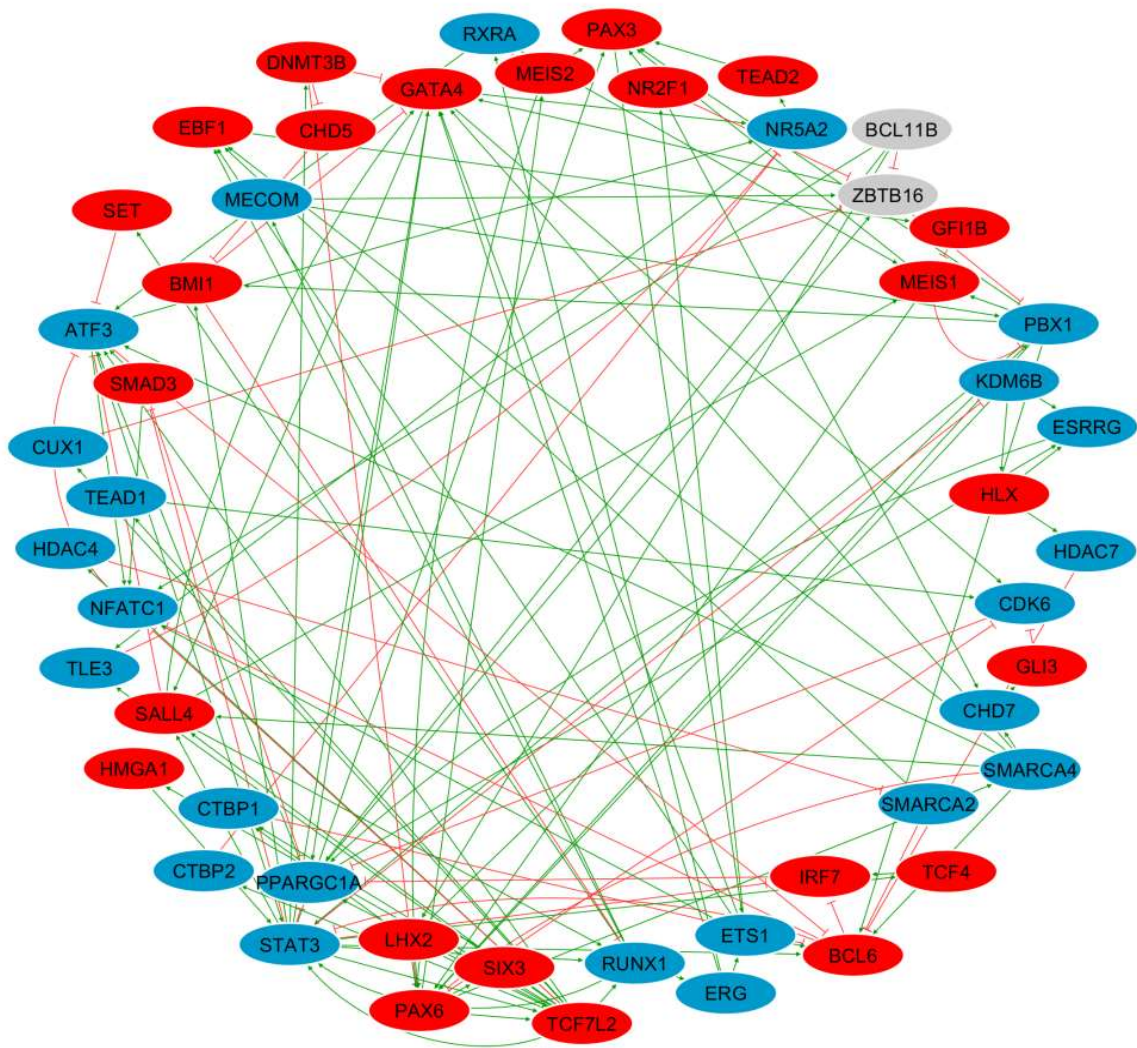
Figure 3.16. Network interactions of top 50 connected genes.

Interaction map depicting the connections between the top 50 most connected Bonferroni significant differentially methylated genes. Where orange lines indicate an inhibitory interaction, green lines indicate an activating interaction, blue ovals indicate genes becoming progressively hypomethylated, red ovals indicate genes becoming progressively hypermethylated and grey ovals indicate genes that have more than one probe annotated to them that have different patterns of methylation change.

3.5 Discussion

In this chapter I have undertaken epigenome wide analyses at base-pair resolution of the DNA methylation changes that occur as iPSCs differentiate into and then mature as neurons. To facilitate this samples from different cellular stages were collected, had DNA extracted and then run on the Illumina EPIC array to quantify DNA methylation levels at over 850,000 loci.

One of the first results of this study showed that stem cell derived neurons have an immature epigenome. This was determined using the Horvath epigenetic age calculator provides a biological age based on DNA methylation data. The highest epigenetic age from any sample from this study was -0.41 years, which would be representative of neurons of an embryo. This result is particularly interesting as neurons derived from this same iPSC line have been shown to be functionally mature and are able to fire mature action potentials at the time points used within this study [145]. In a study conducted by Mertens *et al*, they demonstrated that there are age-related expression changes to *RANBP17* and that neurons derived from stem cells had expression levels of *RANBP17,* which were comparable to embryonic or immature neurons. However, this was not the case with iNs, which are neurons generated directly from fibroblasts and do not undergo an intermediate stem cell phase [273]. Alongside the age-related expression changes to *RANBP17* iNs have also been shown to maintain their epigenetic age unlike the iPSC-derived neurons [169]. Another way it was originally believed may increase or accelerate the epigenetic age of iPSC-derived neurons was to use 3D or organoid models. It's reasonable to think that having the 3D interactions with cells neurons around them, which is more physiologically representative of a brain over 2D culture would increase the biological age. However, using

genome-wide, base-pair resolution DNA methylomic sequencing it has since been demonstrated that cerebral organoid models have a foetal methylomic profile [184]. This included the accumulation of methylation at non-CG loci in super-enhancers which corresponded to forthcoming transcriptional repression in the adult brain and the identification of demethylated regions during organoid development which overlapped with foetal brain regulatory elements [184].

Another important marker of maturity for cells is the number of cell divisions they have gone through. This is particularly of interest for this study as neurons are post-mitotic and therefore should no longer be undergoing cell division. To estimate the number of cell divisions the cells had undergone I used the MiAge calculator developed by Youn and Wang. This analysis demonstrated that after terminal differentiation the cells do indeed stop dividing which is as expected. This suggests that the terminal differentiation of these cells was successful and I have generated neurons which no longer undergo cell division. However, as the D37 samples in general had undergone more cell divisions than the D58 samples it could indicate some technical variation and perhaps suggest that the D37 and D58 samples were plated at different times and that the D37 samples spent longer as NPCs therefore undergoing more rounds of cell division.

It would be interesting to be able to extend this study to further time points to determine whether the epigenetic age of these cells will increase further whilst the mitotic age remains stable. In future studies using iPSC-derived neurons to study diseases of ageing it will be important to consider these metrics of maturity or at least take them into consideration when undertaking analyses.

Another finding to come from this chapter is that there is elevated CpH hemi-methylation in iPSCs when compared to the NPCs and terminally differentiated neurons, which is in concordance with previous literature [181, 274]. This may be a reflection that there are more dynamic gene expression changes occurring during the stem cell stage. However, hemi-methylation of non-CpG loci is also known to occur in neurons and is thought to accumulate during development [275-277]. The fact that it is not possible to see this hemi-methylation in the neuronal cells used in this chapter perhaps adds further evidence to the epigenetic immaturity of the neurons.

To understand the biological consequences of changing DNA methylation throughout differentiation WGCNA and pathway analyses were used to first group together modules of co-methylated loci and then to interrogate the function of these modules. These analyses produced four modules of co-methylated probes, three of which were modules enriched for pathways involved in the generation of neurons. This is to be expected and confirms that the cells I created through were neurons. What is interesting is that the red module, which is made up of genes becoming hypermethylated over time, has very similar pathways coming out to those within the black and blue models, which are made up of progressively hypomethylating genes. As hypomethylation is generally associated with increases in expression hypermethylation associated with decreases in gene expression it would suggest that there are several pathways which are associated with the development of neurons are undergoing increases and decreases in gene expression. This would make sense as there are many different processes and many large-scale changes which are necessary to create neurons. In addition, recent studies have suggested that the consequence of DNA

methylation on gene expression is context dependent and hypermethylation and so it is somewhat generalisable to predict that DNA hypermethylation leads to gene silencing [278, 279]. The other module pulled out through WGCNA and pathway analysis is the greenyellow module. Unlike the other three significant modules this module is associated with biological pathways involved in transcriptional regulation and signalling. As this module is associated with progressive hypomethylation over time it would suggest that there are many genes within these pathways becoming more expressed over time. This is intuitive as the genes that are expressed and the signalling pathways that are used within stem cells are very different from those expressed and used by neurons. It is however worth noting that none of the pathways in the greenyellow module passed FDR correction.

One interesting finding from the creation of the lineage network was that one of the day 37 terminally differentiated neurons clustered more closely with the day 58 terminally differentiated neurons over the other samples within the same cellular stage. This would suggest that this sample has aged quicker than the other samples in the group and is therefore more epigenetically mature. However, this may not be the case as this sample has the second lowest epigenetic age and lowest mitotic age of the day 37 neurons. This could mean that the probes used to determine epigenetic age are not contributing to or do not have a large part in distinguishing between the different cellular stages. This is somewhat logical considering the DNA methylation profile of 391 probes are used to estimate epigenetic age and I generated the trajectory model of the fifth percentile most variable probes, which equates to approximately 42,000 loci. On the other hand, as neurons do not undergo division the fact that the D37 sample is

indistinguishable from the D58 samples is also to be expected; if this sample has matured quicker than the rest of the samples in this group, it is intuitive that it undergone fewer cell divisions.

Similarly to the pathways highlighted in the WGCNA analysis, the pathways highlighted in the hypermethylating and hypomethylating probes in the lineage network are also largely involved in gene regulation and processes important to becoming a neuron. As the majority of Bonferroni significant differentially methylated loci are progressively hypomethylated over time it would suggest that there are more genes becoming expressed at an increased level as cells become more neuronal, although as discussed earlier this is context dependent and depends where the methylation falls within the gene.

From the gene-gene interaction network analysis I was able to generate a network of the 50 most connected genes which played an important role in the generation of the lineage trajectory. Of these genes *STAT3, TCF7L2* and *LHX2* were shown to be the most connected and therefore key genes in the network. These genes have been shown to play vital roles in neuronal survival and function. For example, *STAT3* and other members of the *JAK/STAT* pathway have been shown to play key roles in the control of neuronal proliferation, survival and differentiation [280, 281]. Cells which have been treated with STAT3 inhibitors were shown to be highly susceptible to these even at low concentrations [280]. *TCF7L2* is a transcription factor within the Wnt signalling pathway has been shown to play a crucial role in forebrain development and the regulation of neuronal identity [282]. Finally *LHX2* is homeobox transcriptional regulator that

has been shown to suppress astrogliogenesis in the developing hippocampus, thereby promoting neurogenesis [283] and has also been implicated in the regulation of β-catenin dependent cortical neurogenesis [284]. The implication of these genes in the gene-gene interaction network shows that there are many neuronal specific genes or genes that are highly involved in neuronal differentiation and survival that are key to creating the lineage trajectory and confirms that they are highly influential in the development and differentiation of neurons.

3.6 Conclusion

In this chapter I have characterised genome wide patterns of DNA methylation in order to further understand the epigenomic changes that are occurring throughout neuronal differentiation from iPSCs. I have shown that despite being functionally mature, the resultant neurons still have an immature epigenetic age but also that this epigenetic age does increase throughout differentiation. Although not epigenetically mature the terminally differentiated neurons do appear to have stopped dividing as the estimated number of cell divisions they have undergone does appear to have plateaued, although further time points would be needed to confirm this. In order to provide information on the functional implications of changing DNA methylation patterns I used trajectory inference and pathway analysis. Through these analyses it is clear that there are large amounts of loci undergoing significant DNA methylation changes over time, which are affecting gene regulation within the differentiating cells and that these loci are highly interconnected with one another.

Overall I have identified an epigenomic trajectory signature characteristic of neuronal differentiation and maturation. I have also demonstrated that there are several considerations when modelling epigenetic changes associated with age in iPSC-derived neurons, which should be taken into account in future research studies.

CHAPTER 4 : DETERMINING THE EFFECT OF EPIGENETIC MODULATORS ON DNA METHYLATION IN NEURONS AND MICROGLIA

4.1 Introduction

4.1.1 Histone Proteins

Within the nuclei of all eukaryotic cells can be found a complex interplay of DNA that is wound around octamers of core histone proteins which form nucleosomes. The wrapping of DNA around these histone proteins allows for the 10,000-20,000-fold reduction in DNA size which is necessary to fit the genome into the nucleus [285]. This level of chromatin compaction and therefore transcriptional ability is regulated by conformational changes to the histone proteins including, but not limited to, modifications such as methylation, acetylation, phosphorylation, ubiquitination and sumoylation [286]. These histone tail modifications regulate how easily accessible the transcription start sites (TSS) and other promoter regions within the DNA are to transcription factors and other cellular machinery that are necessary for the transcription of genes. This is achieved through the compaction (heterochromatin) or opening (euchromatin) of chromatin [287]. Methylation and acetylation of the histone tails are the most widely studies modifications. In general histone acetylation is associated with increased gene expression as the positive charge of the acetyl group repels the negative DNA causing it to have a more open conformation [288]. Histone methylation on the other hand can activate and repress gene expression depending on which amino acid has been methylated and how many methyl groups there are on the amino acids [289].

4.1.2 Epigenetic Modulators

There are numerous compounds that have been shown to have an effect through acting on epigenetic mechanisms. As this chapter focuses on the epigenetic

changes caused by different epigenetic modulators I have subsequently described the targets of each group of modulators that are studied in this chapter.

<u>4.1.2.1 Bromodomains</u>

A bromodomain (BRD) is a small (approximately 110) amino acid protein domain that has a conserved three-dimensional structure. Bromodomains recognise acetylated lysines on the N-terminal tails of histone proteins [290]. The domains adopt a bundle of four alpha helices and the differences in the loops can determine the specificity and affinity for different histone peptides and inhibitors [290]. There are 61 BRDs which are expressed in the human proteome, most of which recognise acetylated histone marks however, there are some BRDs that contain atypical domains that have little or no activity towards acetylated histone marks [291].

The modular nature and the diversity in domains has meant that studying the function of BRD-containing proteins has been quite difficult. They can contain a number of distinct reader domains in addition to having enzymatic functionality and playing the role of scaffolding proteins in the chromatin modifying complexes. However, using highly specific BRD inhibitors it is possible to untangle their complex biology and functional effects [291]. BRD inhibitors are a class of drugs that reversibly bind to the BRD regions of the Bromodomain and extra-terminal (BET) motif proteins BRD2, BRD3, BRD4 and BRDT and prevent the protein-protein interaction between the BET proteins and relevant transcription factors [292, 293]. This disruption of action can affect gene transcription and regulation. The development of very selective inhibitors have provided a way to study their

function and unravel the relationships between histone modifications, chromatin biology and DNA methylation.

To date the greatest success in designing BRD inhibitors has been against the BET subfamily of BRD containing proteins. This is largely due to their therapeutic potential for treating diseases such as cancer [294, 295]. The first of these inhibitors to be published was (+)-JQ1, which is a competitive inhibitor of acetylated lysine reading BRDs [296]. There are many more BRD inhibitors that have now published, including, but not limited to, SGC-BP30 which inhibits BRDs present in the histone acetyltransferase (HAT) p300 [297, 298], BI-9564 an inhibitor of the chromatin remodelling complexes BRD7 and BRD9 [299], and BAZ2-ICR which has been shown to inhibit the bromodomain adjacent to zinc-finger domain (BAZ2) chromatin remodelling complex [300].

4.1.2.2 Histone Protein Methyltransferases

Histone modifications, such as methylation, have been shown to be largely localised to areas of the genome that are actively transcribed, which could suggest their function is linked to polymerase activity [301-304]. These modifications also occur in a highly cell type specific manner at enhancers; although there does seem to be similar patterns of histone modifications at promoters between cell types [305]. This could suggest that enhancers are the most variable element of the transcriptional machinery and are what ultimately drives cell type specific gene expression patterns.

Mono-, di-, or tri-methylation of the histone tails has been shown to both induce transcriptional activation and repression as it is dependent on both the residue

164

that is methylated and also the level of methylation [306]. For example, in general lysine tri-methylation at histone 3 lysine 24 (H3K24), H3K36 and H3K79 have all been shown to be associated with active transcription and gene expression whereas lysine di-methylation at H3K9 is a known marker for transcriptional repression [307]. Arginine side chains can be modified through the addition of one methyl group or two methyl groups either symmetrically or asymmetrically. These lysine and arginine modifications are generally carried out by one of two protein families [306]. PR and SET domain proteins are protein lysine methyltransferases (PKMT) and methylate lysines on histone tails whilst the protein arginine methyltransferases (PRMT) such as the Rossman fold proteins modify arginines [308].

4.1.2.3 WD Repeat-Containing Proteins

WD repeat domain proteins are minimally conserved regions of approximately 40-60 amino acids that usually end with a tryptophan and aspartic acid (WD). They are involved in a variety of cellular processes including cell cycle progression, signal transduction, apoptosis and gene regulation.

In terms of epigenetic mechanisms, WD repeat domain 5 (WRD5) is the best characterised protein in terms of its interactions and binding partners. WRD5 has been shown to be a part of the mixed lineage leukaemia complex (MLL). As it is a part of the MLL complex it is involved in the methylation and demethylation of H3K4 [309], which represents a significant epigenetic tag for gene transcriptional activation. Interestingly, alone the WRD5-MLL proteins show little histone methylation activity, but this is greatly increased upon the formation of a larger protein complex [310]. CHD8, a chromatin remodelling enzyme, has been shown

to directly bind to WRD5, and this interaction is known to be responsible for the tri-methylation at the promoters of MLL target genes, which includes *HOXA2* [311]. Alongside binding proteins, WRD5 also has a RNA binding pocket that binds long non-coding RNAs, such as HOTTIP and NeST, facilitating gene transcription [312-314].

One known small molecule inhibitor of WRD5-MLL protein-protein interactions is OICR 9429 [315]. OICR 9429 has been shown to bind in the WRD5-interacting (WIN) peptide binding pocket, therefore disrupting WRD5's interaction with MLL at this same binding pocket [315]. OICR 9429 has demonstrated selective binding to WRD5 compared to other histone methyltransferases (HMTs) or pharmacologically relevant targets and can reduce the proliferation and even induce growth arrest in p30-overexpressing cancer cells [315].

4.1.2.4 Methyl Lysine Readers

Methyl lysine readers (KMR) recognise the methylated tails of histone proteins and are associated with transcriptional repression [316]. One common feature between the different proteins of the KMR family is the methylated lysine binding pocket that contains an "aromatic cage" of amino acids [317]. The KMR family is large, diverse, and has been shown to have relatively weak interactions with histones and not to have any enzymatic activity. As such it has made them a challenging family of proteins to develop chemical inhibitors for [318]. However, one KMR that now has a chemical probe inhibitor is lethal(3)malignant brain tumour-like protein 3 (L3MBTL3) [288]. *L3MBTL3* has been shown to play a role in haematopoiesis [319] and its deletion has also been implicated in diseases such as meduloblastoma [320]. UNC 1215, a potent inhibitor of L3MBTL3, binds

to an arginine residue within the "aromatic cage" binding pocket thus inhibiting its ability to bind methylated lysine residues [288].

4.1.2.5 Histone Lysine Demethylases (HKDM)

The first evidence that histone lysines underwent dynamic regulation in terms of their methylation came from Shi *et al.* in 2004, when they demonstrated that LSD1 uses flavin adenine dinucleotide as a cofactor to oxidise the methyl group on the histone tails into formaldehyde [321]. In this study it was also shown that LSD1 is relatively specific and only demethylates H3K4me1/2, but not H3K4me3 or other H3 lysine residues [321]. Genome-wide chromatin immunoprecipitation mapping has highlighted that LSD1 binds to the promoter and enhancer regions of genes regulating their expression [322, 323]. Through this regulation it is thought that LSD1 plays a role in numerous cellular functions including differentiation and stemness [308, 322, 323], senescence [324], and it has even been implicated in neurodegenerative disorders [325, 326].

The other HKDM targeted within this chapter is the Jumanji domain containing-3 (JMJD3) protein, which catalyses the demethylation of H3K27me2/3 and therefore is associated with increased expression of the genes regulated by that chromatin mark [327, 328]. Interestingly, JMJD3 is essential for stem cell differentiation into neuronal lineages; in the developing spinal cord H3K27me3 regulates the activity of BMP causing the interaction of JMJD3 with the SMAD1/4 transcription factors activating the BMP antagonist Noggin [329]. GSKJ4, an inhibitor of JMJD3, has been shown to mimic α-ketoglutarate binding to JMJD3 and therefore inhibiting it. When treated with GSKJ4, human primary

macrophages had reduced LPS-induced cytokine production therefore highlighting a potential role for JMJD3 in the inflammatory response [330].

4.2 Hypothesis and Aims

Previous work has demonstrated that the epigenetic modulators used in this chapter are known to inhibit proteins involved in different epigenetic mechanisms. Despite this, the epigenomic consequences of these compounds are unknown. Therefore, the hypothesis of this chapter is that these compounds have methylomic consequences on neurons and microglia and that these changes have functional implications on biological pathways.

In order to address this hypothesis this aims of this chapter are:

1. To treat two iPSC cell models with different drugs known to modulate epigenetic mechanisms.
2. To provide the first insight into the DNA methylation changes that are caused by these modulators.
3. To investigate the biological pathways being altered by these epigenetic modulators.

4.3 Methods

4.3.1 Cell Culture

The information in this section contains all the information necessary to grow, maintain and split the iPSC-derived neurons and microglia used in this chapter.

4.3.1.1 Sources of Cells

The iPSC-derived neuronal cells used in this study were grown, maintained and treated by Dr Elena Ribe and her team at the University of Oxford, UK in conjunction with collaborators at the Alzheimer's Research UK Oxford Drug Discovery Institute (ARUK ODDI), according to the protocol below.

The iPSC-derived microglial cells used in this study were grown, maintained and treated by Dr Sally Cowley and her team at the University of Oxford, UK in conjunction with collaborators at the ARUK ODDI, according to the protocol below.

4.3.1.2 Generation of Human iPSC-Derived Cortical Neurons

In this section I will describe the methods used to culture, maintain and differentiate iPSCs into neuronal cells. To generate the cortical neurons we used the iPSC line CTR M3 36S, which were derived from keratinocytes from a middle aged neurotypical male at Kings College London. The keratinocytes were reprogrammed into iPSCs using sendai virus and differentiated into cortical neurons using SMAD inhibition [331].

4.3.1.2.1 iPSC Culture

iPSCs were cultured at 37°C with 5% CO_2 under feeder-free conditions. iPSCs were cultured on 6-well plates (Nunc) that had been coated with Geltrex (Life Technologies) prior to plating and were maintained in 2mL E8F media (Life Technologies). Colonies were passaged when the culture reached approximately 80% confluency. To passage the cells the media was removed and the cells were washed with PBS, and detached using dispase (Life Technologies) by incubating at 37°C for three to four minutes. After this time the dispase was removed and the cells were gently washed with 2mL pre-warmed E8F media. To remove the cells from the base of the well they were gently scraped and pipetted up and down to break up the colonies, but not to reduce them to single cells. The cells were plated at approximately 10,000 cells per cm^2, after which they were returned to the incubator and left for a minimum of 48 hours before handling.

4.3.1.2.2 Neuronal Differentiation

The protocol for neuronal differentiation was adapted from Shi *et al*. 2012. iPSCs were passaged at high density using Versene from Lonza so the cells would be maintained as clusters. After twenty-four hours the SMAD inhibitors 1µM Dorsomorphin and 10µM SB (Sigma) were added to each well in 50% N2 medium (N2 supplemented in DMEM/F12 and 1% glutamax) and 50% B27 medium (B27 supplement in neurobasal medium with 1% glutamax) (all from Life Technologies). The N2/B27 media and SMAD inhibitors were replaced every day for the first seven days. After this, cells were dissociated using Accutase and replated in N2/B27 media containing 10µM Y-27632 Rock inhibitor (Abcam). Neuronal progenitors were plated onto wells coated in laminin for terminal differentiation of neurons at day 21 at 20,000 cells per cm^2 in B27 medium

containing 10µM DAPT and 10µM Rock inhibitor. After 48 hours from induction, the media was replaced with B27 media, the cells were maintained in this media and underwent a 50% media change every three days.

4.3.1.3 Generation of Human iPSC-Derived Microglia

In this section I will describe the methods used to culture, maintain and differentiate iPSCs into microglial cells.

4.3.1.3.1 iPSC Culture

iPSCs were cultured at $37^{\circ}C$ with 5% CO_2 under feeder free conditions. iPSCs were cultured on 6-well plates (Nunc) that had been coated with matrigel (BD Biosciences) prior to plating and were maintained in 2mL Oxford Essential-8 (Ox-E8) media (made in house). Colonies were passaged when the culture reached approximately 80% confluency. To passage the cells the media was removed and the cells were washed with PBS, and detached using dispase (Life Technologies) by incubating at $37^{\circ}C$ for three to four minutes. After this time the dispase was removed and the cells were gently washed with 2mL pre-warmed Ox-E8 media. To remove the cells from the base of the well, they were gently scraped and pipetted up and down to break up the colonies, but not to reduce them to single cells. The cells were plated at approximately 10,000 cells per cm^2, after which they were returned to the incubator and left for a minimum of 48 hours before handling.

4.3.1.3.2 Embryoid Body Formation by Spinning

Spin embryoid bodies were formed using AggreWells^{TM}800 (Stemcell Technologies). iPSCs were washed with PBS and harvested by incubating for

five minutes at 37°C in TrypLE Express (Gibco). The cells were mixed into single cell suspension in the TrypLE by pipetting up and down, collected into a 15mL falcon tube and were diluted 1:10 in PBS. Cells were then counted and spun down. After centrifugation the supernatant was removed, and the cell pellet tapped loose before being resuspended in mTeSR™-1 spin-EB medium. The mTeSR™-1 spin-EB medium consisted of mTeSR™-1 (Stem Cell Technologies), supplemented with 1mM Rock-inhibitor (Y27632; Calbiochem), 50ng/mL BMP-4 (Peprotech), 20ng/mL SCF (Miltenyi Biotec), 50ng/mL VEGF (Peprotech). For AggreWells™800 the plates were prepared by rinsing each AggreWell with PBS and aspirating the PBS. Next, 1mL mTeSR™-1 spin-EB medium was added to the AggreWells and this was centrifuged at 3,000 x g for one to two minutes to remove any microscopic air bubbles. After the plate had been prepared, of 4×10^6 cells were added per well. The plate containing the cells was then centrifuged at 800rpm for three minutes. After centrifugation, the cells in each well were examined to make sure they were evenly distributed across the base of the well. The plate was then left in the incubator for four days. Each day the EBs were fed with spin medium by gently removing 1mL spin medium from the well and gently replacing it by pipetting it in a drop wise manner down the side of each well using a pipette. To harvest the EBs on day four the contents of the wells were pipetted up and down several times using a 5mL serological pipette to dislodge the EBs from the microwells. The contents were taken up and transferred onto a 40μM cell strainer that was inverted over a 50mL falcon tube. The contents were washed out of the well several times with PBS and transferred onto the same cell strainer to collect and wash all EBs on the strainer. This way the EBs remained on top of the inverted strainer and the media/PBS passed through the strainer into the 50mL falcon tube below. The cell strainer containing the EBs was then

gently transferred and inverted over a new 50mL falcon tube so that the EBs were now on the underside of the strainer and could be collected into the new 50mL falcon tube, by passing differentiation media (contents described below) through the strainer. EBs could then be counted by transferring 50uL sample to a 96 well plate under a microscope.

4.3.1.3.2 Directed Differentiation to Produce Microglial Precursors

For differentiation, approximately ten EBs were transferred to one well of a six well plate in 3mL medium, two thirds of the medium were replaced every five days. The medium consisted of X-VIVO^{TM}15 (Lonza) supplemented with 100ng/mL M-CSF (Invitrogen), 25ng/mL IL-3 (R&D Systems), 2mM Glutamax (Invitrogen) 100U/mL penicillin and 100μg/mL streptomycin (Invitrogen) and 0.55mM β-mercaptoethanol (Invitrogen). Once precursors were visible in the supernatant of the cultures (two to three weeks post differentiation beginning), the non-adherent cells were harvested weekly from the supernatant of the EB cultures.

4.3.1.3.3 Microglial Culture and Maturation

Microglia were plated onto treated six well plates (Corning) at a density of 1.5×10^6 cells per well. They were maintained in media consisting of RPMI 1640 (PAA) with 10% fetal bovine serum (PAA), or in X-VIVO^{TM}15 (Lonza) where specifically stated. The medium was supplemented with 100 ng/mL (approx. 1.7×104 units/mL) recombinant human M-CSF (R&D Systems), as well as 2 mM glutamine (PAA), 100 U/mL penicillin and 100 μg/mL streptomycin (PAA). Monocytes were incubated at 37°C, with 5% CO_2 and differentiated for seven days prior to use.

4.3.1.4 Treatment of iPSC-derived Neurons and Microglia with Epigenetic Modulators

Cells were plated out into 36 wells of 6 or 12 well plates at a density of 7.5×10^5 cells per well for the iPSC-derived microglia and 3×10^5 for iPSC-derived neuronal cells. All compounds were used at a final concentration of 3μM (chosen due to the specificity and on-target effect in cells at this concentration) and were incubated on the cells for twenty-four hours. After this twenty-four hour period, each well was washed two times with PBS, which was then aspirated. The plates were then stored at -80°C until required for DNA extraction. The compounds used can be broadly split into five categories: bromodomain inhibitors, histone methyltransferase inhibitors, histone lysine demethylase inhibitors, methyl lysine reader inhibitors and WD40 containing protein inhibitors (table 4.1). Further details about each compound is available at: https://www.thesgc.org/chemical-probes.

An illustration detailing the experimental workflow can be found in figure 4.1 and information for each compound can be found in table 4.1.
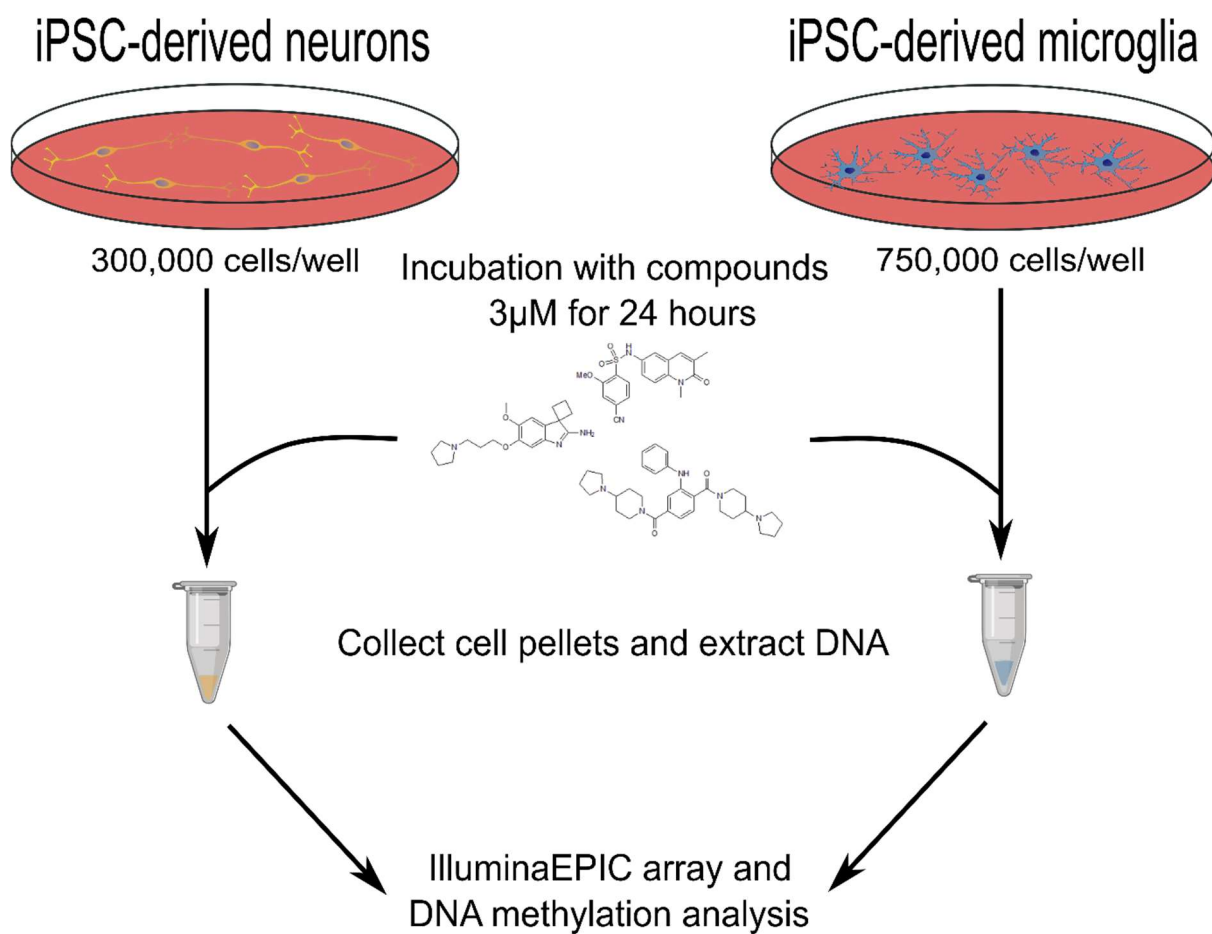
Figure 4.1. Diagram illustrating the experimental workflow.

iPSC-derived neurons and microglia were plated out at densities of 300,000 and 750,000 cells per well, respectively. Both cell types were treated with 29 compounds at 3µM or a DMSO control for 24 hours. Following incubation cells were washed twice in PBS and cells were collected and DNA extracted. Following extraction DNA methylation was quantified on the Illumina EPIC array.

Compound Class	Compound Name	Protein Target	Description
BRD	(+)-JQ1	BET family	Potent, selective BET bromodomain inhibitor
	BAY 299	BRPF2/TAF1	Potent and selective BRD1 and TAF1 inhibitor
	BAZ2-ICR	BAZ2A/2B	Selective BAZ2 inhibitor
	BI 9564	BRD9/7	Potent and selective BRD9 and BRD7 inhibitor
	GSK2801	BAZ2A/2B	Selective BAZ2A and BAZ2B inhibitor
	I-BRD9	BRD9	Potent and selective BRD9 inhibitor
	I-CBP 112	CREBBP/EP300	Selective CBP/p300 BRD inhibitor
	NI 57	BRPF1/2/3	Potent and selective BRPF bromodomain inhibitor
	NVS-CECR2-1	CECR2	Potent and selective inhibitor of CECR2
	OF 1	BRPF1/2/3	Selective BRPF1B and BRPF2 inhibitor
	PFI 3	SMARCA2/4	Potent and selective SMARCA2/4 and polybromo 1 inhibitor
	TP 472	BRD: BRD9/7	Potent BRD9/7 inhibitor
HKDM	GSK LSD 1 dihydrochloride	LSD1	Potent and selective LSD1 inhibitor
	GSKJ4	JMJD3/UTX	Histone KDM inhibitor
KMR	A 395	EED	EED inhibitor
	UNC 1215	L3MBTL3	Potent inhibitor of L3MBTL3 Kme reader domain
MT	A 196	SUV420H1/H2	SUV420H1 and H2 inhibitor
	A 366	G9a/GLP	Potent and selective G9a/GLP inhibitor
	BAY 598	SMYD2	SMYD2 inhibitor
	GSK343	EZH2	EZH2 inhibitor
	GSK591 dihydrochloride	PRMT5	Potent and selective PRMT5 inhibitor
	MS 023 dihydrochloride	PRMT type 1	Potent and selective type I PRMT inhibitor
	MS049 oxalate salt	PRMT4/6	Potent and selective PRMT4 and PRMT6 inhibitor
	RPFI 2 hydrochloride	SETD7	Potent and selective SETD7 inhibitor
	SGC 0946	DOT1L	Highly potent and selective DOT1L inhibitor
	SGC 707	PRMT3	Potent and selective allosteric inhibitor of PRMT3
	TP 064	PRMT4	Potent and selective PRMT4 inhibitor

	UNC 0642	G9a/GLP	Potent and selective G9a and GLP inhibitor
	UNC 1999	EZH2/H1	Potent and selective EZH2/EZH1 inhibitor
WD40	OICR 9429	WDR5	High affinity and selective WDR5 antagonist

Table 4.1. Compound information and description of each treatment.

Listed for each compound is the compound name, its protein target, a description of its action, the supplier it is available from and corresponding catalogue number where available. All compounds in this chapter were used at a concentration of 3µM and were incubated on the cells for 24 hours. Where BRD = bromodomain, KDM = histone lysine demethylase, KMR = methyllysine reader, HMT = histone methyltransferase and WD40 = WD repeat protein family. All compounds are available to buy from Tocris with the exception of A 395 and BAY 598, which were provided by ARUK ODDI and are not available to purchase commercially.

4.3.1.4 DNA Extraction and Methylomic Profiling and Quantification

Please refer to section 2.2 for information on DNA extraction, section 2.3 for details on bisulfite conversion and section 2.4 or figure 2.2 for a detailed outline of the EPIC array protocol.

4.3.2 Data QC

For an outline of the QC and normalisation methods used in this chapter please see section 2.4.2. All data analyses in this chapter were performed using R version 3.4.3. Signal intensities were imported into R using the methylumi package [262]. Initial QC checks were conducted using functions within the methylumi and wateRmelon packages [198, 262]. Using the default settings of one percent within "pfilter", no samples and 2,332 neuronal probes and 2,674 microglial probes were flagged for removal.

4.3.3 Data Analysis

Outlined in this section are the analysis steps conducted in order to assess and quantify the DNA methylation changes occurring when iPSC-derived neurons and microglia are treated with different compounds known to affect epigenetic mechanisms.

4.3.3.1 PCA

In order to look at variation within the dataset, PCA was used. Using the "prcomp" function within the default statistics package within R the top principal components were identified. These principal components were then correlated to known variables including treatment, ChipID and position on BeadChip, array plate (neurons only),

replicate, cell culture plate and the wells within the cell culture plate using spearman correlations.

4.3.3.2 Removing Confounding Variation using Combat

Using the "combat" function within the sva package [332] variation attributed to "replicate" within the microglial samples was removed as this was identified as a significant confounder using PCA (further details are provided below in section 4.4.2.6). For this analysis the batch covariate was replicate number and parametric adjustments were allowed.

4.3.3.3 Identifying DMPs associated with treatment

Linear regression was used to identify DMPs for each drug treatment by comparing each treatment individually to the control treatment (N=810,201 probes that passed QC). In order to investigate whether there was any overlap in differential DNA methylation between compounds with similar functions I used Pearson correlations to compare the effect sizes of the top 100 most significant probes for a given compound to their effect sizes for other compounds in that category using the "cor.test" function in R. Similarly, to explore whether there was an enrichment for the same direction of effect I used a sign test (an exact binomial test). I was also interested to investigate whether similar DNA methylation changes were induced by the compounds in the two different cell types. To this end, I used the sign test and Pearson's correlations to compare the effect sizes of the top 100 most significant DMPs treated with a given compound in one cell type, to their effect sizes in the other cell type.

4.3.3.4 GO Enrichment Analysis

Pathway analysis was used to give biological meaning to nominated CpG sites using the "gometh" function from the missMethyl package [265] alongside the GO repository. The "gometh" function was chosen as it adjusts for the number of CpGs per gene. This was only done in the microglial samples as there were too few consistently differentially methylated probes in the neuronal data. Given the low number of replicates no DMPs reached genome-wide significance. As such, I used a nominal p-value threshold for GO pathway analyses of $p<5.00 \times 10^{-4}$.

4.4 Results

4.4.1 Outcome of the QC Pipeline

This section outlines the results of the QC process undertaken in order to ensure the data was of sufficient quality before undertaking any subsequent analyses.

4.4.1.1 Median Methylated and Unmethylated Sample Intensities

To ensure that the signal intensities for each sample were above background level the methylumi package was used to quantify the fluorescent intensities for each probe [262]. The median methylated and unmethylated intensities were then plotted against one another for each sample colouring them according to either their ChipID (figure 4.2), their position on the BeadChip (figure 4.3), or which plate they were assayed in (neuronal samples only – figure 4.4). It appears that the BeadChip and the position within the Chip that the sample was run on do impact the median intensities, with the position on the BeadChip having a greater effect. In particular both the neuronal and microglial samples run at position R08C01 have the lowest median unmethylated intensities. However, the effect is not large enough to consider removing samples as all samples have median intensities above 1,000 and therefore were not excluded based on this metric.
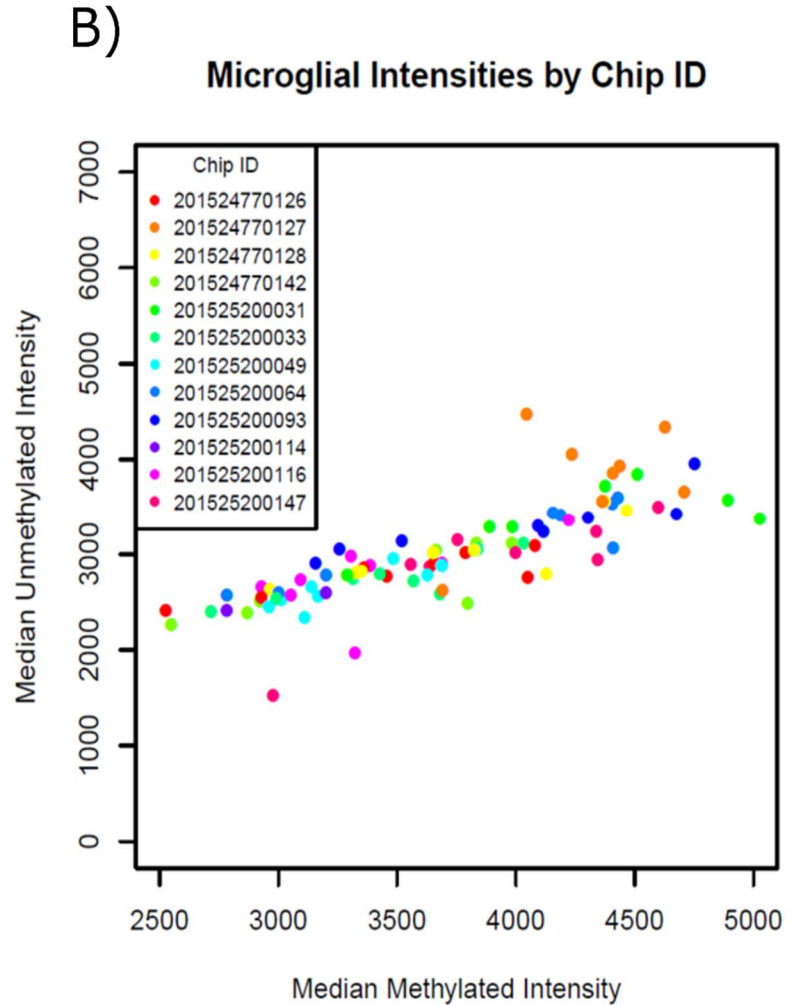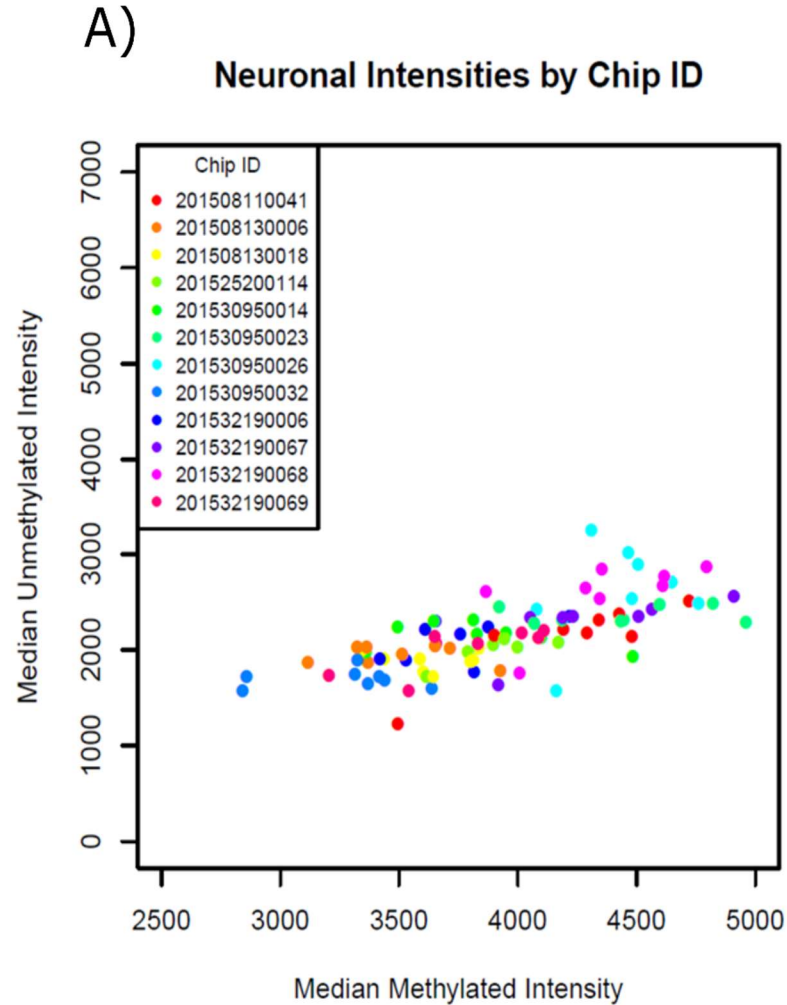
Figure 4.2. Median signal intensities plotted by BeadChip ID.

Intensities for each sample were imported using the methylumi package [262] and the median methylated and unmethylated sample intensities were calculated for each BeadChip. Median signal intensities are coloured by ChipID for the **(A)** neuronal and **(B)** microglial samples
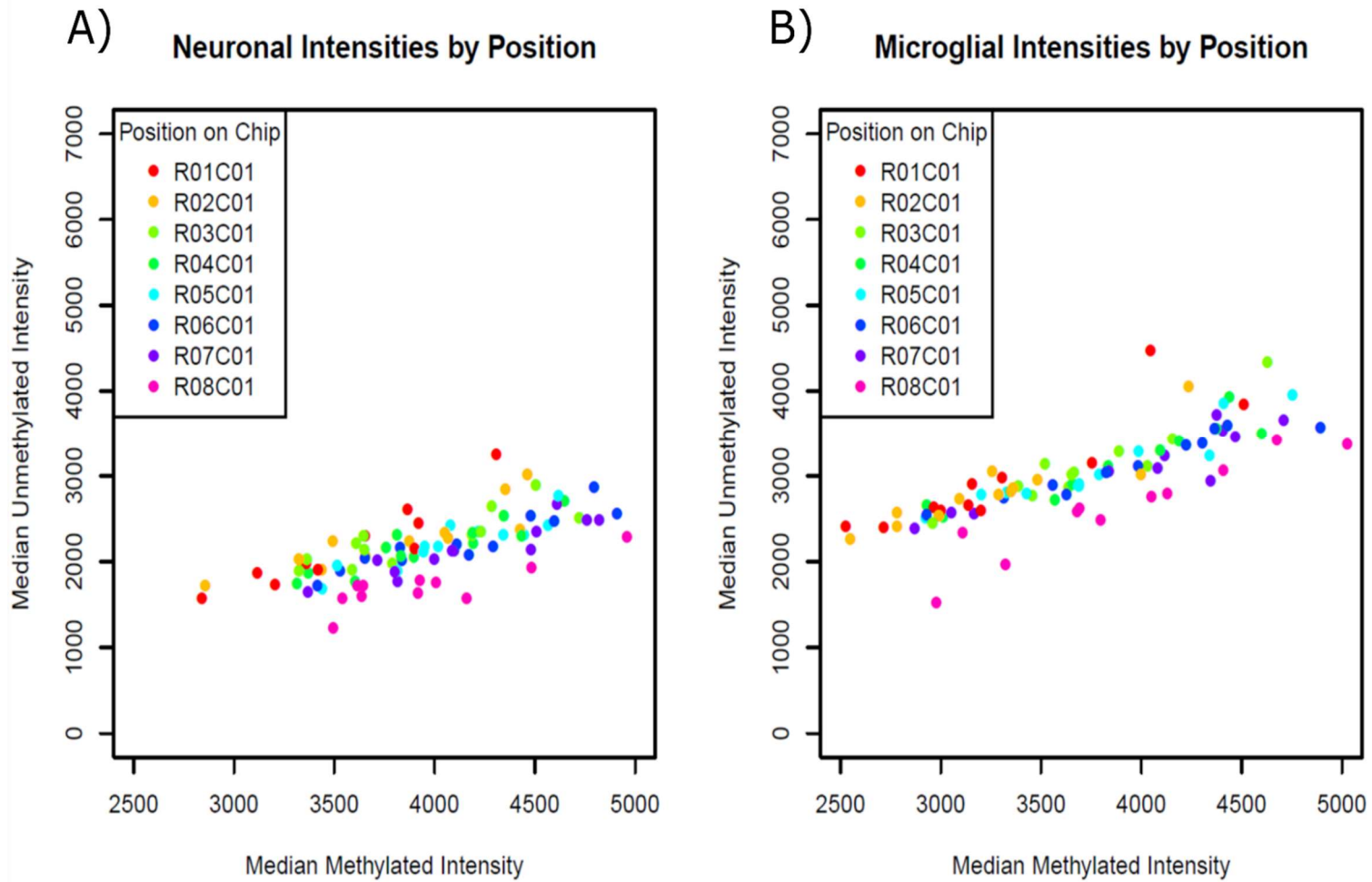
Figure 4.3. Median signal intensities plotted by position on the BeadChip.

Intensities for each sample were imported using the methylumi package [262] and the median methylated and unmethylated sample intensities were calculated for each position on the BeadChip. Median signal intensities are coloured by ChipID for the **(A)** neuronal and **(B)** microglial samples.
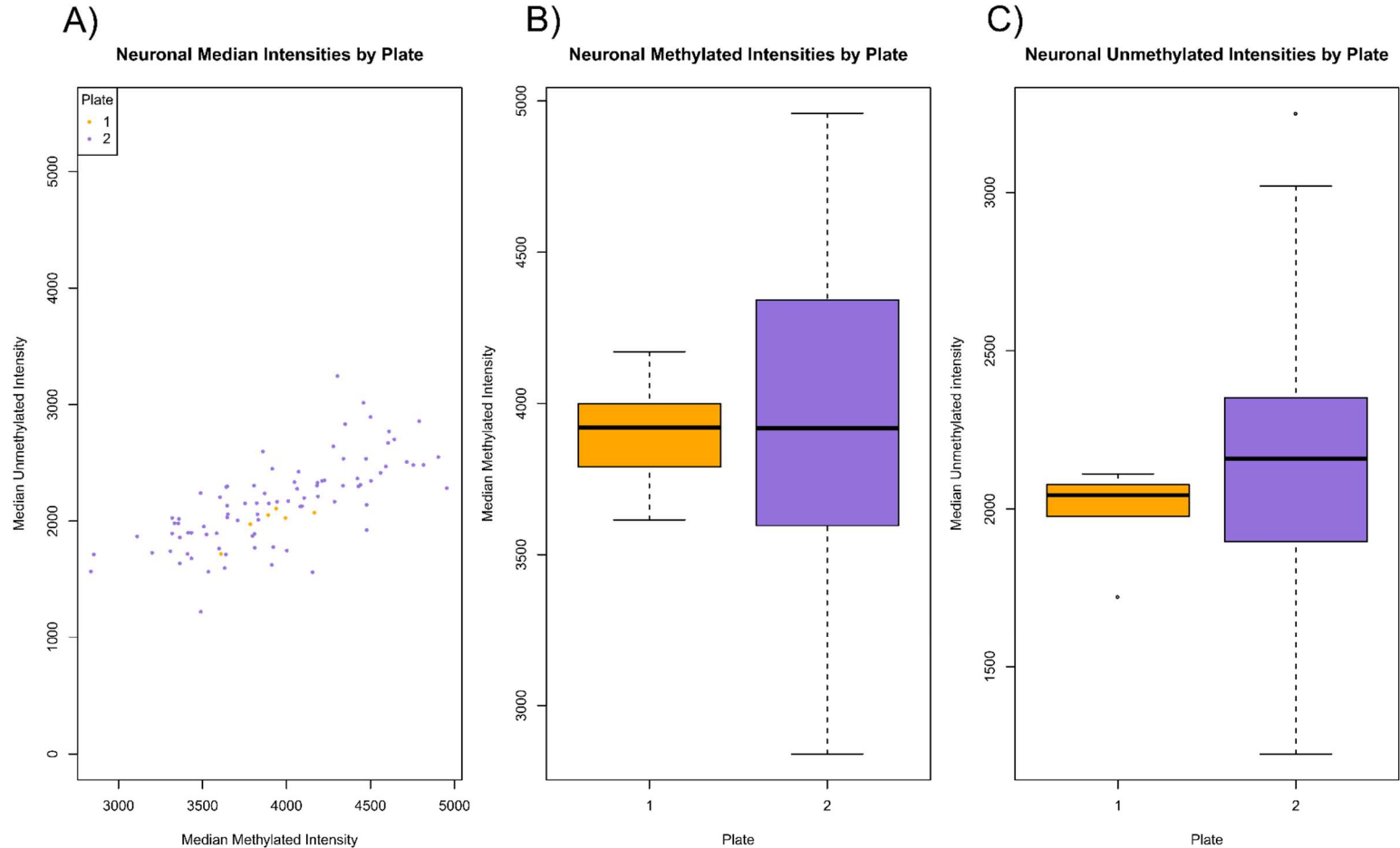
Figure 4.4. Median signal intensities plotted by plate processed in.

Intensities for each sample were imported using the methylumi package [262] and the median methylated and unmethylated sample intensities were calculated for each plate that the neuronal samples were processed in. Shown are **(A)** a scatterplot of the median signal intensities coloured by plate, median **(B)** methylated and **(C)** unmethylated signal intensities plotted by plate represented as a boxplots. As all of the microglial samples were all assayed on the same plate it was not necessary to check the association between plate and methylation intensity. Error bars represent 1.5x the IQR.

4.4.1.2 Bisulfite Conversion Efficiency of Samples

Bisulfite is the process that converts unmethylated cytosines into uracils and therefore allows them to be distinguished from methylated cytosines on the EPIC array. Within the EPIC array BeadChip there are several fully methylated control loci, which allow for the bisulfite conversion efficiency to be calculated. Using the "bscon" function within the R wateRmelon package [198] it is possible to convert the fluorescence intensity of these probes for each sample into an easy to understand percentage conversion efficiency. The lowest generally accepted bisulfite conversion efficiency is 80%, any samples which have a percentage conversion less than this should be removed. All of the samples within this study have a bisulfite conversion efficiency of greater than 92% and therefore do not need to be removed based on this metric (figure 4.5).

4.4.1.3 Neuronal and Microglial have a Bimodal Beta Density Distribution

To ensure our data fell within this metric the β-values for each sample were plotted as a beta density plot. It is clear that for the majority of loci within each sample this holds true (figure 4.6). Interestingly, it appears that the neuronal samples in general are more fully methylated (figure 4.6A) and the microglial samples more fully unmethylated (figure 4.6B).
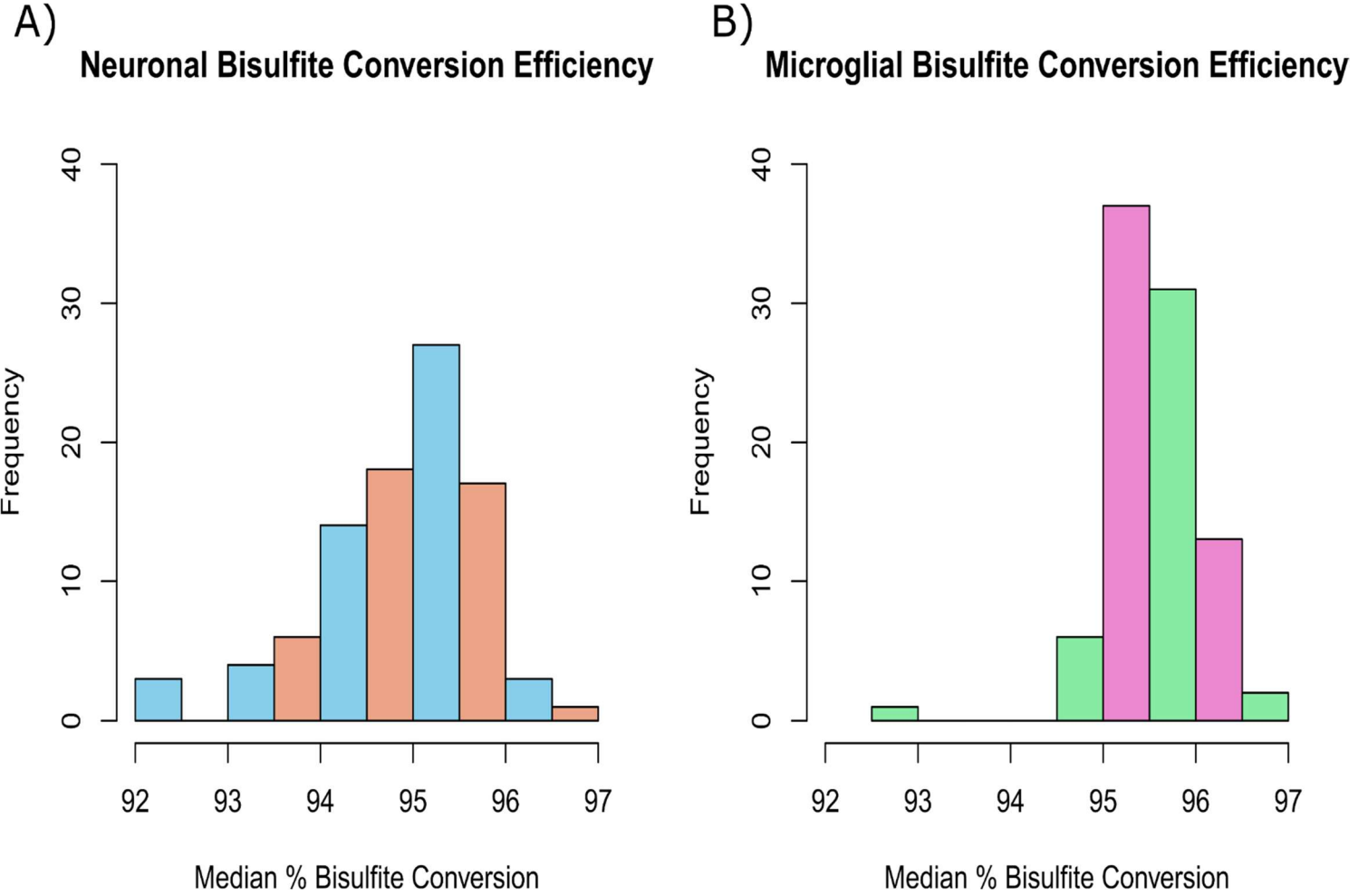
Figure 4.5. Bisulfite conversion efficiency for samples in the study.

Using the fully methylated probes within the array the bisulfite conversion efficiency of each sample was calculated using the "bscon" function in the wateRmelon package and represented as a histogram for the **(A)** neuronal and **(B)** microglial samples.
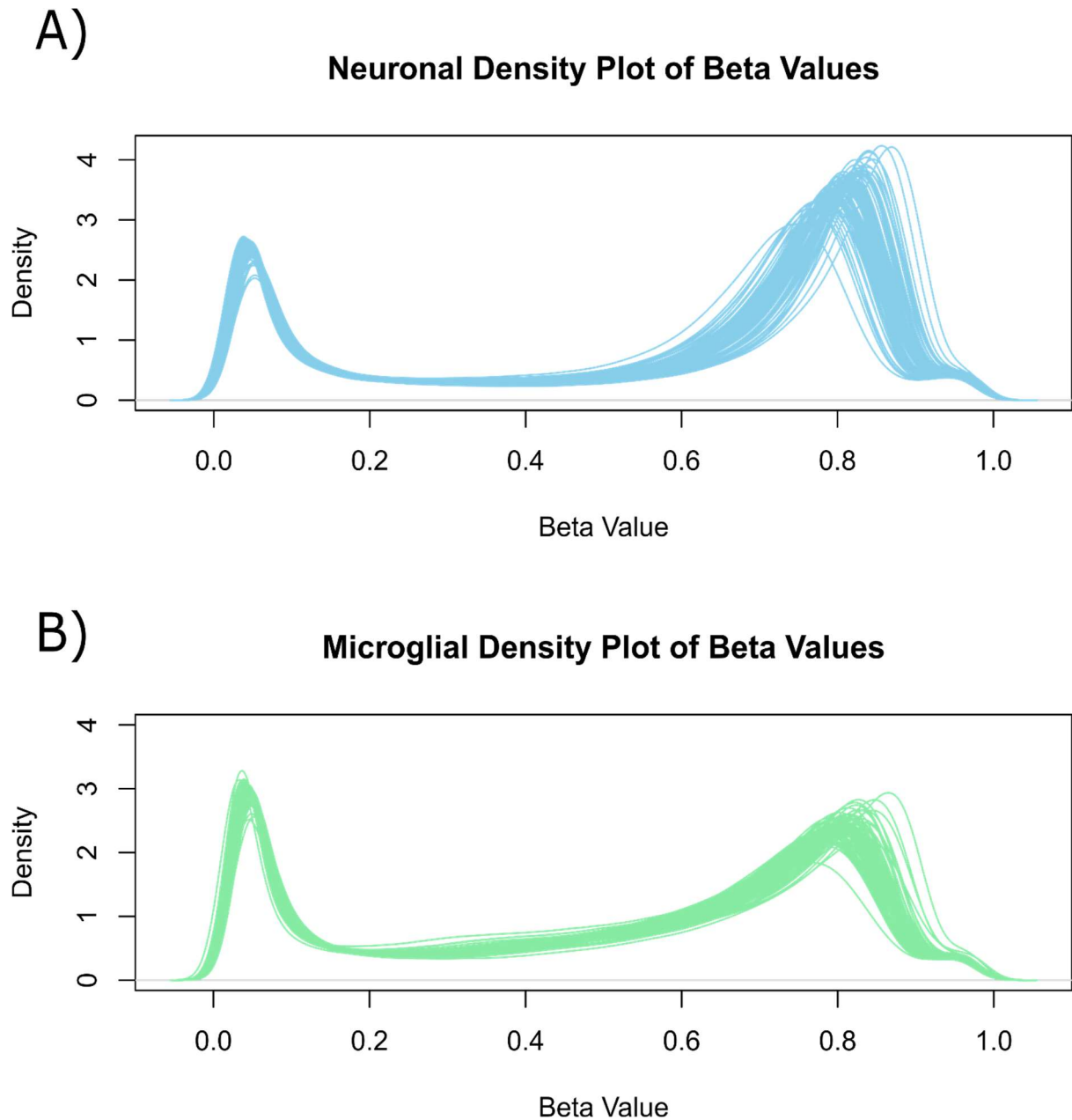
Figure 4.6. Beta-density plots for iPSC-derived neurons and microglia.

The DNA methylation level at each locus was determined using β-values, which are the ratio of fluorescence signal intensity for the methylated and unmethylated beads. The β-values of each probe in the **(A)** neuronal and **(B)** microglial samples were plotted on a beta density plot.

4.4.1.4 No Samples are Removed by P-filtering

The final stage of the QC pipeline is to filter samples and probes based on their detection p-value. Using the "pfilter" function within the wateRmelon package [198] samples that contained more than one percent (by default) probes above the 0.05 detection p-value threshold and probes with any samples having a beadcount less than three or more than one percent above the p-value threshold were removed. Using the default setting of one percent 524 sites that had a beadcount of less than three in five percent of samples and 1,708 sites having one percent with a detection p-value greater than 0.05 were removed from the neuronal samples. Similarly, 499 sites with a low bead count and 2,175 sites with a greater than one percent detection p-value were removed from the microglial samples. However, no whole samples were recommended for removal from either the neuronal or microglial samples.

4.4.2 Data Analysis

In this section I have described the results of the main analyses undertaken in this chapter.

4.4.2.1 iPSC-Derived Neurons have a Lower Epigenetic Age

Using the latest version of the epigenetic age calculator (available from: https://dnamage.genetics.ucla.edu/home) I assessed the epigenetic ages of the neuronal and microglial cells after the treatments with the different epigenetic modulators. Overall the iPSC-derived microglia (figure 4.7B) have a significantly higher epigenetic age than the neurons (p=4.88x10^{-3}, figure 4.7A), although all of the epigenetic ages are still representative of immature cells, with the highest epigenetic age of any of the microglial samples being only ~0.7 years (figure 4.7). There was no

significant difference between treatments within the same cell type as the differences seen between treatments are very small and there are large variations between replicates (neurons: p=0.182 and microglia: p=0.780). There are a couple of exceptions to this, for example the treatment UNC0642 has less variation in epigenetic age between replicates in both the neurons and microglia. There are also some treatments that seem to have a greater effect in the neuronal samples, for instance TP472 decreases epigenetic age in the neurons but not in microglia, where there is an increase in variation. Finally, it is also worth note that UNC1999 seems to cause the greatest consistent decrease in epigenetic age in the neuronal cells. Unfortunately, it was not possible to run the UNC1999 treatment on the EPIC array for the microglial cells.
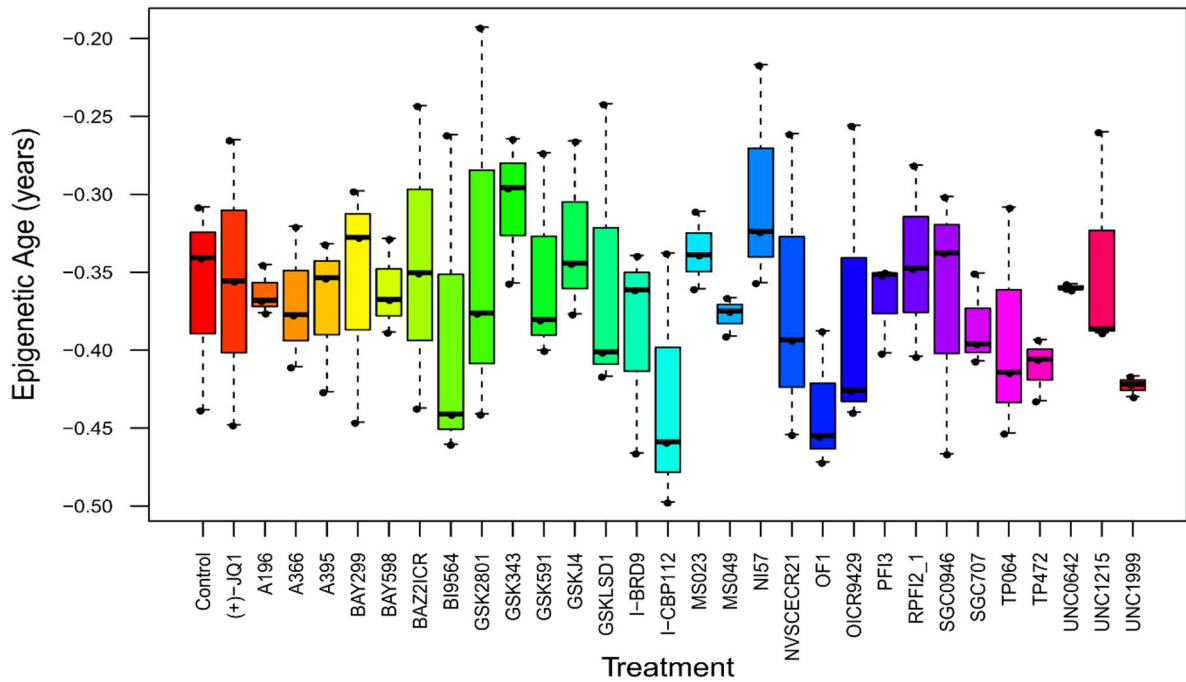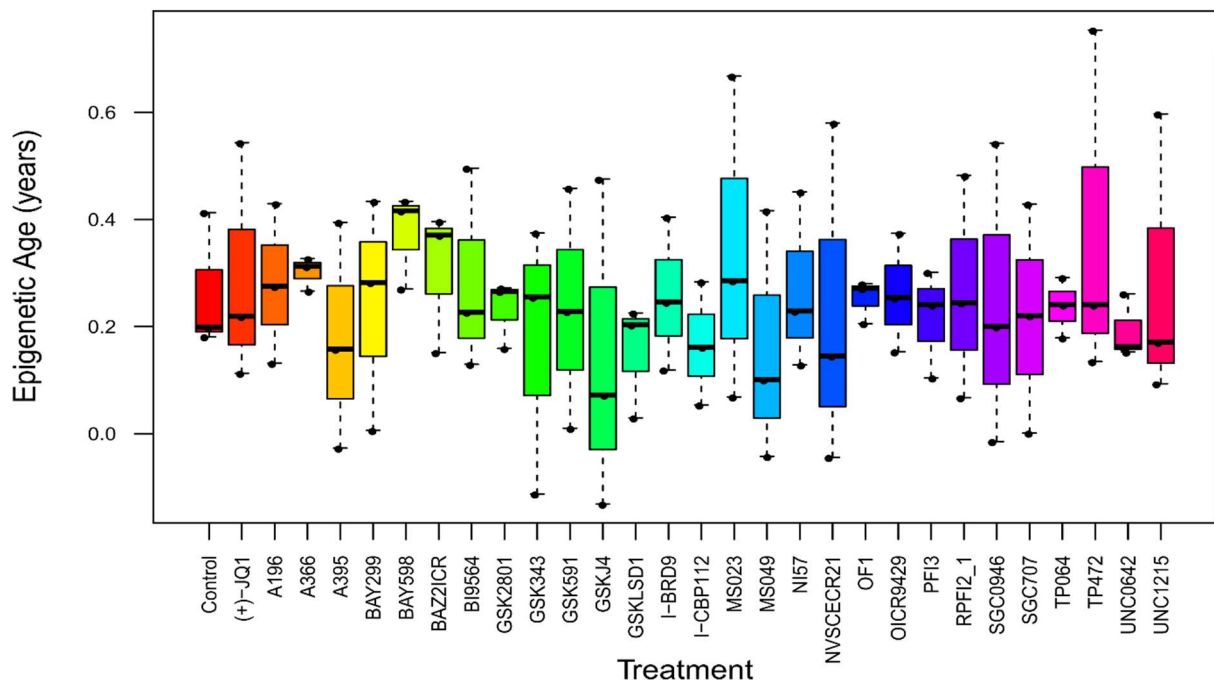
Figure 4.7. iPSC-derived neurons are epigenetically younger than iPSC-derived microglia.

Using the latest iteration of the Horvath epigenetic age calculator [126] the biological or epigenetic ages of each sample were derived. The estimated epigenetic age for each treatment in the **(A)** neuronal and **(B)** microglial samples were then plotted as a boxplot. Error bars represent 1.5x the IQR.

4.4.2.2 iPSC-Derived Microglia have Undergone more Cell Divisions

Using the coefficients of the MiAge calculator created by Youn and Wang [199] I estimated the number cell divisions each of the neuronal and microglial samples had gone through. It is clear that overall the microglial cells (figure 4.8B) had undergone significantly more rounds of cell division than the neuronal cells ($p=5.00 \times 10^{-3}$; figure 4.8A). The microglial control cells have undergone approximately 990 replications on average whereas the neuronal control cells have only been through approximately 450 divisions, less than half that of the microglia. There is also more variation within the microglial cells with some treatments, such as BAY598, causing there to be a 400 cell division spread, although this does seem to be driven by one replicate (figure 4.8B). Due to the large amount of variation in the microglial data it appears that the treatments have a more specific effect on the number of cell divisions in the neurons. For example, A395, GSK LSD1, MS023 and OF1 cause very little variation with there only being a difference of 12, 6, 11 and 7, respectively between the highest and lowest number of cell divisions within each treatment group. However, none of the treatments significantly affect the number of replications in either cell type (neurons: $p=0.266$, microglia: $p=0.414$)
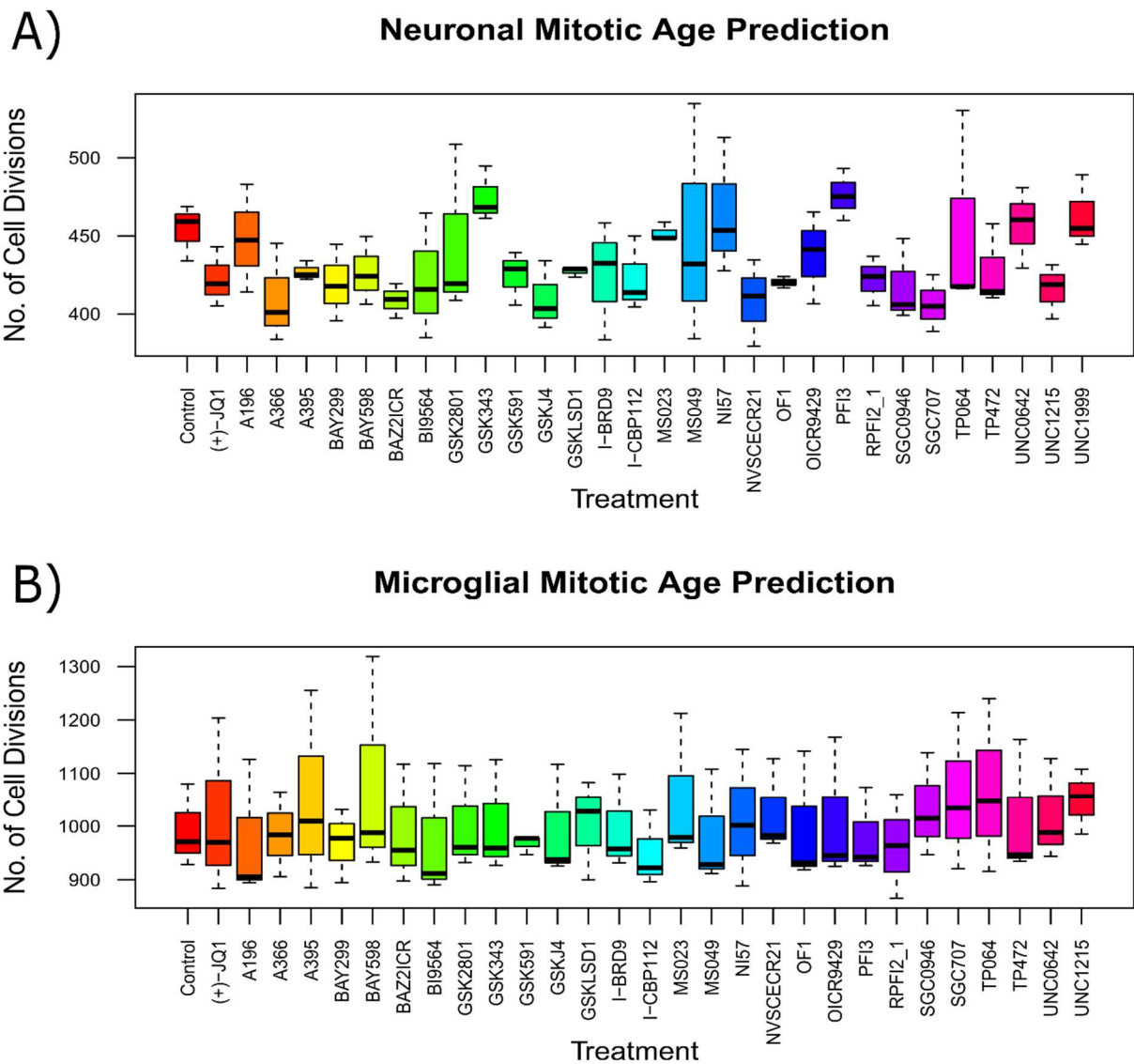
Figure 4.8. iPSC-derived microglia have undergone more rounds of cell division.

Using the coefficients of the MiAge calculator [199] the mitotic ages of each sample were derived. The estimated number of cell divisions for each treatment in the **(A)** neuronal and **(B)** microglial samples were estimated. Error bars represent 1.5x the IQR.

<u>4.4.2.3 Dasen Normalisation</u>

To make it possible to make meaningful comparisons between the data, the "dasen" normalisation function within the wateRmelon package [198] was used. Dasen involves quantile normalisation, which normalises the data by type I and type II probe background levels first. After dasen normalisation, the median methylated and unmethylated signal intensities have a smaller range and are therefore consistent across samples (figure 4.9). Through plotting the normalised β-values it is possible to see that they still have a bimodal distribution and that the unmethylated (β-value between 0 and 0.2) and methylated (β-value between 0.8 and 1) peaks are much more consistent, and this is especially true of the fully methylated probes.

By splitting the probes based on whether they are a type I or type II probe it is clear that for both the neuronal and microglial samples the type I probes contribute more to the unmethylated peak (β-value of less than 0.2; figure 4.10A and C) and the type II probes contribute more to the methylated peak (figure 4.10B and D). The type II microglial fully methylated peak (figure 4.10D) is also a lot smaller than that of the neuronal type II methylated peak (figure 4.10B). This would appear to be because there is an increase in hemi-methylation in the microglial type II probes. Finally, there is a split within the microglial type II fully methylated peak with there being two distinct groups forming.
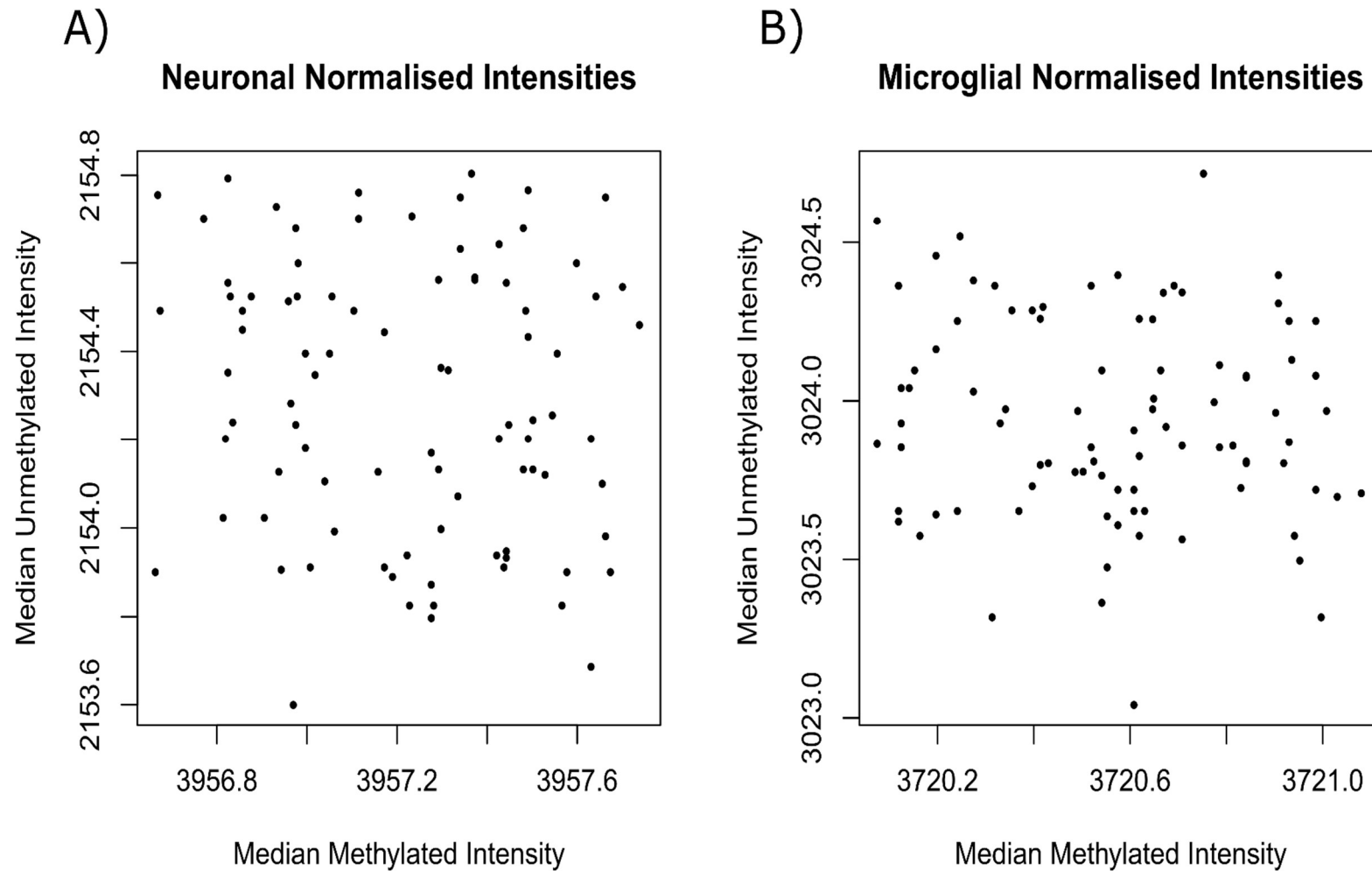
Figure 4.9. Median methylated and unmethylated sample intensities after dasen normalisation.

Quantile normalisation was performed using the dasen function within the wateRmelon package [198] to generate the normalised median methylated and unmethylated signal intensities. Graphical representation of median signal intensities relative to each other for the **(A)** neuronal and **(B)** microglial samples.

A)

Density Plot of Neuronal type I probes After Normalisation

B)

Density Plot of Neuronal type II probes After Normalisation

C)

Density Plot of Microglial type I probes After Normalisation

D)

Density Plot of Microglial type II probes After Normalisation
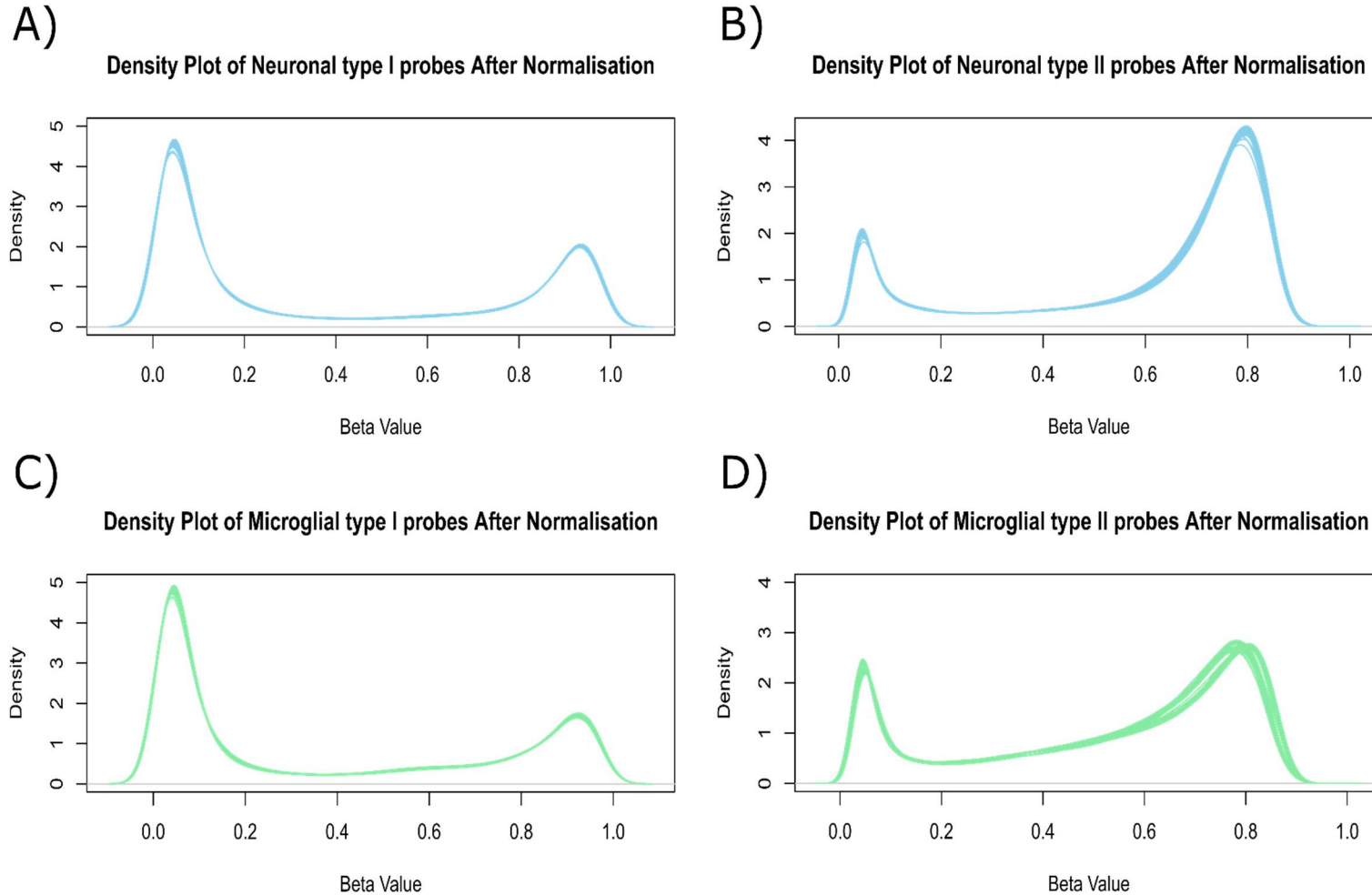
Figure 4.10. Median methylated and unmethylated sample intensities for type I and II probes after dasen normalisation.

Quantile normalisation was performed using dasen [198] to generate the normalised median methylated and unmethylated signal intensities. Probes were separated based on whether they were type I or type II probes and plotted individually. Density plots for **(A)** neuronal type I, **(B)** neuronal type II, **(C)** microglial type I and **(D)** microglial type II probes.

4.4.2.4 There is More Hemi-Methylation in the iPSC-Derived Microglia

Following dasen normalisation, neuronal and microglial probes that were hemi-methylated (having a β-value between 0.2 and 0.8) were extracted and plotted (figure 4.11). From this is it clear that there are a larger proportion of hemi-methylated probes in the microglial samples than that of the neuronal samples. Specifically, there are 512,850 hemi-methylated microglial probes and 476,870 hemi-methylated neuronal probes. In addition, the hemi-methylated probes have a lower β-value in the microglia samples than the neuronal samples, which could account for the smaller type II fully methylated peak in the microglia (figure 4.10D).
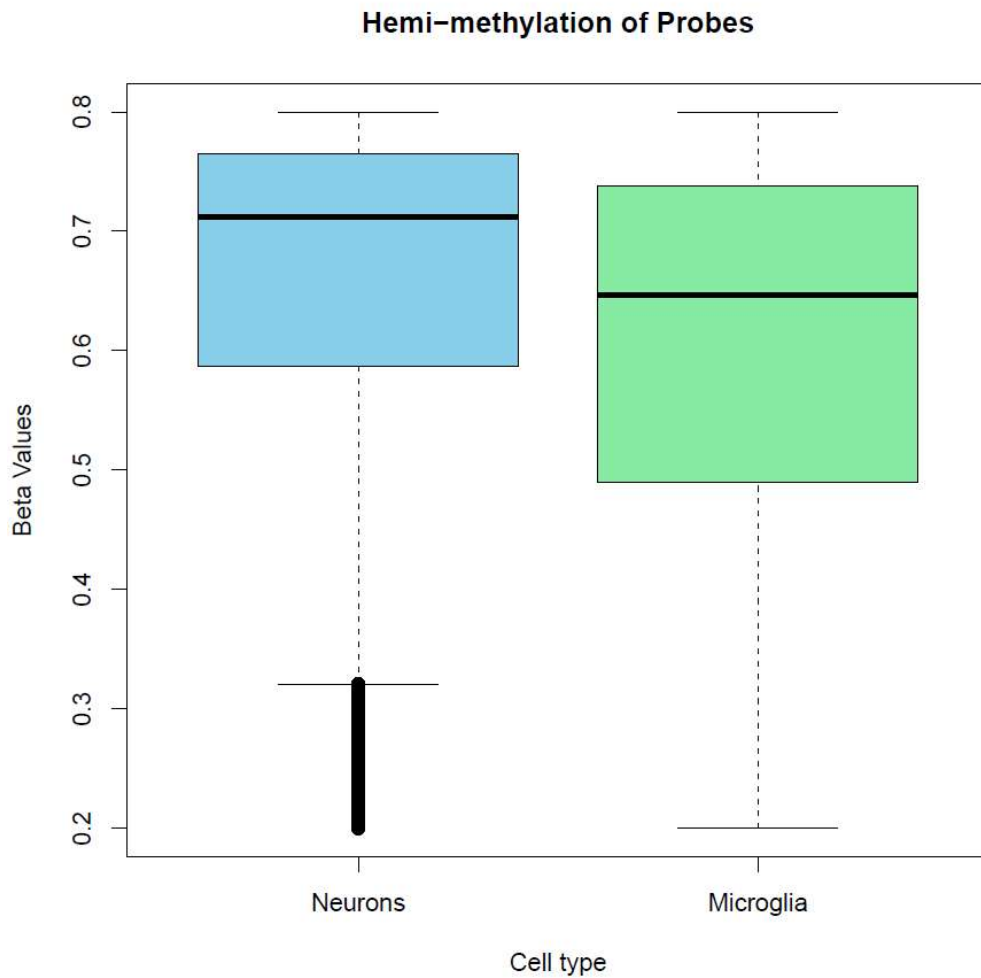
Figure 4.11. iPSC derived-microglial are more hemi-methylated than iPSC-derived neurons.

After dasen normalisation probes containing β-values between 0.2 and 0.8 (hemi-methylated probes) were then plotted, where blue represents the iPSC derived-neurons and green represents the iPSC derived-microglia. Error bars represent 1.5x the IQR.

4.4.2.5 PCA Identifies Variation within Data

Using the "prcomp" function within the default statistics package in R, principal components (PCs) that account for variation within each dataset were identified. The first five PCs were then correlated to known variables. From this it was determined that for the neuronal samples PC1 and PC3 correlate with the array plate the samples were run on, PC2 and PC4 correlate with the position on the BeadChip, and PC5 correlates with ChipID (figure 4.12A). PC1 accounts ~4.11%, PC2 accounts for ~2.72% and PC3 for ~1.92% of variation within the neuronal dataset (table 4.2). Within the microglial samples PC1 and PC2 both correlate with replicate and PC3 and PC4 correlate with position on BeadChip (figure 4.12B). In the microglial samples PC1 accounts for ~42.5%, PC2 for ~12.1% and PC3 for ~1.89% of variation within the data (table 4.3).

Following this, PC1 was plotted against PC2 for both the neuronal and microglial samples with each point being coloured by its corresponding replicate (figure 4.13). This further demonstrates that PC1 and PC2 are associated with replicate in the microglial samples, as the data points group together by replicate (figure 4.13B). There is no grouping of samples by replicate with the neuronal data (figure 4.13A).

	PC1	PC2	PC3	PC4	PC5	PC6	PC7	PC8	PC9	PC10
Standard deviation	4.55	3.70	3.36	3.11	2.88	2.77	2.74	2.68	2.59	2.53
Proportion of Variance	0.04	0.03	0.02	0.02	0.02	0.02	0.01	0.01	0.01	0.01
Cumulative Proportion	0.04	0.07	0.09	0.11	0.13	0.14	0.16	0.17	0.18	0.19674

Table 4.2. Variance explained by the first ten PCs in the neuronal dataset.

Shown for each PC is the standard deviation, proportion of variance explained and the cumulative proportion explained.

	PC1	PC2	PC3	PC4	PC5	PC6	PC7	PC8	PC9	PC10
Standard deviation	20.30	10.83	14.28	3.03	2.93	2.76	2.74	2.68	2.66	2.58
Proportion of Variance	0.42	0.12	0.02	0.01	0.01	0.01	0.01	0.01	0.01	0.01
Cumulative Proportion	0.42	0.55	0.56	0.57	0.58	0.59	0.60	0.61	0.61	0.62

Table 4.3. Variance explained by the first ten PCs in the microglial dataset.

Shown for each PC is the standard deviation, proportion of variance explained and the cumulative proportion explained.
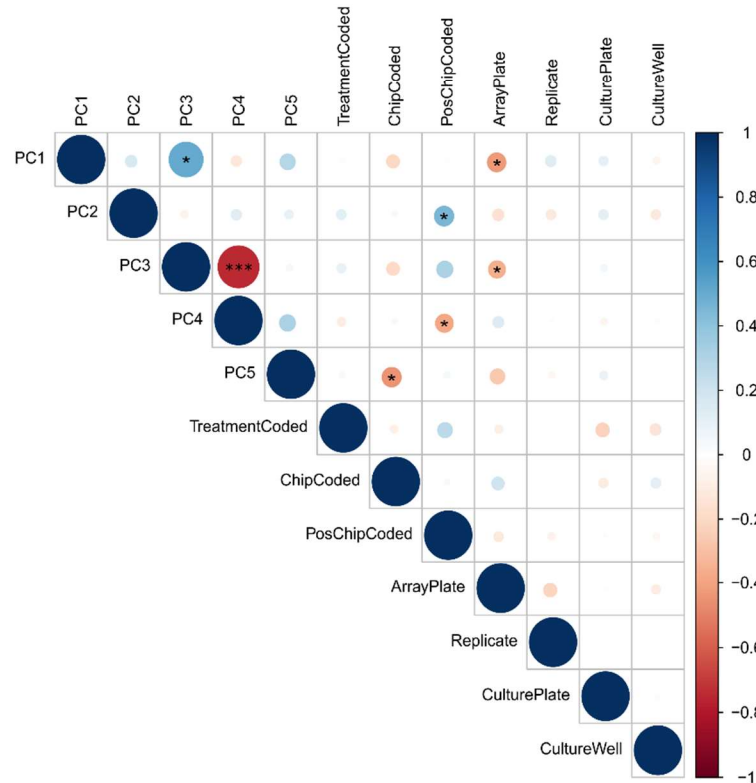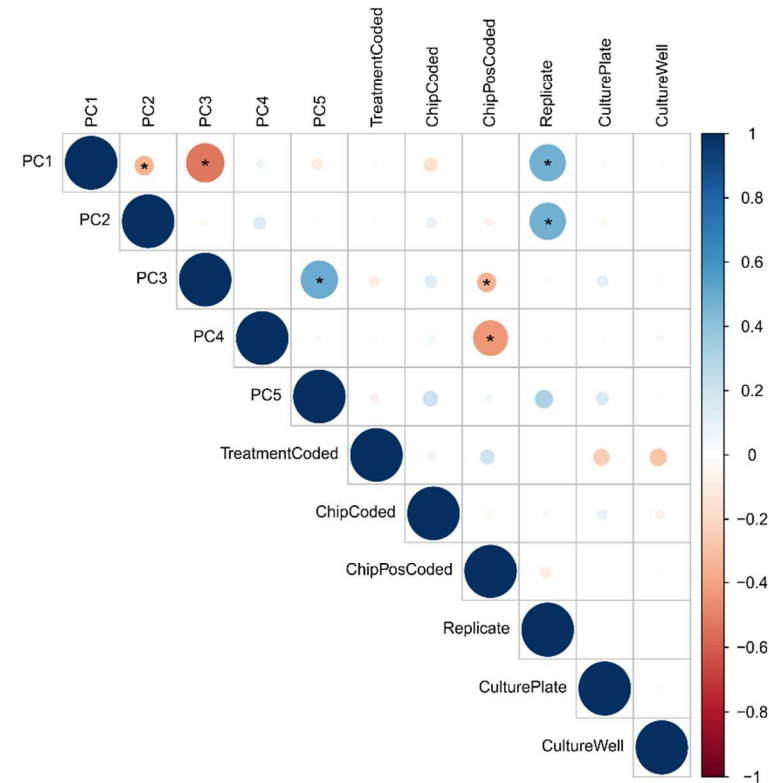
Figure 4.12. Variation in each dataset is identified using principal component analysis.

Using the "prcomp" function within the default statistics package the principal components accounting for variation within the dataset were identified. The first five principal components were then correlated and plotted against known variables for both **(A)** neuronal and **(B)** microglial samples. The known variables were treatment, ChipID, position on Chip, array plate (neurons only), replicate, cell culture plate and well within the cell culture plate. Where blue indicates a positive correlation, red indicates a negative correlation, *=p<0.001, **=p<1e-8 and ***=p<1e-10. The colour intensity and size of the circle are proportional to the correlation coefficients.
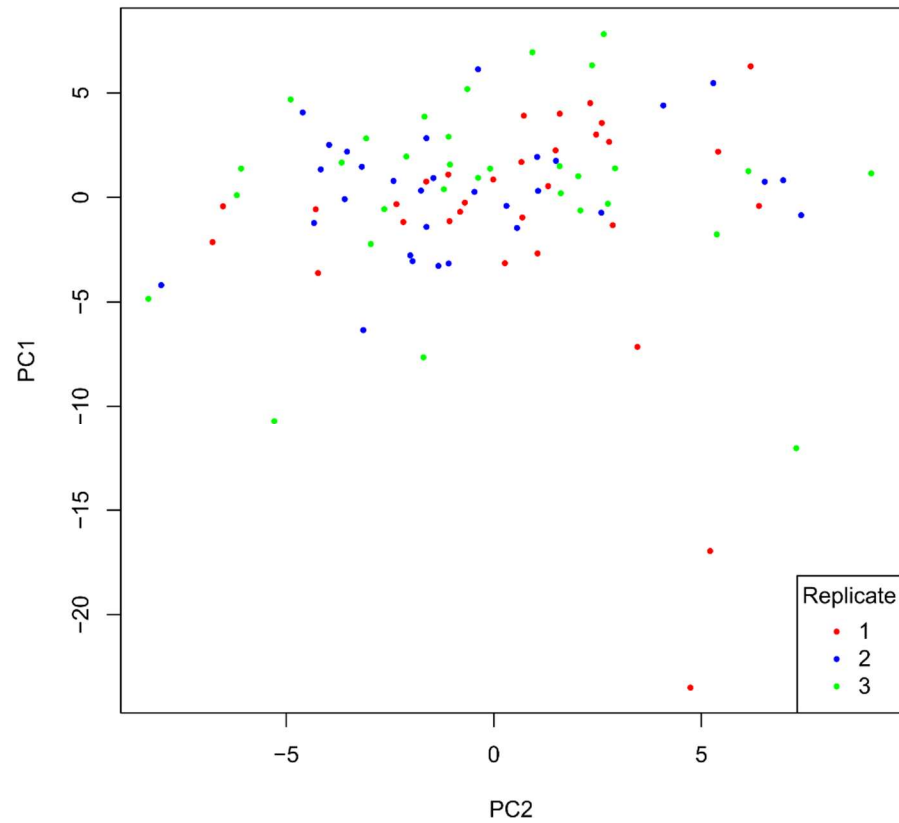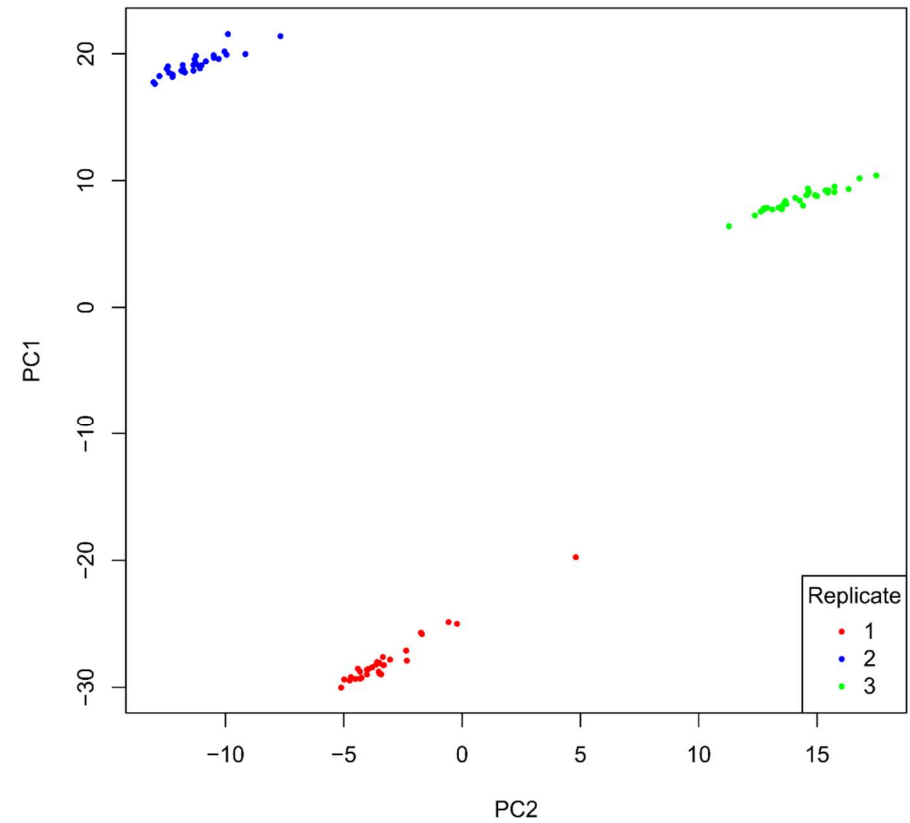
Figure 4.13. PC1 clusters by replicate when plotted against PC2 in the microglial samples.

After PCA, PC1 and PC2 were plotted against one another for the **(A)** neuronal and **(B)** microglial samples to look for clustering within the data. Samples have been coloured by replicate number.

<u>4.4.2.6 Combat Analysis Reduces Variation Induced by Replicate</u>

Using the "combat" function within the SVA package [332] it was possible to reduce the variation in the microglial dataset that was caused by replicate. Following combat analysis it is clear that PC1 and PC2 no longer correlate with replicate (figure 4.14A) and that the samples no longer cluster by replicate when PC1 is plotted against PC2 (figure 4.14B). The proportion of variation accounted for by each PC was also reduced with PC1 accounting for ~5.03%, PC2 for ~2.08% and PC3 for ~1.88% variation in the microglial dataset after combat analysis (table 4.4).

	PC1	PC2	PC3	PC4	PC5	PC6	PC7	PC8	PC9	PC10
Standard deviation	4.65	2.99	2.84	2.83	2.58	2.53	2.47	2.45	2.39	2.37
Proportion of Variance	0.05	0.02	0.02	0.02	0.02	0.01	0.01	0.01	0.01	0.01301
Cumulative Proportion	0.05	0.07	0.09	0.11	0.12	0.14	0.15	0.17	0.18	0.19

Table 4.4. Variance explained by the first ten PCs in the microglial dataset after combat analysis.

Shown for each PC is the standard deviation, proportion of variance explained and the cumulative proportion explained after the microglial samples underwent combat confounder correction.
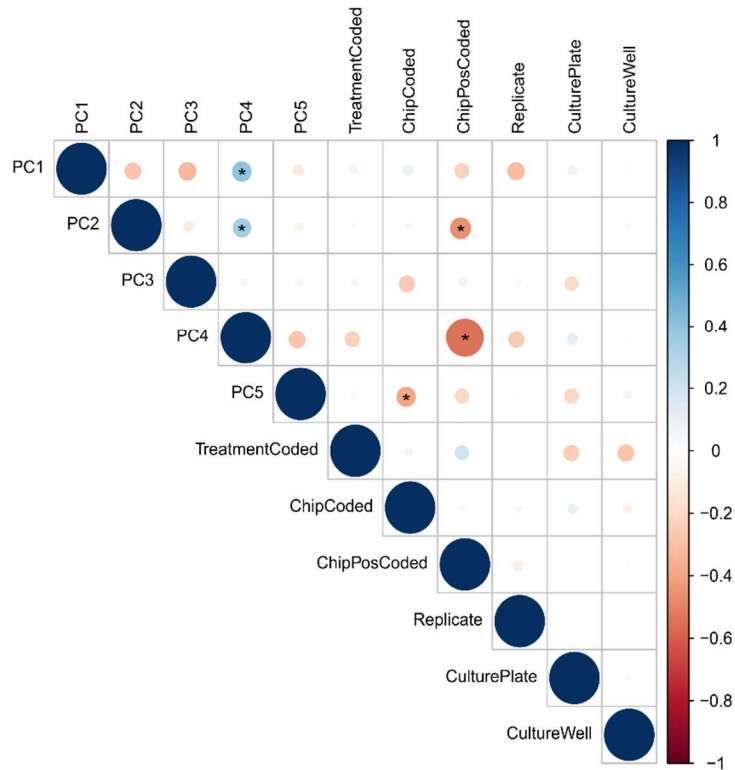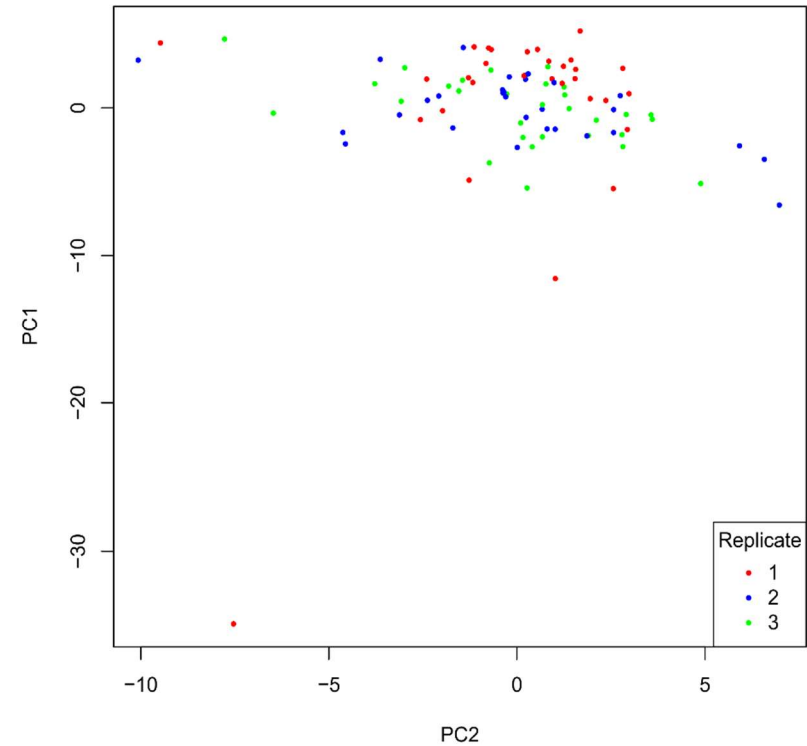
Figure 4.14. Variation caused by replicate in microglial samples is reduced.

Using the "combat" function within the SVA package the variation induced by replicate in the microglial samples was removed from the dataset. **(A)** Following combat analysis the new principal components were calculated and correlated to known variables including treatment, ChipID, position on the Chip, replicate, cell culture plate and the well within the cell culture plate. **(B)** Scatterplot of principal component one plotted against principal component two. *=$p<0.001$, **=$p<1\times10^{-8}$ and ***=$p<1\times10^{-10}$. The colour intensity and size of the circle are proportional to the correlation coefficients.

4.4.2.7 Epigenetic Modulators have Cell Type Specific Effects on Methylation

I used linear regression to identify DMPs associated with each treatment in each cell type separately. Due to the low number of replicates I did not identify any Bonferroni-significant loci but did identify a number of DMPs at a more relaxed p-value threshold of 5×10^{-4}. As a number of compounds have related functions I wanted to identify whether the same probes were differentially methylated across all treatments of the same compound class. To do this I extracted the significant probes (*i.e.* $p<5\times10^{-4}$) from one modulator (the first alphabetically) and extracted the probes that were nominally significant ($p<0.05$) in all other modulators of that same compound class, with this performed for each cell type separately. Interestingly, whilst there were consistent methylation changes seen with compound class in the microglia (BRD: 427, HMT: 429, HKDM: 387, KMR: 369 and WD40: 422 probes nominally significant across all compounds in a class; table 4.5) the same cannot be said of the neuronal samples, as there was only consistent changes in the compound groups with the fewest number of modulators in the group (BRD: 0, HMT: 0, HKDM: 144, KMR: 120 and WD40: 330 significant across all compounds in a class; table 4.5).

To add further meaning to the consistent DNA methylation changes seen in the microglial samples, a pathway analysis was performed on the probes that were consistently differentially methylated across treatments in each compound class. Although few pathways reached FDR significance, several demonstrated nominally significant alterations in specific pathways in cells treated with compounds in the categories of treatment. First, the significant DMPs associated with BRD inhibitor treatment seem to be associated with pathways relating to receptor internalisation binding, endosomal pathways and kidney related pathways such as nephron tubule

and ureteric bud morphogenesis (table 4.6). The pathways associated with HMT inhibitor treatment related to protein targeting to the vacuole, mRNA processing and the AV node (table 4.7). HKDM treatment was related to tight junctions and GTPase activity and regulation (table 4.8). KMR treatment was related to the regulation of chromatin organisation, receptor binding and cell signalling and RNA related process (table 4.9). Finally, WD40 treatment was associated with pathways relating to apoptosis and the immune system including the interleukin-10 production (table 4.10).

Cell Type	Number of consistently DMPs across compound class				
	BRD	HMT	HKDM	KMR	WD40
Neurons	0	0	144	120	330
Microglia	427	429	387	369	422

Table 4.5. Number of consistent DMPs across all compounds of the same type.

Number of consistent nominally significant DMPs across the same compound class in the neurons or microglia. Loci were identified by extracting the significant DMPs ($p < 5 \times 10^{-4}$) from one compound in a given class (the first compound alphabetically) and then noting if they were also nominally significantly ($p < 0.05$) differentially methylated in all of the other compounds of the same type.

GO ID	Term	Ontology	No. of Genes in Term	No. of DMPs	P-value	FDR	Genes
GO:0002090	regulation of receptor internalization	BP	51	5	2.74×10^{-4}	1.000	EGF; ANGPT1; LRRTM1; LRPAP1; NUMB
GO:0005768	endosome	CC	862	20	4.66×10^{-4}	1.000	NISCH; NIPA1; ATP11A; CCDC22; SNX10; EHD4; HLA-DQB1; KIFC1; LRPAP1; OCRL; C11orf59; VAC14; PRKCZ; SPPL2B; C11orf2; RABEP2; FAM108A1; RILP; NUMB; VAMP8
GO:0043393	regulation of protein binding	BP	217	9	0.001	1.000	ANGPT1; LRPAP1; PAX7; PPP2CA; CTNNBIP1; TGFBR3; TIAM1; CFHR5; ARHGEF7
GO:0001658	branching involved in ureteric bud morphogenesis	BP	60	5	0.001	1.000	FGF1; HOXB7; PKD2; CTNNBIP1; SIX1
GO:0099010	modification of postsynaptic structure	BP	17	3	0.002	1.000	CTNNA2; STAU1; TIAM1
GO:0060675	ureteric bud morphogenesis	BP	65	5	0.002	1.000	FGF1; HOXB7; PKD2; CTNNBIP1; SIX1
GO:0072171	mesonephric tubule morphogenesis	BP	66	5	0.002	1.000	FGF1; HOXB7; PKD2; CTNNBIP1; SIX1
GO:0051098	regulation of binding	BP	368	11	0.002	1.000	EGF; ANGPT1; LRPAP1; PAX7; PPP2CA; CTNNBIP1; EBF2; TGFBR3; TIAM1; CFHR5; ARHGEF7
GO:0016323	basolateral plasma membrane	CC	213	8	0.002	1.000	CTNNA2; DLG2; DSP; PKD2; SLC2A9; NDRG4; NUMB; MAP7
GO:0005942	phosphatidylinositol 3-kinase complex	CC	26	3	0.002	1.000	PIK3R5; NRBF2; VAC14
GO:0044431	Golgi apparatus part	CC	915	19	0.003	1.000	YIF1A; GPC5; MAPK8IP3; ATP11A; HLA-DQB1; LRPAP1; OCRL; PODXL2; RAB6B; SERPINA1; A2BP1; VAC14; NSFL1C; SPPL2B; ST3GAL1; C11orf2; AGPAT9; TRAPPC9; ASAP2
GO:0060415	muscle tissue morphogenesis	BP	82	5	0.003	1.000	DSP; IGSF22; PAX7; TGFBR3; TNNC1
GO:0005769	early endosome	CC	336	10	0.003	1.000	NISCH; NIPA1; ATP11A; EHD4; KIFC1; OCRL; VAC14; RABEP2; NUMB; VAMP8
GO:0072078	nephron tubule morphogenesis	BP	74	5	0.003	1.000	FGF1; HOXB7; PKD2; CTNNBIP1; SIX1
GO:0005865	striated muscle thin filament	CC	30	3	0.003	1.000	IGSF22; TNNC1; TNNT3
GO:0048259	regulation of receptor-mediated endocytosis	BP	95	5	0.003	1.000	EGF; ANGPT1; LRRTM1; LRPAP1; NUMB
GO:0072088	nephron epithelium morphogenesis	BP	76	5	0.003	1.000	FGF1; HOXB7; PKD2; CTNNBIP1; SIX1
GO:0036379	myofilament	CC	31	3	0.003	1.000	IGSF22; TNNC1; TNNT3
GO:0099563	modification of synaptic structure	BP	22	3	0.003	1.000	CTNNA2; STAU1; TIAM1
GO:0044440	endosomal part	CC	496	12	0.004	1.000	SNX10; EHD4; HLA-DQB1; LRPAP1; OCRL; C11orf59; VAC14; SPPL2B; C11orf2; FAM108A1; RILP; VAMP8

GO:0048644	muscle organ morphogenesis	BP	88	5	0.004	1.000	DSP; IGSF22; PAX7; TGFBR3; TNNC1
GO:0072028	nephron morphogenesis	BP	78	5	0.004	1.000	FGF1; HOXB7; PKD2; CTNNBIP1; SIX1
GO:0061333	renal tubule morphogenesis	BP	78	5	0.004	1.000	FGF1; HOXB7; PKD2; CTNNBIP1; SIX1
GO:0071556	integral component of lumenal side of endoplasmic reticulum membrane	CC	27	3	0.004	1.000	HLA-DQB1; PKD2; SPPL2B
GO:0098553	lumenal side of endoplasmic reticulum membrane	CC	27	3	0.004	1.000	HLA-DQB1; PKD2; SPPL2B

Table 4.6. Pathways altered upon BRD inhibitor treatment.

Shown are the top 25 most significant pathways after the iPSC-derived microglia were treated with compounds known to inhibit proteins containing bromodomains. Shown for each pathway is the GO ID, the pathway descriptor, the ontology of the pathway, the number of genes in the pathway, the number of DMPs in the pathway, p-value significance, FDR value and the list of significantly differentially methylated genes within the pathway. FDR=false discovery rate, BP=biological pathways, CC=cellular components and MF=molecular functions.

GO ID	Term	Ontology	No. of Genes in Term	No. of DMPs	P-value	FDR	Genes
GO:0086016	AV node cell action potential	BP	11	3	5.39×10^{-4}	1.000	RYR2; CACNA1C; CACNB2
GO:0086027	AV node cell to bundle of His cell signaling	BP	11	3	5.39×10^{-4}	1.000	RYR2; CACNA1C; CACNB2
GO:0086067	AV node cell to bundle of His cell communication	BP	12	3	6.68×10^{-4}	1.000	RYR2; CACNA1C; CACNB2
GO:0019934	cGMP-mediated signaling	BP	33	4	7.07×10^{-4}	1.000	EDNRB; ADNP; KCNC2; NPR1
GO:1900363	regulation of mRNA polyadenylation	BP	16	3	7.51×10^{-4}	1.000	CPEB3; RDBP; CPSF7
GO:0005089	Rho guanyl-nucleotide exchange factor activity	MF	76	6	0.001	1.000	FGD5; MCF2L; PLEKHG5; TRIO; ARHGEF6; ARHGEF10
GO:0097066	response to thyroid hormone	BP	27	3	0.002	1.000	GAS2L1; SIX1; TOMM20
GO:0031440	regulation of mRNA 3'-end processing	BP	27	3	0.003	1.000	CPEB3; RDBP; CPSF7
GO:0086014	atrial cardiac muscle cell action potential	BP	20	3	0.003	1.000	RYR2; CACNA1C; CACNB2
GO:0086026	atrial cardiac muscle cell to AV node cell signaling	BP	20	3	0.003	1.000	RYR2; CACNA1C; CACNB2
GO:0086066	atrial cardiac muscle cell to AV node cell communication	BP	20	3	0.003	1.000	RYR2; CACNA1C; CACNB2
GO:0030016	myofibril	CC	216	8	0.003	1.000	SYNM; SYNE1; RYR2; SPTBN1; TNNI1; CACNA1C; SQSTM1; PDE4DIP
GO:0072665	protein localization to vacuole	BP	55	4	0.003	1.000	VTI1A; SH3BP4; PIK3R4; VPS13D
GO:0019388	galactose catabolic process	BP	10	2	0.004	1.000	GALK2; PGM1
GO:0043292	contractile fiber	CC	227	8	0.004	1.000	SYNM; SYNE1; RYR2; SPTBN1; TNNI1; CACNA1C; SQSTM1; PDE4DIP
GO:0032414	positive regulation of ion transmembrane transporter activity	BP	95	5	0.004	1.000	CFTR; KCNC2; NLGN3; RYR2; CACNB2
GO:0006623	protein targeting to vacuole	BP	30	3	0.004	1.000	VTI1A; PIK3R4; VPS13D
GO:0019935	cyclic-nucleotide-mediated signaling	BP	213	7	0.006	1.000	ADRA2A; EDNRB; ADNP; PCLO; KCNC2; NPR1; BAI3
GO:0050808	synapse organization	BP	381	12	0.006	1.000	DSCAM; EPHA7; PDZRN3; ADNP; PCLO; PALM; PFN2; NLGN3; BAI3; PTPRF; SIX1; CACNB2
GO:0032411	positive regulation of transporter activity	BP	103	5	0.006	1.000	CFTR; KCNC2; NLGN3; RYR2; CACNB2
GO:0098799	outer mitochondrial membrane protein complex	CC	17	2	0.006	1.000	DNAJC11; TOMM20

GO:0051315	attachment of mitotic spindle microtubules to kinetochore	BP	13	2	0.006	1.000	ZNF828; MAD1L1
GO:0031256	leading edge membrane	CC	166	7	0.007	1.000	FGD5; WWC1; SH3YL1; KCNC2; PALM; PSD; SPTBN1
GO:0035023	regulation of Rho protein signal transduction	BP	131	6	0.007	1.000	FGD5; MCF2L; PLEKHG5; TRIO; ARHGEF6; ARHGEF10
GO:0006012	galactose metabolic process	BP	14	2	0.007	1.000	GALK2; PGM1

Table 4.7. Pathways altered upon HMT inhibitor treatment.

Shown are the top 25 most significant pathways after the iPSC-derived microglia were treated with compounds known to inhibit histone methyltransferases. Shown for each pathway is the GO ID, the pathway descriptor, the ontology of the pathway, the number of genes in the pathway, the number of DMPs in the pathway, p-value significance, FDR value and the list of significantly differentially methylated genes within the pathway. FDR=false discovery rate, BP=biological pathways, CC=cellular components and MF=molecular functions.

GO ID	Term	Ontology	No. of Genes in Term	No. of DMPs	P-value	FDR	Genes
GO:2000810	regulation of bicellular tight junction assembly	BP	20	4	4.22×10^{-5}	0.372	NPHP4; PRKACA; PRKCH; FZD5
GO:1901888	regulation of cell junction assembly	BP	87	6	4.90×10^{-4}	1.000	DAPK3; NPHP4; WNT4; PRKACA; PRKCH; FZD5
GO:0043087	regulation of GTPase activity	BP	464	13	0.001	1.000	AGAP11; EPHA4; PLEKHG4; RACGAP1; NTF3; WNT4; RASIP1; PTPRN2; TSC2; PREX2; SYNGAP1; MTSS1L; TBC1D5
GO:0070830	bicellular tight junction assembly	BP	53	4	0.002	1.000	NPHP4; PRKACA; PRKCH; FZD5
GO:0060314	regulation of ryanodine-sensitive calcium-release channel activity	BP	26	3	0.002	1.000	JSRP1; PRKACA; CAMK2D
GO:0120192	tight junction assembly	BP	54	4	0.002	1.000	NPHP4; PRKACA; PRKCH; FZD5
GO:0120193	tight junction organization	BP	57	4	0.002	1.000	NPHP4; PRKACA; PRKCH; FZD5
GO:0015662	ATPase activity, coupled to transmembrane movement of ions, phosphorylative mechanism	MF	33	3	0.003	1.000	FXYD2; ATP2A1; ATP2B1
GO:0016782	transferase activity, transferring sulfur-containing groups	MF	69	4	0.003	1.000	MPST; CHST8; TST; HS3ST3B1
GO:0090075	relaxation of muscle	BP	31	3	0.003	1.000	C5orf20; ATP2A1; CAMK2D
GO:0043297	apical junction assembly	BP	62	4	0.003	1.000	NPHP4; PRKACA; PRKCH; FZD5
GO:1903779	regulation of cardiac conduction	BP	58	4	0.003	1.000	ATP2A1; ATP2B1; PRKACA; CAMK2D
GO:0097546	ciliary base	CC	33	3	0.004	1.000	NPHP4; PRKACA; PRKAR1B
GO:0006040	amino sugar metabolic process	BP	38	3	0.004	1.000	CSGALNACT1; LARGE; GFPT2
GO:1903312	negative regulation of mRNA metabolic process	BP	71	4	0.004	1.000	CIRBP; DHX9; SFRS8; RBM42
GO:0043547	positive regulation of GTPase activity	BP	389	10	0.005	1.000	AGAP11; PLEKHG4; RACGAP1; NTF3; WNT4; TSC2; PREX2; SYNGAP1; MTSS1L; TBC1D5
GO:0051279	regulation of release of sequestered calcium ion into cytosol	BP	80	4	0.007	1.000	JSRP1; PRKACA; PRKCE; CAMK2D
GO:0009101	glycoprotein biosynthetic process	BP	316	8	0.008	1.000	C3orf21; GALNT9; CSGALNACT1; CHST8; B3GNT9; LARGE; GFPT2; HS3ST3B1
GO:0033017	sarcoplasmic reticulum membrane	CC	38	3	0.008	1.000	JSRP1; ATP2A1; CAMK2D
GO:0044273	sulfur compound catabolic process	BP	51	3	0.009	1.000	GGT6; MPST; TST

GO:0071333	cellular response to glucose stimulus	BP	126	5	0.010	1.000	OPA1; PRKACA; PRKCE; PTPRN2; ZNF236
GO:0090630	activation of GTPase activity	BP	83	4	0.010	1.000	PLEKHG4; NTF3; MTSS1L; TBC1D5
GO:0071331	cellular response to hexose stimulus	BP	128	5	0.011	1.000	OPA1; PRKACA; PRKCE; PTPRN2; ZNF236
GO:0030145	manganese ion binding	MF	53	3	0.011	1.000	C3orf21; PRKACA; LARGE
GO:0071326	cellular response to monosaccharide stimulus	BP	129	5	0.011	1.000	OPA1; PRKACA; PRKCE; PTPRN2; ZNF236

Table 4.8. Pathways altered upon HKDM inhibitor treatment.

Shown are the top 25 most significant pathways after the iPSC-derived microglia were treated with compounds known to inhibit histone lysine demethylases. Shown for each pathway is the GO ID, the pathway descriptor, the ontology of the pathway, the number of genes in the pathway, the number of DMPs in the pathway, p-value significance, FDR value and the list of significantly differentially methylated genes within the pathway. FDR=false discovery rate, BP=biological pathways, CC=cellular components and MF=molecular functions.

GO ID	Term	Ontology	No. of Genes in Term	No. of DMPs	P-value	FDR	Genes
GO:0031057	negative regulation of histone modification	BP	40	6	3.12×10^{-6}	0.027	PHF1; KDM3A; SKI; TWIST1; UCN; H2AFY
GO:1905268	negative regulation of chromatin organization	BP	60	6	9.74×10^{-6}	0.043	PHF1; KDM3A; SKI; TWIST1; UCN; H2AFY
GO:0031056	regulation of histone modification	BP	138	7	3.70×10^{-4}	1.000	PHF1; WDR70; KDM3A; SKI; TWIST1; UCN; H2AFY
GO:0008307	structural constituent of muscle	MF	44	4	8.54×10^{-4}	1.000	IGSF22; PLEC1; TTN; ACTN2
GO:1902275	regulation of chromatin organization	BP	174	7	8.74×10^{-4}	1.000	PHF1; WDR70; KDM3A; SKI; TWIST1; UCN; H2AFY
GO:2001251	negative regulation of chromosome organization	BP	142	6	0.001	1.000	PHF1; KDM3A; SKI; TWIST1; UCN; H2AFY
GO:0005104	fibroblast growth factor receptor binding	MF	26	3	0.001	1.000	FGF2; NPTN; KL
GO:0031061	negative regulation of histone methylation	BP	20	3	0.001	1.000	PHF1; KDM3A; H2AFY
GO:0016072	rRNA metabolic process	BP	237	7	0.001	1.000	NGDN; PELP1; UTP11L; H2AFY2; USP36; RPS2; H2AFY
GO:0010996	response to auditory stimulus	BP	23	3	0.002	1.000	USP53; UCN; NRXN1
GO:0030506	ankyrin binding	MF	20	3	0.002	1.000	ATP1A1; PLEC1; SPTBN1
GO:0031430	M band	CC	29	3	0.002	1.000	IGSF22; SPTBN1; TTN
GO:0045595	regulation of cell differentiation	BP	1747	28	0.002	1.000	PQBP1; VAX1; ACAP3; C20orf123; UNC5D; FGF2; NPTN; GLI2; HOXA7; HOXB8; HSPA1A; KDR; MIR9-1; PPP2CA; H2AFY2; KDM3A; PRKCI; CTNNBIP1; PTHLH; PRDM16; SEMA3F; SKI; TPH1; TWIST1; ARHGEF7; BRSK2; NEURL; H2AFY
GO:0044449	contractile fiber part	CC	212	7	0.002	1.000	SYNE1; IGSF22; PLEC1; SPTBN1; TTN; CACNA1C; ACTN2
GO:0030016	myofibril	CC	216	7	0.003	1.000	SYNE1; IGSF22; PLEC1; SPTBN1; TTN; CACNA1C; ACTN2
GO:0045616	regulation of keratinocyte differentiation	BP	39	3	0.003	1.000	HOXA7; H2AFY2; H2AFY
GO:0033120	positive regulation of RNA splicing	BP	35	3	0.003	1.000	ERN1; HSPA1A; NCBP1
GO:0043292	contractile fiber	CC	227	7	0.004	1.000	SYNE1; IGSF22; PLEC1; SPTBN1; TTN; CACNA1C; ACTN2
GO:0051393	alpha-actinin binding	MF	31	3	0.004	1.000	IGSF22; TTN; CACNA1C
GO:0000805	X chromosome	CC	10	2	0.004	1.000	H2AFY2; H2AFY
GO:0040011	locomotion	BP	1812	27	0.004	1.000	NCKAP1; VAX1; CHRM4; ACAP3; UNC5D; FGF2; GCET2; NPTN; GLI2; HOXA7; KDR; LCK; RERE; PRKCI; PTPRK; TRIM27; SEMA3F; SKI; SPTBN1; TWIST1; TRIM26; SYDE1; ARHGEF7; NEURL; NRXN1; CELSR1; ELMO1

GO:0030955	potassium ion binding	MF	10	2	0.004	1.000	ATP1A1; PDXK
GO:1901836	regulation of transcription of nucleolar large rRNA by RNA polymerase I	BP	13	2	0.005	1.000	H2AFY2; H2AFY
GO:0031672	A band	CC	40	3	0.005	1.000	IGSF22; SPTBN1; TTN
GO:0098787	mRNA cleavage involved in mRNA processing	BP	14	2	0.005	1.000	ERN1; NCBP1

Table 4.9. Pathways altered upon KMR inhibitor treatment.

Shown are the top 25 most significant pathways after the iPSC-derived microglia were treated with compounds known to inhibit proteins containing methyl lysine readers. Shown for each pathway is the GO ID, the pathway descriptor, the ontology of the pathway, the number of genes in the pathway, the number of DMPs in the pathway, p-value significance, FDR value and the list of significantly differentially methylated genes within the pathway. FDR=false discovery rate, BP=biological pathways, CC=cellular components and MF=molecular functions.

GO ID	Term	Ontology	No. of Genes in Term	No. of DMPs	P-value	FDR	Genes
GO:0043649	dicarboxylic acid catabolic process	BP	17	3	0.001	1.000	ACOT4; ALDH1L2; GAD1
GO:0048172	regulation of short-term neuronal synaptic plasticity	BP	13	3	0.001	1.000	GRIK2; SYP; PPFIA3
GO:0006110	regulation of glycolytic process	BP	41	4	0.001	1.000	ESRRB; GAPDHS; PRKAG2; HDAC4
GO:0030811	regulation of nucleotide catabolic process	BP	42	4	0.001	1.000	ESRRB; GAPDHS; PRKAG2; HDAC4
GO:0043470	regulation of carbohydrate catabolic process	BP	48	4	0.002	1.000	ESRRB; GAPDHS; PRKAG2; HDAC4
GO:2001169	regulation of ATP biosynthetic process	BP	50	4	0.002	1.000	ESRRB; GAPDHS; PRKAG2; HDAC4
GO:0032786	positive regulation of DNA-templated transcription, elongation	BP	30	3	0.002	1.000	BRD4; ELL3; CCNT1
GO:1902547	regulation of cellular response to vascular endothelial growth factor stimulus	BP	22	3	0.002	1.000	DLL1; MYO1C; ADAMTS12
GO:0051196	regulation of coenzyme metabolic process	BP	55	4	0.003	1.000	ESRRB; GAPDHS; PRKAG2; HDAC4
GO:0043065	positive regulation of apoptotic process	BP	626	15	0.003	1.000	CYP1B1; DAPK3; AES; DFNA5; FAP; TNFAIP8; GRIK2; FBXW7; TRIM39; PRDM11; RPS6KA2; TFDP1; ZBTB16; ARHGEF6; HDAC4
GO:0043068	positive regulation of programmed cell death	BP	630	15	0.003	1.000	CYP1B1; DAPK3; AES; DFNA5; FAP; TNFAIP8; GRIK2; FBXW7; TRIM39; PRDM11; RPS6KA2; TFDP1; ZBTB16; ARHGEF6; HDAC4
GO:0019359	nicotinamide nucleotide biosynthetic process	BP	105	5	0.004	1.000	ESRRB; GAPDHS; PRKAG2; CARKD; HDAC4
GO:0019363	pyridine nucleotide biosynthetic process	BP	105	5	0.004	1.000	ESRRB; GAPDHS; PRKAG2; CARKD; HDAC4
GO:0019369	arachidonic acid metabolic process	BP	49	3	0.004	1.000	MGLL; CYP1B1; TBXAS1
GO:0000083	regulation of transcription involved in G1/S transition of mitotic cell cycle	BP	28	3	0.004	1.000	ESRRB; BRD4; TFDP1
GO:0072525	pyridine-containing compound biosynthetic process	BP	108	5	0.005	1.000	ESRRB; GAPDHS; PRKAG2; CARKD; HDAC4
GO:0032653	regulation of interleukin-10 production	BP	45	3	0.005	1.000	DLL1; BCL3; TNFSF4
GO:0072330	monocarboxylic acid biosynthetic process	BP	287	8	0.005	1.000	MGLL; RDH10; ESRRB; GAD1; GAPDHS; PRKAG2; TBXAS1; HDAC4

GO:1903578	regulation of ATP metabolic process	BP	71	4	0.006	1.000	ESRRB; GAPDHS; PRKAG2; HDAC4
GO:0032613	interleukin-10 production	BP	47	3	0.006	1.000	DLL1; BCL3; TNFSF4
GO:1900371	regulation of purine nucleotide biosynthetic process	BP	71	4	0.006	1.000	ESRRB; GAPDHS; PRKAG2; HDAC4
GO:0010942	positive regulation of cell death	BP	681	15	0.006	1.000	CYP1B1; DAPK3; AES; DFNA5; FAP; TNFAIP8; GRIK2; FBXW7; TRIM39; PRDM11; RPS6KA2; TFDP1; ZBTB16; ARHGEF6; HDAC4
GO:0030808	regulation of nucleotide biosynthetic process	BP	72	4	0.006	1.000	ESRRB; GAPDHS; PRKAG2; HDAC4
GO:0008047	enzyme activator activity	MF	504	12	0.007	1.000	TOM1L1; SH3D20; RASA3; ARHGEF15; RACGAP1; ARF1; PRKAG2; RIN2; ARHGEF10L; CCNT1; STARD13; ARHGEF6
GO:0051193	regulation of cofactor metabolic process	BP	73	4	0.007	1.000	ESRRB; GAPDHS; PRKAG2; HDAC4

Table 4.10. Pathways altered upon WD40 inhibitor treatment.

Shown are the top 25 most significant pathways after the iPSC-derived microglia were treated with compounds known to inhibit proteins containing WD40 domains. Shown for each pathway is the GO ID, the pathway descriptor, the ontology of the pathway, the number of genes in the pathway, the number of DMPs in the pathway, p-value significance, FDR value and the list of significantly differentially methylated genes within the pathway. FDR=false discovery rate, BP=biological pathways, CC=cellular components and MF=molecular functions.

4.4.2.8 There is Significant Correlation of Top DMPs between Compound Types

As there was little consistency in the nominally significantly DMPs identified across compound classes in the neuronal samples I wanted to check whether the treatments within each class were having a consistent effect, in terms of effect size and direction of effect, as due to the limited number of replicates in the study it could be underpowered. When comparing the direction of effect and effect size within each drug class within the neuronal samples it is clear that the direction of effect of the top 100 probes is consistent within the treatments of the same type and that the effect sizes of these top probes also correlate strongly with one another (table 4.11 and figure 4.15). This is also the same within the iPSC-derived microglia, which again show a significant enrichment for the direction of effect and a significant correlation of effect sizes for the top 100 DMPs identified within each drug class (table 4.12 and figure 4.16).

4.4.2.9 There is no Correlation of Top DMPs between Cell Types

To determine whether the treatments had a similar effect in both cell types the top 100 DMPs for each treatment in the neuronal samples were extracted and a sign test and correlation test were performed against the same loci in the microglia treated with the same compound. These analyses highlighted that there is no consistent direction of effect or correlation of effect size in the same drug in both the neurons and microglia (table 4.13 and figure 4.17), suggesting that they are effecting different genes in the different cell types.

Drug Class	Compound Name	Sign Test p-value	Correlation r-value	Correlation p-value
BRD	(+)-JQ1	-	-	-
	BAY299	4.83×10^{-13}	0.80	$<2.20 \times 10^{-16}$
	BAZ2-ICR	2.61×10^{-12}	0.80	$<2.20 \times 10^{-16}$
	BI 9564	4.83×10^{-13}	0.82	$<2.20 \times 10^{-16}$
	GSK2801	3.32×10^{-18}	0.77	$<2.20 \times 10^{-16}$
	I-BRD9	2.61×10^{-12}	0.71	$<2.20 \times 10^{-16}$
	I-CBP 112	2.54×10^{-16}	0.81	$<2.20 \times 10^{-16}$
	NI 57	1.31×10^{-11}	0.72	$<2.20 \times 10^{-16}$
	NVS-CECR2-1	1.91×10^{-15}	0.81	$<2.20 \times 10^{-16}$
	OF 1	8.28×10^{-14}	0.78	$<2.20 \times 10^{-16}$
	PFI 3	2.61×10^{-12}	0.75	$<2.20 \times 10^{-16}$
	TP 472	1.31×10^{-11}	0.81	$<2.20 \times 10^{-16}$
HKDM	GSK LSD 1 dihydrochloride	-	-	-
	GSKJ4	2.54×10^{-16}	0.83	$<2.20 \times 10^{-16}$
HMT	A 196	-	-	-
	A 366	2.70×10^{-10}	0.72	$<2.20 \times 10^{-16}$
	BAY598	5.64×10^{-7}	0.75	$<2.20 \times 10^{-16}$
	GSK343	1.31×10^{-11}	0.72	$<2.20 \times 10^{-16}$
	GSK591 dihydrochloride	8.28×10^{-14}	0.72	$<2.20 \times 10^{-16}$
	MS 023 dihydrochloride	3.06×10^{-17}	0.77	$<2.20 \times 10^{-16}$
	MS049 oxalate salt	4.83×10^{-13}	0.63	3.56×10^{-12}
	RPFI 2 hydrochloride	1.31×10^{-14}	0.78	$<2.20 \times 10^{-16}$
	SGC 0946	8.28×10^{-14}	0.78	$<2.20 \times 10^{-16}$
	SGC 707	1.31×10^{-14}	0.82	$<2.20 \times 10^{-16}$
	TP 064	4.83×10^{-13}	0.78	$<2.20 \times 10^{-16}$
	UNC 0642	3.06×10^{-17}	0.85	$<2.20 \times 10^{-16}$
	UNC 1999	1.31×10^{-11}	0.77	$<2.20 \times 10^{-16}$
KMR	A 395	-	-	-
	UNC 1215	3.32×10^{-18}	0.80	$<2.20 \times 10^{-16}$

Table 4.11. Correlation of effect size and direction of effect for the top 100 most significant DMPs identified in neuronal samples.

Shown are the correlations of effect size for the top 100 most significant DMPs in one compound (the first alphabetically) in a given category, to other compounds in that same drug class within the iPSC-derived neurons. The drug class, compound name, sign test p-value and Pearson correlation are shown for each drug treatment. The compounds that do not have p-values or correlations were the drugs used to assess correlations within the other treatments of the same class. Where BRD=bromodomain inhibitors, HKDM=histone lysine demethylase inhibitors, HMT=histone methyltransferase inhibitors and KMR=methyl lysine reader inhibitors. (+)-JQ1, GSK LSD1, A196 and A 395 were chosen to test against the others as they came first alphabetically.
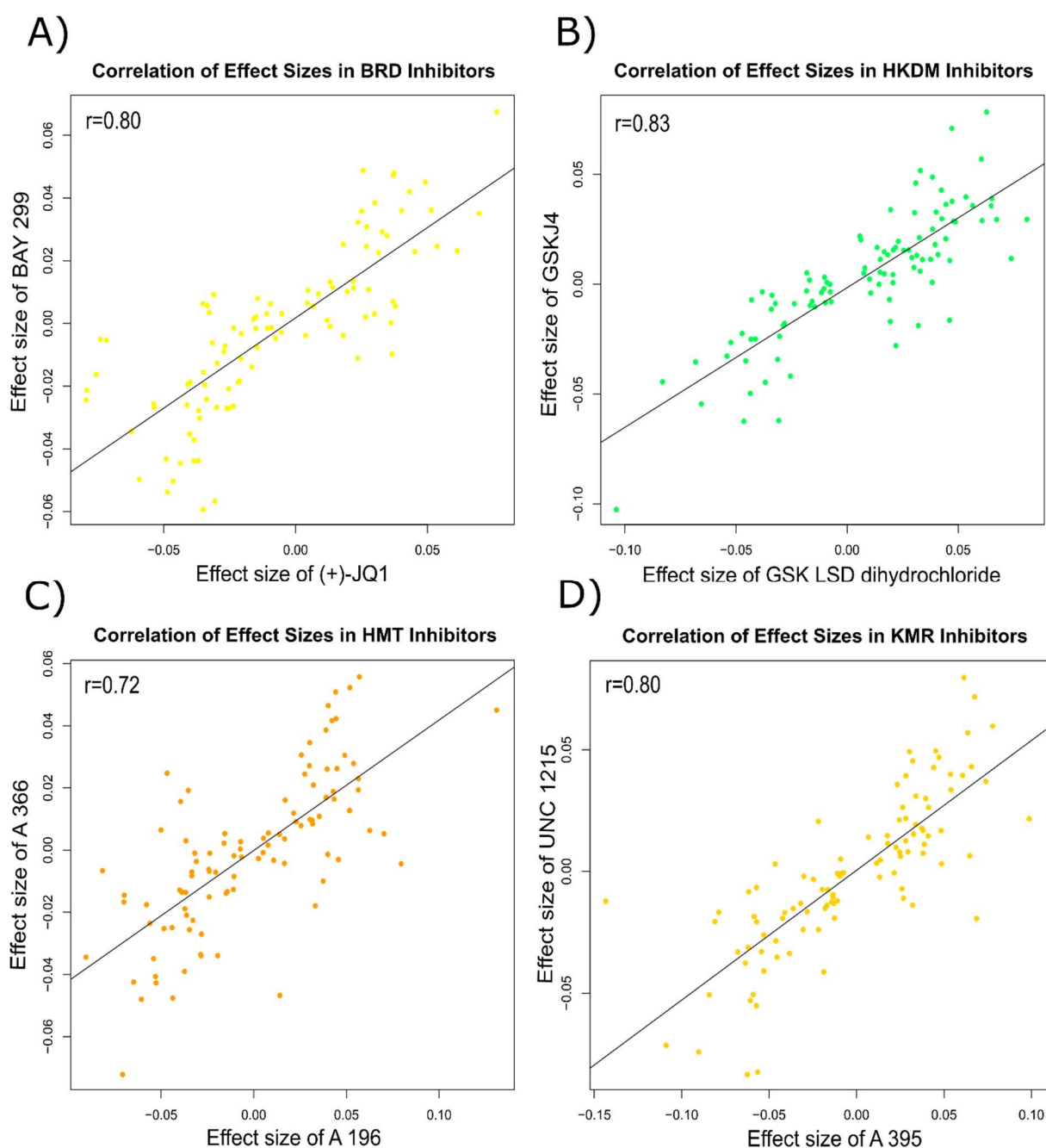
Figure 4.15. The effect size of the top 100 most significant DMPs identified in neurons after treatment with one compound are highly correlated with the effect size of the same probes in neurons treated with another compound in the same drug class.

To assess whether the compounds of the same class were having a consistent effect on DNA methylation, the effect size of the top 100 most significant DMPs identified for one compound were compared to the effect size of the same probes in another compound in the same category using Pearson correlations. Shown as an example are the correlation of effect sizes of two drugs from the **(A)** BRD inhibitors, **(B)** HKDM inhibitors, **(C)** HMT inhibitors and **(D)** KMR inhibitors. For each comparison the correlation (r value) is also given. Where BRD=bromodomain inhibitors, HKDM=histone lysine demethylase inhibitors, HMT=histone methyltransferase inhibitors and KMR=methyl lysine reader inhibitors.

Drug Class	Compound Name	Sign Test p-value	Correlation r-value	Correlation p-value
BRD	(+)-JQ1	-	-	-
	BAY299	1.31×10^{-11}	0.75	$<2.20 \times 10^{-16}$
	BAZ2-ICR	8.28×10^{-14}	0.74	$<2.20 \times 10^{-16}$
	BI 9564	2.61×10^{-12}	0.78	$<2.20 \times 10^{-16}$
	GSK2801	1.31×10^{-11}	0.75	$<2.20 \times 10^{-16}$
	I-BRD9	1.31×10^{-11}	0.75	$<2.20 \times 10^{-16}$
	I-CBP 112	1.12×10^{-9}	0.73	$<2.20 \times 10^{-16}$
	NI 57	4.82×10^{-13}	0.78	$<2.20 \times 10^{-16}$
	NVS-CECR2-1	8.28×10^{-14}	0.78	$<2.20 \times 10^{-16}$
	OF 1	1.31×10^{-11}	0.71	$<2.20 \times 10^{-16}$
	PFI 3	8.28×10^{-14}	0.69	1.69×10^{-15}
	TP 472	6.15×10^{-11}	0.72	$<2.20 \times 10^{-16}$
HKDM	GSK LSD 1 dihydrochloride	-	-	-
	GSKJ4	3.06×10^{-17}	0.80	$<2.20 \times 10^{-16}$
HMT	A 196	-	-	-
	A 366	3.06×10^{-17}	0.78	$<2.20 \times 10^{-16}$
	BAY598	1.67×10^{-6}	0.55	3.93×10^{-9}
	GSK343	2.54×10^{-16}	0.77	$<2.20 \times 10^{-16}$
	GSK591 dihydrochloride	1.59×1^{-8}	0.73	$<2.20 \times 10^{-16}$
	MS 023 dihydrochloride	4.83×10^{-13}	0.80	$<2.20 \times 10^{-16}$
	MS049 oxalate salt	1.91×10^{-15}	0.80	$<2.20 \times 10^{-16}$
	RPFI 2 hydrochloride	8.28×10^{-14}	0.74	$<2.20 \times 10^{-16}$
	SGC 0946	1.31×10^{-14}	0.71	$<2.20 \times 10^{-16}$
	SGC 707	4.34×10^{-9}	0.76	$<2.20 \times 10^{-16}$
	TP 064	1.31×10^{-11}	0.66	1.04×10^{-13}
	UNC 0642	3.32×10^{-18}	0.85	$<2.20 \times 10^{-16}$
KMR	A 395	-	-	-
	UNC 1215	2.70×10^{-11}	0.75	$<2.20 \times 10^{-16}$

Table 4.12. Correlation of effect size and direction of effect for the top 100 most significant DMPs identified in microglial samples.

Shown are the correlations of effect size and direction of effect of the top 100 DMPs in one compound (the first alphabetically) in a given category, to other compounds in that same drug class within the iPSC-derived microglia. The drug class, compound name, sign test p-value and Pearson correlation are shown for each drug treatment. The compounds that do not have p-values or correlations were the drugs used to assess correlations within the other treatments of the same class. Where BRD=bromodomain inhibitors, HKDM=histone lysine demethylase inhibitors, HMT=histone methyltransferase inhibitors and KMR=methyl lysine reader inhibitors. (+)-JQ1, GSK LSD1, A196 and A 395 were chosen to test against the others as they came first alphabetically.
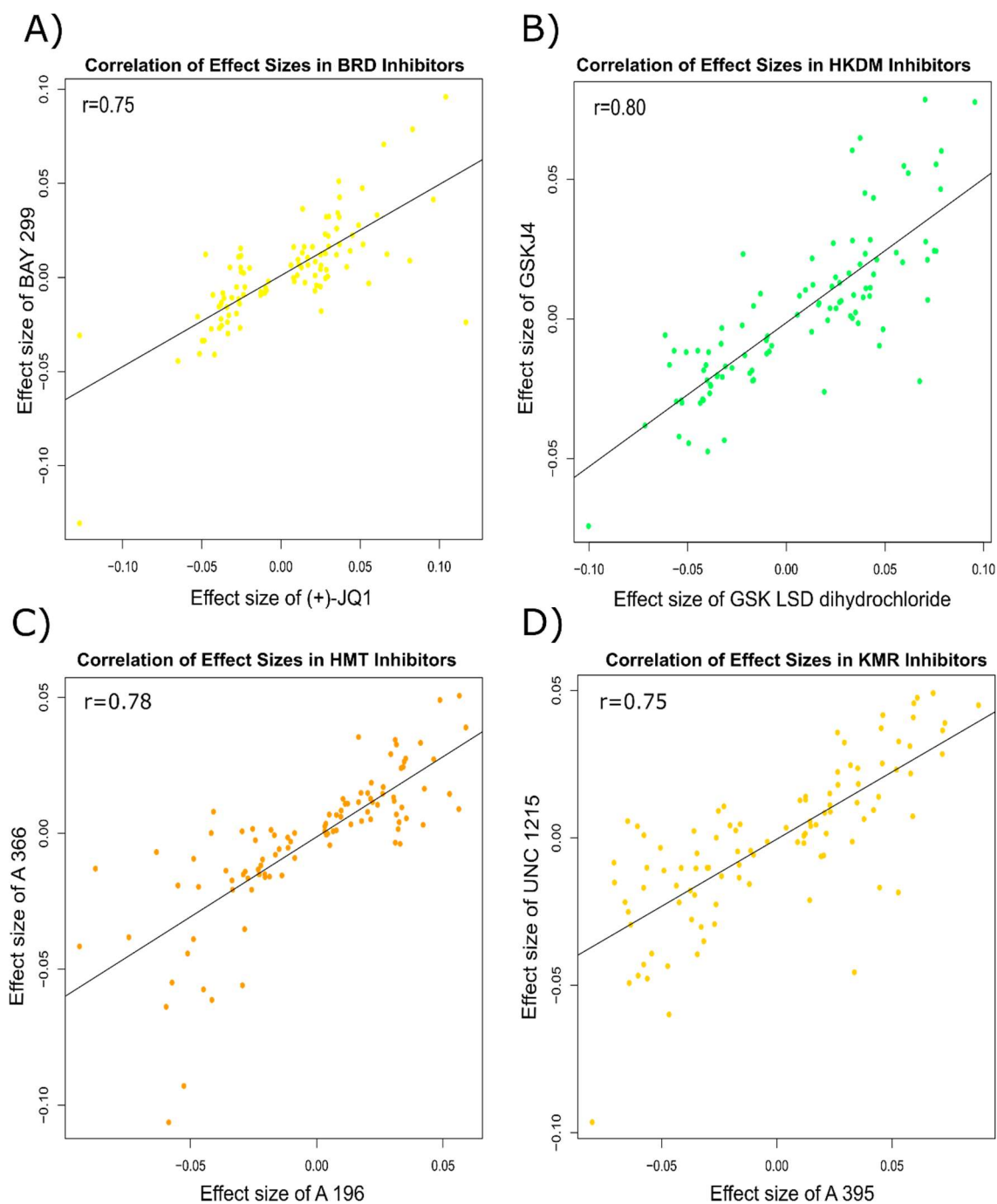
Figure 4.16. The effect size of the top 100 most significant DMPs identified in microglia after treatment with one compound are highly correlated with the effect size of the same probes in microglia treated with another compound of the same drug class.

To assess whether the compounds of the same class were having a consistent effect on DNA methylation, the effect size of the top 100 most significant DMPs were compared to the effect size of the same probes in another compound in the same category using Pearson correlations. Shown as an example are the correlation of effect sizes of two compounds from the **(A)** BRD inhibitors, **(B)** HKDM inhibitors, **(C)** HMT inhibitors and **(D)** KMR inhibitors. For each comparison the correlation (r value) is also given. Where BRD=bromodomain inhibitors, HKDM=histone lysine demethylase inhibitors, HMT=histone methyltransferase inhibitors and KMR=methyl lysine reader inhibitors.

Drug Class	Compound Name	Sign Test p-value	Correlation r-value	Correlation p-value
BRD	(+)-JQ1	0.002	-0.32	0.001
	BAY299	0.617	0.02	0.826
	BAZ2-ICR	1.000	-0.08	0.404
	BI 9564	0.920	0.08	0.451
	GSK2801	0.271	-0.14	0.163
	I-BRD9	0.484	-0.06	0.522
	I-CBP 112	0.271	0.03	0.741
	NI 57	0.193	0.01	0.926
	NVS-CECR2-1	0.133	0.00	0.990
	OF 1	0.920	-0.08	0.428
	PFI 3	0.617	-0.11	0.270
	TP 472	0.271	-0.12	0.250
HKDM	GSK LSD 1 dihydrochloride	0.484	0.10	0.800
	GSKJ4	1.000	-0.03	0.748
HMT	A 196	0.617	-0.19	0.066
	A 366	0.617	-0.06	0.569
	BAY598	0.764	0.01	0.887
	GSK343	0.920	-0.19	0.059
	GSK591 dihydrochloride	0.271	0.01	0.957
	MS 023 dihydrochloride	0.920	0.05	0.617
	MS049 oxalate salt	0.193	0.04	0.691
	RPFI 2 hydrochloride	0.368	0.27	0.007
	SGC 0946	0.271	-0.11	0.288
	SGC 707	0.764	-0.12	0.225
	TP 064	0.484	-0.11	0.276
	UNC 0642	0.920	0.06	0.553
KMR	A 395	0.920	-0.07	0.520
	UNC 1215	0.617	0.03	0.779

Table 4.13. Correlation of effect size and direction of effect for the top 100 most significant DMPs identified in the neurons treated with a compound, with the same probes in microglia treated with the same compound.

Shown are the correlations of effect size and direction of effect of the top 100 DMPs identified in the neurons given a particular compound, with the same probes in microglia treated with the same compound. The compound class, compound name, sign test p-value and Pearson correlation are shown for each drug treatment. Where BRD=bromodomain inhibitors, HKDM=histone lysine demethylase inhibitors, HMT=histone methyltransferase inhibitors and KMR=methyl lysine reader inhibitors.
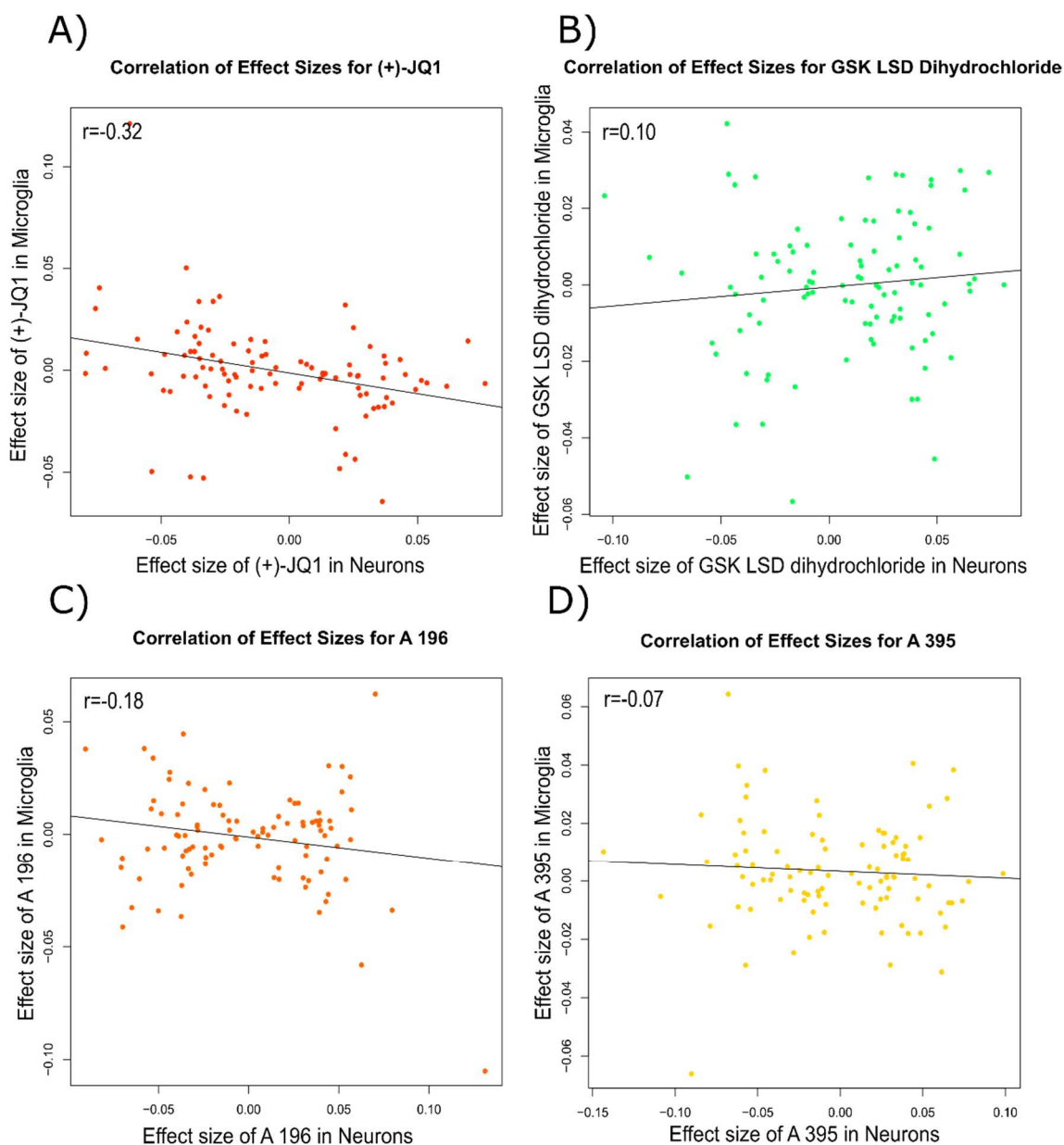
Figure 4.17. There is no correlation of effect sizes for the top 100 most significant DMPs identified in neurons treated with a compound, with the same probes in microglia treated with the same compound.

To assess whether each drug was having a consistent significant effect on the top 100 DMPs identified in the neurons in a particular compound, with the same probes in microglia treated with the same compound binomial testing and Pearsons correlation were used. Shown as an example are the correlations of effect sizes for **(A)** (+)-JQ1, **(B)** GSK LSD dihydrochloride, **(C)** A 196 and **(D)** A 395 within the neurons and microglia. For each comparison the correlation (r value) is also given.

4.5 Discussion

In this chapter I have undertaken epigenome-wide analyses at base-pair resolution of the DNA methylation changes that occur when iPSC-derived neurons and microglia are treated with different compounds that are known to affect different epigenetic mechanisms. To facilitate this, iPSC-derived neurons and microglia were treated with each of the different compounds in triplicate, DNA was extracted and then run on the Illumina EPIC array to quantify the DNA methylation levels at over 850,000 loci.

One of the first things to be shown in this chapter is that both the stem cell derived neurons and microglia have an immature epigenetic or biological age. Consistent with previous chapters the epigenetic ages of the neuronal samples are all foetal with the control sample ages being approximately ~-0.45 to ~-0.30 years. The microglia on the other hand have a significantly higher epigenetic age which for the control group, ranged from ~0.20 and ~0.40 years. This suggests that the iPSC-derived microglia are older in terms of their epigenetic age but despite this are still representative of microglia from an infant. The other marker of "age" used in this chapter was the number of cellular divisions the cells had been through. Again this was higher for the microglial samples, with the neuronal control samples only having undergone ~450 divisions, which is less than half of that of the control microglia, which had been through approximately 1000 cellular divisions. This suggests that the microglia have undergone more divisions, which is likely a reflection of the fact iPSC-derived microglia are proliferative whereas neurons are not.

Interestingly, none of the treatments seemed to have any effect on either the epigenetic or mitotic ages of the neurons or microglia. This lack of effect could be due to the short duration of treatment for the two cell types, which was only 24 hours. Had the cells been exposed to the treatments for longer it is possible that there could have been a greater effect on the epigenetic and mitotic ages of the cells. Despite the lack of significant effect on maturity some of the treatments do seem to have reduced the amount of variation in epigenetic age. For example, UNC 0642 reduced the variation in epigenetic age for both neurons and microglia, suggesting that UNC 0642 has a more specific effect on the loci used to calculate the epigenetic age in both cell types than other treatments. Alongside this, other compounds seemed to have a cell type specific reduction in variation. For example, UNC 1999, MS 049 and A 196 reduced the variation in the neuronal samples yet A 366 OF1 and TP 064 reduced variation in the microglial epigenetic ages. This could suggest that the treatments are having cell type specific effects and that again the loci used to derive the epigenetic age clock are most susceptible to these compounds. Although, as there are few replicates per treatment it is difficult to truly assess the effect of treatments on variation. In terms of mitotic age, the neuronal samples have less variation in terms of number of cellular divisions, which is likely a consequence of all the replicates for the neuronal being plated and processed at once whilst the microglial replicates were plated and processed separately. Aside from GSK 591 the treatments do not seem to reduce the variation in any of the microglial samples. Whereas in the neuronal samples A 395, GSK LSD1 dihydrochloride, MS 023 and OF1 seem to reduce variation. In the future to combat the variation seen in the microglial samples it will be important to plate and collect the replicates all at the same time and to run more replicates per treatment group.

Using linear regression models I aimed to identify DMPs that were associated with each type of treatment. I did not identify any Bonferroni significant DMPs, which is likely due to the low number of replicates per treatment group and in the future it will be of interest to include more samples. However, given the fact that DNA methylation at neighbouring CpG sites is highly correlated, Bonferroni correction is likely overly conservative [333]. To this end I did identify a number of DMPs at a more relaxed p-value threshold of 5.00×10^{-4}, and particularly within the microglial samples a number of these DMPs were also nominally significant ($p < 0.05$) in all of the other treatments targeting the same epigenetic mark *i.e.* BRD, HMT, HKDM or KMR. This suggests that within the microglial cells the treatments of the same category seem to cause similar methylation changes at the same loci. From running pathway analyses on these DMPs it was determined that the inhibitors could be affecting pathways relating to receptor internalisation, GTPase activity, the regulation of chromatin organisation, the regulation of apoptosis and immune relevant pathways. However, it is worth noting that only two of the pathways pass the FDR significance threshold and so cautious interpretation is required. To validate these pathway analyses findings further experimental validation is necessary. In contrary to this very few common DMPs were seen in neurons treated with compounds of the same class. This suggests that unlike in the microglia these treatments had a less specific effect on DNA methylation as the same loci were not significant across the different treatments. This is possibly a reflection of the short treatment time and low number of replicates used, as previously discussed in the future it would be of great interest to treat the cells for longer and also undertake more replicates in order to try and boost the power of the study.

In order to circumnavigate the issue of power I instead decided to look at the direction of effect and effect size for each of the compounds in the same class as these measures are unaffected by the number of replicates. From this it was possible to determine that the compounds of the same class, *i.e.* BRD, HMT or HKDM caused consistent changes in terms of the direction of effect and had highly correlated effect sizes for the top 100 DMPs in both the neurons and microglia. This demonstrates that despite there not being common DMPs within the same treatment groups the treatments are exerting a similar effect on methylation at the same CpGs within the neurons. Interestingly, when the effect size and direction of effect were compared between the neurons and microglia given the same treatment there was no significant consistency in the direction of effect and the effect sizes were not correlated. This infers that the treatments are exerting cell type specific effects on the methylation of the top 100 DMPs. In general, the compounds may have a more specific effect in the microglial cells and this is why there are consistent changes seen across compound categories despite there being little overlap with the top 100 DMPs of the neuronal samples.

Another possibility is that the lack of correlation between the treatments in the different cell types is a result of the different genetic backgrounds of the cell types. A consequence of the neurons and microglia being generated in different labs is that they are derived from different people. It is possible that the differential effect of methylation seen in the different cell types is a reflection of the genotypic differences between them. In order to determine whether this is indeed the case it would be of interest to repeat this experiment using neurons and microglia that have been derived from the same person/cell line. However regardless, based

on the data presented in this chapter, moving forward it would appear that the iPSC-derived microglia are a more interesting model in which to study the effects of these epigenetic modulators. The discordancy between the DNA methylation changes in neurons and microglia potentially demonstrates that the microglia could be the more interesting cell type to further study the effects of the epigenetic modulators. This is because within the microglial samples there are loci which are consistently differentially methylated in all compounds of the same type suggesting that the compounds of the same type have a similar effect in terms of the pathways they are potentially altering.

Alongside assessing methylation it would also be interesting to identify the transcriptomic changes and changes to the specific histone modifications themselves (*i.e.* histone acetylation or methylation) that are associated with each of the treatments. Having both transcriptomic and DNA methylomic information in both cell types and for all treatments would make it possible to determine whether the cellular pathways associated with the differentially expressed genes are similar to the differentially methylated pathways I identified in microglia in the current study. The RNA for these samples has been collected but it wasn't in the remit of this PhD to run the sequencing experiments and undertake the data analysis. Another interesting avenue in which this study could be taken further is to study other epigenetic mechanisms such as histone modifications as a number of the treatments are known to interact with or cause changes to the modifications of histones. Finally, it would be interesting to relate both the DNA methylomic and transcriptomic changes to the loci and pathways that are already known to be altered in the brain or blood of individuals with various diseases known to have a significant epigenetic component, such as AD.

One caveat of this study is that the replicates for the microglial samples were plated out and collected at different times whereas the neuronal replicates were all plated and collected at the same time. By collecting the replicates at different time it introduced variation into the data, which I was able to detect using PCA. As a result of this, and in order to remove the effect of replicate on the data, combat analysis was used. Whilst it is possible to control and reduce this variation it is not the ideal situation as you could potentially also be eliminating variation that is a result of the treatments. When you have very small sample numbers/replicates in the first instance removing any variation could potentially obscure the effect of treatment therefore introducing false negatives.

Finally, in the future it will be important to expand this study to include different drug concentrations and different treatment times. A concentration of 3μM was chosen as all the inhibitors have been shown to have >30-fold selectivity versus other subfamilies and have been demonstrated to have on-target effects in cells at this concentration. Alongside this as this study is exploratory and only the initial effects the modulators have on DNA methylation were to be studied a treatment time of 24 hours was deemed acceptable. However, as modulators such as these could evoke a bi-phasic change within the cell lines used it will therefore be important in the future to determine the effect the compounds have at both different incubation times and at different concentrations.

4.6 Conclusions

In this chapter I have characterised the genome-wide patterns of DNA methylation that are associated with the treatment of iPSC-derived neurons and microglia with different compounds known to affect epigenetic mechanisms. I have again shown that iPSC-derived cells have a foetal or immature epigenome and that the short treatment with the epigenetic modulators does not affect their epigenetic or mitotic age. Within the microglial samples similar DNA methylation changes were observed with compound within the same category, suggesting that the same loci are being affected by related compounds in microglia, which was not the case for the neurons. Alongside this within both the neuronal and microglial samples the compounds of the same type exerted a similar effect in terms of the effect size and direction of effect on DNA methylation. However, when comparing the effect size and direction of effect for the same compound in the two different cell types there was no significant correlation suggesting that the effects of each compound are cell type specific and this warrants further investigation. Through these analyses it is clear that there are large numbers of loci within both the neurons and microglia whose DNA methylation profile is altered upon treatment with the different epigenetic modulators.

Overall, I have identified DNA methylomic variation within iPSC-derived neurons and microglia that is associated with compounds known to regulate epigenetic mechanisms. I have demonstrated that these changes happen in a cell type specific manner and that there are more consistent effects seen within the microglia making them potentially a more interesting cell type to investigate in the future.

CHAPTER 5 : DNA METHYLOMIC VARIATION INDUCED BY LPS CHALLENGE IN A HUMAN MICROGLIAL CELL LINE

5.1 Introduction

5.1.1 Microglial Biology and Response to Immune Challenge

Despite being originally believed to be immune privileged, the CNS is now known to be able to have immunological capability, which differs from that of other peripheral tissues. These immune reactions depend on specialised innate immune cells such as microglia, which are the most common type of CNS-resident immune cells. Unlike other brain cell types, microglia arise from EMPs in the yolk sac [54]. Resting microglia in the adult brain have a small cell body with many highly ramified processes (figure 1.3), a morphology which distinguishes them from other immune cells such as macrophages [58]. Microglial cells have a number of different functions and are critical in neurodevelopment [334-336], synaptogenesis [337-339] and responding to CNS immune challenges [340-342]. Under homeostatic conditions microglial cell bodies remain stationary whilst their processes move and scan the surrounding extracellular space communicating with astrocytes, neurons and blood vessels [343]. However, resting microglia can be activated by a number of CNS challenges including injury, infection, neurodegeneration and protein aggregates [344]. On detecting these insults microglial morphology changes rapidly and they become less ramified, begin to express more inflammatory markers and produce inflammatory mediators. For example, microglia have been shown to express toll like receptors [340] and release cytokines (IL-1β [345], IL-6 [346], TNF-α [347]), chemokines [348] and nitric oxide (NO) [341, 349]. This enables them to recruit other immune cells and initiate a wider immune response.

5.1.2 Neuroinflammation and AD

Despite extensive research, it is still unknown what mechanisms lead to the onset of pathological Aβ and Tau aggregates in the brain in sporadic AD. Recent evidence has suggested that immune mechanisms may play a key role in AD risk and pathogenesis [80, 82]. One common theory surrounding the involvement of microglia in AD is through the recurrent/chronic activation of microglia during ageing or in the presence of Aβ plaques. These recurrent exposures, whether it be to AD related proteins or inflammatory molecules, can trigger morphological changes, leaving the microglia less ramified, and expressing cell surface antigens that are usually reminiscent of activated cells [58-60]. Once activated microglia have a heightened response to inflammatory stimuli, releasing more inflammatory molecules which can be neurotoxic [67].

A number of large scale GWAS studies have identified genetic variation in immune-related genes in LOAD. These GWAS studies have indicated that LOAD is a multifactorial disease with many different SNPs contributing to disease onset [80, 81, 350-354]. These GWAS studies have also revealed that many of the SNPs that are associated with AD reside in genes involved in microglial biology [80, 352, 353]. This includes common variants such as *CLU*, *CR1*, *CD33*, *ABCA7*, *EPHA1* and *MS4A* and more rare variants identified from exome-sequencing studies such as *TREM2* [90, 350, 351, 353, 354]. In recent years there have been several functional studies conducted in order to try and determine the role these variants may play in disease aetiology and to establish the role microglia play in AD onset and progression. For example, *TREM2* has been shown to play a role in regulating microglial phagocytosis [355], and that missense mutations in *TREM2* cause impaired microglial phagocytosis and a reduction in soluble

TREM2 in the cerebrospinal fluid of AD patients [356]. However, in contrast to this in several mouse model of AD, *TREM2* deficiency in microglia was shown to promote survival of microglia and also enhance phagocytosis [357-359]. These findings suggest that the role of *TREM2* in modulating neuroinflammation in AD is complex and therefore further investigation is required, as is the case for many other immune-related AD variants. In general, microglia are thought to regulate the amount of Aβ in the brain through phagocytosis [360]. One interesting feature of microglia in AD brain is that they adopt a polarised morphology and cluster around fibrillar Aβ and extend hypertrophic processes towards the plaques [361]. This provides a physical barrier around the plaques and stops the deposits extending further, promoting the creation of compact plaque micro regions that have little affinity for soluble Aβ$_{1-42}$ [361, 362]. On the other hand regions of the brain that aren't covered by microglial processes are 'hotspots', with high levels of soluble Aβ$_{1-42}$ leading to markedly concentrated protofibrillar Aβ$_{1-42}$ plaque regions [361]. These "hotspots" are neurotoxic given that adjacent axons develop a greater extent of dystrophy compared to those covered by microglia [362].

Alongside GWAS, studies investigating inflammation induced cognitive dysfunction have also linked inflammation seen in the periphery to delirium and acute cognitive impairment resembling that seen in AD [363, 364]. Cytokines are key mediators in the response to inflammation and it is thought that the pro-inflammatory cytokine IL-1β may regulate both the response to infection and be responsible for inflammation induced cognitive decline [365, 366]. In accordance with this, IL-1β has been associated with delirium in patients with septic encephalopathy [367]. The high prevalence of inflammation induced cognitive dysfunction after surgery and systemic infection highlights the deleterious effects

inflammation can have particularly in those who are older and already cognitively impaired [368, 369]. Alongside this it is now apparent that infection can also increase the long term risk of developing dementia [370, 371] or accelerate its progression [372, 373].

5.1.3 Microglial *In Vivo* Models of AD Neuroinflammation

Microglia make up approximately 15% of the total number of cells in the CNS, yet despite this, microglial RNA only makes up < 0.1% of total CNS RNA [374, 375]. This relatively low proportion of total transcripts has made it quite difficult to detect the microglial molecular phenotype from that of neurons, astrocytes and oligodendrocytes in human post-mortem tissues. In order to combat this issue several *in vitro* and *in vivo* model systems have been created. These include immortalised human and rodent cell lines, primary rodent cultures, *in vivo* rodent models and more recently human stem cell models.

In the AD research field, there has traditionally been a large focus on using transgenic mice to model FAD. This is because a lot is understood about murine genetics and there is a wealth of genetic manipulation techniques that are available to develop new mouse models. The vast majority of murine AD models reflect familial AD, with mice expressing human *APP* and *PSEN* genes bearing autosomal dominant mutations [376-381]. However, other mouse models have been developed that express human genes bearing SNPs associated with sporadic AD. The *TREM2* R47H mutation has been shown through whole genome sequencing (WGS) to increase AD risk three fold [382] and so is an important mutation to study in order to understand the role of the immune system in AD onset. As such murine models to study the function of *TREM2* have been

developed, for example mice expressing human *TREM2* or with *TREM2* knocked out [383-385]. In mice expressing wild type human *TREM2* microglia have been shown to cluster around Aβ plaques forming a physical barrier between the plaques and neurons [357, 359, 362, 386]. However, in *TREM2* deficient mice the number of plaque-associated microglia is significantly reduced with there being a concomitant increase in the number of dystropic neurites surrounding the plaques [359, 386].

5.1.4 Microglial *In Vitro* Models of AD Neuroinflammation

Whilst murine *in vivo* models provide three dimensional interactions between microglia and other brain cell types similar to that of the human brain, microglial cultures *in vitro* undoubtedly also provide a useful model for studying neuroinflammation. In particular, *in vitro* models have proven useful for elucidating the basic aspects of neuroinflammation, including intracellular signalling and gene transcription. One example of this was the discovery of the involvement of p38 mitogen-activated protein kinase (MAPK) in the release of inflammatory mediators from microglia. Using BV-2 cells (immortalised mouse microglia), Bachsetter *et al* demonstrated that upon LPS stimulation, the BV-2 cells produced more IL-1β and TNF-α, but that this could be inhibited in a concentration dependent manner by a p38 MAPK inhibitor [387]. This study demonstrated the involvement of MAPK signalling in the response to LPS immune challenge and the potential to modulate cytokine overproduction through the inhibition of this pathway.

Microglial cell culture models have also been useful in disentangling the role of microglia in NO production. In a study using primary rat microglia it was shown

that LPS induced an increase in both inducible nitric oxide synthase (iNOS) reactivity and NO production, but that this could be prevented by parthenolide [388], a pro-inflammatory molecule known to bind and inhibit the cytokine signalling kinase IκB kinase β (IKKβ) [389]. Alongside this, in neuronal-microglial co-cultures LPS has been shown to induce neurotoxicity and cellular dysfunction through the activation of the COX-2 and NOS pathways, resulting in a dramatic increase in prostaglandin and NO production [390-394].

5.1.5 LPS Mechanism of Action

LPS constitutes a large proportion of the outer membrane of gram-negative bacteria and is frequently used *in vitro* and *in vivo* to mimic the presence of an infection. Interestingly, one study has shown that the blood levels of LPS are three times higher in AD patients than that of control populations [395]. Studies have also shown the presence of gram-negative microbes in the erythrocytes of AD patients [396]. LPS cannot itself under physiological conditions enter the brain, therefore it is likely *in vivo* that there are other mechanisms that allow systemic LPS to induce central inflammation, for example degradation of the blood brain barrier (BBB), ischaemia or peripheral cytokines [397, 398]. There is a proposed mechanism of action for LPS induced injury in the AD brain, which is that LPS binds to toll like receptor 4 (TLR4) or CD14 expressed on microglia within the brain [399]. This TLR4 activation then leads to NFκB mediated induction of cytokines including IL-1, IL-6 and TNF-α [400-402]. Very high levels of pro-inflammatory cytokines such as IL-1 and IL-6 can cause myelin injury and can also increase the accumulation of Aβ and APP [403]. This Aβ then can also act on TLR4 causing a feedback loop, further exacerbating the problem [403]. LPS has also been shown to be able to act on the BBB and cause a decrease in

the amount of Aβ being able to leave the brain [398]. Finally, LPS is also known to induce Tau hyperphosphorylation, another protein whose accumulation is a characteristic hallmark of AD [404-406]. Taken together the combination of all these factors could cause or amplify the neurodegeneration seen in AD.

5.1.6 Identifying Methylomic Variation in Microglia following LPS Stimulation

It has previously been demonstrated that there is both epigenetic dysfunction [121, 407-410] and neuroinflammation in AD [60, 61, 68, 411]. As stated above one mechanism through which neuroinflammation and neurodegeneration may be mediated is through recurrent stimulation and activation of microglia by immune activators such as LPS, and this could be mediated via epigenetic mechanisms. With microglial cells representing a relatively small proportion of the cells in the brain it has been difficult to assess the methylomic signature of human microglia *in vivo* following immune challenge. In order to establish what DNA methylomic changes may be occurring following acute exposure to LPS and subsequent recovery, then it is important to model this *in vitro*.

5.2 Hypothesis and Aims

As bacterial infection and neuroinflammation are hypothesised to play a role in the onset of AD this chapter hypothesises that exposure of microglial cells to inflammatory molecules, such as LPS, will have methylomic consequences, that some loci will be more susceptible to this exposure and that these methylomic changes will be associated with changes to biological pathways.

To address this hypothesis the aims of this chapter are:

1. To perform an EWAS of 5-mC levels following LPS challenge in a microglia cell line.

2. To identify DMPs which are associated with immune stimulation and recovery.

3. To assess the biological pathways that are changing following immune stimulation.

5.3 Methods

5.3.1 Cell Culture

The information in this section contains all the information necessary to grow, maintain and passage the microglia cell line used in this chapter.

5.3.1.1 Sources of Cells

The cells used in this study are a primary human immortalised microglia (SV40 cell line) which were bought from Accegen Biotech (ABI-TM009).

5.3.1.2 Maintenance and Passaging of Microglia

Cells were maintained at 37°C and 5% CO_2 in a humidified incubator. The SV40 microglia were maintained in the microglial maintenance medium (MMM) provided by accegen which contains essential and non-essential amino acids, vitamins, organic compounds, inorganic compounds, vitamins, minerals, 5% foetal bovine serum and growth factors necessary for the maintenance of immortalised microglia *in vitro*. The MMM contained 5% HD-fetal bovine serum (ABI-TM009-FBS25), 1% penicillin/streptomycin (ABI-TM009-PS5) and 1% microglial growth supplement (ABI-TM009-MGS5) in 500mL basal medium (ABI-TM009). Media was changed every three days until the cells were 70% confluent, thereafter it was changed every other day until the cells reached ~90% confluency. Once the cells reached approximately 90% confluency they were passaged. Before passaging T75 flasks that were pre-coated with collagen I (Corning; 354485) were washed twice with sterile water. The coated plates, trypsin/EDTA (Fisher scientific; 11580626) solution and trypsin neutraliser solution (Fisher scientific; 11654862) and MMM were pre-warmed to room

temperature, disinfected and placed within a laminar flow hood ready for use. Used media was removed from the flask and cells were washed with 5mL PBS which was then aspirated. A further 5mL PBS was added to the flask before the addition of 5mL trypsin-EDTA for three to five minutes at 37°C. The length of time they were left was determined by how quickly the cells became rounded. After the trypsinisation 5mL of MMM was placed into the flask and the combined 10mL solution transferred in to a 50mL falcon tube already containing 10mL MMM. Using the base of the hand the flask was gently tapped in order to dislodge cells from the base of the flask. 5mL trypsin neutraliser solution was then washed over the base of the flask and placed in the 50mL falcon containing the rest of the cell suspension. The cells were then pelleted through centrifugation at 1000rpm for five minutes. Following this, the number of cells per mL was calculated with a TC20^{TM} automated cell counter (Bio-Rad). Once the number of cells per mL was known it was possible to calculate the dilution factor needed in order to give a density of 10,000 cells/cm^2. This was achieved using the following equation:

$$\frac{Density\ of\ cells\ you\ have\ (cells/mL)}{Density\ of\ cells\ you\ want\ (cells/mL)} = Amount\ of\ cell\ suspension\ per\ T75.$$

Once plated, cells were placed back in the incubator to attach.

5.3.1.3 Stimulation with LPS

Cells were plated out at a density of 10,000 cells/cm^2 into four wells of three individual six-well plates (*i.e.* 12 wells in total). Each plate contained the four replicates for the three different treatments used in this study. Those treatments were: (1) no LPS treatment (control group), (2) 24-hour treatment with 1ug/mL LPS (LPS group) and (3) 24-hour treatment with 1ug/mL LPS followed by a 24-hour recovery period (LPS + recovery group). For the LPS treatments stock

concentrations of LPS (1mg/mL) were diluted 1:1000 into pre-warmed MMM. 48 hours after plating the LPS and LPS + recovery groups had their normal MMM removed and it was replaced with MMM containing 1ug/mL LPS. The control group underwent a normal media change. After 24 hours the control group and LPS treatment groups were washed twice with PBS and collected as pellets using tryspin-EDTA and trypsin neutraliser solution as outlined above. The LPS + recovery group were washed twice with PBS and then the media was replaced with normal MMM. After a further 24 hours on MMM the LPS + recovery group were collected and pelleted using trypsin-EDTA and trypsin neutraliser solution. An outline of the experimental workflow is provided in figure 5.1.
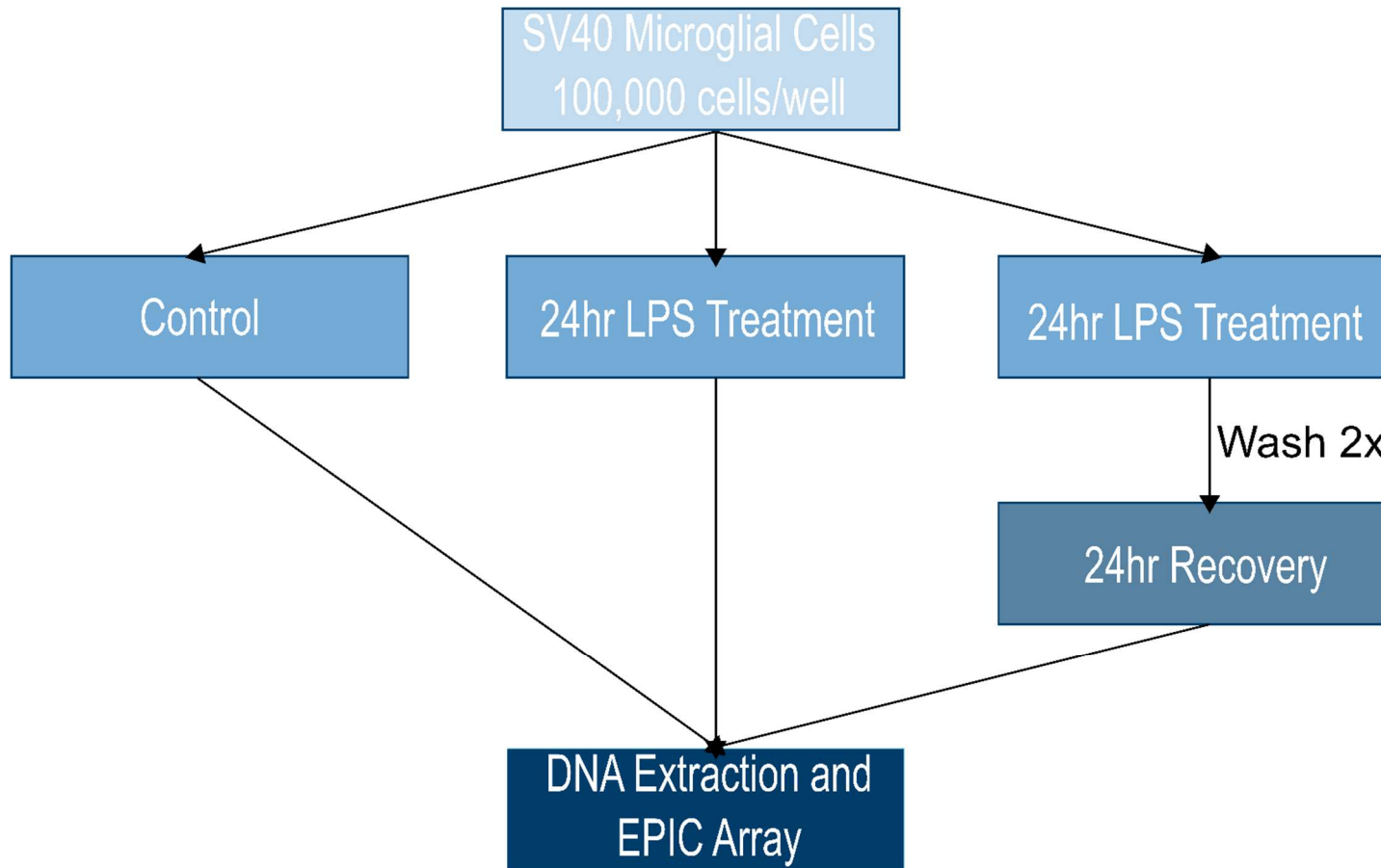
Figure 5.1. Diagram to illustrate the experimental workflow.

SV40 immortalised primary microglial cells were plated out in quadruplet for the three conditions at a density of 100,000 cells per well. 48 hours after plating two of the conditions were treated with 1μg/mL LPS and the cells corresponding to the control condition underwent a normal change of media. 24 hours following this first treatment the LPS and control condition cells were pelleted down and frozen at -80ºC, whilst the LPS + recovery group underwent a change of media to normal MMM and were collected 24 hours later.

5.3.2 DNA Extraction and Methylomic Profiling

DNA was extracted from cell pellets and QC checked as described in section 2.2. 500ng of DNA was bisulfite treated as described in section 2.3. Subsequently bisulfite-treated DNA was analysed for DNA methylation using the EPIC array protocol as described in section 2.4 and in figure 2.2.

5.3.3 Illumina EPIC Data QC

For an outline of the QC and normalisation methods used in this chapter please see sections 2.4.2. All data analyses in this section were performed using R version 3.5.2. Signal intensities were imported into R using the methylumi package [262]. Initial QC checks were conducted using functions within the methylumi and wateRmelon packages [198, 262].

Using the default settings of one percent with "pfilter", no samples, 13,207 sites with a beadcount less than three and 9,180 sites having 1% of samples with a detection p-value of greater than 0.05 were flagged for removal.

5.3.4 Data Analysis

Outlined in this section are the analysis steps conducted in order to assess and quantify the DNA methylation changes occurring immortalised primary microglia are treated with the known immune stimulant, LPS.

5.3.4.1 PCA

In order to look at variation within the dataset PCA was used. Using the "prcomp" function within the default statistics package within R the top principal components

were identified. These principal components were then correlated to known variables, which included treatment, which BeadChip the sample was run on (Chip ID) and position on the BeadChip using spearman correlations.

5.3.4.2 Identification of DMPs

Following normalisation, probes with common (>5% minor allele frequency (MAF)) SNPs within 10 bp of the single base extension and probes with sequences previously identified as potentially hybridizing to multiple genomic loci were excluded [203]. The top 20% most variable probes were identified using the median absolute derivation (N = 158,310 probes). Subsequently, three linear models were used to identify which of these probes were differentially methylated between the three treatment groups (control, LPS, LPS + recovery). We identified four patterns of methylation changes in probes, corresponding to whether they became hyper- or hypomethylated over the 24 hours of LPS treatment and then whether these patterns reverted during the recovery stage (*i.e.* were acute changes), or whether they were persistent through the recovery, as illustrated in figure 5.2. An arbitrary significance threshold of $p < 1\times10^{-3}$ was used to determine whether the probes were differentially methylated between treatment groups.

5.3.4.3 GREAT annotation

Many of the CpG loci covered by the Illumina EPIC array reside in non-coding regions of the genome, meaning it can be difficult to infer meaning to the changes in methylation observed at these loci. Although UCSC gene annotation [271] is provided by Illumina for loci on the EPIC array, there are many loci that lack annotation. In order to gain meaning from these changes and fill in the annotation gaps GREAT was

used to annotate each locus to its nearest gene [412]. Using the chromosomal location of each CpG probe, GREAT was able to annotate each loci to the single nearest gene that is between 1000 kilobases upstream or downstream [412]. Using this annotation method, all bar one probe was annotated to a nearby gene. The function of each of these genes was then manually searched for and recorded.

5.3.4.4 GO Pathway Analysis

GO pathway analysis was performed on each of the four different methylation change categories (i.e. hypermethylating acute, hypermethylating persistent, hypomethylating acute, hypermemethylating persistent). This was performed using the "gometh" function with the missMethyl package, which was selected as it adjusts for the number of CpGs per gene. [265].

In order to add additional meaning to the pathway analysis outputs the online platform REVIGO was used (available at: http://revigo.irb.hr/) [267]. The significantly altered pathways (determined by GO ID) and p-value significance values were added to the online portal with the GO term database being set to *Homo sapiens* and the semantic similarity measure as Resnik. Once analysed the treemaps for the altered BP, MF and CC were generated and created.
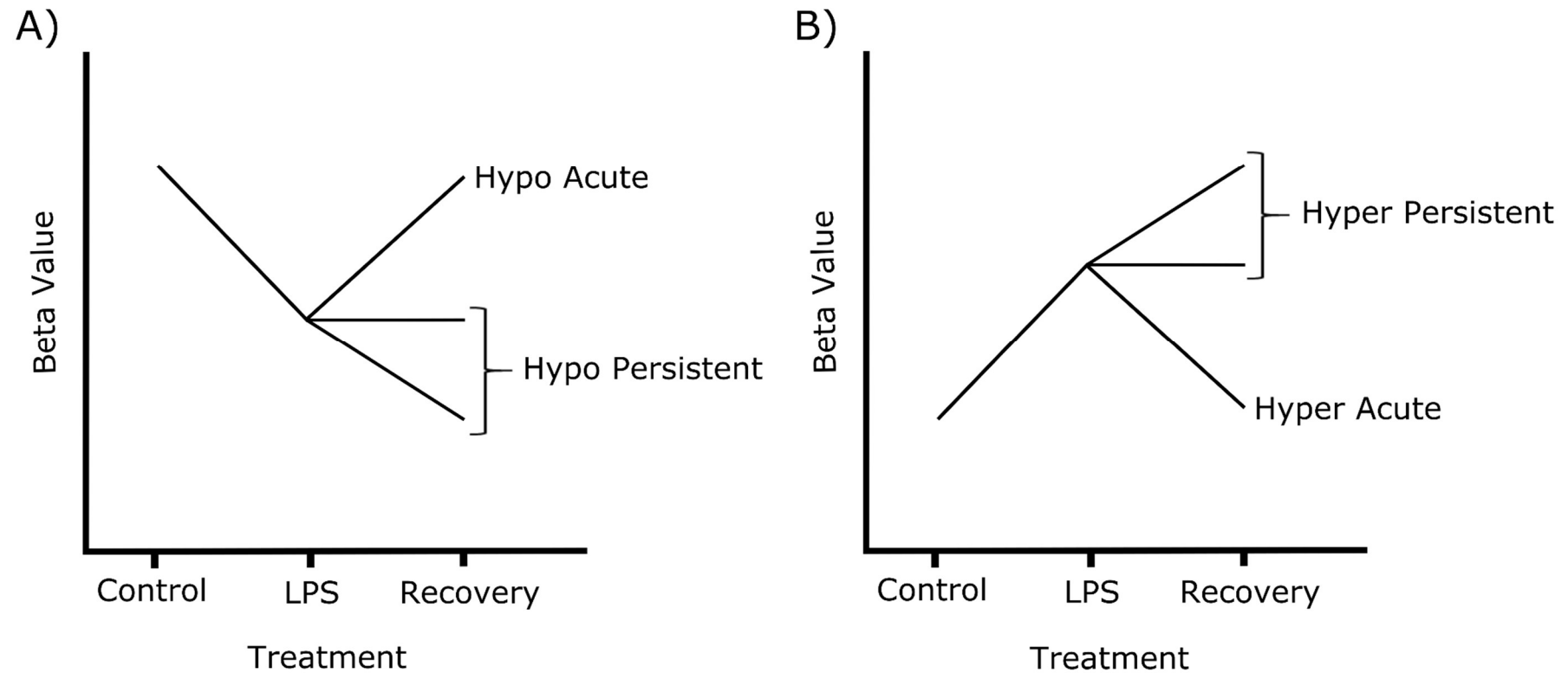
Figure 5.2. Diagrammatical representation of how differentially methylated probes were categorised.

Data analysis was undertaken once the samples had been through QC checks and dasen normalisation. Firstly using the median absolute deviation, the top 20% most variable probes were identified. These probes where then categorised based on whether they were hypomethylated **(A)** or hypermethylated **(B)** between the control and LPS groups. Within this, probes were further categorised depending on whether the methylation reverted to the control level (acute category) or whether the methylation level deviated further from control levels or plateaued (persistent category).

5.4 Results

5.4.1 Outcome of the QC Pipeline

The following section outlines the results of the QC process, which demonstrates that all the samples were of sufficient quality to take forward to the main analyses.

5.4.1.1 Median Methylated and Unmethylated Signal Intensities

In order to check that the signal intensities were above background levels the signal intensities were imported and assessed using the methylumi package [262]. This package extracts and calculates the signal intensities using the fluorescence intensity of each probe. Once the intensities were extracted the median methylated and unmethylated signal intensities for each sample were calculated (table 5.1) and plotted against one another (figure 5.3). The background level of signal intensity is generally assigned a value of 1000 although this is by no means a definitive cut off. Only one of the samples has a value below 1000, which is one of the LPS + recovery samples (LPS_recov_1). As the median unmethylated intensity for this sample was very close to the cut off (value was 997), a decision was made not to drop the sample at this stage and to instead see how it performed when assessed with the other quality control metrics.

Next, I also wanted to see whether there was any variation being introduced by the BeadChip the samples were on (Chip ID) or the position on the BeadChip. As such, the unmethylated and methylated signal intensities were replotted, with the samples coloured both by Chip ID (figure 5.4) and position on the chip (figure 5.5). Although it appeared that the unmethylated intensities of samples run on BeadChip

202073200083 were higher than the other BeadChips (figure 5.4), there was no difference in methylated values and there was no significant difference in methylated or unmethylated intensities between samples run on different chips (methylated intensities: $p=0.70$, unmethylated intensities: $p=0.60$). Similarly, samples run on the first row of the chip had higher median methylated and unmethylated intensities compared to samples run on the second row of the chip, which had higher intensities than those run on the third row of the chip (figure 5.5). However, this pattern is always seen on BeadChips, and there was no significant difference in the ratio of methylated to unmethylated intensities between samples run on different rows of the BeadChip ($p=0.97$).

Treatment	Sample ID	Replicate	Median Methylated Intensity	Median Unmethylated Intensity
No treatment	Control_1	1	2565	1860
	Control_2	2	1714	1296
	Control_3	3	1694	1281
	Control_4	4	2059	1852
LPS	LPS_1	1	1821	1359
	LPS_2	2	1601	1193
	LPS_3	3	1766	1344
	LPS_4	4	1861	1778
LPS + Recovery	LPS_Recov_1	1	1271	997
	LPS_Recov_2	2	2176	1643
	LPS_Recov_3	3	1564	1221
	LPS_Recov_4	4	1705	1669

Table 5.1. Median methylated and unmethylated sample intensities.

Intensities for each sample were imported using the methylumi package [262] and the median methylated and unmethylated sample intensities were calculated.

Median Sample Intensities
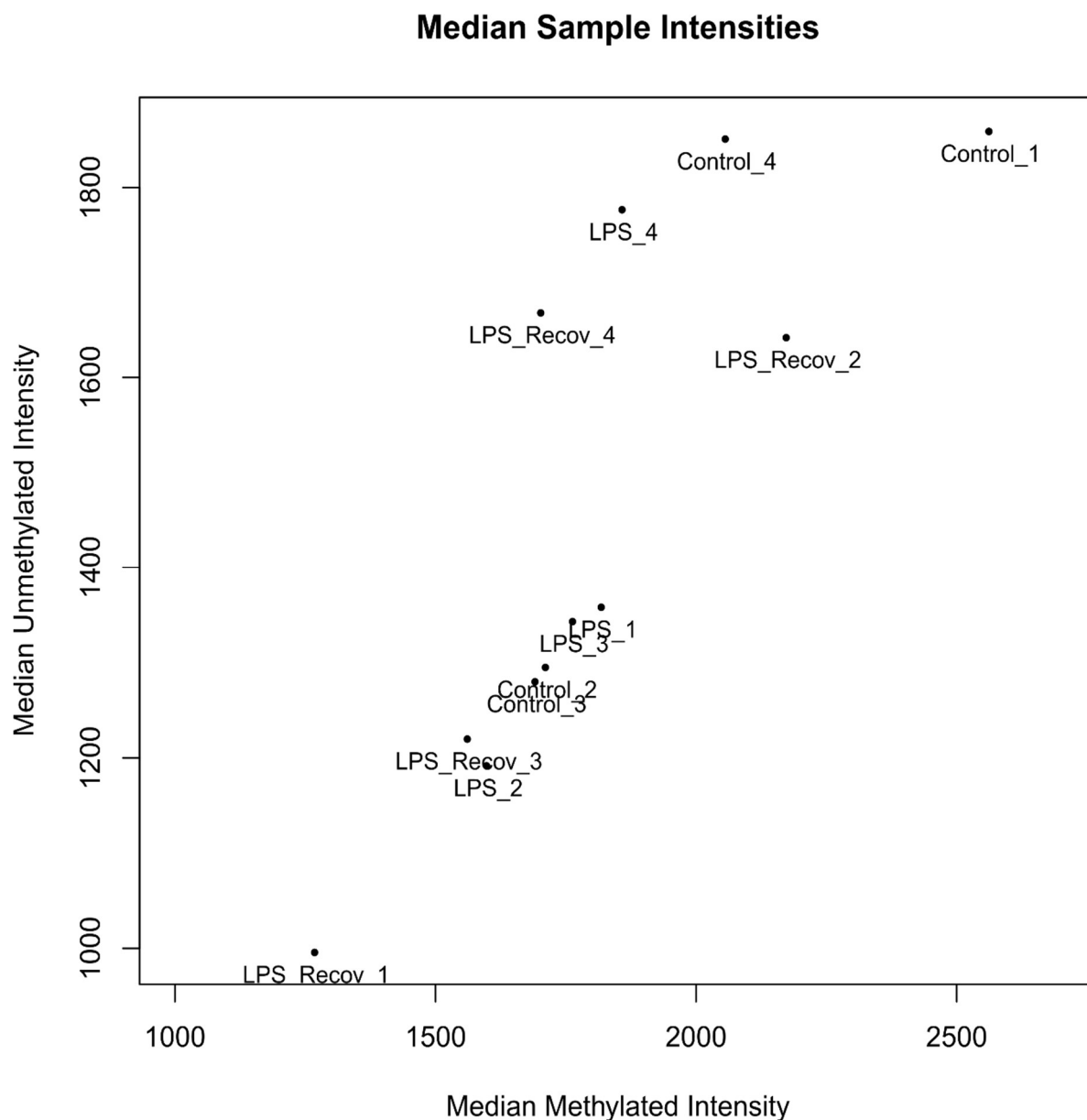
Figure 5.3. Median methylated and unmethylated sample intensities.

Using the methylumi package [262] the signal intensities for samples were extracted and the medians calculated. Shown is a scatterplot plotting the median methylated and unmethylated signal intensities for each sample. Each point is labelled with the corresponding sample ID.
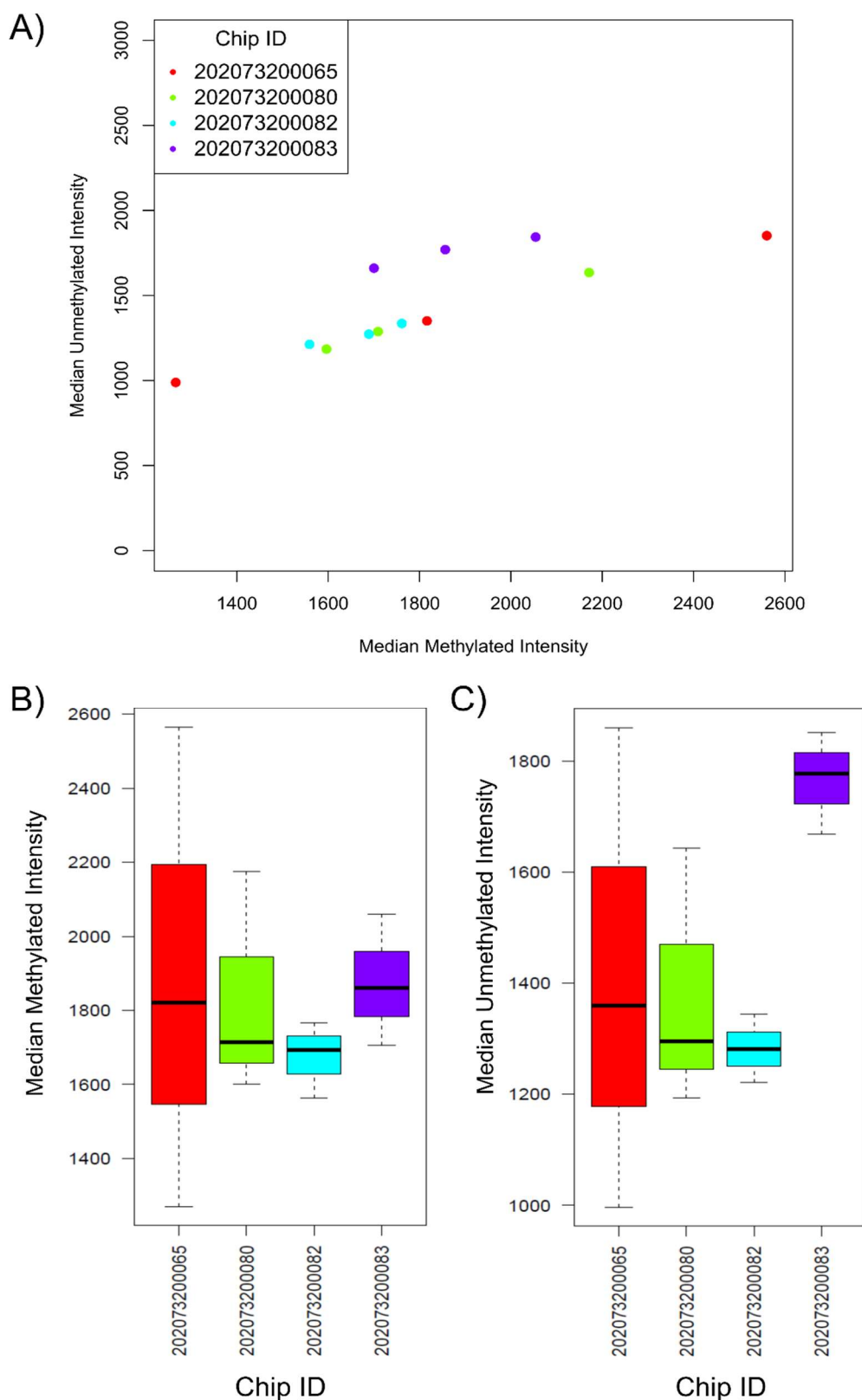
Figure 5.4. Median sample intensities coloured by Chip ID.

Median methylated and unmethylated sample intensities were calculated for each BeadChip **(A)** Median signal intensities coloured by Chip ID represented as a scatterplot. Median **(B)** methylated and **(C)** unmethylated signal intensities coloured by Chip ID represented as a boxplot. Error bars represent 1.5x the IQR.
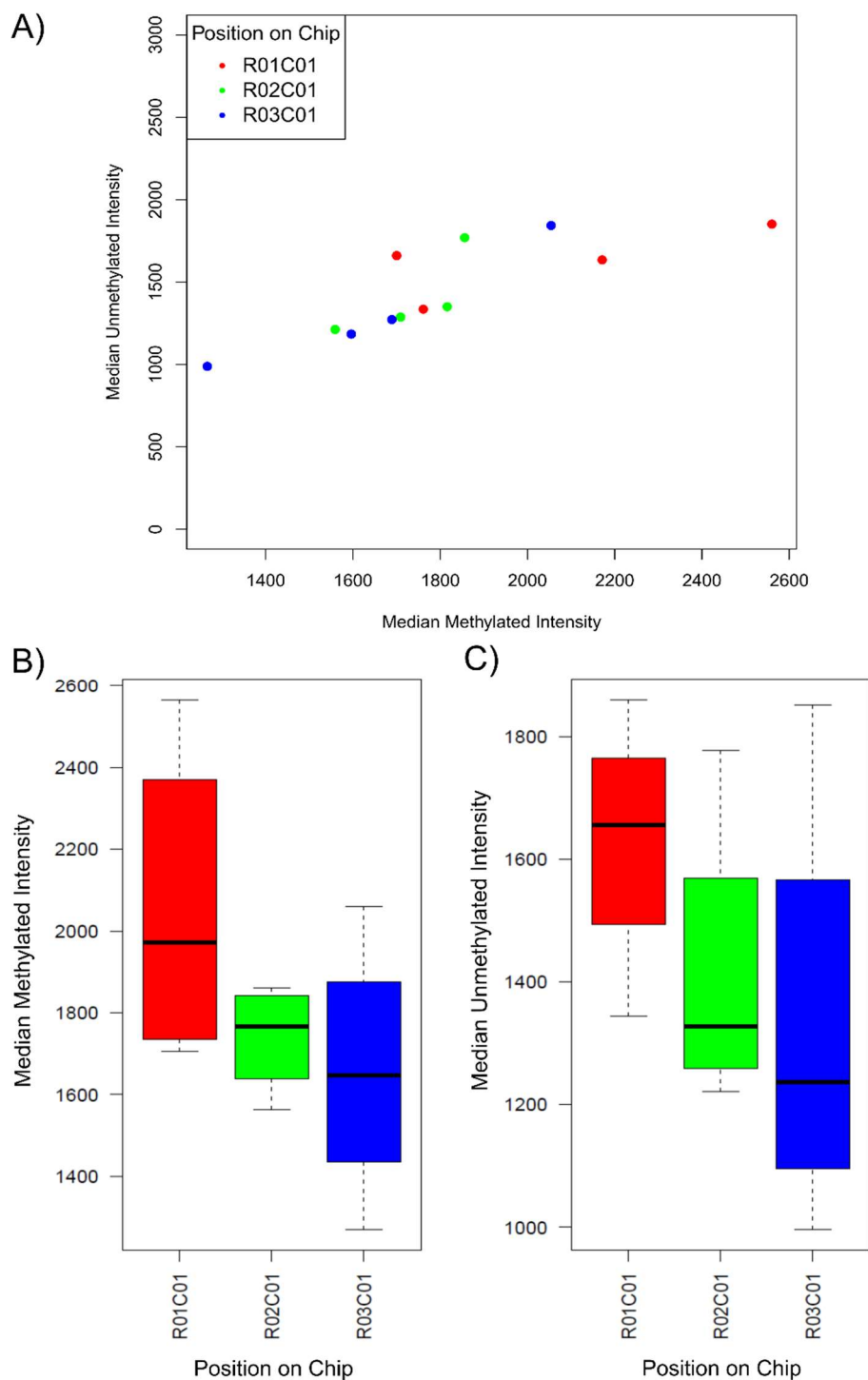
Figure 5.5. Median sample intensities coloured by position on Chip.

Median methylated and unmethylated sample intensities were calculated for each BeadChip **(A)** Median signal intensities coloured by position on chip represented as a scatterplot. Median **(B)** methylated and **(C)** unmethylated signal intensities coloured by position on chip represented as a boxplot. Error bars represent 1.5x the IQR.

5.4.1.2 All Samples have a Good Bisulfite Conversion Efficiency

Bisulfite conversion is the process that converts unmethylated cytosines into uracil and then thymine on PCR amplification and is the process that allows us to distinguish between methylated and unmethylated positions on the array. This therefore allows one to determine how methylated or unmethylated a specific loci is. Therefore, it is important that the bisulfite conversion efficiency of each sample is high. On the EPIC array there are several loci known to be fully methylated, which can be used as controls for bisulfite conversion; it is the fluorescence intensity of these loci that allows us to determine the bisulfite conversion efficiency using the "bscon" function in the wateRmelon package [198]. The lowest generally accepted bisulfite conversion efficiency is 80%. All the samples within this study are well above this cut off with the lowest conversion efficiency being 93.3% (figure 5.6).

5.4.1.3 Beta Density Plot

To determine the methylation at each locus on the EPIC array β-values were generated, which is the ratio of fluorescence signal intensity for the methylated and unmethylated beads. As the value is a ratio all β-values lie between zero and one, where zero indicates that the locus is completely unmethylated and a β-value of one indicates that the locus is fully methylated. The β-values for our samples have a bimodal distribution with most probes being either almost fully methylated or unmethylated, which is as would be expected (figure 5.7).
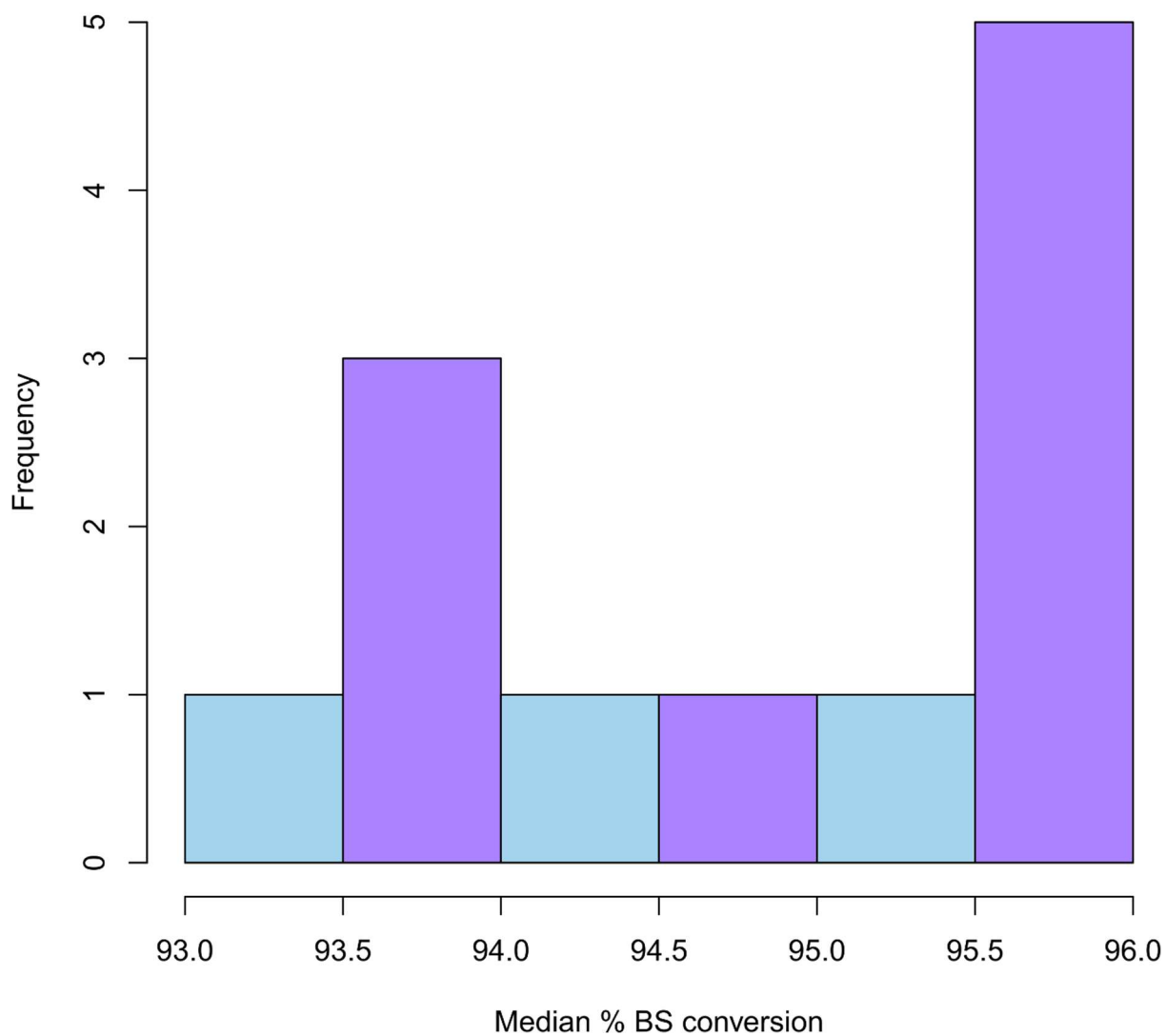
Figure 5.6. Bisulfite conversion efficiency and beta density plot.

Using data from probes on the EPIC array known to be fully methylated, the bisulfite conversion efficiency of each sample was calculated and is represented in a histogram, with median bisulfite (BS) conversion % on the X-axis and the number of samples on the Y-axis.

Density Plot of Beta Values

N = 865323   Bandwidth = 0.01874
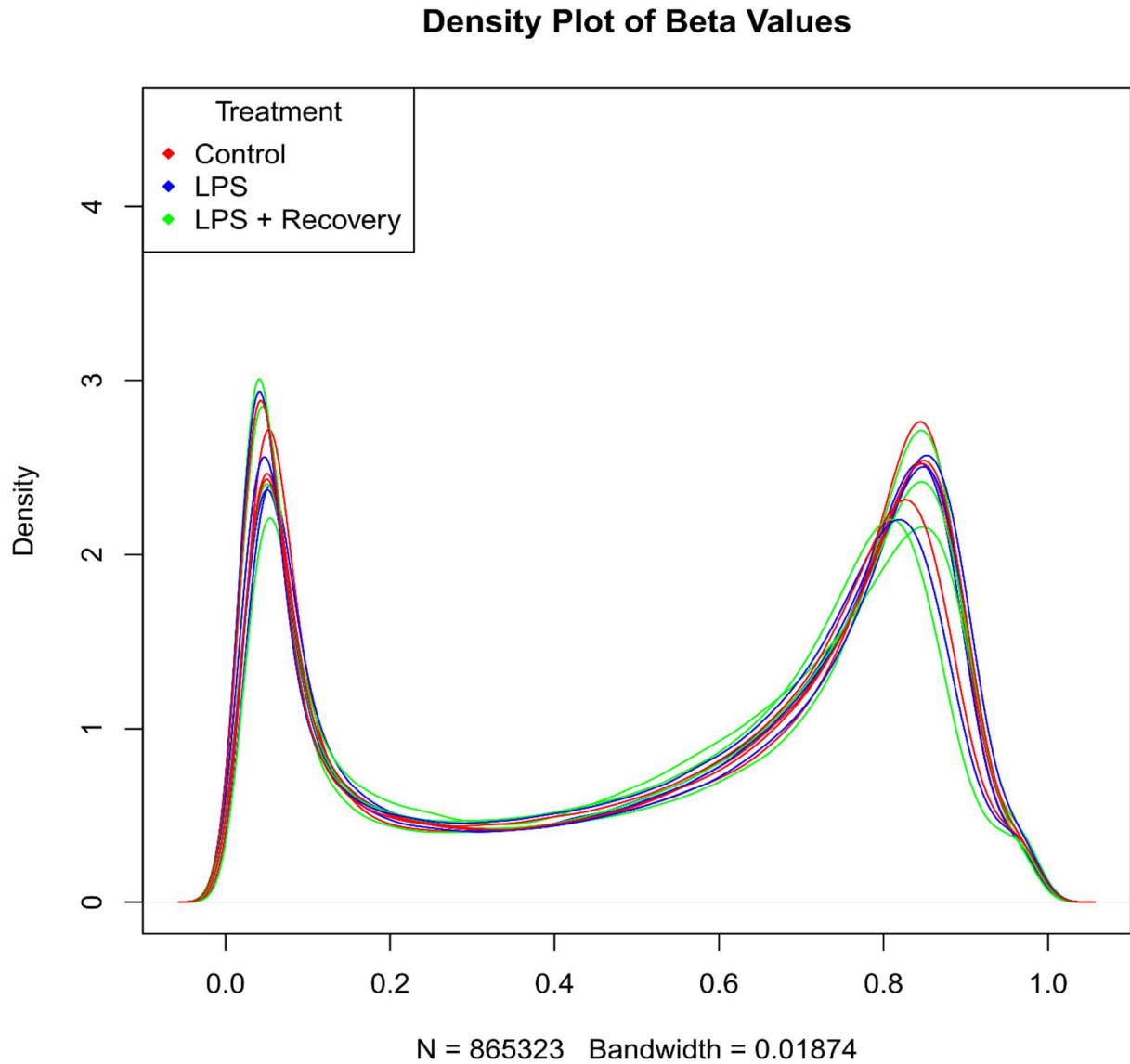
Figure 5.7. Beta density plot.

The DNA methylation level at each locus was determined using β-values, which are the ratio of fluorescence signal intensity for the methylated and unmethylated beads. The beta-values of each probe of each sample were plotted against density.

5.4.1.4 No Samples are Removed by P-filter

The final stage in the QC pipeline is to filter samples and probes by their detection p-value. The "pfilter" function in the wateRmelon package [198] highlights samples or probes that should be removed from the analysis, including samples that contain more than one percent (by default) probes above the 0.05 detection p-value threshold and probes with any samples having a beadcount less than three or more than one percent above the p-value threshold. Using the default settings, 9,180 probes were suggested for removal as they have more than one percent above detection threshold, and 13,207 sites were suggested for removal as there was a beadcount less than three in five percent of samples. These probes were removed from the analysis but no whole samples were flagged for removal. Therefore, all samples were taken forward for the downstream analyses, which are presented in the next section.

5.4.1.5 There Are No Differences in Epigenetic Age between Treatment Groups

Using the latest version of the Horvath epigenetic age calculator (available from: https://dnamage.genetics.ucla.edu/home) I assessed the epigenetic ages of the samples under the different conditions. Overall there seems to be no significant difference between the control, LPS and LPS + recovery groups (table 5.2, figure 5.8), although there is a small, non-significant decrease in epigenetic age between the control and LPS treated groups.

5.4.1.6 There Are No Differences in Mitotic Age

Using the MiAge calculator [199] I estimated the number of cellular divisions that the cells had gone through in each sample, to see if the treatments affected the perceived

number of cell divisions. The MiAge algorithm predicts mitotic age using the DNA methylation profile of 268 probes which are on the Illumina EPIC array. There were no differences in the mitotic ages of the samples (table 5.2, figure 5.9). This suggests that the treatments have not affected the methylation of our samples at these specific probes.

Treatment	Sample ID	Replicate	Epigenetic Age (years)	No. of Cell Divisions
Control	Control_1	1	18.579	3001.784
	Control_2	2	31.968	3104.674
	Control_3	3	19.968	2969.018
	Control_4	4	15.912	2801.034
LPS	LPS_1	1	15.460	3046.159
	LPS_2	2	14.524	3064.258
	LPS_3	3	19.914	2944.178
	LPS_4	4	15.602	2768.622
LPS + Recovery	LPS_Recov_1	1	12.076	2839.904
	LPS_Recov_2	2	23.741	3087.382
	LPS_Recov_3	3	16.186	2954.161
	LPS_Recov_4	4	16.117	2731.298

Table 5.2. Epigenetic and mitotic ages of SV40 microglial treated with LPS.

Using the latest iteration of the Horvath epigenetic age calculator [126] and MiAge calculator [199], the epigenetic or biological age (in years), and mitotic age (number of cell divisions) were calculated for each sample. For each sample shown above is the treatment group, sample ID, replicate number, epigenetic age and mitotic age.

Epigenetic Age Prediction
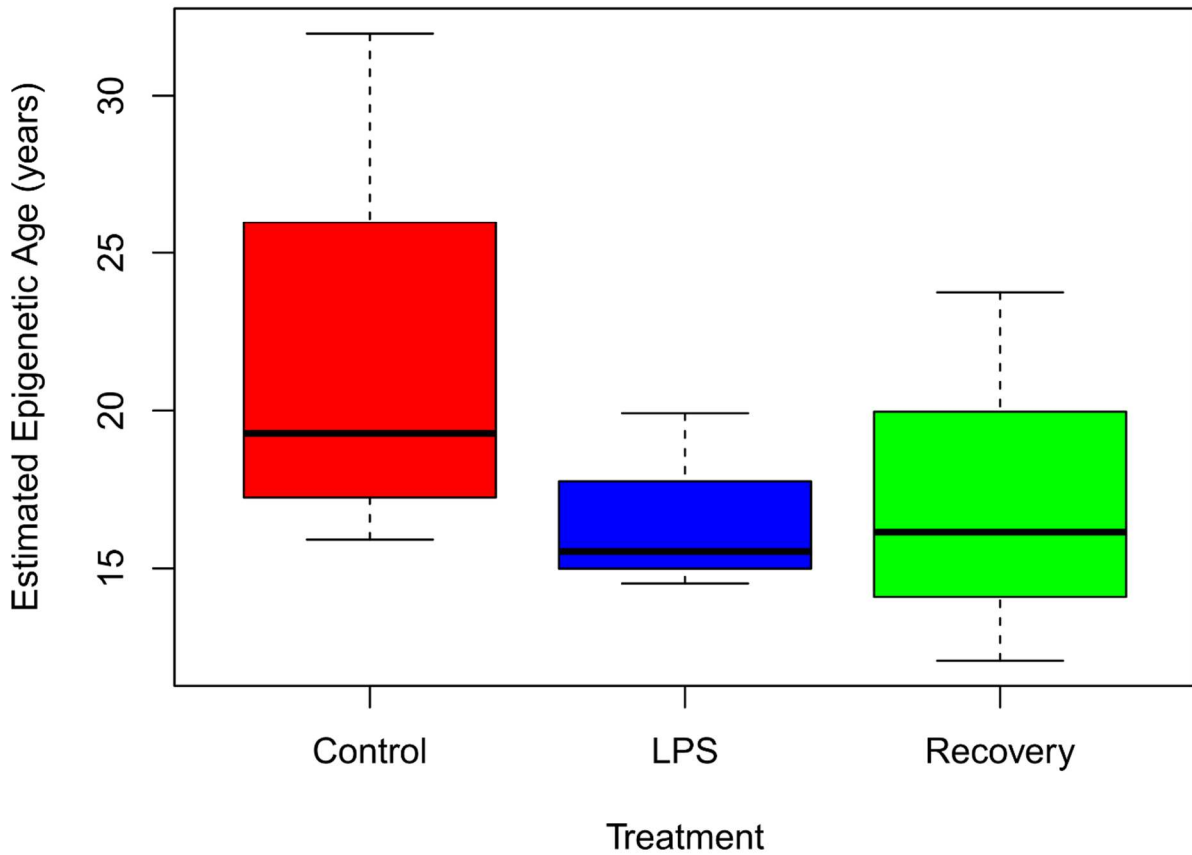
Figure 5.8. Epigenetic age is unaffected by treatment.

Using the new online epigenetic age calculator created by Horvath and colleagues [126] the epigenetic ages of each sample were calculated. Red represents the control group, blue the group treated with LPS for 24 hours and green the cells first treated with LPS for 24 hours and then given a 24 hour recovery period. Error bars represent 1.5x the IQR.

Mitotic Age Prediction
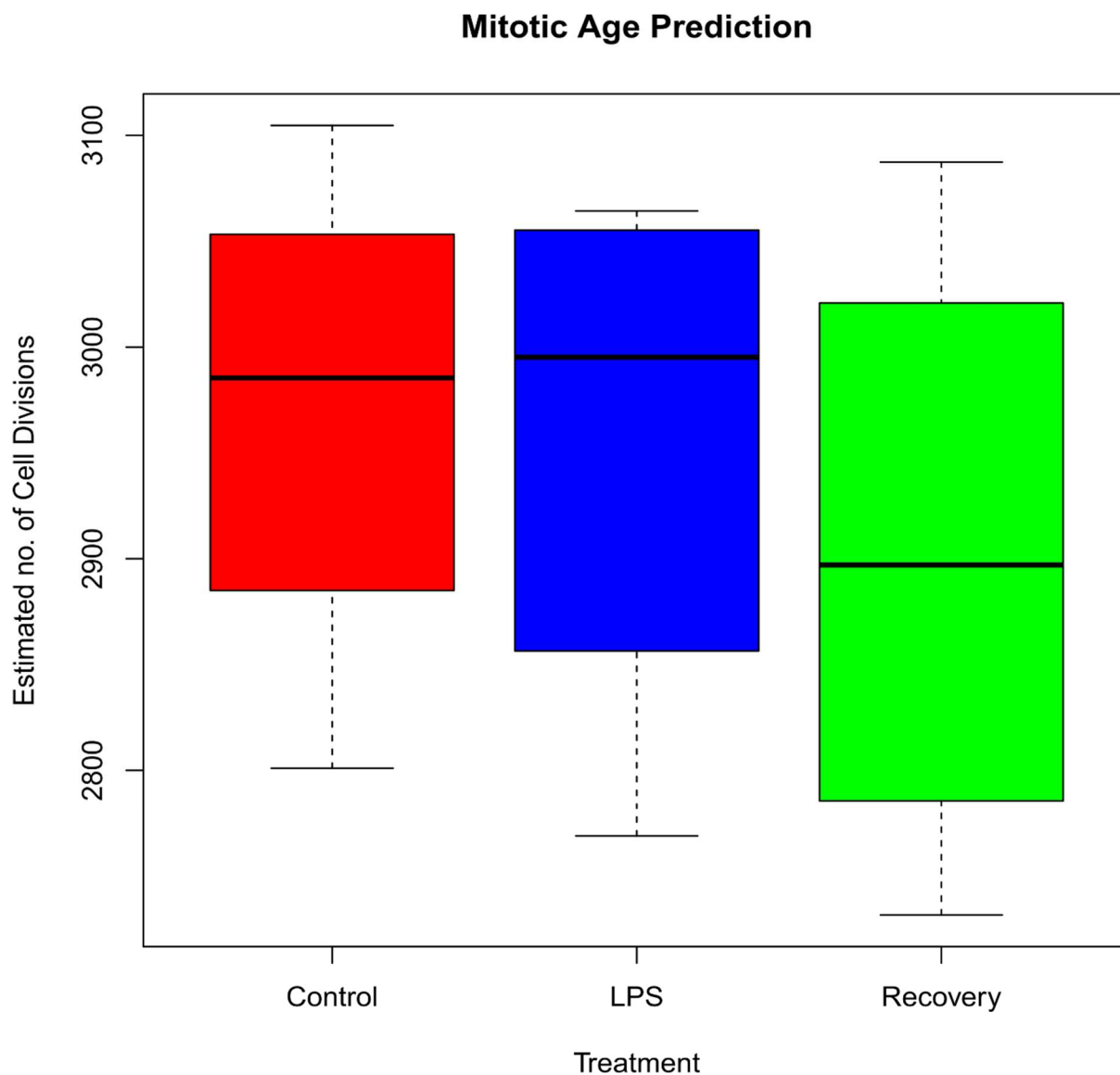
Figure 5.9. Mitotic age is unaffected by treatment.

Using the MiAge calculator [199] the estimated number of cell divisions for each sample were calculated. Where red represents the control group, blue the group treated with LPS for 24 hours and green the cells first treated with LPS for 24 hours and then given a 24 hour recovery period. Error bars represent 1.5x the IQR.

<u>5.4.1.7 Dasen Normalisation</u>

In order to make meaningful comparisons between the samples within the dataset the data was transformed using quantile normalisation using the "dasen" function within the wateRmelon package [198]. After dasen normalisation, there is a lot less variation in the median methylated and unmethylated signal intensities (figure 5.10), with all samples having a median methylated intensity between 1863-1865 and a median unmethylated signal intensity between 1481-1483.

By plotting the normalised β-values it is evident that there are bimodal peaks, which shows that most loci are either fully methylated or fully unmethylated. Across all probes the peaks are much tighter following normalisation (figure 5.11B) compared to before normalisation (figure 5.11A). This was also evident when looked at the type I probes (figure 5.12) and type II probes (figure 5.13) in isolation.

Dasen Normalised Sample Intensities
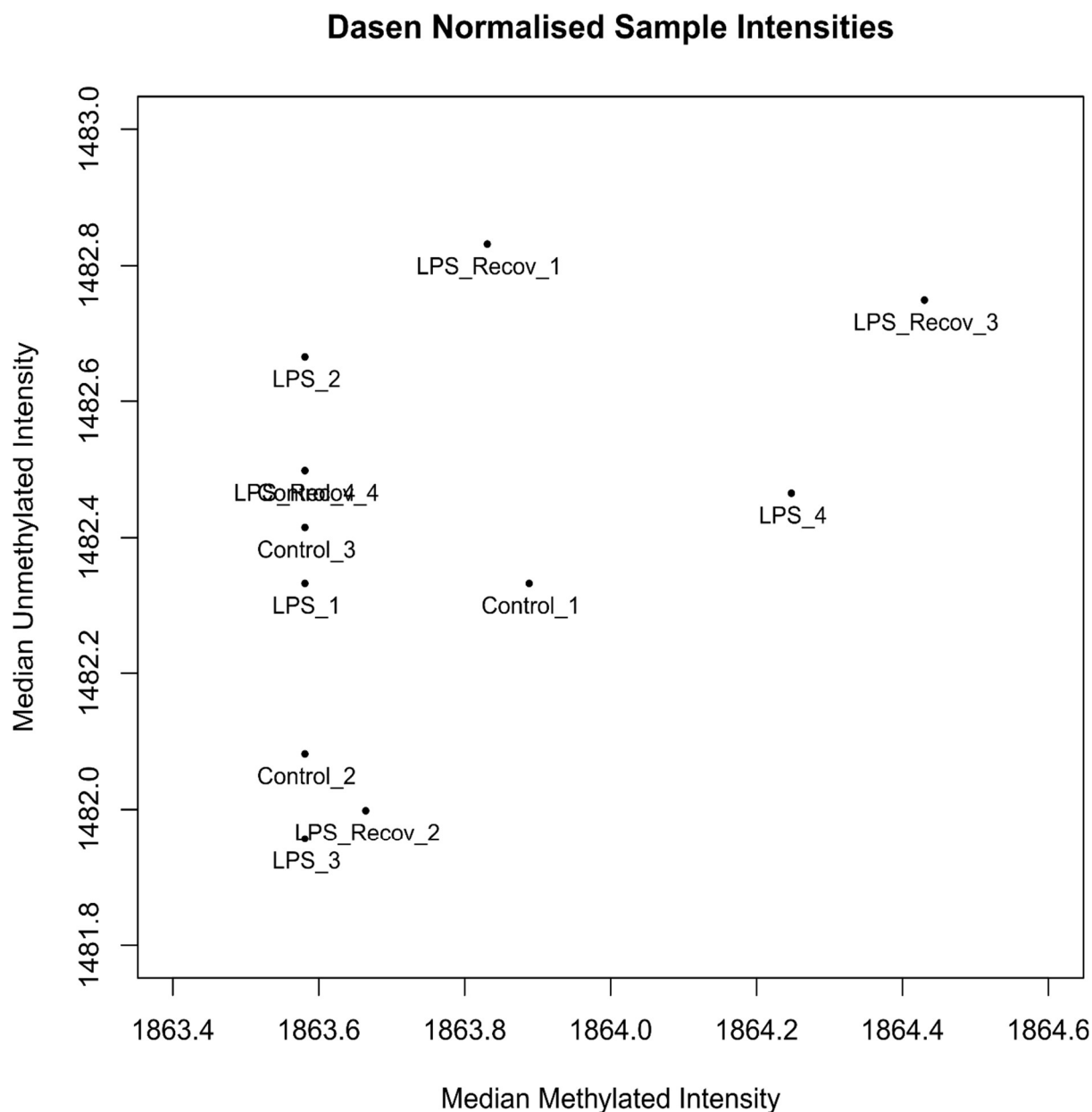
Figure 5.10. Median methylated and unmethylated sample intensities after normalisation.

Quantile normalisation was performed using dasen [198] to generate the normalised median methylated and unmethylated signal intensities. Graphical representation of median signal intensities relative to each other following normalisation. Each point is labelled with the corresponding sample ID.

A)

B)
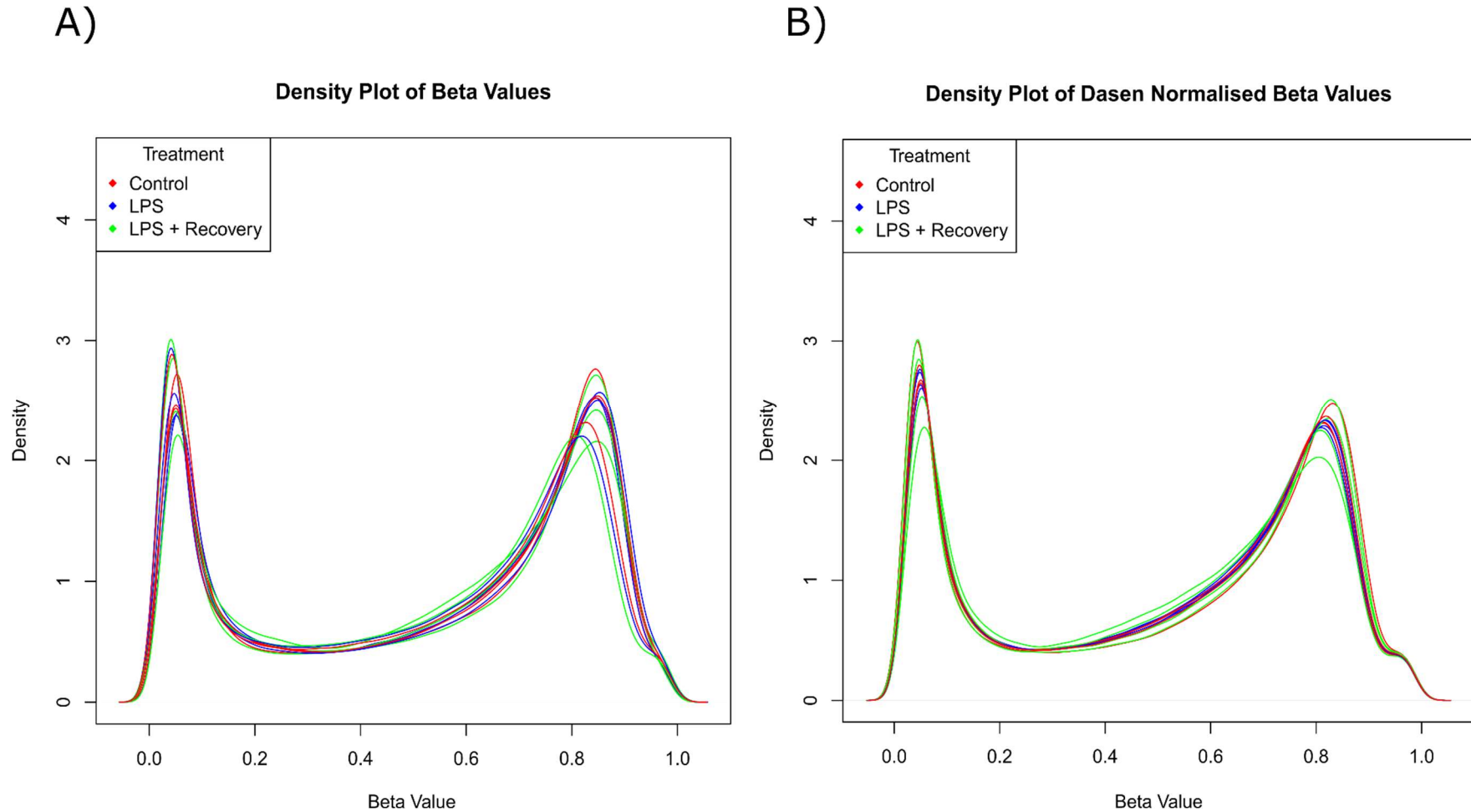
Figure 5.11. Median methylated and unmethylated signal intensities after dasen normalisation.

Quantile normalisation was performed using dasen [198] to generate the normalised median methylated and unmethylated signal intensities. Beta density plot of all samples coloured by treatment **(A)** before and **(B)** after dasen normalisation.

A)

B)
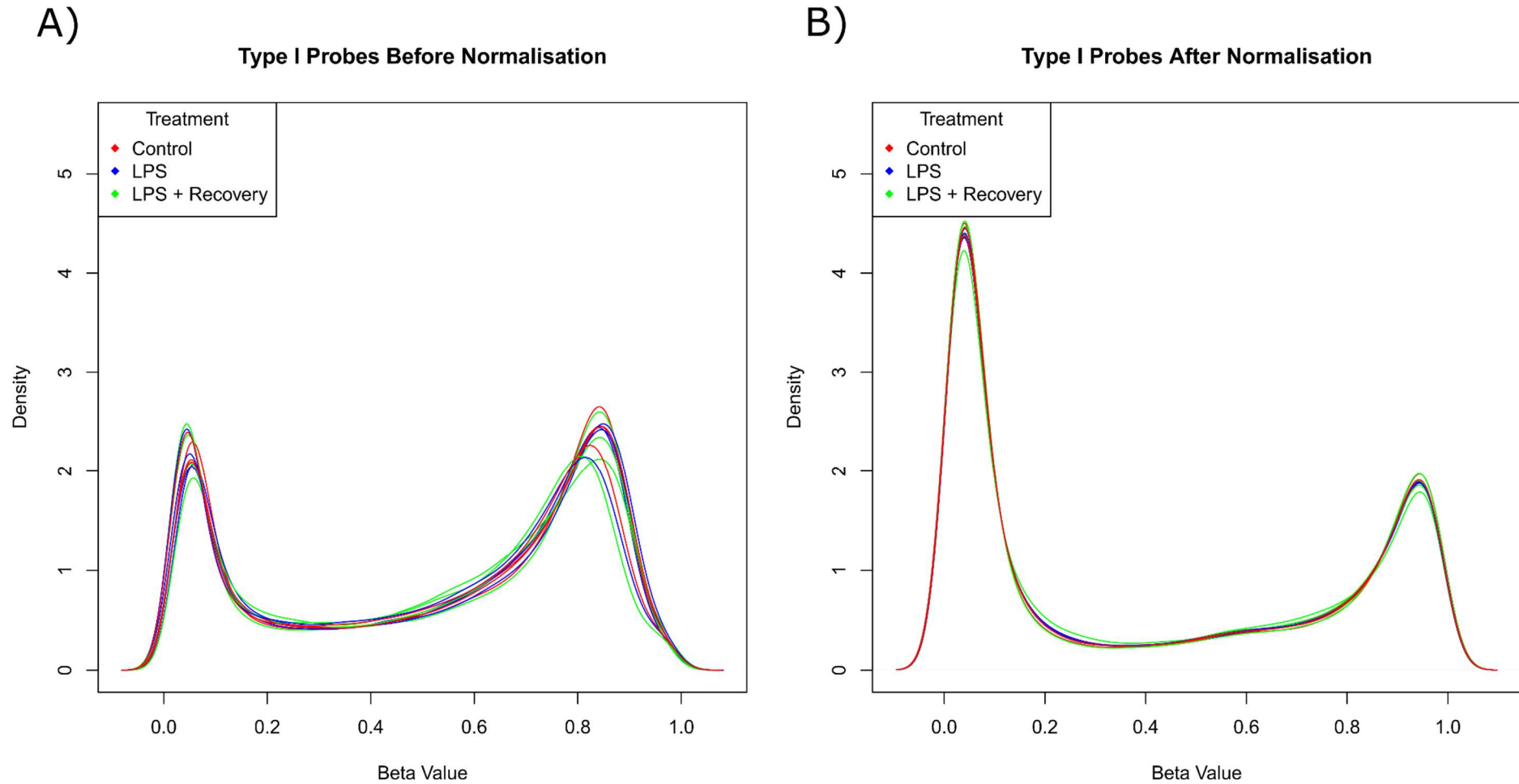
Figure 5.12. Beta density plots of type I probes before and after dasen normalisation.

Probes were separated based on whether they were type I or type II probes. Beta density plots were generated showing the beta values of type I probes **(A)** before and **(B)** after dasen quantile normalisation.
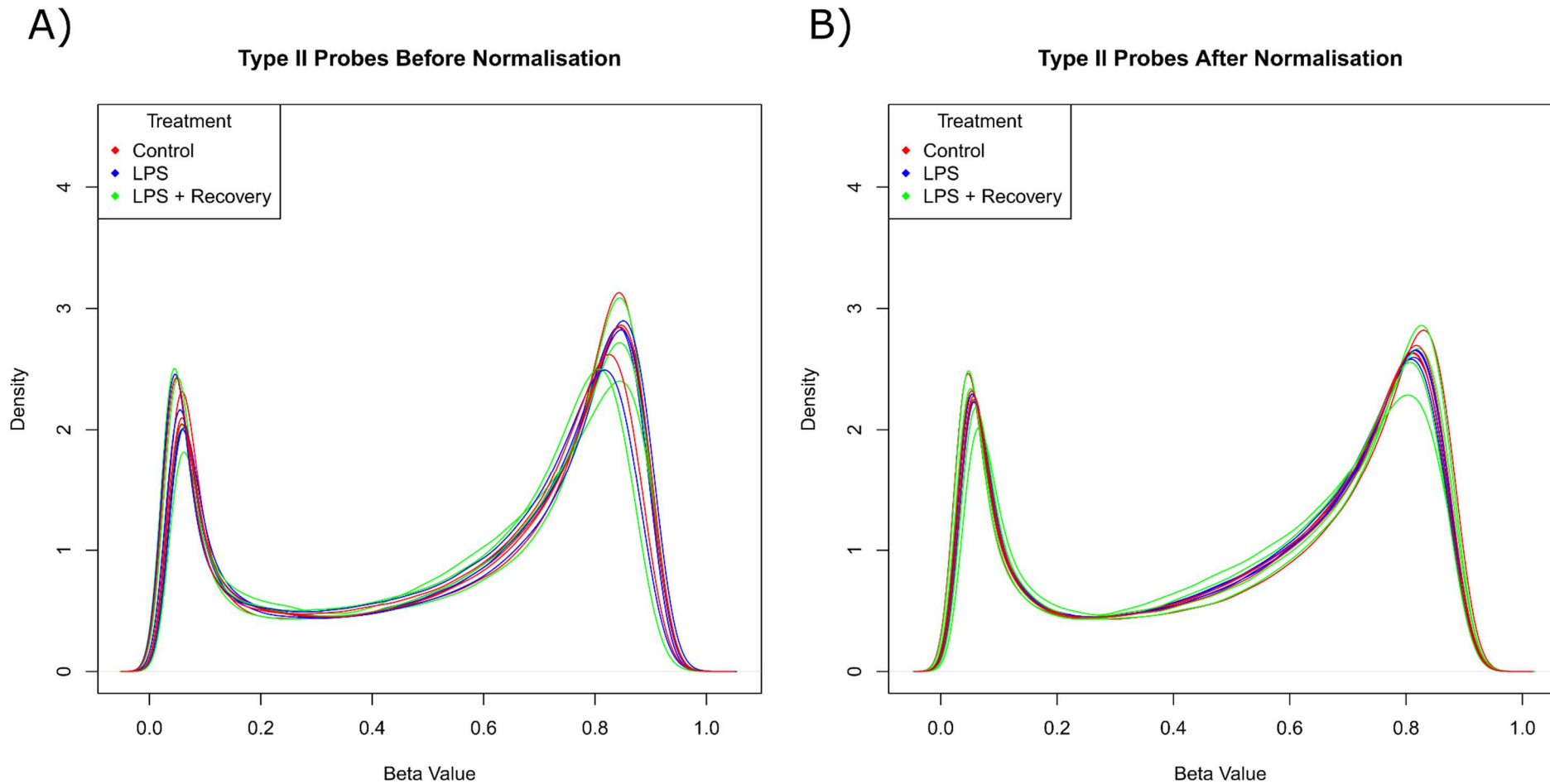
Figure 5.13. Beta density plots of type II probes before and after dasen normalisation.

Probes were separated based on whether they were type I or type II probes. Beta density plots were generated showing the beta values of type II probes **(A)** before and **(B)** after dasen quantile normalisation.

5.4.1.8 There is no Difference in CpH Hemi-Methylation upon Treatment

Following dasen normalisation, the hemi-methylated probes (*i.e.* those with a β-value between 0.2 and 0.8) were grouped together based on whether they were annotated to a CpG or CpH (where H stands for any base other than cytosine) locus (figure 5.14). There was no difference in hemi-methylation at either CpH or CpG probes between treatment groups.

5.4.1.9 Principal Component Analysis Identifies Causes of Variation in the Data

In order to identify sources of confounding variation within the dataset I used principal component analysis. The "prcomp" function in the default statistics package of R was used to detect consistent variation within the dataset and assigned it to different principal components. The first ten principal components generated were able to account for ~95% of the variation within the dataset, with the first and second principal components alone accounting for 22% and 11% of the variation, respectively (table 5.3). Next, I correlated these principal components to known variables, which could be sources of variation in the data. These variables were treatment (plate), the BeadChip the sample was on (Chip ID) and the position within the BeadChip. From this analysis there were no significant correlations and so I did not need to control for any of the principal components, nor variables in the subsequent analyses (figure 5.15).
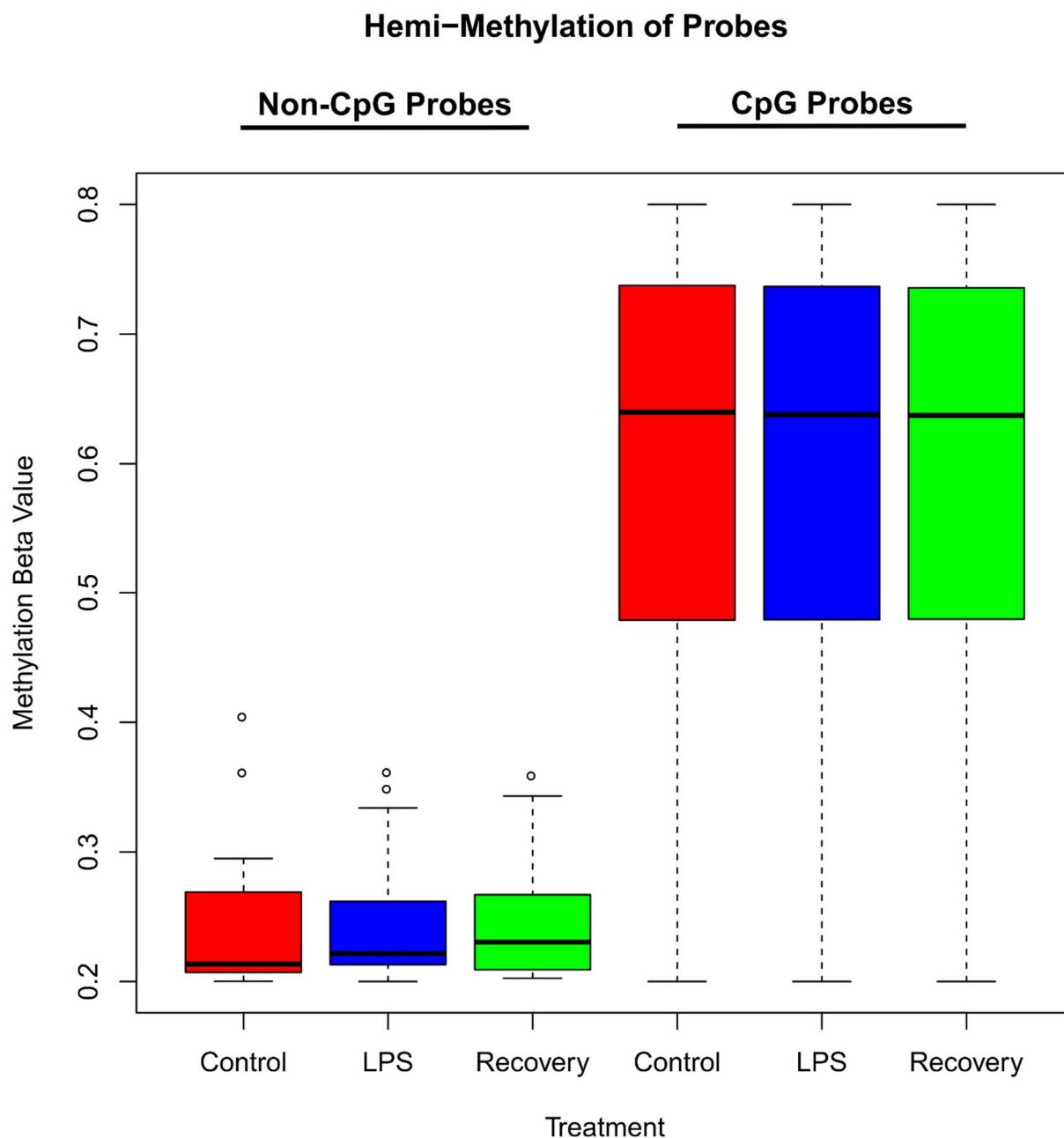
Figure 5.14. Beta-values of hemi-methylated CpG and CpH probes is the same regardless of treatment.

After dasen normalisation probes were grouped on the basis of whether they were a CpG or CpH probe. Shown are box plots of β-value for probes containing beta-values between 0.2 and 0.8 (*i.e.* hemi-methylated probes) for each of the treatment groups. Red represents the control group, blue the LPS treated group and green the cells that were first treated with LPS and then allowed a recovery period. Error bars represent 1.5x the IQR.

	PC1	PC2	PC3	PC4	PC5	PC6	PC7	PC8	PC9	PC10
Standard deviation	16.46	11.84	10.84	10.41	10.12	9.83	9.49	9.38	8.85	8.82
Proportion of Variance	0.22	0.11	0.10	0.09	0.08	0.08	0.07	0.07	0.06	0.06
Cumulative Proportion	0.22	0.34	0.43	0.52	0.60	0.68	0.76	0.83	0.89	0.95

Table 5.3. Table of variation identified by PCA.

Following dasen normalisation, principal component analysis (PCA) was used to identify sources of variance in the data. This table shows the standard deviation, proportion of variance and the cumulative proportion of variance for the first ten principal components.

Correlation Plot of Principal Components and Variables
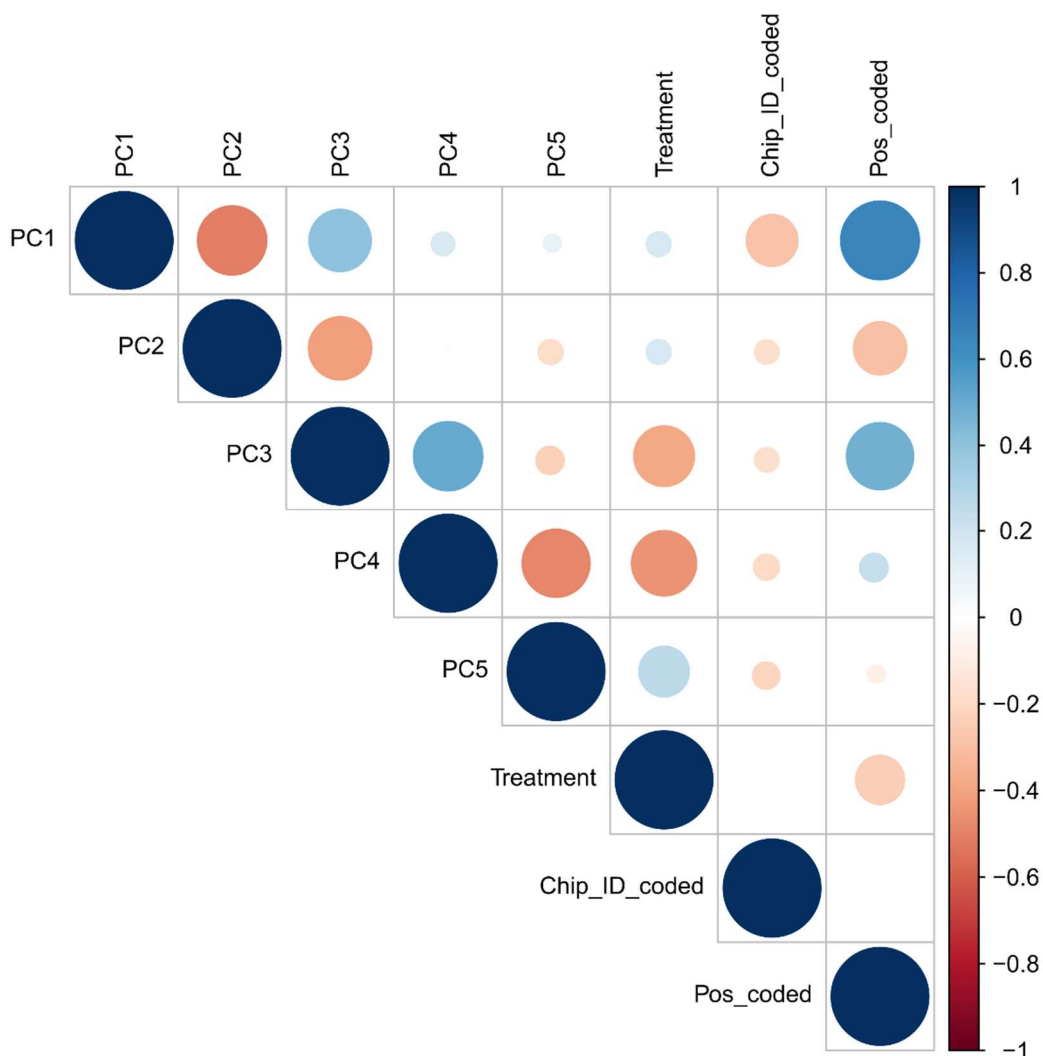
Figure 5.15. Principal component analysis to identify sources of variation with the methylation data.

Following dasen normalisation, PCA was performed and then correlated with known variables to identify sources of variation in the data. Shown is a PCA plot, showing the correlation between treatments, the chip the sample was run on (Chip_ID_coded), and the position of the sample within the chip (Pos_coded) with the first five principal components. Blue indicates a positive correlation, red indicates a negative correlation, with the colour intensity and size of the circle being proportional to the correlation coefficients. None of the correlations of PCs with variables were significant (p>0.05).

5.4.1.10 Identifying Acute and Persistent Changes in DNA Methylation Associated with Treatment

In order to identify DNA methylomic variation associated with LPS treatment, I first identified the 20% most variable probes across all three treatment groups (N = 158,310 probes) and removed from my analysis the remaining, non-varying probes. I then performed three linear regression analyses on this set of 158,310 probes to identify pair-wise differences between the three treatment groups. These probes were then grouped in to four categories (figure 5.2) based on whether they became hyper- or hypomethylated after LPS, and whether this change was acute (*i.e.* was not seen in the LPS + recovery group compared to controls), or persisted during the recovery. Data was analysed in this manner as I hypothesised that probes showing similar methylation patterns over time may have similar biological functions or roles. Therefore, the categories of probes I analysed were (1) acute hypomethylation (2) acute hypermethylation, (3) persistent hypomethylation, and (4) persistent hypermethylation.

The largest numbers of significant differences occurred acutely after LPS treatment, with 97 and 67 significant loci ($p < 1 \times 10^{-3}$ between control and LPS and $p > 0.05$ between LPS and LPS + recovery) being hypomethylated (table 5.4, figure 5.16) or hypermethylated (table 5.5, figure 5.17) after initial LPS treatment, which was not seen after 24 hours of recovery, respectively. There were fewer persistent significantly differentially methylated loci, with eight significant loci persistently hypomethylated (table 5.6, figure 5.18) and just one significant persistently hypermethylated locus (table 5.7, figure 5.19).

There was greatest variation in DNA methylation in the LPS + recovery group compared to the control or the LPS groups, which would explain why I identified considerably fewer persistent differentially methylated loci than acute differentially methylated loci. This could suggest that the microglia were "recovering" from LPS exposure at different rates. Interestingly, there was a pattern of methylation differences within the replicate samples in the LPS + recovery treatment group, and for hypermethylated loci replicates one and three were more consistently hypermethylated than replicates two and four, whilst conversely for hypomethylated loci replicates two and four were more consistently hypermethylated than replicates one and three.

CpG ID	Genomic Location	UCSC Annotation	GREAT Annotation (distance)	Function	Control vs LPS		Control vs LPS+Recovery	
					Δ (%)	P-value	Δ (%)	P-value
cg00664381	Chr1:229892969	DISC1	URB2 (+130989)	Ribosome biogenesis	-7.79	8.35×10^{-6}	-1.33	0.467
cg13642974	Chr11:92611456	-	MTNR1B (-91429)	GPCR in retina	-7.12	$1.10 \times 10.^{5}$	-1.90	0.250
cg18465484	Chr19:16999051	CPAMD8	F2RL3 (-619)	Cell signalling	-8.67	1.12×10^{-5}	-5.31	0.085
cg20564330	Chr1:46924956	EFCAB14-AS1	DMBX1 (-47712)	Transcription factor	-11.51	1.31×10^{-5}	-6.74	0.146
cg14849274	Chr12:51281327	KRT72	METTL7A (-35927)	Methyltransferase	-8.18	2.04×10^{-5}	-6.30	0.160
cg16395123	Chr4:25474382	SEL1L3	ANAPC4 (+95548)	E3 ubiquitin ligase	-8.48	2.12×10^{-5}	-6.18	0.069
cg00252121	Chr13:28773027	MTUS2	PAN3 (+60385)	mRNA degradation	-9.60	2.36×10^{-5}	-3.92	0.127
cg05230522	Chr2:61055411	PUS10	REL (-53244)	Transcription factor	-8.08	2.91×10^{-5}	-3.46	0.162
cg02922817	Chr14:103693366	KIF26A	TNFAIP2 (+103569)	SNARE binding/cell differentiation	-9.65	4.37×10^{-5}	-2.60	0.597
cg24112213	Chr17:69220806	-	SOX9 (-896354)	Transcription factor	-6.91	6.03×10^{-5}	-1.01	0.747
cg08491105	Chr15:22057479	-	OR4M2 (-310998)	Olfactory GPCR	-8.25	6.33×10^{-5}	-5.48	0.218
cg04679277	Chr7:1390554	-	MICALL2 (+108583)	Actin organisation and cell adhesion	-6.71	6.47×10^{-5}	-4.15	0.275
cg24839145	Chr8:5016262	-	CSMD1 (-164325)	Complement control protein	-8.67	8.79×10^{-5}	-3.57	0.073
cg12429593	Chr14:99691999	DEGS2	BCL11B (+45565)	Transcriptional repressor	-9.53	1.01×10^{-4}	-7.13	0.057
cg01751047	Chr16:87785642	CDH15	KLHDC4 (+13912)	Protein binding	-8.01	1.11×10^{-4}	-4.34	0.163
cg21584495	Chr11:17930141	SERGEF	SERGEF (+104567)	Guanine nucleotide exchange factor	-7.98	1.17×10^{-4}	-2.46	0.145
cg23276990	Chr3:113534251	CD200	GRAMD1C (-23013)	Cholesterol transporter	-17.44	1.24×10^{-4}	-11.14	0.080
cg08471790	Chr2:108453832	GCC2	RGPD4 (+10440)	Ran GTPase binding	-12.60	1.24×10^{-4}	-3.80	0.180
cg04413147	Chr21:46399562	FTCD	FAM207A (+39638)	rRNA maturation	-10.23	1.50×10^{-4}	-7.30	0.076
cg13097878	Chr1:65452808	AK4	JAK1 (-20622)	Signal transduction	-6.52	1.75×10^{-4}	-3.20	0.235
cg12736406	Chr11:125918532	KIRREL3	CDON (+14654)	Cell-cell interactions	-6.13	1.88×10^{-4}	-2.87	0.275
cg17023193	Chr1:33333181	AZIN2	FNDC5 (+3232)	Regulation of brown fat differentiation	-5.70	1.92×10^{-4}	1.92	0.622
cg01084189	Chr2:134581807	-	NCKAP5 (-255777)	Microtubule formation	-6.30	2.03×10^{-4}	-5.60	0.074
cg23645046	Chr11:64338820	-	SLC22A11 (+15723)	Sodium-independent transporter	-5.90	2.15×10^{-4}	-1.92	0.263
cg09397963	Chr1:19529973	PQLC2	UBR4 (+6796)	E3 ubiquitin ligase	-7.22	2.26×10^{-4}	-7.06	0.175
cg23228992	Chr18:50887669	-	MBD2 (+863488)	Repression of methylated promoters	-7.13	2.38×10^{-4}	-0.01	0.998

cg08694574	Chr16:84569116	-	TLDC1 (-30753)	mTor signalling	-9.36	2.92×10^{-4}	-4.49	0.377
cg12558795	Chr7:45945361	-	IGFBP3 (+15488)	Insulin-like growth factor I binding	-8.04	2.93×10^{-4}	0.63	0.725
cg09995507	Chr1:21861081	RAP1GAP	ALPL (+25217)	Phosphatase	-5.77	2.97×10^{-4}	-3.60	0.283
cg26254345	Chr10:2961684	-	PFKP (-148027)	Glycolysis regulation	-8.43	3.03×10^{-4}	-2.65	0.639
cg17065901	Chr4:90048410	FAM13A	TIGD2 (+14443)	Nucleic acid binding	-5.80	3.06×10^{-4}	-1.40	0.562
cg03943459	Chr3:142623215	ZBTB38	PCOLCE2 (-15171)	Collagen trimerisation	-7.41	3.08×10^{-4}	-4.39	0.082
cg16856722	Chr3:9895535	CIDEC	RPUSD3 (-9836)	Mitochondrial ribosome assembly	-8.62	3.36×10^{-4}	-3.45	0.295
cg09330885	Chr3:197020882	MUC4	DLG1 (+4564)	Signal transduction/cell proliferation	-7.10	3.41×10^{-4}	-4.82	0.403
cg04196119	Chr10:4507246	-	AKR1E2 (-361199)	Oxidoreductase	-11.84	3.43×10^{-4}	-5.49	0.212
cg25970363	Chr1:47423075	PDZK1IP1	CYP4A11 (-15939)	Cholesterol synthesis	-10.43	3.43×10^{-4}	-1.26	0.780
cg14729068	Chr8:135581283	ZFAT	ZFAT (+143997)	Transcriptional regulator	-5.88	3.44×10^{-4}	-3.06	0.283
cg03431950	Chr18:55050667	-	ST8SIA3 (+32624)	Sialyltransferases	-6.64	3.60×10^{-4}	-3.41	0.156
cg11931360	Chr3:12963820	IQSEC1	IQSEC1 (+45347)	EGF signalling	-8.58	3.66×10^{-4}	-0.76	0.816
cg13001919	Chr7:130842370	PODXL	MKLN1 (-170248)	Ubiquitin degradation	-5.93	3.75×10^{-4}	-1.23	0.700
cg01712984	Chr1:244213389	SMYD3	ZBTB18 (-1195)	Transcriptional repressor	-9.47	3.79×10^{-4}	-5.66	0.366
cg19699170	Chr2:109760023	-	SH3RF3 (+14027)	E3 ubiquitin ligase	-6.30	3.98×10^{-4}	-4.62	0.172
cg24951151	Chr6:70951241	COL19A1	COL9A1 (+61544)	Collagen protein	-9.06	3.99×10^{-4}	-3.79	0.177
cg07612956	Chr7:124865113	-	POT1 (-295079)	Telomere maintenance	-8.75	4.01×10^{-4}	-0.06	0.986
cg09141075	Chr8:874716	-	TDRP (-378936)	Spermatogenesis	-6.09	4.15×10^{-4}	1.41	0.613
cg08314156	Chr11:122446897	-	UBASH3B (-79485)	Protein tyrosine phosphatase	-7.92	4.21×10^{-4}	-5.74	0.086
cg13522359	Chr15:82176542	ADAMTSL3	MEX3B (+161939)	Cell surface interactions	-6.39	4.28×10^{-4}	0.37	0.912
cg26558809	Chr11:9822265	LOC101928008; SBF2	SWAP70 (+136642)	NF-kappaB Signaling.	-11.08	4.39×10^{-4}	-8.30	0.052
cg03544502	Chr14:44467592	KLHL28	FSCB (+508889)	Calcium ion binding	-5.31	4.40×10^{-4}	-0.83	0.646
cg14800299	Chr19:17552465	GLT25D1	TMEM221 (+6910)	Transmembrane protein	-8.28	4.41×10^{-4}	-3.27	0.185
cg03647619	Chr16:65536412	CES2	CDH11 (-380312)	Calcium dependent cell-cell binding	-9.21	4.55×10^{-4}	-3.60	0.369
cg04024417	Chr7:96132284	-	SLC25A13 (-180826)	Mitochdondrial transport protein	-9.29	4.65×10^{-4}	-2.13	0.557
cg00426518	Chr5:115721607	-	SEMA6A (+189022)	Cell-surface receptor signalling	-9.18	4.76×10^{-4}	-7.46	0.093
cg21459713	Chr8:613688	ERICH1	TDRP (-117908)	Spermatogenesis	-7.70	4.89×10^{-4}	-2.50	0.698
cg16075164	Chr13:43580265	-	DNAJC15 (-17073)	Mitochondrial respiratory chain	-8.57	4.94×10^{-4}	-3.96	0.416

cg06790492	Chr17:75570125	TBC1D16	SEPT9 (+292634)	Cytokinesis	-6.62	5.02×10^{-4}	-1.80	0.732
cg18654931	Chr3:156380895	MME	TIPARP (-11738)	Enhancer binding	-8.23	5.07×10^{-4}	-0.23	0.923
cg09451747	Chr4:143761752	INPP4B	INPP4B (+5690)	Phosphatidylinositol signaling	-11.99	5.22×10^{-4}	-7.33	0.069
cg06054708	Chr8:37633059	-	PROSC (+12949)	Regulator of PLP	-8.44	5.47×10^{-4}	-3.13	0.494
cg11527760	Chr4:107392661	TBCK	TBCK (-150010)	Actin organisation	-7.35	5.67×10^{-4}	-6.98	0.055
cg18162371	Chr10:134471866	-	INPP5A (+120543)	Intracellular calcium signalling	-12.43	5.79×10^{-4}	-3.60	0.150
cg16141678	ChrX:3274695	MXRA5	MXRA5 (-10014)	Cell matrix remodelling	-8.67	5.98×10^{-4}	-1.53	0.615
cg02187937	Chr1:20877841	KIF17	CDA (-37599)	Cytidine deaminase	-7.35	6.03×10^{-4}	-3.37	0.288
cg24328431	Chr9:14428351	-	NFIB (-114686)	Transcription factor	-9.79	6.09×10^{-4}	-1.26	0.802
cg02273079	Chr3:167772015	-	GOLIM4 (+41747)	Protein transporter in Golgi	-13.38	6.15×10^{-4}	-8.03	0.102
cg09068998	Chr5:148513916	ABLIM3	ABLIM3 (-7260)	Actin binding	-6.41	6.23×10^{-4}	-1.61	0.664
cg03095244	Chr12:114285006	-	RBM19 (+119104)	Ribosome biogenesis	-6.29	6.30×10^{-4}	-4.15	0.499
cg04815049	Chr21:32189266	HUNK	KRTAP8-1 (-3697)	Keratin associated matrix protein	-7.81	6.37×10^{-4}	-3.56	0.277
cg26577683	Chr1:17765199	ARHGEF10L	RCC2 (+1020)	Regulator of small GTPases	-10.91	6.98×10^{-4}	-3.72	0.074
cg24462058	Chr1:20509731	VWA5B1	UBXN10 (-2846)	Tethering factor	-7.79	7.01×10^{-4}	0.40	0.882
cg21858680	Chr4:85239853	-	NKX6-1 (+179749)	Transcriptional regulator	-9.15	7.04×10^{-4}	-2.66	0.512
cg13734043	Chr17:53625197	EPX	MMD (-125845)	Ion channel protein	-8.30	7.06×10^{-4}	-3.95	0.185
cg01893571	Chr2:38126388	FAM82A1	RMDN2 (-51217)	Regulator of microtubule dynamics	-7.59	7.19×10^{-4}	-0.59	0.936
cg15361587	Chr18:54198203	NEDD4L	TXNL1 (+107672)	Protein disulfide oxioreductase	-11.91	7.21×10^{-4}	-6.29	0.255
cg04407732	Chr10:70142562	-	RUFY2 (+24383)	Endocytosis regulator	-8.50	7.40×10^{-4}	-7.22	0.144
cg18509185	Chr6:108039190	SOBP	SCML4 (+106325)	Transcriptional repressor	-8.17	7.58×10^{-4}	0.58	0.701
cg20229931	Chr21:46472084	LSS	ADARB1 (-22408)	Pre-mRNA editing	-7.68	7.69×10^{-4}	-6.62	0.164
cg05725719	Chr7:150064761	GIMAP5	REPIN1 (-1127)	Nucleic acid binding	-15.34	7.86×10^{-4}	-8.16	0.207
cg08883054	Chr17:58125104	-	HEATR6 (+31187)	RNA binding	-9.35	7.94×10^{-4}	0.05	0.985
cg20216726	Chr22:46176691	-	ATXN10 (+109013)	Akt signalling	-7.66	$7.98 \times 10\text{-}4$	-4.31	0.393
cg20255272	Chr1:1363541	VWA1	TMEM88B (+2034)	PDZ domain binding/signalling	-6.94	8.03×10^{-4}	-3.33	0.500
cg09759578	Chr19:1864405	SCAMP4; ADAT3	KLF16 (-839)	Transcription factor	-8.72	8.14×10^{-4}	-2.52	0.377
cg13450196	Chr2:126981827	-	GYPC (-431681)	GYPC	-8.39	8.25×10^{-4}	4.97	0.085
cg25304968	Chr3:115001494	ATP6V1A	GAP43 (-340862)	Calmodulin binding	-7.88	8.30×10^{-4}	-4.40	0.272

cg16588731	Chr10:133873546	STK32C	JAKMIP3 (-44628)	Microtubule binding/formation	-10.96	8.49×10^{-4}	-2.30	0.423
cg21075278	Chr11:68208663	GAL	PPP6R3 (-19574)	Protein phosphatase	-8.89	8.60×10^{-4}	-6.68	0.389
cg16867466	Chr8:117386061	LINC00536	EIF3H (+381998)	RNA transport/translation initiation	-8.08	9.10×10^{-4}	-3.12	0.271
cg01630199	Chr7:66006511	-	KCTD7 (-199131)	Potassium channel protein	-8.99	9.16×10^{-4}	-2.73	0.597
cg25681958	Chr2:75484984	-	TACR1 (-58159)	Vesicle mediated transport	-6.58	9.17×10^{-4}	-4.97	0.083
cg06823122	Chr3:111008424	-	PVRL3 (+217835)	Cellular adhesion	-9.73	9.30×10^{-4}	-2.15	0.473
cg15319438	Chr7:12681101	-	ARL4A (-45859)	GTP binding protein	-5.64	9.36×10^{-4}	-3.74	0.442
cg03512076	Chr8:103976253	-	ATP6V1C1 (-57037)	ATPase component	-9.07	9.36×10^{-4}	-5.20	0.290
cg03653841	Chr14:36052656	SFTA3	INSM2 (+49409)	Transcriptional repressor	-8.29	9.52×10^{-4}	-1.43	0.493
cg00082939	Chr10:76835299	C10orf41	DUPD1 (-17028)	Phosphatase	-9.57	9.75×10^{-4}	-0.55	0.737
cg25871851	Chr11:113547186	ZBTB16	TMPRSS5 (+29908)	Serine protease	-6.03	9.81×10^{-4}	-0.37	0.861
cg08485684	Chr14:26374866	-	NOVA1 (+692093)	Neuron specific RNA binding	-9.96	9.96×10^{-4}	-3.90	0.549
cg08700546	Chr11:47393251	SLC39A13	SPI1 (+6690)	Transcription factor	-10.79	1.00×10^{-3}	-3.13	0.510

Table 5.4. Probes acutely hypomethylated after treatment with LPS.

Shown are the 97 significantly differentially methylated probes that show acute hypomethylation (control to LPS p-value<1×10^{-3} and LPS to recovery p-value>0.05) after treatment with LPS. For each probe is the CpG ID, the genomic location, the UCSC gene annotation of the probe from Illumina, the GREAT annotation of the probe, the function of the GREAT gene, and the Δ value (% change in methylation) and p-value between both the control to LPS and control to LPS+recovery comparisons. The function of the genes identified through GREAT were found through manual curation.
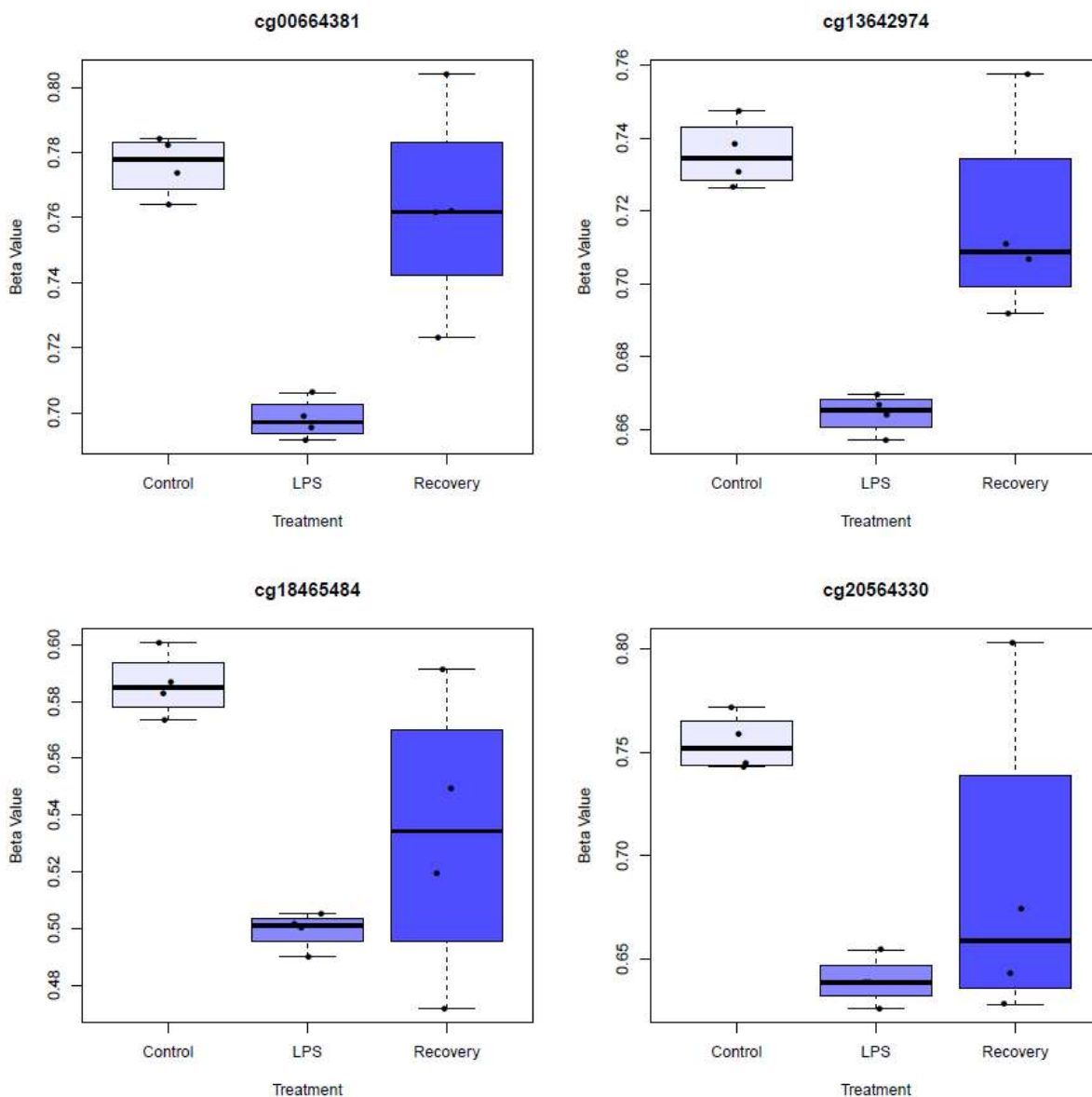
Figure 5.16. Loci demonstrating acute hypomethylation of probes after LPS treatment.

Box plots showing the top four differentially methylated probes that demonstrate acute hypomethylation after LPS treatment, which was not seen after 24 hours recovery. β-values for individual replicates are represented by black dots on each of the box plots. Error bars represent 1.5x the IQR.

CpG ID	Genomic Location	UCSC Annotation	GREAT Annotation (distance)	Function	Control vs LPS		Control vs LPS+Recovery	
					Δ (%)	P-value	Δ (%)	P-value
cg00904273	Chr16:657622	RHOT2/WDR90	RAB40C (+18266)	Component of E3 ubiquitin ligase	8.92	3.93×10^{-5}	1.56	0.550
cg26775104	Chr13:45333858	-	TSC22D1 (-183158)	Transcription factor	7.75	4.34×10^{-5}	4.96	0.069
cg11783901	Chr17:44456999	IGF2BP1	ARL17B (-17870)	GTP binding protein	9.94	7.12×10^{-5}	6.36	0.066
cg06555468	Chr7:2061316	MAD1L1	MAD1L1 (+211561)	Spindle assembly	7.84	8.05×10^{-5}	-1.86	0.406
cg26826339	Chr8:24421976	ADAM7	ADAM7 (+123438)	Protein Interaction and adhesion in sperm-egg fusion	8.88	8.25×10^{-5}	3.60	0.425
cg09076431	Chr1:196155786	LHX9	KCNT2 (+422568)	Voltage gated ion channel protein	6.42	9.15×10^{-5}	5.12	0.053
cg15358079	Chr8:37378803	-	ZNF703 (-174465)	Transcriptional corepressor	5.80	1.32×10^{-4}	4.19	0.214
cg04695063	Chr11:18371116	LDHA	GTF2H1 (+26974)	Part of the general transcription and DNA repair factor IIH	7.06	1.33×10^{-4}	1.63	0.517
cg19100169	Chr5:159620781	CCNJL	FABP6 (+6408)	Fatty acid binding protein	5.53	1.46×10^{-4}	4.33	0.397
cg21336373	Chr17:3754061	P2RX1	C17orf85 (-4517)	mRNA export	9.78	1.57×10^{-4}	3.07	0.100
cg25251543	Chr2:240170336	-	HDAC4 (+152306)	Histone deacetylase	10.64	1.85×10^{-4}	0.28	0.942
cg10139358	Chr18:72763183	ZNF236	ZADH2 (+158119)	Oxioreductase	8.73	2.04×10^{-4}	-0.08	0.985
cg08631134	Chr9:21751378	-	MTAP (-51163)	Adenine and methionine salvage	12.38	2.12×10^{-4}	1.84	0.652
cg25961805	Chr4:121182403	-	MAD2L1 (-194175)	Mitotic checkpoint protein	9.46	2.18×10^{-4}	-0.45	0.834
cg02557865	Chr16:15435558	C16orf45	NPIPA5 (+36592)	Interacts with nuclear pore	16.68	2.29×10^{-4}	3.93	0.199
cg08570033	Chr5:58857790	PDE4D	PDE4D (+331834)	cAMP degradation	9.49	2.44×10^{-4}	4.45	0.121
cg01799429	Chr8:142802747	-	PTP4A3 (+400655)	Protein tyrosine phosphatase	6.42	2.65×10^{-4}	1.14	0.691
cg24744928	Chr1:239757484	-	CHRM3 (-34888)	Muscarinic cholingeric receptor and GPCR	7.85	2.84×10^{-4}	4.28	0.145
cg06046580	Chr2:232465658	MIR1471	C2orf57 (+8084)	Testis expressed protein - function unknown	10.82	2.86×10^{-4}	8.71	0.060
cg09701702	Chr6:101021723	-	SIM1 (-108919)	Transcription factor	7.37	3.20×10^{-4}	0.30	0.950
cg04398416	Chr10:3588486	-	KLF6 (+238980)	Transcription factor	8.93	3.31×10^{-4}	3.20	0.092
cg12765327	Chr14:105434901	-	AHNAK2 (+9792)	Nucleoprotein/calcium signalling	9.36	3.32×10^{-4}	5.94	0.069
cg16899859	Chr4:34346550	-	-	-	9.04	3.35×10^{-4}	2.20	0.256
cg14525769	Chr5:10745140	DAP	DAP (+16243)	Positive mediator of cell death	8.03	3.56×10^{-4}	7.08	0.157
cg05192293	Chr10:71604092	-	COL13A1 (+42405)	Alpha chain of collagen	7.64	3.77×10^{-4}	0.64	0.840
cg18473642	Chr12:122015139	ABCB9	KDM2B (+3749)	Ubiquitin ligase protein	6.80	3.80×10^{-4}	5.74	0.124

cg18158658	Chr9:126064834	NEK6	STRBP (-33980)	Spermatogenesis	4.70	3.96×10^{-4}	-1.43	0.639
cg09696231	Chr19:16346049	EPS15L1	AP1M1 (+37305)	Protein sorting in Golgi network	9.59	3.97×10^{-4}	9.19	0.063
cg08194969	Chr14:64142766	-	SGPP1 (+51990)	Dephosphorylates sphingosine 1-phosphate	10.05	4.02×10^{-4}	6.78	0.078
cg20829955	Chr1:22547616	-	WNT4 (-78158)	Cellular signalling	9.47	4.03×10^{-4}	1.43	0.589
cg00023726	Chr1:2829795	-	ACTRT2 (-108250)	Cytoskeletal organisation	8.75	4.16×10^{-4}	3.70	0.295
cg02206323	Chr17:19189661	MIR1180/B9D1	EPN2EPN2 (+49008)	Clathrin mediated endocytosis	7.87	4.22×10^{-4}	5.19	0.063
cg09425404	Chr21:31641444	TIAM1	KRTAP24-1 (+13831)	Keratin associated matrix protein	7.32	4.55×10^{-4}	-0.10	0.958
cg13724238	Chr11:2828568	-	CDKN1C (+78542)	Inhibitor of G1 cyclin/CDK complexes	3.96	4.78×10^{-4}	-3.95	0.059
cg24307945	Chr2:65363564	-	RAB1A (-6325)	Vesicle trafficking in Golgi	6.03	4.80×10^{-4}	-0.28	0.904
cg22902550	Chr5:136367959	SPOCK1	SPOCK1 (+467077)	Proposed protease inhibitor	12.87	4.82×10^{-4}	6.18	0.074
cg05534427	Chr19:50693390	RTN2/FLJ40125/RTN2	MYH14 (-13511)	Actin dependent motor protein	6.66	5.11×10^{-4}	3.53	0.274
cg02170071	Chr11:59237191	OR10V1	OR4D10 (-7654)	Olfactory GPCR	10.37	5.18×10^{-4}	0.98	0.662
cg05967001	Chr12:111714030	RPH3A	FAM109A (+92894)	Endocytic trafficking	6.92	5.31×10^{-4}	5.99	0.183
cg19076895	Chr6:7578298	-	SNRNP48 (-12133)	Gene regulation and mRNA splicing	6.47	5.47×10^{-4}	4.74	0.145
cg06673910	Chr10:43224783	HNRNPF	BMS1 (-53465)	Ribosome biogenesis	7.75	6.24×10^{-4}	1.45	0.573
cg00828618	Chr19:7660029	FCER2	CAMSAP3 (-758)	Regulation of microtubule dynamics	10.23	6.26×10^{-4}	2.96	0.212
cg22667851	Chr16:11313379	-	SOCS1 (+36656)	Negative regulator of cytokine signalling	7.49	6.27×10^{-4}	5.71	0.071
cg05487589	Chr8:25952113	EBF2	EBF2 (-49201)	Transcription factor	7.78	6.28×10^{-4}	6.88	0.117
cg25654973	Chr8:81355474	-	ZBTB10 (-42427)	Proposed transcriptional regulator	7.29	6.43×10^{-4}	7.00	0.142
cg01736264	Chr1:26320998	PDIK1L	PAFAH2 (+3649)	Platelet homeostasis	8.58	6.44×10^{-4}	5.93	0.067
cg00686823	Chr3:128793728	TPRA1	GP9 (+14119)	Platelet activation	13.64	6.66×10^{-4}	6.52	0.142
cg21554217	Chr5:138877651	-	TMEM173 (-15277)	Regulator of innate immune reponse to infection	11.87	6.78×10^{-4}	3.89	0.268
cg23493306	Chr8:22658435	PEBP4	EGR3 (-107621)	Transcriptional regulation	6.75	6.78×10^{-4}	1.52	0.624
cg21806810	Chr5:35014708	-	AGXT2 (+33489)	Glyoxylate to glycine conversion	8.03	6.81×10^{-4}	0.65	0.745
cg21701994	Chr20:24086020	-	GGTLC1 (-116605)	Glutathione metabolism	8.31	7.10×10^{-4}	2.00	0.524
cg03446846	Chr17:1891356	DPH1/OVCA2	RTN4RL1 (+37282)	Cell surface receptor	6.75	7.17×10^{-4}	0.24	0.934
cg15731551	Chr3:100164386	-	TOMM70A (-44145)	Mitochondrial precursor protein import	10.61	7.31×10^{-4}	5.72	0.250
cg14166835	Chr2:73268254	-	SFXN5 (+30710)	Mitochondrial amino-acid transporter	11.48	7.73×10^{-4}	5.31	0.160

cg07740306	Chr18:75347357	NFATC1	GALR1 (+384853)	GPCR receptor signalling	7.38	7.95×10^{-4}	5.73	0.366
cg26868111	Chr1:116881898	CD58	ATP1A1 (-34590)	Component of NA+/K+ ATPase	5.97	8.02×10^{-4}	0.66	0.732
cg01450803	Chr4:75070018	-	MTHFD2L (+46190)	Formate-tetrahydrofolate ligase activity	8.01	8.03×10^{-4}	4.66	0.197
cg04186484	Chr17:59319760	-	TBX2 (-157496)	Transcription factor	7.44	8.40×10^{-4}	1.77	0.493
cg06106499	Chr2:1088670	SNTG2	SNTG2 (+142117)	Actin/PDZ domain binding	5.81	8.64×10^{-4}	1.25	0.539
cg20134175	Chr20:42195557	JPH2	SGK2 (+821)	Protein tyrosine kinase/glucose transporter	4.70	8.82×10^{-4}	0.66	0.703
cg05050884	Chr3:188050040	ADIPOQ	LPP (+119320)	Cell-cell adhesion	7.61	8.97×10^{-4}	6.90	0.082
cg20682563	Chr5:133488773	TCF7	SKP1 (+23955)	Component of ubiquitin ligase complex	9.06	9.21×10^{-4}	4.70	0.068
cg27286069	Chr11:117987092	PHLDB1	SCN4B (+36442)	Component of voltage gated ion channel	7.85	9.43×10^{-4}	-0.29	0.880
cg08066500	Chr3:2381280	CNTN4	CNTN4 (+100768)	Axon associated cell adhesion molecule	5.77	9.58×10^{-4}	-0.07	0.971
cg12196720	Chr1:160573852	NOS1AP	CD84 (-24559)	Glycoprotein involved in cellular signalling	5.40	9.62×10^{-4}	3.90	0.207
cg11519260	Chr10:42506816	-	ZNF33B (+627175)	Transcriptional regulation	9.89	9.78×10^{-4}	3.70	0.369
cg11003725	Chr14:104420652	KIAA0284	TDRD9 (+25854)	ATP-binding RNA helicase	8.09	9.93×10^{-4}	-1.36	0.590

Table 5.5. Probes acutely hypermethylated after treatment with LPS.

Shown are the 67 significantly differentially methylated probes that show acute hypermethylation (control to LPS p-value<1×10^{-3} and LPS to recovery p-value>0.05) after treatment with LPS. For each probe is the CpG ID, the genomic location, the UCSC gene annotation of the probe from Illumina, the GREAT annotation of the probe, the function of the GREAT gene, and the Δ value (% change in methylation) and p-value between both the control to LPS and control to LPS+recovery comparisons. The function of the genes identified through GREAT were found through manual curation.
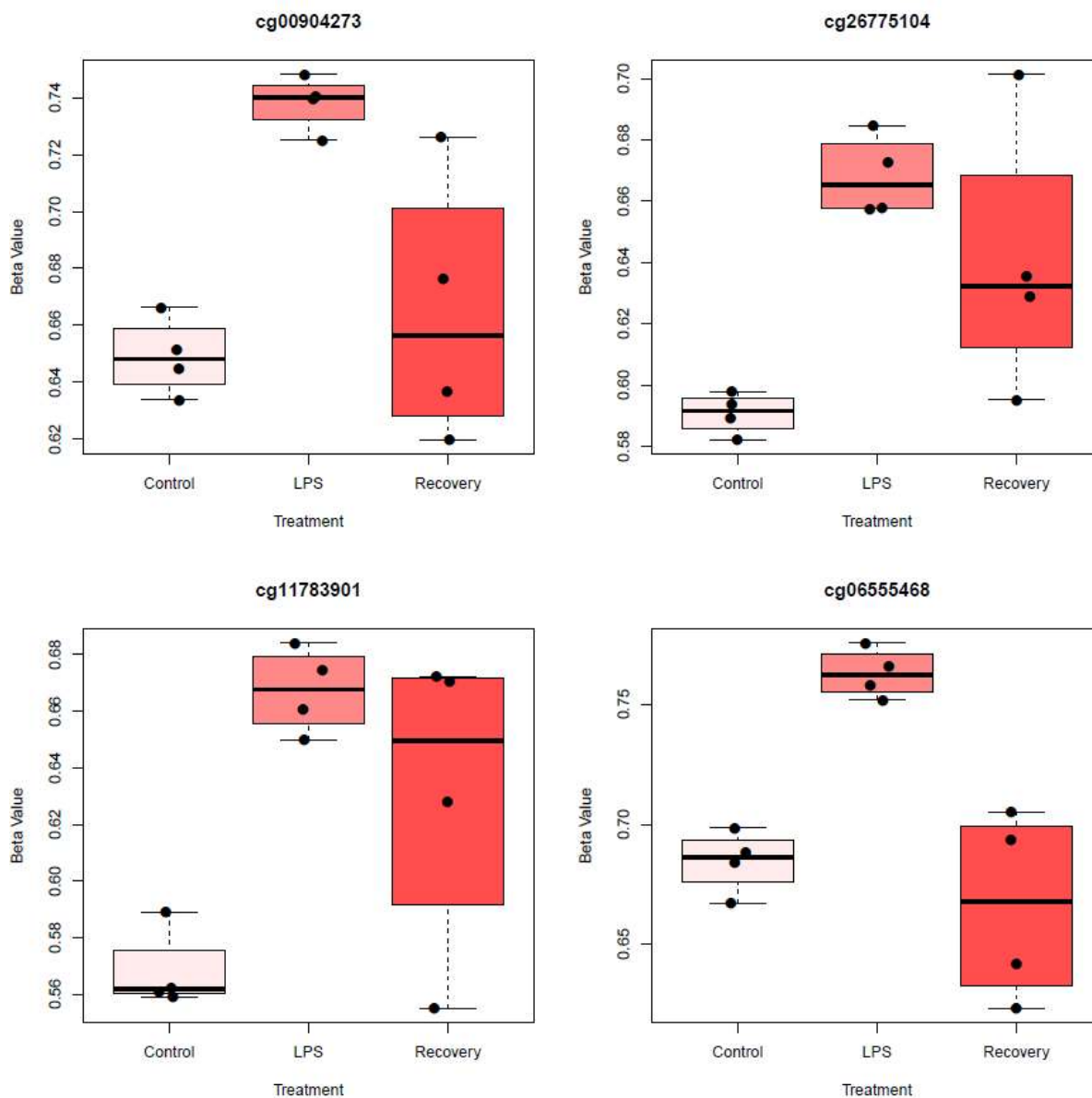
Figure 5.17. Loci demonstrating acute hypermethylation of probes after LPS treatment.

Box plots showing the top four differentially methylated probes that demonstrate acute hypermethylation after LPS treatment, which was not seen after 24 hours recovery. β-values for individual replicates are represented by black dots on each of the box plots. Error bars represent 1.5x the IQR.

CpG ID	Genomic Location	UCSC Annotation	GREAT Annotation (distance)	Function	Control vs LPS		Control vs LPS+Recovery	
					Δ (%)	P-value	Δ (%)	P-value
cg12698829	Chr4:156874061	GUCY1A3	CTSO (+1007)	Cellular protein degradation	-7.41	2.02×10^{-4}	-8.63	3.80×10^{-2}
cg11543559	Chr2:102139055	IL1R1	RFX8 (-47891)	Transcription factor	-5.91	2.91×10^{-4}	-10.12	4.76×10^{-3}
cg23986404	Chr16:49948713	-	ZNF423 (-92064)	Transcription factor	-8.37	3.27×10^{-4}	-9.66	6.96×10^{-3}
cg07022240	ChrX:152694768	PLXNB3	ZFP92 (+10989)	Transcriptional regulation	-7.87	3.91×10^{-4}	-15.15	7.51×10^{-3}
cg20387395	Chr15:56665965	-	TEX9 (+8341)	Suggested ATP binding protein	-7.55	5.29×10^{-4}	-7.58	2.76×10^{-2}
cg10110288	Chr5:55309787	IL6ST	IL6ST (-18967)	Signal transduction	-7.34	6.93×10^{-4}	-7.77	4.82×10^{-3}
cg05084299	Chr1:244126238	SMYD3	ZBTB18 (-88346)	Transcriptional repressor	-7.23	7.33×10^{-4}	-7.66	1.28×10^{-2}
cg13415481	Chr2:234369420	MROH2A	USP40 (+104815)	Deubiquitinating enzyme	-7.44	7.46×10^{-4}	-7.63	4.13×10^{-3}

Table 5.6. Probes persistently hypomethylated after treatment with LPS.

Shown are the 8 significantly differentially methylated probes that show persistent hypomethylation (control to LPS p-value<1.00×10^{-3} and LPS to recovery p-value<0.05) after treatment with LPS. For each probe is the CpG ID, the genomic location, the UCSC gene annotation of the probe from Illumina, the GREAT annotation of the probe, the function of the GREAT gene, and the Δ value (% change in methylation) and p-value between both the control to LPS and control to LPS+recovery comparisons. The function of the genes identified through GREAT were found through manual curation.
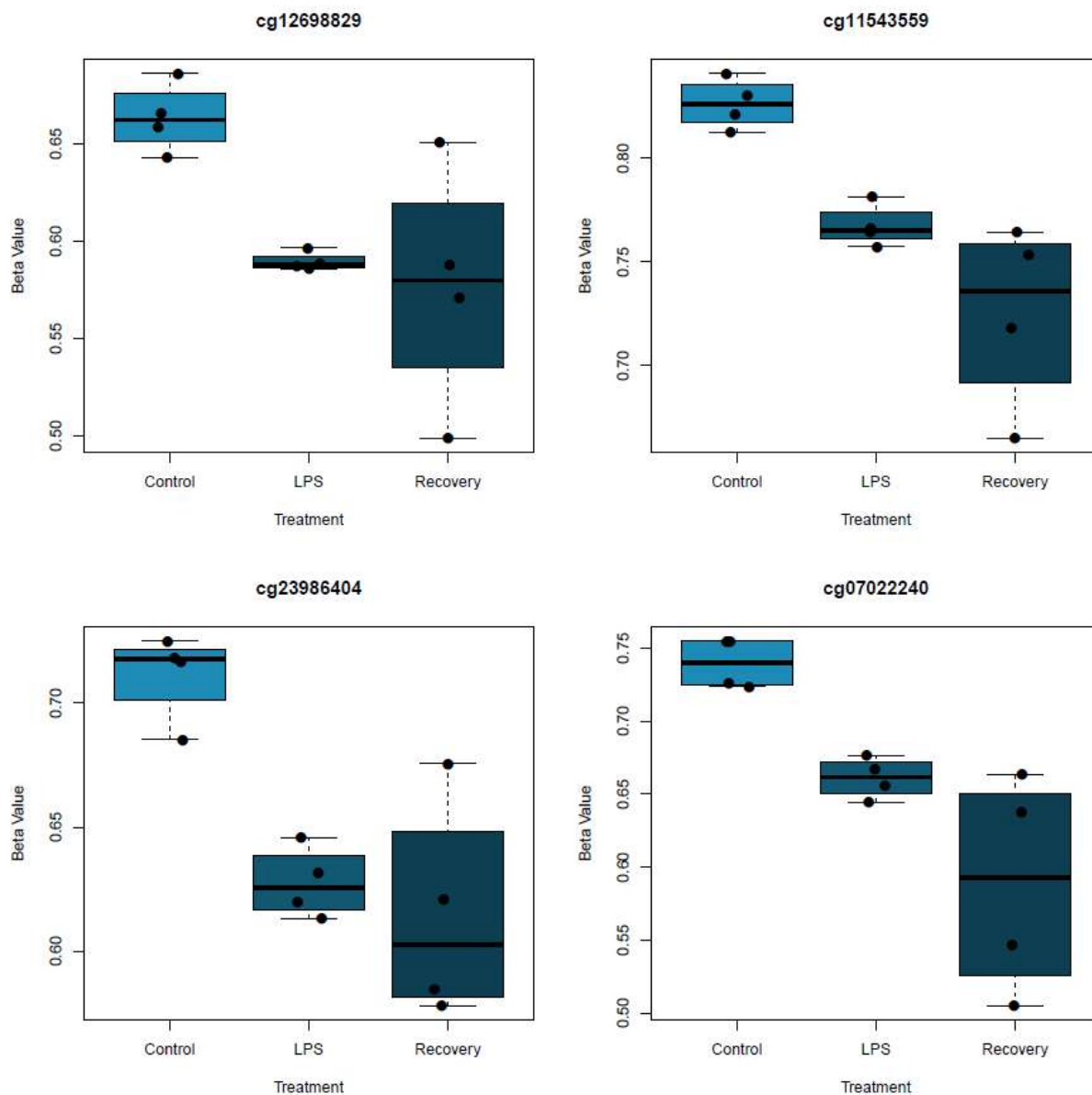
Figure 5.18. Loci demonstrating persistent hypomethylation of probes after LPS treatment.

Box plots showing the top four differentially methylated probes that demonstrate persistent hypomethylation after LPS treatment, which was not seen after 24 hours recovery. β-values for individual replicates are represented by black dots on each of the box plots. Error bars represent 1.5x the IQR.

CpG ID	Genomic Location	UCSC Annotation	GREAT Annotation (distance)	Function	Control vs LPS		Control vs LPS+Recovery	
					Δ (%)	P-value	Δ (%)	P-value
cg09424348	Chr6:30881549	VARS2	MUC22 (+11278)	Glycosylated protein in bacterial/fungal defence	10.76	4.80×10^{-4}	12.66	0.015

Table 5.7. Probe persistently hypermethylated after treatment with LPS.

Shown is the one significantly differentially methylated probe that show persistent hypermethylation (control to LPS p-value<1×10^{-3} and LPS to recovery p-value<0.05) after treatment with LPS. For each probe is the CpG ID, the genomic location, the UCSC gene annotation of the probe from Illumina, the GREAT annotation of the probe, the function of the GREAT gene, and the Δ value (% change in methylation) and p-value between both the control to LPS and control to LPS+recovery comparisons. The function of the genes identified through GREAT were found through manual curation.

cg09424348
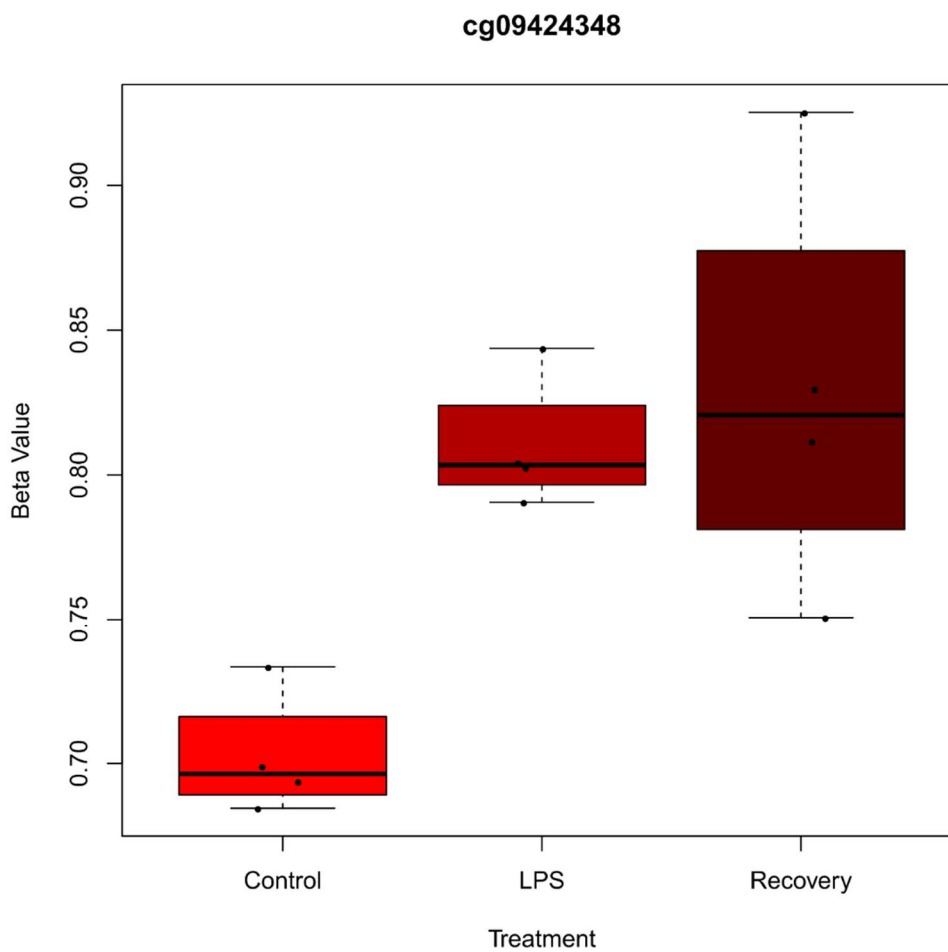
Figure 5.19. Persistent hypermethylation of probes after LPS treatment.

Box plots showing the only differentially methylated probes that demonstrate persistent hypermethylation after LPS treatment, which was not seen after 24 hours recovery. β-values for individual replicates are represented by black dots on each of the box plots. Error bars represent 1.5x the IQR.

5.4.1.11 Specific functional changes in DNA methylation after LPS treatment

Using the chromosomal location of each CpG probe GREAT was used to annotate each locus to the single nearest gene that is either upstream or downstream. Using this annotation method all bar one of the probes was annotated to a nearby gene. The function of each of these genes was then manually searched and recorded.

As I was interested in exploring whether there were any common functions of loci that featured in the four methylation change categories I performed GREAT annotation to determine the genes that are important in the overall response of microglia to LPS. I observed a number of transcription related genes such as *SOX9, RXF8, ZFP92* and *TSC22D1.* Alongside this there were also several genes involved in cellular signalling, for example *F2RL3, JAK1, IL6ST* and *PTP4A3*. Finally, there were also numerous other genes associated with the innate immune system being differentially methylated, including *METTL7A,* a methyltransferase known to be involved in the innate immune response and *C17orf85,* an mRNA export protein known to play a role in the response to cellular stressors such as infections [413].

In addition to manual gene function curation, the "gometh" function within the missMethyl package [265] was used to identify pathways being altered by treatment with LPS. Although ideally I would have performed pathway analysis on each of the four categories of methylation changes separately, given the low number of significant loci in some categories this was not possible and so instead all of the significant loci from all four categories were combined and assessed together, with the overall aim of identifying loci altered after LPS.

In terms of biological pathways (table 5.8, figure 5.20), the largest group of pathways that were altered were those related to extracellular matrix organisation and the regulation of lymphocyte proliferation. Alongside these pathways, there were also changes occurring in genes related to tRNA metabolism and fat cell differentiation. However, it should be noted that none of the pathways from the pathway analysis were FDR significant and therefore it is important to not over interpret the resulting outputs. I observed several changes in molecular functions (table 5.9, figure 5.21), including enzyme activities such as intramolecular transferase and serine-type endopeptidase inhibitor activity, although none of these were FDR-significant. Finally, I also observed changes to cellular components (table 5.10, figure 5.22), relating to lipid particles, organelle membranes, the endoplasmic reticulum and neuromuscular junctions, although again none of these were FDR significant.

GO ID	Term	Ontology	No. Genes in Term	No. of DMPs	P-value	FDR	Genes
GO:0010737	protein kinase A signaling	BP	30	2	0.004	1	GAL; ADIPOQ
GO:1903055	positive regulation of extracellular matrix organization	BP	20	2	0.005	1	PHLDB1; GLT25D1
GO:0006399	tRNA metabolic process	BP	184	3	0.009	1	ADAT3; PUS10; VARS2
GO:0050873	brown fat cell differentiation	BP	40	2	0.010	1	EBF2; ADIPOQ
GO:0032370	positive regulation of lipid transport	BP	58	2	0.014	1	GAL; ADIPOQ
GO:0010470	regulation of gastrulation	BP	42	2	0.015	1	PHLDB1; ADIPOQ
GO:1903053	regulation of extracellular matrix organization	BP	39	2	0.016	1	PHLDB1; GLT25D1
GO:0046324	regulation of glucose import	BP	55	2	0.017	1	RTN2; ADIPOQ
GO:0032945	negative regulation of mononuclear cell proliferation	BP	69	2	0.017	1	GAL; MAD1L1
GO:0050672	negative regulation of lymphocyte proliferation	BP	69	2	0.017	1	GAL; MAD1L1
GO:0070664	negative regulation of leukocyte proliferation	BP	74	2	0.018	1	GAL; MAD1L1
GO:0046323	glucose import	BP	63	2	0.019	1	RTN2; ADIPOQ
GO:0010827	regulation of glucose transmembrane transport	BP	74	2	0.026	1	RTN2; ADIPOQ
GO:1905954	positive regulation of lipid localization	BP	78	2	0.027	1	GAL; ADIPOQ
GO:0008033	tRNA processing	BP	123	2	0.029	1	ADAT3; PUS10
GO:0015850	organic hydroxy compound transport	BP	254	3	0.038	1	P2RX1; GAL; ADIPOQ
GO:1904659	glucose transmembrane transport	BP	101	2	0.041	1	RTN2; ADIPOQ
GO:0032368	regulation of lipid transport	BP	121	2	0.045	1	GAL; ADIPOQ
GO:0008645	hexose transmembrane transport	BP	108	2	0.046	1	RTN2; ADIPOQ
GO:0015749	monosaccharide transmembrane transport	BP	110	2	0.046	1	RTN2; ADIPOQ
GO:0034219	carbohydrate transmembrane transport	BP	112	2	0.047	1	RTN2; ADIPOQ
GO:0120162	positive regulation of cold-induced thermogenesis	BP	96	2	0.049	1	EBF2; ADIPOQ
GO:0016999	antibiotic metabolic process	BP	147	2	0.050	1	FTCD; EPX

Table 5.8. Biological processes altered upon LPS treatment.

Shown are the 23 significantly altered GO BP pathways after treatment with LPS and recovery. Shown for each pathway is the GO ID, the pathway descriptor, the ontology of the pathway, the number of genes in the pathway, the number of DMPs in the pathway, p-value significance, FDR value and the list of significantly differentially methylated genes within the pathway. FDR=false discovery rate.
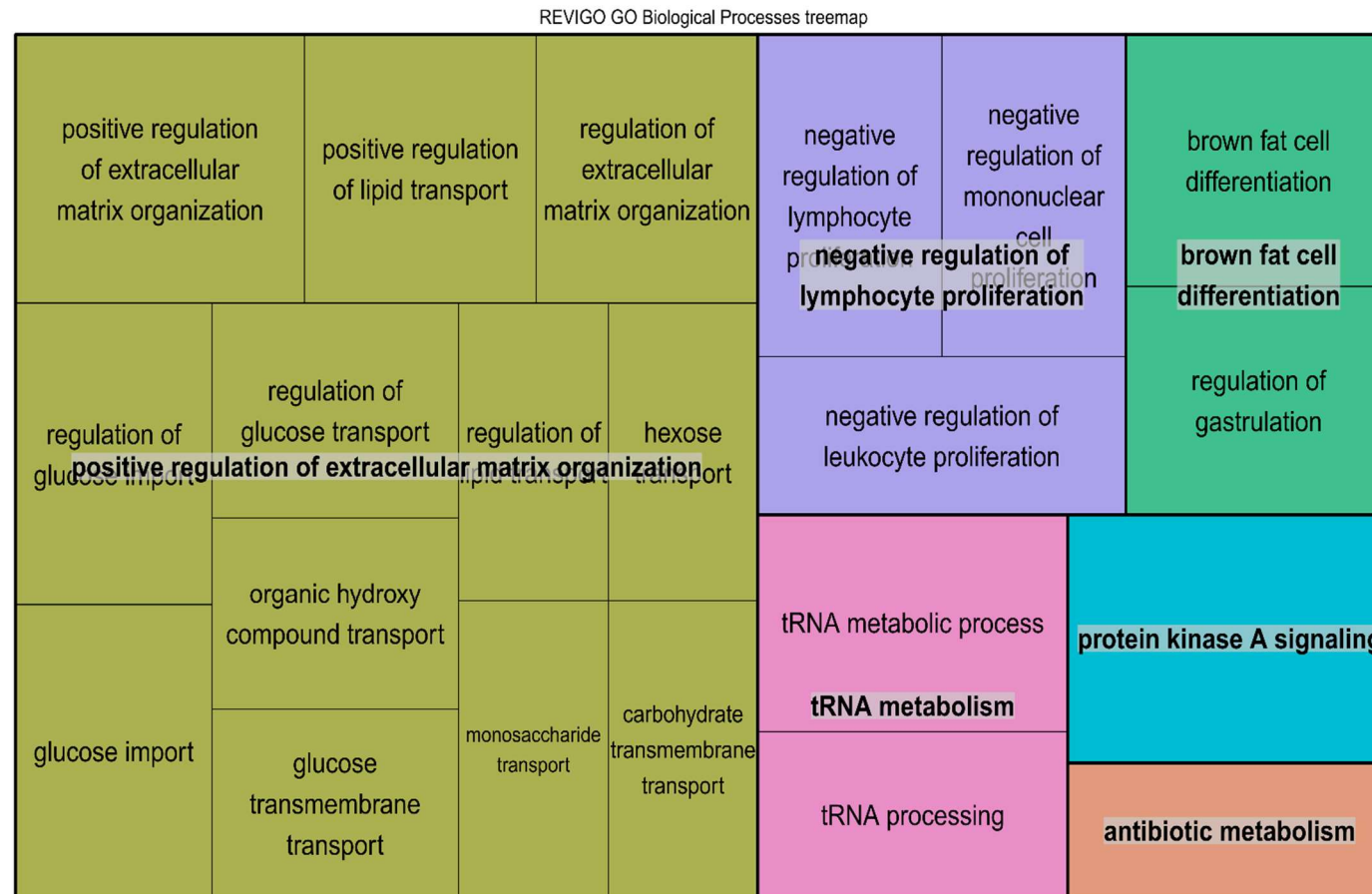
Figure 5.20. Biological processes altered after microglial treatment with LPS.

GO enrichment analysis was performed on the all loci shown to be differentially methylated on LPS treatment. Treemap illustrating the pathways relating to biological processes (BP) is shown. In the treemap, terms relating to the same pathway are grouped together and have been given the same colour, the term that summarizes the grouped pathways is at the centre of each section and is written in bold text.

GO ID	Term	Ontology	No. Genes in Term	No. of DMPs	P-value	FDR	Genes
GO:0016866	intramolecular transferase activity	MF	27	2	0.001	1	PUS10; LSS
GO:0005201	extracellular matrix structural constituent	MF	151	4	0.004	1	MXRA5; MUC4; VWA1; ADIPOQ
GO:0004867	serine-type endopeptidase inhibitor activity	MF	92	2	0.018	1	CPAMD8; SPOCK1
GO:0005179	hormone activity	MF	113	2	0.024	1	GAL; ADIPOQ
GO:0140101	catalytic activity, acting on a tRNA	MF	120	2	0.036	1	PUS10; VARS2
GO:0016853	isomerase activity	MF	141	2	0.040	1	PUS10; LSS

Table 5.9. Molecular functions altered upon LPS treatment.

Shown are the 6 significantly altered GO MF pathways after treatment with LPS and recovery. Shown for each pathway is the GO ID, the pathway descriptor, the ontology of the pathway, the number of genes in the pathway, the number of DMPs in the pathway, p-value significance, FDR value and the list of significantly differentially methylated genes within the pathway. FDR=false discovery rate.

REVIGO GO Molecular Function treemap
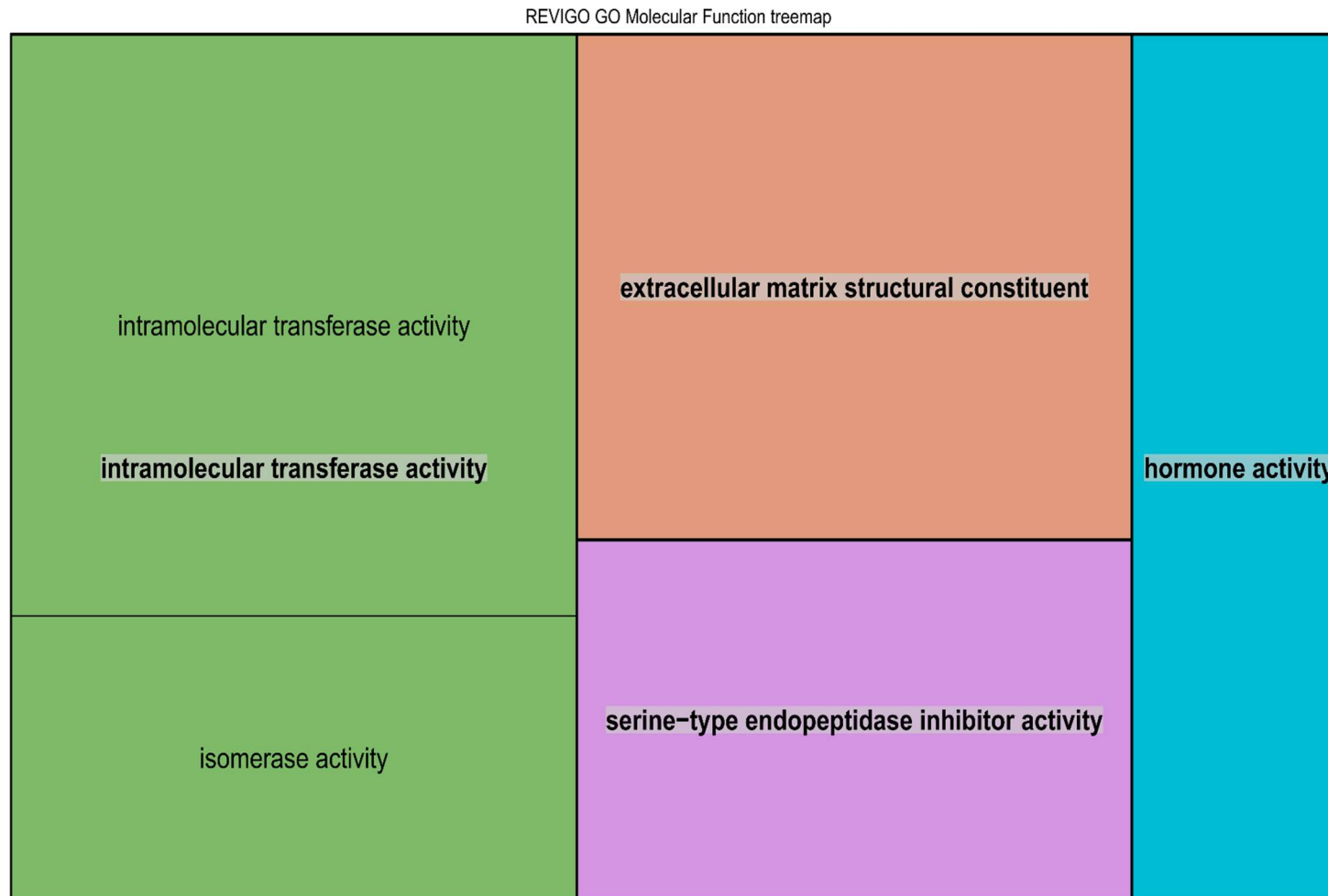
Figure 5.21. Molecular functions altered after microglial treatment with LPS.

GO enrichment analysis was performed on the all loci shown to be differentially methylated on LPS treatment. Treemap illustrating the pathways relating to molecular functions is shown. In the treemap, terms relating to the same pathway are grouped together and have been given the same colour, the term that summarizes the grouped pathways is at the centre of each section and is written in bold text.

GO ID	Term	Ontology	No. Genes in Term	No. of DMPs	P-value	FDR	Genes
GO:0005811	lipid droplet	CC	77	2	0.021	1	LSS; CIDEC
GO:0031301	integral component of organelle membrane	CC	194	3	0.024	1	P2RX1; RHOT2; SLC39A13
GO:0005783	endoplasmic reticulum	CC	1809	11	0.026	1	FTCD; ABCB9; LSS; GIMAP5; RTN2; CIDEC; VWA1; GLT25D1; CES2; SLC39A13; ADIPOQ
GO:0031300	intrinsic component of organelle membrane	CC	216	3	0.032	1	P2RX1; RHOT2; SLC39A13
GO:1902554	serine/threonine protein kinase complex	CC	86	2	0.035	1	GTF2H4; CCNJL
GO:0072686	mitotic spindle	CC	100	2	0.039	1	FAM82A1; MAD1L1
GO:0031594	neuromuscular junction	CC	76	2	0.041	1	CDH15; SPOCK1
GO:0015630	microtubule cytoskeleton	CC	1166	8	0.045	1	FTCD; FAM82A1; WDR90; MTUS2; KIF26A; B9D1; KIAA0284; MAD1L1
GO:0016528	Sarcoplasm	CC	75	2	0.047	1	RTN2; SPOCK1

Table 5.10. Cellular components altered upon LPS treatment

Shown are the 9 significantly altered GO CC pathways after treatment with LPS and recovery. Shown for each pathway is the GO ID, the pathway descriptor, the ontology of the pathway, the number of genes in the pathway, the number of DMPs in the pathway, p-value significance, FDR value and the list of significantly differentially methylated genes within the pathway. FDR=false discovery rate.

REVIGO GO Cellular Component Treemap

lipid particle	integral component of organelle membrane	**serine/threonine protein kinase complex**
lipid particle mitotic spindle	integral component of organelle membrane intrinsic component of organelle membrane	**neuromuscular junction**
microtubule cytoskeleton	**endoplasmic reticulum**	**sarcoplasm**
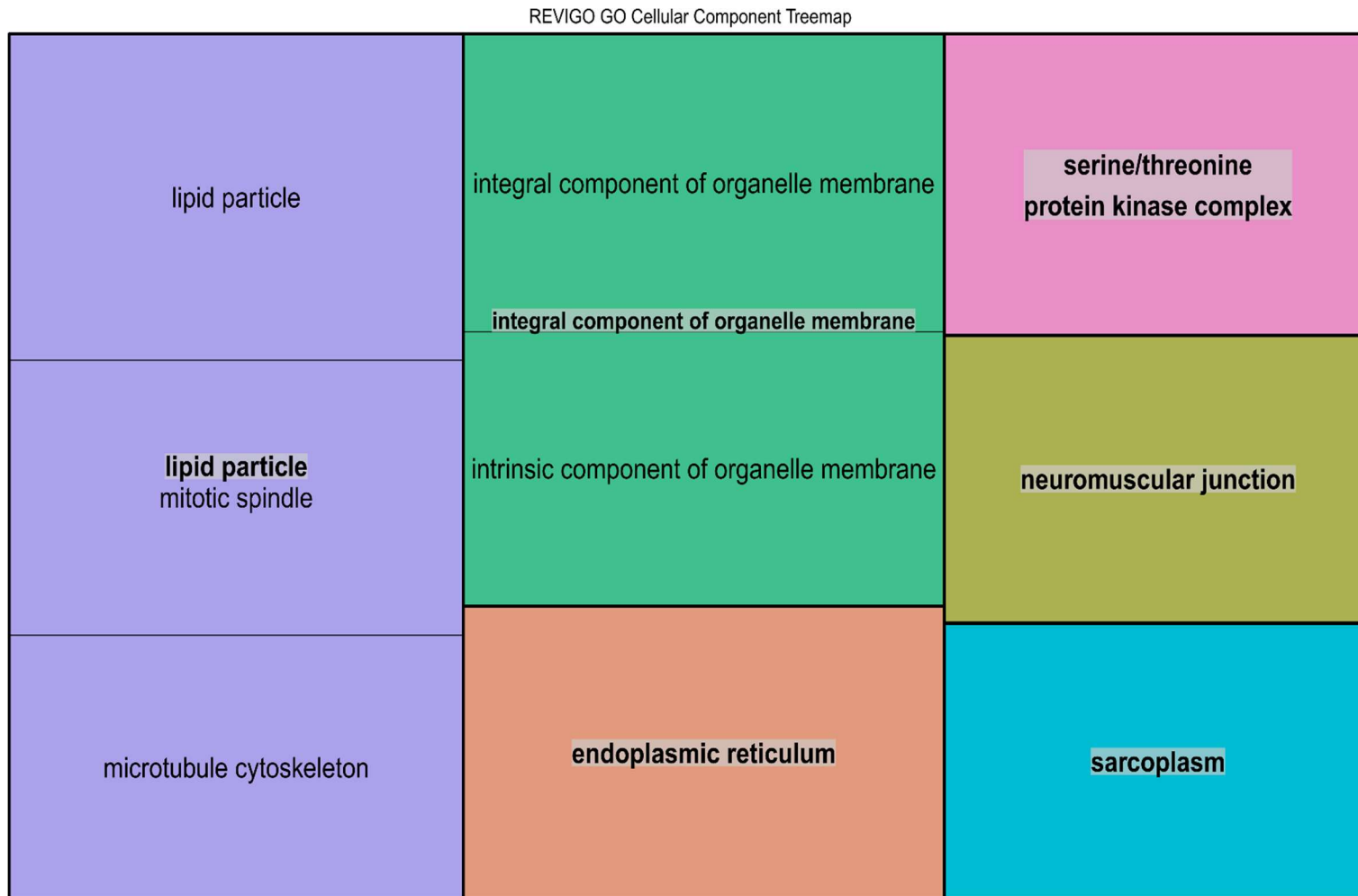
Figure 5.22. Cellular components altered after microglial treatment with LPS.

GO enrichment analysis was performed on the all loci shown to be differentially methylated on LPS treatment. Treemap illustrating the pathways relating to cellular components is shown. In the treemap, terms relating to the same pathway are grouped together and have been given the same colour, the term that summarizes the grouped pathways is at the centre of each section and is written in bold text.

5.5 Discussion

In this chapter I have used the Illumina EPIC array to undertake epigenome-wide analyses of DNA methylation changes occurring upon microglial cell activation and then recovery by a known immune stimulant. This was achieved by treating an immortalised microglial cell line with either LPS for 24 hours, treating with LPS for 24 hours followed by a 24-hour recovery period or undergoing no treatment (control), as outlined in figure 5.1. Once the treatments were completed the cells were collected, DNA was extracted and then run on the EPIC array to provide information on DNA methylation at over 850,000 loci across the genome.

One of the first things that has been shown by this study is that there are no changes to either epigenetic age or mitotic age upon stimulation. This could have numerous explanations. Firstly, as this is an immortalised cell line the process of immortalisation could have made the cells more robust and therefore less susceptible to stimulation. What is of interest is that the epigenetic age of these cells does not reflect the biological age of the person the cells were originally derived from, which was a middle-aged male. This would suggest that the immortalisation process has changed the methylation profile of the cells therefore making them appear epigenetically rejuvenated. Another reason there are no changes upon stimulation could be because the cells were only treated once and for 24-hours. During life and throughout disease course the human body will be exposed to numerous infections and it is possible that it is this repeated exposure to immune stimulation that is causing the robust methylation changes that are found upon post-mortem investigation. In order to test whether these are the reasons there are no significant changes in epigenetic or mitotic age it would be interesting to repeat these experiments in a non-immortalised cellular model and

use recurrent exposures and recoveries to LPS. One example could be to repeatedly expose iPSC-derived microglia or just treat them once with LPS to see if there is any association of repeated exposure to these measures of maturity. Finally, although I showed there were no differences in epigenetic age using the current Horvath age calculator [126], it is worth noting that there are many different epigenetic age clocks [125, 236, 237] and calculators that have now been developed. These all have different advantages and disadvantages, depending on the dataset that they have been developed in. I decided to use the Horvath age calculator in this chapter as I had used it in my previous chapters, as it had demonstrated in chapter 4 that my samples were cortical neurons. It could perhaps be possible that the other epigenetic clocks that are available may be more sensitive to changes in immortalised cell lines, and so future studies could explore the epigenetic age predicted by these different algorithms.

By categorising DMPs into four different categories based on their pattern of methylation change (*e.g.* acute and persistent hypo and hypermethylated probes), I was able to look at which loci are more susceptible to long term changes in methylation and the associated functions of these loci. This allowed me to infer the cellular functions that are perhaps the most affected by immune stimulation. Firstly, as there are many more genes in both of the acute categories it is clear that the majority of differentially methylated loci were more susceptible to short term changes, which had largely disappeared in the recovery group. Again, this could reflect the short term and non-recurrent nature of the stimulation and it would be interesting to see whether the changes in methylation at these loci become more long term upon multiple treatments with LPS. In addition, the fact that I saw greater changes acutely rather than persistently could also reflect

the fact that there was more variation in methylation in the LPS + recovery group samples, compared to the other treatment groups. In the future profiling additional samples per treatment group could reduce this variation, or could demonstrate that this is driven by differences in recovery between samples. It is worth noting that due to the low number of replicates per treatment group (N = 4) and as I only tested a one-off stimulation, none of the loci I identified were Bonferroni-significant. As such I decided to use a more relaxed arbitrary significance threshold of P=1x10^{-3}. Therefore, further replication of results is required. Owing to the fact that the EPIC array profiles ~850,000 methylation sites, and many of these are highly correlated it has been previously shown in previous methylomic studies on the Illumina arrays that Bonferroni significance is overly stringent for EWAS [414], although the field has not yet identified the best p-value threshold for the EPIC array to account for this [415].

Across all of the categories of methylation pattern changes, one type of gene that consistently feature were that of transcriptional regulators. Within the persistent hypomethylation category half of the significant loci were known transcription factors or transcriptional regulators, inferring that changes to transcription are affected more long term. As decreased methylation is generally associated with increases in gene expression it would suggest that immune stimulation is causing an increase in expression of these transcriptional regulators. This would therefore cause expression changes of the targets of the regulators. These changes in DNA methylation are intuitive as exposure to LPS is known to cause immune cell activation which will be regulated and brought about by changes to gene expression. It is however worth noting that the relationship between DNA methylation and gene expression is more complex, with decreased DNA

methylation also associated with gene silencing and alternative splicing, depending on the context. In the future it will therefore be of interest to profile mRNA levels of the genes I have shown are differentially methylated following LPS, to establish this relationship.

Another category of genes that had altered DNA methylation following LPS were those encoding signalling proteins or proteins involved in signalling pathways. The fact that the levels of methylation were both increasing and decreasing depending on the locus would suggest that some signalling pathways become activated, whilst other become less active following LPS exposure. As microglia undertake a variety of different roles in addition to response to LPS/bacteria (*e.g.* phagocytosis, synaptic pruning [416]), then it is not surprising that changes in the activity of different signalling pathways are observed after LPS. It would again be of interest in the future to explore the levels of gene expression of the differentially methylated genes.

In order to get a better idea of the pathways that were changing upon LPS treatment GO pathway analysis using the missMethyl package was used. As there were not enough loci within each category to do this analysis for the categories individually all significant loci across the categories were pooled. By pooling the loci together, it was possible to determine which pathways were possibly impacted following LPS irrespective of the direction or duration of change. Using the REVIGO treemap generator the changing pathways were grouped into biological pathways, molecular functions and cellular components and then further grouped according to their specific function and summarised. From these analyses it appears that DNA methylation levels are particularly

altered in genes involved in extracellular matrix organisation, enzyme activity, signalling and organelle function. One limitation of this analysis is the small number of DMPs used to perform the pathway analysis. Ideally, pathway analysis would be performed on more than 1000 loci, but despite pooling of DMPs there were still only 173 DMPs used. This low number of loci resulted in none of the resulting pathways being FDR significant and therefore cautious interpretation is advised. Another limitation for this analysis was the pooling of the genes in the different categories of methylation changes, as ideally this would be performed on the separate categories. In order to address both of the limitations it could have been an option to analyse the top 1000 DMPs per group. However, as this could introduce a lot of false negatives into the results I decided not to do this.

Looking to the future I feel it is important to take these results further and interrogate DNA methylation upon LPS treatment in more relevant models and more comprehensively. As previously mentioned, this could be undertaken in iPSC-derived microglial lines. Using these cells it would also be of interest to explore the effects of recurrent exposure to LPS and whether there are any loci that are susceptible to persistent changes in DNA methylation upon recurrent stimulation. Using iPSC lines, it would also be possible to look at the effect of genotype on methylation and whether having a microglial relevant mutation, such as those in *TREM2*, *CLU* or *CD33* for example, would affect the changes seen in methylation. As the data generated using this system would be human data it would be possible to look at the overlap in post-mortem brain data, perhaps in people who were known to have an infection at the time of death.

Finally, alongside investigating changes in methylation, it will be important to profile gene expression as well as undertaking more functional assays to assess the effects of LPS on phenotype. It would be particularly interesting to undertake these experiments in the presence of AD relevant proteins such as Aβ, as I am particularly interested in cellular phenotype in the context of AD. This would allow us to confirm that microglial cells are less able to perform phagocytosis of Aβ after stimulation with LPS [417]. Looking at morphological changes and staining for proteins known to have increased expression on immune activation would provide more information on how functionally relevant the assay is. To look at response to injury scratch assays could be used or phagocytosis could be tracked by following the uptake of fluorescently labelled or tagged AD proteins such as Aβ.

5.6 Conclusions

In this chapter I have characterised genome wide patterns of DNA methylation in microglia in order to further understand the epigenomic changes that are occurring upon microglial stimulation with LPS. I have shown that despite treatment and recovery there are no changes in either epigenetic, or mitotic age, which is perhaps a reflection of the cell line used, the low replicate number and the one-off nature of the treatment. In order to understand the functional implications of LPS stimulation, I used both manual and computational assessment of the pathways and cellular functions that were changing. Through these analyses it is clear that there are large amounts of loci undergoing DNA methylation changes on treatment, which is potentially affecting gene regulation, matrix organisation and signalling within the microglial cells. In the future it will be important to expand upon these results by assessing genotype dependent recurrent LPS-induced methylation and functional changes in an iPSC-derived microglial cells.

Overall, I have shown there is methylomic variation occurring upon the stimulation of microglial cells with LPS. This includes increasing and decreasing methylation changes that are short and longer lived. Moving forward it would be of benefit to expand this study further using a different cell line, with more recurrent exposures and using a larger number of replicates.

CHAPTER 6 : DISCUSSION AND FUTURE PERSPECTIVES

6.1 Introduction

The primary aim of thesis was to characterise and expand the existing knowledge about the epigenetic landscape in neuronal and microglial cell lines, in particular the methylomic changes occurring with AD-relevant events, such as time in culture, drug treatment or immune challenge. This discussion will summarise the key findings from each chapter of this thesis and the limitations present within each study.

6.2 Key Findings from this Thesis

6.2.1 Chapter 3: Characterisation of DNA Methylomic Signatures in iPSCs during Neuronal Differentiation

As it is known that epigenetic mechanisms, including DNA methylation, play a role in cell fate, this chapter aimed to demonstrate that there are DNA methylation changes occurring during differentiation and that these changes impact on neuron-related cellular pathways. Using the Illumina EPIC array it was possible to assess the DNA methylation status of over 850,000 loci across the genome at numerous time points throughout the differentiation of iPSCs into neurons.

The first key finding in this study is that the iPSC-derived neurons have a foetal epigenetic age, with the highest age of any sample being -0.41 years. This will be important to bear in mind for future studies, especially when using stem cell derived neurons to study the epigenetic changes occurring in age related diseases. However, it is worth noting that the algorithm used to determine the epigenetic ages of these samples was not trained on foetal brain data. Therefore, it is important that the epigenetic ages of the samples are interpreted with some caution. In the future it will be of interest to test a range of different epigenetic age calculators to explore whether these may demonstrate different ages. However, in the current study it is still interesting that despite not being trained on foetal data that the epigenetic ages of all samples were negative.

Following on from this I performed WGCNA, pathway analysis and trajectory inference modelling to determine the consequences of the DNA methylation changes over time. The WGCNA analysis identified modules of probes largely

relating to pathways involved in neuronal development or the regulation of gene expression. The trajectory inference model identified probes that that were becoming progressively hypo- or hypermethylated with time, and similarly these probes were also largely annotated to genes involved in gene regulation and processes that are important in becoming a neuron. One of the advantages of using two different methods to analyse the data (WGCNA and TI modelling), which identified similar pathways is that we can be more confident that the results seen are genuine and the cells we are generating are neurons.

Finally, to explore the interconnectivity of the probes identified in the trajectory model gene-gene interaction analyses were performed. This identified 2,352 unique genes, of which 602 of those genes formed a network containing 1,158 interactions. Within this network there were 50 highly connected genes, of which 72% were involved in transcriptional regulation and 14% were shown to be involved in epigenetic regulation. Many of the transcription factors identified, including *STAT3*, *TDF7L2* and *LHX2* have been shown to be important for neuronal survival and function [280-282, 418]. The implication of these genes in the network adds more evidence to suggest that there are many neuronal genes that are highly influential in the development and differentiation of neurons.

One caveat of this study is the fact that it was only undertaken in one iPSC cell line and that there were relatively few replicates per group. Having few replicates affects the power in the study and means that it is not possible to detect small changes in DNA methylation. Only using one cell line means that whilst we can say the changes seen here are characteristic of this cell line it is not possible to say this is the same in other iPSC lines. In order to validate the findings of this

study it will be important to repeat the study in several different cell lines, ideally with more replicates; this way we could create a lineage trajectory that is characteristic of all iPSC lines rather than just the one.

6.2.2 Chapter 4: Determining the Utility of Epigenetic Modulators to Treat AD

The aim of this chapter was to characterise the methylomic changes occurring when iPSC-derived neurons and microglia are treated with compounds known to effect epigenetic mechanisms. Whilst the targets of the drugs used in this chapter are known, and have been shown to modulate various epigenetic mechanisms, the consequence on epigenetic markers, such as DNA methylation have never been investigated. This was achieved using the Illumina EPIC array to assess DNA methylation patterns across the genome.

As demonstrated in chapter 3, the iPSC-derived neurons in this chapter all have a foetal epigenome, with the highest epigenetic age of any sample being ~-0.2 years. In addition to this the epigenetic ages of iPSC-derived microglia were also assessed. Whilst the majority of microglial samples did not have a foetal epigenetic age, the age they were predicted to be was still immature and ranged from ~0 to 0.7 years. This suggests that whilst still young the microglia are epigenetically older than the neuronal samples, which may reflect that they still proliferate once generated. Interestingly, none of the treatments in either of the cell types had an impact on the epigenetic age of the samples. This could be a result of the short nature of treatment or show that the epigenetic modulators do not affect the methylation levels of the loci that are used to calculate epigenetic age. As drugs are not often given as a one-off treatment it would be worthwhile

assessing the epigenetic age and methylation changes that occur after a longer term treatment with these compounds.

Using linear regression modelling I tried to identify DMPs in the neurons and microglia that were nominally consistently significant across the drugs of the same class, *i.e.* BRD, HMT, HKDM or KMR inhibitor. Whilst there were consistent nominally significant changes seen across the drug classes in the microglial samples (BRD: 427, HMT: 429, HKDM: 387 and KMR: 369) the same was not true in the neurons BRD: 0, HMT: 0, HKDM: 144 and KMR: 120), where the only consistent nominally significant changes that were seen were in the groups containing the fewest modulators. This suggests that the modulators are having a much more constant effect on DNA methylation in microglia than in neurons, or that there is more variation in the neurons than the microglia, meaning there are less significant changes in the neurons. However, it is worth noting that although I saw little overlap in the number of nominally significant methylation changes in neurons, I did observe similar effect sizes for compounds in the same drug class. For example, when I compared the effect size of the 100 most significant DMPs identified in neurons for one compound in a class, to other compounds in that class I saw a significant correlation and enrichment of direction of effect. Similarly, when I performed the same tests in the microglia I also observed significant correlations and enrichments of direction of effect. Interestingly, when I compared the effect size and direction of effect of the top 100 DMPs in one treatment in the neuronal samples to the same treatment in the microglial samples there was no correlation or enrichment for a direction of effect. This demonstrates that the modulators are a different effect in the two difference cell types.

One caveat of this study is that it was underpowered, and therefore it was not possible to find any methylation changes that reached genome-wide (Bonferroni) significance. As power is linked to the number of replicates, in the future the replicate number would need to be increased in order to detect DMPs and DMRs that are Bonferroni significant. It may also be possible to see more significant changes if the treatments were delivered for longer than 24-hours. As previously mentioned drugs used to treat chronic diseases are seldom given as a one off and so it would be valuable to assess the long term effects these drugs would have on DNA methylation.

Another potential pitfall in this study is that the neurons and microglia were generated from different cell lines. As a result of this, the different cell types will have different genetic backgrounds and this could affect the way the treatments alter the DNA methylome. In the future it will be of interest to repeat these experiments using neurons and microglia generated from the same iPSC line to eliminate the different genotypes as a confounder. Similarly, it will be of interest to explore this in multiple iPSC lines to ensure any findings are consistent across different genetic backgrounds.

Finally, in the future it would be interesting to assess other epigenetic markers other than DNA methylation. As a lot of the targets of the drugs are known to interact with histone-related proteins it, looking at histone modifications and chromatin accessibility would provide more information on the epigenetic consequences of these modulators. Alongside this looking at the corresponding gene expression changes within the cells would allow us to determine whether the cellular pathways implicated by the methylation data are the same being

pulled out by the transcriptomic data. Being able to take a multi-omics approach would also mean we could determine whether the methylation changes are causing gene expression changes therefore further disentangling the cellular effects of the modulators.

6.2.3 Chapter 5: DNA Methylomic Variation Induced by LPS Challenge in a Human Microglial Cell Line

The aim of study was to determine DNA methylation changes that occur when microglial cells are exposed to known immune stimulants such as LPS and the cellular consequences that these changes have. This was achieved by treating immortalised human primary microglia for 24 hours with LPS, 24 hours with LPS followed by a 24 hour recovery period or no treatment (*i.e.* control), the genome wide DNA methylation changes were then profiled using the Illumina EPIC array.

One of the first results of this study demonstrated that neither treatment nor treatment and recovery from LPS stimulation affects the epigenetic or mitotic age of the microglial cells. As previously discussed, there are several reasons this could be. Firstly, the immortalisation of the cells is likely to have impacted the methylome of the cells and could have therefore made them less susceptible to LPS-induced methylation changes. Secondly, the treatment and recovery periods may have been too short. As the treatment and recovery periods were both only 24 hours it is possible that this was not a long enough time for significant changes to manifest. To improve this study in the future it would be interesting to assess the methylomic changes recurring after longer treatment or recurrent exposures.

In order to determine the probes that were susceptible to long term changes to methylation and the associated functions of these loci I categorised the DMPs into four categories based on their methylation changes (*i.e.* acute or persistent hypo- and hypermethylated probes). This approach allowed me to infer the cellular pathways and functions that were more susceptible to immune stimulation. As there are more probes in both of the acute groups it is clear that the majority of DMPs were more susceptible to short term changes that largely disappear during the recovery period. This may be due to the short term nature of the treatment period, and in the future it would be interesting to see if any of these loci become persistently differentially methylated after longer or recurrent treatment. Across the four categories there was one type of gene that was more consistently differentially methylated, these were transcriptional regulators. In fact half of the DMPs in the persistent hypomethylation category were transcription factors or transcriptional regulators. As decreased methylation is generally associated with increased transcription it would suggest that there is increased expression of transcriptional regulators upon LPS stimulation. However, as the relationship between DNA methylation and gene expression is context dependent it would also be interesting to study the mRNA changes associated with LPS treatment to see if the expression of these regulators is in fact decreasing.

As there weren't enough loci in each individual category to perform pathway analysis separately the four categories of DMPs were pooled to get a general view of the pathways potentially impacted by LPS treatment irrespective of the direction or duration of the change. These analyses demonstrated that DNA methylation changes are particularly observed in genes involved in extracellular matrix organisation, signalling and organelle function. However, to confirm that

these pathways are changing functional experiments are required. One limitation of analysing the data in this way is the small number of DMPs put into the pathway analysis. Ideally >1,000 DMPs would be used for each category and each category would have been run separately. However, in the current study I did not use this approach as taking the top 1,000 DMPs for each group would have introduced a lot of false negatives, which could have made the data more difficult to interpret.

One of the largest limitations of this study is the small number of replicates used. The low sample number in conjunction with the short treatment time are likely the reasons it wasn't possible to detect any Bonferroni significant loci. This lack of power means that further replication of the results in the future is necessary. In addition to this adding more replicates to this study should also counteract some of the large variation seen in some of the results. For instance the variation seen in the LPS + recovery group suggests that some of the replicates are recovering from treatment faster than others and could be the reason I identified fewer persistently differentially methylated loci. By adding more replicates into the study I would be able to reduce this variation and determine whether there is a genuine difference in the recovery rates of samples.

Finally looking to the future I think it will not only be important to increase the treatment length or use recurrent treatments to assess LPS-induced methylation changes. However, one issue with recurrent exposure to LPS is cells can become tolerant to the treatment [419-421], so in addition to LPS, it would also be interesting to look at the methylation changes occurring upon Lipoteichoic acid (LTA). I think it will be of great importance to profile the LPS-changes in a more

relevant cellular model and profile the changes more comprehensively. This could include the use of iPSC-derived microglial lines containing different relevant mutations, such as *TREM2, CLU* or *CD33.* Using these non-immortalised human lines it would then be possible to see if there is any overlap with human post mortem data, perhaps in people who were known to have an infection at time of death. In addition, I believe it would also be of interest to profile the DNA methylation changes observed in iPSC-microglia upon stimulation with pathological proteins such as Aβ or Tau.

6.3 General Discussion, Limitations and Future Perspectives

6.3.1 Biological Implications of the Key Findings

Through each chapter of this thesis I have demonstrated that there are methylomic changes occurring in neuronal and microglial cell lines that have been exposed to AD-relevant exposures such as time in culture, drug treatment and immune stimulation. As DNA methylation is known to regulate gene expression [99, 422-424] and there are many loci at which the methylation levels are changing it is likely that each of these exposures are causing changes gene expression changes at numerous loci therefore potentially impacting certain cellular pathways.

One of the most consistent changes seen throughout this thesis is changes to methylation at loci associated with transcriptional regulation. In chapter 3, 72% of the loci within the gene-gene interaction network were known transcriptional regulators and ten of the MFs identified through pathway analysis using the loci becoming progressively hypermethylated with time were related to transcription regulatory region DNA binding. Similarly, in chapter 5 half of the loci in the persistent hypomethylation category were found to be involved in transcriptional regulation through manual curation. As hypomethylation is generally associated with increases in gene expression it would suggest that LPS treatment is causing an increase in the expression of these regulators. Due to the nature of the treatments in these chapters, *i.e.* differentiation (chapter 3) and immune challenge (chapter 5) it is not surprising that transcriptional regulation is affected. Expression changes to some of the loci identified in these chapters have previously been demonstrated through other methods [425-429]. However, in

order to assess the true biological impact the exposures are having more experiments will need to be performed, these could include quantitative polymerase chain reaction (qPCR) to look at gene expression changes and assays to look at changes to cellular function.

Another broad category of proteins affected consistently throughout this thesis is that of signalling proteins. In chapter 3 six of the BPs identified through pathway analysis using the loci becoming progressively hypermethylated with time were related to cell-surface receptor signalling. Alongside this two of the compound classes in microglia were shown to affect the methylation of loci known to be involved in cell signalling pathways; these include the BRD inhibitors which affected loci associated with protein tyrosine kinase activity and the KMR inhibitors which affected loci associated with phosphatidylinositol 3-kinase signalling. Finally, LPS treatment in chapter 5 was associated with changes to methylation at loci involved in protein tyrosine kinase A signalling and serine/threonine kinases. These data taken together suggest that AD relevant exposures are associated with changes in cellular signalling, which has been previously demonstrated using different methods [430-433]. However, although associated it is important to note that without undertaking specific functional assays the changes to these signalling pathways is not certain in these conditions in these cell lines.

Finally, although there is commonality in regards to the types of loci undergoing methylation changes as the work has been undertaken in cell lines grown in 2D culture these results likely only reflect a small proportion of the changes occurring in the brain. In order to have a better understanding of how these data relate to

disease it would be interesting to compare them to post-mortem human brain data or data generated from organoid co-culture models.

6.3.2 Limitations

As outlined above there are numerous limitations associated with the chapters of this thesis and with studying epigenetic changes. In this section I will outline the limitations that are common to most chapters and what could be done in the future to address these limitations.

6.3.2.1 Low Sample Number

One consistent limitation throughout this thesis and is often a common problem for cell culture based studies, is that of the low number of samples. Whilst it is possible to use a lower number of replicates for *in vitro* studies as it is possible to eliminate confounders such as sex, medication, or age that are common caveats in studies using human samples, having a low sample number does often mean that statistical significance, particularly in -omics based studies are not often reached. This is due to the relationship between p-value, sample size and the power to detect changes in methylation [434-436]. By increasing the sample size in further studies it will be possible to more accurately determine whether there are type I or II errors being introduced into the results therefore possibly leading to misinterpretation of findings. It will also possible to use the data in the chapters of this thesis to undertake power calculations in order to determine the ideal samples sizes moving forward. Power calculations were not performed before undertaking the experiments presented in this thesis as they represent the first DNA methylomic studies in this context and so no preliminary data was available to estimate power. In the analyses I present a higher importance has been placed

on direction of effect and the correlation of effect size in some cases, in addition to a more relaxed arbitrary significance threshold chosen. It has previously been demonstrated that due to the high degree of correlation between the probes on the Illumina EPIC array the Bonferroni significance threshold is likely too stringent and therefore likely to introduce type II errors. Owing to this it was deemed acceptable to use more relaxed thresholds in my studies, but to note that further replication of results is required before solid conclusions can be drawn.

6.3.2.2 Use of Different Cell Lines

It is critical to note that there is a different cell line used in each of the chapters of this thesis. Whilst this was not originally planned due to issues with building management and power failures I have had to rely upon collaborators to provide iPSC-derived cells to use in each chapter. The first issue to occur was due to lack of communication between the technical staff in the Hatherly laboratories. As a result of the mis-communication the liquid nitrogen tanks storing the vast majority of the neuronal lines I had developed, evaporated and meant all of the cell stored in the tank were destroyed. Following this loss it took numerous months to get stocks of the various lines from collaborators and to regenerate the iPSC-derived neurons. Owing to the lack of redundancy in the liquid nitrogen facilities at the Hatherly laboratories whilst cell lines were being re-acquired I decided to move my tissue culture work to the RILD building, as that is where our research group is primarily based. Unfortunately, a year later within the RILD building there was a power failure overnight and the backup generators failed. This power outage affected the tissue culture facilities and resulted in the incubators cooling down to $\sim 12^\circ$C. Whilst the cells were still alive the next morning I decided the cells could not be kept for experiments as this persistent decrease in temperature would

likely have affected the methylome of the cells. As a result of this second system failure I lost iPSC-derived neurons which had been maturing in culture for approximately six months and cell lines of different genetic background. A further four months of work was lost later that year whilst I was away at a conference and my cells were being looked after by someone else. Unfortunately all of these issues were beyond my control, and has meant that we have used different lines for different chapters, with substantially less replicates than originally planned. However, ideally all of the experiments in this thesis would have been undertaken in cells of the same genetic background with substantially more replicates.

6.3.2.3 Caveats of EWAS Studies and Profiling Cytosine Modifications

The Illlumina platform has become one of the most popular ways to interrogate DNA methylation across the genome and has been used extensively to study methylomic variation within AD [120, 121, 437]. However, despite its extensive use there are limitations which should be taken into account. Firstly, standard BS conversion does not allow you to distinguish between DNA methylation and another cytosine modifications (DNA hydroxymethylation). As a result of this, the results from the array are a combination of both these cytosine modifications rather than just 5-mC. As 5-hmC is a DNA modification that in particular has been shown to be elevated in the brain and during development [438, 439] and the majority of cells used in this thesis are iPSC-derived neurons, which I have shown to be epigenetically foetal or immature then it would be of interest to profile this modification in isolation in the future. It is now possible to simultaneously profile 5-hmC and 5-mC, by adding an oxidation step prior to bisulfite treatment, which converts 5-hmC to 5-fC. Following BS treatment the 5-fC is converted to a uracil and so upon PCR amplification becomes a thymine, whilst methylated loci are

protected from the conversion and therefore will remain as cytosine. Subsequently, running oxidative-BS samples on the array generates a measure of 5-mC in isolation, and by running a matched BS sample in parallel you can subtract the oxidative-BS signal from the BS signal generating a 5-hmC value for each locus. In order to determine whether the methylation changes detected (particularly in chapters 4 and 5) are indeed changes to DNA methylation rather than hydroxymethylation it would be of interest in the future to also run oxidative BS converted DNA on the EPIC array to disentangle the relationship between cellular maturity, drug treatment and hydroxymethylation changes.

6.3.2.4 Determination of Age

Looking to the future, I think it will be important to further explore the epigenetic age of the iPSC-derived neurons and microglia used in this thesis. The methodology used to generate the epigenetic or biological age of the samples used in this thesis was the most up to date version of Horvath's epigenetic age calculator [126]. However, it is worth noting that the algorithm used to calculate epigenetic age was not trained on foetal data. As the DNA methylation profile is dynamic throughout brain development [440], the epigenetic ages presented in each chapter should not be interpreted as a robust read out of age. The interpretation of this should be that despite not being trained on foetal or infant data the epigenetic ages of the sample in this thesis are still predicted to be foetal. In the future it will be of interest to explore other epigenetic age calculators and to culture cells for a long period of time to investigate whether this impacts their epigenetic age. It will also be of interest to examine the epigenetic age of iNs under the different treatments outlined in each chapter, as iNs have been shown retain their age-related epigenetic signature [441].

In order to combat this other metrics of cellular maturity or ways of measuring the biological age of iPSC-derived cells should be considered in the future in addition to epigenetic age. One way in which this could be achieved in through the use of RNA-sequencing and measuring the expression of genes known to increase or decrease throughout development. This could include the measuring the expression level of pluripotency genes such as *NANOG*, mature neuronal markers such as *β-III-Tubulin* or subtype specific markers such as choline acetyltransferase to determine the type of neuron being generated. As telomerase is known to be active in iPSCs [442, 443] determining the telomere length of the resultant iPSC-derived neurons and relating it healthy human post mortem brain data I believe would also be of value.

6.4 Conclusions

Overall the data outlined in this thesis has provided evidence that it is possible to generate iPSC-derived neurons and that there are epigenetic changes occurring in neuronal and microglial cell models that are exposed to AD-relevant exposures such as time in culture, drug treatment and immune challenge. However, despite this there are still several questions which remain unanswered. These include:

1. What is the best way to mature iPSC-derived cells in culture and the best way of measuring cellular age?

2. Whether longer treatment with the epigenetic modulators used in chapter 4 could alter epigenetic age or be used to reverse the epigenetic changes seen in disease.

3. Whether recurrent exposure to LPS or other relevant pathological proteins will have a more profound effect on resulting cells.

Looking to the future using multi-omics approaches and different conditions throughout neuronal differentiation and maturation will offer the best tools in which to answer these questions.

APPENDIX A : USING INDUCED PLURIPOTENT STEM CELLS TO EXPLORE GENETIC AND EPIGENETIC VARIATION ASSOCIATED WITH ALZHEIMER'S DISEASE

Epigenomics
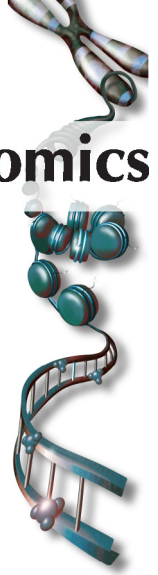
Using induced pluripotent stem cells to explore genetic and epigenetic variation associated with Alzheimer's disease

Jennifer Imm[1], Talitha L Kerrigan[1], Aaron Jeffries[1] & Katie Lunnon*,[1]

[1]Institute of Clinical and Biomedical Science, University of Exeter Medical School, Exeter University, Exeter, UK

* Author for correspondence: k.lunnon@exeter.ac.uk

It is thought that both genetic and epigenetic variation play a role in Alzheimer's disease initiation and progression. With the advent of somatic cell reprogramming into induced pluripotent stem cells it is now possible to generate patient-derived cells that are able to more accurately model and recapitulate disease. Furthermore, by combining this with recent advances in (epi)genome editing technologies, it is possible to begin to examine the functional consequence of previously nominated genetic variants and infer epigenetic causality from recently identified epigenetic variants. In this review, we explore the role of genetic and epigenetic variation in Alzheimer's disease and how the functional relevance of nominated loci can be investigated using induced pluripotent stem cells and (epi)genome editing techniques.

Alzheimer's disease

Alzheimer's disease (AD) is the most prevalent neurodegenerative disorder and accounts for approximately 60–80% of all dementia cases worldwide [1]. Dementia is estimated to affect 46.8 million people worldwide, with this set to double every 20 years reaching 131.5 million in 2050 [2]. The disease is characterized by the accumulation of amyloid beta (Aβ) plaques, intracellular neurofibrillary tangles of hyperphosphorylated tau [3] and loss of synaptic connections [4]; taken together these lead to neuronal cell death. This is accompanied by cognitive and behavioral changes, such as memory impairments, language disturbance and hallucinations. The early cognitive decline in AD can be attributed to the degeneration of cholinergic neuronal cells found in the cortical and limbic brain regions such as the hippocampus [5] and the basal forebrain [6].

The deposition of senile plaques and tangles does not occur at random, but follows a distinct and characteristic pattern [7–10], starting in the neocortex and then the hippocampus [11], while other regions, such as the cerebellum, remain relatively unaffected [12]. This specific topographical distribution correlates with, and explains, the characteristic symptoms of AD; the hippocampus and neocortex are well known for being involved in controlling emotions, memory and higher brain function [13,14]. The cerebellum on the other hand is responsible for coordination, motor and voluntary movements, and there are far fewer aberrations in these in AD patients when compared with the prevalence of other symptoms [15]. There is already considerable pathology before the disease is diagnosed [16], with the onset of symptoms sometimes occurring at least 10 years after Aβ is first deposited [17]. This apparent delay in the appearance of symptoms is caused by there being a threshold of cholinergic loss before the brain can no longer compensate and ameliorate the deficit [11]. Although, much progress has been made in understanding the cellular pathology of AD, the treatments currently available only temporarily alleviate some symptoms and do not modify the underlying pathology.

Genetic variation associated with AD

Given, the high heritability estimates (~60–80%) for AD based on quantitative genetic studies [18], initial etiological studies have focused on identifying a genetic basis for disease. Although some AD cases are caused by autosomal

Future Medicine

Table 1. Summary table of single nucleotide polymorphisms (SNPs) associated with Alzheimer's disease (AD), which reach genome-wide significance in Lambert *et al.* (2013).

SNP	Chr: position	Closest gene	Odds ratio
rs6656401	1:207692049	CR1	1.18
rs6733839	2:127892810	BIN1	1.22
rs10948363	6:47487762	CD2AP	1.10
rs11771145	7:143110762	EPHA1	0.90
rs9331896	8:27467686	CLU	0.86
rs983392	11:59923508	MS4A6A	0.90
rs10792832	11:85867875	PICALM	0.87
rs4147929	19:1063443	ABCA7	1.15
rs3865444	19:51727962	CD33	0.94
rs9271192	6:32578530	HLA-DRB5– HLA-DRB1	1.11
rs28834970	8:27195121	PTK2B	1.10
rs11218343	11:121435587	SORL1	0.77
rs10498633	14:92926952	SLC24A4 RIN3	0.91
rs8093731	18:29088958	DSG2	0.73
rs35349669	2:234068476	INPP5D	1.08
rs190982	5:88223420	MEF2C	0.93
rs2718058	7:37841534	NME8	0.93
rs1476679	7:100004446	ZCWPW1	0.91
rs10838725	11:47557871	CELF1	1.08
rs17125944	14:53400629	FERMT2	1.14
rs7274581	20:55018260	CASS4	0.88

Chr: Chromosome.
Data taken with permission from [25].

dominant mutations in three genes (*APP*, *PSEN1*, *PSEN2*), these account for less than 5% of AD prevalence and are early-onset, occurring before the age of 65 years. Most AD cases are late-onset (>65 years) and sporadic, with no defined etiology. However in recent years, large cohort collections and the relatively inexpensive cost of assessing genetic variation through genome-wide association studies (GWAS) has allowed the identification of common variants associated with risk of developing AD. These studies have demonstrated that late-onset Alzheimer's disease (LOAD) is thought to be multifactorial with many different genes and single nucleotide polymorphisms (SNPs) being implicated in, and contributing to, disease onset and progression [18]. The most robustly associated gene with LOAD is *APOE*, which encodes a polymorphic glycoprotein that is involved in the transport of cholesterol and other lipids [19] alongside neuronal growth [20] and tissue repair [21]. There are three isoforms of *APOE*: ε2, ε3 and ε4, which can be distinguished by cysteine to arginine substitutions at the amino acid positions 112 and 158 [22]. The ε4 variant confers increased risk of developing LOAD, with each additional copy of the risk allele lowering the mean age of onset [23]. While *APOE* ε4 accounts for approximately 20% of genetic risk for developing LOAD it cannot explain all of disease incidence, as not everyone who is homozygous for ε4 actually develops AD [24]. Aside from *APOE* there are numerous other risk loci SNPs that have been implicated in AD. The most recent meta-analysis of nearly 75,000 individuals nominated 19 common genetic variants, of which 11 were novel disease loci [25] (Table 1). Interestingly, many of the GWAS loci that have been nominated for AD can be linked to amyloid processing or inflammation. While risk variants that have been identified from GWAS only confer a relatively modest effect size, with odds ratios between 0.73 and 1.22 per loci investigated [26], it is thought that these could act cumulatively to cause the onset of degeneration. Scientists have generated polygenic risk scores (PRS) for AD, which combine the effects of many disease-associated SNPs to predict disease risk [27] and recently it has been reported that the PRS prediction captures nearly all common genetic risk for AD [28]. However, another study has demonstrated that collectively common SNPs for AD only account for a third of phenotypic variance in AD [29]. Recent efforts to explain the missing heritability of AD have used sequencing approaches to identify rare variants, with a larger effect size, with SNPs in *PLD3*, *TREM2*, *TM2D3* and *PICALM* being nominated in recent years [30–34].

Despite the fact that GWAS and sequencing efforts have been successful in identifying novel genes involved in AD, the majority of SNPs lie outside of coding regions of the genome. These variants are thus unlikely to have direct structural or functional effects on their gene's protein product, and are more likely to affect gene regulation at other loci. By integrating genetic variation with transcriptomic measurements in the same samples, for example from microarray or RNA sequencing experiments, it is possible to correlate disease associated genetic variants with changes in gene expression to identify expression quantitative trait loci (eQTLs). Such disease-associated eQTLs can occur both within the same gene (in *cis*) or distally within another gene (in *trans*). Recent research indicates that SNPs may change expression by initially altering the binding ability of one 'pioneering' transcription factor (TF), which then recruits other TFs. This was shown to occur at a CTCF motif, which if disrupted affects the binding of five different TFs [35]. However, if there are two or more variants in perfect linkage disequilibrium (LD) with one another, the nonrandom association of loci at different genomic locations, then it is not possible to distinguish which variant is acting as the eQTL. To further complicate matters, many eQTLs act in a cell-type-specific manner [36]. This is particularly relevant when studying heterogeneous tissues such as the brain or blood, or in a disease such as AD, where cellular abundance is known to be altered [37,38]. In the context of AD, one recent study demonstrated enrichment for monocyte-specific eQTLs at disease-associated loci, suggesting a role of the innate immune system in AD pathology [39]. In support of this, Karch *et al.*, tested whether GWAS LOAD SNPs act as cis-eQTLs for LOAD GWAS genes [40]. They were able to show the AD SNP rs1476679 in *ZCWPW1*, was significantly associated with the expression of *PILRB* and *GATS* in most brain regions, including the hippocampus. Interestingly, PILRB acts as a binding partner for TYROBP, both of which can be found on microglia [41]. The expression of TYROBP is restricted to cells of the immune system such as microglia, and has been shown to be upregulated in the brains of patients with LOAD. In a recent gene-regulatory network analysis TYROBP was shown to be a key causal regulator of a microglial/immune module highlighted as the module most associated with pathophysiology of LOAD. This microglia/immune module was also shown to contain a number of AD GWAS risk loci, such as *CD33*, *MS4A4A* and *MS4A6A* [39]. Furthermore, TREM2, which has been recently nominated from sequencing studies, is known to interact and signal through TRYOBP [39]. Taken together many network level analyses have highlighted a role for microglia and neuroinflammation in AD risk [39,40,42,43].

A role for epigenomic dysfunction in AD?

Recently, increased understanding about the functional complexity of the genome has led to growing recognition about the likely role of nonsequence-based 'epigenetic' variation in AD [44]. Epigenetic processes mediate the reversible regulation of gene expression, occurring independently of DNA sequence, acting principally through chemical modifications to DNA and nucleosomal histone proteins (Figure 1). The most widely studied epigenetic modification in human studies is that of DNA methylation, given it is the most stable and longest lasting change.

In general, *in vitro* studies have suggested that there is a trend toward global DNA hypomethylation in AD. For example, one study demonstrated global hypomethylation in a glioblastoma cell line with the APP^{SWE} mutation, which occurs in familial AD [45]. Likewise, it was shown that there are lower DNA methylation levels in brain microvascular endothelial cells that were exposed to high levels of synthetic $A\beta_{1-40}$ [46]. However, in contrast to this a more recent study using neuroblastoma cells exposed to synthetic $A\beta_{1-40}$ showed no significant change in DNA methylation levels [47]. In the context of human postmortem brain samples there are also some conflicting results; contrasting studies have shown decreased levels of global DNA methylation in AD-associated brain regions such as the entorhinal cortex [48] and hippocampus [49], while others report no change [50,51] or even increased levels in the frontal cortex [52] and hippocampus [53].

In recent years, advances in genomic technology have allowed the first genome-scale studies of DNA methylation in AD [54,55]. To date, all published studies have utilized the Illumina Infinium 450 K Methylation Beadarray (450 K array) to examine DNA methylation changes at >485,000 loci in postmortem brain samples. Although, these epigenome-wide association studies (EWAS) have been performed on independent sample cohorts, in a range of anatomically distinct cortical brain regions, a number of consistently differentially methylated genes have been identified [56]. Most notably one such gene to be robustly hypermethylated in AD cortex is *ANK1* [54,55]. Interestingly, disease-associated *ANK1* hypermethylation has been observed in a tissue-specific manner, with brain regions affected by AD pathology (entorhinal cortex, superior temporal gyrus and prefrontal cortex) showing significant hypermethylation, while the cerebellum, a region largely unaffected by pathology, and premortem blood show no disease-associated changes. The majority of genes identified by EWAS are distinct from those nominated in GWAS with the exception of *BIN1*. However, despite different genes being identified with the two approaches
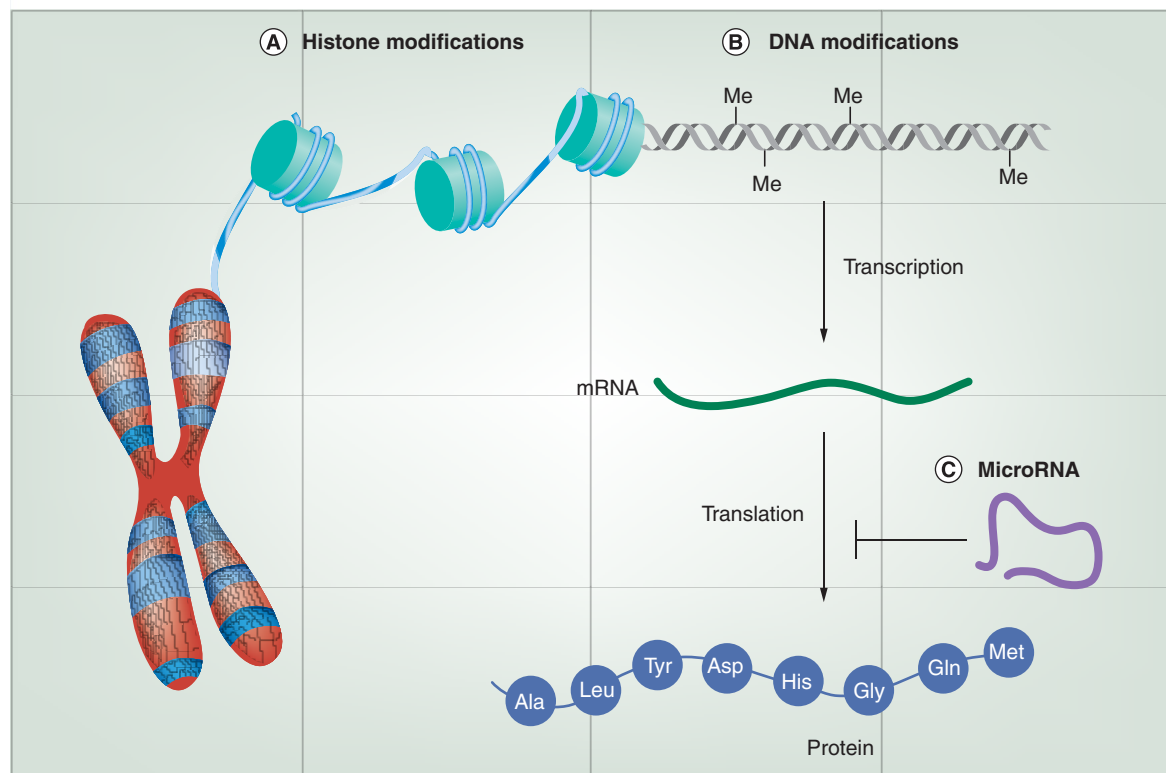
Figure 1.   Diagram to illustrate the different epigenetic mechanisms that have been identified. (A) Regulation of chromatic structure through post-translational modifications to histone proteins. This can include: acetylation, methylation, SUMOylation, ubiquitylation, citrullination and ADP-ribosylation. **(B)** Addition of chemical tags to DNA to the 5' end of a cytosine nucleotide. This creates 5mC – the most commonly studied epigenetic mark, 5hmC, 5caC and 5fC. **(C)** Small RNA molecules, such as microRNA can also affect gene expression either through degrading mRNA or altering protein translation.
5caC: 5-carboxylcytosine; 5fC: 5-formylcytosine; 5hmC: 5-hydroxymethycytosine; 5mC: 5-methylcytosine.

many of these do reside in common pathways [57]. Since the publication of the initial EWAS analyses, there have been additional studies identifying additional differentially methylated genes in AD, including *CRTC1* [58], *APOE* [59] and *TREM2* [60].

To date, the majority of AD EWAS have focussed on DNA methylation, with histone modifications considerably less well studied. However, one study has shown that the histone deacetylase (HDAC) inhibitor, sodium butyrate, can improve cognitive function, synaptic density and plasticity in mouse models with inducible overexpression of p25 protein [61]. P25 has been shown to be linked to numerous features of AD such as amyloid and tau pathology alongside memory loss and neurodegeneration [62–64]. Similarly, another study has shown improved memory function in transgenic APPPS1–21 mice after treatment with sodium butyrate [65]. Furthermore, memory improvements were seen even when it was administered at the latest stages of amyloid pathology and were associated with increased expression of genes implicated in associative learning. Other studies have also shown HDACs to have therapeutic utility, such as Depakote [66], phenylbutryic acid [67] and trichostatin A [68]. While these studies are encouraging and show the potential utility of HDACs as therapeutic agents there are, however, a couple of considerations with this approach. First, most models, including the ones we describe, are models of familial AD, which use small numbers of animals and, as such, results should not be over interpreted. Alongside this, these studies use pan-HDAC inhibitors, which are all known to affect multiple HDACs. While, it is useful to know that there may be some involvement of histone modifications or HDACs in AD initiation or progression, these studies do not highlight specifically which ones are implicated. In order to address this, a number of groups have crossed APPPS1–21 mice with those lacking certain HDACs. APPPS1–21 mice that lack HDAC5 show exaggerated memory impairment [69], while those lacking HDAC6 have improved memory, but this is achieved

without changing amyloid deposition [70]. Another HDAC that could have potential as a therapeutic target is HDAC2, as mice with reduced HDAC2 show increased memory and synaptic plasticity [71]. Therefore, it appears that only specific HDACs show promise as potential drug targets. When using certain HDACs it is important to be aware that they can also affect DNA methylation. For instance, it has been shown that Depakote can cause extensive DNA methylation changes including demethylation changes at specific genes such as *MMP2, MAGEB2* and *WIF1*, which have been implicated in tumor growth and metastasis [72]. This study supports the concept that various epigenetic marks are in a dynamic relationship with one another and that you cannot necessarily target one without affecting another. Finally, as with any potential drug that is tested on model systems, such as mice, it is important to remember that these rarely translate effectively into humans. One good example of this comes from studies which demonstrated the utility of anti-amyloid antibodies [73]. In these APP-transgenic mice, just one injection of m266, an anti-APP mouse antibody, was able to reverse cognitive deficits without reducing amyloid plaque burden [73]. However, when taken to Phase III clinical trials, the human antibody, Solanezumab, did not reduce cognitive decline in those with mild dementia due to AD [74].

Induced pluripotent stem cells: new models for late-onset Alzheimer's disease?

To fully understand and elucidate the mechanisms of disease etiology, extensive modeling must take place. Traditionally, this has been achieved by a number of methods, including both animal (murine) models and primary patient cell lines. While both of these approaches have their own merits, they can prove inconvenient and do not completely and accurately reflect human disease. At present, the AD research field has had a heavy focus on disease modeling through the use of transgenic mouse models [75], as there is a well-developed understanding of genetic manipulation techniques in this organism. Furthermore, mice are more phylo-genetically related to humans than other simpler model organisms such as *Drosophila melanogaster* and *Caenorhabditis elegans*, although these do allow for more experimental control than mice. Due to the close relation of mice and humans they also have good utility for studying familial AD, through the use of transgenic mice containing mutations in the *APP* and *PSEN* genes. This has led to advances in our understanding of multiple aspects of AD, in particular amyloid pathology and the differential effects of the various Aβ peptides. However, despite the extensive use of these transgenic models to study AD, they do not accurately recapitulate AD, as the mice do not display overt neurodegeneration [76–78] or have amyloid plaques [79]. While proven useful for modeling autosomal disease, such as familial AD, the mouse models do not have extensive utility for studying sporadic AD, which has both polygenic and environmental components. Even if it was possible to model the genetics of sporadic AD in transgenic mice the effect sizes of each associated variant would be small and therefore difficult to determine phenotypic outcome. However, there have been murine studies that have targeted replacement of the endogenous murine *Apoe* gene with human *APOE-ε4*. These mice demonstrated reduced spatial learning and a reduction in dendritic spine density in the medial entorhinal cortex [80]. In another study, where *APOE (both ε3/ε3 and ε4/ε4)* mice were crossed with mice containing a mutant human form of *APP*, the *APOE-ε4xAPP* mice displayed significantly worse spatial memory performance than their *APOE-ε3xAPP* counterparts, but this was also associated with insulin dysfunction [81].

A more promising avenue for modeling SNPs in complex diseases, such as sporadic AD, is through the use of stem cell technology. Embryonic stem cells (ESCs), which are derived from the inner cell mass of an embryo (blastocyst), have the ability to differentiate into any cell in the body [82]. Due to their inherent plasticity, and as genomic variation can be assessed relatively inexpensively through PCR, microarray, or sequencing technology, there is the potential that they could be used to study the effect of disease-associated SNPs on the functionality of specific cell types. However, while being useful, the ethical issues implicated with using embryo-derived ESCs are numerous. Recent advances in stem cell technology have allowed the production of stem cells derived from adult tissue, such as blood, urine and keratinocytes [83]. These induced pluripotent stem cells (iPSCs) have almost identical characteristics to ESCs: they share the same morphology, can differentiate into any cell type in the body, have unlimited growth and have the same expression pattern of genes [84]; potentially making them a very powerful tool in research.

There are, however, a number of caveats when utilizing iPSCs to model complex diseases that must be considered. Associated with inducing pluripotency are the global cellular epigenetic changes that allow the cells to alter gene expression in order for them to be functionally identical to ESCs. Despite, being functionally identical, several groups report that iPSCs have different DNA methylation profiles and gene expression patterns to ESCs [85–88]. Some groups attribute this variation due to an 'epigenetic memory' where iPSCs show residual DNA methylation patterns that are typical of the tissue they originate from [89]. These differentially methylated regions (DMRs) were

shown to affect the differentiation potential of the newly formed iPSCs. For example, iPSCs derived from neural and fibroblast progenitors maintained DNA methylation marks at sites associated with hematopoietic lineages, which decreased the potential for these iPSCs to form blood cells. Subsequently, it is possible to reverse these restricting methyl marks by increasing the cells passage number or treatment with chromatin modifying compounds [89]. This treatment is associated with a decrease in DNA methylation at hematopoietic loci and therefore an increase in blood cell fate potential. Therefore, although it would appear that this epigenetic memory can affect the differentiation potential of cells initially, this effect is actually only transient. It has also been observed that certain subsets of cells can become stuck in a partially reprogrammed state. This is due to inefficient DNA demethylation at certain sites or the incomplete repression of TFs [90]. Despite this, these aberrations can be rectified using RNA inhibition of TFs or treatment with DNA methylase inhibitors. Another potential source of epigenetic variation between ESCs and iPSCs is the microenvironment in which the iPSCs have been generated. Cooper and Newman have demonstrated that there is some correlation between cells' gene expression patterns and the laboratory the cell lines are derived from [91,92]. This demonstrates that the environment can affect the epigenome and therefore, downstream gene expression of cell lines. To fully assess the differences in the epigenomes between iPSCs and ESCs, Lister *et al.*, utilized a shotgun bisulphite sequencing technique (MethylC-seq) to look at the whole-genome DNA methylome at single base-pair resolution [93]. This demonstrated that, overall, ESCs and iPSCs are similar, but that there are some inherent differences between their DNA methylomes. The reprogramming of somatic cells generated hundreds of DMRs that could be attributed to both memory from the somatic cell and iPSC specific DNA methylation patterns that are susceptible during the reprogramming process as many DMRs were consistent across independent iPSC lines [86]. All of these studies demonstrate that there are fundamental differences in both the epigenome and gene expression patterns of ESCs and iPSCs. However, there are ways to rectify some of these differences meaning that iPSCs still have utility as disease models, although the differences must be taken into account when interpreting results.

Since, the introduction of iPSC technology there have been increasingly more studies utilizing iPSCs for disease modeling and small molecule testing as, theoretically, iPSCs are an exact genetic match of the patient they are derived from. To accurately model AD using iPSCs, the generation of specific neuronal populations are usually necessary, particularly iPSC derived cortical and cholinergic neurons. Generating these requires certain factors, including SB431542 and LDN-193189 [94], which act as inhibitors of TGF-βI and BMP type I receptors respectively. This inhibition prevents SMAD phosphorylation, suppressing cellular renewal and promoting cortical differentiation [95,96]. A good iPSC model of AD would not only be the correct cell type of interest, but also show the neuropathological features and characteristics of the disease. There have been several studies that have reported that iPSCs show certain disease features [97–100]. More specifically, in AD iPSCs have also been used to show Aβ-induced synaptotoxicity [101]. In this study, Nieweg *et al.* demonstrated not only that Aβ altered AMPA receptors postsynaptically and impaired axonal vesicle clustering, but also increased the phosphorylation status of tau, another key characteristic hallmark of AD. Alongside aberrations in tau phosphorylation, degeneration of cortical neurons is also a very prominent clinical feature of AD, and it is believed that this causes the onset of symptoms. Therefore, to truly understand AD as a disease, being able to recapitulate this neuronal cell death is vital. One recent study has shown that iPSC-derived basal forebrain cholinergic neurons heterozygous for *APOE* (ε3/ε4) are more susceptible to glutamate-mediated cell death, while also showing an increased $A\beta_{42}/A\beta_{40}$ ratio when compared with basal forebrain cholinergic neurons generated from healthy age matched control patients [102].

One of the major utilities for using iPSCs to study AD is the ability to examine the effects of genetic variants with a relatively small effect size on phenotype. One study that took advantage of this has demonstrated that iPSC-derived neurons carrying genetic variants in *SORL1*, which increase LOAD risk, have reduced response to BDNF treatment. This not only manifests at the level of *SORL1* expression but also impacts APP processing [103]. Furthermore, given that AD has a polygenic component; it is also possible to assess the effect of different combinations of disease-associated SNPs. As it is possible to use iPSCs to generate patient specific neuronal cells, there is the potential to generate libraries of cells with varying combinations of LOAD-associated SNPs and therefore, different susceptibilities to disease. Interestingly, two studies have demonstrated this variability in susceptibility using LOAD iPSC-derived neurons [104,105]. In the first, undertaken by Israel *et al.*, they found that neurons from one patient, but not from another, showed AD-associated phenotypes. This included altered levels of secreted $A\beta_{1-40}$, higher aGSK3 levels and had significantly increased p-tau/total tau [104]. The second study, conducted by Kondo *et al.*, showed differential intracellular Aβ oligomer accumulation, inducing endoplasmic reticulum and oxidative stress [105]. Taken together these studies show how different genetic backgrounds can alter disease initiation and progression as

well as the complex genetic interplay there is in LOAD. However, being able to investigate the effects of different PRS on living and developing neuronal populations will provide more valuable insight into the role genetic variants play in terms of physiological/cellular aberrations and disease progression in LOAD. Importantly, data that is generated through the usage of iPSCs can therefore be compared and contrasted with data collected from molecular studies in human postmortem tissue to potentially elucidate the disease-specific effects.

Using genetic editing to elucidate the functional consequence of disease-associated variation

Using iPSCs and recent advances in epigenetic editing technology, it is becoming possible to start teasing apart the underlying mechanisms that may be driving AD pathogenesis. Clustered regularly interspersed short palindromic repeats (CRISPR) uses RNA-guided Cas9 nucleases to introduce DNA breaks which can be repaired through homologous recombination, indel mutations or with a vector carrying a desired mutation [106]. CRIPSR can be used provided that the sequence of interest is unique compared with the rest of the genome and is upstream of a protospacer adjacent motif (PAM) sequence. The PAM sequence is typically three to five nucleotides long and serves as a binding region for the Cas9 to bind. Unfortunately, this is a requirement of the method and can be technically challenging. Despite, the PAM sequences being relatively common throughout the human genome they can often be in the incorrect location relative to the sequence of interest and can make modifying the gene difficult. Furthermore, if the target locus has high homology to another region in the genome then there is the potential for off-target effects resulting in inadvertent mutations [107,108].

The main advantage of the CRISPR-Cas9 system is that you can create isogenic control lines that only show genetic variation at your disease-specific loci. One recent example of this in the AD field comes from Pires *et al.*, who successfully corrected the A79V *PSEN1* mutation in a patient AD iPSC cell line [109]. These types of control lines are extremely beneficial for studying disease-associated genetic variation, as they enable the minimization of genetic variability as both disease and control lines have the same genetic background. Such isogenic lines have been recently used to study familial AD [105,110,111]. One study has shown iPSCs harboring the *APP*SWE and *PSEN1* M146V mutations have increased total Aβ production, and up to a three-fold increase in the $A\beta_{42}/A\beta_{40}$ ratio when compared with their isogenic controls. These changes have been shown to correlate to neuronal identity, maturity and mutation load [112].

While, it proves relatively simple to use this technique to study the effects of causative mutations, such as those in familial AD, other genetic variants like SNPs associated with sporadic AD are more problematic to model. This is due to the fact that they may only be relevant to diseases such as AD in specific combinations. As an extension to the CRISPR system, it is possible to alter multiple loci using CRISPR-multiplexing [113]. In this system, multiple guide RNAs are assembled into the same vector and transfected into the cells allowing the targeting of multiple loci. This tool will undoubtedly prove incredibly useful for LOAD research as it will allow researchers to modify up to seven loci. By modifying multiple disease-associated SNPs, one could investigate the effects of various combinations on cell physiology, protein expression and aggregation. This approach would work very well for the LOAD risk SNPs *BIN1*, *CLU* and *PICALM*, for example, as these have all been shown to interact with Aβ/tau [114–117]. Therefore, by altering these specific SNPs one could investigate how tau and Aβ pathology changes over time. Another interesting point is that this methodology would allow one to investigate the interaction between disease-associated SNPs with reported relationships, for example *PICALM* and the *APOE* ε4 allele. In a previous study of familial AD patients, a homozygous *PICALM* genotype (rs3851179) was shown to modulate prefrontal cortex volume and cognitive impairment in carriers of the *APOE* ε4 allele [118]. As both proteins are involved in the same Aβ clearance pathway [119,120], it is thought that alterations in the endocytic functions of *PICALM* may synergistically affect *APOE* ε4. This could mean there is a higher likelihood of Aβ remaining in the brain and therefore increasing plaque formation.

Establishing causality

An important step for research is to establish whether disease-associated variation is causing disease. This is simpler to test when examining genetic variation, as we know that the SNP has been present in an individual throughout their life course, prior to disease onset. However, when investigating the functional effects of disease-associated epigenetic variation, the relationship is less clear, and it is difficult to determine whether epigenetic changes are a cause, or a consequence, of the disease process. While previous postmortem brain studies have provided valuable physiologically relevant information about epigenetic changes occurring at later disease stages it is difficult to establish if those alterations actually initiated disease, or are secondary to the disease process, therefore making it

difficult to infer causality. First, because this is crucial for the design of effective drug therapies to combat disease, and second, because AD neuropathology generally occurs at least 10 years before symptomatic onset, it is important to understand the root causes to be able to monitor and diagnose the disease in its very earliest stages. iPSCs have real utility for determining whether associations identified in EWAS analyses could represent a secondary effect of disease, or could be driving disease progression. Using a modified version of the CRISPR-Cas9 technology it has become possible to alter DNA methylation at specific loci. By fusing the Cas9 protein with the enzymatic domains of TET1 or DNMT3A it is possible to remove, or add methyl groups to DNA respectively [121]. This method builds on previous work [122,123] where Tet1 and Dnmt3a were fused to TALE proteins to achieve the same effect. By being able to manipulate the epigenetic landscape of cells, particularly at loci associated with disease it will enable researchers to establish whether disease-associated epigenetic variation is causative. These techniques have already been utilized in diseases such as cancer [124,125], but to our knowledge have not yet been reported in AD research. The epigenetic status of genes such as *ANK1,* which have robust changes in AD, would be an excellent initial target for this new methodology. It has the potential to reveal whether the DNA methylation changes seen are truly causative and precede disease initiation, or whether they are a consequence of progression. Even if, it is the latter and it is found that these alterations do not cause disease, but occur in the earliest stages of the disease, they could potentially be used as a biomarker for diagnosis prior to symptomatic onset. Alongside this, such changes also tell us something about the disease process and its progression. Given that recent studies have demonstrated robust epigenetic alterations in AD, iPSCs could become a valuable tool in which these studies could be taken further. However, to undertake epigenetic studies in these cells it will be very important to fully understand the epigenetic landscape of the iPSCs themselves, both throughout differentiation and at maturity.

Current challenges to progress

While it is possible to create disease-relevant cells using iPSCs, as with any model, iPSCs also have their limitations. A large concern when using iPSC-derived neurons to model disease is that the resulting neurons represent an immature and fetal population [126–129]. This is of particular concern when studying diseases of aging, such as LOAD. However, efforts are being made to overcome this particular issue. For example, by expressing a mutant form of *LMNA*, which is known to cause premature aging. By expressing progerin in the iPSC-derived dopaminergic neurons, it was possible to create phenotypes that were resultant of both the induced aging and genetic susceptibility [130]. The aged Parkinson's disease neurons had marked dendrite neurodegeneration, reduced tyrosine-hydroxylase expression and displayed epigenetic markers of aging that were not present in the control populations. Another study directly reprogrammed fibroblasts into neurons, skipping iPSC pluripotency stages, in an attempt to overcome iPSC immaturity [131]. As this protocol does not induce pluripotency the inducible neurons display both age-related epigenetic and transcriptomic signatures, showing age-associated decreases in RanBP17, a nuclear transport receptor. While these neurons would prove useful for studying diseases of aged cells, such as AD, it is difficult to make large amounts of primary material as these cells cannot be propagated, unlike the iPSCs.

Future perspective

Since, the pioneering work by Takahashi and Yamanaka in 2006, the use of iPSCs has been able to significantly advance complex disease research. They have enabled researchers to more accurately recapitulate disease phenotypes in a cell culture system. While iPSCs are far from being used therapeutically, they have proven useful for investigating the molecular and genetic underpinnings of LOAD. Once there have been more extensive investigations into the effects of SNP burden and their molecular targets, iPSCs can be used to test the effectiveness of new therapeutic interventions. Although, at present iPSC generation and differentiation are costly and time consuming, differentiation protocols are quickening, and the use of an individual's own iPSCs to select their appropriate treatment would be a first step toward personalized medicine, potentially improving the patient's life.

While, it is still unknown whether the global epigenetic changes that occur during iPSC generation affect the end epitype of cells, there is still promise that these cells could be used to study the epigenetics of complex diseases. If epigenetic aberrations do prove to be an issue, then these will have to be taken into account during experimental design and analysis. However, before identified changes can be targeted for therapeutic intervention, it will be important to determine whether they are causal; with the recent advances in genetic and epigenetic editing technology this will soon be possible. Finally, while there are many questions that still remain unanswered and many challenges ahead when addressing these, with the correct model and methodologies these will hopefully be overcome.

Executive summary

Alzheimer's disease
- Most prevalent neurodegenerative disorder causing 60–80% of dementia cases worldwide.
- Characterized by extracellular depositions of amyloid β-protein and intracellular neurofibrillary tangles of paired helical filaments of tau.

Genetic variation associated with Alzheimer's disease
- Through the use of genome wide association studies (GWAS) a number of single nucleotide polymorphisms (SNPs) have been associated with late onset Alzheimer's disease (AD).
- Many GWAS loci implicated in disease have been linked to amyloid processing and inflammation.

A role for epigenomic dysfunction in Alzheimer's disease?
- Recent epigenome wide association studies (EWAS) have identified a number of loci that are differentially methylated in disease.
- The majority of genes identified by EWAS are distinct from those nominated in GWAS with the exception of *BIN1*.

Induced pluripotent stem cells: new models for late-onset Alzheimer's disease?
- Through somatic cell reprogramming, it is possible to generate induced pluripotent stem cell (iPSC) derived neuronal cells.
- These iPSC-derived neuronal cells have been shown to reflect some disease features.
- iPSC-derived neuronal cells can be used to assess the effect of polygenic risk on physiological/cellular changes and disease progression.

Using genetic editing to elucidate the functional consequence of disease-associated variation
- Clustered regularly interspersed short palindromic repeats (CRISPR) uses RNA guided Cas9 nucleases to introduce modifications in the genome.
- CRISPR-multiplexing can be used to edit multiple loci within the genome.

Establishing causality
- iPSC models have utility in determining whether loci identified from GWAS and EWAS are causative in the disease process.
- Using CRISPR, the epigenetic landscape of cells can be altered to establish whether DNA methylation changes associated with disease are causative.

References

Papers of special note have been highlighted as: • of interest; •• of considerable interest

1   What is dementia? www.alz.org/what-is-dementia.asp

2   Prince M, Wimo A, Guerchet M, Ali G, Wu Y, Prina M. The global impact of dementia: an analysis of prevalence, incidence, cost and trends. *Alzheimer. Dis. Int.* 1–87 (2015).

3   Blurton-Jones M, Laferla FM. Pathways by which Abeta facilitates tau pathology. *Curr. Alzheimer Res.* 3(5), 437–448 (2006).

4   Butterfield DA, Boyd-Kimball D. Amyloid beta-peptide(1–42) contributes to the oxidative stress and neurodegeneration found in Alzheimer disease brain. *Brain Pathol.* 14(4), 426–432 (2004).

5   Braak H, Braak E. Neuropathological stageing of Alzheimer-related changes. *Acta Neuropathol.* 82(4), 239–259 (1991).

6   Rasool CG, Svendsen CN, Selkoe DJ. Neurofibrillary degeneration of cholinergic and noncholinergic neurons of the basal forebrain in Alzheimer's disease. *Ann. Neurol.* 20(4), 482–488 (1986).

7   Braak H, Braak E. Demonstration of amyloid deposits and neurofibrillary changes in whole brain sections. *Brain Pathol.* 1(3), 213–216 (1991).

8   Kalus P, Braak H, Braak E, Bohl J. The presubicular region in Alzheimer's disease: topography of amyloid deposits and neurofibrillary changes. *Brain Res.* 494(1), 198–203 (1989).

9   Rogers J, Morrison JH. Quantitative morphology and regional and laminar distributions of senile plaques in Alzheimer's disease. *J. Neurosci.* 5(10), 2801–2808 (1985).

10   Van Hoesen GW, Hyman BT. Hippocampal formation: anatomy and the patterns of pathology in Alzheimer's disease. *Prog. Brain Res.* 83, 445–457 (1990).

11   Francis PT, Palmer AM, Snape M, Wilcock GK. The cholinergic hypothesis of Alzheimer's disease: a review of progress. *J. Neurol. Neurosurg. Psychiatry* 66(2), 137–147 (1999).

12   Thal DR, Rub U, Orantes M, Braak H. Phases of A beta-deposition in the human brain and its relevance for the development of AD. *Neurology* 58(12), 1791–1800 (2002).

13   Cragg BG. Autonomic functions of the hippocampus. *Nature* 182(4636), 675–676 (1958).

14   Diamond IT, Hall WC. Evolution of neocortex. *Science* 164(3877), 251–262 (1969).

15   Morris RG, Garrud P, Rawlins JN, O'keefe J. Place navigation impaired in rats with hippocampal lesions. *Nature* 297(5868), 681–683 (1982).

16   Jack CR, Jr., Knopman DS, Jagust WJ *et al.* Hypothetical model of dynamic biomarkers of the Alzheimer's pathological cascade. *Lancet Neurol.* 9(1), 119–128 (2010).

17   Price JL, Morris JC. Tangles and plaques in nondemented aging and "preclinical" Alzheimer's disease. *Ann. Neurol.* 45(3), 358–368 (1999).

18   Gatz M, Reynolds CA, Fratiglioni L *et al.* Role of genes and environments for explaining Alzheimer disease. *Arch. Gen. Psychiatry* 63(2), 168–174 (2006).

19   Poirier J. Apolipoprotein E, cholesterol transport and synthesis in sporadic Alzheimer's disease. *Neurobiol. Aging* 26(3), 355–361 (2005).

20   Nathan BP, Bellosta S, Sanan DA, Weisgraber KH, Mahley RW, Pitas RE. Differential effects of apolipoproteins E3 and E4 on neuronal growth *in vitro*. *Science* 264(5160), 850–852 (1994).

21   Huang Y. Abeta-independent roles of apolipoprotein E4 in the pathogenesis of Alzheimer's disease. *Trends Mol. Med.* 16(6), 287–294 (2010).

22   Zlokovic BV. Cerebrovascular effects of apolipoprotein E: implications for Alzheimer disease. *JAMA Neurol.* 70(4), 440–444 (2013).

23   Corder EH, Saunders AM, Strittmatter WJ *et al.* Gene dose of apolipoprotein E type 4 allele and the risk of Alzheimer's disease in late onset families. *Science* 261(5123), 921–923 (1993).

24   Slooter AJ, Cruts M, Kalmijn S *et al.* Risk estimates of dementia by apolipoprotein E genotypes from a population-based incidence study: the Rotterdam Study. *Arch. Neurol.* 55(7), 964–968 (1998).

25   Lambert JC, Ibrahim-Verbaas CA, Harold D *et al.* Meta-analysis of 74,046 individuals identifies 11 new susceptibility loci for Alzheimer's disease. *Nat. Genet.* 45(12), 1452–1458 (2013).
●●   **Identified 19 loci associated with Alzheimer's disease (AD), 11 of which had not previously been implicated, highlighting new pathways that could play a role in AD.**

26   Ebbert MT, Ridge PG, Wilson AR *et al.* Population-based analysis of Alzheimer's disease risk alleles implicates genetic interactions. *Biol. Psychiatry* 75(9), 732–737 (2014).

27   Escott-Price V, Sims R, Bannister C *et al.* Common polygenic variation enhances risk prediction for Alzheimer's disease. *Brain* 138(Pt 12), 3673–3684 (2015).

28   Escott-Price V, Shoai M, Pither R, Williams J, Hardy J. Polygenic score prediction captures nearly all common genetic risk for Alzheimer's disease. *Neurobiol. Aging* 49, 214.e217–214.e211 (2017).

29   Ridge PG, Mukherjee S, Crane PK, Kauwe JS, Alzheimer's Disease Genetics C. Alzheimer's disease: analyzing the missing heritability. *PLoS ONE* 8(11), e79771 (2013).

30   Cruchaga C, Karch CM, Jin SC *et al.* Rare coding variants in the phospholipase D3 gene confer risk for Alzheimer's disease. *Nature* 505(7484), 550–554 (2014).

31   Jakobsdottir J, Van Der Lee SJ. Rare functional variant in TM2D3 is associated with late-onset Alzheimer's disease. *PLoS Genet.* 12(10), e1006327 (2016).

32   Jonsson T, Stefansson H, Steinberg S *et al.* Variant of TREM2 associated with the risk of Alzheimer's disease. *N. Engl. J. Med.* 368(2), 107–116 (2013).

33   Guerreiro R, Wojtas A, Bras J *et al.* TREM2 variants in Alzheimer's disease. *N. Engl. J. Med.* 368(2), 117–127 (2013).

34   Lord J, Turton J, Medway C *et al.* Next generation sequencing of CLU, PICALM and CR1: pitfalls and potential solutions. *Int. J. Mol. Epidemiol. Genet.* 3(4), 262–275 (2012).

35   Tehranchi AK, Myrthil M, Martin T, Hie BL, Golan D, Fraser HB. Pooled chIP-seq links variation in transcription factor binding to complex disease risk. *Cell* 165(3), 730–741 (2016).

36   Zhernakova DV, Deelen P. Identification of context-dependent expression quantitative trait loci in whole blood. *Nat. Genet.* 49(1), 139–145 (2016).

37   Serrano-Pozo A, Frosch MP, Masliah E, Hyman BT. Neuropathological alterations in Alzheimer disease. *Cold Spring Harb. Perspect. Med.* 1(1), a006189 (2011).

38   Lunnon K, Ibrahim Z, Proitsi P *et al.* Mitochondrial dysfunction and immune activation are detectable in early Alzheimer's disease blood. *J. Alzheimers Dis.* 30(3), 685–710 (2012).

39   Zhang B, Gaiteri C, Bodea LG *et al.* Integrated systems approach identifies genetic nodes and networks in late-onset Alzheimer's disease. *Cell* 153(3), 707–720 (2013).

••   **Used postmortem brain tissue to construct a gene-regulatory network of late onset Alzheimer's disease. Demonstrated immune- and microglia-specific network which contained TYROBP, a binding partner of TREM2, as a key regulator.**

40   Karch CM, Ezerskiy LA, Bertelsen S, Goate AM. Alzheimer's disease risk polymorphisms regulate gene expression in the ZCWPW1 and the CELF1 loci. *PLoS ONE* 11(2), e0148717 (2016).

41   Tato CM, Joyce-Shaikh B, Banerjee A *et al.* The Myeloid receptor PILRβ mediates the balance of inflammatory responses through regulation of IL-27 production. *PLoS ONE* 7(3), e31680 (2012).

42   Li X, Long J, He T, Belshaw R, Scott J. Integrated genomic approaches identify major pathways and upstream regulators in late onset Alzheimer's disease. *Sci. Rep.* 5, 12393 (2015).

43   Wes PD, Easton A, Corradi J *et al.* Tau overexpression impacts a neuroinflammation gene expression network perturbed in Alzheimer's disease. *PLoS ONE* 9(8), e106050 (2014).

44   Lunnon K, Mill J. Epigenetic studies in Alzheimer's disease: current findings, caveats, and considerations for future studies. *Am. J. Med. Genet. B Neuropsychiatr. Genet.* 162b(8), 789–799 (2013).

45   Sung HY, Choi EN, Ahn Jo S, Oh S, Ahn JH. Amyloid protein-mediated differential DNA methylation status regulates gene expression in Alzheimer's disease model cell line. *Biochem. Biophys. Res. Commun.* 414(4), 700–705 (2011).

46   Chen KL, Wang SS, Yang YY, Yuan RY, Chen RM, Hu CJ. The epigenetic effects of amyloid-beta(1–40) on global DNA and neprilysin genes in murine cerebral endothelial cells. *Biochem. Biophys. Res. Commun.* 378(1), 57–61 (2009).

47   Taher N, Mckenzie C, Garrett R, Baker M, Fox N, Isaacs GD. Amyloid-beta alters the DNA methylation status of cell-fate genes in an Alzheimer's disease model. *J. Alzheimers Dis.* 38(4), 831–844 (2014).

48   Mastroeni D, Grover A, Delvaux E, Whiteside C, Coleman PD, Rogers J. Epigenetic changes in Alzheimer's disease: decrements in DNA methylation. *Neurobiol. Aging* 31(12), 2025–2037 (2010).

49   Chouliaras L, Mastroeni D, Delvaux E *et al.* Consistent decrease in global DNA methylation and hydroxymethylation in the hippocampus of Alzheimer's disease patients. *Neurobiol. Aging* 34(9), 2091–2099 (2013).

50   Lashley T, Gami P, Valizadeh N, Li A, Revesz T, Balazs R. Alterations in global DNA methylation and hydroxymethylation are not detected in Alzheimer's disease. *Neuropathol. Appl. Neurobiol.* 41(4), 497–506 (2015).

51   Condliffe D, Wong A, Troakes C *et al.* Cross-region reduction in 5-hydroxymethylcytosine in Alzheimer's disease brain. *Neurobiol. Aging* 35(8), 1850–1854 (2014).

52   Coppieters N, Dieriks BV, Lill C, Faull RL, Curtis MA, Dragunow M. Global changes in DNA methylation and hydroxymethylation in Alzheimer's disease human brain. *Neurobiol. Aging* 35(6), 1334–1344 (2014).

53   Bradley-Whitman MA, Lovell MA. Epigenetic changes in the progression of Alzheimer's disease. *Mech. Ageing Dev.* 134(10), 486–495 (2013).

54   Lunnon K, Smith R, Hannon E *et al.* Methylomic profiling implicates cortical deregulation of ANK1 in Alzheimer's disease. *Nat. Neurosci.* 17(9), 1164–1170 (2014).

••   **One of the first epigenome-wide association studies published and robustly implicate epigenetic dysregulation of ANK1 in AD.**

55   De Jager PL, Srivastava G, Lunnon K, Burgess J, Schalkwyk LC. Alzheimer's disease: early alterations in brain DNA methylation at ANK1, BIN1, RHBDF2 and other loci. *Nat. Neurosci.* 17(9), 1156–1163 (2014).

••   **One of first epigenome-wide association studies published.**

56   Lord J, Cruchaga C. The epigenetic landscape of Alzheimer's disease. *Nat. Neurosci.* 17(9), 1138–1140 (2014).

57   Smith AR, Mill J, Smith RG, Lunnon K. Elucidating novel dysfunctional pathways in Alzheimer's disease by integrating loci identified in genetic and epigenetic studies. *Neuroepigenetics* 6, 32–50 (2016).

58   Mendioroz M, Celarain N, Altuna M *et al.* CRTC1 gene is differentially methylated in the human hippocampus in Alzheimer's disease. *Alzheimers Res. Ther.* 8(1), 15 (2016).

59   Foraker J, Millard SP, Leong L *et al.* The APOE gene is differentially methylated in Alzheimer's disease. *J. Alzheimers Dis.* 48(3), 745–755 (2015).

60   Smith AR, Smith RG, Condliffe D *et al.* Increased DNA methylation near TREM2 is consistently seen in the superior temporal gyrus in Alzheimer's disease brain. *Neurobiol. Aging* 47, 35–40 (2016).

61   Fischer A, Sananbenesi F, Wang X, Dobbin M, Tsai LH. Recovery of learning and memory is associated with chromatin remodelling. *Nature* 447(7141), 178–182 (2007).

62   Cruz JC, Tseng HC, Goldman JA, Shih H, Tsai LH. Aberrant Cdk5 activation by p25 triggers pathological events leading to neurodegeneration and neurofibrillary tangles. *Neuron* 40(3), 471–483 (2003).

63   Cruz JC, Kim D, Moy LY *et al.* p25/cyclin-dependent kinase 5 induces production and intraneuronal accumulation of amyloid beta *in vivo*. *J. Neurosci.* 26(41), 10536–10541 (2006).

64   Fischer A, Sananbenesi F, Pang PT, Lu B, Tsai LH. Opposing roles of transient and prolonged expression of p25 in synaptic plasticity and hippocampus-dependent memory. *Neuron* 48(5), 825–838 (2005).

65   Govindarajan N, Agis-Balboa RC, Walter J, Sananbenesi F, Fischer A. Sodium butyrate improves memory function in an Alzheimer's disease mouse model when administered at an advanced stage of disease progression. *J. Alzheimers Dis.* 26(1), 187–197 (2011).

66   Kilgore M, Miller CA, Fass DM *et al.* Inhibitors of class 1 histone deacetylases reverse contextual memory deficits in a mouse model of Alzheimer's disease. *Neuropsychopharmacology* 35(4), 870–880 (2010).

67   Wiley JC, Pettan-Brewer C, Ladiges WC. Phenylbutyric acid reduces amyloid plaques and rescues cognitive behavior in AD transgenic mice. *Aging Cell* 10(3), 418–428 (2011).

68   Francis YI, Fa M, Ashraf H *et al.* Dysregulation of histone acetylation in the APP/PS1 mouse model of Alzheimer's disease. *J. Alzheimers Dis.* 18(1), 131–139 (2009).

69   Agis-Balboa RC, Pavelka Z, Kerimoglu C, Fischer A. Loss of HDAC5 impairs memory function: implications for Alzheimer's disease. *J. Alzheimers Dis.* 33(1), 35–44 (2013).

70   Govindarajan N, Rao P, Burkhardt S *et al.* Reducing HDAC6 ameliorates cognitive deficits in a mouse model for Alzheimer's disease. *EMBO Mol. Med.* 5(1), 52–63 (2013).

71   Graff J, Rei D, Guan JS *et al.* An epigenetic blockade of cognitive functions in the neurodegenerating brain. *Nature* 483(7388), 222–226 (2012).

72   Milutinovic S, D'alessio AC, Detich N, Szyf M. Valproate induces widespread epigenetic reprogramming which involves demethylation of specific genes. *Carcinogenesis* 28(3), 560–571 (2007).

73   Dodart JC, Bales KR, Gannon KS *et al.* Immunization reverses memory deficits without reducing brain Abeta burden in Alzheimer's disease model. *Nat. Neurosci.* 5(5), 452–457 (2002).

74   Sacks CA, Avorn J, Kesselheim AS. The failure of solanezumab – how the FDA saved taxpayers billions. *N. Engl. J. Med.* 376(18), 1706–1708 (2017).

75   Mcgowan E, Eriksen J, Hutton M. A decade of modeling Alzheimer's disease in transgenic mice. *Trends Genet.* 22(5), 281–289 (2006).

76   Takeuchi A, Irizarry MC, Duff K *et al.* Age-related amyloid beta deposition in transgenic mice overexpressing both Alzheimer mutant presenilin 1 and amyloid beta precursor protein Swedish mutant is not associated with global neuronal loss. *Am. J. Pathol.* 157(1), 331–339 (2000).

77   Irizarry MC, McNamara M, Fedorchak K, Hsiao K, Hyman BT. APPSw transgenic mice develop age-related A beta deposits and neuropil abnormalities, but no neuronal loss in CA1. *J. Neuropathol. Exp. Neurol.* 56(9), 965–973 (1997).

78   Irizarry MC, Soriano F, Mcnamara M *et al.* Abeta deposition is associated with neuropil changes, but not with overt neuronal loss in the human amyloid precursor protein V717F (PDAPP) transgenic mouse. *J. Neurosci.* 17(18), 7053–7059 (1997).

79   Kitazawa M, Medeiros R, Laferla FM. Transgenic mouse models of Alzheimer disease: developing a better model as a tool for therapeutic interventions. *Curr. Pharm. Des.* 18(8), 1131–1147 (2012).

80   Rodriguez GA, Burns MP, Weeber EJ, Rebeck GW. Young APOE4 targeted replacement mice exhibit poor spatial learning and memory, with reduced dendritic spine density in the medial entorhinal cortex. *Learn. Mem.* 20(5), 256–266 (2013).

81   Chan ES, Shetty MS, Sajikumar S, Chen C, Soong TW, Wong B-S. ApoE4 expression accelerates hippocampus-dependent cognitive deficits by enhancing Aβ impairment of insulin signaling in an Alzheimer's disease mouse model. *Sci. Rep.* 6, 26119 (2016).

82   Evans MJ, Kaufman MH. Establishment in culture of pluripotential cells from mouse embryos. *Nature* 292(5819), 154–156 (1981).

83   Takahashi K, Yamanaka S. Induction of pluripotent stem cells from mouse embryonic and adult fibroblast cultures by defined factors. *Cell* 126(4), 663–676 (2006).

••   **Demonstrated which factors were important for the maintenance and induction of the stem-cell phenotype, therefore allowing for the generation of induced pluripotent stem cells (iPSCs).**

84   Yamanaka S. A fresh look at iPS cells. *Cell* 137(1), 13–17 (2009).

85   Chin MH, Mason MJ, Xie W *et al.* Induced pluripotent stem cells and embryonic stem cells are distinguished by gene expression signatures. *Cell Stem Cell* 5(1), 111–123 (2009).

86   Lister R, Pelizzola M, Kida YS *et al.* Hotspots of aberrant epigenomic reprogramming in human induced pluripotent stem cells. *Nature* 471(7336), 68–73 (2011).

87   Mallon BS, Chenoweth JG, Johnson KR *et al.* StemCellDB: the human pluripotent stem cell database at the National Institutes of Health. *Stem Cell Res.* 10(1), 57–66 (2013).

88   Mallon BS, Hamilton RS, Kozhich OA *et al.* Comparison of the molecular profiles of human embryonic and induced pluripotent stem cells of isogenic origin. *Stem Cell Res.* 12(2), 376–386 (2014).

89   Kim K, Doi A, Wen B *et al.* Epigenetic memory in induced pluripotent stem cells. *Nature* 467(7313), 285–290 (2010).

90   Mikkelsen TS, Hanna J, Zhang X *et al.* Dissecting direct reprogramming through integrative genomic analysis. *Nature* 454(7200), 49–55 (2008).

91   Newman AM, Cooper JB. Lab-specific gene expression signatures in pluripotent stem cells. *Cell Stem Cell* 7(2), 258–262 (2010).

92   Newman AM, Cooper JB. AutoSOME: a clustering method for identifying gene expression modules without prior knowledge of cluster number. *BMC Bioinform.* 11, 117 (2010).

93   Lister R, Pelizzola M, Dowen RH *et al.* Human DNA methylomes at base resolution show widespread epigenomic differences. *Nature* 462(7271), 315–322 (2009).

94   Chambers SM, Fasano CA, Papapetrou EP, Tomishima M, Sadelain M, Studer L. Highly efficient neural conversion of human ES and iPS cells by dual inhibition of SMAD signaling. *Nat. Biotechnol.* 27(3), 275–280 (2009).

95   Lopez-Coviella I, Mellott TM, Kovacheva VP *et al.* Developmental pattern of expression of BMP receptors and Smads and activation of Smad1 and Smad5 by BMP9 in mouse basal forebrain. *Brain Res.* 1088(1), 49–56 (2006).

96   Shi Y, Kirwan P, Livesey FJ. Directed differentiation of human pluripotent stem cells to cerebral cortex neurons and neural networks. *Nat. Protoc.* 7(10), 1836–1846 (2012).

●●   **Found a robust and reproducible way of creating corticol neurons from iPSCs, a method for investigating AD with iPSCs.**

97   Moretti A, Bellin M, Welling A *et al.* Patient-specific induced pluripotent stem-cell models for long-QT syndrome. *N. Engl. J. Med.* 363(15), 1397–1409 (2010).

98   Lee G, Papapetrou EP, Kim H *et al.* Modelling pathogenesis and treatment of familial dysautonomia using patient-specific iPSCs. *Nature* 461(7262), 402–406 (2009).

99   Carvajal-Vergara X, Sevilla A, D'souza SL *et al.* Patient-specific induced pluripotent stem-cell-derived models of LEOPARD syndrome. *Nature* 465(7299), 808–812 (2010).

100   Marchetto MC, Carromeu C, Acab A *et al.* A model for neural development and treatment of Rett syndrome using human induced pluripotent stem cells. *Cell* 143(4), 527–539 (2010).

101   Nieweg K, Andreyeva A, Van Stegen B, Tanriover G, Gottmann K. Alzheimer's disease-related amyloid-beta induces synaptotoxicity in human iPS cell-derived neurons. *Cell Death Dis.* 6, e1709 (2015).

102   Duan L, Bhattacharyya BJ, Belmadani A, Pan L, Miller RJ, Kessler JA. Stem cell derived basal forebrain cholinergic neurons from Alzheimer's disease patients are more susceptible to cell death. *Mol. Neurodegener.* 9, 3 (2014).

●●   **Demonstrates that iPSC-derived neurons are able to recapitulate disease phenotypes and are more susceptible to glutamate-meditaed cell death.**

103   Young Jessica E, Boulanger-Weill J, Williams Daniel A *et al.* Elucidating molecular phenotypes caused by the SORL1 Alzheimer's disease genetic risk factor using human induced pluripotent stem cells. *Cell Stem Cell* 16(4), 373–385 (2015).

104   Israel MA, Yuan SH, Bardy C *et al.* Probing sporadic and familial Alzheimer's disease using induced pluripotent stem cells. *Nature* 482(7384), 216–220 (2012).

105   Kondo T, Asai M, Tsukita K *et al.* Modeling Alzheimer's disease with iPSCs reveals stress phenotypes associated with intracellular Abeta and differential drug responsiveness. *Cell Stem Cell* 12(4), 487–496 (2013).

106   Byrne SM, Mali P, Church GM. Genome editing in human stem cells. *Methods Enzymol.* 546, 119–138 (2014).

107   Mali P, Yang L, Esvelt KM *et al.* RNA-Guided human genome engineering via Cas9. *Science* 339(6121), 823–826 (2013).

108   Cong L, Ran FA, Cox D *et al.* Multiplex genome engineering using CRISPR/cas systems. *Science* 339(6121), 819–823 (2013).

109   Pires C, Schmid B, Petraeus C *et al.* Generation of a gene-corrected isogenic control cell line from an Alzheimer's disease patient iPSC line carrying a A79V mutation in PSEN1. *Stem Cell Res.* 17(2), 285–288 (2016).

110   Woodruff G, Young JE, Martinez FJ *et al.* The presenilin-1 DeltaE9 mutation results in reduced gamma-secretase activity, but not total loss of PS1 function, in isogenic human stem cells. *Cell Rep.* 5(4), 974–985 (2013).

111   Choi SH, Kim YH, Hebisch M *et al.* A three-dimensional human neural cell culture model of Alzheimer's disease. *Nature* 515(7526), 274–278 (2014).

112   Paquet D, Kwart D, Chen A *et al.* Efficient introduction of specific homozygous and heterozygous mutations using CRISPR/Cas9. *Nature* 533(7601), 125–129 (2016).

113   Cong L, Ran FA, Cox D *et al.* Multiplex genome engineering using CRISPR/Cas systems. *Science* 339(6121), 819–823 (2013).

114   Holler CJ, Davis PR, Beckett TL *et al.* Bridging integrator 1 (BIN1) protein expression increases in the Alzheimer's disease brain and correlates with neurofibrillary tangle pathology. *J. Alzheimers Dis.* 42(4), 1221–1227 (2014).

115   Harold D, Abraham R, Hollingworth P *et al.* Genome-wide association study identifies variants at CLU and PICALM associated with Alzheimer's disease. *Nat. Genet.* 41(10), 1088–1093 (2009).

116   Xu W, Tan L, Yu JT. The role of PICALM in Alzheimer's disease. *Mol. Neurobiol.* 52(1), 399–413 (2015).

117   Karch CM, Goate AM. Alzheimer's disease risk genes and mechanisms of disease pathogenesis. *Biol. Psychiatry* 77(1), 43–51 (2015).

118 Morgen K, Ramirez A, Frolich L *et al.* Genetic interaction of PICALM and APOE is associated with brain atrophy and cognitive impairment in Alzheimer's disease. *Alzheimers Dement.* 10(5 Suppl.), S269–S276 (2014).

119 Nordstedt C, Caporaso GL, Thyberg J, Gandy SE, Greengard P. Identification of the Alzheimer beta/A4 amyloid precursor protein in clathrin-coated vesicles purified from PC12 cells. *J. Biol. Chem.* 268(1), 608–612 (1993).

120 Cirrito JR, Kang JE, Lee J *et al.* Endocytosis is required for synaptic activity-dependent release of amyloid-beta *in vivo*. *Neuron* 58(1), 42–51 (2008).

121 Liu XS, Wu H, Ji X *et al.* Editing DNA Methylation in the Mammalian Genome. *Cell* 167(1), 233.e217–247.e217 (2016).

122 Bernstein DL, Le Lay JE, Ruano EG, Kaestner KH. TALE-mediated epigenetic suppression of CDKN2A increases replication in human fibroblasts. *J. Clin. Invest.* 125(5), 1998–2006 (2015).

123 Maeder ML, Angstman JF, Richardson ME *et al.* Targeted DNA demethylation and activation of endogenous genes using programmable TALE-TET1 fusion proteins. *Nat. Biotechnol.* 31(12), 1137–1142 (2013).

124 Rivenbark AG, Stolzenburg S, Beltran AS *et al.* Epigenetic reprogramming of cancer cells via targeted DNA methylation. *Epigenetics* 7(4), 350–360 (2012).

125 Nunna S, Reinhardt R, Ragozin S, Jeltsch A. Targeted methylation of the epithelial cell adhesion molecule (EpCAM) promoter to silence its expression in ovarian cancer cells. *PLoS ONE* 9(1), e87703 (2014).

126 Weick JP. Functional properties of human stem cell-derived neurons in health and disease. *Stem Cells Int.* 2016, 4190438 (2016).

127 Stein JL, De La Torre-Ubieta L, Tian Y *et al.* A quantitative framework to evaluate modeling of cortical development by neural stem cells. *Neuron* 83(1), 69–86 (2014).

128 Mariani J, Simonini MV, Palejev D *et al.* Modeling human cortical development *in vitro* using induced pluripotent stem cells. *Proc. Natl Acad. Sci. USA* 109(31), 12770–12775 (2012).

129 Livesey MR, Magnani D, Hardingham GE, Chandran S, Wyllie DJA. Functional properties of *in vitro* excitatory cortical neurons derived from human pluripotent stem cells. *J. Physiol.* 594(22), 6573–6582 (2016).

130 Miller JD. Human iPSC-based modeling of late-onset disease via progerin-induced aging. *Cell Stem Cell* 13(6), 691–705 (2013).

131 Mertens J, Paquola AC, Ku M *et al.* Directly reprogrammed human neurons retain aging-associated transcriptomic signatures and reveal age-related nucleocytoplasmic defects. *Cell Stem Cell* 17(6), 705–718 (2015).

●● **Demonstrates that iPSC-derived neurons do not retain age-related signatures, but induced neurons do display age-specific transcriptomic signatures and have age-associated decreases in RanBP17.**

APPENDIX B : <u>MICROGLIA IN ALZHEIMER'S DISEASE: A ROLE FOR ION CHANNELS</u>

frontiers
in Neuroscience

Microglia in Alzheimer's Disease: A Role for Ion Channels

Laura Thei [1], Jennifer Imm [2], Eleni Kaisis [1], Mark L. Dallas [1] and Talitha L. Kerrigan [2]*

[1] Reading School of Pharmacy, University of Reading, Reading, United Kingdom, [2] University of Exeter Medical School, University of Exeter, Exeter, United Kingdom

Alzheimer's disease is the most common form of dementia, it is estimated to affect over 40 million people worldwide. Classically, the disease has been characterized by the neuropathological hallmarks of aggregated extracellular amyloid-β and intracellular paired helical filaments of hyperphosphorylated tau. A wealth of evidence indicates a pivotal role for the innate immune system, such as microglia, and inflammation in the pathology of Alzheimer's disease. The over production and aggregation of Alzheimer's associated proteins results in chronic inflammation and disrupts microglial clearance of these depositions. Despite being non-excitable, microglia express a diverse array of ion channels which shape their physiological functions. In support of this, there is a growing body of evidence pointing to the involvement of microglial ion channels contributing to neurodegenerative diseases such as Alzheimer's disease. In this review, we discuss the evidence for an array of microglia ion channels and their importance in modulating microglial homeostasis and how this process could be disrupted in Alzheimer's disease. One promising avenue for assessing the role that microglia play in the initiation and progression of Alzheimer's disease is through using induced pluripotent stem cell derived microglia. Here, we examine what is already understood in terms of the molecular underpinnings of inflammation in Alzheimer's disease, and the utility that inducible pluripotent stem cell derived microglia may have to advance this knowledge. We outline the variability that occurs between the use of animal and human models with regards to the importance of microglial ion channels in generating a relevant functional model of brain inflammation. Overcoming these hurdles will be pivotal in order to develop new drug targets and progress our understanding of the pathological mechanisms involved in Alzheimer's disease.

Keywords: microglia, Alzheimer's disease, ion channel, stem cells, iPSCs

INTRODUCTION

Alzheimer's disease (AD) is the most prevalent neurodegenerative disorder and accounts for approximately 60–80% of all dementia cases worldwide (Alzheimer'sstatistics, 2016). Initial studies focussed on trying to identify a genetic basis to the disease (Gatz et al., 2006). Although some AD cases are caused by defined mutations in one of three genes (APP, PSEN1 and PSEN2) these account for fewer than 10% of all cases and occur before 65 years of age. The majority of cases are sporadic, have no defined etiology and occurs at or after a mean age of 65. Our understanding has progressed through evidence obtained from large cohort studies identifying genetic variants which are associated with and potentially result in the late onset form of AD (LOAD). These

genome wide association studies (GWAS) have demonstrated that LOAD is a multifactorial disease with many different genes and single nucleotide polymorphisms contributing to disease onset (Gatz et al., 2006). The most strongly associated gene with LOAD is Apolipoprotein E (APOE), which encodes a polymorphic glycoprotein that is involved in cholesterol and other lipid transport (Poirier, 2005) alongside tissue repair (Huang, 2010) and neuronal growth (Nathan et al., 1994). There are three isoforms of APOE, ε2, ε3, and ε4 that all correspond to cysteine to arginine substitutions at the amino acid positions 112 and 158 (Zlokovic, 2013). The ε4 variant confers increased risk of developing LOAD, and each additional copy of the ε4 allele lowers the mean age of onset (Corder et al., 1993). Neurodegenerative diseases such as AD were traditionally considered to be ''neurocentric,'' however recent findings are challenging this view, implicating glia as primary targets. GWAS studies reveal there have been a number of single nucleotide polymorphisms that are associated with AD which reside in genes involved in microglial biology. These include common variants such as CR1 (complement receptor 1), CD33 (sialic acid binding Ig-like lectin 3), CLU (clusterin), ABCA7 (ATP-binding cassette, sub family A, member 7), MS4A (membrane-spanning 4-domain family, subfamily A) and EPHA1 (ephrin type-A receptor 1) (Bertram et al., 2008; Harold et al., 2009; Hollingworth et al., 2011; Naj et al., 2011; Lambert et al., 2013; Zhang et al., 2013), and also more rare coding variants in genes such as TREM2 (triggering receptor expressed on myeloid cells 2) (Guerreiro et al., 2013; Jonsson et al., 2013). TREM2 is a cell surface receptor of the immunoglobulin superfamily that is expressed on microglia (reviewed by Colonna and Wang, 2016). Several variants within TREM2 appear to significantly increase the risk of developing AD (Jin et al., 2014; Song et al., 2017), in particular rs75932628, an SNP that confers an arginine to histidine change at amino acid 47 (R47H) (Guerreiro et al., 2013; Jonsson et al., 2013). Although TREM2 polymorphisms are associated with a risk of late-onset AD (Guerreiro et al., 2013), their role in neurodegenerative diseases is controversial. Indeed, recent evidence proposes that the TREM2-APOE pathway induces a microglia phenotypic switch from a homeostatic to neurodegenerative phenotype (Krasemann et al., 2017). One of the main functions of TREM2 is regulating microglial phagocytosis (Hsieh et al., 2009), and as a ligand for TREM2 in microglia, APOE binds to dead neurons and increases Trem2-mediated phagocytosis (Atagi et al., 2015). Interestingly, Kleinberger et al. (2014) showed that missense mutations in TREM2 resulted in impaired phagocytic activity with a reduced level of soluble TREM2 in cerebrospinal fluid (CSF) of AD patients. Indeed TREM2 deficiency has been shown to alter microglial function in both primary microglial cultures and in mouse models of AD where a decrease in plaque-associated microglia are observed alongside an increase in apoptosis of both resting and activated microglia and reduced phagocytosis (Ulrich et al., 2014; Jay et al., 2015, 2017). These findings suggest that the role of TREM2 in modulating inflammation may be more complex than previously appreciated and may be dependent on the cell type in which it is expressed and the inflammatory context in which it is studied. For a more in depth discussion we refer the reader to the following very comprehensive review articles (Colonna and Wang, 2016; Ulrich et al., 2017; Li and Zhang, 2018).

Microglia are thought to regulate the degree of Aβ deposition by phagocytosis with potentially protective impact on AD progression (Lee and Landreth, 2010). One striking feature of the behavior of microglia in the AD brain is their marked clustering around fibrillar Aβ deposits and they adopt a polarized morphology with hypertrophic processes extending toward plaques (Condello et al., 2015). This aids as a protective physical barrier mechanism through which the Aβ fibrils cannot extend, promoting the formation of highly compact plaque micro regions that have minimal affinity for soluble $A\beta_{1-42}$ (Condello et al., 2015; Yuan et al., 2016). Conversely, areas not covered by microglia processes display "hotspots" with very high soluble $A\beta_{1-42}$ affinity, leading to markedly concentrated protofibrillar Aβ42 plaque regions (Condello et al., 2015). These "hotspots" are neurotoxic given that adjacent axons develop a greater extent of dystrophy compared to those covered by microglia (Yuan et al., 2016).

On the other hand, most studies in TREM2- deficient AD-like mice have shown reduced number of microglia around Aβ plaques (Jay et al., 2015; Wang et al., 2015). Similar reports suggest that in R47H human mutants, microglial processes were also unable to form a robust barrier, resulting in a decreased Aβ fibril compaction (Yuan et al., 2016). With the decrease in microglial number, there are less compact Aβ fibrils and a higher ratio of $A\beta_{1-42}$ plaques (Yuan et al., 2016; Ulland et al., 2017), therefore a deficient rather than an exacerbated microglial response could give rise to the development of sporadic AD. Once activated by pathological triggers, like neuronal death or protein aggregates, microglia extend their processes to the site of injury, migrate to the lesion and initiate an innate immune response (Heneka et al., 2015). Mounting evidence from polymorphisms linking microglial dysfunction to AD could have a causal role in disease onset and progression and are not just a consequence of neuropathological hallmarks that are characteristic of AD.

THE INNATE IMMUNE SYSTEM IN AD

Of increasing interest is the involvement of the innate immune system in AD, particularly the role of microglia. Microglia are the resident immune cells in the brain and spinal cord, and play important roles in neurodevelopment, immune surveillance, disease and homeostasis (Nayak et al., 2014). Unlike neurons and other glial cell types, microglia are of haematopoietic lineage, arise early during development (Hutchins et al., 1990), and are derived from erythromyeloid progenitors (EMPs) in the yolk sac (Ginhoux et al., 2010).

Microglia can exist in several morphological/phenotypic states depending on the environment they are in or the factors they are stimulated by. From a highly processed state, the microglia become more amoeboid with increased numbers of intracellular vesicles in preparation for engulfment of foreign particles. These differential states have been termed accordingly as "classical activation," "alternative activation," and "acquired deactivation"

(Colton, 2009; Colton and Wilcock, 2010). Previous studies defined these states as separate from one another, a profiling index of M1 or M2 phenotyping suggesting a pro- or anti-inflammatory state respectively. More recently it has become more apparent that this is derived from the idea that microglia are central macrophages and so must follow by the same "kill or cure" switch seen in these cell types. However, microglia can exist in multiple phases with the same cell producing markers of both pro- and anti- inflammatory components depending on stimulus. Usage of M1/M2 profile terminology fails to capture the heterogeneity of microglia which is a vital to their local and global physiological responses (Mosser et al., 2017).

Classical activation, considered to be pro-inflammatory, is stimulated by IFN-γ and is associated with the production of cytokines such as TNF-α and IL-1β and nitric oxide production (Li et al., 2004; Block et al., 2007). On the other hand, alternative activation, is defined by the release of anti-inflammatory cytokines IL-4 and IL-13 and arginase 2. This results in gene expression to promote tissue repair and extracellular matrix reconstruction (Ponomarev et al., 2007; Colton, 2009). Acquired deactivation, is mainly seen in the presence of apoptotic cells and is characterized by the release of IL-10, TGF-β, IL-6, and CSF1 and the production of scavenger receptors (Sawada et al., 1999; Colton, 2009; Colton and Wilcock, 2010; Saijo and Glass, 2011). Microglial phagocytosis relies on specific receptors expressed on the cell surface and their downstream signaling pathways to instigate engulfment of harmful particulates (**Figure 1**).

Microglia mediate the innate immune response of the brain and are involved in the phagocytosis and clearance of debris, pathogens, and toxins. Their dysfunction and increased Aβ accumulation is universal to AD patients and not just those with familial APP mutations. This suggests that Aβ build-up is due to poor clearance and not APP proteolysis. Microglia will secrete both pro- and anti-inflammatory factors, which can either be beneficial or detrimental in neurodegenerative diseases. Here exists extensive literature showing that inflammation is integral to AD progression, facilitating Aβ deposition, neuronal loss and cognitive deficits. Brains from AD patients and those from murine models of Aβ pathology uniformly display high expression of pro-inflammatory cyto- and chemokines including TNFα, IFNγ, IL-1β, and IL-6 (Zheng et al., 2016). IL-1β and TNFα can impair neuronal function by suppression of long-term potentiation of synaptic transmission (LTP) (Rowan et al., 2007). Multiple interactions as well as elevated expression of additional cytokines/chemokines and innate immune receptors favor a pro-inflammatory activation state in AD.

Accumulating evidence demonstrates that inflammasomes, which cleave precursors of interleukin-1β (IL-1β) and IL-18 to generate their active forms, play an important role in the inflammatory response in the CNS and in AD pathogenesis. The inflammasome is an inducible, high molecular weight, protein complex consisting of the antigen sensor protein NLRP3, adaptor protein ASC, and pro-caspase 1 (Heneka et al., 2015). The complexing of these three components results in cleavage of caspase 1 and instigates a cascade of pro-inflammatory cytokine activation of the IL-1b family. In murine mutants where APP/PS1

was crossed with NLRP3-/- mice, a decrease in cC1 and IL-1β is observed (Heneka et al., 2013).

Conversely an anti-inflammatory profile of microglia also contributes to Aβ pathology. In murine models where IL-10 was either knocked down or knocked out in the APP/PS1 model, a decrease in Aβ load, increases phagocytosis and reduces microglial APOE expression was observed (Chakrabarty et al., 2015). Further studies showed that this was due to preventing downstream pathways involving Jak1/Stat3 and consequential transcription factor activity (Guillot-Sestier et al., 2015). Additionally, primary microglia treated with fibrillar Aβ$_{1-42}$ and recombinant IL-10 showed that fibrillar Aβ$_{1-42}$ is prevented from inducing a pro-inflammatory response of cytokine release including CCL5, CXC10, and TNFα, suggesting a push to an anti-inflammatory profile (Chakrabarty et al., 2015).

Therefore, it is pertinent to think that the Aβ activates microglia and results in an innate immune response. Indeed, it has been shown that exposure of microglia to fibrillar Aβ by CD36, a class B scavenger receptor (Coraci et al., 2002), causes the formation of a heterodimer of the TLR4 and TLR6 through NF-κB signaling (Stewart et al., 2010). However, on deletion of MyD88, an adaptor protein essential for downstream TLR signaling, there was a significant decrease in both Aβ load and microglial activation in APP/PS1 mice (Lim et al., 2011). Despite this the MyD88 deletion only resulted in minor improvements in cognitive functions (Lim et al., 2012).

Microglial activation by Aβ does not necessarily only occur after Aβ deposition but can also occur before plaques are even formed. Maezawa and colleagues have shown that nanomolar concentrations of Aβ oligomers activated microglia and that they required another scavenger receptor, SR-A, and the Ca^{2+}-activated potassium channel KCa3.1 (Maezawa et al., 2011). Another group has also shown microglial activation precedes Aβ aggregation in APP[V717I] transgenic mice and that this coincides with increased BACE1 activation (Heneka et al., 2005).

Intracellular neurofibrillary tangles of hyperphosphorylated tau are another pathological hallmark of AD. However, the exact mechanisms which lead to the hyperphosphorylation of tau are still unclear. Previously, it has been demonstrated that neuro-inflammation positively correlates with tau aggregation, hyperphosphorylation and neurodegeneration in several models (Sheng et al., 1997; Sheffield et al., 2000; Bellucci et al., 2004, 2011; Ikeda et al., 2005; Yoshiyama et al., 2007).

Microglial activation also precedes tau pathology in the P301S tauopathy model (Yoshiyama et al., 2007). In the triple transgenic model of AD, lipopolysaccharide administration significantly increased tau phosphorylation through toll like receptor 4 signaling (Kitazawa et al., 2005). Interestingly, one paper has demonstrated that microglia may be involved in the propagation of tau pathology through non-synaptic transmission in mammals (Asai et al., 2015). Asai et al. (2015) used two different tau mouse models to show that tau propagation is mediated through microglia which phagocytose tau-positive neurons or synapses and secrete tau protein in exosomes, efficiently transmitting tau to neurons. They also demonstrated that this propagation is sensitive to microglial depletion and inhibition of nSMase2 activity. On the other

FIGURE 1 | Morphological phenotype of Microglia. An illustration depicting the different phenotypic states. These are "classical activation," "alternative activation," and "acquired deactivation." Classical activation, otherwise considered to be the M1 phenotype and so is pro-inflammatory, is stimulated by IFN-γ and is associated with the production of cytokines such as TNF-α and IL-1β. Subsequently the alternative activation, or M2 phenotype, defined by the release of anti-inflammatory cytokines IL-4 and IL-13. The third activation phenotype, acquired deactivation, is thought to be a subtype of the M2 phenotype, releases IL-10 and TGF-β. Activation does not inclusively mean a phagocytic phenotype in microglia. For this to occur, antigen sensing receptors are made available on the cell surface to allow pathogen recognition. In Alzheimer's disease, the best known of these is TREM2 but others include Toll-like receptors and members of the complement system.

hand, significant ablation of microglia in a mouse model of amyloidopathy indicated that Aβ formation, maintenance and associated neuritic dystrophy was not depended on microglia (Grathwohl et al., 2009). Interestingly, (Krabbe et al., 2013) reported that Aβ may directly affect microglial function. This *in vivo* study detected a significant inverse correlation between Aβ plaque burden and microglial phagocytic activity (Krabbe et al., 2013). They found that microglial dysfunction develops early during AD in an Aβ-dependent fashion and can be restored by interventional anti-Aβ approaches, such as Aβ vaccination (Krabbe et al., 2013).

MICROGLIA PHYSIOLOGY AND ION CHANNELS

Studies have highlighted the importance of microglia in brain ionic homeostasis (Annunziato et al., 2013; Szalay et al., 2016; Shibata and Suzuki, 2017). For example, depletion of microglia results in the loss of potassium chloride induced neuronal depolarisation (Szalay et al., 2016) and the microglia KCa3.1 channel has been proposed as a valid therapeutic target for modulating cortical spreading depression (Shibata and Suzuki, 2017). Therefore ion channels and transporters, regulating ionic flux, are essential regulators of a variety of microglial functions, including proliferation, morphological changes, migration, cytokine release and reactive oxygen species production (Schilling and Eder, 2015). Ion channel expression in microglial cells is tightly regulated, with the expression of most ion channel types noticeably depending on the cells' functional

state (Eder, 1998, 2005, 2010; Kettenmann et al., 2011). Despite being non-excitable cells, the plethora of voltage-gated ion channels present in microglia suggests they play a prominent role in both physiological as well as pathological states. Brain inflammation is a characteristic of AD and numerous studies have demonstrated that microglia can directly interact with neurons to induce inflammation (Hashioka et al., 2012). Due to this interaction, the study of microglial ion channels may shed light on brain inflammation seen in neurodegenerative diseases such as AD (Silei et al., 1999). In this review, we have summarized the most prominent ion channels involved in microglial cells which may contribute to AD pathology, as demonstrated in **Figure 2**.

POTASSIUM CHANNELS

Potassium channels are present in all cells within the body and have many diverse functions. In particular, they are capable of regulating cell excitability and influence action potential waveform. To identify therapeutic targets to modulate microglial activation, numerous studies are addressing the contributions of several K^+ channels. Based on both their structural and functional properties, K^+ channels have been subdivided into specific families. They have transmembrane helices (TMs) spanning the lipid bilayer (Kuang et al., 2015). The largest of these consist of K^+ channels that are activated by membrane depolarisation, with subsequent families consisting of channels that are activated by altered intracellular Ca^{2+} ions and others that are constitutively active. Based on the structure and function,

FIGURE 2 | Illustration depicting presence of ion channels observed in microglial models and which of these have confirmed activity in Alzheimer's disease associated microglia. Strength of evidence is depicted in bold to un-bold text. In addition each channel is pre-fixed with the species in which they have been investigated: h, human; m, mouse; r, rat.
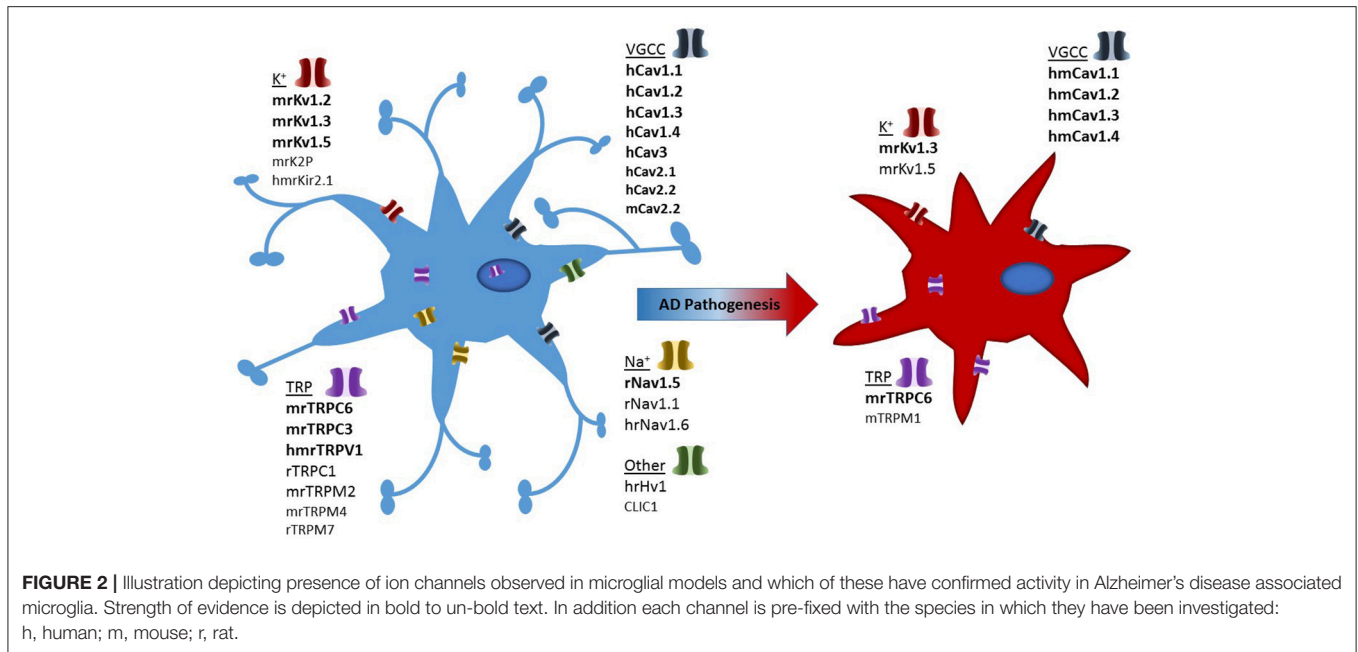
the channels are categorized into three major classes: the voltage-gated (Kv) (six TMs), inwardly rectifying (Kir) (two TMs), and tandem pore domain (K2P) (four TMs) channels (Kuang et al., 2015). K^+ channels are particularly important in microglia since their activation can induce membrane hyperpolarisations, which are essential for driving Ca^{2+} influx through inward rectifying Ca^{2+}-Release-Activated-Ca^{2+} channels (CRAC) (Kraft, 2015; Nguyen et al., 2017a) ATP-activated P2X receptors (Burnstock, 2015) and other Ca^{2+}-permeable cation channels (Kettenmann et al., 2011).

Voltage-Gated Potassium Channels

Kv channels form an exceedingly diverse group, their structure consists of six TMs, of which the first four helices (S1–S4) form the voltage sensor domain (VSD) (Jiang Y. et al., 2003; Long et al., 2007). The last two helices (S5–S6, corresponding to the outer and inner helices in KcsA, respectively) form the pore-forming domain. The VSD senses the membrane potential alteration, and is followed by a conformational change that is coupled to gate the pore-forming domain (Long et al., 2005). In more general terms Kv currents can be classified into showing A-type (inactivating) or delayed rectifier behavior (non-inactivating). The Kv channels present in microglia to date have been summarized in **Table 1** and mainly comprises of delayed rectifier Kv channels.

Kv1.2, Kv1.3, and Kv1.5 transcripts and protein have been detected in both primary rat and mouse microglia (Kotecha and Schlichter, 1999; Khanna et al., 2001; Fordyce et al., 2005; Pannasch et al., 2006; Li et al., 2011). Microglia are widely distributed throughout the brain; however some regions express much higher levels than others (Lawson et al., 1990). The hippocampus, an area particularly affected by AD, is rich with microglia and is especially sensitive to cerebrovascular insults which have been shown to rapidly activate microglia (Wu and Ling, 1998). The reasons for the highly variable expression

of Kv channels and the role this plays in non-excitable cells such as microglia are not well understood. It is now known that microglia in culture can express different proteins when compared to microglia *in situ* in brain slices or *in vivo* (Boucsein et al., 2003; Butovsky et al., 2014; Yamasaki et al., 2014; Gosselin et al., 2017). Earlier studies mostly used cultured microglia from enzymatically dissociated tissue, thus removing cell– cell contacts and key secretory products such as growth factors affecting Kv channel expression itself (Kettenmann et al., 1990; Ganter et al., 1992; Draheim et al., 1999). *In vitro* studies are currently the only way to stimulate microglia in isolation in order to elucidate similarities and differences in how different species respond (Lam et al., 2017).

It is becoming more apparent that altered expression of Kv channels could trigger the mechanisms underlying microglial polarity and could characterize these microglial states (Saijo and Glass, 2011; Maezawa et al., 2012). In a study on freshly isolated microglial cells, Kotecha and Schlichter (1999) found both Kv1.3 and Kv1.5, the former being associated with proliferating cells and the latter with non-proliferating cells. This shift in microglial activation also results in changes in the physiological properties of the cells (Kotecha and Schlichter, 1999). Resting microglia express Kv1.5 channels and upon activation and proliferation they upregulate Kv1.3 and down-regulate Kv1.5 channels (Pannasch et al., 2006). Kv1.3 channels migrate to the cell surface while Kv1.5 channels are internalized, making Kv1.3 channels not only functionally relevant but highly susceptible to pharmacological manipulation through selective channel blockers. As we have highlighted, majority of microglial studies use animal models, in particular rodents. Lam et al. (2017) found distinct variability between the different rodent models in expressing different Kv channels. It is also apparent that Kv channel expression of microglial cells in brain slices from juvenile mice (P5-P9) differs to some extent from that of cells

TABLE 1 | Microglia ion channels and their functionality after cell activation.

Channel type	Subunit	Expression and modulation	Proposed functions	Models	References
Voltage-gated Calcium Channels (VGCC)	N-type $Ca_V2.2$ Possible L-type $(Cav1.X)$	Very low expression levels at both protein and mRNA level	$Cav2.2$ control chemokine release from microglia $Cav1.2$ and 1.3 activity results in proliferation, increased intracellular Ca^{2+} with Aβ, microglial survival and pro-inflammatory action	Rat, mouse and Human primary cultures BV2 cell lines	Silei et al., 1999 Hashioka et al., 2012 Nicoletti et al., 2017 Espinosa-Parrilla et al., 2015
Inwardly rectifying potassium current (K_{ir})	$K_{ir}2.1$	Generally expressed in activated microglia; very low densities in resting microglia Modulated by intracellular factors, such as, G-proteins, intracellular calcium, pH and protein kinase C (PKC) LPS reduces or enhances current density in cultured murine microglia.	Sets a negative resting membrane potential (RMP)	Rat, mouse and primary and secondary cultures BV2 cell line Adult mouse brain slices	Schilling et al., 2000 Eder et al., 1999 Draheim et al., 1999 Boucsein et al., 2003 Kettenmann et al., 1993, 2011; Nörenberg et al., 1994a; Fischer et al., 1995; Chung et al., 1999; Franchini et al., 2004
Delayed outwardly rectifying potassium current (K_{dr})	$K_V1.3$ $K_V1.5$ To a lesser extent $K_V1.1$ $K_V1.2$	Transiently up-regulated upon stimulation with LPS interferon-β, TNF-α, TGF-β, GM-CSF, pH, Aβ, prostaglandin E2 receptor activation. Hypoxic insults increase Kv1.2 expression in adult microglial cells	Re-establishing a negative RMP during membrane oscillations Both $K_V1.3$ and $K_V1.5$ play a role in proliferation and ROS production $K_V1.3$ is involved the respiratory burst $K_V1.5$ is involved in NO release $K_V1.1$ and $K_V1.2$ involved LPS-induced release of TNF-α, interleukin-1β, endothelins and NO	Rat and mouse primary cultures Human brain slices and primary cultures	Nörenberg et al., 1994a; Schilling et al., 2000; Fordyce et al., 2005 Jou et al., 1998; Kotecha and Schlichter, 1999; Khanna et al., 2001 Pannasch et al., 2006; Eder, 1998 Chung et al., 1999 Eder and Heinemann, 1996
Ca^{2+}-dependent potassium channels (KCa)	Large conductance: KCa1.1 Small conductance: KCa2.1 KCa2.2 KCa2.3 KCa3.1	KCa2.3 channels are predominantly expressed in both cultures and healthy striatum tissue; LPS treatment or ischemic insult increased the level of expression.	Blocking KCa2.2/KCa2.3 with CyPPA reduces cytokine release Migration was inhibited when KCa1.1 was blocked with charybdotoxin and clotrimazole Small conductance channels are linked to NO release, MAPK signaling and respiratory burst Inhibition of KCa2.3 affected microglial activation and reduced microglial neurotoxicity.	Calf, rat, mouse, human, adult, and new born rat primary cultures and brain slices	Walz et al., 1993 McLarnon et al., 1997; McLarnon et al., 2001; Bordey and Spencer, 2003 Khanna et al., 2001 Spranger et al., 1998 Papavlassopoulos et al., 2006; Stock et al., 2006; Kaushal et al., 2007
Two-Pore Domain Potassium Channel (K2P)	K2P13.1 (THIK-1)	High RNA expression in resting microglia Age-dependent decrease of mRNA	Maintaining RMP. Mediates release of the pro-inflammatory cytokine interleukin-1β from activated microglia Regulates microglial ramification	Rat hippocampal brain slices and primary cultures	Madry et al., 2018

(Continued)

TABLE 1 | Continued

Channel type	Subunit	Expression and modulation	Proposed functions	Models	References
Voltage-gated Na$^+$ channels	Na$_V$1.1, Na$_V$1.5 Na$_V$1.6	Na$_V$1.6 expression correlates with the transition between resting and activated microglia in EAE Protein and mRNA for Na$_V$1.6 were detected in EAE mice spinal cord and optic nerve, as well as in MS-affected human spinal cord.	Phagocytosis and cell volume regulation Treatment of LPS-activated microglia with TTX or phenytoin reduced IL-α1, IL-1β, and TNF-α secretion Decreased motility responses to ATP Phenytoin reduced microglial activation in EAE model	Rat primary cultures	Craner et al., 2005 Korotzer and Cotman, 1992 Nörenberg et al., 1994b Schmidtmayer et al., 1994 Eder, 2005 Black et al., 2009
Transient Receptor Potential channels (TRP)	TRPC1, 3, 6 TRPM2, 4 TRPV1, 2 and to a lesser extent other TRPs	Low expression of RNA in resting microglia. Transiently up-regulated upon stimulation with LPS, ATP, or BDNF	Activation of TRPs contributes to microglial Ca^{2+} signaling and are linked to IL-6 release, NO, TNFα associated initiation of microglial cells death Contribute to the regulation of transcription factors' function, including NFkB, NRF2, and AP-1, cytokine production, cell proliferation, activation, apoptosis and oxidative stress	Rat and mouse primary cultures BV-2 cell lines Human primary cultures	Sun et al., 2014 Mizoguchi et al., 2014 Liu et al., 2017 Huang et al., 2017 Sappington and Calkins, 2008 Schilling and Eder, 2011
Proton channels	H$_V$1 voltage-activated H$^+$ channels	Unknown	Single-channel conductance fS range High sensitivity to extracellular pH; associated with generation of respiratory burst Disruption of cytoskeleton leads to a 50% reduction in H$^+$ current amplitude Cell swelling potentiates H$^+$ currents.	Mouse, rat and human primary cultures	Eder et al., 1995; Klee et al., 1998, 1999 Tian et al., 2016 Wu et al., 2012
Chloride channels	CLIC-1	mRNA highly expressed in mammalian microglia channel protein relocation from cytosol to membrane after Aβ	Morphological changes based on Cl$^-$ responses to stretch	Rat and bovine primary cultures	Visentin et al., 1995; Schlichter et al., 1996 McLarnon et al., 1995 Skaper et al., 2013 Milton et al., 2008 Paradisi et al., 2008

in adult mice (Boucsein et al., 2003; Schilling and Eder, 2007; Menteyne et al., 2009; Arnoux et al., 2013, 2014). The passive membrane properties and Kv channel expression of microglial cells undergo substantial changes upon aging (Schilling and Eder, 2015). In comparison with microglia of young adult mice, microglial cells of aged mice are characterized by more negative resting membrane potentials, decreased input resistances and upregulated expression of inward rectifier and outward rectifier Kv channels. Interestingly, the outward rectifier Kv channel current is strongly age-dependent both *in vitro* and *in vivo* (Schilling and Eder, 2015). It is clear from the literature that the way in which we study Kv channel physiology in microglia varies dramatically and depends on the methodology used (Lam et al., 2017).

Further complications include the potential for strain differences in rodents (Becker, 2016), and genetic polymorphisms and epigenetic changes in humans (Boche and Nicoll, 2010). There is considerable debate as to how closely mouse models resemble human responses in inflammatory diseases (Seok et al., 2013; Takao and Miyakawa, 2015). A better understanding of microglial K^+ channel regulation and expression patterns in neurodegenerative states could also yield targets for drug development using K^+ channel blockers.

Voltage-Gated Potassium Channels and AD

Microglia are the key inflammatory cells in AD that mediate neuro-inflammation, and Kv channels are key regulators of microglial function, in particular Kv1.3 (Rangaraju et al., 2015). In animal models of AD, Aβ-induced priming of microglial NADPH oxidative activity depends on Kv1.3 channels, however the exact mechanisms that contribute to this priming is still poorly explored (Kotecha and Schlichter, 1999; Schilling and Eder, 2011). It is thought that the activity of Kv channels lead to membrane hyperpolarization, this Kv1.3 channel-induced membrane hyperpolarisation could enhance Ca^{2+} influx through Transient receptor potential (TRP) channels (see section Calcium Channels; Schilling and Eder, 2011) aiding in the translocation of PKC and therefore leading to NADPH oxidative priming. Franciosi et al. (2006) demonstrated that the broad spectrum Kv channel inhibitor 4-aminopyridine (4-AP) suppressed microglial activation *in vivo* and reduced microglia-induced neuronal death (Franciosi et al., 2006). This inhibition using 4-AP, which also blocks Kv1.3 channels, could attribute to inhibition of microglial priming and subsequent reduction of microglial ROS production, supporting a role for Kv1.3 channels as a therapeutic target in AD (Schilling and Eder, 2011). More recently immunohistochemistry experiments on human brain cortices revealed the presence of Kv1.3 channels in cortical microglia at levels higher than non-AD controls (Rangaraju et al., 2015). This particular study also revealed a "plaque-like" pattern of Kv1.3, suggesting that it may be possible for Aβ to interact with Kv1.3. Interestingly, Aβ$_{1-42}$ oligomers, but not soluble Aβ, accelerate the activation and inactivation kinetics of Kv1.3 channels in lipid bilayers without altering channel conductance (Lioudyno et al., 2012). It is possible that altered channel conductance of Kv1.3 channels could affect calcium fluxes in neurons and microglia, however the relevance of this potential Aβ-Kv1.3-interaction remains to

be clarified. Another study by Chung et al. (2001) also confirmed that Aβ was capable of upregulating Kv1.3 as well as the Kv1.5 channel current density. More recently, low levels of soluble oligomeric Aβ have been reported to upregulate primary cultured microglial activity as well as Kv1.3 at transcript and as protein levels (Maezawa et al., 2017). Electrophysiological studies using whole-cell patch clamp also revealed enhanced outward rectifier current, characteristic of homotetrameric Kv1.3 channels. Pharmacological characterization revealed that the currents were sensitive to the Kv1.3 specific blockers ShK-186 (Tarcha et al., 2012), margatoxin (Garcia-Calvo et al., 1993) and the selective Kv1.3 blocker PAP-1 [5-(4-phenoxybutoxy) psoralen (Schmitz et al., 2005). Oligomeric Aβ further induced a significant increase in Kv1.3 current density compared to unstimulated microglia (Maezawa et al., 2017). Following long-term treatment of an APP/PS1 mouse model, the selective Kv1.3 blocker PAP-1 mitigated some key AD-like phenotypes such as reducing Aβ deposition as well as restoring hippocampal synaptic plasticity. The observation that pharmacological targeting of Kv1.3 channels in microglia with the selective inhibitor PAP-1 supports PAP-1 as a promising potential for neuro-immunomodulation therapy and the treatment of neurodegenerative diseases such as AD.

The age-dependent changes in microglial Kv1.3 noted in 5xFAD mice followed a similar trend—initially an age-dependent increase, then a substantial decrease between 10 and 15 months of age. We suspect that these changes in K^+ channel expression form part of the age-related changes in microglial function, documented by several lines of investigation, such as altered responses to Aβ aggregates or downregulation of "sensome" genes (Hickman et al., 2008; Cameron et al., 2012; Heneka et al., 2013; Hickman and El Khoury, 2013; Johansson et al., 2015) ever, this downregulation is not reflected in a human study in which Kv1.3 expression remains robust in microglia, particularly in the later stages of AD (Rangaraju et al., 2015). More recently transcriptomic data from Rangaraju et al. (2018), revealed that Kv1.3 plays a distinct role in disease-associated-microglia in the 5XFAD mouse model (Rangaraju et al., 2018). It is pertinent to say that the evidence presented here from the existing human and rodent studies, show Kv1.3 could be a therapeutic target even at the late stage of the disease. Similar to what we have previously discussed, it appears that the current transgenic models of AD do not replicate the patterns of microglia activation in human AD. Many potential treatments identified in rodents have failed in human clinical trials. To narrow this translational gap, it is essential to investigate and acknowledge species similarities and differences. With the promises of stem cell therapy and use of iPSCs to model diseases in a dish, pharmacological manipulation on a more directly available human source may reveal further species differences.

Other Potassium Channels

Recent evidence has suggested that two-pore domain K^+ (K2P) channels may play a role in microglia physiology (Madry et al., 2018). Functional investigations provide data to support the involvement of THIK-1 in the cytokine release of microglia *in situ*. This study revealed two functionally and

mechanistically distinct modes of microglial motility. THIK-1 regulates microglial ramification, surveillance and interleukin-1β release (Madry et al., 2018). This is the first study of its kind to implicate K2P channels in microglia physiology. Future work will provide a better understanding of its role *in vivo* as well as neuro-inflammatory responses. The impairment of motility of microglial processes that occurs in some pathological conditions, e.g., in models of Alzheimer's disease with Aβ plaque deposition (Koenigsknecht-Talboo et al., 2008; Krabbe et al., 2013; Condello et al., 2015) raises the question of whether the dependence of surveillance on THIK-1 activity can be employed therapeutically for the treatment of AD (Madry et al., 2018). Currently there has been no direct experimental evidence linking THIK-1 to AD.

Another important K$^+$ channel that has been shown to play a key role in microglia activation by modulating Ca^{2+} signaling and membrane potential is calcium-activated KCa3.1 (also known as IK1, SK4 or KCNN4) channels (Maezawa et al., 2012). This channel is predominantly expressed in microglia and has been a potential target for both industry and academia as a potential drug target for AD (as reviewed by Maezawa et al., 2012).

The strong inwardly rectifying K$^+$ (Kir) channel belong to a family of K$^+$ channels that have only two membrane-spanning domains and are responsible for stabilization of the resting membrane potential (V_{rest}) near to the K$^+$ equilibrium potential (E_K) (Kettenmann et al., 1990; Tsai et al., 2013). Blocking Kir channels depolarizes the cell and decreases the driving force for inwardly transported Ca^{2+} in microglia. In a study by (Tsai et al., 2013), addition of the AD drug memantine suppressed Kir as well as depolarized the membrane potential of BV-2 cells. This block of Kir2.1 channels could represent one of the important mechanisms underlying its actions on the functional activities of microglial cells. It remains unclear what the *in vivo* function of Kir are, an area showing significant promise for AD.

Interestingly, in the transgenic mouse model of AD (5xFAD) (Wendt et al., 2017) reported that the impairment in phagocytic function of microglia was due to altered purinergic signaling. They found evidence of altered physiological phenotype only of microglia in 5xFAD mice that were located close to Aβ plaques (Wendt et al., 2017). Supporting the idea that functional and pathological alterations of microglia in AD may be a consequence of their association with Aβ plaques. Their detailed study on the 5xFAD model revealed an initial induction of Kir current, followed by subsequent activation of outwardly rectifying currents at a later age. Therefore the induction of Kir current could be considered a first response followed up with outward K$^+$ current developing at a later stage of microglial activation, similar to their previous studies (Boucsein et al., 2000; Kettenmann et al., 2011). This data supports the fact that microglia can undergo chronic changes in physiological properties in a disease model over a prolonged period. It appears from the literature that Kv1.3, KCa3.1, and Kir 2.1 inhibitors seem to constitute relatively general anti-inflammatory effects and it could therefore be useful to preferentially target detrimental pro-inflammatory microglia functions associated with neuro-inflammation, such as AD (Nguyen et al., 2017b). A more recent study

investigated the effects of Aβ plaque-dependent morphological and electrophysiological heterogeneity of microglia in the AD mouse model, TgCRND8. Plescher et al. (2018) revealed increased K$^+$ currents in plaque-associated but not plaque distant microglia. They believe that this electrophysiological heterogeneity is likely to reflect the different functional states of the microglia in TgCRND8 (Plescher et al., 2018). Their finding that outwardly rectifying currents (Kv 1.3) were confined to a subset of plaque associated microglial cells emphasizes the potential of specific ion channel inhibitors to target only specific (i.e., detrimental) subtypes of microglia in AD (Plescher et al., 2018).

VOLTAGE-GATED SODIUM CHANNELS

Sodium voltage channels (NaV) are formed of one pore-α-subunit associated with one/more β-subunits. The α-subunit acts as the "voltage sensor" being activated by changes in membrane potential (Payandeh et al., 2011). The β-subunits have multiple roles, from modulating channel gating and regulating channel expression, to interacting with the cytoskeleton and the extracellular matrix, as cell adhesion molecules (Brackenbury and Isom, 2008). It is now known that there are nine pore forming α-subunits of sodium channels, Nav1.1-Nav1.9, encoded by genes SCN1A-SCN11A (Catterall et al., 2005), which associate with one or more non-pore-forming β- subunits encoded by SCN1B-SCN4B (Brackenbury and Isom, 2011). In addition to being expressed in cells capable of generating action potentials, sodium channels have also been identified in cells that have not traditionally been considered to be electrically excitable ("non-excitable cells"), leading to speculation as to their functional role (Pappalardo et al., 2016). Sodium channels contribute to multiple, varied cellular functions in these cells including phagocytosis (Carrithers et al., 2007), migration (Kis-Toth et al., 2011), and proliferation (Wu et al., 2006). Voltage-gated sodium channels have been documented in immune cells such as macrophages (Schmidtmayer et al., 1994; Carrithers et al., 2007, 2009, 2011; Black et al., 2013).

Patch-clamp recordings have since confirmed the expression of functional sodium channels in microglia (Korotzer and Cotman, 1992; Nicholson and Randall, 2009; Persson et al., 2014). A number of voltage-gated ion channels have been identified in microglia, in particularly, voltage-gated Na$^+$ channels isoforms (VGSC): Nav1.1, Nav1.5, and Nav1.6 (Craner et al., 2005; Black and Waxman, 2012).

In vitro, microglia derived from mixed glial cultures from neonatal rats, exhibit immunolabeling for Nav1.1, Nav1.5, and Nav1.6, which is most prominent, while Nav1.2, Nav1.3, Nav1.7, Nav1.8, and Nav1.9 are not detectable above background levels (Black et al., 2009). Whole-cell voltage clamp experiments on cultured rat microglia revealed that, depolarization-induced sodium currents were elicited and then completely blocked by 0.3 μM TTX, consistent with the presence of functional TTX-S sodium channels (Persson et al., 2014). Similarly, microglia within normal CNS tissues exhibit low levels of Nav1.6 immunolabeling *in situ* (Black and Waxman, 2012).

There is a handful of electrophysiological studies of cultures of human microglia derived from native tissue which reports the presence of Na^+ currents (Nörenberg et al., 1994b; Nicholson and Randall, 2009), however, these are not observed in every laboratory (McLarnon et al., 1997). Na^+ currents have also been reported in rat microglia (Korotzer and Cotman, 1992). A study in mice provides evidence that Nav1.6, plays a central role in the infiltration and phagocytosis of microglia in experimental autoimmune encephalomyelitis. Furthermore, the same channel is reported to be up-regulated in macrophages and microglia in the lesions of multiple sclerosis patients (Craner et al., 2005). To date there is no direct evidence for the involvement of microglial VGSC in AD. This same group, however, also report the presence of Nav1.1 and Nav1.5 in cultured rat microglia and demonstrate their function in many key microglial processes (Black et al., 2009). Although Aβ is a known activator for microglia, treatment of the human microglial cell line with Aβ (12 h, 10 μM) there was no significant change in Na^+ current or Nav1.5 expression (Nicholson and Randall, 2009). Although there is clear involvement for VGSC in microglial function its role in AD remain less well defined. This could be due to a number of different contributing factors such as species variation, individual laboratory protocols, as well as non-standardized preparation of exogenous Aβ and Aβ species selection.

TRANSIENT RECEPTOR POTENTIAL CHANNELS

Transient receptor potential (TRP) channels are non-selective, non-voltage gated cation channels, ubiquitously expressed in mammalian cells. The TRP gene was initially discovered in Drosophilla where mutant gene expressing animals showed impaired vision due to dysregulated Ca^{2+} influx into photoreceptor cells. TRP channels play important physiological role in cells by their regulation of temperature, chemoception, mechanoception, and nocioception. There are 30 known members of the mammalian superfamily, which can be divided up into six subfamilies, based on amino acid sequence homology. These are: TRPA (Ankyrin); TRPC (Canonical); TRPM (Melastatin); TRPML (Mucolipin); TRPP (Polycystin); and TRPV (Vanilloid). TRP channels are tetramers made of monomeric subunits that include a six trans-membrane (TM) domain with a pore-forming loop between TM 5 and 6. In addition, their C- and N-termini are intracellular. Functionally, they act by changing cytoplasmic free Ca^{2+} concentrations via Ca^{2+} permeable pore or by modulating ionic movement via changes to the membrane potential. Microglia are evidenced to express some TRP subfamily members, including those of the TRPC, TRPM, and TRPV families.

TRPA

The smallest of the TRP subfamilies. Its only mammalian member is TRPA1, a mechano- and chemo-sensor. Its name is derived from the 14 N-terminal ankyrin repeats. To date there is no evidence that it is present in microglia, although it's

silencing in dorsal root ganglion results in reduced microglia activation following hyperalgesia (Meotti et al., 2017). Similarly, there is no evidence of the presence of TRPML nor TRPP channels being expressed in nor influencing function of microglia.

TRPC

The TRPC subfamily consists of seven homologs (C1-7), with TRPC2 being exclusively expressed in mouse. TRPC members share a structural motif in the COOH-terminal tail, TRP box, located close to the intracellular border of TM6. In addition, they contain three or four N-terminal ankyrin repeats.

TRPC channels are activated via the stimulation of GPCRs and receptor tyrosine kinases, leading to phospholipase C, inositol 1,4,5-triphosphate, and diacylglycerol production. This stimulation results in a biphasic Ca^{2+} release with a first phase ER release, followed by sustained Ca^{2+} influx across the membrane. TRPC channels are known mostly as store operated Ca^{2+} entry (SOCE) mediators.

In microglia, all seven members have shown RNA expression in *in vitro* cell line models, although only C1 and C3 have been reported *in vivo*. TRPC1 is a non-selective Na^+/Ca^{2+} permeable channel with known function in cell survival and proliferation. Their expression is commonly on organelle membranes such as ER and intracellular vesicles. TRPC1 negatively regulates the ORAI1 Ca^{2+} channel resulting in suppression of NKkB, JNK and ERK1/2 signaling from microglia (Sun et al., 2014).

TRPC3 is widely expressed in the CNS where it has modulation via the growth factor BDNF to induce axonal guidance, neuronal survival, and postsynaptic glutamate transmission. In microglia, pre-treatment with BDNF inhibits NO and TNF-α upregulation, via sustained Ca^{2+} influx through upregulated TRPC3 channels at the plasma membrane. Effects were reversed using the siRNA against TRPC3 (Mizoguchi et al., 2014).

TRPM

The TRPM subfamily has eight mammalian members. Unlike TRPA/C there are no N-terminus anykin repeats, instead having functional protein domains, in addition to the TRP box, in the C-terminus. TRPM's are non-selective cation channels with a verity of cellular functions including temperature sensing, osmolarity, redox, Mg^{2+} homeostasis, proliferation, and cell death. These channels can be subdivided further into four groups: M1/3; M4/5; M6/7; M2/8. M1, 2, 4, and 7 have all been reported as present in microglia.

TRPM1 was the first to be cloned, in 1998 (Harteneck, 2005), however its function and activation remains unknown. TRPM1 has a high capacitance for splice variance, similarly so with TRPM3-with whom M1 shares strong sequence homology. In murine models of AD (5XFAD/MHCII+) high levels of Aβ plaque burden correlated to an increase in TRPM1 gene expression compared to age matched control animals (Yin et al., 2017).

M2 contains an adapted adenosine 5$'$-diphosphoribose ribose (ADPR)-recognizing Nudix box domain at its c-terminus. It is a redox modulator, activated by reactive oxygen species,

ADP ribose, NAD$^+$ and Ca^{2+}. M2 will mediate the release of lysosomal Zn^{2+} stores in response to reactive oxygen species, leading to increased cytosolic Zn^{2+} levels, leading to regulation of cell motility and actin remodeling. Additionally, Ca^{2+} influx via TRPM2 leads to increased intracellular insulin release in pancreatic β-cells (Uchida et al., 2011). A number of studies, both *in vitro* and *in vivo* confirm TRPM2 expression and activity in microglia.

In a TRPM2 KO mouse model, microglia show an abolishment of Ca^{2+} influx after LPS or IFNγ stimulation. Activation by these stimuli results in Pyk2-mediated activation of p38 MAPK and JNK signaling as well as an increase in nitric oxide production (Miyake et al., 2014). Similarly studies of MCAO-induced hypoxia in TRPM2 KO mice saw reduced MG activation, reduced cytokine expression and increased brain volume after damage (Huang et al., 2017). Lastly, TRPM2 channels are functionally expressed in the murine microglia cell line BV2. Here these channels have been shown to be involved in LPC-induced p38 MAPK phosphorylation. LPC-induced intracellular Ca^{2+} increase and inward currents dependent on TRPM2 channels (Jeong et al., 2017).

TRPM4 are non-selective cation channels with a greater affinity for Na^{2+} over Ca^{2+}. TRPM4 are activated by increased intracellular Ca^{2+} due to changes in cell membrane potential, ATP, PKC-dependent phosphorylation and calmodulin (CaM) binding to the channels C-terminal CaM domain (Nilius et al., 2005). Functional channels were detected in the mouse primary microglia, both quiescent and active. Here they are thought to mediate membrane depolarisation, in correlation to Ca^{2+} influx (Beck et al., 2008). Sulfonylurea receptor 1 activates TRPM4 channels in mouse primary microglia. Receptor binding regulates NOS and NO transcription on microglia activation via LPS action at TLR4 (Kurland et al., 2016).

TRPM7, like TRPM6, is a channel-enzyme. It is Mg^{2+}, Zn^{2+}, and Ca^{2+} permeable with a strong outward rectifying current-voltage relationship. In addition to its ionic pore, it contains a tyrosine kinase domain on its N-terminal. Activity at both pore region and kinase domain are implemented to be involved in the channels activity. For example, in rat brain microglia there is a strong increase of intracellular Mg^{2+} via the channel, however the currents generated were kinase activity-dependant and not due to pore, nor cell, activation (Jiang X. et al., 2003). TRPM7 also plays a role in cell motility. Migration and invasion of M1 (pro-apoptotic) microglia was observed in rat primary and MLS-9 microglia after priming with LPS (Siddiqui et al., 2014). In addition, flow cytometry and Ca^{2+} imaging studies in neonatal mouse microglia saw an increase in intracellular Ca^{2+} with cell activation by PolyI:C. Increased Ca^{2+} led to a correlated increase in TNFα and P38, in a TRPM7-dependent manner.

TRPV

The final sub-family are the vanilloids, the largest (1-6) and most in depth studies of the TRP channel families. All TRPVs are highly selective to Ca^{2+}. The most well-known is TRPV1 for its actions as a thermosensor (temperatures >43C). V1 mediates heat response and inflammation in addition to nociceptive responses to capsaicin, the main "heat" compound of chili

peppers. In addition, application of compounds with a pH <5.9 will shift the temperature gated threshold of these channels to 20–23 C. Heat-mediated activation is shared quality with other TRPV members, specifically 2, 3, and 4. However, these channels are insensitive to capsaicin and pH. V5 and V6 are not thermosensors but have enhanced selectivity to Ca^{2+} over other monovalent cations. Lastly, all TRPV channels are functionally regulated by their insertion, or retention to the plasma membrane.

TRPV1 has a high protein expression in microglia, with the majority of these channels showing co-localisation to organelles including the golgi, ER, lysosomes, and mitochondria. Interestingly, at resting state there is very little expression at the plasma membrane (Miyake et al., 2015). In a model of rat spinal cord injury, activation of TRPV1 channels, via I.V injection of capsaicin, gave increased expression of SOD1 and pro-inflammatory cytokines from spinal microglia (Talbot et al., 2012). Similar influence on pro-inflammatory markers were observed in retinal microglia where activation of TRPV1 resulted in increased IL-6 and NFkB expression (Sappington and Calkins, 2008). Expression of TRPV1 protein and function was confirmed in HMO6 human microglial cell line. Application of capsaicin resulted in increased intracellular Ca^{2+}, and subsequently cytochrome C and cleaved caspase 3 release (Kim et al., 2006). Together this suggests a strong role of TRPV1 in the pro-inflammatory profile of microglia.

Little is known about the other TRPV channels in microglia, although an RNA-based analysis by Raboune et al. (2014). showed upregulation of TRPV1-4 in BV2 cells following cell activation by N-acyl amide.

Microglial TRP Channels in AD

Aβ accumulation, one of the major hallmarks of AD, commonly results in excitotoxicity and cell death via the disruption of normal Ca^{2+} homeostasis and release of pro-inflammatory factors such as ROS, NO, and cytokine release. The previous section highlights the role of TRP channels in intracellular Ca^{2+} regulation as well as differentially switching the phenotype of microglia between M1 (pro-apoptotic) and M2 (pro-survival). Despite this there is little research into glial TRP channel activity in AD, with most of the focus being on neuronal responses.

Aβ treatment of BV-2 cells gave an upregulation of protein and mRNA for TRPC6 that is dependent on NFkB activity. When these cells had TRPC6 knocked down via siRNA, the condition media was neuroprotective to cultured hippocampal cells compared to sham BV2 cells. Neuronal influence of TRPC6 activates via an upregulation of COX2 downstream (Liu et al., 2017). By using familial AD mouse models- APP23 and 5XFAD, plaque associated microglia from these animals were homogenized and run through flow cytometry to observe upregulated genes. From these TRPM1 was pulled out, however its role in AD remains unclear (Yin et al., 2017). BV2 cells treated with either fibrillary or soluble Aβ saw high levels of ROS which was attenuated with simultaneous application of TRPV1 via I-RTX (Schilling and Eder, 2011).

CALCIUM CHANNELS

Plasma membrane calcium channels are subdivided into three main groups according to their manner of activation; the voltage-gated calcium channels (VGCCs), the store-operating calcium channels (SOCs) and the receptor-operated calcium channels (ROCs). VGCCs specifically, play a vital role in maintaining calcium homeostasis, with important roles in cellular processes such as neurotransmission, control of gene expression, hormone secretion and cell apoptosis (Ertel et al., 2000; Valerie et al., 2013). Therefore, developing therapeutics that target these channels may be of benefit in treating various diseases of the CNS, such as AD. Structurally VGCCs consists of the α1 pore-forming subunit consisting of four transmembrane domains, the cytoplasmic β subunit, the peripheral α2δ and occasionally the γ accessory subunit (Ertel et al., 2000). VGCCs are divided into subfamilies according to their pore-forming subunit; the high voltage-activated channels known as Cav1 (Cav1.1-1.4) and Cav2 (Cav2.1-2.3), and the low voltage-activated Cav3 channels (Cav3.1-3.3) (Ertel et al., 2000).

Voltage-Gated Calcium Channels

To date, evidence suggesting the existence of microglial VGCCs and their involvement in AD is limited. Although numerous studies, mainly via electrophysiology and Fura-2 calcium imaging, have proven that various agents such as Aβ, ATP, and K^+, cause an increase in intracellular Ca^{2+}, the mechanism by which this phenomenon occurs is still under debate (Korotzer et al., 1995; McLarnon et al., 1999; Valerie et al., 2013). Thus, there is no clear indication of the existence of microglial VGCCs or whether the increase in intracellular Ca^{2+} is due to other factors such as ion exchange transporters or opening of intracellular stores (Korotzer et al., 1995; McLarnon et al., 1999; Valerie et al., 2013).

The majority of human studies, have investigated the presence and functionality of VGCCs in human glioblastoma cell lines, consisting of a mixed culture of glial cells, including astrocytes and microglia. Therefore, a major limitation of human *in vitro* studies, is that identifying VGCCs in glioblastoma cells does not necessarily indicate the presence of these channels in microglia. For instance, Valerie et al. (2013), demonstrated that pharmacological inhibition via the calcium channel blocker (CCB) mibefradil, or siRNA-induced downregulation of the Cav3 channel (T-type current) in human glioblastoma cell lines, led to cell apoptosis. Additionally, Nicoletti et al. (2017) demonstrated that Cav2.1 and Cav2.2 are involved in glial proliferation, through using of pharmacological tools (Nicoletti et al., 2017). Furthermore, via the use of an Iba-1 antibody, a marker of inflammation, and immunohistochemistry, in an *in vivo* rodent glioblastoma model (GL261 glioma cells), it was revealed that the degree of Iba-1 positive microglia had increased following N-type inhibition. This highlights a role of microglial VGCCs not only in cell proliferation and microglial survival, but also in inducing their pro-inflammatory action (Nicoletti et al., 2017). Evidence from human glial cells, demonstrates that VGCCs are expressed in human microglia, and that microglia VGCCs may also have

a role in neurotoxicity (Hashioka et al., 2012). Prior to 48-h treatment with LPS and IFN-γ to induce inflammation, primary human microglial cells were treated with the L-type blocker nimodipine, significantly reducing neuronal toxicity induced by the microglia (Hashioka et al., 2012). In contrast to other studies, Hashioka et al. (2012) provided more conclusive evidence in indicating the presence of microglial VGCCs due to the use of primary human microglia and not a cell line consisting of a mixed glial population. A 1999 study demonstrated a more direct involvement of microglia VGCCs with progression of AD by investigating how $Aβ_{25-35}$ alters Ca^{2+} signaling in human microglia (Silei et al., 1999). Incubation with Aβ caused an increase in microglia proliferation and additionally an increase in intracellular Ca^{2+} levels (Silei et al., 1999). As no significant increase in microglial intracellular Ca^{2+} levels were observed when microglia were incubated in Ca^{2+} -free media, it was suggested that this change was due to VGCC-mediated Ca^{2+} influx (Silei et al., 1999). This was verified via co-incubation of microglia with Aβ and the CCBs verapamil, nifedipine and diltiazem which lead to a half-reduction in intracellular levels (Silei et al., 1999). Moreover, incubation of peptide-treated microglia with nifedipine not only lead to a reduction in intracellular Ca^{2+}, but also significantly prevented the increase in microglia proliferation induced by the peptide. Therefore, this study proposes that Aβ has the ability to increase microglia number and also induce their activation and consequently inflammatory action, through a VGCC manner (Silei et al., 1999).

In contrast to human studies, the majority of studies using animal models, have not provided conclusive evidence to indicate the existence and activity of VGCCs in microglia (Toescu et al., 1998; Silei et al., 1999).

A possible explanation for this, could be that microglial VGCC expression and activity is species-dependent. For instance, studies have shown that rodent microglia can express very low levels of VGCC activity which may even remain undetected (Toescu et al., 1998). Toescu et al. (1998), demonstrated that adding ATP to microglia isolated from murine cortex lead to a significant increase in intracellular Ca^{2+} levels. In contrast, KCl induced microglial depolarisation, did not lead to an increase in intracellular Ca^{2+} thus it was proposed that increased Ca^{2+} levels involved VGCC independent pathway (Toescu et al., 1998). Prolonged elevation in intracellular Ca^{2+} levels can activate pathways involved in regulation of gene expression such as the Ca^{2+}-calmodulin pathway, and therefore altered Ca^{2+} signaling in microglia may occur as a pathway for microglia activation and may even induce the progression of various pathological conditions such as AD (Toescu et al., 1998).

Although the majority of animal model studies have not definitively proven the existence of the channels in microglia, a few were able to provide some evidence indicating their existence. In a study carried out in 2014 by Saeugusa and Tanabe, where rodent lines were created where expression of Cav2.2 was suppressed, they indicated dynamic modulation of microglia Cav2.2 in regulation of pain related behavior. (Saegusa and Tanabe, 2014). Saeugusa and Tanabe also highlight neuronal

and microglial crosstalk, in controlling response to pathology (Saegusa and Tanabe, 2014). A more recent study investigated how microglial activation, verified by immunostaining and morphological changes, alters the activity of the L-type currents in an *in vivo* animal model for neurodegeneration, and in the *in vitro* BV2 cell line (Espinosa-Parrilla et al., 2015). Comparison of microglia before and after LPS and IFNγ stimulation revealed differences as seen via immunostaining and molecular approaches such as western blotting and PCR (Espinosa-Parrilla et al., 2015). Additionally, as depolarisation of LPS/IFNγ treated microglia demonstrated changes in intracellular Ca^{2+} by treatment with either nifedipine or Bay K8644 (agonist), it was suggested that VGCCs, may form part of the mechanism involved in the activation of microglia, inducing their pro-inflammatory action (Espinosa-Parrilla et al., 2015).

To summarize, even though human microglia studies have proposed the existence of functional VGCCs, the majority of the studies were carried out in mixed glial cell lines. Additionally, animal studies have either demonstrated very low expression of VGCCs in microglia or were not able to prove their existence, either at a functional or expression level (protein and mRNA). Thus, due to the limited and contradicting evidence on human and rodent microglial VGCC existence, the use of human induced pluripotent stem cells (iPSCs) may allow a more effective study of microglial ion channel role in neuro-inflammation observed in neurodegenerative diseases such as AD.

CHLORIDE CHANNELS

Chloride channels are a diverse superfamily of channels proteins, incorporating the volume regulated chloride channels, the ClC proteins, Ca^{2+} activated chloride channels, CFTR and maxi chloride channels (Alexander et al., 2017). Studies have identified Cl^- channels in rat (Visentin et al., 1995; Schlichter et al., 1996), bovine (McLarnon et al., 1995) and human microglia (McLarnon et al., 1997). These have mainly been based on pharmacological studies using a range of Cl^- channel blockers (e.g. nifluemic acid). Pharmacological modulation of Cl- channels indicates a role for in the regulation of microglia process outgrowth (Hines et al., 2009). However, the lack of specific pharmacological tools has hindered our progress in identifying specific channel entities, and indeed their contribution to microglia physiology. This is backed up with a lack of experimental evidence as to the molecular identity of the channels that have been suggested to be responsible for experimental observations. While the molecular identity remains to be resolved, evidence indicates that is a similar fashion to Cl^- currents within lymphocytes, microglia Cl^- conductance are responsive to stretch (Lewis et al., 1993; Steinert and Grissmer, 1997). Interestingly CLIC1 an intracellular chloride channel has received some attention with relation to amyloid pathology (Novarino et al., 2004; Milton et al., 2008; Paradisi et al., 2008). This suggests a role for modulation of chloride conductances in microglial generation of reactive oxygen species, but robust evidence for this is lacking in relevant *in situ* models of microglia.

VOLTAGE GATED PROTON CHANNELS (HV1)

Voltage-gated proton channels (H_v1; Alexander et al., 2017) reportedly consist of 4 proton sensitive transmembrane domains which are sensitive to both membrane depolarisation and transmembrane pH gradient (DeCoursey, 2008; Capasso et al., 2011). There is widespread expression of these channels within the central nervous system, highlighting both regional and cellular variation (Eder et al., 1995; McLarnon et al., 1997). Functional evidence comes from both studies carried out on murine microglia (Eder et al., 1995; Klee et al., 1998, 1999), rat (Visentin et al., 1995), and human microglia (McLarnon et al., 1997). There is also evidence to link Hv1 to both microglia polarity and brain responses to stroke (Wu et al., 2012; Tian et al., 2016). This could be pertinent given the link between hypoxia and Alzheimer's disease (Peers et al., 2007). However, one drawback from these studies is the use of culture preparations. This is pertinent given that work on brain slices was unable to detect any H^+ conductance *in situ* (De Simoni et al., 2008). This again raises the question about membrane properties in cultured preparations in contrast to *in situ* set ups. In addition there are questions around the physiological role of these channels when present in microglia (Eder and Decoursey, 2001) It is well established that microglial reactive oxygen species contribute to neuronal cell death in AD (see review Block et al., 2007). This process likely involved the build-up of protons within microglia, which will impact on the flux through Hv1 channels. However, a direct demonstration of the involvement of H_V1 in this process is lacking. There is greater evidence to indicate the involvement of other channels (e.g., Kv1.3) which are discussed elsewhere in this article.

MODELING MICROGLIAL INVOLVEMENT

To fully understand a disease and its etiology it is necessary that extensive modeling takes place. By tradition this has been through the use of a number of different model systems including both animal (murine) models and primary patient cell lines. Currently in AD research there is a large focus on the use of animal models, particularly transgenic mice (McGowan et al., 2006), as a lot is understood about their genetics and the availability of well-characterized genetic manipulation techniques in this organism. Not only this, mice are more closely phylo-genetically related to humans than other model systems such as *Caenorhabiditis elegans* or *Drosophila melanogaster*. The genetic similarities between humans and mice means that they have utility in studying the familial aspect of AD by using transgenic mice that contain mutations in the APP and PSEN genes. There are over 100 different transgenic mouse models available to study the familial aspect of AD, with some models containing five different mutations in the APP and PSEN genes (Oakley et al., 2006).

As it is widely accepted that Aβ plaques and neurofibrillary tangles cause neuro-inflammation, models which overexpress mutant human versions of APP have been shown to present

microglial activation (Bornemann et al., 2001; Wright et al., 2013). In addition to this it was shown that there were significant increases in CD38-positive microglia before Aβ deposition which also correlated with neuronal cell death in the CA1 region of the hippocampus (Wright et al., 2013). The inflammatory processes of in another APP mouse model, Tg2576, were investigated by looking at individual microglial cells using *in vivo* multiphoton imaging. Meyer-Luehmann and his colleagues showed that Aβ plaques can form within days and once formed it only takes 1–2 days before microglial cells begin to aggregate around the depositions. Alongside this accumulation of microglia is accompanied by changes to neurite morphology (Meyer-Luehmann et al., 2008). Whilst these have their advantages, they also have a number of limitations. These types of models do not accurately recapitulate human pathology as they do not develop the robust tauopathy or neuronal cell death that is seen in human disease without the addition of extra transgenes such as tau (Ribé et al., 2005).

The triple-transgenic model of AD, which contains the APP_{SWE}, Presenilin-1 ($PSEN_{M146V}$) and tau mutations (tau_{P301L}) offers the advantage that they develop Aβ plaques, tau tangles, synaptic dysfunction and LTP deficits which all manifest in an age-related manner (Oddo et al., 2003). Janelsins et al. demonstrated that this model shows a 14.8 fold increase of TNF-α and 10.8 fold increase in MCP-1 mRNA in 6 month old triple transgenic mice when compared to 2 month old mice. However these increases were only seen in the entorhinal cortex and could not be replicated in the hippocampus, suggesting that different cell types or environments may be responsible for the differential transcript levels and inflammatory responses in these disease relevant brain regions (Janelsins et al., 2005).

Mouse models containing just tau mutations have also been investigated in terms of neuro-inflammatory response and they too also display microglial changes (Wes et al., 2014; Cook et al., 2015). For example, the P301S tau model whose neurons develop bundles of hyperphosphorylated tau also have significant increases in inflammatory molecules such as IL-1β and COX-2 within the tau-positive neurons. Alongside this they also demonstrated that there were activated microglia throughout the brain and spinal cord, but that these microglia could be predominantly found surrounding the tau-positive neurons (Bellucci et al., 2004). Interestingly, this microglial activation was shown to begin before neurofibrillary tangle formation, but could be ameliorated using an immunosuppressive drug, FK506, early in life increasing life span and attenuating tau pathology (Yoshiyama et al., 2007). One important thing to bear in mind that mutations in tau do not cause AD but instead cause frontotemporal dementia. So whilst these models can provide useful information about how mutations in tau can cause cellular dysfunction and neurodegeneration they do not completely replicate AD in terms of other pathological markers (Wolfe, 2012).

Whilst proven useful for modeling autosomal disease, such as the familial form of AD, as previously mentioned, these murine models do not accurately recapitulate AD. A more promising avenue for modeling complex diseases, such as sporadic AD, is through the use of stem cell technology. Embryonic stem cells (ESCs) are derived from the inner cell mass, or blastocyst, of an embryo and can differentiate into any cell in the body (Evans and Kaufman, 1981). Despite their many potential uses, the ethical issues surrounding the use of embryo-derived cells are numerous. However, recent advances in stem cell technology have meant that it is now possible to derive stem cells from differentiated adult cells/tissue. Takahashi et al. showed it was possible to use ectopic transcription factors to induce pluripotency and ESC properties (Takahashi and Yamanaka, 2006). These transcription factors were known for being important in the long term maintenance of ES cell phenotype (Oct3/4 and Sox2) and pluripotency (c-myc and Klf4) (Takahashi and Yamanaka, 2006). These iPSCs are almost identical to ESCs in terms of their characteristics. They are able to differentiate into any cell type in the body, have infinite potential to grow, share the same morphology and have the same expression pattern of genes (Yamanaka, 2009); making them a potentially very powerful tool for complex disease research.

Primary microglia cultures are often used to study neuro-inflammation, they can be derived from rat or mouse brain before birth or early on in development. In addition, human microglia cultures have also been established from fetal brain (McLarnon et al., 1997). One method of generating these cells was developed by Giulian and Baker (1986) and involving a specific process of adhesion and agitation. These cells are often used as they show similarities to microglial cells *in vitro*, however, the process of extraction and culture itself alters microglial phenotype (Caldeira et al., 2014). Given the degree of variability in ion channel distribution during development and aging (Harry, 2013), using this type of model for investigating neurodegeneration is less than ideal. Another method to study microglia is through the use of retroviral-immortalized cell lines, such as the mouse and rat microglial cell lines N9 and BV-2 respectively (Righi et al., 1989; Blasi et al., 1990). These cell lines offer an advantage in the fact that they are fast to grow, and large numbers of cells can be generated quickly. However, as they have been immortalized using oncogenes which means they differ from primary microglia as they have increased adhesion and proliferation and can vary in terms of their morphology (Horvath et al., 2008).

Until recently, being able to generate iPSC-derived microglia has been elusive, with previous attempts being met with skepticism as the microglia were made from induced hematopoietic stem cells (HSCs). HSCs have the potential to give rise to other cell types such as blood derived macrophages and as already stated microglia arise from EMPs. In order to generate EMPs from the iPSCs, Muffat and his colleagues developed a serum free media that contains high levels of IL-34 and colony stimulating factor 1 (CSF1) (Muffat and Li, 2016). These conditions were chosen as the media mimics the brain cerebrospinal fluid and the factors have been shown to be necessary for microglia differentiation and maintenance. Under these conditions they found that the cells soon formed rope-like structures that when plated onto low adherence plates gave rise to highly adherent pluripotent stem cell–derived microglia-like cells (pMGLs). These cells express many of the markers that would be expected from microglia, such as TMEM119, P2RY12/13, HEXB and GPR34. Alongside this they

are also highly phagocytic and gene transcriptomic analysis demonstrated they resemble human primary fetal and adult microglia (Muffat and Li, 2016). This is not the only protocol that has been published which describes the derivation of microglia from iPSCs, subsequently there have been four more protocols released. In fact the next two papers described the generation of iPSC-derived microglia going through a hematopoietic progenitor cell (HPC) stage. Both methodologies use defined media systems that contain a number of growth factors including IL-3, BMP4 and L-ascorbic acid to generate HPCs (Abud et al., 2017; Pandya et al., 2017). Both protocols take about 10 days to generate HPCs at which point they were checked for markers of the hematopoietic lineage such as CD43 before differentiating for a further 2 weeks using another media to form induced microglia like cells (iMGLs). One way in which these protocols differ is that Pandya et al. (2017) co-culture the HPCs with astrocytes to enhance microglial differentiation. This is not the only protocol that uses co-culture to generate iPSC-derived microglia, a paper released by Walter Haenseler also uses co-culture but neuronal microglial co-culture instead (Haenseler et al., 2017).

Whilst iPSC-based models offer a number of advantages to modeling complex diseases there are a number of limitations that should also be considered. Firstly, the cells which are derived from iPSCs have been found to display the functional and epigenetic signatures of fetal neurons and do not maintain the features, such as telomere length and mitochondrial metabolism, of the cells from which they were originally derived (Lapasset

et al., 2011). One of the current major stumbling blocks for iPSC research (control and those derived from patients with specific neurodegenerative disorders), is the lack of standard culturing or differentiation methods (Wen et al., 2016). Resulting in the unavailability of established protocols to generate entirely pure populations of a specific cell type, therefore making cross lab comparisons particularly difficult. However, more recently the availability of human tissue as well as iPSCs have provided new opportunities for academic and industry-based researchers to identify optimal cell types and culture conditions to efficiently generate stable, defined and reproducible cell types for their specific research–with limited variability. Whilst this may not be an issue for some studies, when trying to investigate diseases of aging such as AD it could pose more problems as cells may not show age related phenotypes or degeneration. One way in which it may be possible to overcome this is through maintain and aging the cells in culture for as long as possible.

One of the challenges to date has been modeling sporadic AD in both rodent and human models of disease, with familial AD mutations accounting for only 5–10% of all AD cases (Kim et al., 2017). Excitingly, Lin et al. (2018) describes the first experiments in which CRISPR/Cas9 technology has been used to generate isogenic APOE4 iPSC-derived microglia. In this study the APOE4-like microglia exhibited altered morphology correlating to the reduced Aβ phagocytosis seen in rodent models. They found that consistently converting APOE4 to APOE3 in brain cell types from sporadic AD iPSCs was sufficient to diminish multiple AD-related pathologies (Lin et al., 2018).

TABLE 2 | Comparison of multiple transcriptome studies of regulated microglial genes, relating to ion channels, in models of aging or Alzheimer's disease.

Species	Sample type	Potassium channels	Sodium channels	TRP channels	Calcium channels	Others	Reference
Human	iPSC	KCNA5, KCNK13, KCNN4	SCN5A	TRPM2, TRPM4, TRPM8, TRPV1, TRPV2	CACNA1S	HVCN1, CLIC1	Haenseler et al., 2017
Human	Biopsy primary microglia culture	KCNK13, KCNN1, KCNN4	Not determined	TRPC1, TRPC2, TRPM2, TRPM3, TRPM4, TRPM7, TRPMV1, TRPV2, TRPV4	Not determined	HVCN1, CLIC1	Gosselin et al., 2017
Human	Purified from post-mortem dorsal lateral pre-frontal cortex	KCNN4	Not determined	TRPM2, TRPV2	Not determined	CLIC1	Olah et al., 2018
Human	Purified from post-mortem dorsal lateral pre-frontal cortex	KCNJ2, KCNK13, KCNN4	Not determined	TRPM2, TRPM7, TRPV1, TRPV2	CACNA1A, CACNA1D	HVCN1, CLIC1	Olah et al., 2018
Human	Purified from post-mortem right parietal cortex	KCNK13, KCNN4	Not determined	TRPC2, TRPV2, TRPV4	Not determined	CLIC1	Galatro et al., 2017
Human	Purified from post-mortem right parietal cortex	KCNN4	Not determined	Not determined	CACNA1F	Not determined	Galatro et al., 2017
Mouse	Primary microglia culture	KCNA3, KCNK13, KCNN4	Not determined	TRPM4	CACNA1A, CACNA1D	Not determined	Gosselin et al., 2017
Mouse	Collated Meta-Analysis	KCNA1, KCNA2, KCNN1, KCNN3	Not determined	TRPA1, TRPC1, TRPC3, TRPC4, TRPC6, TRPC7, TRPM3, TRPM8, TRPV1, TRPV6	Not determined	HVCN1	Olah et al., 2018
Rat	Primary microglia culture	KCNK13, KCNN4	Not determined	TRPC4, TRPC6, TRPM2, TRPM4, TRPV1	Not determined	CLIC1	Bohlen et al., 2017

Regulation threshold was set at a 3-fold change over all studies. Anything below this is referred to as not determined.

They also showed that in their iPSC-derived microglia, TREM2 was positively correlated to the APOE4 genotype. This data is consistent with reports showing increased levels of soluble TREM2 in cerebrospinal fluid of AD patients (Heslegrave et al., 2016). Similarly, protocols for microglia differentiated from patients carrying missense mutations in TREM2 (that are causal for frontotemporal dementia-like syndrome and Nasu-Hakola disease). These studies found subtle effects on microglia biology, consistent with the adult onset of disease in individuals with these mutations (Brownjohn et al., 2018). These particular studies establish a reference for human cell-type-specific changes associated with the risk of developing AD, providing critical insight into potential treatments for sporadic AD.

As more is understood about the developmental origin and unique identity of microglia, recent studies have attempted to circumvent this issue by deriving microglia from iPSCs in order to study human and cell-type-specific biology and disease (Muffat et al., 2016; Abud et al., 2017; Douvaras et al., 2017; Haenseler et al., 2017; Pandya et al., 2017; Takata et al., 2017; Brownjohn et al., 2018; Lin et al., 2018). At the whole-transcriptome level, microglia generated by the methods reported here most closely resemble cultured primary microglia (Brownjohn et al., 2018). Due to a lack of unique surface markers, it has historically been difficult to distinguish microglia from other macrophages and cells of myeloid lineage. It is only recently that a distinct transcriptomic profile of microglia has emerged (Hickman et al., 2013; Butovsky et al., 2014; Holtman et al., 2015; Bennett et al., 2016; Gosselin et al., 2017; Keren-Shaul et al., 2017; Krasemann et al., 2017). In this review we have highlighted the similarities between rodent and human microglia transcriptomics and have identified key ion channels prominent in human iPSC-derived microglia, some of which we have already been highlighted earlier in this review as prominent targets associated with AD (**Table 2**) including KCNK13, KCNN4, TRPV2, HVCN1, and CLIC1. Indeed, the ion channels found from iPSC-derived microglia to date mirror those found in aged-human tissue (Olah et al., 2018).

Finally, the characterization of the electrophysiological properties of neurons derived from iPSCs are extremely limited and even fewer reports on the functional properties of iPSC-derived glia (microglia and astrocytes). However, with the development of standardized methods and differentiation protocols and, importantly, broader *functional* characterization of the complex collection of ion channels and receptors expressed in defined glial and neuronal subtypes from iPSCs, their significance in drug discovery and neuroscience will become increasingly valuable.

CONCLUDING REMARKS

Microglial research has expanded dramatically in the last 5 years, this combined with the lack of new therapeutic options for treating complex neurological conditions highlights the potential of these cells to provide a viable alternative. For this to be realized a clearer picture of human microglial physiology needs to be established. The development of iPSC technology has been a great advance in these efforts, but robust protocols are still in their infancy (Douvaras et al., 2017; Haenseler et al., 2017; Brownjohn et al., 2018). With microglia being dependent *in situ* environments the need to generate more complex 3D models is even greater. While the development of 3D scaffolds continues at pace (Saliba et al., 2018), some initial research indicates the possibility of 3D microglia cultures (Cho et al., 2018). The challenge will now be to incorporate the diverse range of cells into these cultures with the ability to provided measurable outcomes (e.g. electrophysiology). Establishing robust and reproducible protocols will also allow us to progress into addressing the role of microglia in pathological states. This is vital if we are to achieve a therapeutic purpose for targeting microglia ion channels.

The role of ion channels is extensive within the central nervous system, however as non-excitable cells microglia channels often get overlooked. Here we have examined the microglia ion channel landscape and the evidence that supports the involvement in Alzheimer's disease pathogenesis. While there is still work to be done as highlighted above, this review indicates that microglia ion channels play a pivotal role in their physiology and can contribute to the fight against dementia.

AUTHOR CONTRIBUTIONS

TK and MD contributed to the initial design and conception of the review. LT, JI, EK, MD, and TK wrote individual sections of the review. TK wrote the first draft of the manuscript. LT and JI prepared figures. TK and LT outlined the tables and compiled final version of manuscript. All authors approved, read and revised final version before submission.

REFERENCES

Abud, E. M., Ramirez, R. N., Martinez, E. S., Healy, L. M., Nguyen, C. H.H., Newman, S. A., et al. (2017). iPSC-derived human microglia-like cells to study neurological diseases. *Neuron* 94: 278–293.e9. doi: 10.1016/j.neuron.2017.03.042

Alexander, S. P., Kelly, E., Marrion, N. V., Peters, J. A., Faccenda, E., Harding, S. D., et al. (2017). The concise guide to pharmacology 2017/18: other ion channels. *Br. J. Pharmacol.* 174(Suppl. 1), S195–S207. doi: 10.1111/bph.13881

Alzheimer'sstatistics (2016). *2016 Alzheimer's Statistics*. AvailableOnline at: http://www.alzheimers.net/resources/alzheimers-statistics/ (Accessed December 13, 2016).

Annunziato, L., Boscia, F., and Pignataro, G. (2013). Ionic transporter activity in astrocytes, microglia, and oligodendrocytes during brain

ischemia. *J. Cereb. Blood Flow Metab.* 33, 969–982. doi: 10.1038/jcbfm.2013.44

Arnoux, I., Hoshiko, M., Mandavy, L., Avignone, E., Yamamoto, N., and Audinat, E. (2013). Adaptive phenotype of microglial cells during the normal postnatal development of the somatosensory "Barrel" cortex. *Glia* 61, 1582–1594. doi: 10.1002/glia.22503

Arnoux, I., Hoshiko, M., Sanz Diez, A., and Audinat, E. (2014). Paradoxical effects of minocycline in the developing mouse somatosensory cortex. *Glia* 62, 399–410. doi: 10.1002/glia.22612

Asai, H., Ikezu, S., Tsunoda, S., Medalla, M., Luebke, J., Haydar, T., et al. (2015). Depletion of microglia and inhibition of exosome synthesis halt tau propagation. *Nat. Neurosci.* 18, 1584–1593. doi: 10.1038/nn.4132

Atagi, Y., Liu, C. C., Painter, M. M., Chen, X. F., Verbeeck, C., Zheng, H., et al. (2015). Apolipoprotein E is a ligand for triggering receptor

expressed on myeloid cells 2 (TREM2). *J. Biol. Chem.* 290, 26043–26050. doi: 10.1074/jbc.M115.679043

Beck, A., Penner, R., and Fleig, A. (2008). Lipopolysaccharide-induced down-regulation of Ca^{2+} release-activated Ca^{2+} currents (I CRAC) but not Ca^{2+}-activated TRPM4-like currents (I CAN) in cultured mouse microglial cells. *J. Physiol.* 586, 427–439. doi: 10.1113/jphysiol.2007.145151

Becker, K. J. (2016). Strain-related differences in the immune response: relevance to human stroke. *Transl. Stroke. Res.* 7, 303–312. doi: 10.1007/s12975-016-0455-9

Bellucci, A., Bugiani, O., Ghetti, B., and Spillantini, M. G. (2011). Presence of reactive microglia and neuroinflammatory mediators in a case of frontotemporal dementia with P301S mutation. *Neurodegener. Dis.* 8, 221–229. doi: 10.1159/000322228

Bellucci, A., Westwood, A. J., Ingram, E., Casamenti, F., Goedert, M., and Spillantini, M. G. (2004). Induction of inflammatory mediators and microglial activation in mice transgenic for mutant human P301S tau protein. *Am. J. Pathol.* 165, 1643–1652. doi: 10.1016/S0002-9440(10)63421-9

Bennett, M. L., Bennett, F. C., Liddelow, S. A., Ajami, B., Zamanian, J. L., Fernhoff, N. B., et al. (2016). New tools for studying microglia in the mouse and human CNS. *Proc. Natl. Acad. Sci. U. S. A.* 113, E1738–E1746. doi: 10.1073/pnas.1525528113

Bertram, L., Lange, C., Mullin, K., Parkinson, M., Hsiao, M., Hogan, M. F., et al. (2008). Genome-wide association analysis reveals putative Alzheimer's disease susceptibility loci in addition to APOE. *Am. J. Hum. Genet.* 83, 623–632. doi: 10.1016/j.ajhg.2008.10.008

Black, J. A., Liu, S., and Waxman, S. G. (2009). Sodium channel activity modulates multiple functions in microglia. *Glia* 57, 1072–1081. doi: 10.1002/glia.20830

Black, J. A., Newcombe, J., and Waxman, S. G., (2013). Nav1.5 sodium channels in macrophages in multiple sclerosis lesions. *Mult. Scler.* 19, 532–542. doi: 10.1177/1352458512460417

Black, J. A., and Waxman, S. G. (2012). Sodium channels and microglial function. *Exp. Neurol.* 234, 302–315. doi: 10.1016/j.expneurol.2011.09.030

Blasi, E., Barluzzi, R., Bocchini, V., Mazzolla, R., and Bistoni, F. (1990). Immortalization of murine microglial cells by a v-raf/v-myc carrying retrovirus. *J. Neuroimmunol.* 27, 229–237. doi: 10.1016/0165-5728(90)90073-V

Block, M. L., Zecca, L., and Hong, J. S. (2007). Microglia-mediated neurotoxicity: uncovering the molecular mechanisms. *Nat. Rev. Neurosci.* 8, 57–69. doi: 10.1038/nrn2038

Boche, D and Nicoll, J. A. (2010). Are we getting to grips with Alzheimer's disease at last? *Brain* 133, 1297–1299. doi: 10.1093/brain/awq099

Bohlen, C. J., Bennett, F. C., Tucker, A. F., Collins, H. Y., Mulinyawe, S. B., and Barres, B. A. (2017). Diverse requirements for microglial survival, specification, and function revealed by defined-medium cultures. *Neuron* 94, 759–773.e758. doi: 10.1016/j.neuron.2017.04.043

Bordey, A., and Spencer, D. D. (2003). Chemokine modulation of high-conductance Ca^{2+}-sensitive K^+ currents in microglia from human hippocampi. *Eur. J. Neurosci.* 18, 2893–2898. doi: 10.1111/j.1460-9568.2003.03021.x

Bornemann, K. D., Wiederhold, K. H., Pauli, C., Ermini, F., Stalder, M., Schnell, L., et al. (2001). Aβ-Induced inflammatory processes in microglia cells of APP23 transgenic mice. *Am. J. Pathol.* 158, 63–73. doi: 10.1016/S0002-9440(10)63945-4

Boucsein, C., Kettenmann, H., and Nolte, C. (2000). Electrophysiological properties of microglial cells in normal and pathologic rat brain slices. *Eur. J. Neurosci.* 12, 2049–2058. doi: 10.1046/j.1460-9568.2000.00100.x

Boucsein, C., Zacharias, R., Farber, K., Pavlovic, S., Hanisch, U. K., and Kettenmann, H. (2003). Purinergic receptors on microglial cells: functional expression in acute brain slices and modulation of microglial activation *in vitro*. *Eur. J. Neurosci.* 17, 2267–2276. doi: 10.1046/j.1460-9568.2003.02663.x

Brackenbury, W. J., and Isom, L. L. (2008). Voltage-gated Na^+ channels: potential for beta subunits as therapeutic targets. *Expert Opin. Ther. Targets* 12, 1191–1203. doi: 10.1517/14728222.12.9.1191

Brackenbury, W. J., and Isom, L. L. (2011). Na channel beta subunits: overachievers of the ion channel family. *Front. Pharmacol.* 2:53. doi: 10.3389/fphar.2011.00053

Brownjohn, P. W., Smith, J., Solanki, R., Lohmann, E., Houlden, H., Hardy, J., et al. (2018). Functional studies of missense TREM2 mutations in human stem cell-derived microglia. *Stem Cell Rep.* 10, 1294–1307. doi: 10.1016/j.stemcr.2018.03.003

Burnstock, G. (2015). Physiopathological roles of P2X receptors in the central nervous system. *Curr. Med. Chem.* 22, 819–844. doi: 10.2174/0929867321666140706130415

Butovsky, O., Jedrychowski, M. P., Moore, C. S., Cialic, R., Lanser, A. J., Gabriely, G., et al. (2014). Identification of a unique TGF-beta-dependent molecular and functional signature in microglia. *Nat. Neurosci.* 17, 131–143. doi: 10.1038/nn.3599

Caldeira, C., Oliveira, A. F., Cunha, C., Vaz, A. R., Falcao, A. S., Fernandes, A., et al. (2014). Microglia change from a reactive to an age-like phenotype with the time in culture. *Front. Cell Neurosci.* 8:152. doi: 10.3389/fncel.2014.00152

Cameron, B., Tse, W., Lamb, R., Li, X., Lamb, B. T., and Landreth, G. E., (2012). Loss of interleukin receptor-associated kinase 4 signaling suppresses amyloid pathology and alters microglial phenotype in a mouse model of Alzheimer's disease. *J. Neurosci.* 32, 15112–15123. doi: 10.1523/JNEUROSCI.1729-12.2012

Capasso, M., Decoursey, T. E., and Dyer, M. J. (2011). pH regulation and beyond: unanticipated functions for the voltage-gated proton channel, HVCN1. *Trends Cell Biol.* 21, 20–28. doi: 10.1016/j.tcb.2010.09.006

Carrithers, L. M., Hulseberg, P., Sandor, M., and Carrithers, M. D. (2011). The human macrophage sodium channel NaV1.5 regulates mycobacteria processing through organelle polarization and localized calcium oscillations. *FEMS Immunol. Med. Microbiol.* 63, 319–327. doi: 10.1111/j.1574-695X.2011.00853.x

Carrithers, M. D., Chatterjee, G., Carrithers, L. M., Offoha, R., Iheagwara, U., Rahner, C., et al. (2009). Regulation of podosome formation in macrophages by a splice variant of the sodium channel SCN8A. *J. Biol. Chem.* 284, 8114–8126. doi: 10.1074/jbc.M801892200

Carrithers, M. D., Dib-Hajj, S., Carrithers, L. M., Tokmoulina, G., Pypaert, M., Jonas, E. A., et al. (2007). Expression of the voltage-gated sodium channel NaV1.5 in the macrophage late endosome regulates endosomal acidification. *J. Immunol.* 178, 7822–7832. doi: 10.4049/jimmunol.178.12.7822

Catterall, W. A., Goldin, A. L., and Waxman, S. G. (2005). International union of pharmacology. XLVII. Nomenclature and structure-function relationships of voltage-gated sodium channels. *Pharmacol. Rev.* 57, 397–409. doi: 10.1124/pr.57.4.4

Chakrabarty, P., Li, A., Ceballos-Diaz, C., Eddy, J. A., Funk, C. C., Moore, B., et al. (2015). IL-10 alters immunoproteostasis in APP mice, increasing plaque burden and worsening cognitive behavior. *Neuron* 85, 519–533. doi: 10.1016/j.neuron.2014.11.020

Cho, H. J., Verbridge, S. S., Davalos, R. V., and Lee, Y. W. (2018). Development of an *in vitro* 3D brain tissue model mimicking *in vivo*-like pro-inflammatory and pro-oxidative responses. *Ann. Biomed. Eng.* 46, 877–887. doi: 10.1007/s10439-018-2004-z

Chung, S., Jung, W., and Lee, M. Y. (1999). Inward and outward rectifying potassium currents set membrane potentials in activated rat microglia. *Neurosci. Lett.* 262, 121–124. doi: 10.1016/S0304-3940(99)00053-1

Chung, S., Lee, J., Joe, E. H., and Uhm, D. Y. (2001). Beta-amyloid peptide induces the expression of voltage dependent outward rectifying K^+ channels in rat microglia. *Neurosci. Lett.* 300, 67–70. doi: 10.1016/S0304-3940(01)01516-6

Colonna, M., and Wang, Y. (2016). TREM2 variants: new keys to decipher Alzheimer disease pathogenesis. *Nat. Rev. Neurosci.* 17, 201–207. doi: 10.1038/nrn.2016.7

Colton, C., and Wilcock, D. M. (2010). Assessing activation states in microglia. *CNS Neurol. Disord. Drug Targets* 9, 174–191. doi: 10.2174/187152710791012053

Colton, C. A. (2009). Heterogeneity of microglial activation in the innate immune response in the brain. *J. Neuroimmune. Pharmacol.* 4, 399–418. doi: 10.1007/s11481-009-9164-4

Condello, C., Yuan, P., Schain, A., and Grutzendler, J. (2015). Microglia constitute a barrier that prevents neurotoxic protofibrillar Abeta42 hotspots around plaques. *Nat. Commun.* 6:6176: doi: 10.1038/ncomms7176

Cook, C., Kang, S. S., Carlomagno, Y., Lin, W. L., Yue, M., Kurti, A., et al. (2015). Tau deposition drives neuropathological, inflammatory and behavioral abnormalities independently of neuronal loss in a novel mouse model. *Hum. Mol. Genet.* 24, 6198–6212. doi: 10.1093/hmg/ddv336

Coraci, I. S., Husemann, J., Berman, J. W., Hulette, C., Dufour, J. H., Campanella, G. K., et al. (2002). CD36, a class B scavenger receptor, is expressed on microglia in Alzheimer's disease brains and can mediate production of reactive oxygen species in response to beta-amyloid fibrils. *Am. J. Pathol.* 160, 101–112. doi: 10.1016/S0002-9440(10)64354-4

Corder, E. H., Saunders, A. M., Strittmatter, W. J., Schmechel, D. E., Gaskell, P. C., Small, G. W., et al. (1993). Gene dose of apolipoprotein E type 4 allele and the risk of Alzheimer's disease in late onset families. *Science* 261, 921–923. doi: 10.1126/science.8346443

Craner, M. J., Damarjian, T. G., Liu, S., Hains, B. C., Lo, A. C., Black, J. A., et al. (2005). Sodium channels contribute to microglia/macrophage activation and function in EAE and MS. *Glia* 49, 220–229. doi: 10.1002/glia.20112

De Simoni, A., Allen, N. J., and Attwell, D. (2008). Charge compensation for NADPH oxidase activity in microglia in rat brain slices does not involve a proton current. *Eur. J. Neurosci.* 28, 1146–1156. doi: 10.1111/j.1460-9568.2008.06417.x

DeCoursey, T. E. (2008). Voltage-gated proton channels. *Cell Mol. Life Sci.* 65, 2554–2573. doi: 10.1007/s00018-008-8056-8

Douvaras, P., Sun, B., Wang, M., Kruglikov, I., Lallos, G., Zimmer, M., et al. (2017). Directed differentiation of human pluripotent stem cells to microglia. *Stem Cell Rep.* 8, 1516–1524. doi: 10.1016/j.stemcr.2017.04.023

Draheim, H. J., Prinz, M., Weber, J. R., Weiser, T., Kettenmann, H., and Hanisch, U. K. (1999). Induction of potassium channels in mouse brain microglia: cells acquire responsiveness to pneumococcal cell wall components during late development. *Neuroscience* 89, 1379–1390. doi: 10.1016/S0306-4522(98)00407-2

Eder, C. (1998). Ion channels in microglia (brain macrophages). *Am. J. Physiol.* 275, C327–C342. doi: 10.1152/ajpcell.1998.275.2.C327

Eder, C. (2005). Regulation of microglial behavior by ion channel activity. *J. Neurosci. Res.* 81, 314–321. doi: 10.1002/jnr.20476

Eder, C. (2010). Ion channels in monocytes and microglia/brain macrophages: promising therapeutic targets for neurological diseases. *J. Neuroimmunol.* 224, 51–55. doi: 10.1016/j.jneuroim.2010.05.008

Eder, C., and Decoursey, T. E. (2001). Voltage-gated proton channels in microglia. *Prog. Neurobiol.* 64, 277–305. doi: 10.1016/S0301-0082(00)00062-9

Eder, C., Fischer, H. G., Hadding, U., and Heinemann, U. (1995). Properties of voltage-gated currents of microglia developed using macrophage colony-stimulating factor. *Pflugers Arch.* 430, 526–533. doi: 10.1007/BF00373889

Eder, C., and Heinemann, U. (1996). Proton modulation of outward K⁺ currents in interferon-gamma-activated microglia. *Neurosci. Lett.* 206, 101–104. doi: 10.1016/S0304-3940(96)12433-2

Eder, C., Schilling, T., Heinemann, U., Haas, D., Hailer, N., and Nitsch, R. (1999). Morphological, immunophenotypical and electrophysiological properties of resting microglia *in vitro*. *Eur. J. Neurosci.* 11, 4251–4261. doi: 10.1046/j.1460-9568.1999.00852.x

Ertel, E. A., Campbell, K. P., Harpold, M. M., Hofmann, F., Mori, Y., Perez-Reyes, E., et al. (2000). Nomenclature of voltage-gated calcium channels. *Neuron* 25, 533–535. doi: 10.1016/S0896-6273(00)81057-0

Espinosa-Parrilla, J. F., Martinez-Moreno, M., Gasull, X., Mahy, N., and Rodriguez, M. J. (2015). The L-type voltage-gated calcium channel modulates microglial pro-inflammatory activity. *Mol. Cell. Neurosci.* 64, 104–115. doi: 10.1016/j.mcn.2014.12.004

Evans, M. J., and Kaufman, M. H. (1981). Establishment in culture of pluripotential cells from mouse embryos. *Nature* 292, 154–156. doi: 10.1038/292154a0

Fischer, H. G., Eder, C., Hadding, U., and Heinemann, U. (1995). Cytokine-dependent K⁺ channel profile of microglia at immunologically defined functional states. *Neuroscience* 64, 183–191. doi: 10.1016/0306-4522(94)00398-O

Fordyce, C. B., Jagasia, R., Zhu, X., and Schlichter, L. C. (2005). Microglia Kv1.3 channels contribute to their ability to kill neurons. *J. Neurosci.* 25, 7139–7149. doi: 10.1523/JNEUROSCI.1251-05.2005

Franchini, L., Levi, G., and Visentin, S. (2004). Inwardly rectifying K⁺ channels influence Ca²⁺ entry due to nucleotide receptor activation in microglia. *Cell Calcium* 35, 449–459. doi: 10.1016/j.ceca.2003.11.001

Franciosi, S., Ryu, J. K., Choi, H. B., Radov, L., Kim, S. U., and Mclarnon, J. G. (2006). Broad-spectrum effects of 4-aminopyridine to modulate amyloid beta1-42-induced cell signaling and functional responses in human microglia. *J. Neurosci.* 26, 11652–11664. doi: 10.1523/JNEUROSCI.2490-06.2006

Galatro, T. F., Holtman, I. R., Lerario, A. M., Vainchtein, I. D., Brouwer, N., Sola, P. R., et al. (2017). Transcriptomic analysis of purified human cortical microglia reveals age-associated changes. *Nat. Neurosci.* 20:1162. doi: 10.1038/nn.4597

Ganter, S., Northoff, H., Mannel, D., and Gebicke-Harter, P. J. (1992). Growth control of cultured microglia. *J. Neurosci. Res.* 33, 218–230. doi: 10.1002/jnr.490330205

Garcia-Calvo, M., Leonard, R. J., Novick, J., Stevens, S. P., Schmalhofer, W., Kaczorowski, G. J., et al. (1993). Purification, characterization, and biosynthesis of margatoxin, a component of *Centruroides margaritatus* venom that selectively inhibits voltage-dependent potassium channels. *J. Biol. Chem.* 268, 18866–18874.

Gatz, M., Reynolds, C. A., Fratiglioni, L., Johansson, B., Mortimer, J. A., Berg, S., et al. (2006). Role of genes and environments for explaining Alzheimer disease. *Arch. Gen. Psychiatr.* 63, 168–174. doi: 10.1001/archpsyc.63.2.168

Ginhoux, F., Greter, M., Leboeuf, M., Nandi, S., See, P., Gokhan, S., et al. (2010). Fate mapping analysis reveals that adult microglia derive from primitive macrophages. *Science* 330, 841–845. doi: 10.1126/science.1194637

Giulian, D., and Baker, T. J. (1986). Characterization of ameboid microglia isolated from developing mammalian brain. *J. Neurosci.* 6, 2163–2178. doi: 10.1523/JNEUROSCI.06-08-02163.1986

Gosselin, D., Skola, D., Coufal, N. G., Holtman, I. R., Schlachetzki, J. C.M., Sajti, E., et al. (2017). An environment-dependent transcriptional network specifies human microglia identity. *Science* 356:eaal3222. doi: 10.1126/science.aal3222

Grathwohl, S. A., Kalin, R. E., Bolmont, T., Prokop, S., Winkelmann, G., Kaeser, S. A., et al. (2009). Formation and maintenance of Alzheimer's disease beta-amyloid plaques in the absence of microglia. *Nat. Neurosci.* 12, 1361–1363. doi: 10.1038/nn.2432

Guerreiro, R., Wojtas, A., Bras, J., Carrasquillo, M., Rogaeva, E., Majounie, E., et al. (2013). TREM2 variants in Alzheimer's disease. *N. Engl. J. Med.* 368, 117–127. doi: 10.1056/NEJMoa1211851

Guillot-Sestier, M. V., Doty, K. R., Gate, D., Rodriguez, J. Jr., Leung, B. P., Rezai-Zadeh, K., et al. (2015). Il10 deficiency rebalances innate immunity to mitigate Alzheimer-like pathology. *Neuron* 85, 534–548. doi: 10.1016/j.neuron.2014.12.068

Haenseler, W., Sansom, S. N., Buchrieser, J., Newey, S. E., Moore, C. S., Nicholls, F. J., et al. (2017). A highly efficient human pluripotent stem cell microglia model displays a neuronal-co-culture-specific expression profile and inflammatory response. *Stem Cell Rep.* 8, 1727–1742. doi: 10.1016/j.stemcr.2017.05.017

Harold, D., Abraham, R., Hollingworth, P., Sims, R., Gerrish, A., Hamshere, M. L., et al. (2009). Genome-wide association study identifies variants at CLU and PICALM associated with Alzheimer's disease. *Nat. Genet.* 41, 1088–1093. doi: 10.1038/ng.440

Harry, G. J. (2013). Microglia during development and aging. *Pharmacol. Ther.* 139, 313–326. doi: 10.1016/j.pharmthera.2013.04.013

Harteneck, C. (2005). Function and pharmacology of TRPM cation channels. *Naunyn Schmiedebergs Arch. Pharmacol.* 371, 307–314. doi: 10.1007/s00210-005-1034-x

Hashioka, S., Klegeris, A., and Mcgeer, P. L. (2012). Inhibition of human astrocyte and microglia neurotoxicity by calcium channel blockers. *Neuropharmacology* 63, 685–691. doi: 10.1016/j.neuropharm.2012.05.033

Heneka, M. T., Carson, M. J., El Khoury, J., Landreth, G. E., Brosseron, F., Feinstein, D. L., et al. (2015). Neuroinflammation in Alzheimer's disease. *Lancet Neurol.* 14, 388–405. doi: 10.1016/S1474-4422(15)70016-5

Heneka, M. T., Kummer, M. P., Stutz, A., Delekate, A., Schwartz, S., Vieira-Saecker, A., et al. (2013). NLRP3 is activated in Alzheimer's disease and contributes to pathology in APP/PS1 mice. *Nature* 493, 674–678. doi: 10.1038/nature11729

Heneka, M. T., Sastre, M., Dumitrescu-Ozimek, L., Dewachter, I., Walter, J., Klockgether, T., et al. (2005). Focal glial activation coincides with increased BACE1 activation and precedes amyloid plaque deposition in APP[V717I] transgenic mice. *J. Neuroinflammation.* 2:22. doi: 10.1186/1742-2094-2-22

Heslegrave, A., Heywood, W., Paterson, R., Magdalinou, N., Svensson, J., Johansson, P., et al. (2016). Increased cerebrospinal fluid soluble TREM2 concentration in Alzheimer's disease. *Mol. Neurodegener.* 11:3. doi: 10.1186/s13024-016-0071-x

Hickey, S. E., Allison, E. K., and El Khoury, J. (2008). Microglial dysfunction and defective beta-amyloid clearance pathways in aging Alzheimer's disease mice. *J. Neurosci.* 28, 8354–8360. doi: 10.1523/JNEUROSCI.0616-08.2008

Hickman, S. E., and El Khoury, J. (2013). The neuroimmune system in Alzheimer's disease: the glass is half full. *J. Alzheimers Dis.* 33(Suppl. 1), S295–302. doi: 10.3233/JAD-2012-129027

Hickman, S. E., Kingery, N. D., Ohsumi, T. K., Borowsky, M. L., Wang, L. C., Means, T. K., et al. (2013). The microglial sensome revealed by direct RNA sequencing. *Nat. Neurosci.* 16, 1896–1905. doi: 10.1038/nn.3554

Hines, D. J., Hines, R. M., Mulligan, S. J., and Macvicar, B. A. (2009). Microglia processes block the spread of damage in the brain and require functional chloride channels. *Glia* 57, 1610–1618. doi: 10.1002/glia.20874

Hollingworth, P., Harold, D., Sims, R., Gerrish, A., Lambert, J. C., Carrasquillo, M. M., et al. (2011). Common variants at ABCA7, MS4A6A/MS4A4E, EPHA1, CD33 and CD2AP are associated with Alzheimer's disease. *Nat. Genet.* 43, 429–435. doi: 10.1038/ng.803

Holtman, I. R., Raj, D. D., Miller, J. A., Schaafsma, W., Yin, Z., Brouwer, N., et al. (2015). Induction of a common microglia gene expression signature by aging and neurodegenerative conditions: a co-expression meta-analysis. *Acta Neuropathol. Commun.* 3:31. doi: 10.1186/s40478-015-0203-5

Horvath, R. J., Nutile-Mcmenemy, N., Alkaitis, M. S., and Deleo, J. A. (2008). Differential migration, LPS-induced cytokine, chemokine, and NO expression in immortalized BV-2 and HAPI cell lines and primary microglial cultures. *J. Neurochem.* 107, 557–569. doi: 10.1111/j.1471-4159.2008.05633.x

Hsieh, C. L., Koike, M., Spusta, S. C., Niemi, E. C., Yenari, M., Nakamura, M. C., et al. (2009). A role for TREM2 ligands in the phagocytosis of apoptotic neuronal cells by microglia. *J. Neurochem.* 109, 1144–1156. doi: 10.1111/j.1471-4159.2009.06042.x

Huang, S., Turlova, E., Li, F., Bao, M.-H., Szeto, V., Wong, R., et al. (2017). Transient receptor potential melastatin 2 channels (TRPM2) mediate neonatal hypoxic-ischemic brain injury in mice. *Exp. Neurol.* 296, 32–40. doi: 10.1016/j.expneurol.2017.06.023

Huang, Y. (2010). A beta-independent roles of apolipoprotein E4 in the pathogenesis of Alzheimer's disease. *Trends Mol. Med.* 16, 287–294. doi: 10.1016/j.molmed.2010.04.004

Hutchins, K. D., Dickson, D. W., Rashbaum, W. K., and Lyman, W. D. (1990). Localization of morphologically distinct microglial populations in the developing human fetal brain: implications for ontogeny. *Brain Res. Dev. Brain Res.* 55, 95–102. doi: 10.1016/0165-3806(90)90109-C

Ikeda, M., Shoji, M., Kawarai, T., Kawarabayashi, T., Matsubara, E., Murakami, T., et al. (2005). Accumulation of filamentous tau in the cerebral cortex of human tau R406W transgenic mice. *Am. J. Pathol.* 166, 521–531. doi: 10.1016/S0002-9440(10)62274-2

Janelsins, M. C., Mastrangelo, M. A., Oddo, S., Laferla, F. M., Federoff, H. J., and Bowers, W. J. (2005). Early correlation of microglial activation with enhanced tumor necrosis factor-alpha and monocyte chemoattractant protein-1 expression specifically within the entorhinal cortex of triple transgenic Alzheimer's disease mice. *J. Neuroinflammation* 2:23. doi: 10.1186/1742-2094-2-23

Jay, T. R., Hirsch, A. M., Broihier, M. L., Miller, C. M., Neilson, L. E., Ransohoff, R. M., et al. (2017). Disease progression-dependent effects of TREM2 deficiency in a mouse model of Alzheimer's Disease. *J. Neurosci.* 37, 637–647. doi: 10.1523/JNEUROSCI.2110-16.2016

Jay, T. R., Miller, C. M., Cheng, P. J., Graham, L. C., Bemiller, S., Broihier, M. L., et al. (2015). TREM2 deficiency eliminates TREM^{2+} inflammatory macrophages and ameliorates pathology in Alzheimer's disease mouse models. *J. Exp. Med.* 212, 287–295. doi: 10.1084/jem.20142322

Jeong, H., Kim, Y. H., Lee, Y., Jung, S. J., and Oh, S. B. (2017). TRPM2 contributes to LPC-induced intracellular Ca^{2+} influx and microglial activation. *Biochem. Biophys. Res. Commun.* 485, 301–306. doi: 10.1016/j.bbrc.2017.02.087

Jiang, X., Newell, E. W., and Schlichter, L. C. (2003). Regulation of a TRPM7-like current in rat brain microglia. *J. Biol. Chem.* 278, 42867–42876. doi: 10.1074/jbc.M304487200

Jiang, Y., Lee, A., Chen, J., Ruta, V., Cadene, M., Chait, B. T., et al. (2003). X-ray structure of a voltage-dependent K$^+$ channel. *Nature* 423, 33–41. doi: 10.1038/nature01580

Jin, S. C., Benitez, B. A., Karch, C. M., Cooper, B., Skorupa, T., Carrell, D., et al. (2014). Coding variants in TREM2 increase risk for Alzheimer's disease. *Hum. Mol. Genet.* 23, 5838–5846. doi: 10.1093/hmg/ddu277

Johansson, J. U., Woodling, N. S., Brown, H. D., Wang, Q., and Andreasson, K. I. (2015). Microarray analysis of the *in vivo* response of microglia to Abeta peptides in mice with conditional deletion of the prostaglandin EP2 receptor. *Genom. Data* 5, 268–271. doi: 10.1016/j.gdata.2015.06.011

Jonsson, T., Stefansson, H., Steinberg, S., Jonsdottir, I., Jonsson, P. V., Snaedal, J., et al. (2013). Variant of TREM2 associated with the risk of Alzheimer's disease. *N. Engl. J. Med.* 368, 107–116. doi: 10.1056/NEJMoa1211103

Jou, I., Pyo, H., Chung, S., Jung, S. Y., Gwag, B. J., and Joe, E. H. (1998). Expression of Kv1.5 K$^+$ channels in activated microglia *in vivo*. *Glia* 24, 408–414.

Kaushal, V., Koeberle, P. D., Wang, Y., and Schlichter, L. C. (2007). The Ca^{2+}-activated K$^+$ channel KCNN4/KCa3.1 contributes to microglia activation and nitric oxide-dependent neurodegeneration. *J. Neurosci.* 27, 234–244. doi: 10.1523/JNEUROSCI.3593-06.2007

Keren-Shaul, H., Spinrad, A., Weiner, A., Matcovitch-Natan, O., Dvir-Szternfeld, R., Ulland, T. K., et al. (2017). A unique microglia type associated with restricting development of Alzheimer's disease. *Cell* 169, 1276–1290 e1217. doi: 10.1016/j.cell.2017.05.018

Kettenmann, H., Banati, R., and Walz, W. (1993). Electrophysiological behavior of microglia. *Glia* 7, 93–101. doi: 10.1002/glia.440070115

Kettenmann, H., Hanisch, U. K., Noda, M., and Verkhratsky, A. (2011). Physiology of microglia. *Physiol. Rev.* 91, 461–553. doi: 10.1152/physrev.00011.2010

Kettenmann, H., Hoppe, D., Gottmann, K., Banati, R., and Kreutzberg, G. (1990). Cultured microglial cells have a distinct pattern of membrane channels different from peritoneal macrophages. *J. Neurosci. Res.* 26, 278–287. doi: 10.1002/jnr.490260303

Khanna, R., Roy, L., Zhu, X., and Schlichter, L. C. (2001). K$^+$ channels and the microglial respiratory burst. *Am. J. Physiol. Cell Physiol.* 280, C796–806. doi: 10.1152/ajpcell.2001.280.4.C796

Kim, H., Yoo, J., Shin, J., Chang, Y., Jung, J., Jo, D.-G., et al. (2017). Modelling APOE ε3/4 allele-associated sporadic Alzheimer's disease in an induced neuron. *Brain* 140, 2193–2209. doi: 10.1093/brain/awx144

Kim, S. R., Kim, S. U., Oh, U., and Jin, B. K. (2006). Transient receptor potential vanilloid subtype 1 mediates microglial cell death *in vivo* and *in vitro* via Ca^{2+}-mediated mitochondrial damage and cytochrome c release. *J. Immunol.* 177, 4322–4329. doi: 10.4049/jimmunol.177.7.4322

Kis-Toth, K., Hajdu, P., Bacskai, I., Szilagyi, O., Papp, F., Szanto, A., et al. (2011). Voltage-gated sodium channel Nav1.7 maintains the membrane potential and regulates the activation and chemokine-induced migration of a monocyte-derived dendritic cell subset. *J. Immunol.* 187, 1273–1280. doi: 10.4049/jimmunol.1003345

Kitazawa, M., Oddo, S., Yamasaki, T. R., Green, K. N., and Laferla, F. M. (2005). Lipopolysaccharide-induced inflammation exacerbates tau pathology by a cyclin-dependent kinase 5-mediated pathway in a transgenic model of Alzheimer's disease. *J. Neurosci.* 25, 8843–8853. doi: 10.1523/JNEUROSCI.2868-05.2005

Klee, R., Heinemann, U., and Eder, C. (1998). Changes in proton currents in murine microglia induced by cytoskeletal disruptive agents. *Neurosci. Lett.* 247, 191–194. doi: 10.1016/S0304-3940(98)00322-X

Klee, R., Heinemann, U., and Eder, C. (1999). Voltage-gated proton currents in microglia of distinct morphology and functional state. *Neuroscience* 91, 1415–1424. doi: 10.1016/S0306-4522(98)00710-6

Kleinberger, G., Yamanishi, Y., Suarez-Calvet, M., Czirr, E., Lohmann, E., Cuyvers, E., et al. (2014). TREM2 mutations implicated in neurodegeneration impair cell surface transport and phagocytosis. *Sci. Transl. Med.* 6:243ra286. doi: 10.1126/scitranslmed.3009093

Koenigsknecht-Talboo, J., Meyer-Luehmann, M., Parsadanian, M., Garcia-Alloza, M., Finn, M. B., Hyman, B. T., et al. (2008). Rapid microglial response around amyloid pathology after systemic anti-Abeta antibody administration in PDAPP mice. *J. Neurosci.* 28, 14156–14164. doi: 10.1523/JNEUROSCI.4147-08.2008

Korotzer, A. R., and Cotman, C. W. (1992). Voltage-gated currents expressed by rat microglia in culture. *Glia* 6, 81–88. doi: 10.1002/glia.440060202

Korotzer, A. R., Whittemore, E. R., and Cotman, C. W. (1995). Differential regulation by beta-amyloid peptides of intracellular free Ca^{2+} concentration in cultured rat microglia. *Eur. J. Pharmacol.* 288, 125–130. doi: 10.1016/0922-4106(95)90006-3

Kotecha, S. A., and Schlichter, L. C. (1999). A Kv1.5 to Kv1.3 switch in endogenous hippocampal microglia and a role in proliferation. *J. Neurosci.* 19, 10680–10693. doi: 10.1523/JNEUROSCI.19-24-10680.1999

Krabbe, G., Halle, A., Matyash, V., Rinnenthal, J. L., Eom, G. D., Bernhardt, U., et al. (2013). Functional impairment of microglia coincides with beta-amyloid

deposition in mice with Alzheimer-like pathology. *PLoS ONE* 8:e60921. doi: 10.1371/journal.pone.0060921

Kraft, R. (2015). STIM and ORAI proteins in the nervous system. *Channels* 9, 244–252. doi: 10.1080/19336950.2015.1071747

Krasemann, S., Madore, C., Cialic, R., Baufeld, C., Calcagno, N., El Fatimy, R., et al. (2017). The TREM2-APOE pathway drives the transcriptional phenotype of dysfunctional microglia in neurodegenerative diseases. *Immunity* 47, 566–581 e569. doi: 10.1016/j.immuni.2017.08.008

Kuang, Q., Purhonen, P., and Hebert, H. (2015). Structure of potassium channels. *Cell Mol. Life Sci.* 72, 3677–3693. doi: 10.1007/s00018-015-1948-5

Kurland, D. B., Gerzanich, V., Karimy, J. K., Woo, S. K., Vennekens, R., Freichel, M., et al. (2016). The Sur1-Trpm4 channel regulates NOS2 transcription in TLR4-activated microglia. *J. Neuroinflammation* 13:130. doi: 10.1186/s12974-016-0599-2

Lam, D., Lively, S., and Schlichter, L. C., (2017). Responses of rat and mouse primary microglia to pro- and anti-inflammatory stimuli: molecular profiles, K(+) channels and migration. *J. Neuroinflammation* 14:166. doi: 10.1186/s12974-017-0941-3

Lambert, J. C., Ibrahim-Verbaas, C. A., Harold, D., Naj, A. C., Sims, R., Bellenguez, C., et al. (2013). Meta-analysis of 74,046 individuals identifies 11 new susceptibility loci for Alzheimer's disease. *Nat. Genet.* 45, 1452–1458. doi: 10.1038/ng.2802

Lapasset, L., Milhavet, O., Prieur, A., Besnard, E., Babled, A., Ait-Hamou, N., et al. (2011). Rejuvenating senescent and centenarian human cells by reprogramming through the pluripotent state. *Genes Dev.* 25, 2248–2253. doi: 10.1101/gad.173922.111

Lawson, L. J., Perry, V. H., Dri, P., and Gordon, S. (1990). Heterogeneity in the distribution and morphology of microglia in the normal adult-mouse brain. *Neuroscience* 39, 151–170. doi: 10.1016/0306-4522(90)90229-W

Lee, C. Y., and Landreth, G. E. (2010). The role of microglia in amyloid clearance from the AD brain. *J. Neural. Transm (Vienna)* 117, 949–960. doi: 10.1007/s00702-010-0433-4

Lewis, R. S., Ross, P. E., and Cahalan, M. D. (1993). Chloride channels activated by osmotic stress in T lymphocytes. *J. Gen. Physiol.* 101, 801–826. doi: 10.1085/jgp.101.6.801

Li, F., Zhu, S., Wu, C., Yan, C., Liu, Y., and Shugan, L. (2011). Neuroinflammation and cell therapy for Parkinson's disease. *Front. Biosci (Schol Ed)* 3, 1407–1420. doi: 10.2741/232

Li, J. T., and Zhang, Y. (2018). TREM2 regulates innate immunity in Alzheimer's disease. *J. Neuroinflammation* 15:107. doi: 10.1186/s12974-018-1148-y

Li, R., Huang, Y. G., Fang, D., and Le, W. D. (2004). (-)-Epigallocatechin gallate inhibits lipopolysaccharide-induced microglial activation and protects against inflammation-mediated dopaminergic neuronal injury. *J. Neurosci. Res.* 78, 723–731. doi: 10.1002/jnr.20315

Lim, J.-E., Kou, J., Song, M., Pattanayak, A., Jin, J., Lalonde, R., et al. (2011). MyD88 deficiency ameliorates β-Amyloidosis in an animal model of alzheimer's disease. *Am. J. Pathol.* 179, 1095–1103. doi: 10.1016/j.ajpath.2011.05.045

Lim, J. E., Song, M., Jin, J., Kou, J., Pattanayak, A., Lalonde, R., et al. (2012). The effects of MyD88 deficiency on exploratory activity, anxiety, motor coordination, and spatial learning in C57BL/6 and APPswe/PS1dE9 mice. *Behav. Brain Res.* 227, 36–42. doi: 10.1016/j.bbr.2011.10.027

Lin, Y. T., Seo, J., Gao, F., Feldman, H. M., Wen, H. L., Penney, J., et al. (2018). APOE4 causes widespread molecular and cellular alterations associated with alzheimer's disease phenotypes in human iPSC-derived brain cell types. *Neuron.* 98, 1141–1154.e7. doi: 10.1016/j.neuron.2018.05.008

Lioudyno, M. I., Broccio, M., Sokolov, Y., Rasool, S., Wu, J., Alkire, M. T., et al. (2012). Effect of synthetic abeta peptide oligomers and fluorinated solvents on Kv1.3 channel properties and membrane conductance. *PLoS ONE* 7:e35090. doi: 10.1371/journal.pone.0035090

Liu, N., Zhuang, Y., Zhou, Z., Zhao, J., Chen, Q., and Zheng, J. (2017). NF-kappaB dependent up-regulation of TRPC6 by Abeta in BV-2 microglia cells increases COX-2 expression and contributes to hippocampus neuron damage. *Neurosci. Lett.* 651, 1–8. doi: 10.1016/j.neulet.2017.04.056

Long, S. B., Campbell, E. B., and Mackinnon, R. (2005). Crystal structure of a mammalian voltage-dependent Shaker family K$^+$ channel. *Science* 309, 897–903. doi: 10.1126/science.1116269

Long, S. B., Tao, X., Campbell, E. B., and Mackinnon, R. (2007). Atomic structure of a voltage-dependent K$^+$ channel in a lipid membrane-like environment. *Nature* 450, 376–382. doi: 10.1038/nature06265

Madry, C., Kyrargyri, V., Arancibia-Carcamo, I. L., Jolivet, R., Kohsaka, S., Bryan, R. M., et al. (2018). Microglial ramification, surveillance, and interleukin-1β release are regulated by the two-pore domain K$^+$ channel THIK-1. *Neuron* 97, 299.e6–312.e6 e296. doi: 10.1016/j.neuron.2017.12.002

Maezawa, I., Jenkins, D. P., Jin, B. E., and Wulff, H. (2012). Microglial KCa3.1 channels as a potential therapeutic target for Alzheimer's disease. *Int. J. Alzheimers Dis.* 2012:868972. doi: 10.1155/2012/868972

Maezawa, I., Nguyen, H. M., Di Lucente, J., Jenkins, D. P., Singh, V., Hilt, S., et al. (2017). Kv1.3 inhibition as a potential microglia-targeted therapy for Alzheimer's disease: preclinical proof of concept. *Brain.* 141, 596-612. doi: 10.1093/brain/awx346

Maezawa, I., Zimin, P. I., Wulff, H., and Jin, L. W. (2011). Amyloid-beta protein oligomer at low nanomolar concentrations activates microglia and induces microglial neurotoxicity. *J. Biol. Chem.* 286, 3693–3706. doi: 10.1074/jbc.M110.135244

McGowan, E., Eriksen, J., and Hutton, M. (2006). A decade of modeling Alzheimer's disease in transgenic mice. *Trends Genet.* 22, 281–289. doi: 10.1016/j.tig.2006.03.007

McLarnon, J. G., Franciosi, S., Wang, X., Bae, J. H., Choi, H. B., and Kim, S. U. (2001). Acute actions of tumor necrosis factor-alpha on intracellular Ca(2+) and K(+) currents in human microglia. *Neuroscience* 104, 1175–1184. doi: 10.1016/S0306-4522(01)00119-1

McLarnon, J. G., Sawyer, D., and Kim, S. U. (1995). Cation and anion unitary ion channel currents in cultured bovine microglia. *Brain Res.* 693, 8–20. doi: 10.1016/0006-8993(95)00664-C

McLarnon, J. G., Xu, R., Lee, Y. B., and Kim, S. U. (1997). Ion channels of human microglia in culture. *Neuroscience* 78, 1217–1228. doi: 10.1016/S0306-4522(96)00680-X

McLarnon, J. G., Zhang, L., Goghari, V., Lee, Y. B., Walz, W., Krieger, C., et al. (1999). Effects of ATP and elevated K$^+$ on K$^+$ currents and intracellular Ca^{2+} in human microglia. *Neuroscience* 91, 343–352. doi: 10.1016/S0306-4522(98)00491-6

Menteyne, A., Levavasseur, F., Audinat, E., and Avignone, E. (2009). Predominant functional expression of Kv1.3 by activated microglia of the hippocampus after Status epilepticus. *PLoS ONE* 4:e6770. doi: 10.1371/journal.pone.0006770

Meotti, F. C., Figueiredo, C. P., Manjavachi, M., and Calixto, J. B. (2017). The transient receptor potential ankyrin-1 mediates mechanical hyperalgesia induced by the activation of B1 receptor in mice. *Biochem. Pharmacol.* 125, 75–83. doi: 10.1016/j.bcp.2016.11.003

Meyer-Luehmann, M., Spires-Jones, T. L., Prada, C., Garcia-Alloza, M., De Calignon, A., Rozkalne, A., et al. (2008). Rapid appearance and local toxicity of amyloid-[bgr] plaques in a mouse model of Alzheimer/'s disease. *Nature* 451, 720–724. doi: 10.1038/nature06616

Milton, R. H., Abeti, R., Averaimo, S., Debiasi, S., Vitellaro, L., Jiang, L., et al. (2008). CLIC1 function is required for beta-amyloid-induced generation of reactive oxygen species by microglia. *J. Neurosci.* 28, 11488–11499. doi: 10.1523/JNEUROSCI.2431-08.2008

Miyake, T., Shirakawa, H., Kusano, A., Sakimoto, S., Konno, M., Nakagawa, T., et al. (2014). TRPM2 contributes to LPS/IFNγ-induced production of nitric oxide via the p38/JNK pathway in microglia. *Biochem. Biophys. Res. Commun.* 444, 212–217. doi: 10.1016/j.bbrc.2014.01.022

Miyake, T., Shirakawa, H., Nakagawa, T., and Kaneko, S. (2015). Activation of mitochondrial transient receptor potential vanilloid 1 channel contributes to microglial migration. *Glia* 63, 1870–1882. doi: 10.1002/glia.22854

Mizoguchi, Y., Kato, T. A., Seki, Y., Ohgidani, M., Sagata, N., Horikawa, H., et al. (2014). Brain-derived neurotrophic factor (BDNF) induces sustained intracellular Ca(2+) elevation through the up-regulation of surface transient receptor potential 3 (TRPC3) channels in rodent microglia. *J. Biol. Chem.* 289, 18549–18555. doi: 10.1074/jbc.M114.555334

Mosser, C. A., Baptista, S., Arnoux, I., and Audinat, E. (2017). Microglia in CNS development: Shaping the brain for the future. *Prog. Neurobiol.* 149–150, 1–20. doi: 10.1016/j.pneurobio.2017.01.002

Muffat, J., and Li, Y. (2016). Efficient derivation of microglia-like cells from human pluripotent stem cells. *Nat. Med.* 22, 1358–1367. doi: 10.1038/nm.4189

Muffat, J., Li, Y., Yuan, B., Mitalipova, M., Omer, A., Corcoran, S., et al. (2016). Efficient derivation of microglia-like cells from human pluripotent stem cells. *Nat. Med.* 22, 1358–1367. doi: 10.1038/nm.41890

Naj, A. C., Jun, G., Beecham, G. W., Wang, L. S., Vardarajan, B. N., Buros, J., et al. (2011). Common variants at MS4A4/MS4A6E, CD2AP, CD33 and EPHA1 are associated with late-onset Alzheimer's disease. *Nat. Genet.* 43, 436–441. doi: 10.1038/ng.801

Nathan, B. P., Bellosta, S., Sanan, D. A., Weisgraber, K. H., Mahley, R. W., and Pitas, R. E., (1994). Differential effects of apolipoproteins E3 and E4 on neuronal growth *in vitro. Science* 264, 850–852. doi: 10.1126/science.8171342

Nayak, D., Roth, T. L., and Mcgavern, D. B. (2014). Microglia development and function. *Annu. Rev. Immunol.* 32, 367–402. doi: 10.1146/annurev-immunol-032713-120240

Nguyen, H. M., Blomster, L. V., Christophersen, P., and Wulff, H. (2017a). Potassium channel expression and function in microglia: plasticity and possible species variations. *Channels (Austin)* 11, 305–315. doi: 10.1080/19336950.2017.1300738

Nguyen, H. M., Grossinger, E. M., Horiuchi, M., Davis, K. W., Jin, L. W., Maezawa, I., et al. (2017b). Differential Kv1.3, KCa3.1, and Kir2.1 expression in "classically" and "alternatively" activated microglia. *Glia* 65, 106–121. doi: 10.1002/glia.23078

Nicholson, E., and Randall, A. D. (2009). Na(v)1.5 sodium channels in a human microglial cell line. *J. Neuroimmunol.* 215, 25–30. doi: 10.1016/j.jneuroim.2009.07.009

Nicoletti, N. F., Erig, T. C., Zanin, R. F., Roxo, M. R., Ferreira, N. P., Gomez, M. V., et al. (2017). Pre-clinical evaluation of voltage-gated calcium channel blockers derived from the spider P. nigriventer in glioma progression. *Toxicon* 129, 58–67. doi: 10.1016/j.toxicon.2017.02.001

Nilius, B., Prenen, J., Tang, J., Wang, C., Owsianik, G., Janssens, A., et al. (2005). Regulation of the Ca^{2+} sensitivity of the nonselective cation channel TRPM4. *J. Biol. Chem.* 280, 6423–6433. doi: 10.1074/jbc.M411089200

Nörenberg, W., Gebicke-Haerter, P. J., and Illes, P. (1994a). Voltage-dependent potassium channels in activated rat microglia. *J. Physiol.* 475, 15–32.

Nörenberg, W., Illes, P., and Gebicke-Haerter, P. J. (1994b). Sodium channel in isolated human brain macrophages (microglia). *Glia* 10, 165–172.

Novarino, G., Fabrizi, C., Tonini, R., Denti, M. A., Malchiodi-Albedi, F., Lauro, G. M., et al. (2004). Involvement of the intracellular ion channel CLIC1 in microglia-mediated beta-amyloid-induced neurotoxicity. *J. Neurosci.* 24, 5322–5330. doi: 10.1523/JNEUROSCI.1170-04.2004

Oakley, H., Cole, S. L., Logan, S., Maus, E., Shao, P., Craft, J., et al. (2006). Intraneuronal beta-amyloid aggregates, neurodegeneration, and neuron loss in transgenic mice with five familial Alzheimer's disease mutations: potential factors in amyloid plaque formation. *J. Neurosci.* 26, 10129–10140. doi: 10.1523/JNEUROSCI.1202-06.2006

Oddo, S., Caccamo, A., Shepherd, J. D., Murphy, M. P., Golde, T. E., Kayed, R., et al. (2003). Triple-transgenic model of Alzheimer's disease with plaques and tangles: intracellular Abeta and synaptic dysfunction. *Neuron* 39, 409–421. doi: 10.1016/S0896-6273(03)00434-3

Olah, M., Patrick, E., Villani, A.-C., Xu, J., White, C. C., Ryan, K. J., et al. (2018). A transcriptomic atlas of aged human microglia. *Nat. Commun.* 9:539. doi: 10.1038/s41467-018-02926-5

Pandya, H., Shen, M. J., Ichikawa, D. M., Sedlock, A. B., Choi, Y., Johnson, K. R., et al. (2017). Differentiation of human and murine induced pluripotent stem cells to microglia-like cells. *Nat. Neurosci.* 20, 753–759. doi: 10.1038/nn.4534

Pannasch, U., Farber, K., Nolte, C., Blonski, M., Yan Chiu, S., Messing, A., et al. (2006). The potassium channels Kv1.5 and Kv1.3 modulate distinct functions of microglia. *Mol. Cell Neurosci.* 33, 401–411. doi: 10.1016/j.mcn.2006.08.009

Papavlassopoulos, M., Stamme, C., Thon, L., Adam, D., Hillemann, D., Seydel, U., et al. (2006). MaxiK blockade selectively inhibits the lipopolysaccharide-induced I kappa B-alpha /NF-kappa B signaling pathway in macrophages. *J. Immunol.* 177, 4086–4093. doi: 10.4049/jimmunol.177.6.4086

Pappalardo, L. W., Black, J. A., and Waxman, S. G. (2016). Sodium channels in astroglia and microglia. *Glia* 64, 1628–1645. doi: 10.1002/glia.22967

Paradisi, S., Matteucci, A., Fabrizi, C., Denti, M. A., Abeti, R., Breit, S. N., et al. (2008). Blockade of chloride intracellular ion channel 1 stimulates Abeta phagocytosis. *J. Neurosci. Res.* 86, 2488–2498. doi: 10.1002/jnr.21693

Payandeh, J., Scheuer, T., Zheng, N., and Catterall, W. A. (2011). The crystal structure of a voltage-gated sodium channel. *Nature* 475, 353–358. doi: 10.1038/nature10238

Peers, C., Pearson, H. A., and Boyle, J. P. (2007). Hypoxia and Alzheimer's disease. *Essays Biochem.* 43, 153–164. doi: 10.1042/bse0430153

Persson, A. K., Estacion, M., Ahn, H., Liu, S., Stamboulian-Platel, S., Waxman, S. G., et al. (2014). Contribution of sodium channels to lamellipodial protrusion and Rac1 and ERK1/2 activation in ATP-stimulated microglia. *Glia* 62, 2080–2095. doi: 10.1002/glia.22728

Plescher, M., Seifert, G., Hansen, J. N., Bedner, P., Steinhauser, C., and Halle, A. (2018). Plaque-dependent morphological and electrophysiological heterogeneity of microglia in an Alzheimer's disease mouse model. *Glia* 66, 1464–1480. doi: 10.1002/glia.23318

Poirier, J. (2005). Apolipoprotein E, cholesterol transport and synthesis in sporadic Alzheimer's disease. *Neurobiol. Aging* 26, 355–361. doi: 10.1016/j.neurobiolaging.2004.09.003

Ponomarev, E. D., Maresz, K., Tan, Y., and Dittel, B. N. (2007). CNS-derived interleukin-4 is essential for the regulation of autoimmune inflammation and induces a state of alternative activation in microglial cells. *J. Neurosci.* 27, 10714–10721. doi: 10.1523/JNEUROSCI.1922-07.2007

Raboune, S., Stuart, J. M., Leishman, E., Takacs, S. M., Rhodes, B., Basnet, A., et al. (2014). Novel endogenous N-acyl amides activate TRPV1-4 receptors, BV-2 microglia, and are regulated in brain in an acute model of inflammation. *Front. Cell Neurosci.* 8:195. doi: 10.3389/fncel.2014.00195

Rangaraju, S., Dammer, E. B., Raza, S. A., Rathakrishnan, P., Xiao, H., Gao, T., et al. (2018). Identification and therapeutic modulation of a pro-inflammatory subset of disease-associated-microglia in Alzheimer's disease. *Mol. Neurodegener.* 13;24. doi: 10.1186/s13024-018-0254-8

Rangaraju, S., Gearing, M., Jin, L. W., and Levey, A. (2015). Potassium channel Kv1.3 is highly expressed by microglia in human Alzheimer's disease. *J. Alzheimers Dis.* 44, 797–808. doi: 10.3233/JAD-141704

Ribé, E. M., Perez, M., Puig, B., Gich, I., Lim, F., Cuadrado, M., et al. (2005). Accelerated amyloid deposition, neurofibrillary degeneration and neuronal loss in double mutant APP/tau transgenic mice. *Neurobiol. Dis.* 20, 814–822. doi: 10.1016/j.nbd.2005.05.027

Righi, M., Mori, L., De Libero, G., Sironi, M., Biondi, A., Mantovani, A., et al. (1989). Monokine production by microglial cell clones. *Eur. J. Immunol.* 19, 1443–1448. doi: 10.1002/eji.1830190815

Rowan, M. J., Klyubin, I., Wang, Q., Hu, N. W., and Anwyl, R. (2007). Synaptic memory mechanisms: Alzheimer's disease amyloid beta-peptide-induced dysfunction. *Biochem. Soc. Trans.* 35, 1219–1223. doi: 10.1042/BST0351219

Saegusa, H., and Tanabe, T. (2014). N-type voltage-dependent Ca^{2+} channel in non-excitable microglial cells in mice is involved in the pathophysiology of neuropathic pain. *Biochem. Biophys. Res. Commun.* 450, 142–147. doi: 10.1016/j.bbrc.2014.05.103

Saijo, K., and Glass, C. K. (2011). Microglial cell origin and phenotypes in health and disease. *Nat. Rev. Immunol.* 11, 775–787. doi: 10.1038/nri3086

Saliba, J., Daou, A., Damiati, S., Saliba, J., El-Sabban, M., and Mhanna, R., (2018). Development of microplatforms to mimic the *in vivo* architecture of CNS and PNS physiology and their diseases. *Genes (Basel)* 9:E285. doi: 10.3390/genes9060285

Sappington, R. M., and Calkins, D. J. (2008). Contribution of TRPV1 to microglia-derived IL-6 and NFkappaB translocation with elevated hydrostatic pressure. *Invest. Ophthalmol. Vis. Sci.* 49, 3004–3017. doi: 10.1167/iovs.07-1355

Sawada, M., Suzumura, A., Hosoya, H., Marunouchi, T., and Nagatsu, T. (1999). Interleukin-10 inhibits both production of cytokines and expression of cytokine receptors in microglia. *J. Neurochem.* 72, 1466–1471. doi: 10.1046/j.1471-4159.1999.721466.x

Schilling, T., and Eder, C. (2007). Ion channel expression in resting and activated microglia of hippocampal slices from juvenile mice. *Brain Res.* 1186, 21–28. doi: 10.1016/j.brainres.2007.10.027

Schilling, T., and Eder, C. (2011). Amyloid-beta-induced reactive oxygen species production and priming are differentially regulated by ion channels in microglia. *J. Cell Physiol.* 226, 3295–3302. doi: 10.1002/jcp.22675

Schilling, T., and Eder, C. (2015). Microglial K^+ channel expression in young adult and aged mice. *Glia* 63, 664–672. doi: 10.1002/glia.22776

Schilling, T., Quandt, F. N., Cherny, V. V., Zhou, W., Heinemann, U., Decoursey, T. E., et al. (2000). Upregulation of Kv1.3 K$^+$ channels in microglia deactivated by TGF-beta. *Am. J. Physiol. Cell Physiol.* 279, C1123–1134. doi: 10.1152/ajpcell.2000.279.4.C1123

Schlichter, L. C., Sakellaropoulos, G., Ballyk, B., Pennefather, P. S., and Phipps, D. J., (1996). Properties of K$^+$ and Cl$^-$ channels and their involvement in proliferation of rat microglial cells. *Glia* 17, 225–236.

Schmidtmayer, J., Jacobsen, C., Miksch, G., and Sievers, J. (1994). Blood monocytes and spleen macrophages differentiate into microglia-like cells on monolayers of astrocytes: membrane currents. *Glia* 12, 259–267. doi: 10.1002/glia.440120403

Schmitz, A., Sankaranarayanan, A., Azam, P., Schmidt-Lassen, K., Homerick, D., Hansel, W., et al. (2005). Design of PAP-1, a selective small molecule Kv1.3 blocker, for the suppression of effector memory T cells in autoimmune diseases. *Mol. Pharmacol.* 68, 1254–1270. doi: 10.1124/mol.105.015669

Seok, J., Warren, H. S., Cuenca, A. G., Mindrinos, M. N., Baker, H. V., Xu, W., et al. (2013). Genomic responses in mouse models poorly mimic human inflammatory diseases. *Proc. Natl. Acad. Sci. U. S.A.* 110, 3507–3512. doi: 10.1073/pnas.1222878110

Sheffield, L. G., Marquis, J. G., and Berman, N. E. (2000). Regional distribution of cortical microglia parallels that of neurofibrillary tangles in Alzheimer's disease. *Neurosci. Lett.* 285, 165–168. doi: 10.1016/S0304-3940(00)01037-5

Sheng, J. G., Mrak, R. E., and Griffin, W. S. (1997). Glial-neuronal interactions in Alzheimer disease: progressive association of IL-1alpha+ microglia and S100β+ astrocytes with neurofibrillary tangle stages. *J. Neuropathol. Exp. Neurol.* 56, 285–290. doi: 10.1097/00005072-199703000-00007

Shibata, M., and Suzuki, N. (2017). Exploring the role of microglia in cortical spreading depression in neurological disease. *J. Cereb. Blood Flow Metab.* 37, 1182–1191. doi: 10.1177/0271678X17690537

Siddiqui, T., Lively, S., Ferreira, R., Wong, R., and Schlichter, L. C. (2014). Expression and contributions of TRPM7 and KCa2.3/SK3 channels to the increased migration and invasion of microglia in anti-inflammatory activation states. *PLoS ONE* 9:e106087. doi: 10.1371/journal.pone.0106087

Silei, V., Fabrizi, C., Venturini, G., Salmona, M., Bugiani, O., Tagliavini, F., et al. (1999). Activation of microglial cells by PrP and beta-amyloid fragments raises intracellular calcium through L-type voltage sensitive calcium channels. *Brain Res.* 818, 168–170. doi: 10.1016/S0006-8993(98)01272-4

Skaper, S.D., Facci, L., and Giusti, P. (2013). Intracellular ion channel CLIC1: involvement in microglia-mediated β-amyloid peptide (1-42) neurotoxicity. Neurochem. Res. 38, 1801-1808. doi: 10.1007/s11064-013-1084-2

Song, W., Hooli, B., Mullin, K., Jin, S. C., Cella, M., Ulland, T. K., et al. (2017). Alzheimer's disease-associated TREM2 variants exhibit either decreased or increased ligand-dependent activation. *Alzheimers Dement.* 13, 381–387. doi: 10.1016/j.jalz.2016.07.004

Spranger, M., Kiprianova, I., Krempien, S., and Schwab, S. (1998). Reoxygenation increases the release of reactive oxygen intermediates in murine microglia. *J. Cereb. Blood Flow Metab.* 18, 670–674. doi: 10.1097/00004647-199806000-00009

Steinert, M., and Grissmer, S. (1997). Novel activation stimulus of chloride channels by potassium in human osteoblasts and human leukaemic T lymphocytes. *J. Physiol.* 500(Pt. 3), 653–660.

Stewart, C. R., Stuart, L. M., Wilkinson, K., Van Gils, J. M., Deng, J., Halle, A., et al. (2010). CD36 ligands promote sterile inflammation through assembly of a Toll-like receptor 4 and 6 heterodimer. *Nat. Immunol.* 11, 155–161. doi: 10.1038/ni.1836

Stock, C., Schilling, T., Schwab, A., and Eder, C. (2006). Lysophosphatidylcholine stimulates IL-1beta release from microglia via a P2X7 receptor-independent mechanism. *J. Immunol.* 177, 8560–8568. doi: 10.4049/jimmunol.177.12.8560

Sun, C.-K., Zhen, Y.-Y., Lu, H.-I., Sung, P.-H., Chang, L.-T., Tsai, T.-H., et al. (2014). Reducing TRPC1 expression through liposome-mediated siRNA delivery markedly attenuates hypoxia-induced pulmonary arterial hypertension in a murine model. *Stem Cells Int.* 2014:316214. doi: 10.1155/2014/316214

Szalay, G., Martinecz, B., Lenart, N., Kornyei, Z., Orsolits, B., Judak, L., et al. (2016). Microglia protect against brain injury and their selective elimination dysregulates neuronal network activity after stroke. *Nat. Commun.* 7:11499. doi: 10.1038/ncomms11499

Takahashi, K., and Yamanaka, S. (2006). Induction of pluripotent stem cells from mouse embryonic and adult fibroblast cultures by defined factors. *Cell* 126, 663–676. doi: 10.1016/j.cell.2006.07.024

Takao, K., and Miyakawa, T. (2015). Genomic responses in mouse models greatly mimic human inflammatory diseases. *Proc. Natl. Acad. Sci. U.S.A.* 112, 1167–1172. doi: 10.1073/pnas.1401965111

Takata, K., Kozaki, T., Lee, C. Z.W., Thion, M. S., Otsuka, M., Lim, S., et al. (2017). Induced-pluripotent-stem-cell-derived primitive macrophages provide a platform for modeling tissue-resident macrophage differentiation and function. *Immunity* 47, 183–198 e186. doi: 10.1016/j.immuni.2017.06.017.

Talbot, S., Dias, J. P., Lahjouji, K., Bogo, M. R., Campos, M. M., Gaudreau, P., et al. (2012). Activation of TRPV1 by capsaicin induces functional kinin B(1) receptor in rat spinal cord microglia. *J. Neuroinflammation* 9:16. doi: 10.1186/1742-2094-9-16

Tarcha, E. J., Chi, V., Munoz-Elias, E. J., Bailey, D., Londono, L. M., Upadhyay, S. K., et al. (2012). Durable pharmacological responses from the peptide ShK-186, a specific Kv1.3 channel inhibitor that suppresses T cell mediators of autoimmune disease. *J. Pharmacol. Exp. Ther.* 342, 642–653. doi: 10.1124/jpet.112.191890

Tian, D. S., Li, C. Y., Qin, C., Murugan, M., Wu, L. J., and Liu, J. L. (2016). Deficiency in the voltage-gated proton channel Hv1 increases M2 polarization of microglia and attenuates brain damage from photothrombotic ischemic stroke. *J. Neurochem.* 139, 96–105. doi: 10.1111/jnc.13751

Toescu, E. C., Moller, T., Kettenmann, H., and Verkhratsky, A. (1998). Long-term activation of capacitative Ca^{2+} entry in mouse microglial cells. *Neuroscience* 86, 925–935. doi: 10.1016/S0306-4522(98)00123-7

Tsai, K. L., Chang, H. F., and Wu, S. N. (2013). The inhibition of inwardly rectifying K$^+$ channels by memantine in macrophages and microglial cells. *Cell Physiol. Biochem.* 31, 938–951. doi: 10.1159/000350112

Uchida, K., Dezaki, K., Damdindorj, B., Inada, H., Shiuchi, T., Mori, Y., et al. (2011). Lack of TRPM2 impaired insulin secretion and glucose metabolisms in mice. *Diabetes* 60, 119–126. doi: 10.2337/db10-0276

Ulland, T. K., Song, W. M., Huang, S. C., Ulrich, J. D., Sergushichev, A., Beatty, W. L., et al. (2017). TREM2 maintains microglial metabolic fitness in Alzheimer's disease. *Cell* 170, 649–663 e613. doi: 10.1016/j.cell.2017.07.023.

Ulrich, J. D., Finn, M. B., Wang, Y., Shen, A., Mahan, T. E., Jiang, H., et al. (2014). Altered microglial response to Abeta plaques in APPPS1-21 mice heterozygous for TREM2. *Mol. Neurodegener.* 9:20. doi: 10.1186/1750-1326-9-20

Ulrich, J. D., Ulland, T. K., Colonna, M., and Holtzman, D. M. (2017). Elucidating the role of TREM2 in Alzheimer's disease. *Neuron* 94, 237–248. doi: 10.1016/j.neuron.2017.02.042

Valerie, N. C., Dziegielewska, B., Hosing, A. S., Augustin, E., Gray, L. S., Brautigan, D. L., et al. (2013). Inhibition of T-type calcium channels disrupts Akt signaling and promotes apoptosis in glioblastoma cells. *Biochem. Pharmacol.* 85, 888–897. doi: 10.1016/j.bcp.2012.12.017

Visentin, S., Agresti, C., Patrizio, M., and Levi, G. (1995). Ion channels in rat microglia and their different sensitivity to lipopolysaccharide and interferon-gamma. *J. Neurosci. Res.* 42, 439–451. doi: 10.1002/jnr.490420402

Walz, W., Ilschner, S., Ohlemeyer, C., Banati, R., and Kettenmann, H. (1993). Extracellular ATP activates a cation conductance and a K$^+$ conductance in cultured microglial cells from mouse brain. *J. Neurosci.* 13, 4403–4411. doi: 10.1523/JNEUROSCI.13-10-04403.1993

Wang, Y., Cella, M., Mallinson, K., Ulrich, J. D., Young, K. L., Robinette, M. L., et al. (2015). TREM2 lipid sensing sustains the microglial response in an Alzheimer's disease model. *Cell* 160, 1061–1071. doi: 10.1016/j.cell.2015.01.049

Wen, Z., Christian, K. M., Song, H., and Ming, G. L. (2016). Modeling psychiatric disorders with patient-derived iPSCs. *Curr. Opin. Neurobiol.* 36, 118–127. doi: 10.1016/j.conb.2015.11.003

Wendt, S., Maricos, M., Vana, N., Meyer, N., Guneykaya, D., Semtner, M., et al. (2017). Changes in phagocytosis and potassium channel activity in microglia of 5xFAD mice indicate alterations in purinergic signaling in a mouse model of Alzheimer's disease. *Neurobiol. Aging* 58, 41–53. doi: 10.1016/j.neurobiolaging.2017.05.027

Wes, P. D., Easton, A., Corradi, J., Barten, D. M., Devidze, N., Decarr, L. B., et al. (2014). Tau overexpression impacts a neuroinflammation gene expression network perturbed in Alzheimer's disease. *PLoS ONE* 9:e106050. doi: 10.1371/journal.pone.0106050

Wolfe, M. S. (2012). The role of tau in neurodegenerative diseases and its potential as a therapeutic target. *Scientifica* 2012:796024. doi: 10.6064/2012/796024

Wright, A. L., Zinn, R., Hohensinn, B., Konen, L. M., Beynon, S. B., Tan, R. P., et al. (2013). Neuroinflammation and neuronal loss precede Abeta plaque deposition in the hAPP-J20 mouse model of Alzheimer's disease. *PLoS ONE* 8:e59586. doi: 10.1371/journal.pone.0059586

Wu, L. J., Wu, G., Akhavan Sharif, M. R., Baker, A., Jia, Y., Fahey, F. H., et al. (2012). The voltage-gated proton channel Hv1 enhances brain damage from ischemic stroke. *Nat. Neurosci.* 15, 565–573. doi: 10.1038/nn.3059

Wu, W. K., Li, G. R., Wong, H. P., Hui, M. K., Tai, E. K., Lam, E. K., et al. (2006). Involvement of Kv1.1 and Nav1.5 in proliferation of gastric epithelial cells. *J. Cell Physiol.* 207, 437–444. doi: 10.1002/jcp.20576

Wu, Y. P., and Ling, E. A. (1998). Induction of microglial and astrocytic response in the adult rat lumbar spinal cord following middle cerebral artery occlusion. *Exp. Brain Res.* 118, 235–242. doi: 10.1007/s002210050277

Yamanaka, S. (2009). A fresh look at iPS cells. *Cell* 137, 13–17. doi: 10.1016/j.cell.2009.03.034

Yamasaki, R., Lu, H., Butovsky, O., Ohno, N., Rietsch, A. M., Cialic, R., et al. (2014). Differential roles of microglia and monocytes in the inflamed central nervous system. *J. Exp. Med.* 211, 1533–1549. doi: 10.1084/jem.20132477

Yin, Z., Raj, D., Saiepour, N., Van Dam, D., Brouwer, N., Holtman, I. R., et al. (2017). Immune hyperreactivity of Abeta plaque-associated microglia in Alzheimer's disease. *Neurobiol. Aging* 55, 115–122. doi: 10.1016/j.neurobiolaging.2017.03.021

Yoshiyama, Y., Higuchi, M., Zhang, B., Huang, S. M., Iwata, N., Saido, T. C., et al. (2007). Synapse loss and microglial activation precede tangles in a P301S tauopathy mouse model. *Neuron* 53, 337–351. doi: 10.1016/j.neuron.2007.01.010

Yuan, P., Condello, C., Keene, C. D., Wang, Y., Bird, T. D., Paul, S. M., et al. (2016). TREM2 haplodeficiency in mice and humans impairs the microglia barrier function leading to decreased amyloid compaction and severe axonal dystrophy. *Neuron* 92, 252–264. doi: 10.1016/j.neuron.2016.09.016

Zhang, B., Gaiteri, C., Bodea, L. G., Wang, Z., Mcelwee, J., Podtelezhnikov, A. A., et al. (2013). Integrated systems approach identifies genetic nodes and networks in late-onset Alzheimer's disease. *Cell* 153, 707–720. doi: 10.1016/j.cell.2013.03.030

Zheng, C., Zhou, X.-W., and Wang, J.-Z. (2016). The dual roles of cytokines in Alzheimer's disease: update on interleukins, TNF-α, TGF-β and IFN-γ. *Transl. Neurodegener.* 5:7. doi: 10.1186/s40035-016-0054-4

Zlokovic, B. V. (2013). Cerebrovascular effects of apolipoprotein E: implications for Alzheimer disease. *J. Am. Med. Assoc. Neurol* 70, 440–444. doi: 10.1001/jamaneurol.2013.2152

Conflict of Interest Statement: The authors declare that the research was conducted in the absence of any commercial or financial relationships that could be construed as a potential conflict of interest.

APPENDIX C : <u>CHARACTERIZATION OF DNA METHYLOMIC SIGNATURES IN INDUCED PLURIPOTENT STEM CELLS DURING NEURONAL DIFFERENTIATION</u>

SHORT COMMUNICATION

Characterization of DNA Methylomic signatures in induced pluripotent stem cells during neuronal differentiation

ABSTRACT

Background

In development, inducing pluripotency and differentiation into different cell types results in global epigenetic changes, although the extent this occurs in induced pluripotent stem cell (iPSC)-based neuronal models has not been extensively characterized.

Methods

iPSC colonies (33Qn1 line) were differentiated and collected at four time-points. DNA methylation was assessed using the Illumina EPIC array. After dimensionality reduction, we identified dynamic changes during differentiation using a data-driven trajectory inference method.

Discussion

We identified 5,866 Bonferroni-significant loci during differentiation. A gene-gene interaction network analysis identified 50 densely connected genes that are influential in the differentiation of neurons, with *STAT3* being the gene with the highest connectivity.

Conclusions

We have profiled DNA methylation during iPSC-derived neuronal differentiation and identified an epigenetic trajectory signature associated with maturation.

INTRODUCTION

DNA methylation is the most widely studied epigenetic change, as it is the most stable and long-lasting modification; there is a vast array of literature linking DNA methylation changes in various cell types with aging [239, 242, 243, 260, 430, 431]. Changes to the epigenome occur throughout the life course in all tissues and cell types [432-435]. In humans, these changes begin very early, with dynamic DNA methylation changes reported across fetal development [426], and further changes throughout the life course as we age [436].

In recent years, owing to advances in genomic technology, a number of epigenome-wide association studies (EWAS) of DNA methylation have been undertaken in various age-related complex diseases, including, for example, Alzheimer's disease (AD) [405, 407, 437]. Whilst these studies have provided considerable insight into the epigenomic landscape of the disease, they were performed on post-mortem brain tissue and so only offer a snapshot of what is occurring at the end stages of disease and provide no evidence for epigenetic causality. In order to better understand the molecular mechanisms underlying disease onset and progression, it is necessary to monitor epigenetic changes at multiple time points throughout the disease course. However, this is not possible in human studies of inaccessible tissues such as the brain.

One promising avenue for longitudinal modeling of neurological diseases is through the use of induced pluripotent stem cell (iPSC)-derived neuronal cells, as iPSCs are derived from human tissue, can be monitored over time and in theory can be transformed into any cell type in the body [1]. In recent years iPSC-derived neurons have been increasingly used to model various neurological diseases by, for example, utilizing a patient line bearing a specific disease-associated genetic mutation [438, 439]. Furthermore, through recent advances in epigenetic editing technology it is now feasible to model disease-associated DNA methylomic variation. However, there are some potential caveats with this approach; whilst differentiated iPSC-derived neurons have mature electrophysiological features, including spontaneous electrical activity,

regenerative induced action potential train activity and hyperpolarized resting membrane potentials [273], they do not retain their age-related transcriptomic profile [285]. This lack of transcriptional maturity has led researchers to question whether iPSC-derived neurons are an appropriate model to study age-related diseases such as AD. Furthermore, much like the erasure and re-establishment of epigenetic marks after fertilization, there are global DNA methylation changes that occur upon inducing pluripotency [440], which are essential for efficient reprogramming [441]. However, to our knowledge, no studies have yet longitudinally profiled DNA methylation patterns and the epigenetic "age" of iPSC-derived neurons during differentiation and maturation. This is an important area to address before utilizing these to model neuroepigenetic changes in neurological diseases, particularly those that are associated with aging. In this study, we have differentiated iPSCs into cortical neurons and assessed their DNA methylation profile at different time points during differentiation and maturation to identify DNA methylomic trajectories of neuronal aging.

MATERIALS AND METHODS

iPSC culture and neuronal differentiation

This study was performed using one extensively characterised feeder-free human iPSC line (33Qn1), originally derived from human fibroblasts by transfection of episomal plasmid vectors expressing the six transcription factors Oct4, Sox2, Klf4, cMyc, Nanog, and Lin28) [442]. Differentiation was achieved using the SCM1/2 protocol outlined in [273]. Briefly, iPSCs were maintained on vitronectin coated plates in Essential 8 flex medium, passaged using dispase according to the manufacturer's instructions (Stem Cell Technologies) and were collected four days after initial plating for DNA extraction (Day 0 - iPSCs). Neuronal differentiation was started at approximately 70% confluency. Differentiation into neuronal precursors was achieved using SLI media (Advanced DMEM:F12 (with Glutamax); 1 % Penicillin/Streptomycin (all from Life Technologies); 10 µM SB431542 (Abcam, Cambridge, Cambs. U.K.); 1 µM LDN 193189 (Stemgent, Cambridge, MA, U.S.A); 1.5 µM IWR1 (Tocris Bioscience, Abingdon, Oxon., U.K.), and;

2 % NeuroBrew-21 without RA (Miltenyi Biotec: Bisley, Surry, U.K) for the first eight days followed by LI media for another eight days (Advanced DMEM:F12, 2 mM L-glutamine, 1 % Penicillin/Streptomycin, 200 nM LDN 193189, 1.5 µM IWR1, and: 2 % NeuroBrew-21 without RA), after which neuronal precursor cells (NPCs) were collected for DNA extraction (Day 16 – NPCs). The remaining neuronal precursors were then terminally differentiated and matured as described previously [129] using the sequential addition of the SCM1 for seven days (SCM1 contained: Advanced DMEM:F12 (with Glutamax); 1 % penicillin/streptomycin; 2 % NeuroBrew21 (Miltenyi Biotec); 2 μM PD0332991 (Selleckchem); 10 μM DAPT (Sigma-Aldrich); 0.6 mM $CaCl_2$ (to give 1.8mM total $CaCl_2$ in final complete medium, (Sigma-Aldrich)), 200 μM ascorbic acid (Sigma-Aldrich), 10 ng/mL BDNF (Miltenyi Biotec); 1 μM LM22A4 (Tocris Bioscience); 10 μM Forskolin (FSK, Tocris Bioscience), 3 μM CHIR 99021 (Tocris Bioscience), and; 300 μM GABA (Tocris Bioscience)) and then SCM2 for the remainder of the maturation period for a further 37 and 58 days (SCM2 contained: 1:1 Advanced DMEM/F12 (with Glutamax): Neurobasal A (Life Technologies); 1 % penicillin/streptomycin (Life Technologies), 2 % NeuroBrew21 with RA (Miltenyi Biotec); 2 μM PD0332991 (Selleckchem); 3 μM CHIR 99021 (Tocris Bioscience); 0.3 mM $CaCl_2$ (to give 1.8 mM total $CaCl_2$ in final complete medium (Sigma-Aldrich)); 200 μM ascorbic acid (Sigma-Aldrich); 10 ng/mL BDNF (Miltenyi Biotec)). At these time points the cells were collected for DNA extraction (Day 37 and Day 58 – mature neurons). At each time point cells were collected separately from four wells, representing four technical replicates. All collected cells were washed with PBS, pelleted down, frozen and stored at -80°C

Genome-wide quantification of DNA methylation

DNA was extracted from the 16 cell pellets using a standard phenol chloroform protocol. Subsequently, 500ng of genomic DNA was sodium bisulfite converted using the Zymo EZ 96 DNA methylation kit (Zymo Research) according to the manufacturer's instructions. Samples were profiled using the Illumina Infinium Human Methylation EPIC BeadChip (Illumina) and the Illumina HiScan System (Ilumina).

All data analysis was done in R version 3.5.2 (Eggshell Igloo). The methylumi package [443] was used to extract signal intensities for each CpG probe and perform initial QC, with data normalization and pre-processing using the WateRmelon package [153]. Additional QC checks were performed using the p-filter function within the methylumi package, assessing bisulfite conversion efficiency, and the median methylated and unmethylated sample intensities as previously described [437]. Two iPSC samples failed the p-filter checks and had low median (un)methylated sample intensities. As a result, they were removed from the study. For the remaining 14 samples the data were normalized with the *dasen* function from the wateRmelon package [444]. Prior to any analyses, probes with common (>5% minor allele frequency [MAF]) single nucleotide polymorphisms (SNPs) within 10 bp of the single base extension and probes with sequences previously identified as potentially hybridizing to multiple genomic loci were excluded [445], resulting in a final dataset of 847,103 probes. For each of the 14 samples the mitotic age and epigenetic age were calculated [154, 155]. Epigenetic age was calculated using the latest iteration of the Horvath *et al* age calculator using the online portal; available at: https://dnamage.genetics.ucla.edu/new.

Probe filtering and dimensionality reduction

Median absolute deviation (MAD) was computed as a robust measure of variability for each CpG site across the four cell stages and the upper fifth percentile value was used as a cut-off to determine the most variably methylated loci (41,811 loci). Principal component analysis (PCA) without scaling the probes by their variance was then applied to obtain a lower-dimensional feature subspace, representing the information explaining most of the variance in the dataset.

Pseudotime trajectory analysis

A pseudotime trajectory through the cell stages was inferred and plotted using the "infer_trajectory" and "draw_trajectory_plot" functions in the SCORPIUS package, respectively [270]. The first two principal components of the DNA methylation data was subjected as coordinate of the samples to 'infer_trajectory' function which performs k-

means clustering, calculates distance matrix between cluster centres and finds the shortest path connecting all cluster centres using a custom distance function, and finally fits a curve to the given data using principal curves [270].

Next, to identify the loci with the largest contribution to the trajectory inference, we regressed each CpG site's methylation values on the pseudotime variable that had been inferred by trajectory analysis, using a general additive model (GAM). This allowed the detection of non-linear methylation patterns throughout neuronal differentiation. The loci that remained significant after Bonferroni correction for 41,811 tests were considered as robust markers of neuronal differentiation and subjected to further downstream analyses.

Gene Ontology and pathway enrichment analyses

We performed Gene Ontology (GO) pathway analysis using the missMethyl R package [277], which adjusts for the number of CpGs per gene.

Gene-gene interaction network analysis

We used Metacore (Clarivate Analytics) to obtain a set of directed functional regulatory interactions between the unique genes annotated to the CpG sites with the largest contribution to the trajectory inference. The MetaCore database contains a compilation of manually curated and experimentally validated directed gene-gene interactions based on existing literature. Its high level of manual curation ensures the creation of highly confident interaction network maps. The network reconstruction was restricted to interactions reported in humans from the categories "transcriptional regulation", "influence on expression", "co-regulation of transcription", and "regulation", with the interaction type (*i.e.* activation or inhibition) provided when available. Subsequently, the R package igraph (version 1.1.2) [446] was used to extract the strongly connected component (SCC) from the network obtained through Metacore. The 'network analyzer' tool from Cytoscape (version 3.4.0) [281] was used to conduct a network topological analysis in order to identify key genes with high centrality and connectivity in the network.

RESULTS

iPSC-derived neurons have an immature epigenome

One concern when using iPSC-derived neurons to study diseases of advanced age is the biological age of the neurons. We used the Horvath epigenetic age calculator to predict epigenetic age based on DNA methylation profiles assessed by the EPIC array [154]. The epigenetic age of the iPSCs was negative (*i.e.* fetal), with the age then increasing through differentiation and maturation (**Figure 1A**). However, even the most mature neurons we studied (Day 58) still had a negative epigenetic age (~-0.4 years).

Another important metric of aging is the number of cell divisions, which is particularly interesting to assess in our study as differentiated neurons are post-mitotic. Using the MiAge calculator [155] we observed an increase in mitotic age from the iPSC stage to the NPC stage and to Day 37 mature neurons (**Figure 1B**). However, this then plateaued in the Day 58 mature neurons. This suggests that whilst the cells are differentiating into NPCs and, for at least the first 37 days post terminal differentiation, the cells are still replicating. However, at some point after 37 days post terminal differentiation the cells stop dividing and become senescent.

Cell trajectory modeling highlights methylation patterns during differentiation

In order to further explore how DNA methylation levels change throughout neuronal differentiation and maturation, we generated a cellular lineage trajectory signature to identify groups of loci that become progressively hyper- or hypomethylated throughout differentiation. First, we reduced the dimensionality of the dataset containing the most variable CpG probes (41,811 loci), to 14 principal components (PCs), of which the first two explained 78% of the variation in that dataset. These two PCs were used as coordinates of samples to cluster them according to stage of differentiation/maturation (**Figure 2A**). Samples within each cellular stage clustered together, with the exception of one Day 37 neuron sample, which clustered with the Day 58 neuron samples. This could indicate that this sample had aged quicker than the others in the same group; however, when we checked the "epigenetic age" of this sample, it was surprisingly the

second youngest of the four Day 37 neuronal samples. To ensure this sample was not a general outlier we clustered all 14 samples based on Euclidean distance (prior to the trajectory inference analysis). This highlighted that this Day 37 sample was not an outlier in general and clustered together with the Day 58 samples (**Supplementary Figure 1**).

Using the pseudotime generated in the trajectory analysis as a predictor, a GAM was fitted to the 41,811 probes in order to identify the loci that contributed the most to the trajectory inference model. In total we identified 5,866 of the 41,811 loci that showed Bonferroni-significant variation in methylation across the cell stages (**Supplementary Table 1**, **Figure 2B**), which we termed the "epigenetic trajectory signature". An example of the large scale DNA methylation changes occurring through differentiation is highlighted by the cg00908292 probe, which is intergenic and located closest to the *CCR7* gene P_{Bonf}= 7.16x10^{-9}. This locus is hemi-methylated in iPSCs, becoming progressively de-methylated over time and is largely unmethylated in the terminally differentiated mature neurons (**Figure 2C**).

Pathway analysis of loci contributing to cell trajectories implicates development, signalling and transcription

We used GO enrichment analysis to identify the pathways that are changing most significantly throughout neuronal differentiation. We took the 5,866 loci that comprised the epigenetic trajectory signature and grouped these according to whether they were becoming gradually hypermethylated (N=1,661) or hypomethylated (N=4,205) over time. The progressively hypermethylated loci resided in genes that featured in pathways relating to head development, signalling, cell surface receptor signalling, transcriptional activity and cell-cell junctions. (**Supplementary Table 2, Supplementary Figure 2**). The progressively hypomethylated loci were associated with neuron projection development, synaptic activity and gated channel activity (**Supplementary Tables 3**, **Supplementary Figure 3**).

<u>Transcriptional regulation is a highly interconnected process throughout differentiation</u>

To explore the connectivity between key genes that display progressive DNA methylomic changes through differentiation, we performed gene-gene interaction analyses on the 2,352 unique genes that were annotated (Illumina [UCSC] annotation) to the 5,866 loci comprising the epigenetic trajectory signature. The prior knowledge network (PKN) obtained from MetaCore contained 602 genes and 1,158 interactions. Only one strongly connected component (SCC) existed in this network (i.e. there is only one sub-network in which every gene can be reached through any other gene in the same sub-network), comprised of 50 genes and 138 interactions between them (**Supplementary Table 4**, **Figure 3**). The conducted topological network analysis highlighted the key genes in this SCC with outstanding topological characteristics, including out-degree (set of target genes it regulates), in-degree (set of upstream regulating genes), betweenness centrality (most influential genes based on their shortest paths to other genes in the network), and clustering coefficient (a measure of gene tendency to cluster with other genes in the network). *STAT3* was the gene with the highest connectivity (Neighbourhood Connectivity = 9.43, Clustering Coefficient = 0.02) in the SCC, according to its in-degree (9) and out-degree (62), suggesting it may play a key regulatory role in this SCC. Previously, alterations in STAT3 signalling have already been observed to be associated with age-related changes in different cell types [447, 448].

DISCUSSION

In this study we have used the Illumina Infinium EPIC array to profile DNA methylation in iPSCs and throughout their differentiation and maturation into neurons. One of the concerns regarding using iPSC-derived neurons to study diseases of aging is that they have been reported to lose their age-associated transcriptomic signatures [285]. Similarly, in our study we have shown that iPSCs, NPCs and post-terminally differentiated neurons have an immature epigenomic profile according to the Horvath epigenetic age calculator. This is particularly interesting given that these iPSC-derived neurons have been previously shown to be functionally mature at these time points [273].

Mertens and colleagues showed that although neurons derived from iPSCs lose their age-related transcriptional profiles and were comparable to embryonic or immature neurons, this was not the case with inducible neurons (iNs), which are neurons generated directly from fibroblasts that do not go through the intermediate stem cell phase [285]. Alongside the age-related transcriptomic profiles of iNs, they also exhibit age-dependent nucleocytoplasmic compartmentalisation and maintenance of epigenetic age, unlike iPSC-derived neurons. In the future, it will be of interest to assess the mitotic age and epigenetic trajectories of iNs. It will also be important to utilize a number of different iPSC lines and to culture the iPSC-derived neurons for longer than 58 days, to explore how this affects the epigenetic age and epigenetic trajectory. Another important point to consider is that the epigenetic age calculator is reported to be inaccurate in juvenile samples, presumably because DNA methylation changes are more dynamic in children [449]. As all of the samples used in our study were estimated to have an epigenetic age <1 year, it is possible that these predictions are inaccurate, and the biological age of the samples is greater than predicted. Another important marker of aging for cells is their number of divisions, which is particularly interesting in the context of our study as the differentiated neurons (Day 37 and 58) are post-mitotic and therefore should no longer be dividing. We showed that although the mean mitotic age increased from the iPSC stage through to 37 days post-differentiation, this plateaued at day 58, indicating that the neurons had become post mitotic. This decrease could be due to imperfect differentiation in some of the day 37 samples, causing there to be contamination of proliferating non-neural cells. The fact that the mitotic and epigenetic age show different patterns across differentiation/maturation, with the epigenetic age still increasing at day 58, corroborates previous findings that epigenetic age does not reflect mitotic age [247].

One interesting observation from the creation of the cell lineage network was that one of the day 37 terminally differentiated neuron samples clustered more closely with the day 58 terminally differentiated neuron samples, than with other samples of the same cellular

stage. We considered that this sample may have "aged" faster than the other day 37 neurons however, upon further investigation this sample actually had the second lowest epigenetic age and has the lowest mitotic age of the day 37 group. This could therefore suggest that the probes used to determine epigenetic age are not contributing to the epigenetic trajectory signature we identified that distinguished between the different cellular stages.

Our pathway analysis highlighted that probes comprising the epigenetic trajectory signature are largely involved in gene regulation and neural development. The gene-gene interaction network analysis of the epigenetic trajectory signature identified a highly connected, epigenetically altered sub-network of 50 genes, featuring 138 interactions. *STAT3* was the most connected gene in the SCC subnetwork. This gene is known to be involved in neuronal survival and function, for example, *STAT3* and other members of the JAK/STAT pathway have been shown to play key roles in the control of neuronal proliferation, survival and differentiation [292, 293]. Primary neuronal and SH-SY5Y cells have been shown to be highly susceptible to treatment with the STAT3 inhibitor tryphostin, with a significant percentage of both cell types (80-100%) dying even at low concentrations [292]. The fact that *STAT3* was identified as a key gene by the network analysis highlights its importance in the epigenetic trajectory signature, which is further confirmed by its already proven pivotal role in the development and differentiation of neurons.

CONCLUSION

In this study, we have characterized genome-wide patterns of DNA methylation and identified an epigenetic trajectory signature of 5,866 loci that become progressively hypermethylated or hypomethylated during the course of neuronal differentiation and maturation from iPSCs. These loci reside in genes that were over-represented in processes related to gene regulation and transcription.

FUTURE PERSPECTIVE

Since the creation of iPSCs they have been increasingly used to study neurological and neurodegenerative diseases. However, to date iPSC-derived neurons have not been usedto study the epigenetic aberrations known to be associated with various age-related disease. Here we have investigated DNA methylation changes occurring throughout iPSC-derived neuronal differentiation in order to better understand iPSC-derived neurons as a model system in the context of the epigenome. One caveat of our study is that we have examined only one iPSC line (33Qn1). Looking into the future, it will therefore be important to explore whether our epigenetic trajectory signature is reproducible in neurons derived from other iPSC lines. Similarly, it will be of interest to compare iPSC-derived neurons to iN-derived neurons, and to profile neurons beyond 58 days post-terminal differentiation. Another important logical next step for the future will be the profiling of other types of epigenetic markers, such as histone modifications and general chromatin accessibility. Ultimately, different types of epigenetic information will need to be integrated with matched transcriptomic data in order to deconvolute the role of the dynamic epigenetic landscape in the neuronal differentiation process.

EXECUTIVE SUMMARY

Induced pluripotent stem cells (iPSCs)

- Through the introduction of pluripotency factors into differentiated adult cells it is possible to create iPSCs.
- Induction of pluripotency leads to global epigenetic changes.

Epigenetic and mitotic age change throughout neuronal differentiation

- Epigenetic age increases as iPSCs differentiate into neurons. However. even day 58 neurons have a fetal epigenetic age.

- Mitotic age increases initially during differentiation but after terminal differentiation plateaus.

DNA methylation changes occur at a large number of loci

- Bonferroni significant changes to DNA methylation changes occurred at 5,866 loci.

- 1,661 of these loci became progressively hypermethylated during differentiation

Gene-gene interaction analysis nominates *STAT3* as a key gene in differentiation

- A gene-gene interaction analysis identified 50 genes, with 138 interactions, with *STAT3* being the most connected gene.

REFERENCES

Papers of particular significance have been highlighted as: * of interest or ** of considerable interest

1. Bell JT, Tsai P-C, Yang T-P et al. Epigenome-Wide Scans Identify Differentially Methylated Regions for Age and Age-Related Phenotypes in a Healthy Ageing Population. PLOS Genetics 8(4), e1002629 (2012).
2. Horvath S, Zhang Y, Langfelder P et al. Aging effects on DNA methylation modules in human brain and blood tissue. Genome biology 13(10), R97 (2012).
3. Rodriguez-Rodero S, Fernandez-Morera JL, Fernandez AF, Menendez-Torre E, Fraga MF. Epigenetic regulation of aging. Discovery medicine 10(52), 225-233 (2010).
4. Murgatroyd C, Wu Y, Bockmuhl Y, Spengler D. The Janus face of DNA methylation in aging. Aging 2(2), 107-110 (2010).
5. Bollati V, Schwartz J, Wright R et al. Decline in genomic DNA methylation through aging in a cohort of elderly subjects. Mechanisms of ageing and development 130(4), 234-239 (2009).
6. Fraga MF, Esteller M. Epigenetics and aging: the targets and the marks. Trends in genetics : TIG 23(8), 413-418 (2007).
7. Christiansen L, Lenart A, Tan Q et al. DNA methylation age is associated with mortality in a longitudinal Danish twin study. Aging Cell 15(1), 149-154 (2016).
8. Hernandez DG, Nalls MA, Gibbs JR et al. Distinct DNA methylation changes highly correlated with chronological age in the human brain. Human Molecular Genetics 20(6), 1164-1172 (2011).
9. Ronn T, Volkov P, Gillberg L et al. Impact of age, BMI and HbA1c levels on the genome-wide DNA methylation and mRNA expression patterns in human adipose tissue and identification of epigenetic biomarkers in blood. Human Molecular Genetics 24(13), 3792-3813 (2015).

10.   Maegawa S, Hinkal G, Kim HS et al. Widespread and tissue specific age-related DNA methylation changes in mice. Genome Res 20(3), 332-340 (2010).
11.   Spiers H, Hannon E, Schalkwyk LC et al. Methylomic trajectories across human fetal brain development. Genome research 25(3), 338-352 (2015).
*Shows that there are widespread changes in DNA methylation across human fetal brain development.
12.   Horvath S, Raj K. DNA methylation-based biomarkers and the epigenetic clock theory of ageing. Nature Reviews Genetics 19(6), 371-384 (2018).
13.   Lunnon K, Smith R, Hannon E et al. Methylomic profiling implicates cortical deregulation of ANK1 in Alzheimer's disease. Nature neuroscience 17(9), 1164-1170 (2014).
*Paper highlighting DNA methylation aberrations in neurodegenerative disease.
14.   Smith AR, Smith RG, Pishva E et al. Parallel profiling of DNA methylation and hydroxymethylation highlights neuropathology-associated epigenetic variation in Alzheimer's disease. Clinical epigenetics 11(1), 52 (2019).
15.   Smith RG, Hannon E, De Jager PL et al. Elevated DNA methylation across a 48-kb region spanning the HOXA gene cluster is associated with Alzheimer's disease neuropathology. Alzheimer's & dementia : the journal of the Alzheimer's Association 14(12), 1580-1588 (2018).
16.   Imm J, Kerrigan TL, Jeffries A, Lunnon K. Using induced pluripotent stem cells to explore genetic and epigenetic variation associated with Alzheimer's disease. Epigenomics 9(11), 1455-1468 (2017).
17.   Muratore CR, Rice HC, Srikanth P et al. The familial Alzheimer's disease APPV717I mutation alters APP processing and Tau expression in iPSC-derived neurons. Human Molecular Genetics 23(13), 3523-3536 (2014).
18.   Woodruff G, Young JE, Martinez FJ et al. The presenilin-1 DeltaE9 mutation results in reduced gamma-secretase activity, but not total loss of PS1 function, in isogenic human stem cells. Cell reports 5(4), 974-985 (2013).
19.   Telezhkin V, Schnell C, Yarova P et al. Forced cell cycle exit and modulation of GABAA, CREB, and GSK3beta signaling promote functional maturation of induced pluripotent stem cell-derived neurons. American journal of physiology. Cell physiology 310(7), C520-541 (2016).
**Paper demonstrates a method to accelerate maturation of iPSC-derived neuronal cells.
20.   Mertens J, Paquola ACM, Ku M et al. Directly Reprogrammed Human Neurons Retain Aging-Associated Transcriptomic Signatures and Reveal Age-Related Nucleocytoplasmic Defects. Cell stem cell 17(6), 705-718 (2015).
*Paper showing that induced neurons retain their age-related transcriptomic profile whilst iPSC-derived neurons do not.
21.   De Carvalho DD, You JS, Jones PA. DNA Methylation and Cellular Reprogramming. Trends in cell biology 20(10), 609-617 (2010).
22.   Watanabe A, Yamada Y, Yamanaka S. Epigenetic regulation in pluripotent stem cells: a key to breaking the epigenetic barrier. Philosophical transactions of the Royal Society of London. Series B, Biological sciences 368(1609), 20120292-20120292 (2013).
23.   The hd ipsc consortium. Induced Pluripotent Stem Cells from Patients with Huntington's Disease Show CAG-Repeat-Expansion-Associated Phenotypes. Cell stem cell 11(2), 264-278 (2012).
24.   Telezhkin V, Schnell C, Yarova P et al. Forced cell cycle exit and modulation of GABAA, CREB, and GSK3β signaling promote functional maturation of induced pluripotent stem cell-derived neurons. American Journal of Physiology-Cell Physiology 310(10), (2016).
25.   Davis S, Du P, Triche JT, Bootwalla M. methylumi: Handle Illumina methylation data. R package version 2.26.0. doi:10.18129/B9.bioc.methylumi (2017).
26.   Pidsley R, Cc YW, Volta M, Lunnon K, Mill J, Schalkwyk LC. A data-driven approach to preprocessing Illumina 450K methylation array data. BMC genomics 14 293 (2013).

27.   Pidsley R, Y Wong CC, Volta M, Lunnon K, Mill J, Schalkwyk LC. A data-driven
       approach to preprocessing Illumina 450K methylation array data. BMC
       Genomics 14(1), 293 (2013).
*Paper that is fundamental in the pre-processing of DNA methylation data.
28.   Mccartney DL, Walker RM, Morris SW, Mcintosh AM, Porteous DJ, Evans KL.
       Identification of polymorphic and off-target probe binding sites on the Illumina
       Infinium MethylationEPIC BeadChip. Genom Data 9 22-24 (2016).
29.   Horvath S, Oshima J, Martin GM et al. Epigenetic clock for skin and blood cells
       applied to Hutchinson Gilford Progeria Syndrome and ex vivo studies. Aging
       10(7), 1758-1775 (2018).
**This paper is the basis of the newest epigenetic age calculator used in this study.
30.   Youn A, Wang S. The MiAge Calculator: a DNA methylation-based mitotic age
       calculator of human tissue types. Epigenetics 13(2), 192-206 (2018).
**This paper introduces the mitotic age calculator used in this study.
31.   Cannoodt R, Saelens W, Sichien D et al. SCORPIUS improves trajectory
       inference and identifies novel modules in dendritic cell development. bioRxiv
       doi:10.1101/079509 079509 (2016).
**This study introduces the SCORPIOUS trajectory inference methodology used in this
       paper.
32.   Phipson B, Maksimovic J, Oshlack A. missMethyl: an R package for analyzing
       data from Illumina's HumanMethylation450 platform. Bioinformatics (Oxford,
       England) 32(2), 286-288 (2016).
33.   Csardi G, Nepusz T. The igraph software package for complex network
       research. InterJournal Complex Systems 1695 (2006).
34.   Shannon P, Markiel A, Ozier O et al. Cytoscape: a software environment for
       integrated models of biomolecular interaction networks. Genome research
       13(11), 2498-2504 (2003).
35.   O'brown ZK, Van Nostrand EL, Higgins JP, Kim SK. The Inflammatory
       Transcription Factors NFkappaB, STAT1 and STAT3 Drive Age-Associated
       Transcriptional Changes in the Human Kidney. PLoS Genet 11(12), e1005734
       (2015).
36.   Chazaud B, Mouchiroud G. Inflamm-aging: STAT3 signaling pushes muscle
       stem cells off balance. Cell stem cell 15(4), 401-402 (2014).
37.   Mcewen LM, O'donnell KJ, Mcgill MG et al. The PedBE clock accurately
       estimates DNA methylation age in pediatric buccal cells. Proceedings of the
       National Academy of Sciences of the United States of America
       doi:10.1073/pnas.1820843116 (2019).
38.   Horvath S. DNA methylation age of human tissues and cell types. Genome
       biology 14(10), R115 (2013).
*Outlines the first iteration of the epigenetic age calculator.
39.   Yadav A, Kalita A, Dhillon S, Banerjee K. JAK/STAT3 pathway is involved in
       survival of neurons in response to insulin-like growth factor and negatively
       regulated by suppressor of cytokine signaling-3. The Journal of biological
       chemistry 280(36), 31830-31840 (2005).
40.   Snyder M, Huang XY, Zhang JJ. Stat3 is essential for neuronal differentiation
       through direct transcriptional regulation of the Sox6 gene. FEBS Lett 585(1),
       148-152 (2011).

Figure 1: The predicted biological ages of iPSC-derived neurons through differentiation. As two iPSC samples did not pass the quality control checks there are only two samples in the iPSC group of each graph. (**A**) The estimated epigenetic age (Y-axis) of the four cellular stages (X-axis) increased throughout differentiation, with the Day 58 neurons having the highest epigenetic age, although the mean age was still <0.5 years. (**B**) The estimated mitotic age (number of cell divisions - Y-axis) of the four cellular stages (X-axis) increased until 37 days post-terminal differentiation, after which point it plateaued suggesting the day 58 neurons had become senescent.
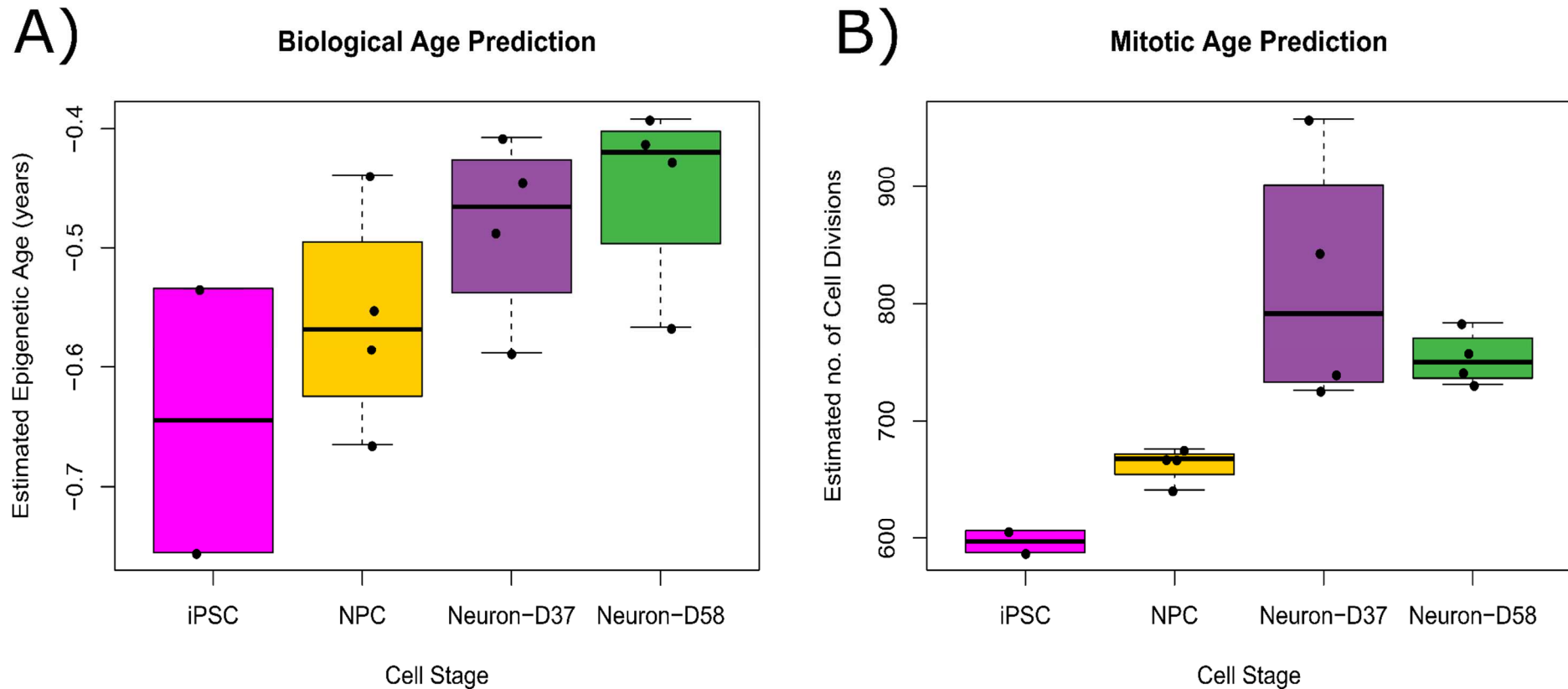
Figure 2: Trajectory inference modelling identifies a signature of 5,866 probes that distinguish cell stage. (**A**) To create the trajectory model dimensionality reduction was first performed, using PCA, followed by estimating pseudo-time to model the lineage trajectory. The different samples grouped together based on the first two principal components. (**B**) Using the pseudo-time estimation a generalised additive model was used to determine which of the 5,866 probes were becoming hypomethylated (blue) or hypermethylated (red) over time. The patterns of hypomethylation and hypermethylation could distinguish the different cell stages. (**C**) The DNA methylation patterns occurring at the most significant probe throughout differentiation. Left: plot of beta-value (Y-axis) against pseudotime (X-axis) and right: plot of beta-value (Y-axis) against cellular stage (X-axis).

A)

B)

C)
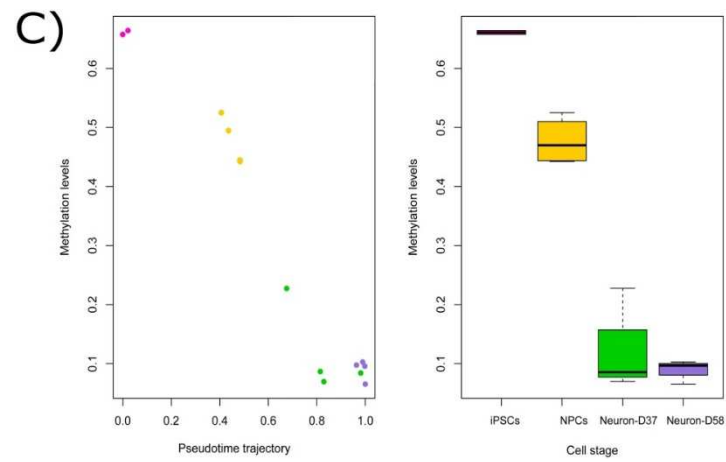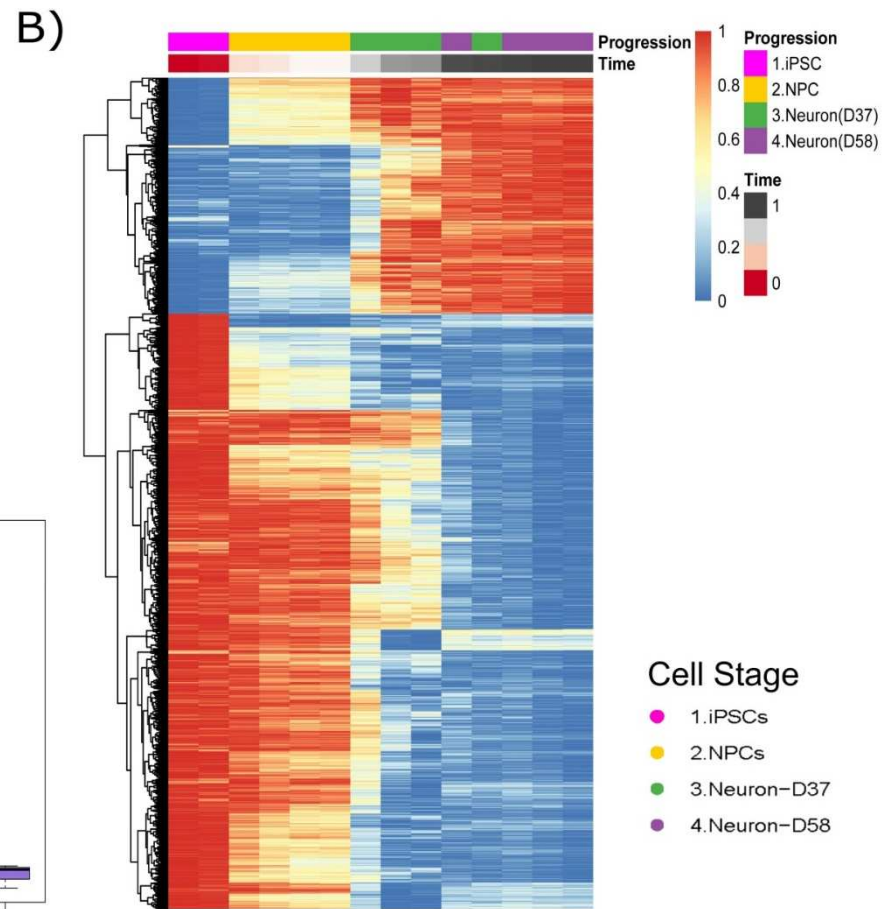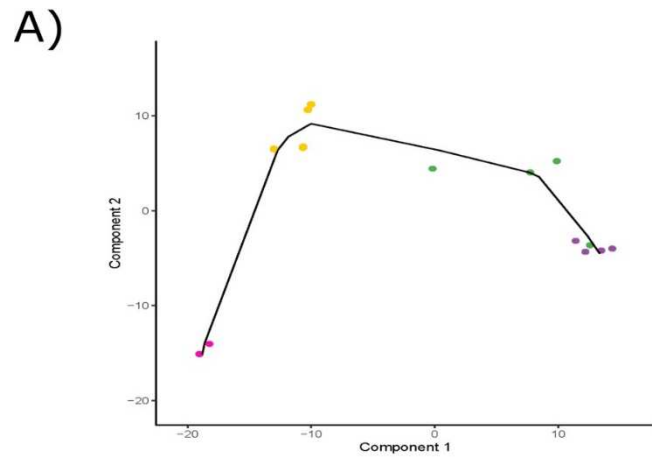
Figure 3: A subnetwork of 50 genes constituting the strongly connected component (SCC) in the gene-gene interaction network. Directed gene-gene interaction network was constructed for 2,352 unique genes that were annotated to the 5,866 loci comprising the epigenetic trajectory signature. The prior knowledge network (PKN) obtained from Metacore contained 602 genes and 1,158 interactions. Only one strongly connected component (SCC) in this network, comprising of 50 genes and 138 interactions between them was identified, blue nodes indicate genes becoming progressively hypomethylated, red nodes indicate genes becoming progressively hypermethylated and grey ovals indicate genes that have more than one probe annotated to them that have different patterns of methylation change.
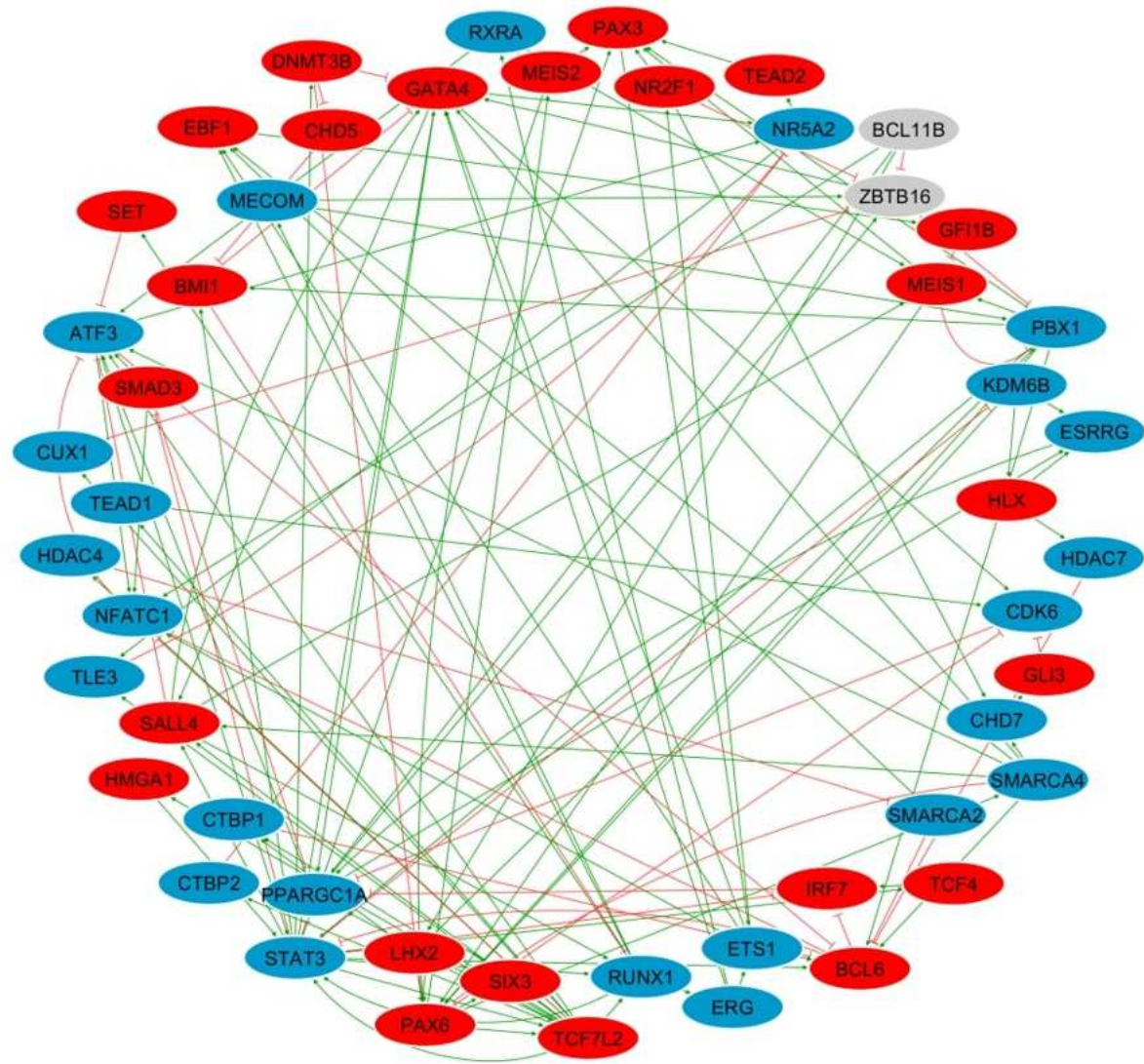
Supplementary figure 1: Clustering of 14 samples based on Euclidean distance prior Trajectory inference analysis. One sample from Day 37 is clustered together with the Day 58 samples

Sample dendrogram and Day indicator
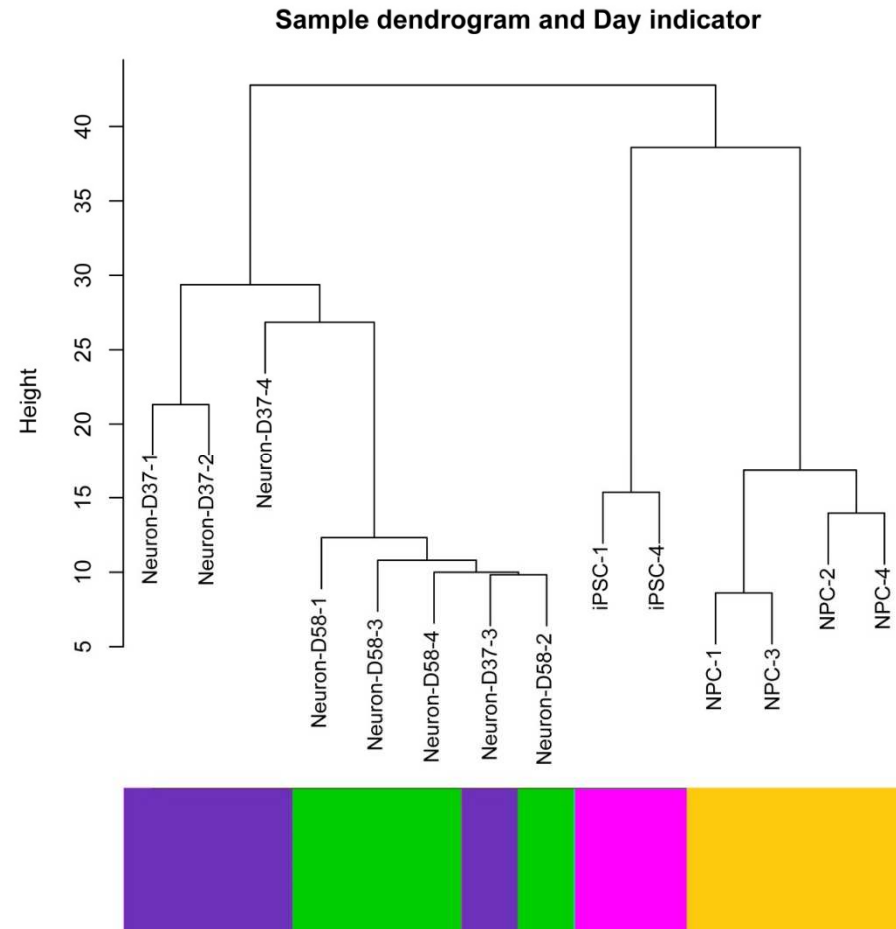
Supplementary figure 2: Pathway analysis of loci becoming progressively hypermethylated throughout differentiation. Gene ontology (GO) enrichment analysis was performed on the 1,661 loci shown to become progressively hypermethylated throughout neuronal differentiation. Treemaps illustrating the pathways relating to (**A**) biological pathways (BP), (**B**) cellular components (CC) and (**C**) molecular functions (MF) that are changing throughout differentiation are shown. For each treemap, terms relating to the same pathway are grouped together and have been given the same colour, the term that summarizes the grouped pathways is at the centre of each section and is written in bold text.
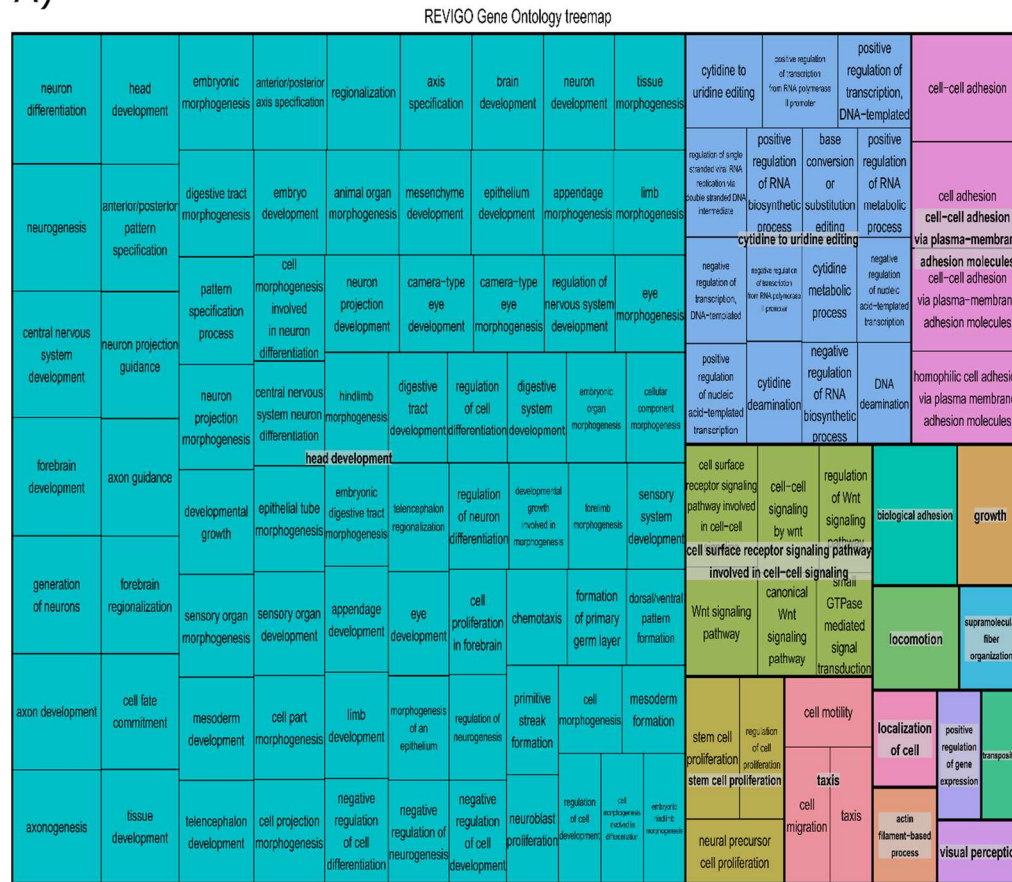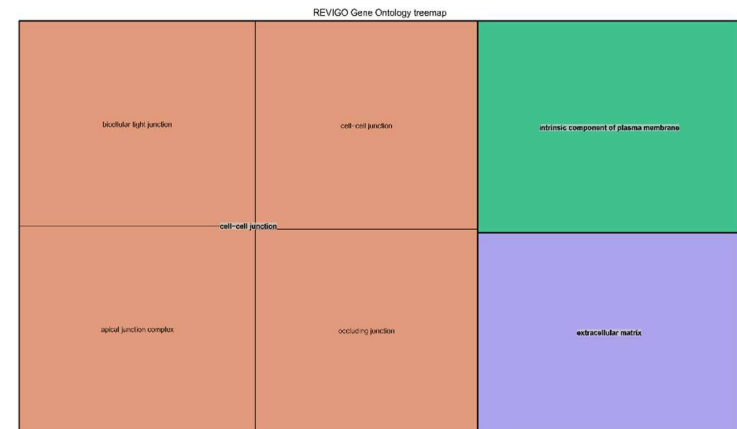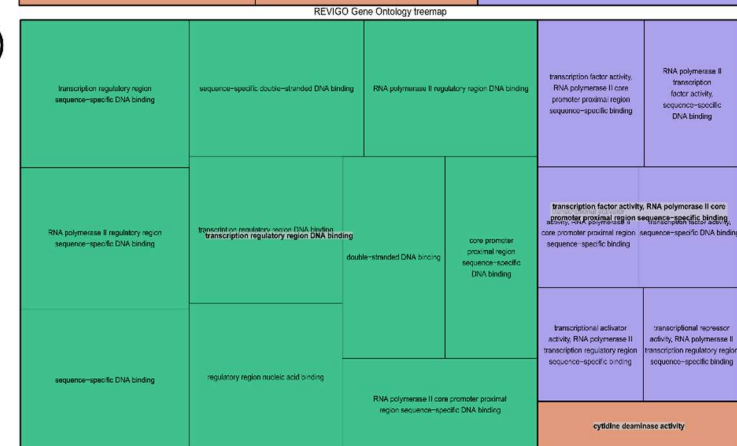
Supplementary figure 3: Pathway analysis of loci becoming progressively hypomethylated throughout differentiation. Gene ontology (GO) enrichment analysis was performed on the 4,205 loci shown to become progressively hypomethylated throughout neuronal differentiation. Treemaps illustrating the pathways relating to (**A**) biological pathways (BP), (**B**) cellular components (CC) and (**C**) molecular functions (MF) that are changing throughout differentiation are shown. For each treemap, terms relating to the same pathway are grouped together and have been given the same colour, the term that summarizes the grouped pathways is at the centre of each section and is written in bold text.

A)
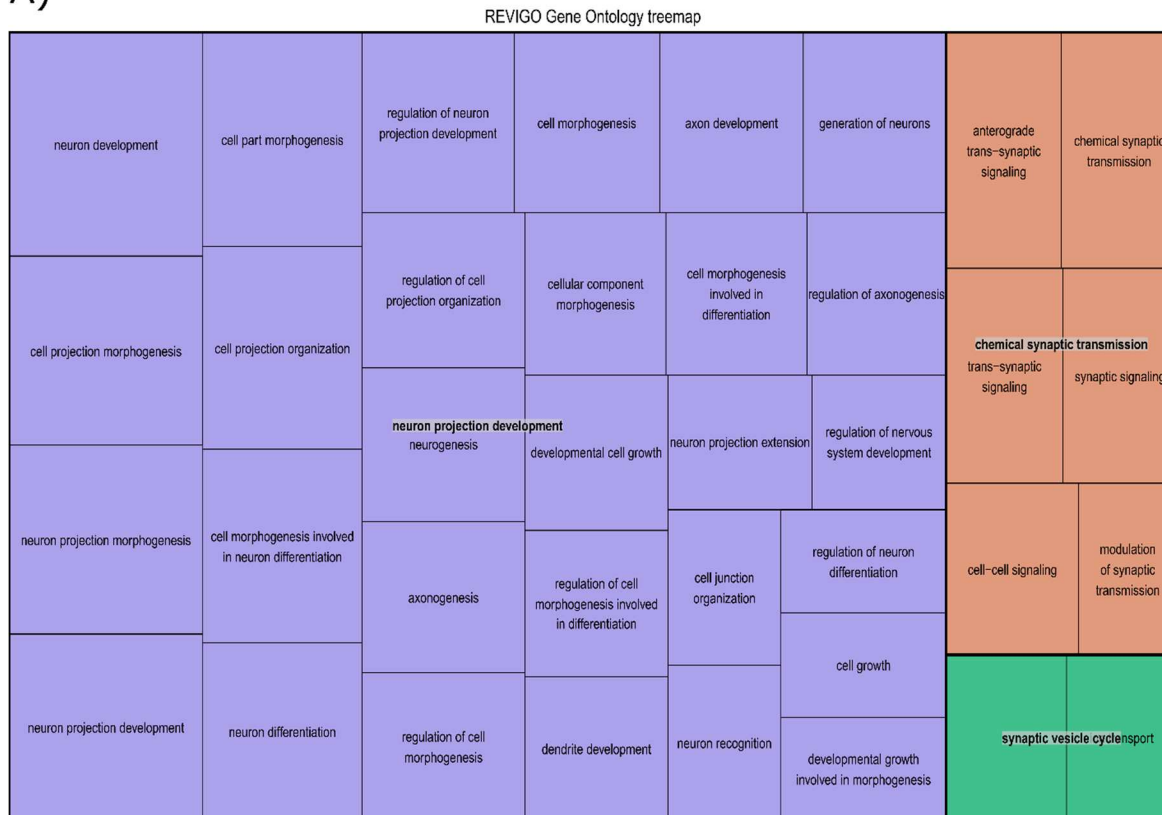
B)
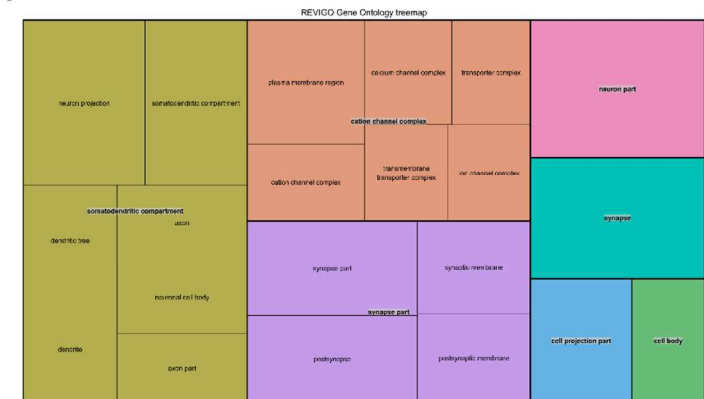
C)

References

1.   Imm, J., et al., *Using induced pluripotent stem cells to explore genetic and epigenetic variation associated with Alzheimer's disease.* Epigenomics, 2017. **9**(11): p. 1455-1468.

2.   Association, A.s. *What Is Dementia?* ; Available from: http://www.alz.org/what-is-dementia.asp.

3.   Blurton-Jones, M. and F.M. Laferla, *Pathways by which Abeta facilitates tau pathology.* Curr Alzheimer Res, 2006. **3**(5): p. 437-48.

4.   Butterfield, D.A. and D. Boyd-Kimball, *Amyloid beta-peptide(1-42) contributes to the oxidative stress and neurodegeneration found in Alzheimer disease brain.* Brain Pathol, 2004. **14**(4): p. 426-32.

5.   Braak, H. and E. Braak, *Neuropathological stageing of Alzheimer-related changes.* Acta Neuropathol, 1991. **82**(4): p. 239-59.

6.   Rasool, C.G., C.N. Svendsen, and D.J. Selkoe, *Neurofibrillary degeneration of cholinergic and noncholinergic neurons of the basal forebrain in Alzheimer's disease.* Ann Neurol, 1986. **20**(4): p. 482-8.

7.   Zhu, X.C., et al., *Rate of early onset Alzheimer's disease: a systematic review and meta-analysis.* Ann Transl Med, 2015. **3**(3).

8.   Gatz, M., et al., *Role of genes and environments for explaining Alzheimer disease.* Arch Gen Psychiatry, 2006. **63**(2): p. 168-74.

9.   Prince, M., et al., *The Global Impact of Dementia: An Analysis of Prevalence, Incidence, Cost and Trends.* Alzheimers's Disease International, 2015: p. 1-87.

10.   Prince, M., et al., *World Alzheimer Report 2015 The Global Impact of Dementia An analysis of prevalence, incidence, cost and trends.* Alzheimer's Disease International, 2015: p. 1-87.

11.   United Nations, D.o.E.a.S.A., Population Division., *World Population Ageing 2017 - Highlights.* 2017.

12.   Braak, H. and E. Braak, *Demonstration of amyloid deposits and neurofibrillary changes in whole brain sections.* Brain Pathol, 1991. **1**(3): p. 213-6.

13.   Kalus, P., et al., *The presubicular region in Alzheimer's disease: topography of amyloid deposits and neurofibrillary changes.* Brain Res, 1989. **494**(1): p. 198-203.

14.   Rogers, J. and J.H. Morrison, *Quantitative morphology and regional and laminar distributions of senile plaques in Alzheimer's disease.* J Neurosci, 1985. **5**(10): p. 2801-8.

15.   Van Hoesen, G.W. and B.T. Hyman, *Hippocampal formation: anatomy and the patterns of pathology in Alzheimer's disease.* Prog Brain Res, 1990. **83**: p. 445-57.

16.   Francis, P.T., et al., *The cholinergic hypothesis of Alzheimer's disease: a review of progress.* J Neurol Neurosurg Psychiatry, 1999. **66**(2): p. 137-47.

17.   Thal, D.R., et al., *Phases of A beta-deposition in the human brain and its relevance for the development of AD.* Neurology, 2002. **58**(12): p. 1791-800.

18.   Cragg, B.G., *Autonomic functions of the hippocampus.* Nature, 1958. **182**(4636): p. 675-6.

19.   Diamond, I.T. and W.C. Hall, *Evolution of neocortex.* Science, 1969. **164**(3877): p. 251-62.

20.   Morris, R.G., et al., *Place navigation impaired in rats with hippocampal lesions.* Nature, 1982. **297**(5868): p. 681-3.

21. Jack, C.R., Jr., et al., *Hypothetical model of dynamic biomarkers of the Alzheimer's pathological cascade.* Lancet Neurol, 2010. **9**(1): p. 119-28.

22. Price, J.L. and J.C. Morris, *Tangles and plaques in nondemented aging and "preclinical" Alzheimer's disease.* Ann Neurol, 1999. **45**(3): p. 358-68.

23. O'Brien, R.J. and P.C. Wong, *Amyloid precursor protein processing and Alzheimer's disease.* Annu Rev Neurosci, 2011. **34**: p. 185-204.

24. Levy-Lahad, E., et al., *Candidate gene for the chromosome 1 familial Alzheimer's disease locus.* Science, 1995. **269**(5226): p. 973-7.

25. Rogaev, E.I., et al., *Familial Alzheimer's disease in kindreds with missense mutations in a gene on chromosome 1 related to the Alzheimer's disease type 3 gene.* Nature, 1995. **376**(6543): p. 775-8.

26. Sherrington, R., et al., *Cloning of a gene bearing missense mutations in early-onset familial Alzheimer's disease.* Nature, 1995. **375**(6534): p. 754-60.

27. Parihar, M.S. and G.J. Brewer, *Amyloid-beta as a modulator of synaptic plasticity.* J Alzheimers Dis, 2010. **22**(3): p. 741-63.

28. Takashima, A., et al., *Activation of tau protein kinase I/glycogen synthase kinase-3beta by amyloid beta peptide (25-35) enhances phosphorylation of tau in hippocampal neurons.* Neurosci Res, 1998. **31**(4): p. 317-23.

29. Atwood, C.S., et al., *Amyloid-beta: a chameleon walking in two worlds: a review of the trophic and toxic properties of amyloid-beta.* Brain Res Brain Res Rev, 2003. **43**(1): p. 1-16.

30. Ahmed, M., et al., *Structural conversion of neurotoxic amyloid-beta(1-42) oligomers to fibrils.* Nat Struct Mol Biol, 2010. **17**(5): p. 561-7.

31. Bird, T.D., *Genetic aspects of Alzheimer disease.* Genet Med, 2008. **10**(4): p. 231-9.

32. Weingarten, M.D., et al., *A protein factor essential for microtubule assembly.* Proc Natl Acad Sci U S A, 1975. **72**(5): p. 1858-62.

33. Kolarova, M., et al., *Structure and Pathology of Tau Protein in Alzheimer Disease.* International Journal of Alzheimer’s Disease, 2012. **2012**: p. 13.

34. Zempel, H. and E. Mandelkow, *Lost after translation: missorting of Tau protein and consequences for Alzheimer disease.* Trends Neurosci, 2014. **37**(12): p. 721-32.

35. Alonso, A.C., et al., *Role of abnormally phosphorylated tau in the breakdown of microtubules in Alzheimer disease.* Proc Natl Acad Sci U S A, 1994. **91**(12): p. 5562-6.

36. Li, B., et al., *Disruption of microtubule network by Alzheimer abnormally hyperphosphorylated tau.* Acta Neuropathol, 2007. **113**(5): p. 501-11.

37. Terry, R.D., *The pathogenesis of Alzheimer disease: an alternative to the amyloid hypothesis.* J Neuropathol Exp Neurol, 1996. **55**(10): p. 1023-5.

38. Metaxas, A. and S.J. Kempf, *Neurofibrillary tangles in Alzheimer's disease: elucidation of the molecular mechanism by immunohistochemistry and tau protein phospho-proteomics.* Neural regeneration research, 2016. **11**(10): p. 1579-1581.

39. Alonso, A.C., I. Grundke-Iqbal, and K. Iqbal, *Alzheimer's disease hyperphosphorylated tau sequesters normal tau into tangles of filaments and disassembles microtubules.* Nat Med, 1996. **2**(7): p. 783-7.

40. Bierer, L.M., et al., *Neocortical neurofibrillary tangles correlate with dementia severity in Alzheimer's disease.* Arch Neurol, 1995. **52**(1): p. 81-8.

41. Hutton, M., et al., *Association of missense and 5'-splice-site mutations in tau with the inherited dementia FTDP-17.* Nature, 1998. **393**(6686): p. 702-705.

42. Spillantini, M.G., et al., *Mutation in the tau gene in familial multiple system tauopathy with presenile dementia.* Proceedings of the National Academy of Sciences of the United States of America, 1998. **95**(13): p. 7737-7741.

43. Poorkaj, P., et al., *Tau is a candidate gene for chromosome 17 frontotemporal dementia.* Annals of Neurology, 1998. **43**(6): p. 815-825.

44. Hong, M., et al., *Mutation-specific functional impairments in distinct tau isoforms of hereditary FTDP-17.* Science, 1998. **282**(5395): p. 1914-1917.

45. Dayanandan, R., et al., *Mutations in tau reduce its microtubule binding properties in intact cells and affect its phosphorylation.* FEBS Letters, 1999. **446**(2-3): p. 228-232.

46. Rizzu, P., et al., *High Prevalence of Mutations in the Microtubule-Associated Protein Tau in a Population Study of Frontotemporal Dementia in the Netherlands.* The American Journal of Human Genetics, 1999. **64**(2): p. 414-421.

47. Hasegawa, M., M.J. Smith, and M. Goedert, *Tau proteins with FTDP-17 mutations have a reduced ability to promote microtubule assembly.* FEBS Letters, 1998. **437**(3): p. 207-210.

48. P, P., et al., *Tau Is a Candidate Gene for Chromosome 17 Frontotemporal Dementia.* Annals of neurology, 1998. **43**(6).

49. HR, M., et al., *Mutation in the Tau Exon 10 Splice Site Region in Familial Frontotemporal Dementia.* Annals of neurology, 1999. **45**(2).

50. Hutton, M., et al., *Association of missense and 5'-splice-site mutations in tau with the inherited dementia FTDP-17.* Nature, 2020. **393**(6686): p. 702-705.

51. L, V., et al., *Structure of Tau Exon 10 Splicing Regulatory Element RNA and Destabilization by Mutations of Frontotemporal Dementia and Parkinsonism Linked to Chromosome 17.* Proceedings of the National Academy of Sciences of the United States of America, 1999. **96**(14).

52. M, H., et al., *Mutation-specific Functional Impairments in Distinct Tau Isoforms of Hereditary FTDP-17.* Science (New York, N.Y.), 1998. **282**(5395).

53. AJ, W., et al., *Is Tau in the Absence of Amyloid on the Alzheimer's Continuum?: A Study of Discordant PET Positivity.* Brain communications, 2020. **2**(1).

54. Nayak, D., T.L. Roth, and D.B. McGavern, *Microglia development and function.* Annu Rev Immunol, 2014. **32**: p. 367-402.

55. Hutchins, K.D., et al., *Localization of morphologically distinct microglial populations in the developing human fetal brain: implications for ontogeny.* Brain Res Dev Brain Res, 1990. **55**(1): p. 95-102.

56. Ginhoux, F., et al., *Fate mapping analysis reveals that adult microglia derive from primitive macrophages.* Science, 2010. **330**(6005): p. 841-5.

57. Hansen, D.V., J.E. Hanson, and M. Sheng, *Microglia in Alzheimer's disease.* J Cell Biol, 2018. **217**(2): p. 459-472.

58. Glenn, J.A., et al., *Characterisation of ramified microglial cells: detailed morphology, morphological plasticity and proliferative capability.* J Anat, 1992. **180 (Pt 1)**(Pt 1): p. 109-18.

59. Perry, V.H., J.A. Nicoll, and C. Holmes, *Microglia in neurodegenerative disease.* Nat Rev Neurol, 2010. **6**(4): p. 193-201.

60. Perry, V.H. and C. Holmes, *Microglial priming in neurodegenerative disease.* Nature Reviews Neurology, 2014. **10**: p. 217.

61. Perry, V.H., *The influence of systemic inflammation on inflammation in the brain: implications for chronic neurodegenerative disease.* Brain Behav Immun, 2004. **18**(5): p. 407-13.

62. Perry, V.H., C. Cunningham, and C. Holmes, *Systemic infections and inflammation affect chronic neurodegeneration.* Nat Rev Immunol, 2007. **7**(2): p. 161-7.

63. Frank, M.G., et al., *mRNA up-regulation of MHC II and pivotal pro-inflammatory genes in normal brain aging.* Neurobiol Aging, 2006. **27**(5): p. 717-22.

64. Godbout, J.P., et al., *Exaggerated neuroinflammation and sickness behavior in aged mice following activation of the peripheral innate immune system.* Faseb j, 2005. **19**(10): p. 1329-31.

65. VanGuilder, H.D., et al., *Concurrent hippocampal induction of MHC II pathway components and glial activation with advanced aging is not correlated with cognitive impairment.* J Neuroinflammation, 2011. **8**: p. 138.

66. Henry, C.J., et al., *Peripheral lipopolysaccharide (LPS) challenge promotes microglial hyperactivity in aged mice that is associated with exaggerated induction of both pro-inflammatory IL-1beta and anti-inflammatory IL-10 cytokines.* Brain Behav Immun, 2009. **23**(3): p. 309-17.

67. Mrak, R.E. and W.S. Griffin, *Common inflammatory mechanisms in Lewy body disease and Alzheimer disease.* J Neuropathol Exp Neurol, 2007. **66**(8): p. 683-6.

68. Maezawa, I., et al., *Amyloid-beta protein oligomer at low nanomolar concentrations activates microglia and induces microglial neurotoxicity.* J Biol Chem, 2011. **286**(5): p. 3693-706.

69. de Craen, A.J., et al., *Meta-analysis of nonsteroidal antiinflammatory drug use and risk of dementia.* Am J Epidemiol, 2005. **161**(2): p. 114-20.

70. Chen, J., et al., *Inhibition of AGEs/RAGE/Rho/ROCK pathway suppresses non-specific neuroinflammation by regulating BV2 microglial M1/M2 polarization through the NF-kappaB pathway.* J Neuroimmunol, 2017. **305**: p. 108-114.

71. H, E.H., H.N. Noristani, and F.E. Perrin, *Microglia Responses in Acute and Chronic Neurological Diseases: What Microglia-Specific Transcriptomic Studies Taught (and did Not Teach) Us.* Front Aging Neurosci, 2017. **9**: p. 227.

72. Bolos, M., J.R. Perea, and J. Avila, *Alzheimer's disease as an inflammatory disease.* Biomol Concepts, 2017. **8**(1): p. 37-43.

73. Breitner, J.C., et al., *Extended results of the Alzheimer's disease anti-inflammatory prevention trial.* Alzheimers Dement, 2011. **7**(4): p. 402-11.

74. Poirier, J., *Apolipoprotein E, cholesterol transport and synthesis in sporadic Alzheimer's disease.* Neurobiol Aging, 2005. **26**(3): p. 355-61.

75. Nathan, B.P., et al., *Differential effects of apolipoproteins E3 and E4 on neuronal growth in vitro.* Science, 1994. **264**(5160): p. 850-2.

76. Huang, Y., *Abeta-independent roles of apolipoprotein E4 in the pathogenesis of Alzheimer's disease.* Trends Mol Med, 2010. **16**(6): p. 287-94.

77. Zlokovic, B.V., *Cerebrovascular effects of apolipoprotein E: implications for Alzheimer disease.* JAMA Neurol, 2013. **70**(4): p. 440-4.

78. Corder, E.H., et al., *Gene dose of apolipoprotein E type 4 allele and the risk of Alzheimer's disease in late onset families.* Science, 1993. **261**(5123): p. 921-3.

79. Slooter, A.J., et al., *Risk estimates of dementia by apolipoprotein E genotypes from a population-based incidence study: the Rotterdam Study.* Arch Neurol, 1998. **55**(7): p. 964-8.

80. Lambert, J.C., et al., *Meta-analysis of 74,046 individuals identifies 11 new susceptibility loci for Alzheimer's disease.* Nat Genet, 2013. **45**(12): p. 1452-8.

81. Kunkle, B.W., et al., *Genetic meta-analysis of diagnosed Alzheimer's disease identifies new risk loci and implicates Aβ, tau, immunity and lipid processing.* Nature Genetics, 2019. **51**(3): p. 414-430.

82. Jansen, I.E., et al., *Genome-wide meta-analysis identifies new loci and functional pathways influencing Alzheimer's disease risk.* Nature Genetics, 2019. **51**(3): p. 404-413.

83. Ebbert, M.T., et al., *Population-based analysis of Alzheimer's disease risk alleles implicates genetic interactions.* Biol Psychiatry, 2014. **75**(9): p. 732-7.

84. Escott-Price, V., et al., *Common polygenic variation enhances risk prediction for Alzheimer's disease.* Brain, 2015. **138**(Pt 12): p. 3673-84.

85. Escott-Price, V., et al., *Polygenic score prediction captures nearly all common genetic risk for Alzheimer's disease.* Neurobiol Aging, 2017. **49**: p. 214.e7-214.e11.

86. Ridge, P.G., et al., *Alzheimer's disease: analyzing the missing heritability.* PLoS One, 2013. **8**(11): p. e79771.

87. Cruchaga, C., et al., *Rare coding variants in the phospholipase D3 gene confer risk for Alzheimer's disease.* Nature, 2014. **505**(7484): p. 550-4.

88. Jakobsdottir, J. and S.J. van der Lee, *Rare Functional Variant in TM2D3 is Associated with Late-Onset Alzheimer's Disease.* 2016. **12**(10): p. e1006327.

89. Jonsson, T., et al., *Variant of TREM2 associated with the risk of Alzheimer's disease.* N Engl J Med, 2013. **368**(2): p. 107-16.

90. Guerreiro, R., et al., *TREM2 variants in Alzheimer's disease.* N Engl J Med, 2013. **368**(2): p. 117-27.

91. Lord, J., et al., *Next generation sequencing of CLU, PICALM and CR1: pitfalls and potential solutions.* Int J Mol Epidemiol Genet, 2012. **3**(4): p. 262-75.

92. Henikoff, S. and M.A. Matzke, *Exploring and explaining epigenetic effects.* Trends Genet, 1997. **13**(8): p. 293-5.

93. Jaenisch, R. and A. Bird, *Epigenetic regulation of gene expression: how the genome integrates intrinsic and environmental signals.* Nat Genet, 2003. **33 Suppl**: p. 245-54.

94. Lande-Diner, L., et al., *Role of DNA methylation in stable gene repression.* J Biol Chem, 2007. **282**(16): p. 12194-200.

95. Almouzni, G. and H. Cedar, *Maintenance of Epigenetic Information.* Cold Spring Harb Perspect Biol, 2016. **8**(5).

96. Lunnon, K. and J. Mill, *Epigenetic studies in Alzheimer's disease: current findings, caveats, and considerations for future studies.* Am J Med Genet B Neuropsychiatr Genet, 2013. **162b**(8): p. 789-99.

97. Klose, R.J. and A.P. Bird, *Genomic DNA methylation: the mark and its mediators.* Trends Biochem Sci, 2006. **31**(2): p. 89-97.

98. Aran, D., et al., *Replication timing-related and gene body-specific methylation of active human genes.* Hum Mol Genet, 2011. **20**(4): p. 670-80.

99. Ball, M.P., et al., *Targeted and genome-scale strategies reveal gene-body methylation signatures in human cells.* Nat Biotechnol, 2009. **27**(4): p. 361-8.

100. Rauch, T.A., et al., *A human B cell methylome at 100-base pair resolution.* Proc Natl Acad Sci U S A, 2009. **106**(3): p. 671-8.

101. Wyatt, G.R. and S.S. Cohen, *The bases of the nucleic acids of some bacterial and animal viruses: the occurrence of 5-hydroxymethylcytosine.* Biochem J, 1953. **55**(5): p. 774-82.

102. Penn, N.W., et al., *The presence of 5-hydroxymethylcytosine in animal deoxyribonucleic acid.* Biochem J, 1972. **126**(4): p. 781-90.

103. Inoue, A., et al., *Generation and replication-dependent dilution of 5fC and 5caC during mouse preimplantation development.* Cell Research, 2011. **21**: p. 1670.

104. Ito, S., et al., *Tet proteins can convert 5-methylcytosine to 5-formylcytosine and 5-carboxylcytosine.* Science, 2011. **333**(6047): p. 1300-3.

105. Globisch, D., et al., *Tissue Distribution of 5-Hydroxymethylcytosine and Search for Active Demethylation Intermediates.* PLOS ONE, 2010. **5**(12): p. e15367.

106. Kriaucionis, S. and N. Heintz, *The nuclear DNA base 5-hydroxymethylcytosine is present in Purkinje neurons and the brain.* Science, 2009. **324**(5929): p. 929-30.

107. Li, W. and M. Liu, *Distribution of 5-Hydroxymethylcytosine in Different Human Tissues.* Journal of Nucleic Acids, 2011. **2011**.

108. Ficz, G., et al., *Dynamic regulation of 5-hydroxymethylcytosine in mouse ES cells and during differentiation.* Nature, 2011. **473**(7347): p. 398-402.

109. Tahiliani, M., et al., *Conversion of 5-Methylcytosine to 5-Hydroxymethylcytosine in Mammalian DNA by MLL Partner TET1.* Science, 2009. **324**(5929): p. 930-935.

110. Freudenberg, J.M., et al., *Acute depletion of Tet1-dependent 5-hydroxymethylcytosine levels impairs LIF/Stat3 signaling and results in loss of embryonic stem cell identity.* Nucleic Acids Res, 2012. **40**(8): p. 3364-77.

111. Ito, S., et al., *Role of Tet proteins in 5mC to 5hmC conversion, ES-cell self-renewal and inner cell mass specification.* Nature, 2010. **466**: p. 1129.

112. Sherwani, S.I. and H.A. Khan, *Role of 5-hydroxymethylcytosine in neurodegeneration.* Gene, 2015. **570**(1): p. 17-24.

113. Chouliaras, L., et al., *Consistent decrease in global DNA methylation and hydroxymethylation in the hippocampus of Alzheimer's disease patients.* Neurobiol Aging, 2013. **34**(9): p. 2091-9.

114. Mastroeni, D., et al., *Epigenetic changes in Alzheimer's disease: decrements in DNA methylation.* Neurobiol Aging, 2010. **31**(12): p. 2025-37.

115. Mastroeni, D., et al., *Epigenetic differences in cortical neurons from a pair of monozygotic twins discordant for Alzheimer's disease.* PLoS One, 2009. **4**(8): p. e6617.

116. Bradley-Whitman, M.A. and M.A. Lovell, *Epigenetic changes in the progression of Alzheimer's disease.* Mech Ageing Dev, 2013. **134**(10): p. 486-95.

117. Coppieters, N., et al., *Global changes in DNA methylation and hydroxymethylation in Alzheimer's disease human brain.* Neurobiol Aging, 2014. **35**(6): p. 1334-44.

118. Bakulski, K.M., et al., *Genome-wide DNA methylation differences between late-onset Alzheimer's disease and cognitively normal controls in human frontal cortex.* J Alzheimers Dis, 2012. **29**(3): p. 571-88.

119. Sanchez-Mut, J.V., et al., *Promoter hypermethylation of the phosphatase DUSP22 mediates PKA-dependent TAU phosphorylation and CREB activation in Alzheimer's disease.* Hippocampus, 2014. **24**(4): p. 363-8.

120. Lunnon, K., et al., *Methylomic profiling implicates cortical deregulation of ANK1 in Alzheimer's disease.* Nature Neuroscience, 2014. **17**: p. 1164.

121. De Jager, P.L., et al., *Alzheimer's disease: early alterations in brain DNA methylation at ANK1, BIN1, RHBDF2 and other loci.* Nat Neurosci, 2014. **17**(9): p. 1156-63.

122. Smith, A.R., et al., *A cross-brain regions study of ANK1 DNA methylation in different neurodegenerative diseases.* Neurobiol Aging, 2019. **74**: p. 70-76.

123. Smith, R.G., et al., *Elevated DNA methylation across a 48-kb region spanning the HOXA gene cluster is associated with Alzheimer's disease neuropathology.* Alzheimer's & Dementia, 2018. **14**(12): p. 1580-1588.

124. Gasparoni, G., et al., *DNA methylation analysis on purified neurons and glia dissects age and Alzheimer's disease-specific changes in the human cortex.* Epigenetics & chromatin, 2018. **11**(1): p. 41-41.

125. Horvath, S., *DNA methylation age of human tissues and cell types.* Genome Biol, 2013. **14**(10): p. R115.

126. Horvath, S., et al., *Epigenetic clock for skin and blood cells applied to Hutchinson Gilford Progeria Syndrome and ex vivo studies.* Aging (Albany NY), 2018. **10**(7): p. 1758-1775.

127. McCartney, D.L., et al., *Investigating the relationship between DNA methylation age acceleration and risk factors for Alzheimer's disease.* Alzheimer's & dementia (Amsterdam, Netherlands), 2018. **10**: p. 429-437.

128. McGowan, E., J. Eriksen, and M. Hutton, *A decade of modeling Alzheimer's disease in transgenic mice.* Trends Genet, 2006. **22**(5): p. 281-9.

129. Takeuchi, A., et al., *Age-related amyloid beta deposition in transgenic mice overexpressing both Alzheimer mutant presenilin 1 and amyloid beta precursor protein Swedish mutant is not associated with global neuronal loss.* Am J Pathol, 2000. **157**(1): p. 331-9.

130. Irizarry, M.C., et al., *APPSw transgenic mice develop age-related A beta deposits and neuropil abnormalities, but no neuronal loss in CA1.* J Neuropathol Exp Neurol, 1997. **56**(9): p. 965-73.

131. Irizarry, M.C., et al., *Abeta deposition is associated with neuropil changes, but not with overt neuronal loss in the human amyloid precursor protein V717F (PDAPP) transgenic mouse.* J Neurosci, 1997. **17**(18): p. 7053-9.

132. Kitazawa, M., R. Medeiros, and F.M. Laferla, *Transgenic mouse models of Alzheimer disease: developing a better model as a tool for therapeutic interventions.* Curr Pharm Des, 2012. **18**(8): p. 1131-47.

133. Rodriguez, G.A., et al., *Young APOE4 targeted replacement mice exhibit poor spatial learning and memory, with reduced dendritic spine density in the medial entorhinal cortex.* Learn Mem, 2013. **20**(5): p. 256-66.

134.   Chan, E.S., et al., *ApoE4 expression accelerates hippocampus-dependent cognitive deficits by enhancing Aβ impairment of insulin signaling in an Alzheimer's disease mouse model.* Scientific Reports, 2016. **6**: p. 26119.

135.   Evans, M.J. and M.H. Kaufman, *Establishment in culture of pluripotential cells from mouse embryos.* Nature, 1981. **292**(5819): p. 154-6.

136.   Takahashi, K. and S. Yamanaka, *Induction of pluripotent stem cells from mouse embryonic and adult fibroblast cultures by defined factors.* Cell, 2006. **126**(4): p. 663-676.

137.   Yamanaka, S., *A fresh look at iPS cells.* Cell, 2009. **137**(1): p. 13-7.

138.   Bar, S., et al., *Global Characterization of X Chromosome Inactivation in Human Pluripotent Stem Cells.* Cell Rep, 2019. **27**(1): p. 20-29.e3.

139.   Chambers, S.M., et al., *Highly efficient neural conversion of human ES and iPS cells by dual inhibition of SMAD signaling.* Nat Biotechnol, 2009. **27**(3): p. 275-80.

140.   Tomishima, M., *StemBook*. Neural induction – Dual SMAD inhibition. 2012, Cambridge, MA.

141.   Muratore, C.R., et al., *Comparison and Optimization of hiPSC Forebrain Cortical Differentiation Protocols.* PLOS ONE, 2014. **9**(8): p. e105807.

142.   McAllister, A.K., *Neurotrophins and neuronal differentiation in the central nervous system.* Cellular and Molecular Life Sciences CMLS, 2001. **58**(8): p. 1054-1060.

143.   Shin, D.M., et al., *Ascorbic acid responsive genes during neuronal differentiation of embryonic stem cells.* Neuroreport, 2004. **15**(12): p. 1959-63.

144.   Uesaka, T., M. Nagashimada, and H. Enomoto, *GDNF signaling levels control migration and neuronal differentiation of enteric ganglion precursors.* J Neurosci, 2013. **33**(41): p. 16372-82.

145.   Telezhkin, V., et al., *Forced cell cycle exit and modulation of GABAA, CREB, and GSK3β signaling promote functional maturation of induced pluripotent stem cell-derived neurons.* American Journal of Physiology-Cell Physiology, 2016. **310**(10).

146.   L, W., et al., *β-Amyloid 1-42 Oligomers Impair Function of Human Embryonic Stem Cell-Derived Forebrain Cholinergic Neurons.* PloS one, 2010. **5**(12).

147.   X, X., et al., *Prevention of β-Amyloid Induced Toxicity in Human iPS Cell-Derived Neurons by Inhibition of Cyclin-dependent Kinases and Associated Cell Cycle Events.* Stem cell research, 2013. **10**(2).

148.   T, K., et al., *Modeling Alzheimer's Disease With iPSCs Reveals Stress Phenotypes Associated With Intracellular Aβ and Differential Drug Responsiveness.* Cell stem cell, 2013. **12**(4).

149.   Nieweg, K., et al., *Alzheimer's disease-related amyloid-beta induces synaptotoxicity in human iPS cell-derived neurons.* Cell Death Dis, 2015. **6**: p. e1709.

150.   BJ, B., et al., *Physiological Aβ Concentrations Produce a More Biomimetic Representation of the Alzheimer's Disease Phenotype in iPSC Derived Human Neurons.* ACS chemical neuroscience, 2018. **9**(7).

151.   YT, L., et al., *APOE4 Causes Widespread Molecular and Cellular Alterations Associated With Alzheimer's Disease Phenotypes in Human iPSC-Derived Brain Cell Types.* Neuron, 2018. **98**(6).

152.   Ochalek, A., et al., *Neurons derived from sporadic Alzheimer's disease iPSCs reveal elevated TAU hyperphosphorylation, increased amyloid*

levels, and GSK3B activation. Alzheimer's Research & Therapy, 2017. **9**(1): p. 1-19.

153. Ortiz-Virumbrales, M., et al., *CRISPR/Cas9-Correctable mutation-related molecular and physiological phenotypes in iPSC-derived Alzheimer's PSEN2 N141I neurons.* Acta Neuropathologica Communications, 2017. **5**(1): p. 1-20.

154. CR, M., et al., *Cell-type Dependent Alzheimer's Disease Phenotypes: Probing the Biology of Selective Neuronal Vulnerability.* Stem cell reports, 2017. **9**(6).

155. T, Y., et al., *Modeling Familial Alzheimer's Disease With Induced Pluripotent Stem Cells.* Human molecular genetics, 2011. **20**(23).

156. CR, M., et al., *The Familial Alzheimer's Disease APPV717I Mutation Alters APP Processing and Tau Expression in iPSC-derived Neurons.* Human molecular genetics, 2014. **23**(13).

157. T, S., et al., *Developmental Regulation of Tau Splicing Is Disrupted in Stem Cell-Derived Neurons From Frontotemporal Dementia Patients With the 10 + 16 Splice-Site Mutation in MAPT.* Human molecular genetics, 2015. **24**(18).

158. MA, I., et al., *Probing Sporadic and Familial Alzheimer's Disease Using Induced Pluripotent Stem Cells.* Nature, 2012. **482**(7384).

159. Muffat, J., et al., *Efficient derivation of microglia-like cells from human pluripotent stem cells.* Nat Med, 2016. **22**(11): p. 1358-1367.

160. Abud, E.M., et al., *iPSC-Derived Human Microglia-like Cells to Study Neurological Diseases.* Neuron, 2017. **94**(2): p. 278-293.e9.

161. Pandya, H., et al., *Differentiation of human and murine induced pluripotent stem cells to microglia-like cells.* Nat Neurosci, 2017. **20**(5): p. 753-759.

162. Haenseler, W., et al., *A Highly Efficient Human Pluripotent Stem Cell Microglia Model Displays a Neuronal-Co-culture-Specific Expression Profile and Inflammatory Response.* Stem Cell Reports, 2017. **8**(6): p. 1727-1742.

163. Douvaras, P., et al., *Directed Differentiation of Human Pluripotent Stem Cells to Microglia.* Stem Cell Reports, 2017. **8**(6): p. 1516-1524.

164. Xiang, X.Y., et al., *The Trem2 R47H Alzheimer's risk variant impairs splicing and reduces Trem2 mRNA and protein in mice but not in humans.* Molecular Neurodegeneration, 2018. **13**.

165. Brownjohn, P.W., et al., *Functional Studies of Missense TREM2 Mutations in Human Stem Cell-Derived Microglia.* Stem Cell Reports, 2018. **10**(4): p. 1294-1307.

166. Lin, Y.T., et al., *APOE4 Causes Widespread Molecular and Cellular Alterations Associated with Alzheimer's Disease Phenotypes in Human iPSC-Derived Brain Cell Types.* Neuron, 2018. **98**(6): p. 1141-1154.e7.

167. Vierbuchen, T., et al., *Direct conversion of fibroblasts to functional neurons by defined factors.* Nature, 2010. **463**(7284): p. 1035-1041.

168. J, M., et al., *Directly Reprogrammed Human Neurons Retain Aging-Associated Transcriptomic Signatures and Reveal Age-Related Nucleocytoplasmic Defects.* Cell stem cell, 2015. **17**(6).

169. CJ, H., et al., *Maintenance of Age in Human Neurons Generated by microRNA-based Neuronal Conversion of Fibroblasts.* eLife, 2016. **5**.

170. S, S., et al., *Quantitative Model of Cell Cycle Arrest and Cellular Senescence in Primary Human Fibroblasts.* PloS one, 2012. **7**(8).

171. LT, G., et al., *Representing Diversity in the Dish: Using Patient-Derived in Vitro Models to Recreate the Heterogeneity of Neurological Disease.* Frontiers in neuroscience, 2018. **12**.

172. T, A., et al., *Efficient and Rapid Generation of Induced Pluripotent Stem Cells From Human Keratinocytes.* Nature biotechnology, 2008. **26**(11).

173. K, O. and Y. S, *Induced Pluripotent Stem Cells: Opportunities and Challenges.* Philosophical transactions of the Royal Society of London. Series B, Biological sciences, 2011. **366**(1575).

174. Lancaster, M.A., et al., *Cerebral organoids model human brain development and microcephaly.* Nature, 2013. **501**(7467).

175. C, G., et al., *Modeling Amyloid Beta and Tau Pathology in Human Cerebral Organoids.* Molecular psychiatry, 2018. **23**(12).

176. Park, J., et al., *A 3D human triculture system modeling neurodegeneration and neuroinflammation in Alzheimer's disease.* Nature Neuroscience, 2018. **21**(7): p. 941-951.

177. Y, G. and H. C, *Brain Organoids: A Next Step for Humanized Alzheimer's Disease Models?* Molecular psychiatry, 2019. **24**(4).

178. E, D.L. and K. AR, *The Use of Brain Organoids to Investigate Neural Development and Disease.* Nature reviews. Neuroscience, 2017. **18**(10).

179. Waddington, C.H., *The Strategy of the Genes. A Discussion of Some Aspects of Theoretical Biology* 1957: Allen and Unwin.

180. Chin, M.H., et al., *Induced pluripotent stem cells and embryonic stem cells are distinguished by gene expression signatures.* Cell Stem Cell, 2009. **5**(1): p. 111-23.

181. Lister, R., et al., *Hotspots of aberrant epigenomic reprogramming in human induced pluripotent stem cells.* Nature, 2011. **471**(7336): p. 68-73.

182. Mallon, B.S., et al., *StemCellDB: the human pluripotent stem cell database at the National Institutes of Health.* Stem Cell Res, 2013. **10**(1): p. 57-66.

183. Mallon, B.S., et al., *Comparison of the molecular profiles of human embryonic and induced pluripotent stem cells of isogenic origin.* Stem Cell Res, 2014. **12**(2): p. 376-86.

184. Luo, C., et al., *Cerebral Organoids Recapitulate Epigenomic Signatures of the Human Fetal Brain.* Cell Rep, 2016. **17**(12): p. 3369-84.

185. Kim, K., et al., *Epigenetic memory in induced pluripotent stem cells.* Nature, 2010. **467**(7313): p. 285-90.

186. Mikkelsen, T.S., et al., *Dissecting direct reprogramming through integrative genomic analysis.* Nature, 2008. **454**(7200): p. 49-55.

187. Newman, A.M. and J.B. Cooper, *Lab-specific gene expression signatures in pluripotent stem cells.* Cell Stem Cell, 2010. **7**(2): p. 258-62.

188. Newman, A.M. and J.B. Cooper, *AutoSOME: a clustering method for identifying gene expression modules without prior knowledge of cluster number.* BMC Bioinformatics, 2010. **11**: p. 117.

189. Lister, R., et al., *Human DNA methylomes at base resolution show widespread epigenomic differences.* Nature, 2009. **462**(7271): p. 315-22.

190. Plomin, R., M. Owen, and P. McGuffin, *The genetic basis of complex human behaviors.* Science, 1994. **264**(5166): p. 1733-1739.

191. *Induced pluripotent stem cells from patients with Huntington's disease show CAG-repeat-expansion-associated phenotypes.* Cell Stem Cell, 2012. **11**(2): p. 264-78.

192. Cocks, G., et al., *The utility of patient specific induced pluripotent stem cells for the modelling of Autistic Spectrum Disorders.* Psychopharmacology, 2014. **231**(6): p. 1079-1088.

193. Fernandes, H.J., et al., *ER Stress and Autophagic Perturbations Lead to Elevated Extracellular α-Synuclein in GBA-N370S Parkinson's iPSC-Derived Dopamine Neurons.* Stem Cell Reports, 2016. **6**(3): p. 342-56.

194. Sambrook, J. and D.W. Russell, *Purification of nucleic acids by extraction with phenol:chloroform.* CSH Protoc, 2006. **2006**(1).

195. Frommer, M., et al., *A genomic sequencing protocol that yields a positive display of 5-methylcytosine residues in individual DNA strands.* Proc Natl Acad Sci U S A, 1992. **89**(5): p. 1827-31.

196. Illumina. *Infinium® MethylationEPIC BeadChip.* 2017 20/12/2018]; Available from: https://www.illumina.com/content/dam/illumina-marketing/documents/products/datasheets/humanmethylationepic-data-sheet-1070-2015-008.pdf.

197. Pidsley, R., et al., *Critical evaluation of the Illumina MethylationEPIC BeadChip microarray for whole-genome DNA methylation profiling.* Genome Biol, 2016. **17**(1): p. 208.

198. Pidsley, R., et al., *A data-driven approach to preprocessing Illumina 450K methylation array data.* BMC Genomics, 2013. **14**: p. 293.

199. Youn, A. and S. Wang, *The MiAge Calculator: a DNA methylation-based mitotic age calculator of human tissue types.* Epigenetics, 2018. **13**(2): p. 192-206.

200. Dedeurwaerder, S., et al., *Evaluation of the Infinium Methylation 450K technology.* Epigenomics, 2011. **3**(6): p. 771-84.

201. Chen, Y.-a., et al., *Discovery of cross-reactive probes and polymorphic CpGs in the Illumina Infinium HumanMethylation450 microarray.* Epigenetics, 2013. **8**(2): p. 203-209.

202. Price, M.E., et al., *Additional annotation enhances potential for biologically-relevant analysis of the Illumina Infinium HumanMethylation450 BeadChip array.* Epigenetics Chromatin, 2013. **6**(1): p. 4.

203. McCartney, D.L., et al., *Identification of polymorphic and off-target probe binding sites on the Illumina Infinium MethylationEPIC BeadChip.* Genomics Data, 2016. **9**: p. 22-24.

204. Terman, A., B. Gustafsson, and U.T. Brunk, *Autophagy, organelles and ageing.* J Pathol, 2007. **211**(2): p. 134-43.

205. Lee, H.C. and Y.H. Wei, *Mitochondria and aging.* Adv Exp Med Biol, 2012. **942**: p. 311-27.

206. Phillip, J.M., et al., *The Mechanobiology of Aging.* Annu Rev Biomed Eng, 2015. **17**: p. 113-141.

207. Booth, L.N. and A. Brunet, *The Aging Epigenome.* Mol Cell, 2016. **62**(5): p. 728-44.

208. Peleg, S., et al., *The Metabolic Impact on Histone Acetylation and Transcription in Ageing.* Trends Biochem Sci, 2016. **41**(8): p. 700-711.

209. Wheeler, H.E. and S.K. Kim, *Genetics and genomics of human ageing.* Philos Trans R Soc Lond B Biol Sci, 2011. **366**(1561): p. 43-50.

210. Green, D.R., L. Galluzzi, and G. Kroemer, *Mitochondria and the autophagy-inflammation-cell death axis in organismal aging.* Science, 2011. **333**(6046): p. 1109-12.

211. Harman, D., *THE FREE RADICAL THEORY OF AGING: EFFECT OF AGE ON SERUM COPPER LEVELS.* J Gerontol, 1965. **20**: p. 151-3.

212. Hekimi, S., J. Lapointe, and Y. Wen, *Taking a "good" look at free radicals in the aging process.* Trends Cell Biol, 2011. **21**(10): p. 569-76.

213. Kuilman, T., et al., *The essence of senescence.* Genes Dev, 2010. **24**(22): p. 2463-79.

214. Campisi, J. and F. d'Adda di Fagagna, *Cellular senescence: when bad things happen to good cells.* Nat Rev Mol Cell Biol, 2007. **8**(9): p. 729-40.

215. Collado, M., M.A. Blasco, and M. Serrano, *Cellular senescence in cancer and aging.* Cell, 2007. **130**(2): p. 223-33.

216. Bodnar, A.G., et al., *Extension of life-span by introduction of telomerase into normal human cells.* Science, 1998. **279**(5349): p. 349-52.

217. Ressler, S., et al., *p16INK4A is a robust in vivo biomarker of cellular aging in human skin.* Aging Cell, 2006. **5**(5): p. 379-89.

218. Krishnamurthy, J., et al., *Ink4a/Arf expression is a biomarker of aging.* J Clin Invest, 2004. **114**(9): p. 1299-307.

219. Jeck, W.R., A.P. Siebold, and N.E. Sharpless, *Review: a meta-analysis of GWAS and age-associated diseases.* Aging Cell, 2012. **11**(5): p. 727-31.

220. Li, H., et al., *Alternative splicing in aging and age-related diseases.* Translational Medicine of Aging, 2017. **1**: p. 32-40.

221. Lisowiec, J., et al., *Structural determinants for alternative splicing regulation of the MAPT pre-mRNA.* RNA Biol, 2015. **12**(3): p. 330-42.

222. Tollervey, J.R., et al., *Analysis of alternative splicing associated with aging and neurodegeneration in the human brain.* Genome Res, 2011. **21**(10): p. 1572-82.

223. Buee, L., et al., *Tau protein isoforms, phosphorylation and role in neurodegenerative disorders.* Brain Res Brain Res Rev, 2000. **33**(1): p. 95-130.

224. De Sandre-Giovannoli, A., et al., *Lamin a truncation in Hutchinson-Gilford progeria.* Science, 2003. **300**(5628): p. 2055.

225. Eriksson, M., et al., *Recurrent de novo point mutations in lamin A cause Hutchinson-Gilford progeria syndrome.* Nature, 2003. **423**(6937): p. 293-8.

226. Makous, N., et al., *Cardiovascular manifestations in progeria. Report of clinical and pathologic findings in a patient with severe arteriosclerotic heart disease and aortic stenosis.* American Heart Journal, 1962. **64**(3): p. 334-346.

227. Lu, T., et al., *Gene regulation and DNA damage in the ageing human brain.* Nature, 2004. **429**(6994): p. 883-91.

228. Bell, J.T., et al., *Epigenome-Wide Scans Identify Differentially Methylated Regions for Age and Age-Related Phenotypes in a Healthy Ageing Population.* PLOS Genetics, 2012. **8**(4): p. e1002629.

229. Horvath, S., et al., *Aging effects on DNA methylation modules in human brain and blood tissue.* Genome Biology, 2012. **13**(10): p. R97.

230. Murgatroyd, C., et al., *The Janus face of DNA methylation in aging.* Aging (Albany NY), 2010. **2**(2): p. 107-10.

231. Bollati, V., et al., *Decline in genomic DNA methylation through aging in a cohort of elderly subjects.* Mechanisms of Ageing and Development, 2009. **130**(4): p. 234-239.

232. Fraga, M.F. and M. Esteller, *Epigenetics and aging: the targets and the marks.* Trends Genet, 2007. **23**(8): p. 413-8.

233. Bjornsson, H.T., et al., *Intra-individual Change Over Time in DNA Methylation With Familial Clustering.* JAMA, 2008. **299**(24): p. 2877-2883.

234. Christensen, B.C., et al., *Aging and environmental exposures alter tissue-specific DNA methylation dependent upon CpG island context.* PLoS Genet, 2009. **5**(8): p. e1000602.

235. Teschendorff, A.E., et al., *Age-dependent DNA methylation of genes that are suppressed in stem cells is a hallmark of cancer.* Genome Res, 2010. **20**(4): p. 440-6.

236. Hannum, G., et al., *Genome-wide methylation profiles reveal quantitative views of human aging rates.* Mol Cell, 2013. **49**(2): p. 359-367.

237. Weidner, C.I., et al., *Aging of blood can be tracked by DNA methylation changes at just three CpG sites.* Genome Biology, 2014. **15**(2): p. R24.

238. Levine, M.E., et al., *An epigenetic biomarker of aging for lifespan and healthspan.* Aging (Albany NY), 2018. **10**(4): p. 573-591.

239. Herbstman, J.B., et al., *Predictors and consequences of global DNA methylation in cord blood and at three years.* PLoS One, 2013. **8**(9): p. e72824.

240. Martino, D.J., et al., *Evidence for age-related and individual-specific changes in DNA methylation profile of mononuclear cells during early immune development in humans.* Epigenetics, 2011. **6**(9): p. 1085-94.

241. Fraga, M.F., et al., *Epigenetic differences arise during the lifetime of monozygotic twins.* Proceedings of the National Academy of Sciences of the United States of America, 2005. **102**(30): p. 10604-10609.

242. Tan, Q., et al., *Twins for epigenetic studies of human aging and development.* Ageing Res Rev, 2013. **12**(1): p. 182-7.

243. Mohn, F., et al., *Lineage-specific polycomb targets and de novo DNA methylation define restriction and potential of neuronal progenitors.* Mol Cell, 2008. **30**(6): p. 755-66.

244. Siegmund, K.D., et al., *DNA methylation in the human cerebral cortex is dynamically regulated throughout the life span and involves differentiated neurons.* PLoS One, 2007. **2**(9): p. e895.

245. Numata, S., et al., *DNA methylation signatures in development and aging of the human prefrontal cortex.* Am J Hum Genet, 2012. **90**(2): p. 260-72.

246. Glisky, E.L., *Frontiers in Neuroscience*

Changes in Cognitive Function in Human Aging, in *Brain Aging: Models, Methods, and Mechanisms*, D.R. Riddle, Editor. 2007, CRC Press/Taylor & Francis

Taylor & Francis Group, LLC.: Boca Raton (FL).

247. Jones, M.J., S.J. Goodman, and M.S. Kobor, *DNA methylation and healthy human aging.* Aging Cell, 2015. **14**(6): p. 924-32.

248. Murgatroyd, C., et al., *The Janus face of DNA methylation in aging.* Aging (Albany NY), 2010. **2**(2): p. 107-10.

249. Levenson, J.M., et al., *Evidence that DNA (cytosine-5) methyltransferase regulates synaptic plasticity in the hippocampus.* J Biol Chem, 2006. **281**(23): p. 15763-73.

250. Liu, L., et al., *DNA methylation impacts on learning and memory in aging.* Neurobiol Aging, 2009. **30**(4): p. 549-60.

251. Oliveira, A.M., T.J. Hemstedt, and H. Bading, *Rescue of aging-associated decline in Dnmt3a2 expression restores cognitive abilities.* Nat Neurosci, 2012. **15**(8): p. 1111-3.

252. Tanay, A. and A. Regev, *Scaling single-cell genomics from phenomenology to mechanism.* Nature, 2017. **541**(7637): p. 331-338.

253. Etzrodt, M., M. Endele, and T. Schroeder, *Quantitative single-cell approaches to stem cell research.* Cell Stem Cell, 2014. **15**(5): p. 546-58.

254. Trapnell, C., *Defining cell types and states with single-cell genomics.* Genome Res, 2015. **25**(10): p. 1491-8.

255. Schlitzer, A., et al., *Identification of cDC1- and cDC2-committed DC progenitors reveals early lineage priming at the common DC progenitor stage in the bone marrow.* Nat Immunol, 2015. **16**(7): p. 718-28.

256. Haghverdi, L., et al., *Diffusion pseudotime robustly reconstructs lineage branching.* Nat Methods, 2016. **13**(10): p. 845-8.

257. Matsumoto, H. and H. Kiryu, *SCOUP: a probabilistic model based on the Ornstein-Uhlenbeck process to analyze single-cell expression data during differentiation.* BMC Bioinformatics, 2016. **17**(1): p. 232.

258. Cannoodt, R., et al., *SCORPIUS improves trajectory inference and identifies novel modules in dendritic cell development.* bioRxiv, 2016: p. 079509.

259. Camp, J.G., et al., *Human cerebral organoids recapitulate gene expression programs of fetal neocortex development.* Proc Natl Acad Sci U S A, 2015. **112**(51): p. 15672-7.

260. Mattis, V.B., et al., *Induced Pluripotent Stem Cells from Patients with Huntington's Disease Show CAG Repeat Expansion Associated Phenotypes.* Cell Stem Cell, 2012. **11**(2): p. 264-78.

261. Telezhkin, V., et al., *Forced cell cycle exit and modulation of GABAA, CREB, and GSK3beta signaling promote functional maturation of induced pluripotent stem cell-derived neurons.* Am J Physiol Cell Physiol, 2016. **310**(7): p. C520-41.

262. Davis S., D.P., Bilke S., Triche, Jr. T., Bootwalla M., *methylumi: Handle Illumina methylation data. R package version 2.30.0.* 2019.

263. Langfelder, P. and S. Horvath, *WGCNA: an R package for weighted correlation network analysis.* BMC Bioinformatics, 2008. **9**: p. 559.

264. Langfelder, P. and S. Horvath, *WGCNA: an R package for weighted correlation network analysis.* BMC Bioinformatics, 2008. **9**(1): p. 559.

265. Phipson, B., J. Maksimovic, and A. Oshlack, *missMethyl: an R package for analyzing data from Illumina's HumanMethylation450 platform.* Bioinformatics, 2016. **32**(2): p. 286-8.

266. Lunnon, K., et al., *Variation in 5-hydroxymethylcytosine across human cortex and cerebellum.* Genome Biol, 2016. **17**: p. 27.

267. Supek, F., et al., *REVIGO Summarizes and Visualizes Long Lists of Gene Ontology Terms.* PLOS ONE, 2011. **6**(7): p. e21800.

268. G. Csardi, a.T.N., *The igraph software package for complex network research.* InterJournal Complex Systems, 2006. **1965**: p. 1965.

269. Shannon, P., et al., *Cytoscape: a software environment for integrated models of biomolecular interaction networks.* Genome Res, 2003. **13**(11): p. 2498-504.

270. Jeffries, A.R., et al., *Erasure and reestablishment of random allelic expression imbalance after epigenetic reprogramming.* Rna, 2016. **22**(10): p. 1620-30.

271. Kent, W.J., et al., *The human genome browser at UCSC.* Genome Res, 2002. **12**(6): p. 996-1006.

272. McLean, C.Y., et al., *GREAT improves functional interpretation of cis-regulatory regions.* Nature Biotechnology, 2010. **28**(5): p. 495-501.

273. Mertens, J., et al., *Directly Reprogrammed Human Neurons Retain Aging-Associated Transcriptomic Signatures and Reveal Age-Related Nucleocytoplasmic Defects.* Cell Stem Cell, 2015. **17**(6): p. 705-718.

274. Ma, H., et al., *Abnormalities in human pluripotent cells due to reprogramming mechanisms.* Nature, 2014. **511**(7508): p. 177-83.

275. Guo, J.U., et al., *Distribution, recognition and regulation of non-CpG methylation in the adult mammalian brain.* Nat Neurosci, 2014. **17**(2): p. 215-22.

276. Xie, W., et al., *Base-resolution analyses of sequence and parent-of-origin dependent DNA methylation in the mouse genome.* Cell, 2012. **148**(4): p. 816-31.

277. Varley, K.E., et al., *Dynamic DNA methylation across diverse human cell lines and tissues.* Genome Res, 2013. **23**(3): p. 555-67.

278. Keshet, I., J. Lieman-Hurwitz, and H. Cedar, *DNA methylation affects the formation of active chromatin.* Cell, 1986. **44**(4): p. 535-543.

279. Bird, A., *The essentials of DNA methylation.* Cell, 1992. **70**(1): p. 5-8.

280. Yadav, A., et al., *JAK/STAT3 pathway is involved in survival of neurons in response to insulin-like growth factor and negatively regulated by suppressor of cytokine signaling-3.* J Biol Chem, 2005. **280**(36): p. 31830-40.

281. Snyder, M., X.Y. Huang, and J.J. Zhang, *Stat3 is essential for neuronal differentiation through direct transcriptional regulation of the Sox6 gene.* FEBS Lett, 2011. **585**(1): p. 148-52.

282. Lee, M., et al., *Tcf7l2 plays crucial roles in forebrain development through regulation of thalamic and habenular neuron identity and connectivity.* Dev Biol, 2017. **424**(1): p. 62-76.

283. Subramanian, L., et al., *Transcription factor Lhx2 is necessary and sufficient to suppress astrogliogenesis and promote neurogenesis in the developing hippocampus.* 2011.

284. LC, H., et al., *Lhx2 Regulates the Timing of β-Catenin-Dependent Cortical Neurogenesis.* Proceedings of the National Academy of Sciences of the United States of America, 2015. **112**(39).

285. Zentner, G.E. and S. Henikoff, *Regulation of nucleosome dynamics by histone modifications.* Nat Struct Mol Biol, 2013. **20**(3): p. 259-66.

286. Sadakierska-Chudy, A. and M. Filip, *A comprehensive view of the epigenetic landscape. Part II: Histone post-translational modification, nucleosome level, and chromatin regulation by ncRNAs.* Neurotox Res, 2015. **27**(2): p. 172-97.

287. Tamaru, H., *Confining euchromatin/heterochromatin territory: jumonji crosses the line.* Genes & development, 2010. **24**(14): p. 1465-1478.

288. James, L.I., et al., *Discovery of a chemical probe for the L3MBTL3 methyllysine reader domain.* Nature Chemical Biology, 2013. **9**(3): p. 184-191.

289. Hughes, R.M., et al., *Recognition of trimethyllysine by a chromodomain is not driven by the hydrophobic effect.* Proceedings of the National Academy of Sciences, 2007. **104**(27): p. 11184-11188.

290. Zeng, L. and M.-M. Zhou, *Bromodomain: an acetyl-lysine binding domain.* FEBS Letters, 2002. **513**(1): p. 124-128.

291. Wu, Q., et al., *A chemical toolbox for the study of bromodomains and epigenetic signaling.* Nature Communications, 2019. **10**(1): p. 1915.

292. Filippakopoulos, P., et al., *Selective inhibition of BET bromodomains.* Nature, 2010. **468**(7327): p. 1067-1073.

293. Vidler, L.R., et al., *Druggability Analysis and Structural Classification of Bromodomain Acetyl-lysine Binding Sites.* Journal of Medicinal Chemistry, 2012. **55**(17): p. 7346-7359.

294. Jung, M., et al., *Targeting BET bromodomains for cancer treatment.* Epigenomics, 2015. **7**(3): p. 487-501.

295. Filippakopoulos, P. and S. Knapp, *Targeting bromodomains: epigenetic readers of lysine acetylation.* Nat Rev Drug Discov, 2014. **13**(5): p. 337-56.

296. Filippakopoulos, P., et al., *Selective inhibition of BET bromodomains.* Nature, 2010. **468**(7327): p. 1067-73.

297. Conery, A.R., et al., *Bromodomain inhibition of the transcriptional coactivators CBP/EP300 as a therapeutic strategy to target the IRF4 network in multiple myeloma.* Elife, 2016. **5**.

298. Hay, D.A., et al., *Discovery and Optimization of Small-Molecule Ligands for the CBP/p300 Bromodomains.* Journal of the American Chemical Society, 2014. **136**(26): p. 9308-9319.

299. Martin, L.J., et al., *Structure-Based Design of an in Vivo Active Selective BRD9 Inhibitor.* Journal of Medicinal Chemistry, 2016. **59**(10): p. 4462-4475.

300. Drouin, L., et al., *Structure enabled design of BAZ2-ICR, a chemical probe targeting the bromodomains of BAZ2A and BAZ2B.* J Med Chem, 2015. **58**(5): p. 2553-9.

301. Heintzman, N.D., et al., *Histone modifications at human enhancers reflect global cell-type-specific gene expression.* Nature, 2009. **459**(7243): p. 108-112.

302. Ernst, J., et al., *Mapping and analysis of chromatin state dynamics in nine human cell types.* Nature, 2011. **473**(7345): p. 43-49.

303. Calo, E. and J. Wysocka, *Modification of Enhancer Chromatin: What, How, and Why?* Molecular Cell, 2013. **49**(5): p. 825-837.

304. Creyghton, M.P., et al., *Histone H3K27ac separates active from poised enhancers and predicts developmental state.* Proceedings of the National Academy of Sciences, 2010. **107**(50): p. 21931-21936.

305. Zhang, Z. and M.Q. Zhang, *Histone modification profiles are predictive for tissue/cell-type specific expression of both protein-coding and microRNA genes.* BMC Bioinformatics, 2011. **12**(1): p. 155.

306. Scheer, S., et al., *A chemical biology toolbox to study protein methyltransferases and epigenetic signaling.* Nature Communications, 2019. **10**(1): p. 19.

307. Greer, E.L. and Y. Shi, *Histone methylation: a dynamic mark in health, disease and inheritance.* Nature reviews. Genetics, 2012. **13**(5): p. 343-357.

308. Amente, S., L. Lania, and B. Majello, *The histone LSD1 demethylase in stemness and cancer transcription programs.* Biochim Biophys Acta, 2013. **1829**(10): p. 981-6.

309. Yokoyama, A., et al., *Leukemia proto-oncoprotein MLL forms a SET1-like histone methyltransferase complex with menin to regulate Hox gene expression.* Molecular and cellular biology, 2004. **24**(13): p. 5639-5649.

310. Dou, Y., et al., *Regulation of MLL1 H3K4 methyltransferase activity by its core components.* Nat Struct Mol Biol, 2006. **13**(8): p. 713-9.

311. Yates, J.A., et al., *Regulation of HOXA2 gene expression by the ATP-dependent chromatin remodeling enzyme CHD8.* FEBS Lett, 2010. **584**(4): p. 689-93.

312. Wang, K.C., et al., *A long noncoding RNA maintains active chromatin to coordinate homeotic gene expression.* Nature, 2011. **472**(7341): p. 120-4.

313. Gomez, J.A., et al., *The NeST long ncRNA controls microbial susceptibility and epigenetic activation of the interferon-gamma locus.* Cell, 2013. **152**(4): p. 743-54.

314. Guo, X., et al., *A Linc1405/Eomes Complex Promotes Cardiac Mesoderm Specification and Cardiogenesis.* Cell Stem Cell, 2018. **22**(6): p. 893-908.e6.

315. Grebien, F., et al., *Pharmacological targeting of the Wdr5-MLL interaction in C/EBPα N-terminal leukemia.* Nature Chemical Biology, 2015. **11**(8): p. 571-578.

316. Golbabapour, S., et al., *Gene silencing and Polycomb group proteins: an overview of their structure, mechanisms and phylogenetics.* Omics : a journal of integrative biology, 2013. **17**(6): p. 283-296.

317. Li, H., et al., *Structural Basis for Lower Lysine Methylation State-Specific Readout by MBT Repeats of L3MBTL1 and an Engineered PHD Finger.* Molecular Cell, 2007. **28**(4): p. 677-691.

318. Frye, S.V., T. Heightman, and J. Jin, *Chapter 20 - Targeting Methyl Lysine*, in *Annual Reports in Medicinal Chemistry*, J.E. Macor, Editor. 2010, Academic Press. p. 329-343.

319. Perna, F., et al., *Depletion of L3MBTL1 promotes the erythroid differentiation of human hematopoietic progenitor cells: possible role in 20q− polycythemia vera.* Blood, 2010. **116**(15): p. 2812-2821.

320. Northcott, P.A., et al., *Multiple recurrent genetic events converge on control of histone lysine methylation in medulloblastoma.* Nature Genetics, 2009. **41**(4): p. 465-472.

321. Shi, Y., et al., *Histone demethylation mediated by the nuclear amine oxidase homolog LSD1.* Cell, 2004. **119**(7): p. 941-53.

322. Maiques-Diaz, A., et al., *Enhancer Activation by Pharmacologic Displacement of LSD1 from GFI1 Induces Differentiation in Acute Myeloid Leukemia.* Cell Rep, 2018. **22**(13): p. 3641-3659.

323. Whyte, W.A., et al., *Enhancer decommissioning by LSD1 during embryonic stem cell differentiation.* Nature, 2012. **482**(7384): p. 221-5.

324. Castex, J., et al., *Inactivation of Lsd1 triggers senescence in trophoblast stem cells by induction of Sirt4.* Cell Death Dis, 2017. **8**(2): p. e2631.

325. Ambrosio, S. and B. Majello, *Targeting Histone Demethylase LSD1/KDM1a in Neurodegenerative Diseases.* J Exp Neurosci, 2018. **12**: p. 1179069518765743.

326. Christopher, M.A., et al., *LSD1 protects against hippocampal and cortical neurodegeneration.* Nat Commun, 2017. **8**(1): p. 805.

327. Mansour, A.A., et al., *The H3K27 demethylase Utx regulates somatic and germ cell epigenetic reprogramming.* Nature, 2012. **488**(7411): p. 409-13.

328. Ohtani, K., et al., *Jmjd3 controls mesodermal and cardiovascular differentiation of embryonic stem cells.* Circ Res, 2013. **113**(7): p. 856-62.

329. Akizu, N., et al., *H3K27me3 regulates BMP activity in developing spinal cord.* Development, 2010. **137**(17): p. 2915-25.

330. Kruidenier, L., et al., *A selective jumonji H3K27 demethylase inhibitor modulates the proinflammatory macrophage response.* Nature, 2012. **488**(7411): p. 404-408.

331. Shi, Y., et al., *Human cerebral cortex development from pluripotent stem cells to functional excitatory synapses.* Nature neuroscience, 2012. **15**(3): p. 477-S1.

332. Leek, J.T., et al., *The sva package for removing batch effects and other unwanted variation in high-throughput experiments.* Bioinformatics, 2012. **28**(6): p. 882-3.

333. Mansell, G., et al., *Guidance for DNA methylation studies: statistical insights from the Illumina EPIC array.* BMC Genomics, 2019. **20**(1): p. 366.

334. Marin-Teva, J.L., et al., *Microglia promote the death of developing Purkinje cells.* Neuron, 2004. **41**(4): p. 535-47.

335. Paolicelli, R.C., et al., *Synaptic pruning by microglia is necessary for normal brain development.* Science, 2011. **333**(6048): p. 1456-8.

336. Schafer, D.P., et al., *Microglia sculpt postnatal neural circuits in an activity and complement-dependent manner.* Neuron, 2012. **74**(4): p. 691-705.

337. Miyamoto, A., et al., *Microglia contact induces synapse formation in developing somatosensory cortex.* Nat Commun, 2016. **7**: p. 12540.

338. Lim, S.H., et al., *Neuronal synapse formation induced by microglia and interleukin 10.* PLoS One, 2013. **8**(11): p. e81218.

339. Parkhurst, C.N., et al., *Microglia promote learning-dependent synapse formation through brain-derived neurotrophic factor.* Cell, 2013. **155**(7): p. 1596-609.

340. Bsibsi, M., et al., *Broad expression of Toll-like receptors in the human central nervous system.* J Neuropathol Exp Neurol, 2002. **61**(11): p. 1013-21.

341. Banati, R.B., et al., *Cytotoxicity of microglia.* Glia, 1993. **7**(1): p. 111-8.

342. Hartlage-Rubsamen, M., R. Lemke, and R. Schliebs, *Interleukin-1beta, inducible nitric oxide synthase, and nuclear factor-kappaB are induced in morphologically distinct microglia after rat hippocampal lipopolysaccharide/interferon-gamma injection.* J Neurosci Res, 1999. **57**(3): p. 388-98.

343. Nimmerjahn, A., F. Kirchhoff, and F. Helmchen, *Resting microglial cells are highly dynamic surveillants of brain parenchyma in vivo.* Science, 2005. **308**(5726): p. 1314-8.

344. Dheen, S.T., C. Kaur, and E.A. Ling, *Microglial activation and its implications in the brain diseases.* Curr Med Chem, 2007. **14**(11): p. 1189-97.

345. Kaushik, D.K., et al., *Interleukin-1beta orchestrates underlying inflammatory responses in microglia via Kruppel-like factor 4.* J Neurochem, 2013. **127**(2): p. 233-44.

346. Suzumura, A., M. Sawada, and T. Marunouchi, *Selective induction of interleukin-6 in mouse microglia by granulocyte-macrophage colony-stimulating factor.* Brain Res, 1996. **713**(1-2): p. 192-8.

347. Floden, A.M., S. Li, and C.K. Combs, *Beta-amyloid-stimulated microglia induce neuron death via synergistic stimulation of tumor necrosis factor alpha and NMDA receptors.* J Neurosci, 2005. **25**(10): p. 2566-75.

348. Fischer, F.R., et al., *RANTES-Induced Chemokine Cascade in Dendritic Cells.* The Journal of Immunology, 2001. **167**(3): p. 1637-1643.

349. Nakamichi, K., et al., *Double-stranded RNA stimulates chemokine expression in microglia through vacuolar pH-dependent activation of intracellular signaling pathways.* J Neurochem, 2005. **95**(1): p. 273-83.

350. Lambert, J.C., et al., *Genome-wide association study identifies variants at CLU and CR1 associated with Alzheimer's disease.* Nat Genet, 2009. **41**(10): p. 1094-9.

351. Harold, D., et al., *Genome-wide association study identifies variants at CLU and PICALM associated with Alzheimer's disease.* Nat Genet, 2009. **41**(10): p. 1088-93.

352. Seshadri, S., et al., *Genome-wide analysis of genetic loci associated with Alzheimer disease.* JAMA, 2010. **303**(18): p. 1832-40.

353. Hollingworth, P., et al., *Common variants at ABCA7, MS4A6A/MS4A4E, EPHA1, CD33 and CD2AP are associated with Alzheimer's disease.* Nat Genet, 2011. **43**(5): p. 429-35.

354. Naj, A.C., et al., *Common variants at MS4A4/MS4A6E, CD2AP, CD33 and EPHA1 are associated with late-onset Alzheimer's disease.* Nat Genet, 2011. **43**(5): p. 436-41.

355. Hsieh, C.L., et al., *A role for TREM2 ligands in the phagocytosis of apoptotic neuronal cells by microglia.* J Neurochem, 2009. **109**(4): p. 1144-56.

356. Kleinberger, G., et al., *TREM2 mutations implicated in neurodegeneration impair cell surface transport and phagocytosis.* Sci Transl Med, 2014. **6**(243): p. 243ra86.

357. Ulrich, J.D., et al., *Altered microglial response to Abeta plaques in APPPS1-21 mice heterozygous for TREM2.* Mol Neurodegener, 2014. **9**: p. 20.

358. Jay, T.R., et al., *Disease Progression-Dependent Effects of TREM2 Deficiency in a Mouse Model of Alzheimer's Disease.* J Neurosci, 2017. **37**(3): p. 637-647.

359. Jay, T.R., et al., *TREM2 deficiency eliminates TREM2+ inflammatory macrophages and ameliorates pathology in Alzheimer's disease mouse models.* J Exp Med, 2015. **212**(3): p. 287-95.

360. Lee, C.Y. and G.E. Landreth, *The role of microglia in amyloid clearance from the AD brain.* J Neural Transm (Vienna), 2010. **117**(8): p. 949-60.

361. Condello, C., et al., *Microglia constitute a barrier that prevents neurotoxic protofibrillar Abeta42 hotspots around plaques.* Nat Commun, 2015. **6**: p. 6176.

362. Yuan, P., et al., *TREM2 Haplodeficiency in Mice and Humans Impairs the Microglia Barrier Function Leading to Decreased Amyloid Compaction and Severe Axonal Dystrophy.* Neuron, 2016. **90**(4): p. 724-39.

363. GEORGE, J., et al., *Causes and prognosis of delirium in elderly patients admitted to a district general hospital.* Age and Ageing, 2020. **26**(6): p. 423-427.

364. Elie, M., et al., *Delirium Risk Factors in Elderly Hospitalized Patients.* J Gen Intern Med, 1998. **13**(3): p. 204-12.

365. Dantzer, R., et al., *From inflammation to sickness and depression: when the immune system subjugates the brain.* Nature Reviews Neuroscience, 2020. **9**(1): p. 46-56.

366. Gosselin, D. and S. Rivest, *MyD88 signaling in brain endothelial cells is essential for the neuronal activity and glucocorticoid release during systemic inflammation.* Molecular Psychiatry, 2008. **13**(5): p. 480-497.

367. Serantes, R., et al., *Interleukin-1β Enhances GABAA Receptor Cell-surface Expression by a Phosphatidylinositol 3-Kinase/Akt Pathway.* 2006.

368. DHJ, D., et al., *Worsening Cognitive Impairment and Neurodegenerative Pathology Progressively Increase Risk for Delirium.* The American journal of geriatric psychiatry : official journal of the American Association for Geriatric Psychiatry, 2015. **23**(4).

369. Fong, T.G., et al., *The Interface of Delirium and Dementia in Older Persons.* Lancet Neurol, 2015. **14**(8): p. 823-32.

370. Davis, D.H.J., et al., *Delirium is a strong risk factor for dementia in the oldest-old: a population-based cohort study.* Brain, 2020. **135**(9): p. 2809-2816.

371. MacLullich, A.M.J., et al., *Delirium and long-term cognitive impairment.* https://doi.org/10.1080/09540260802675031, 2009.

372. Fong, T.G., et al., *Delirium accelerates cognitive decline in Alzheimer disease.* 2009.

373. Holmes, C., et al., *Systemic inflammation and disease progression in Alzheimer disease.* 2009.

374. Carson, M.J., et al., *A rose by any other name? The potential consequences of microglial heterogeneity during CNS health and disease.* Neurotherapeutics, 2007. **4**(4): p. 571-9.

375. Melchior, B., S.S. Puntambekar, and M.J. Carson, *Microglia and the control of autoreactive T cell responses.* Neurochem Int, 2006. **49**(2): p. 145-53.

376. Moran, P.M., et al., *Age-related learning deficits in transgenic mice expressing the 751-amino acid isoform of human beta-amyloid precursor protein.* Proc Natl Acad Sci U S A, 1995. **92**(12): p. 5341-5.

377. Lamb, B.T., et al., *Introduction and expression of the 400 kilobase amyloid precursor protein gene in transgenic mice [corrected].* Nat Genet, 1993. **5**(1): p. 22-30.

378. Buxbaum, J.D., et al., *Expression of APP in brains of transgenic mice containing the entire human APP gene.* Biochem Biophys Res Commun, 1993. **197**(2): p. 639-45.

379. Yamaguchi, F., et al., *Transgenic mice for the amyloid precursor protein 695 isoform have impaired spatial memory.* Neuroreport, 1991. **2**(12): p. 781-4.

380. Xia, D., et al., *Presenilin-1 knockin mice reveal loss-of-function mechanism for familial Alzheimer's disease.* Neuron, 2015. **85**(5): p. 967-981.

381. Lok, K., et al., *Characterization of the APP/PS1 mouse model of Alzheimer's disease in senescence accelerated background.* Neurosci Lett, 2013. **557 Pt B**: p. 84-9.

382. Jonsson, T., et al., *Variant of TREM2 associated with the risk of Alzheimer's disease.* The New England journal of medicine, 2013. **368**(2): p. 107-116.

383. Song, W.M., et al., *Humanized TREM2 mice reveal microglia-intrinsic and -extrinsic effects of R47H polymorphism.* J Exp Med, 2018. **215**(3): p. 745-760.

384. Kang, S.S., et al., *Behavioral and transcriptomic analysis of Trem2-null mice: not all knockout mice are created equal.* Hum Mol Genet, 2018. **27**(2): p. 211-223.

385. Filipello, F., et al., *The Microglial Innate Immune Receptor TREM2 Is Required for Synapse Elimination and Normal Brain Connectivity.* Immunity, 2018. **48**(5): p. 979-991.e8.

386. Wang, Y., et al., *TREM2 lipid sensing sustains the microglial response in an Alzheimer's disease model.* Cell, 2015. **160**(6): p. 1061-71.

387. Bachstetter, A.D., et al., *Microglial p38α MAPK is a key regulator of proinflammatory cytokine up-regulation induced by toll-like receptor (TLR) ligands or beta-amyloid (Aβ).* Journal of neuroinflammation, 2011. **8**: p. 79-79.

388. Fiebich, B.L., et al., *Inhibition of LPS-induced p42/44 MAP kinase activation and iNOS/NO synthesis by parthenolide in rat primary microglial cells.* J Neuroimmunol, 2002. **132**(1-2): p. 18-24.

389. Kwok, B.H., et al., *The anti-inflammatory natural product parthenolide from the medicinal herb Feverfew directly binds to and inhibits IkappaB kinase.* Chem Biol, 2001. **8**(8): p. 759-66.

390. McMillian, M., et al., *Selective killing of cholinergic neurons by microglial activation in basal forebrain mixed neuronal/glial cultures.* Biochem Biophys Res Commun, 1995. **215**(2): p. 572-7.

391. Hoozemans, J.J., et al., *The role of cyclo-oxygenase 1 and 2 activity in prostaglandin E(2) secretion by cultured human adult microglia: implications for Alzheimer's disease.* Brain Res, 2002. **951**(2): p. 218-26.

392. Shi, J., et al., *The prostaglandin E2 E-prostanoid 4 receptor exerts anti-inflammatory effects in brain innate immunity.* J Immunol, 2010. **184**(12): p. 7207-18.

393. Jeohn, G.H., et al., *p38 MAP kinase is involved in lipopolysaccharide-induced dopaminergic neuronal cell death in rat mesencephalic neuron-glia cultures.* Ann N Y Acad Sci, 2002. **962**: p. 332-46.

394. Fiebich, B.L., R.D. Butcher, and P.J. Gebicke-Haerter, *Protein kinase C-mediated regulation of inducible nitric oxide synthase expression in cultured microglial cells.* J Neuroimmunol, 1998. **92**(1-2): p. 170-8.

395. Zhang, R., et al., *Circulating endotoxin and systemic immune activation in sporadic amyotrophic lateral sclerosis (sALS).* Journal of neuroimmunology, 2009. **206**(1-2): p. 121-124.

396. Bester, J., et al., *Viscoelastic and ultrastructural characteristics of whole blood and plasma in Alzheimer-type dementia, and the possible role of bacterial lipopolysaccharides (LPS).* Oncotarget, 2015. **6**(34): p. 35284-303.

397. Banks, W.A. and M.A. Erickson, *The blood-brain barrier and immune function and dysfunction.* Neurobiol Dis, 2010. **37**(1): p. 26-32.

398. Banks, W.A., et al., *Lipopolysaccharide-induced blood-brain barrier disruption: roles of cyclooxygenase, oxidative stress, neuroinflammation, and elements of the neurovascular unit.* J Neuroinflammation, 2015. **12**: p. 223.

399. Lehnardt, S., et al., *The toll-like receptor TLR4 is necessary for lipopolysaccharide-induced oligodendrocyte injury in the CNS.* J Neurosci, 2002. **22**(7): p. 2478-86.

400. Beurel, E. and R.S. Jope, *Lipopolysaccharide-induced interleukin-6 production is controlled by glycogen synthase kinase-3 and STAT3 in the brain.* Journal of Neuroinflammation, 2009. **6**(1): p. 9.

401. de Bont, N., et al., *LPS-induced release of IL-1 beta, IL-1Ra, IL-6, and TNF-alpha in whole blood from patients with familial hypercholesterolemia: no effect of cholesterol-lowering treatment.* J Interferon Cytokine Res, 2006. **26**(2): p. 101-7.

402. Wan, Y., et al., *Role of lipopolysaccharide (LPS), interleukin-1, interleukin-6, tumor necrosis factor, and dexamethasone in regulation of LPS-binding protein expression in normal hepatocytes and hepatocytes from LPS-treated rats.* Infect Immun, 1995. **63**(7): p. 2435-42.

403. Wu, D., et al., *The role of the TLR4/NF-kappaB signaling pathway in Abeta accumulation in primary hippocampal neurons.* Sheng Li Xue Bao, 2015. **67**(3): p. 319-28.

404. Kitazawa, M., et al., *Lipopolysaccharide-induced inflammation exacerbates tau pathology by a cyclin-dependent kinase 5-mediated pathway in a transgenic model of Alzheimer's disease.* J Neurosci, 2005. **25**(39): p. 8843-53.

405. Liu, J., et al., *Suppression of LPS-induced tau hyperphosphorylation by serum amyloid A.* J Neuroinflammation, 2016. **13**: p. 28.

406. Lee, D.C., et al., *LPS- induced inflammation exacerbates phospho-tau pathology in rTg4510 mice.* J Neuroinflammation, 2010. **7**: p. 56.

407. Smith, R.G., et al., *Elevated DNA methylation across a 48-kb region spanning the HOXA gene cluster is associated with Alzheimer's disease neuropathology.* Alzheimers Dement, 2018. **14**(12): p. 1580-1588.

408. Condliffe, D., et al., *Cross-region reduction in 5-hydroxymethylcytosine in Alzheimer's disease brain.* Neurobiol Aging, 2014. **35**(8): p. 1850-4.

409. Lunnon, K., et al., *Methylomic profiling implicates cortical deregulation of ANK1 in Alzheimer's disease.* Nat Neurosci, 2014. **17**(9): p. 1164-70.

410. Smith, A.R., et al., *Increased DNA methylation near TREM2 is consistently seen in the superior temporal gyrus in Alzheimer's disease brain.* Neurobiol Aging, 2016. **47**: p. 35-40.

411. Cunningham, C., et al., *Systemic inflammation induces acute behavioral and cognitive changes and accelerates neurodegenerative disease.* Biol Psychiatry, 2009. **65**(4): p. 304-12.

412. McLean, C.Y., et al., *GREAT improves functional interpretation of cis-regulatory regions.* Nat Biotechnol, 2010. **28**(5): p. 495-501.

413. Gebhardt, A., et al., *mRNA export through an additional cap-binding complex consisting of NCBP1 and NCBP3.* Nature Communications, 2015. **6**(1): p. 8192.

414. Ong, M.L. and J.D. Holbrook, *Novel region discovery method for Infinium 450K DNA methylation data reveals changes associated with aging in muscle and neuronal pathways.* Aging Cell, 2014. **13**(1): p. 142-55.

415. Mansell, G., et al., *Guidance for DNA methylation studies: statistical insights from the Illumina EPIC array.* BMC genomics, 2019. **20**(1): p. 366-366.

416. Tremblay, M.-È., et al., *The role of microglia in the healthy brain.* The Journal of neuroscience : the official journal of the Society for Neuroscience, 2011. **31**(45): p. 16064-16069.

417. Pan, X.D., et al., *Microglial phagocytosis induced by fibrillar beta-amyloid is attenuated by oligomeric beta-amyloid: implications for Alzheimer's disease.* Mol Neurodegener, 2011. **6**: p. 45.

418. Kallur, T., et al., *Pax6 promotes neurogenesis in human neural stem cells.* Mol Cell Neurosci, 2008. **38**(4): p. 616-28.

419. Vergadi, E., K. Vaporidi, and C. Tsatsanis, *Regulation of Endotoxin Tolerance and Compensatory Anti-inflammatory Response Syndrome by Non-coding RNAs.* Frontiers in Immunology, 2018. **9**(2705).

420. O'Carroll, C., A. Fagan, and R. Carmody, *Regulation of LPS Tolerance in Macrophages (48.2).* The Journal of Immunology, 2012. **188**(1 Supplement): p. 48.2-48.2.

421. Seeley, J.J. and S. Ghosh, *Molecular mechanisms of innate memory and tolerance to LPS.* J Leukoc Biol, 2017. **101**(1): p. 107-119.

422. Klose, R.J. and A.P. Bird, *Genomic DNA methylation: the mark and its mediators.* Trends in Biochemical Sciences, 2006. **31**(2): p. 89-97.

423. Aran, D., et al., *Replication timing-related and gene body-specific methylation of active human genes.* Human Molecular Genetics, 2011. **20**(4): p. 670-680.

424. TA, R., et al., *A Human B Cell Methylome at 100-base Pair Resolution.* Proceedings of the National Academy of Sciences of the United States of America, 2009. **106**(3).

425. Gurok, U., et al., *Gene Expression Changes in the Course of Neural Progenitor Cell Differentiation.* J Neurosci, 2004. **24**(26): p. 5982-6002.

426. Manuel, M.N., et al., *Regulation of cerebral cortical neurogenesis by the Pax6 transcription factor.* Front Cell Neurosci, 2015. **9**.

427. Hou, P.S., et al., *LHX2 regulates the neural differentiation of human embryonic stem cells via transcriptional modulation of PAX6 and CER1*, in *Nucleic Acids Res*. 2013. p. 7753-70.

428. Cho, C.E., et al., *A modular analysis of microglia gene expression, insights into the aged phenotype*, in *BMC Genomics*. 2019.

429. Pulido-Salgado, M., et al., *RNA-Seq transcriptomic profiling of primary murine microglia treated with LPS or LPS + IFNγ*, in *Sci Rep*. 2018.

430. Mizuno, S., et al., *AlzPathway: a comprehensive map of signaling pathways of Alzheimer's disease.* BMC Systems Biology, 2012. **6**(1): p. 1-10.

431. GJ, H., et al., *Mechanisms of Cell Signaling and Inflammation in Alzheimer's Disease.* Current drug targets. Inflammation and allergy, 2005. **4**(2).

432. Haque, M.E., et al., *Importance of GPCR-Mediated Microglial Activation in Alzheimer's Disease.* Front Cell Neurosci, 2018. **12**.

433. CC, L., et al., *Deficiency in LRP6-mediated Wnt Signaling Contributes to Synaptic Abnormalities and Amyloid Pathology in Alzheimer's Disease.* Neuron, 2014. **84**(1).

434. Greenland, S., et al., *Statistical tests, P values, confidence intervals, and power: a guide to misinterpretations.* European journal of epidemiology, 2016. **31**(4): p. 337-350.

435. Kadam, P. and S. Bhalerao, *Sample size calculation.* International journal of Ayurveda research, 2010. **1**(1): p. 55-57.

436. Jones, S.R., S. Carley, and M. Harrison, *An introduction to power and sample size estimation.* Emergency Medicine Journal, 2003. **20**(5): p. 453-458.

437. Watson, C.T., et al., *Genome-wide DNA methylation profiling in the superior temporal gyrus reveals epigenetic signatures associated with Alzheimer's disease.* Genome Med, 2016. **8**(1): p. 5.

438. Wang, T., et al., *Genome-wide DNA hydroxymethylation changes are associated with neurodevelopmental genes in the developing human cerebellum.* Hum Mol Genet, 2012. **21**(26): p. 5500-10.

439. Kriaucionis, S. and N. Heintz, *The nuclear DNA base 5-hydroxymethylcytosine is present in Purkinje neurons and the brain.* Science (New York, N.Y.), 2009. **324**(5929): p. 929-930.

440. Spiers, H., et al., *Methylomic trajectories across human fetal brain development.* Genome research, 2015. **25**(3): p. 338-352.

441. Huh, C.J., et al., *Maintenance of age in human neurons generated by microRNA-based neuronal conversion of fibroblasts.* eLife, 2016. **5**: p. e18648.

442. Blasco, M.A., *Telomere length, stem cells and aging.* Nat Chem Biol, 2007. **3**(10): p. 640-9.

443. Hiyama, E. and K. Hiyama, *Telomere and telomerase in stem cells.* Br J Cancer, 2007. **96**(7): p. 1020-4.